AAAS

Science

11 DECEMBER 2025

NASA goes hunting for city-killer asteroids **p. 1094**

Insulating windows with nanotube coatings **pp. 1104 & 1171**

Methane emissions from energy facilities **p. 1151**



DETECTING HEAT

Plant thermal radiation attracts pollinators **pp. 1100 & 1164**

Thank You To Our 2025 Founding **Institutional Partners and Members**





We are honored to recognize the universities leading the way as AAAS Institutional Partners and Members. These institutions have collectively helped to strengthen the scientific enterprise, foster interdisciplinary collaboration, and empower the next generation of STEMM professionals.

PARTNERS

Arizona State University

UTMB THE UNIVERSITY OF TEXAS MEDICAL BRANCH

MEMBERS

THE GEORGE WASHINGTON UNIVERSITY WASHINGTON, DC

THE UNIVERSITY OF MISSISSIPPI

Penn University of Pennsylvania

THE UNIVERSITY OF TENNESSEE KNOXVILLE

THE UNIVERSITY OF ARIZONA

Curious to learn how your institution can join in our efforts to advance science and serve society? Please visit **aaas.org/InstitutionalProgram**

AAAS

CONTENTS

11 DECEMBER 2025 | VOLUME 390 | ISSUE 6778



1094

An asteroid hunter prepares for its mission to deep space.

PHOTO: NASA

EDITORIAL

1083 Pandemic security needs national leadership
—M. D. Van Kerkhove and C. Ihekweazu

NEWS

1084 Cancer-fighting cells made in body help patients
Approach could be faster than making CAR-T cells in the lab—and early results are encouraging —M. Leslie

1086 Warm, humid 'atmospheric rivers' threaten Antarctica
Growing more common as the climate warms, these once-rare events could ultimately accelerate ice loss
—T. Vernimmen

1088 Replenishing sapped groundwater could trigger small earthquakes
A boom in aquifer injection projects could unlock long-quiet faults
—H. Richter

1089 AI tools aim to speed up outbreak modeling
DARPA program could help researchers build transparent, editable models of viral spread in days instead of weeks
—S. Scoles

1090 Could adding light sensors to nerve cells help switch off diseases?
Optogenetics is poised to move from a research tool to new therapies—if scientists can show it's safe —K. Servick

FEATURES

1094 Planet protector
More than half of the "city killer" asteroids that might threaten Earth remain undiscovered. With an infrared eye, NASA's NEO Surveyor aims to find them
—R. G. Andrews
PODCAST

COMMENTARY

PERSPECTIVES

1100 Infrared as a pollination signal
Relying on infrared communication over visual color could have limited cycad evolution
—B. J. Glover and A. A. R. Webb
RESEARCH ARTICLE p. 1164

1102 Chromosome shattering in cancer
A protein that cuts double-stranded DNA contributes to chromosome scrambling in human cancer cells
—S. Clarke and M. Imieliński
RESEARCH ARTICLE p. 1156

1104 Invisible heat insulators
A nanotube network with precisely engineered pores could replace insulating components in windows —L. Li and W. Li
RESEARCH ARTICLE p. 1171

1105 Deep mantle clues to Earth's watery beginning
Minerals in the lower mantle may store more water than previously estimated —M. Walter
RESEARCH ARTICLE p. 1177

BOOKS ET AL.

1107 Dealing with distressing dreams
A sleep scientist offers hope for nightmare sufferers —J. Herndon

1108 The statusocratic dilemma
An organizational theorist probes the hidden drivers of social power
—S. M. S. Krammer

LETTERS

1109 Landmark marine mammal laws under threat —M. S. Leslie *et al.*

1110 Communities can enforce China's national parks
—S. Gao and Q. Shao

science.org/journal/sciimmunol



READY TO PUT THE SPOTLIGHT ON YOUR RESEARCH?

Submit your research:
cts.ScienceMag.org

Science Immunology
AAAS

Twitter: @SciImmunology
Facebook: @ScienceImmunology

1110 Arctic route demands advanced marine coatings
—T. Zhang and L. Wang

ANALYSIS

POLICY ARTICLE

1112 Mapping the online manipulation economy
A market perspective on digital manipulation may help improve online trust and safety —A. Dek *et al.*

RESEARCH

HIGHLIGHTS

1115 From *Science* and other journals

RESEARCH SUMMARIES

1118 Photosynthesis
Locating the missing chlorophylls f in far-red photosystem
—G. Consoli *et al.*

1119 Cell biology
Mechanosensitive genomic enhancers potentiate the cellular response to matrix stiffness
—B. D. Cosgrove *et al.*

1120 Genomics
Multispecies pangenomes reveal a pervasive influence of population size on structural variation
—S. V. Edwards *et al.*

1121 Reproduction
Comparative analysis of human and mouse ovaries across age
—E. A. Gaylord *et al.*

1122 Organic chemistry
Three-component assembly and structure-function relationships of (−)-gukulenin —A V. Gupta *et al.*

1123 Immunology
Hepatic leukemia factor directs tissue residency of proinflammatory memory CD4$^+$ T cells
—M. Kiuchi *et al.*



1120
A pangenome of three jays, including the pictured Woodhouse's scrub-jay, reveals population dynamics.

PHOTO: KALEB ANDERSON

1124 Neuroscience
Cortical glutamatergic and GABAergic inputs support learning-driven hippocampal stability
—V. Robert *et al.*

RESEARCH ARTICLES

Quantum simulation

1125 Shapiro steps in strongly-interacting Fermi gases
—G. Del Pace *et al.*

1130 Observation of Shapiro steps in an ultracold atomic Josephson junction
—E. Bernhart *et al.*

Metabolism

1134 NUDT5 regulates purine metabolism and thiopurine sensitivity by interacting with PPAT —Z. Wu *et al.*

1143 A non-enzymatic role of Nudix hydrolase 5 in repressing purine de novo synthesis
—T.-A. Nguyen *et al.*

1151 Methane emissions
Global energy sector methane emissions estimated by using facility-level satellite observations
—D. Jervis *et al.*
PERSPECTIVE p. 1102

1156 Molecular biology
Chromothripsis and ecDNA initiated by N4BP2 nuclease fragmentation of cytoplasm-exposed chromosomes
—K. Krupina *et al.*
PERSPECTIVE p. 1102

1164 Evolution
Infrared radiation is an ancient pollination signal
—W. A. Valencia-Montoya *et al.*
PERSPECTIVE p. 1110; PODCAST

1171 Thermal management
Mesoporous optically clear heat insulators for sustainable building envelopes —A. Bhardwaj *et al.*
PERSPECTIVE p. 1104

1177 Mineral physics
Substantial water retained early in Earth's deep mantle —W. Lu *et al.*
PERSPECTIVE p. 1105

ON THE COVER



Cycad plants use thermogenesis to warm their reproductive cones. A beetle dusted with pollen and fluorescent dyes lands on the warm cone of a cycad. High concentrations of dye have been deposited on the cone's hottest regions during previous visits by other labeled beetles. Beetle pollinators use these thermal infrared patterns as a guide to locate host pollen and ovulate cones. See pages 1100 and 1164. Credit: Michael Calonje, Montgomery Botanical Center

ON THE PODCAST

Hunting asteroids from space, and talking to pollinators with heat

WORKING LIFE

1182 The experiment I didn't plan —M. Gulia-Nuss

1082 *Science* Staff
1181 *Science* Careers

Science **serves as a forum for discussion of important issues related to the advancement of science by publishing material on which a consensus has been reached as well as including the presentation of minority or conflicting points of view. Accordingly, all articles published in *Science*—including editorials, news, commentary, and book reviews—are signed and reflect the individual views of the authors and not official points of view adopted by AAAS or the institutions with which the authors are affiliated.** *Science* (ISSN 0036-8075) is published weekly on Thursday, except last week in December, by the American Association for the Advancement of Science, 1200 New York Avenue, NW, Washington, DC 20005. Periodicals mail postage (publication No. 484460) paid at Washington, DC, and additional mailing offices. Copyright © 2025 by the American Association for the Advancement of Science. The title *Science* is a registered trademark of the AAAS. Domestic individual membership, including subscription (12 months): $165 ($74 allocated to subscription). Domestic institutional subscription (51 issues): $2865; Foreign postage extra: Air assist delivery: $135. First class, airmail, student, and emeritus rates on request. Canadian rates with GST available upon request, GST #125488122. Publications Mail Agreement Number 1069624. **Printed in the U.S.A. Change of address:** Allow 4 weeks, giving old and new addresses and 8-digit account number. **Postmaster:** Send change of address to AAAS, P.O. Box 96178, Washington, DC 20090–6178. **Single-copy sales:** $15 each plus shipping and handling available from backissues.science.org; bulk rate on request. **Authorization to reproduce** material for internal or personal use under circumstances not falling within the fair use provisions of the Copyright Act can be obtained through the Copyright Clearance Center (CCC), www.copyright.com. The identification code for *Science* is 0036-8075. *Science* is indexed in the *Reader's Guide to Periodical Literature* and in several specialized indexes.

Science AAAS

EDITOR-IN-CHIEF Holden Thorp, hthorp@aaas.org

EXECUTIVE EDITOR Valda Vinson

EDITORS, RESEARCH Sacha Vignieri, Jake S. Yeston **EDITOR, COMMENTARY** Lisa D. Chong

DEPUTY EXECUTIVE EDITOR Lauren Kmec

DEPUTY EDITORS Stella M. Hurtley (UK), Phillip D. Szuromi **SENIOR EDITORS** Caroline Ash (UK), Michael A. Funk, Angela Hessler, Di Jiang, Priscilla N. Kelly, Marc S. Lavine (Canada), Sarah Lempriere (UK), Mattia Maroso, Yevgeniya Nusinovich, Ian S. Osborne (UK), Joana Osório (UK), L. Bryan Ray, H. Jesse Smith, Keith T. Smith (UK), Jelena Stajic, Peter Stern (UK), Yury V. Suleymanov, Valerie B. Thompson, Brad Wible **ASSOCIATE EDITORS** Jack Huang, Sumin Jin, Bianca Lopez, Sarah Ross (UK), Madeleine Seale (UK), Corinne Simonti, Ekeoma Uzogara **SENIOR LETTERS EDITOR** Jennifer Sills **NEWSLETTER EDITOR** Christie Wilcox **RESEARCH & DATA ANALYST** Jessica L. Slater **LEAD CONTENT PRODUCTION EDITORS** Chris Filiatreau, Harry Jach **SR. CONTENT PRODUCTION EDITOR** Amelia Beyna **CONTENT PRODUCTION EDITORS** Anne Abraham, Robert French, Julia Haber-Katris, Nida Masiulis, Abigail Shashikanth, Suzanne M. White **SENIOR PROGRAM ASSOCIATE** Maryrose Madrid **EDITORIAL MANAGER** Joi S. Granger **EDITORIAL ASSOCIATES** Aneera Dobbins, Lisa Johnson, Jerry Richardson, Anita Wynn **SENIOR EDITORIAL COORDINATORS** Alexander Kief, Ronmel Navas, Isabel Schnaidt, Alice Whaley (UK), Brian White **EDITORIAL COORDINATORS** Samuel Bates, Clair Goodhead (UK), Kat Kirkman, Daniel Young **ADMINISTRATIVE COORDINATOR** Karalee P. Rogers **ASI DIRECTOR, OPERATIONS** Janet Clements (UK) **ASI OFFICE MANAGER** Carly Hayward (UK) **ASI SR. OFFICE ADMINISTRATORS** Simon Brignell (UK), Jessica Waldock (UK) **COMMUNICATIONS DIRECTOR** Meagan Phelan **DEPUTY DIRECTOR** Matthew Wright **SENIOR WRITERS** Walter Beckwith, Joseph Cariz, Abigail Eisenstadt **WRITER** Mahathi Ramaswamy **SENIOR COMMUNICATIONS ASSOCIATES** Zachary Graber, Sarah Woods **COMMUNICATIONS ASSOCIATES** Kiara Brooks, Haley Riley, Mackenzie Williams

NEWS EDITOR Tim Appenzeller

NEWS MANAGING EDITOR John Travis **INTERNATIONAL EDITOR** David Malakoff **DEPUTY NEWS EDITORS** Rachel Bernstein, Martin Enserink, David Grimm, Eric Hand, Michael Price, Kelly Servick, Matt Warren (Europe) **SENIOR CORRESPONDENTS** Daniel Clery (UK), Jon Cohen, Jeffrey Mervis **ASSOCIATE EDITORS** Michael Greshko, Katie Langin **NEWS REPORTERS** Jeffrey Brainard, Adrian Cho, Phie Jacobs, Jocelyn Kaiser, Robert F. Service, Jennie Erin Smith, Erik Stokstad, Paul Voosen **CONSULTING EDITOR** Elizabeth Culotta **CONTRIBUTING CORRESPONDENTS** Vaishnavi Chandrashekhar, Dan Charles, Warren Cornwall, Andrew Curry (Berlin), Ann Gibbons, Kai Kupferschmidt (Berlin), Andrew Lawler, Mitch Leslie, Virginia Morell, Dennis Normile (Tokyo), Catherine Offord, Cathleen O'Grady, Elisabeth Pain (Careers), Charles Piller, Zack Savitsky, Richard Stone (Senior Asia Correspondent), Gretchen Vogel (Berlin), Lizzie Wade (Mexico City) **INTERNS** Celina Zhao **COPY EDITORS** Julia Cole (Senior Copy Editor), Hannah Knighton, Cyra Master (Copy Chief) **ADMINISTRATIVE SUPPORT** Meagan Weiland

CREATIVE DIRECTOR Beth Rakouskas

DESIGN MANAGING EDITOR Chrystal Smith **GRAPHICS MANAGING EDITOR** Chris Bickel **PHOTOGRAPHY MANAGING EDITOR** Emily Petersen **MULTIMEDIA MANAGING PRODUCER** Kevin McLean **DIGITAL DIRECTOR** Kara Estelle-Powers **DESIGN EDITOR** Marcy Atarod **DESIGNER** Noelle Jessup **SENIOR SCIENTIFIC ILLUSTRATOR** Noelle Burgess **SCIENTIFIC ILLUSTRATORS** Austin Fisher, Kellie Holoski, Ashley Mastin **SENIOR GRAPHICS EDITOR** Monica Hersher **GRAPHICS EDITOR** Veronica Penney **SENIOR PHOTO EDITOR** Charles Borst **PHOTO EDITOR** Elizabeth Billman **SENIOR PODCAST PRODUCER** Sarah Crespi **SENIOR VIDEO PRODUCER** Meagan Cantwell **SOCIAL MEDIA STRATEGIST** Jessica Hubbard **SOCIAL MEDIA PRODUCER** Sabrina Jenkins **WEB DESIGNER** Jennie Pajerowski

CHIEF EXECUTIVE OFFICER AND EXECUTIVE PUBLISHER

Sudip Parikh

PUBLISHER, SCIENCE FAMILY OF JOURNALS Bill Moran

DIRECTOR, BUSINESS OPERATIONS & ANALYSIS Eric Knott **MANAGER, BUSINESS OPERATIONS** Jessica Tierney **SENIOR MANAGER, BUSINESS ANALYSIS** Cory Lipman **BUSINESS ANALYSTS** Kurt Ennis, Maggie Clark, Isacco Fusi **BUSINESS OPERATIONS ADMINISTRATOR** Taylor Fisher **DIGITAL SPECIALIST** Marissa Zuckerman **ASSOCIATE DIRECTOR OF PRODUCTION AND PLATFORM** Jason Hillman **SENIOR MANAGER, PUBLISHING AND CONTENT SYSTEMS** Marcus Spiegler **CONTENT OPERATIONS MANAGER** Rebecca Doshi **PUBLISHING PLATFORM MANAGER** Jessica Loayza **PUBLISHING SYSTEMS SPECIALIST, PROJECT COORDINATOR** Jacob Hedrick **SENIOR PRODUCTION SPECIALIST** Kristin Wowk **PRODUCTION SPECIALISTS** Kelsey Cartelli, Audrey Diggs **SPECIAL PROJECTS ASSOCIATE** Shantel Agnew

MARKETING DIRECTOR Sharice Collins **ASSOCIATE DIRECTOR, MARKETING** Justin Sawyers **GLOBAL MARKETING MANAGER** Allison Pritchard **ASSOCIATE DIRECTOR, MARKETING SYSTEMS & STRATEGY** Aimee Aponte **SENIOR MARKETING MANAGER** Shawana Arnold **MARKETING MANAGER** Ashley Evans **MARKETING ASSOCIATES** Hugues Beaulieu, Ashley Hylton, Lorena Chirinos Rodriguez, Jenna Voris **MARKETING ASSISTANT** Courtney Ford **SENIOR DESIGNER** Kim Huynh

DIRECTOR AND SENIOR EDITOR, CUSTOM PUBLISHING Erika Gebel Berg **ADVERTISING PRODUCTION OPERATIONS MANAGER** Deborah Tompkins **DESIGNER, CUSTOM PUBLISHING** Jeremy Huntsinger **SENIOR TRAFFIC ASSOCIATE** Christine Hall

DIRECTOR, PRODUCT MANAGEMENT Kris Bishop **PRODUCT DEVELOPMENT MANAGER** Scott Chernoff **ASSOCIATE DIRECTOR, PUBLISHING INTELLIGENCE** Rasmus Andersen **SR. PRODUCT ASSOCIATE** Robert Koepke **PRODUCT ASSOCIATES** Caroline Breul, Anne Mason

ASSOCIATE DIRECTOR, INSTITUTIONAL LICENSING MARKETING Kess Knight **ASSOCIATE DIRECTOR, INSTITUTIONAL LICENSING SALES** Ryan Rexroth **INSTITUTIONAL LICENSING MANAGER** Nazim Mohammedi, Claudia Paulsen-Young **SENIOR MANAGER, INSTITUTIONAL LICENSING OPERATIONS** Judy Lillibridge **MANAGER, RENEWAL & RETENTION** Lana Guz **SYSTEMS & OPERATIONS ANALYST** Ben Teincuff **FULFILLMENT ANALYST** Aminta Reyes

ASSOCIATE DIRECTOR, INTERNATIONAL Roger Goncalves **ASSOCIATE DIRECTOR, US ADVERTISING** Stephanie O'Connor **US MID WEST, MID ATLANTIC AND SOUTH EAST SALES MANAGER** Chris Hoag **DIRECTOR, OUTREACH AND STRATEGIC PARTNERSHIPS, ASIA** Shoupeng Liu **SALES REP, ROW** Sarah Lelarge **SALES ADMIN ASSISTANT, ROW** Victoria Glasbey **DIRECTOR OF GLOBAL COLLABORATION AND ACADEMIC PUBLISHING RELATIONS, ASIA** Xiaoying Chu **ASSOCIATE DIRECTOR, INTERNATIONAL COLLABORATION** Grace Yao **SALES MANAGER** Danny Zhao **MARKETING MANAGER** Kilo Lan **ASCA CORPORATION, JAPAN** Rie Rambelli (Tokyo), Miyuki Tani (Osaka)

DIRECTOR, COPYRIGHT, LICENSING AND SPECIAL PROJECTS Emilie David **RIGHTS AND PERMISSIONS ASSOCIATE** Elizabeth Sandler **LICENSING ASSOCIATE** Virginia Warren **RIGHTS AND LICENSING COORDINATOR** Dana James **CONTRACT SUPPORT SPECIALIST** Michael Wheeler

EDITORIAL
science_editors@aaas.org

NEWS
science_news@aaas.org

INFORMATION FOR AUTHORS
science.org/authors/
science-information-authors

REPRINTS AND PERMISSIONS
science.org/help/
reprints-and-permissions

MULTIMEDIA CONTACTS
SciencePodcast@aaas.org
ScienceVideo@aaas.org

MEDIA CONTACTS
scipak@aaas.org

PRODUCT ADVERTISING & CUSTOM PUBLISHING
advertising.science.org
science_advertising@aaas.org

CLASSIFIED ADVERTISING
advertising.science.org/
science-careers
advertise@sciencecareers.org

JOB POSTING CUSTOMER SERVICE
employers.sciencecareers.org
support@sciencecareers.org

MEMBERSHIP AND INDIVIDUAL SUBSCRIPTIONS
science.org/subscriptions

MEMBER BENEFITS
aaas.org/membership/
benefits

INSTITUTIONAL SALES AND SITE LICENSES
science.org/librarian

AAAS BOARD OF DIRECTORS

CHAIR Joseph S. Francisco

IMMEDIATE PAST PRESIDENT
Willie E. May

PRESIDENT
Theresa A. Maldonado

PRESIDENT-ELECT
Marina Picciotto

TREASURER Carolyn N. Ainslie

COUNCIL CHAIR
Ichiro Nishimura

CHIEF EXECUTIVE OFFICER
Sudip Parikh

BOARD
Mark Dingfield
Morton Ann Gernsbacher
Kathleen Hall Jamieson
Jane Maienschein
Babak Parviz
Gabriela Popescu
Juan S. Ramírez Lugo
Susan M. Rosenberg
Vassiliki Betty Smocovitis
Roger Wakimoto

BOARD OF REVIEWING EDITORS (Statistics board members indicated with **S**)

Erin Adams, *U. of Chicago*
Takuzo Aida, *U. of Tokyo*
Leslie Aiello, *Wenner-Gren Fdn.*
Anastassia Alexandrova, *UCLA*
Mohammed AlQuraishi, *Columbia U.*
James Analytis, *UC Berkeley*
Paola Arlotta, *Harvard U.*
Madan Babu, *St. Jude*
Jennifer Balch, *U. of Colorado*
Nenad Ban, *ETH Zürich*
Carolina Barillas-Mury, *NIH, NIAID*
Christopher Barratt, *U. of Dundee*
François Barthelat, *U. of Colorado Boulder*
Franz Bauer, *Universidad de Tarapacá*
Andreas Baumler, *UC Davis*
Carlo Beenakker, *Leiden U.*
Sarah Bergbreiter, *Carnegie Mellon U.*
Kiros T. Berhane, *Columbia U.*
Aude Bernheim, *Inst. Pasteur*
Joseph J. Berry, *NREL*
Aditi Bhargav, *UCSF*
Dominique Bonnet, *Francis Crick Inst.*
Chris Bowler, *École Normale Supérieure*
Ian Boyd, *U. of St. Andrews*
Malcolm Brenner, *Baylor Coll. of Med.*
Ron Brookmeyer, *UCLA* (**S**)
Christian Büchel, *UKE Hamburg*
Johannes Buchner, *TUM*
Dennis Burton, *Scripps Res.*
Carter Tribley Butts, *UC Irvine*
György Buzsáki, *NYU School of Med.*
Annmarie Carlton, *UC Irvine*
Jane Carlton, *Johns Hopkins U.*
Pedro Carvalho, *U. of Oxford*
Simon Cauchemez, *Inst. Pasteur*
Ling-Ling Chen, *SIBCB, CAS*
Hilde Cheroutre, *La Jolla Inst.*
Wendy Cho, *UIUC*
Ib Chorkendorff, *Denmark TU*
Chunaram Choudhary, *Københavns U.*
Karlene Cimprich, *Stanford U.*
Laura Colgin, *UT Austin*
James J. Collins, *MIT*
Robert Cook-Deegan, *Arizona State U.*
Carolyn Coyne, *Duke U.*
Roberta Croce, *VU Amsterdam*
Ismaila Dabo, *Penn State U.*
Nicolas Dauphas, *U. of Chicago*
Claude Desplan, *NYU*
Sandra Díaz, *U. Nacional de Córdoba*
Samuel Díaz-Muñoz, *UC Davis*
Ulrike Diebold, *TU Wien*
Stefanie Dimmeler, *Goethe-U. Frankfurt*
Hong Ding, *Inst. of Physics, CAS*
Dennis Discher, *UPenn*
Jennifer A. Doudna, *UC Berkeley*
Ruth Drdla-Schutting, *Med. U. Vienna*
Raissa M. D'Souza, *UC Davis*
Bruce Dunn, *UCLA*
William Dunphy, *Caltech*
Scott Edwards, *Harvard U.*
Todd A. Ehlers, *U. of Glasgow*
Tobias Erb, *MPS, MPI Terrestrial Microbiology*
Beate Escher, *UFZ & U. of Tübingen*
Barry Everitt, *U. of Cambridge*
Vanessa Ezenwa, *U. of Georgia*
Toren Finkel, *U. of Pitt. Med. Ctr.*
Natascha Förster Schreiber, *MPI Extraterrestrial Phys.*
Serita Frey, *U. of New Hampshire*
Elaine Fuchs, *Rockefeller U.*
Caixia Gao, *Inst. of Genetics and Developmental Bio., CAS*
Daniel Geschwind, *UCLA*
Lindsey Gillson, *U. of Cape Town*
Alemu Gonsamo Gosa, *McMaster U.*
Simon Greenhill, *U. of Auckland*
Gillian Griffiths, *U. of Cambridge*
Nicolas Gruber, *ETH Zürich*
Hua Guo, *U. of New Mexico*
Taekjip Ha, *Johns Hopkins U.*
Daniel Haber, *Mass. General Hos..*
Hamida Hammad, *VIB IRC*
Brian Hare, *Duke U.*
Kelley Harris, *U. of Wash*
Carl-Philipp Heisenberg, *IST Austria*
Emiel Hensen, *TU Eindhoven*
Christoph Hess, *U. of Basel & U. of Cambridge*
Brian Hie, *Stanford U.*
Heather Hickman, *NIAID, NIH*
Janneke Hille Ris Lambers, *ETH Zürich*
Kai-Uwe Hinrichs, *U. of Bremen*
Pinshane Huang, *UIUC*
Christina Hulbe, *U. of Otago, New Zealand*
Gwyneth Ingram, *ENS Lyon*
Darrell Irvine, *Scripps Res.*
Erich Jarvis, *Rockefeller U.*
Peter Jonas, *IST Austria*
Sheena Josselyn, *U. of Toronto*
Matt Kaeberlein, *U. of Wash.*
Daniel Kammen, *UC Berkeley*
Kisuk Kang, *Seoul Nat. U.*
Vedika Khemani, *Stanford U.*
V. Narry Kim, *Seoul Nat. U.*
Nancy Knowlton, *Smithsonian*
Etienne Koechlin, *École Normale Supérieure*
LaShanda Korley, *U. of Delaware*
Paul Kubes, *U. of Calgary*
Deborah Kurrasch, *U of Calgary*
Laura Lackner, *Northwestern U.*
Mitchell A. Lazar, *UPenn*
Hedwig Lee, *Duke U.*
Fei Li, *Xi'an Jiaotong U.*
Jianyu Li, *McGill U.*
Ryan Lively, *Georgia Tech*
Luis Liz-Marzán, *CIC biomaGUNE*
Omar Lizardo, *UCLA*
Jonathan Losos, *WUSTL*
Ke Lu, *Inst. of Metal Res., CAS*
Christian Lüscher, *U. of Geneva*
Jean Lynch-Stieglitz, *Georgia Tech*
David Lyons, *U. of Edinburgh*
Fabienne Mackay, *QIMR Berghofer*
Vidya Madhavan, *UIUC*
Anne Magurran, *U. of St. Andrews*
Oscar Marín, *King's Coll. London*
Matthew Marinella, *Arizona State U.*
Charles Marshall, *UC Berkeley*
Christopher Marx, *U. of Idaho*
Geraldine Masson, *CNRS*
Jennifer McElwain, *Trinity College Dublin*
Scott McIntosh, *NCAR*
Rodrigo Medellín, *U. Nacional Autónoma de México*
Mayank Mehta, *UCLA*
C. Jessica Metcalf, *Princeton U.*
Tom Misteli, *NCI, NIH*
Jeffery Molkentin, *Cincinnati Children's Hospital Medical Center*
Alison Motsinger-Reif, *NIEHS, NIH* (**S**)
Rosa Moysés, *U. of São Paulo School of Medicine*
Carey Nadell, *Dartmouth College*
Thi Hoang Duong Nguyen, *MRC LMB*
Pilar Ossorio, *U. of Wisconsin*
Andrew Oswald, *U. of Warwick*
Isabella Pagano, *Istituto Nazionale di Astrofisica*
Giovanni Parmigiani, *Dana-Farber* (**S**)
Zak Page, *UT Austin*
Pierre Paoletti, *Ecole Normale Supérieure, Paris*
Sergiu Pasca, *Stanford U.*
Julie Pfeiffer, *UT Southwestern Med. Ctr.*
Philip Phillips, *UIUC*
Matthieu Piel, *Inst. Curie*
Kathrin Plath, *UCLA*
Martin Plenio, *Ulm U.*
Katherine Pollard, *UCSF*
Elvira Poloczanska, *Alfred-Wegener-Inst.*
Julia Pongratz, *Ludwig Maximilians U.*
Philippe Poulin, *CNRS*
Suzie Pun, *U. of Wash*
Lei Stanley Qi, *Stanford U.*
Simona Radutoiu, *Aarhus U.*
Maanasa Raghavan, *U. of Chicago*
Trevor Robbins, *U. of Cambridge*
Adrienne Roeder, *Cornell U.*
Joeri Rogelj, *Imperial Coll. London*
John Rubenstein, *SickKids*
Sylvie Roke, *École Polytechnique Fédérale de Lausanne*
Yvette Running Horse Collin, *Toulouse U.*
Mike Ryan, *UT Austin*
Alberto Salleo, *Stanford U.*
Miquel Salmeron, *Lawrence Berkeley Nat. Lab*
Nitin Samarth, *Penn State U.*
Erica Ollmann Saphire, *La Jolla Inst.*
Joachim Saur, *U. zu Köln*
Alexander Schier, *Harvard U.*
Susannah Scott, *UC Santa Barbara*
Anuj Shah, *U. of Chicago*
Vladimir Shalaev, *Purdue U.*
Jie Shan, *Cornell U.*
Jay Shendure, *U. of Wash.*
Steve Sherwood, *U. of New South Wales*
Ken Shirasu, *RIKEN CSRS*
Robert Siliciano, *JHU School of Med.*
Emma Slack, *ETH Zürich & U. of Oxford*
Richard Smith, *UNC* (**S**)
Ivan Soltesz, *Stanford U.*
John Speakman, *U. of Aberdeen*
Allan C. Spradling, *Carnegie Institution for Sci.*
V. S. Subrahmanian, *Northwestern U.*
Sandip Sukhtankar, *U. of Virginia*
Tavneet Suri, *MIT*
Naomi Tague, *UC Santa Barbara*
A. Alec Talin, *Sandia Natl. Labs*
Patrick Tan, *Duke-NUS Med. School*
Sarah Teichmann, *Wellcome Sanger Inst.*
Dörthe Tetzlaff, *Leibniz Institute of Freshwater Ecology and Inland Fisheries*
Amanda Thomas, *UC Davis*
Rocio Titiunik, *Princeton U.*
Shubha Tole, *Tata Inst. of Fundamental Res.*
Maria-Elena Torres Padilla, *Helmholtz Zentrum München*
Kimani Toussaint, *Brown U.*
Barbara Treutlein, *ETH Zürich*
Li-Huei Tsai, *MIT*
Jason Tylianakis, *U. of Canterbury*
Matthew Vander Heiden, *MIT*
Jo Van Ginderachter, *VIB, U. of Ghent*
Ivo Vankelecom, *KU Leuven*
Henrique Veiga-Fernandes, *Champalimaud Fdn.*
Elizabeth Villa, *UC San Diego*
Bert Vogelstein, *Johns Hopkins U.*
David Wallach, *Weizmann Inst.*
Jane-Ling Wang, *UC Davis* (**S**)
Jessica Ware, *Amer. Mus. of Natural Hist.*
David Waxman, *Fudan U.*
Alex Webb, *U. of Cambridge*
Chris Wikle, *U. of Missouri* (**S**)
Ian A. Wilson, *Scripps Res.* (**S**)
Marjorie Weber, *U. of Michigan*
Sylvia Wirth, *ISC Marc Jeannerod*
Hao Wu, *Harvard U.*
Amir Yacoby, *Harvard U.*
Benjamin Youngblood, *St. Jude*
Kenneth Zaret, *UPenn School of Med.*
Lidong Zhao, *Beihang U.*
Bing Zhu, *Inst. of Biophysics, CAS*
Xiaowei Zhuang, *Harvard U.*
Maria Zuber, *MIT*

Pandemic security needs national leadership

Maria D. Van Kerkhove and **Chikwe Ihekweazu**

In a world facing escalating risks from conflict, climate change, and emerging infectious diseases, health systems are the first line of defense for protecting people, economies, and stability. Although pandemic preparedness is often framed as a global endeavor, readiness can only be successfully realized through strong national approaches that work alongside global strategies. The tools and networks already exist to help countries achieve this. What remains is the sustained commitment of governments to finance and implement those tools.

The threat of another pandemic is not theoretical. Rapid urbanization, ecological disruption, human mobility, climate-driven spread of organisms that transmit disease, and the risk of pathogens spilling over from animals to humans are converging to increase the risk of outbreaks worldwide. For example, avian influenza H5N1 is infecting new animal species and occasionally humans; the first outbreaks of Marburg virus in Ethiopia and Rwanda were reported this year; and over the past 2 years, Western Europe has seen unprecedented transmission of dengue and chikungunya viruses.

Ultimately, national preparedness is a strategic choice.

Since the peak of the COVID-19 pandemic, governments have reduced investments in public health, while increasing military defense spending. These reductions are short-sighted. Governments must embed preparedness in their health systems. A shift toward continuous, country-led readiness is critical to national stability. In 2023, the World Health Organization (WHO) launched the Health Emergency Preparedness, Response and Resilience (HEPR) framework to support this shift in five key areas: surveillance, clinical care, protecting communities, access to medical countermeasures, and emergency operations. Although WHO provides evidence-based guidance, global coordination, and technical support, each country must translate prevention and control strategies into operational effectiveness.

COVID-19 demonstrated the value of sustained national investment in HEPR capacities. Countries with strong emergency response systems could act quickly because they had learned from earlier outbreaks. For example, nations affected by severe acute respiratory syndrome (SARS) in 2002–2003 rapidly activated emergency operations, surveillance, and hospital surge systems when SARS-CoV-2 emerged. Similarly, countries in West Africa were better positioned to mobilize testing, contact tracing, and isolation systems because of their experience with Ebola virus. Although WHO issued global alerts and technical guidance within days of the first COVID-19 cases in early 2020, strong national leadership enabled early contact tracing, targeted diagnostic testing, genomic surveillance, and supportive clinical care, preventing health systems from being overwhelmed.

Additionally, many countries now operate all-hazards emergency operation centers within national public health agencies. These integrate disease surveillance, medical countermeasure logistics, and clinical care, and also coordinate partnerships, including those for disasters such as floods and earthquakes. In parallel, many governments have established national public health agencies or centers for disease control to work alongside ministries of health. With WHO guidance and capacity-building support, these institutions play a critical role in detecting outbreaks early and preventing localized events from becoming global crises.

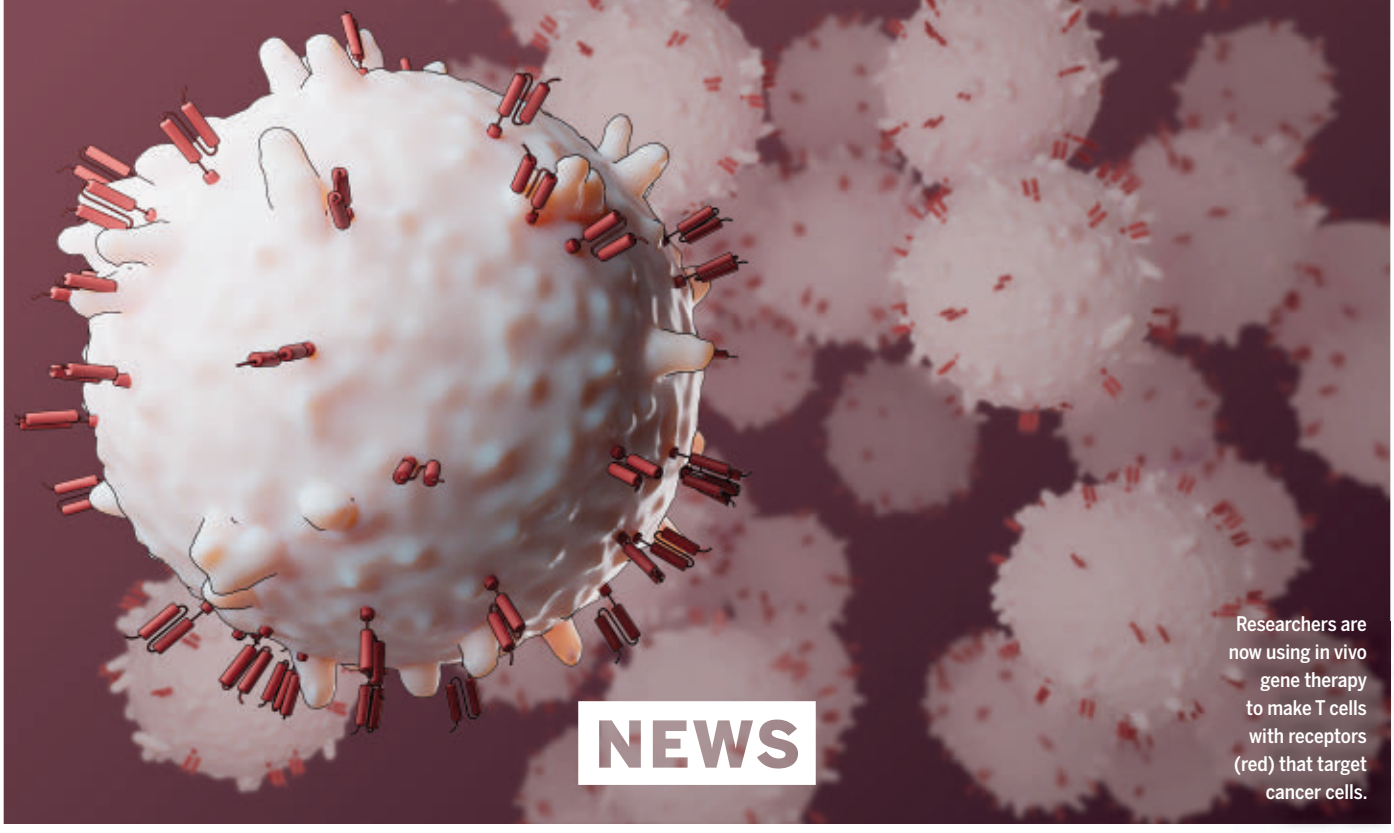
The economic case for preparedness is undeniable. COVID-19 caused an estimated global economic loss of more than USD 16 trillion in 2020. By contrast, the annual cost of building and maintaining core preparedness capacities is a fraction of that—estimated by the World Bank at USD 10 to 11 billion per year. Still, financing preparedness remains challenging. Global mechanisms such as the Pandemic Fund, established in 2022 by WHO and the World Bank, have awarded over USD 1.385 billion to low- and lower-middle-income countries to close critical capacity gaps. In addition, the International Monetary Fund, World Bank, and WHO have embedded preparedness into the USD 60 billion Resilience and Sustainability Trust, which provides affordable, long-term financing for preparedness.

WHO provides essential surge capacity and cross-border coordination, but these efforts complement—not replace—national capabilities. Countries also have access to technical partnerships such as the Global Outbreak Alert and Response Network, established in 2020, which links research institutions, universities, and health organizations to provide expertise and operational support. The Global Health Emergency Corps was launched by WHO in 2023 to strengthen workforce readiness through training and deployment. Yet sustained preparedness ultimately depends on national investments in emergency medical teams, public health professionals, and community health workers, as well as trust-building efforts co-developed with local leaders and civil society.

Ultimately, national preparedness is a strategic choice. The WHO 2025 Pandemic Agreement and strengthened International Health Regulations signal growing political commitment to shared global responsibility. However, political will alone is not enough. Sustained investment in preparedness is not optional—it is a cornerstone of economic stability, public trust, and global safety. □

Maria D. Van Kerkhove is director of the Department of Epidemic and Pandemic Management, Health Emergency Preparedness and Response Programme, World Health Organization, Geneva, Switzerland. vankerkhovem@who.int **Chikwe Ihekweazu** is executive director of the Health Emergency Preparedness and Response Programme, World Health Organization, Geneva, Switzerland. cihekweazu@who.int

10.1126/science.aee5227



NEWS

Researchers are now using in vivo gene therapy to make T cells with receptors (red) that target cancer cells.

ILLUSTRATION: N. BURGESS/*SCIENCE*

BIOMEDICINE

Cancer-fighting cells made in body help patients

Approach could be faster than making CAR-T cells in the lab—and early results are encouraging

MITCH LESLIE

Immune cells engineered to home in on cancer cells like guided missiles can be lifesavers—if patients can get them in time. Currently, their T cells must be harvested and given a surface protein, a chimeric antigen receptor (CAR), through genetic manipulation, a slow and expensive lab process. Making the cells directly inside the body should be faster, and early clinical data now suggest the strategy can work. In one of the first trials, the approach induced the so-called in vivo CAR-T cells in four patients with multiple myeloma, a blood cancer, and evicted the malignant cells from their bone marrow.

The results, presented this week at the American Society of Hematology (ASH) annual meeting, are preliminary but "really impressive," says cancer biologist Bin He of the Houston Methodist Research Institute, who isn't connected to the work. Moreover, the trial is the second this year to unveil positive findings from in vivo CAR-T cells for multiple myeloma. Patients in the earlier study suffered significant side effects, likely because of the viruses that ferried the needed genes into the immune cells, although the problems were less severe in the newer trial, despite using the same class of virus. "The question is no longer can you really do this," says Yvonne Chen, a cancer immunotherapy researcher at the University of California, Los Angeles. "The question now is can you reach the level of efficacy that's expected and will the safety profile meet the target."

CAR-T cells, which *Science* named as part of its 2013 Breakthrough of the Year, were first approved by U.S. regulators in 2017 and are now standard treatment for several types of blood cancers, including multiple myeloma. Specialized facilities turn a patient's T cells into cancer fighters by exposing them to viruses that infect them and deliver the *CAR* gene. Researchers are now looking to broaden the cells' repertoire, testing them against solid tumors, autoimmune diseases, and other illnesses.

But some patients die of their cancers during the month it typically takes to make CAR-T cells. And the high cost, usually in the hundreds of thousands of dollars, puts the treatment out of reach for many people. Before patients can receive their upgraded T cells, they also need risky chemotherapy to wipe out their natural T cells.

These drawbacks explain why researchers are so enthusiastic about the potential of making the cells in the body. "The field is gradually switching from ex vivo to in vivo CAR-T cells," says immunobioengineer Matthias Stephan of the Fred Hutchinson Cancer Center.

The two multiple myeloma trials followed a similar strategy, infusing a genetically altered virus known as a lentivirus, which carries the DNA sequence for a CAR, and letting it spread through the patient's T cells. Each virus carries an antibody that allows it to attach to a T cell target. Once a virus latches on, it enters and releases the DNA, which spurs synthesis of the receptor.

In July, researchers reported in *The Lancet* on four patients with multiple myeloma who received a lentivirus crafted by EsoBiotec of Belgium and Shenzhen Pregene Biopharma of China. All four patients showed significant improvement, as indicated by cell

and molecular measurements, hematologist Heng Mei of the Huazhong University of Science and Technology and colleagues revealed. In two patients, abnormal cells had vanished from the bone marrow after 3 months and a telltale cancer protein was no longer detectable in the blood. The other two patients didn't benefit as much, but the myeloma cells disappeared from their bone marrow after 2 months.

The treatment also produced what Mei called a "remarkable" effect in two patients: eliminating tumors that had grown outside the bone marrow, which other treatments often fail to control. The results "highlight the promise of the in vivo approach for achieving deep responses in difficult-to-treat sites," he says.

In three of the patients, however, blood pressure plunged shortly after the virus infusions. Two patients also required supplementary oxygen, and one showed mental slowing and confusion. All recovered after receiving treatment, but such problems typically don't occur with conventional CAR-T cells, Mei says. On the other hand, labmade CAR-T cells often trigger cytokine release syndrome (CRS), in which a surge of immune system molecules causes fever, chills, and other symptoms—and occasionally death. All four of the patients in the in vivo CAR-T cell trial developed CRS, but only at the lowest level of severity, the researchers reported.

At the ASH meeting, hematologist Joy Ho of the Royal Prince Alfred Hospital reported similar positive results for the second trial, sponsored by Boston-based Kelonia Therapeutics. One month after receiving a gene-carrying lentivirus developed by Kelonia, all four patients with previously untreatable multiple myeloma had no detectable cancer cells in their bone marrow. The cells were still absent in the one patient tested after 5 months. "The depth of response was very profound," Ho says.

The side effects were milder than in the other trial, for unclear reasons. CRS did occur in three of the patients, but the symptoms disappeared after treatment. "I think it gives us a glimpse into the future," Ho says. "In vivo CAR-T for multiple myeloma is here and hopefully it will stay."

The results from both trials are an important step forward, but much more evidence is needed, says molecular virologist Christian Buchholz of the Paul Ehrlich Institute, who produced the first in vivo CAR-T cells in mice that carried human blood cells. Researchers must closely follow these patients, probably over several years, before they can draw conclusions about the safety and effectiveness of the approach, he stresses. The lentiviruses pose a particular safety concern because they integrate their cargo into the DNA of host cells—a possible trigger for cancer.

The Kelonia trial will continue to add patients, and at least two other companies have launched in vivo CAR-T clinical trials that use lentiviruses. But EsoBiotec's trial has been halted, Mei says, partly because AstraZeneca bought the company in March—one of four biotechs working on the technology that Big Pharma scooped up this year.

The startup Capstan Therapeutics (now owned by AbbVie) has begun a clinical trial of an alternative nonvirus strategy that relies on small spheres known as lipid nanoparticles to deliver an RNA molecule coding for the CAR to T cells. These particles, similar to those in some COVID-19 vaccines, may be less likely to rile the immune system. Moreover, because the RNA doesn't integrate into the T cells' genomes, they only make the CAR for a short time, which may reduce side effects. The approach also allays the lentivirus cancer fears.

Other companies are planning trials of the nanoparticle CAR-T approach in cancer. This year, researchers reported using nanoparticles to generate in vivo CAR-T cells in patients with lupus.

Conventional CAR-T cells have enabled some multiple myeloma patients to stave off the return of their cancer for more than 5 years. Whether any of the in vivo approaches will provide such lasting benefits remains to be seen. Still, He says, the field is progressing fast. "Patients should be optimistic." □



IN FOCUS

New Zealand's early voyagers

New radiocarbon dates obtained from rope fibers found inside a buried canoe suggest it belonged to some of the earliest people to arrive on New Zealand's Chatham Islands—among the last places settled by Polynesian voyagers. Researchers reported last month that the canoe, known as a *waka* in Polynesian languages, dates to between 1440 C.E. and 1470 C.E. That aligns with the first archaeological traces of human settlement on Rēkohu, as the main island of the Chathams is known to the Indigenous Moriori people. Researchers and Moriori leaders hope studying the canoe, which includes carefully notched panels (above), will provide insights into the technology used to settle dozens of far-flung islands. —Veronika Meduna

PHOTO: VINCENT DIX

CLIMATE

Warm, humid ‘atmospheric rivers’ threaten Antarctica

Growing more common as the climate warms, these once-rare events could ultimately accelerate ice loss

TIM VERNIMMEN



A weather balloon is launched into an atmospheric river from King Sejong Station in Antarctica.

PHOTO: IRINA GORODETSKAYA

In May 2009, a strange weather pattern swept across Princess Elisabeth station, a remote Belgian research outpost in East Antarctica. Amid heavy snow, the air warmed by nearly 20°C, to –11°C. In 2 days, the storm dumped half a meter of snow in a region that is normally desert-dry.

Using weather data from the station, meteorologist Irina Gorodetskaya, now at the University of Porto, identified three more of these unusual storms in the following months. Together they deposited three-quarters of the normal annual snowfall in a handful of days, breaking records. Weather maps showed how a strong low-pressure area had pulled moist air south, where a high-pressure ridge channeled it straight toward the frozen continent.

The pattern, never described before in Antarctica, looked much like what, in places like California, meteorologists call “atmospheric rivers”: narrow streams of moist air that originate over tropical oceans and are blown thousands of kilometers to land, delivering large amounts of rain or snow.

Since the four atmospheric rivers in 2009, 30 more have hit the region. Climate change is the driver, Gorodetskaya says. “In warmer air, the moisture level will increase, which will make these rivers stronger and more frequent.” A recent study in *Communications Earth & Environment* makes a similar prediction. “Our models project that by the end of the century, there may be up to twice as many events with high enough moisture levels to qualify as atmospheric rivers today,” says lead author Michelle Maclennan, a meteorologist at the British Antarctic Survey.

These unprecedented pulses of heat and moisture could threaten the stability of coastal glaciers and ice shelves already weakened by decades of warming, researchers warned at a September meeting on Antarctic climate change at the United Kingdom’s Royal Society. “These systems now seem to be increasingly predisposed to collapse,” said Mike Bentley, a geoscientist at Durham University. In at least one case so far, an atmospheric river appears to have triggered the breakup of a coastal ice shelf.

Gorodetskaya continues to study the phenomenon in various ways, including with weather balloons launched from South Korea’s King Sejong Station on a windswept island just north of the Antarctic Peninsula. The work is challenging, she says. “We have special permission to go out in this weather. Nobody else usually does. We are considered to be the freaks of the station.” The gale-force winds can damage the 1-meter-wide balloons before they are airborne. “The challenge is to launch the balloon without breaking it. We’re losing many. It’s quite emotional.”

When she and her colleagues are successful, data on the unusual conditions in atmospheric rivers come pouring in. In Antarctica, precipitation normally falls as snow. But when an atmospheric river arrives, snow and ice particles can melt on the way down, Gorodetskaya says. “The transition zone from snow to

rain can be 2 to 3 kilometers up." The warm, moist air can spread far inland, bringing heavy rain or snow to normally dry regions, she says.

That may seem beneficial: The West Antarctic Ice Sheet has lost mass for decades, at an accelerating rate, as glaciers slide more quickly into the sea. But in 2022, "we saw so much precipitation from just a few extreme events that if you add it all up over the continent, the [Antarctic] ice sheet gained mass," says meteorologist Kyle Clem of the Victoria University of Wellington. Over the long term, however, intense precipitation may have unwelcome effects on the ice.

The top of the ice sheet usually consists of firn, snow riddled with tiny air holes that acts as a sponge, absorbing any accumulating meltwater. But large amounts of wet snow tend to freeze into a solid layer that causes meltwater or rain to pool rather than soak in, Bentley says. The dark puddles absorb more solar heat than a frozen surface would, which speeds up melting.

If extra water reaches the bedrock, it can lubricate the base of the glacier and accelerate its slide toward the ocean. If it collects in crevasses in the ice instead, its weight can deepen and widen them. This process can precondition coastal ice shelves for breakup, Bentley says. It may have proved fatal to East Antarctica's Conger ice shelf, a mass the size of Los Angeles that suddenly disintegrated in 2022.

The shelf had been shrinking and thinning since 2000, Bentley says. But its collapse came after an atmospheric river in March 2022 caused temperatures in East Antarctica to spike by 45°C. At the beginning of the year the ice shelf still measured 1200 square kilometers. But "in March, during this intense warming event, it just disappeared," Bentley recounts.

And surprisingly, it did so with no signs of surface melt. Strong winds during the storm probably dealt the final blow, causing the shelf to break into pieces, Bentley says. "We use the word 'glacial' to describe slow processes, but this was astonishingly fast."

In 2024, East Antarctica experienced another very warm period, this time in the dead of winter. "Extreme events caused by atmospheric rivers are transient. But this one lasted weeks," Clem says. Researchers are now documenting the consequences, and pondering the exact nature of yet another disturbance that human greenhouse gas emissions appear to be inflicting on Antarctica. □

Tim Vernimmen is a science journalist based near Antwerp, Belgium.

THEY SAID IT

This has a great potential to cause harm, and I simply hope that the committee will accept its responsibility when this harm is caused.

Neuroscientist Joseph Hibbeln, member of the Advisory Committee on Immunization Practices at the U.S. Centers for Disease Control and Prevention, after the panel voted 8-3 on 5 December to eliminate a long-standing recommendation that all infants in the United States receive the hepatitis B vaccine at birth.

IN EU NEWS

A GREEN LIGHT FOR GENE-EDITED CROPS

Plant genetic engineers received an early holiday present when the European Parliament and member nations of the European Union agreed to loosen regulations on the commercialization of gene-edited crops. The long-awaited deal, announced last week, has its origins in a 2018 decision by the European Court of Justice. It ruled that crops created through gene editing, which enables breeders to reshuffle or tweak a plant's own genes, should be regulated as strictly as crops engineered to include DNA from other organisms. Under the new rules, set to begin in 2028, companies will face no major hurdles to releasing gene-edited plants with minor changes that could have been accomplished via traditional breeding. In a nod to EU trade politics, crops carrying two common traits that have long dominated genetically modified crops in the United States—herbicide tolerance and insect protection—will still face tougher rules. Negotiators rejected a demand to bar companies from patenting gene-edited crops, but firms releasing new varieties must reveal their patents in a public database. —Erik Stokstad

X FACES FINE FOR NOT SHARING DATA

The social media company X is facing a fine of €120 million, in part because it hasn't made its data available to scientists, the European Commission announced on 5 December. By violating the European Union's Digital Services Act (DSA), the company is "effectively undermining research into several systemic risks in the European Union," the Commission said. It is the first time the Commission has levied a fine under the DSA, which was adopted in 2022 to hold digital platforms accountable. It opened an investigation into X in December 2023 and in July 2024 released preliminary findings that the company had breached the DSA. Since then, researchers had been waiting to find out whether the Commission would follow through in spite of mounting pressure from the United States to drop the investigation. X must now submit a plan on how to address the issues or face periodic penalty payments. The fine is likely just the beginning of an enforcement battle between the EU and U.S. tech platforms, says Stephan Lewandowsky, a misinformation researcher at the University of Bristol. "At present, a few billionaires in Silicon Valley are shaping the information diet of 450 million Europeans without much accountability, and the fine for X is a signal that Europe is not willing to tolerate this foreign intervention forever." —Kai Kupferschmidt

IN OTHER NEWS

HERBICIDE PAPER RETRACTED

The journal *Regulatory Toxicology and Pharmacology* retracted a paper published in 2000 that claimed to find no evidence that the chemical giant Monsanto's widely used glyphosate herbicide, Roundup, caused cancer. In 2017, a lawsuit uncovered internal emails suggesting the company's employees helped ghostwrite the paper, which was authored by three scientists. In a scathing retraction notice posted on 28 November, Co–Editor-in-Chief Martin van den Berg wrote that the paper was withdrawn because of "serious ethical concerns" and questions about the validity of the research findings. An analysis published earlier this year showed the now-retracted paper was in the top 0.1% of studies cited in glyphosate-related academic research and that citation rates had barely budged after the revelations of Monsanto's hidden involvement.
—Warren Cornwall



Seismic stations in Virginia can sense tremors that may be triggered by recharging the Potomac Aquifer.

PHOTO: RYAN POLLYEA

SEISMOLOGY

Replenishing sapped groundwater could trigger small earthquakes

A boom in aquifer injection projects could unlock long-quiet faults

HANNAH RICHTER

Near the Atlantic Ocean, along the banks of the James River, 10 stainless steel pipes penetrate hundreds of meters into the silts and sands beneath southeastern Virginia. Next year, the Hampton Roads Sanitation District (HRSD) will begin to inject about 60 million liters of treated wastewater through the pipes each day, as part of a project to refill the giant but shrinking Potomac Aquifer, which stores water underground in the pore spaces of compacted layers of sand. When completed, the $2.8 billion project will be the largest of its kind in the Mid-Atlantic region.

Similar projects are planned or underway elsewhere in the country, all aiming to keep water flowing to households, businesses, and farms that have overpumped aquifers for decades. But the projects could come with an unwanted side effect: earthquakes. "Anytime fluids are injected deep underground and in large volumes, injection-induced seismicity is a concern," says Ryan Pollyea, a geoscientist at the Virginia Polytechnic Institute and State University (Virginia Tech) who leads a research project related to the Virginia injection project, the Sustainable Water Initiative for Tomorrow.

Aquifers supply about half of the United States's freshwater. Overpumping has drawn down these reserves, leading to sinking of the overlying land and, in places where oceans are nearby, saltwater intrusions. In southeastern Virginia—an area already vulnerable to rising sea levels—water levels in the Potomac Aquifer have dropped more than 30 meters in some places, says HRSD hydrogeologist Dan Holloway.

Water managers in California's Orange County began to experiment with recharging aquifers nearly a century ago, says Adam Hutchinson, recharge planning manager for the Orange County Water District. Initially, they simply let water seep into the ground naturally, from giant holding ponds. But such surface water recharge is slow, and works best in places with large tracts of undeveloped land and loose, permeable soils. (The Potomac Aquifer, in contrast, is capped by a thick clay "lid" that inhibits natural recharge.)

So in the 1970s, Orange County sped up the process by taking water purified to drinking standards at sewage treatment plants and injecting it directly into the depleted aquifers. Hutchinson says the projects helped restore pressure in the aquifer, keeping saltwater intrusions from the Pacific Ocean at bay, while

allowing Orange County farmers and residents to maintain their water-hungry ways. The country took notice: Water managers from Texas to Florida began to implement their own injection projects.

But Earth's bedrock is full of faults, weak zones where slabs of crust grind past one another and generate earthquakes. Many sit dormant in the "basement" rocks below aquifers. When injected water seeps into these rocks, it raises the pore pressure—taking some of the load off the rocks. This decreases the stresses that normally keep faults clamped shut, leading to slip—and earthquakes.

"[When] the crust is in a very critical state, it requires a very small modification in the stress system to trigger some earthquakes," says Nicola D'Agostino, a geodesist at Italy's National Institute of Geophysics and Volcanology. Such earthquakes can take months or even years to show up, and they can appear tens of kilometers beyond the injection site. Even if injection stops, years of tremors may already be baked in. "It is not a simple switch on, switch off problem," says Pier Luigi Bragato, a seismologist at Italy's National Institute of Oceanography and Applied Geophysics.

No earthquakes tied to aquifers have yet been reported, but human-induced seismicity has unfolded countless times in the oil and gas industry, which injects wastewater from fracking operations into deep rock layers that are disconnected from aquifers. In Oklahoma and Texas, these "astronomical volumes" can trigger daily quakes, says Katie Smye, a geologist at the Bureau of Economic Geology at the University of Texas at Austin. Although most are too small to feel, a 2011 magnitude 5.7 quake in Oklahoma destroyed homes and buckled a highway, and a magnitude 5.4 quake in Texas caused the evacuation of a hospital building in 2022.

In 2019, HRSD approached Pollyea, who previously studied seismicity tied to oil and gas, to look at the earthquake threat from its plans. He and his team set up five seismic stations around the planned injection sites to establish a baseline of the region's background rumblings. They also built a geological model of the aquifer and other subsurface layers, applying estimates of the rocks' properties and the orientation of known faults. The model also factors in the speed of injection, which determines whether fluid pressure is forced deeper into fault-ridden rocks.

Using the model, Pollyea and his team tested proposed injection rates as high as nearly 10 million liters per day per well—some 50% greater than planned. The highest injection rate resulted in a pore pressure less than one-sixth of the pressure in a car tire, but still enough to cause seismicity, they reported in a paper in June. Last month, they reported more reassuring news for the Virginia project: A relatively impermeable layer of clay in the Potomac Aquifer should slow the seepage of water into basement rocks, potentially limiting earthquakes.

Demand for aquifer recharge may grow in regions such as California and Virginia because of thirsty data centers, which need vast amounts of water to cool the computers that power artificial intelligence, says Lorrie Council, underground injection control policy director at the nonprofit Ground Water Protection Council. "That stresses the whole water supply," she says. "I think we're going to see more [injection projects] in the future in places you wouldn't necessarily expect." She is already discussing aquifer injection projects in historically water-rich states such as Washington, Oregon, and Ohio.

That's all the more reason to ensure that earthquakes don't derail otherwise promising aquifer injection projects, D'Agostino says. Given Virginia's relatively quiet crust, dangerous quakes that cause severe damage are unlikely. But "imagine, suddenly, you get earthquakes in places where they were very rare before," he says. Even if small, people are sure to notice—and infrastructure might not be designed to withstand it. And multiple small earthquakes increase the probability of a larger one, adds John Ogunleye, a geoscience graduate student in Pollyea's lab at Virginia Tech.

As these projects come online, it's important to keep in mind that "we do not control how the earth responds to our forcing," D'Agostino says. "As soon as we start interfering with the crust, we should be careful." □

Hannah Richter is a journalist in Washington, D.C.

ARTIFICIAL INTELLIGENCE

AI tools aim to speed up outbreak modeling

DARPA program could help researchers build transparent, editable models of viral spread in days instead of weeks **SARAH SCOLES**

As SARS-CoV-2 radiated across the planet in 2020, epidemiologists scrambled to predict its spread—and its deadly consequences. Often, they turned to models that not only simulate viral transmission and hospitalization rates, but can also predict the effect of interventions: masks, vaccines, or travel bans.

But in addition to being computationally intensive, models in epidemiology and other disciplines can be black boxes: millions of lines of legacy code subject to finicky tunings by operators at research organizations scattered around the world. They don't always provide clear guidance. "The models that are used are often kind of brittle and nonexplainable," says Erica Briscoe, who was a program manager for the Automating Scientific Knowledge Extraction and Modeling (ASKEM) project at the Defense Advanced Research Projects Agency (DARPA).

In the wake of the pandemic, ASKEM set out to do better. Launched in 2022, the $29.4 million program aims to develop artificial intelligence (AI)-based tools that can make model building easier, faster, and more transparent.

Three years later, the ASKEM program, which includes nine teams with members from universities, companies, and government labs, has now published some of its tools for researchers and policymakers to use and assess. There's "real potential" for them to speed up model building during an outbreak, says Mohsen Malekinejad, an epidemiologist at the University of California San Francisco who helped evaluate the ASKEM products. "In a pandemic, time is always our biggest constraint. We need to have the information. We need to have it fast," he says. "We simply don't have enough data-skilled modelers for every single emergence, or every different type of public health need."

A common problem with models, epidemiological or otherwise, is that the mechanisms coded into them—the physics of airflow, say—are buried in thousands or millions of lines of software. Introducing new physics, biology, or behavior requires disentangling how those lines of code interact with each other. "What you really want to do as a scientist or a scientific modeler is to think about the actual science," says Brandon

Rose, chief technology officer at Jataware, an AI research and software company participating in ASKEM.

The program's AI tools automate that coding, allowing researchers to construct, update, and combine models at a higher level of abstraction. To make this work, ASKEM teams designed AI systems that can consume scientific literature—about disease transmission in a particular region, say—and extract the equations and knowledge needed to create or update a given model. The systems also pull out descriptions of those model components, so that users can manipulate and refer to them.

Other ASKEM teams found ways to build models by leveraging the expertise locked inside the minds of scientists. Many researchers record their ideas in Jupyter notebooks—web-based lab notebooks that mix code, narrative text, and visuals all in one place. One ASKEM project developed a way to ingest those notebooks, extract the underlying mathematical descriptions, and turn them into a model.

> **"In a pandemic, time is always our biggest constraint."**
>
> **Mohsen Malekinejad**
> University of California San Francisco

Another ASKEM project produced graphical interfaces through which scientists can interact with and edit the models, without touching the code itself. The interface also documents every decision—from code changes to scientific assumptions. "We had to present the results back to the researcher in a way that they could make sense of it and validate that the results were accurate," says Pascale Proulx, managing partner at Uncharted Software, an ASKEM participant.

Parshin Shojaee, a graduate student in computer science at the Virginia Polytechnic Institute and State University who wasn't involved with ASKEM, doesn't see ASKEM's knowledge-extraction efforts as particularly innovative. Scientists can routinely do a similar thing when they customize large language models such as ChatGPT by training them on scientific literature. What she finds more notable is how the tools allow researchers to interact with and edit models in a transparent way.

After completing the tools, DARPA tasked MITRE, a nonprofit research organization, with testing them. One test scenario was to create a model simulating coinfection with influenza, respiratory syncytial virus, and COVID-19, all circulating together as they do in the real world. The resulting model integrated the viruses' different transmission and seasonal patterns, while gauging the effects of interventions such as wearing masks and testing. Another what-if was very specific: Testers were asked to model the impact of a vaccination campaign on the cost of hospitalization for hepatitis A in a state's unhoused drug users.

In the final results, testers found that the ASKEM tools, when pitted against standard modeling workflows, could create models 83% faster. "They were able to build practically useful models in a 40-hour work week for multiple problems," says James Fairbanks, a computational scientist and engineer at the University of Florida and an ASKEM participant. Because of the ASKEM models' enhanced transparency, testers also found that decision-makers would be more confident in ASKEM's outputs than in those of traditional models.

Much of what's come out of the project is open source, and some teams have published in the scientific literature. A modeling and simulation workbench called Terarium, for instance, is available on Github, a collaboration platform for software developers. DARPA is working to find agencies or programs within the health, defense, and intelligence communities that might want to take advantage of ASKEM.

Whether the tools will be adopted more widely by epidemiologists—or other kinds of scientists—remains to be seen. "Scientists often are individualistic," says Philip Shapira, a professor of public policy at the Georgia Institute of Technology. "They want to do things themselves and build it themselves, and they might not trust what others provide."

But Fairbanks hopes epidemiologists will take advantage of the tools. "We're not here to make the best epidemiology model," he says. "We're here to give you, the scientists, the tools to build whatever you want as effectively as possible." □

Sarah Scoles is a science journalist based in Colorado.

BIOMEDICINE

Could adding light sensors to nerve cells help switch off diseases?

Optogenetics is poised to move from a research tool to new therapies—if scientists can show it's safe

KELLY SERVICK

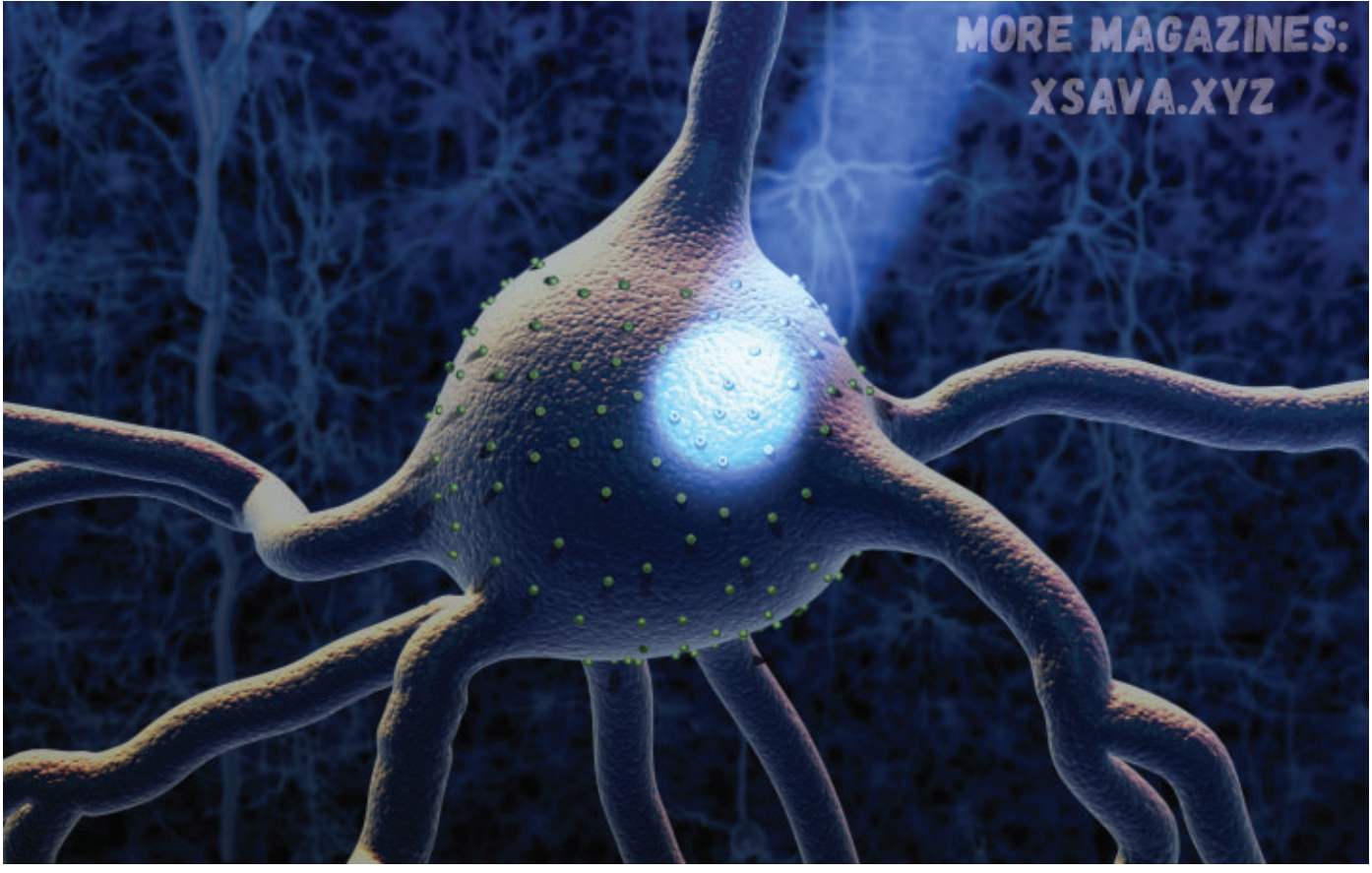
In the past 20 years, mice with glowing cables sprouting from their heads have become a staple of neuroscience. They reflect the rise of optogenetics, in which neurons are engineered to contain light-sensitive proteins called opsins, allowing pulses of light to turn them on or off. The method has powered thousands of basic experiments into the brain circuits that drive behavior and underlie disease.

As this research tool matured, hopes arose for using it as a treatment, too. Compared with the electrical or magnetic brain stimulation approaches already in use, optogenetics offers a way to more precisely target and manipulate the exact cell types driving brain disorders.

So far only one optogenetic application—addressing certain kinds of vision loss by introducing opsins into cells in the eye—has made it into human trials. But promising early results from the treatment, along with the discovery of more sensitive and sophisticated opsins, are inspiring researchers to look beyond the eye and target peripheral nerves or even the deep brain. Tests of these strategies in animal models of epilepsy, amyotrophic lateral sclerosis (ALS), and other disorders have been encouraging, researchers reported last month at the annual meeting of the Society for Neuroscience (SfN) in San Diego. One company is hoping to launch a human trial for an optogenetic pain treatment by 2027.

"We definitely don't want to oversell the idea of using optogenetics [on human brains] any time soon, but we also are firmly convinced that this is now the right moment to be thinking about this seriously," University of Geneva neurologist and neuroscientist Christian Lüscher told an SfN session he chaired, in which participants presented a newly published road map for bringing optogenetics to the clinic. Still, the speakers acknowledged major remaining challenges, including possible risks of inserting genes for opsins—many of which are derived from algae or other microbes—into a person's nerves or brain cells.

MORE MAGAZINES:
XSAVA.XYZ



Adding proteins (green) to nerve cells to make them respond to light could help control the circuits driving various brain disorders.

IMAGE: MCGOVERN INSTITUTE/MASSACHUSETTS INSTITUTE OF TECHNOLOGY

In 2021, about 15 years after scientists laid the foundation for optogenetics by showing that algae opsins made neurons respond to light, researchers published the first results from a participant in an optogenetics trial. The man had lost the light-sensitive cells in his retina to the inherited disease retinitis pigmentosa. The team, from the French company GenSight Biologics and its collaborators, injected a virus carrying an algae-derived opsin gene into his eye, targeting retinal ganglion cells. Those cells normally relay visual information to the optic nerve, but the added gene made them sensitive to reddish light. Wearing special goggles to project patterns of light onto the retina, the man could find and count dark objects on a table, although he was still unable to make out faces, letters, or colors.

GenSight's initial 10-person trial is ongoing, and other companies are pursuing similar strategies. The 2021 result was an "important breakthrough, as it demonstrated the feasibility of optogenetic therapy," says neurophotonics and optical neuroscience researcher Valentina Emiliani, whose team at the Vision Institute in Paris is working to improve the visual resolution of the technology.

Speech-language pathologist Teresa Lever of the University of Missouri now hopes to use optogenetics to enable people with ALS to retain the ability to swallow as the disease progressively destroys neurons that help control tongue muscles. In a poster at the meeting, her Ph.D. student, biomedical engineer Apaala Basak, presented experiments where the team injected the tongues of mice with green algae opsin genes, which were taken up by both tongue muscle fibers and the neurons in the brainstem that project to and control these muscles. Pulses of light onto the tongue activated these light-sensitive muscle fibers and nerve endings, making the tongue contract. The team plans to test whether activating the tongue strengthens it enough to help mice with ALS-like symptoms drink water. Lever is seeking industry partners to move the technology toward a clinical trial that would equip patients who have received similar opsin gene injections with a retainerlike device that emits light.

Another strategy, under development by the Boston-based company Modulight Biotherapeutics, takes aim at the trigeminal nerve in the face, which can cause excruciating chronic pain when damaged or irritated. In an outpatient procedure, physicians would inject an opsin gene into the nerve through a natural opening in the skull above the upper jaw; flashes of light either shined on the face or delivered via an implanted fiber would dampen the activity of pain-signaling cells. The team hopes to start a human trial in 2 years.

Modulight and others also hope to deliver opsins to cells deep in the human brain, where the proteins could be used to turn disease-related neurons or circuits on or off in response to light delivered by an implanted fiber. They might, for example, dampen specific cells in the hippocampus that set off a storm of electrical activity in a hard-to-treat form of epilepsy, or disrupt the activity of cells in the subthalamic nucleus that drive abnormal movements in Parkinson's disease.

Among the existing treatments for those two conditions is deep brain stimulation, where an implanted wire delivers electricity to regulate cell activity. But because these electrodes affect a large swath of nearby cells, "it's like trying to play the piano by hitting it with a large mallet," says Newcastle University neuroscientist Andrew Jackson, who previously led a multicenter effort to explore optogenetics for treating epilepsy. Optogenetics should be much

more precise—able, for example, to dampen excitatory cells that ramp up seizures while leaving nearby inhibitory cells alone—because the opsin genes can be delivered to just the desired cells.

In a big-brained animal such as a human, the cells that researchers endow with opsins and want to stimulate might be far apart. The intensity of light needed to trigger them risks overheating and damaging the brain, says Yotam Eldar, Modulight's co-founder and CEO. So Eldar and collaborators have been experimenting with a highly sensitive opsin called eOPN3, recently discovered in mosquitoes, for which lower light intensities should suffice. It also responds to red light, which is "really good at penetrating biologic tissue" Eldar explains.

At the SfN meeting, Eldar and Mayo Clinic biomedical engineer Filip Mivalt described a first attempt to use eOPN3 to suppress seizures in a breed of miniature pig—which, like humans, has a relatively large and deeply folded brain. The team introduced the opsin gene into the hippocampi of three pigs, inserted a fine, light-emitting fiber into this region, and then injected a seizure-inducing compound called kainic acid. Light suppressed the seizure in seconds, the team reported at the meeting, and in a preprint earlier this year.

"I was quite impressed," says Jackson, who hopes to collaborate with Modulight to test the approach in nonhuman primates, alongside a technique for probing the brain with light to predict oncoming seizures.

A key hurdle optogenetic researchers must clear is showing they can safely get opsin genes into a person's brain cells. Adeno-associated viruses (AAVs), injected either directly into brain tissue or into the bloodstream, are a standard vehicle for gene therapies. But they have triggered dangerous immune reactions and other side effects, and the U.S. Food and Drug Administration has halted some clinical studies after participants died.

"AAV-based gene therapies are still evolving," said Stanford University neuroscientist and optogenetics pioneer Karl Deisseroth during the SfN session. Using the lowest possible doses may help, he said, and he noted that no safety problems have surfaced in the optogenetics vision trials to date.

To Jackson, the biggest safety concern remains the opsins themselves. "How do you demonstrate and convince yourself that the expression of these foreign proteins in the brain isn't going to be harmful … over the lifetime of the participant?" he wonders. That's a fair question, others in the field agree. Eldar says his team has seen no dangerous reactions to eOPN3 in rodent and pig studies so far, but he acknowledges more safety testing is needed.

Yet the need for more precise and effective neurological treatments is reason to persist, Eldar says. "We can't do the same things over and over and expect new results. We need new tools." □

IN FOCUS

A spider's serpentine silk

A mesmerizing image of two silk threads spun by the Australian net-casting spider (*Asianopis subrufa*) was the winner of this year's Royal Society Publishing Photography Competition. Shot with a scanning electron microscope by spider researcher Martín Ramírez of Argentina's National Scientific and Technical Research Council, it captures looping lengths of silk just 50 microns long. The spiders are ambush predators that toss a web with their forelegs to snare passing insects. That strategy, Ramírez notes, requires strong but "incredibly stretchy" silk that can snap back to its original length. —David Malakoff

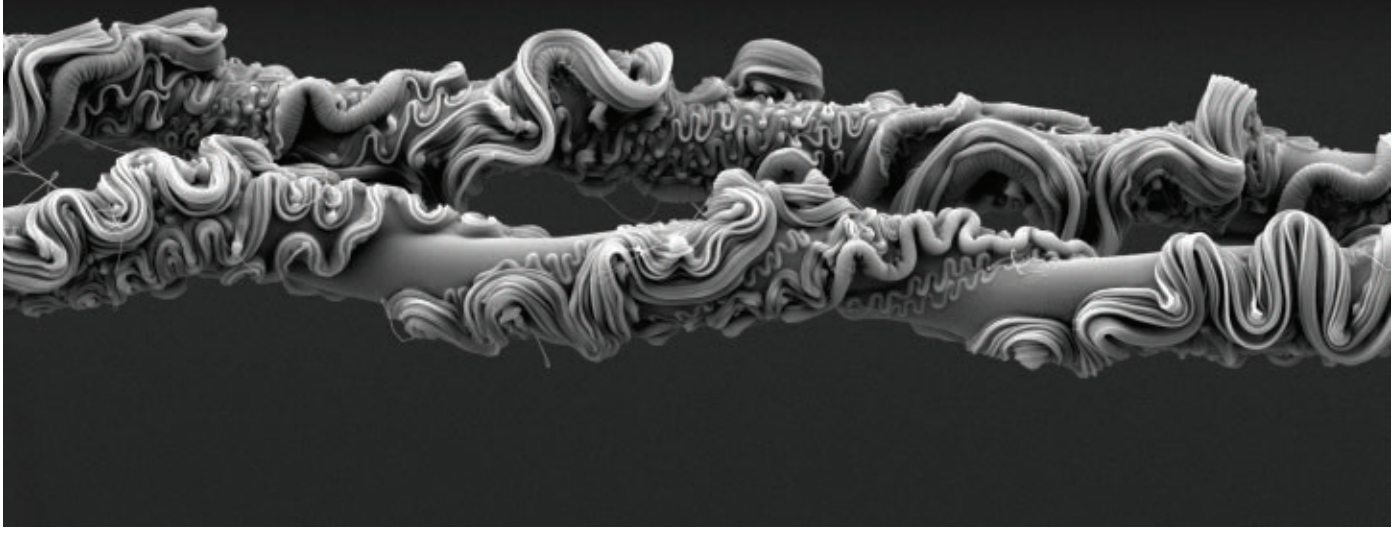


PHOTO: MARTÍN J. RAMÍREZ, SAMPLE OBTAINED BY JONAS WOLFF



AAAS.ORG/COMMUNITY







AAAS' Member Community is a one-stop destination for scientists and STEM enthusiasts alike. It's "Where Science Gets Social": a community where facts matter, ideas are big and there's always a reason to come hang out, share, discuss and explore.

Member COMMUNITY
AAAS

AMERICAN ASSOCIATION FOR THE ADVANCEMENT OF SCIENCE

FEATURES

PLANET PROTECTOR

More than half of the "city killer" asteroids that might threaten Earth remain undiscovered. With an infrared eye, NASA's NEO Surveyor aims to find them

ROBIN GEORGE ANDREWS



Wrapped in thermal blankets, the Near-Earth Object Surveyor is subjected to cold, airless conditions inside a NASA vacuum chamber.

On a commercial thoroughfare in old town Pasadena, California, a stone's throw from NASA's Jet Propulsion Laboratory (JPL), you'll find the Neon Retro Arcade. Among its collection of vintage video games is the 1979 Atari classic *Asteroids*, in which a pixelated spaceship shoots down a barrage of space rocks to stave off fatal collisions. After long days of work at JPL, Amy Mainzer used to rack up high scores on that console. "It was a hoot," she says. It was also apt, considering she oversees a space mission designed to spot dangerous asteroids before they crash into Earth.

That mission, the Near-Earth Object (NEO) Surveyor, was conceived in the early 2000s and finally got the green light in 2022. Its components are now being built, tested, and assembled in clean rooms across the United States ahead of its planned launch in September 2027. "We're in the thick of building everything," says Mainzer, NEO Surveyor's principal investigator and now an astronomer at the University of California, Los Angeles (UCLA). "It's really amazing to see things we've seen on PowerPoint slides and on cocktail napkins for years and years and years now as real pieces of hardware."

The mission has one overarching goal: to help planetary defenders find nearly all near-Earth asteroids at least 140 meters in length—a population that is still mostly undetected. These asteroids are sometimes called city killers, and for good reason: A direct strike on a large metropolis could unleash the destructive energy of 300 million tons of TNT. Put another way, that's six times the yield of the Tsar Bomba, the most powerful nuclear bomb ever detonated.

Many of these asteroids are invisible to astronomers: They can hide in the glare of the Sun, loop about on eccentric orbits most telescopes can't see, and camouflage themselves with dark coatings. But NEO Surveyor, observing in the infrared from a vantage that lets it stare closer to the Sun, will see those hidden asteroids glow like fireflies in the night.

Thanks to its heightened perception, the observatory will also offer planetary scientists valuable information about the diversity of the primordial materials that went into making the Solar System. But it is first and foremost a planetary defense mission. "We are trying to find killer asteroids and protect the planet," says Ed Swenka, NEO Surveyor's flight system manager at JPL.

If humanity is lucky, the mission will find that no sizable asteroids are on an Earth-bound trajectory for the foreseeable future. But if a perilous space rock is identified, it will give governments valuable time to mount a mission to deflect or destroy it. "We're on the precipice of actually knowing whether there's an asteroid out there with our name on it," says Richard Binzel, an asteroid expert at the Massachusetts Institute of Technology (MIT).

WHEN I MEET MAINZER in her office at UCLA, she shows me the unofficial NEO Surveyor mission patch. It depicts a *Tyrannosaurus rex* screaming at an Earth-bound asteroid above two words: NEVER AGAIN. "It's not officially blessed by NASA," she says, with a grin.

Although habitually upbeat, Mainzer's tone shifts slightly as she discusses the serious side of her work. She was the scientific adviser to *Don't Look Up*, a darkly comedic movie featuring a comet plunging toward the planet—and astronomers being dismissed by ignorant politicians. The film's key lesson, she says, also applies to the real world: "If we can't all agree that getting hit by an asteroid is a bad thing, then we can't agree on much."

Fortunately, planetary defense has long held bipartisan sway with the public, members of Congress, and various occupants of the White House. "It's a mission that sells itself," says Casey Dreier, chief of space policy at the Planetary Society, an advocacy organization. "As long as one wants to continue the human race into the future, it's a hard value proposition to ignore."

The asteroids of concern aren't the millions of rocks that orbit the Sun in a belt between Mars and Jupiter. These objects are usually on stable, long-term orbits aligned with the plane of the Solar System, along which the planets also sit. That makes them easy to monitor.

But some are yanked from the belt by collisions or by gravitational tugs from planets—typically Jupiter. These strays can end up flying on trajectories that cross Earth's own circumsolar path. Their orbits are "splattered all over the sky," Mainzer says. "It's a pain to find them."

Earth is struck continuously by the smallest members of this population: grit and gravel that burns up in the atmosphere as meteors or shooting stars. A few are larger and sturdy enough to survive the fiery descent to terra firma. UCLA's meteorite collection includes the remains of some of these interlopers. A hefty rocky stela is marked with ripples scored into it as it plunged to Earth. Several metallic pallasites sparkling with green-yellow olivine crystals resemble iridescent stained-glass windows. But the most impactful object is the most innocuous looking: a dark rock that fits comfortably in my palm.

On 15 February 2013, a 20-meter asteroid exploded above the Russian city of Chelyabinsk with the energy of 500,000 tons of TNT—about 15 times greater than the combined yield of the atomic bombs dropped on Japan's Hiroshima and Nagasaki. Miraculously, nobody died. The asteroid came in at a shallow angle and had to push through more of Earth's atmosphere during its dive, which caused it to explode at high altitude. Nevertheless, the shock wave shattered windows across the region, blasting shards of glass into unsuspecting bystanders. Some 1500 people went to the hospital with injuries.

Most of the Chelyabinsk meteor vaporized in the atmosphere. But some of it survived—including the



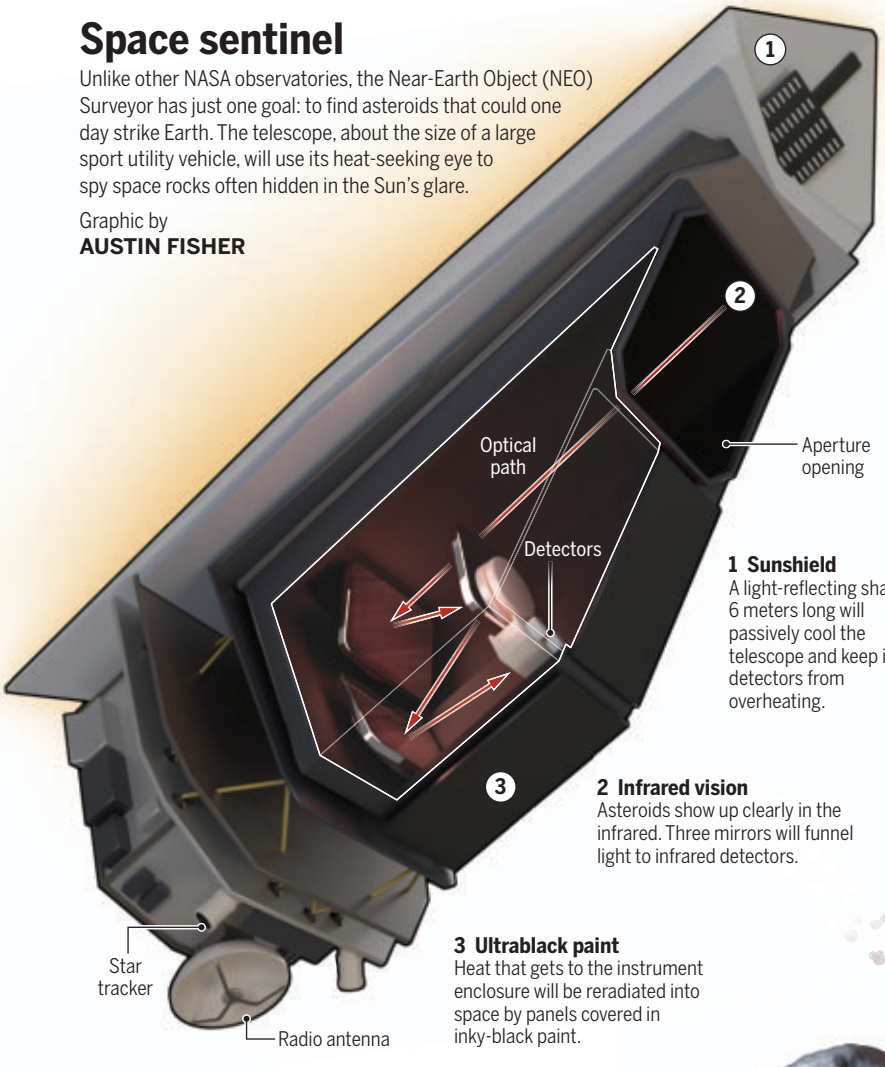
For 2 decades, Amy Mainzer worked to get an asteroid spotter in space. With the Near-Earth Object Surveyor, that plan is finally becoming a reality.

PHOTOS: SELIN FILIZ/*DAILY BRUIN*; (OPPOSITE PAGE) NASA

Space sentinel

Unlike other NASA observatories, the Near-Earth Object (NEO) Surveyor has just one goal: to find asteroids that could one day strike Earth. The telescope, about the size of a large sport utility vehicle, will use its heat-seeking eye to spy space rocks often hidden in the Sun's glare.

Graphic by
AUSTIN FISHER

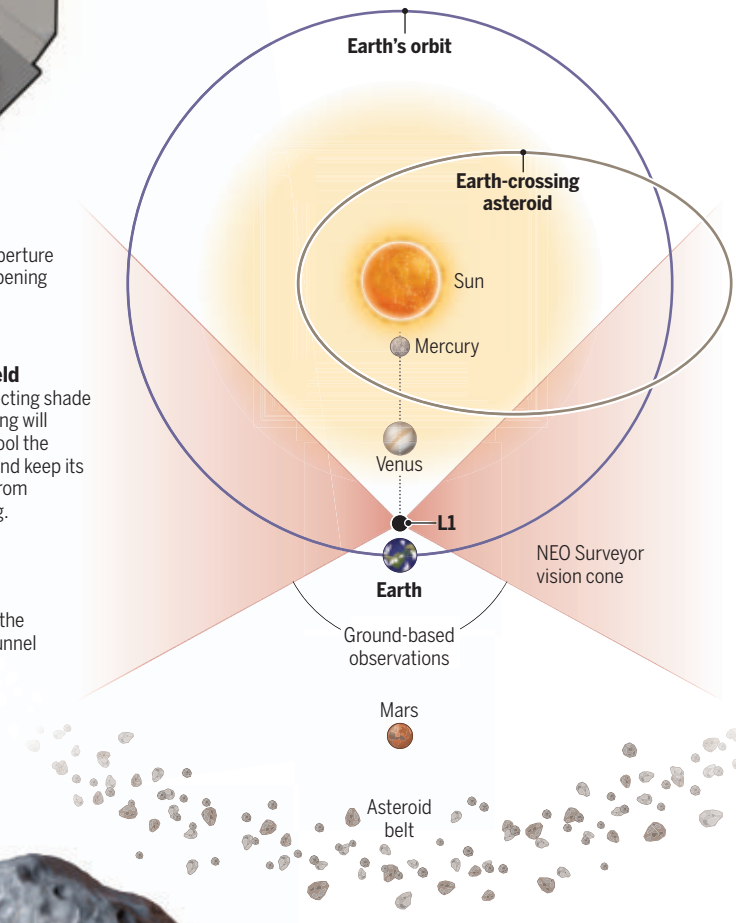


1 Sunshield
A light-reflecting shade 6 meters long will passively cool the telescope and keep its detectors from overheating.

2 Infrared vision
Asteroids show up clearly in the infrared. Three mirrors will funnel light to infrared detectors.

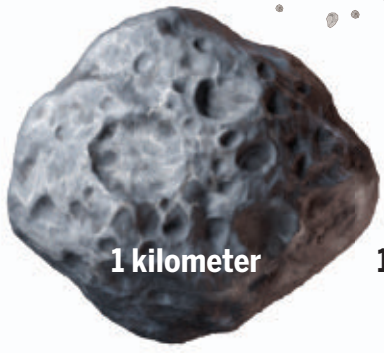
3 Ultrablack paint
Heat that gets to the instrument enclosure will be reradiated into space by panels covered in inky-black paint.

Staring near the Sun
Ground-based telescopes, observing at night and pointing away from the Sun, can scrutinize the asteroid belt, but sometimes struggle to find objects in Earth-crossing orbits. NEO Surveyor's position at L1, 1.5 million kilometers sunward of Earth, means it can constantly look inside Earth's orbit, to within 45° of the Sun.



City flatteners
The impact of a 140-meter-wide asteroid in midtown Manhattan would generate a blast strong enough to topple steel-framed buildings across much of the island.





	1 kilometer	140 meters	50 meters
Percent discovered	95%	45%	7%
Estimated near-Earth asteroid population	900	25,000	230,000
Destructive energy (megatons TNT)	100,000	300	10
Impact recurrence interval (years)	700,000	20,000	1000
How bad?	Worldwide devastation and risk of civilizational upheaval	Capable of annihilating a large city, injuring and killing millions	Highly destructive to a metropolis, like a small nuclear blast

CREDITS: (GRAPHIC) A. FISHER/*SCIENCE*; (DATA) R. MARCUS, J. MELOSH, G. COLLINS/EARTH IMPACT EFFECTS PROGRAM; (MAP) V. PENNEY/*SCIENCE*

piece I held. "It was pulled out of a lake by divers," Mainzer says.

Worrisomely, the Chelyabinsk asteroid was an ambush: It emerged from the direction of the Sun, and astronomers didn't see it coming.

The event served as a wake-up call for NASA, which soon after established its Planetary Defense Coordination Office. It manages a network of ground-based observatories and has made steady progress in fulfilling earlier congressional mandates. One, set in 1998, tasked NASA with finding at least 90% of the "planet killer" asteroids bigger than 1 kilometer. A second, in 2005, tasked the agency with discovering at least 90% of the 140-meter-and-up city killers. (The blast from an asteroid of that size would be roughly 600 times more destructive than Chelyabinsk, because a doubling in diameter increases a space rock's kinetic energy by eight times.)

Until all of them are found, scientists can only make educated guesses about the overall number of planet killers and city killers. Larger asteroids are far more rare than smaller ones, and overall populations can be approximated based on the space rocks discovered to date. According to NASA's most recent assessment, 95% of the estimated 900 planet killers in near-Earth space have now been found. But of the roughly 25,000 city killers predicted to exist, less than half have been spotted. When it comes to the expected 230,000 or so 50-meter asteroids, the number falls below 10%.

Optical telescopes—those relying on light we can see—aren't especially well-suited to spot them. About 40% of asteroids are made of dark, carbon-rich material that reflects little sunlight, effectively giving these rocks a stealth coating. The camouflage also keeps astronomers from getting an accurate measure of an asteroid's size, as a larger rock with a surface like charcoal bounces back the same amount of light as a smaller one with a shiny coating.

In addition, many near-Earth asteroids are thought to spend much of their time on trajectories interior to our planet's orbit, which means ground-based observatories must look toward the Sun to try to find them. To avoid being blinded, they can only search during the brief minutes of twilight before sunrise and after sunset. Peering for a few minutes each day through Earth's obfuscating atmosphere into a sky increasingly graffitied by the glinting tracks of reflective satellites isn't an efficient asteroid-seeking strategy.

That leaves just one solution to the problem. "You need an asset in space," says Kelly Fast, acting head of NASA's Planetary Defense Coordination Office. And it needs to watch the heavens not at optical wavelengths, but in the infrared.

NO MATTER WHETHER they are coated in dark or shiny dust, all asteroids appear like bonfires in the dark to an infrared observer. Not only does an asteroid's thermal glow stand out, it also allows astronomers to calculate the asteroid's diameter down to about 10%.

Space-based observatories have demonstrated time and again that thermal scopes are superlative asteroid spotters. Chief among them was the Wide-field Infrared Survey Explorer, or WISE mission. Launched in 2009, WISE perused countless stars and galaxies until it was put into hibernation in 2011. But in 2013, it was reactivated as NEOWISE under Mainzer's leadership.

NEOWISE orbited Earth around the poles so it could see as much of the night sky as quickly as possible. That meant it could take a good look at the main asteroid belt, which is in a fixed position. Over the next 11 years, the satellite discovered tens of thousands of asteroids in the main belt. But because of its orbit, it had slim chances of capturing fast-moving near-Earth asteroids, including those hiding far above or below the plane of the Solar System. It found a total of 215 new near-Earth asteroids and comets—a welcome number but far from enough for planetary defenders.

Mainzer didn't want to just find a handful of potentially hazardous space rocks here and there. "Can we make it work at scale?" she says. Could she "mass-produce asteroid discovery?"

Her first proposal for a dedicated near-Earth asteroid hunter came in the early 2000s in the form of NEOCam: an infrared space observatory looking toward the Sun. Back then, planetary defense was still considered to be a part of NASA's planetary science division. That meant that in the fierce competition for funding, NEOCam was pitted against concepts like Lucy (a mission to Jupiter's Trojan asteroids) and Psyche (a mission to a metal asteroid). It lost out each time, partly because the science return of an explicit planetary defense mission wasn't considered to be as substantial as from the other proposals. Treating NEOCam primarily as a science mission "was kind of like trying to fit a round peg into a square hole," says Cristina Thomas, a planetary astronomer at Northern Arizona University.

In 2016, in the wake of the Chelyabinsk event, NASA leadership had an epiphany: You can't do planetary science if an asteroid smacks into Earth and kills everyone. That year, it set up its Planetary Defense Coordination Office. And in 2019, NEOCam was made a directed mission and was taken out of the competitive realm and given a dedicated stream of funding. Mainzer's team made the case that the proposed spacecraft would fulfill the congressional mandate: Simulations show that even if every other asteroid-hunting observatory was deactivated, it alone would find 90% of all the city killers—and plenty of the 50-meter hazards, too. After being convinced the space observatory could execute its noble task, NASA gave the mission the official go-ahead in December 2022.

> "We are trying to find killer asteroids and protect the planet."
>
> **Ed Swenka**
> Near-Earth Object Surveyor team

NEO Surveyor was born. And engineers, building on several decades of infrared surveys, got to work on a brand-new, all-seeing eye.

JPL'S HIGH BAY 1 CLEAN ROOM is where NASA's best known robotic spacecraft are assembled and put through their paces. The outer Solar System adventurer Voyager 1 was forged here, as was every single one of the space agency's Mars rovers. In April—after putting on an all-enveloping, particulate-trapping bunny suit—I was invited into that hallowed hanger. Inside, surrounded by a coterie of engineers, was NEO Surveyor's instrument enclosure, a sleek-looking car-size sarcophagus



In 2013, a 20-meter asteroid exploded above Chelyabinsk, Russia (above). Meteorite hunters recovered many small fragments (opposite page).

that will hold the mission's killer app: its heat-seeking scope.

A specialized radiation splitter within the instrument enclosure will slice the infrared light into two beams at distinct wavelengths where asteroids are brightest. Two infrared retinas will absorb most of the photons from those beams. "It took us a long time to build these detectors," Mainzer says. "Nobody has anything better on the whole planet."

After NEO Surveyor launches on a SpaceX Falcon 9 rocket from Florida, the spacecraft will travel for about 2 months to a gravitationally balanced spot between Earth and the Sun some 1.5 million kilometers away. This anchor point, known as L1, not only will allow NEO Surveyor to maintain its position for at least 12 years with minimal use of fuel, but will also offer unobstructed views of asteroids hidden in the space closer to the Sun.

That ceaseless view of the Sun also presents a problem: NEO Surveyor will get cooked at extremely high temperatures. Aside from not wanting electronics to overheat, engineers also want to prevent the enclosure itself from warming up and radiating in the infrared—which could reduce the sensitivity of its detectors. The team could have opted to cool NEO Surveyor with cryogenic fluids, like liquid nitrogen. But those run out. Instead, engineers went with a 6-meter-long sunshade—a mirrorlike shield decorated with solar panels that will power the spacecraft.

Inevitably, some heat will still sneak past the sunshade. Fortunately, there's a low-tech solution for that, too. Dark surfaces efficiently radiate heat and cool down, so the team has smothered panels of NEO Surveyor's instrument enclosure in what Mainzer calls "a weird black paint," so inky black that, to my eye, the flat panels looked like dimensionless, cavernous voids. During my visit, the enclosure was still a work in progress. But when complete, NEO Surveyor will resemble a shining star from one side, and a pool of shadows from the other.

LIKE THE ORIGINAL NEOCAM, NEO Surveyor's hyperacuity will open new research avenues for planetary scientists, those to whom asteroids aren't just rocky missiles, but time capsules.

Asteroids are relics of the formation of the Solar System 4.6 billion years ago. They come in a stunning variety of flavors—from dense, metal-rich orbs to icy rocks brimming with organic matter. Some are mechanically rigid behemoths, whereas others are weakly cohesive rubble piles. "Every asteroid that we've been to has surprised us in some way," says Kathryn Kumamoto, head of the planetary defense research program at Lawrence Livermore National Laboratory. "That just tells us we don't know enough about the asteroid population as a whole."

NEO Surveyor will discover an entirely new population of space rocks. It will learn little more than their location, size, and shape. But other telescopes—including JWST, a large NASA infrared observatory—can zoom in and study each new asteroid up close.

One question astronomers hope to address is the source of Earth's oceans. Astronomers used to think icy comets were the main water carriers. But the smart money is now on waterlogged asteroids: They hang about closer to the planet than comets, and impact us far more frequently. Moreover, the isotopic composition of the water within comets doesn't always resemble that of the water in Earth's seas, whereas water trapped in a recently found meteorite was a near-perfect match. Finding similarly soggy asteroids in the near-Earth population would add weight to this hypothesis.

Such data will delight not just planetary scientists, but also planetary defenders, who want to know what asteroids are made of as well as where they are hiding. Attempting to deflect or blow up a damp rubble pile would require a very different spaceflight campaign than defending Earth from a monolithic metallic mountain.

Protecting the planet is a profound assignment, and two other astronomical powerhouses are expected to charge into the fray alongside NEO Surveyor. First up is the Vera C. Rubin Observatory, a gigantic telescope in Chile that will begin its decadelong sweep of the night sky

PHOTO: MARAT AHMETVALEEV/GEOPHOTO/ZUMA



PHOTO: DETLEV VAN RAVENSWAAY/PICTURE PRESS/REDUX

later this year. Although many of its targets lie outside the Solar System, it is also set to find 3.7 million main belt asteroids and 89,000 near-Earth asteroids. Its twilight surveys have some overlap with NEO Surveyor's own viewing angle. "But NEO Surveyor's going to spend a lot more time there and find anything that we miss," says Mario Jurić, an astronomer at the University of Washington and a Rubin project scientist.

The second is a mission in the planning stages at the European Space Agency (ESA) called the Near-Earth Object Mission in the Infra-Red, or NEOMIR. If greenlit by ESA leadership, it would launch sometime in the 2030s and join NEO Surveyor at L1. NEO Surveyor can look as close as 45° away from the Sun, but NEOMIR plans to peer even closer—down to 30°, says Luca Conversi, an ESA researcher and NEOMIR lead. Its infrared detectors are also designed to take many short-exposure images of the Sun's surroundings, like the burst mode on a smartphone camera. Simulations show this approach would allow NEOMIR to spot Chelyabinsk-size asteroids flying toward Earth from the Sun's direction.

In case the array of astronomical forces sounds like overkill, this year brought a reminder of the threat. For a moment, it looked like Earth might genuinely be in peril from an asteroid—one that had almost escaped the notice of planetary defenders entirely.

THE OBJECT—dubbed 2024 YR4—had just flown past Earth when a small NASA-funded telescope in Chile spotted it in late December 2024. By February, astronomers calculated there was a 1-in-32 chance it would hit the planet on a later pass, in 2032. The optical telescopes tracking it estimated it could be as small as 40 meters or as large as 90 meters. At the lower end of the scale, a direct strike on a city would cause widespread damage and injure thousands. At the higher end, that city would suffer a mass casualty catastrophe.

By early this year, 2024 YR4 was quickly fading from view. If astronomers couldn't track its orbit closely enough to nail down those impact odds, they would have to wait for its next close approach in 2028—just 4 years away from a potential collision. Planetary defenders weren't sure they could mount an effective deflection mission in time.

To everyone's great relief, observers did manage to scope out 2024 YR4 long enough to rule out an Earth impact in 2032. And at the tail end of the crisis, scientists got permission to point JWST at the asteroid. Its thermal eye quickly revealed the asteroid's true size: 60 meters, a comfortable city wrecker, if not killer.

Had it been around, NEO Surveyor would have rendered all the drama moot. Mainzer opens her laptop and pulls up a chart showing how 2024 YR4 would have moved across her spacecraft's field of view. "There," she says, pointing to the year 2012. If NEO Surveyor had existed back then, "We had a pretty good chance at spotting it."

THIS YEAR, NASA's planetary scientists came under unprecedented attack—not from the skies, but from the White House. A budget proposal from President Donald Trump asked Congress to kill off dozens of Solar System exploration missions. And the cancellation requests included not just spacecraft in their conceptual stages, but several still zooming through space. One notable example was OSIRIS-APEX, which had collected samples from one asteroid and was subsequently retasked with chasing down and studying another for planetary defense research purposes. Whether Congress will accede to the demands of the White House is uncertain. But NEO Surveyor was not marked for termination. For now, it remains on track for a 2027 launch.

"Even in this administration, they have continued it and seemingly embraced it," Dreier says. "You almost can't fully allow yourself to believe it's actually happening after the journey it's been through."

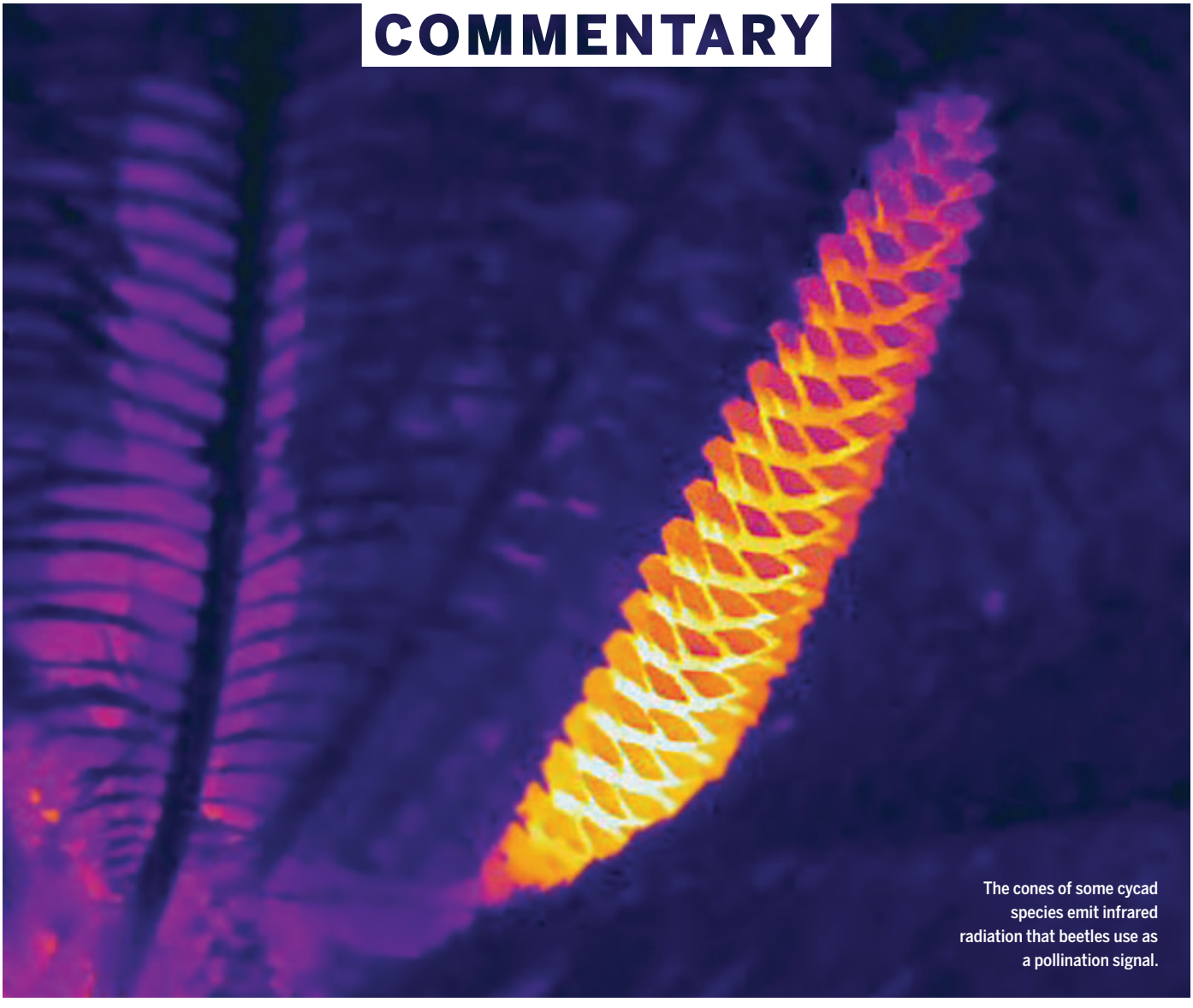
He sees it as a happy example of science-informed policy. Back in the 1990s, scientists presented Congress with compelling evidence about the threat of hidden asteroids. Congress legislated NASA to go find them, and NEO Surveyor is the culmination of that effort. "It's good that we can find things we can agree on," Mainzer says.

MIT's Binzel frames the consequences of this agreement more bluntly. If NEO Surveyor discovers a sizable asteroid heading our way, it "could be the most important contribution that planetary science has ever made to humanity."

At the end of my meeting with Mainzer, I wonder whether that immense responsibility weighs on her. Her team's work could contribute to saving millions of lives someday. Does she ever dwell on that?

"Let's put it this way: We'll be really happy if we can get it launched," she says. "The rest will work itself out." □

Robin George Andrews is a science journalist based in London.



The cones of some cycad species emit infrared radiation that beetles use as a pollination signal.

EVOLUTIONARY BIOLOGY

Infrared as a pollination signal

Relying on infrared communication over visual color could have limited cycad evolution

Beverley J. Glover and **Alex A. R. Webb**

Understanding the relationships between long-dead organisms is tricky. Flowering plants (angiosperms, a group within the seed plants) are pollinated by a wide diversity of animals, which use scent and color as long-range and mid- to short-range signals, respectively. But the fossil record indicates that other seed-plant lineages that arose earlier were also likely pollinated by insects, despite little evidence of color-based signaling. On page 1164 of this issue, Valencia-Montoya *et al.* (*1*) demonstrate that one of these earlier diverging seed-plant lineages, the cycads, use infrared radiation at dusk as a signal to attract beetle pollinators. In the beetle antennae, similar receptors to those used by predators, such as snakes, to detect prey allow the insects to find the cycads' thermogenic reproductive structures in the dark. This discovery explains ancient pollinator attraction and might also explain why some animal-pollinated groups diversified more than others.

Previous work has suggested that the earliest pollinating interactions likely involved heat as a reward and as a mechanism to enhance signaling through scent volatilization (*2*). Thermogenesis originated at least 200 million years ago, long before the angiosperms (*2*), and recent studies converge on an origin of insect pollination at least 163 million years ago (*3*). Such studies imply that insect pollination was relatively common among seed-plant groups that were present before

PHOTO: WENDY A. VALENCIA MONTOYA, HARVARD UNIVERSITY

the rapid diversification (radiation) of the angiosperms. For example, a fossil of a fly with long tubular mouthparts was found associated with pollen of a member of the Bennettitales, an extinct group with flower-like structures (*4*). Insect pollination is therefore ancient and associated from its early origins with thermogenic plants.

Valencia-Montoya *et al*. focused on pollination of the cycads, a seed-plant group more closely related to conifers than to angiosperms, and considerably more ancient. Extant cycads are mostly found in the tropics and produce woody trunks, large leathery leaves, and reproductive structures that resemble large pine cones. The cones of some cycad species produce heat, presumably as a pollinator attractant. The authors demonstrated that cones from multiple cycad species in the genus *Zamia* are thermogenic. In field experiments, they observed that cones of male plants produce heat as night falls, with cones of female plants warming up 3 hours later. Valencia-Montoya *et al*. found that *Rhopalotria furfuracea*, the beetle pollinator of the cycad *Zamia furfuracea*, is attracted to the warm areas of cones, sequentially visiting males and then females. Using artificial cones covered in protective materials, the authors show that beetles respond to emitted infrared rather than sensing warmth through touch or convective heating. The results of subsequent electrophysiological, behavioral, and pharmacological experiments with *R. furfuracea* and a different cycad-pollinating beetle, *Pharaxonotha floridana,* strongly suggested that transient receptor potential ankyrin 1 (TRPA1), a cation channel expressed in antennal neurons of these beetles, is activated by infrared to generate neuronal signals that allow the beetle to detect warm cycad reproductive cones. TRPA1 receptors in animals regulate the activity of sensory neurons in response to different stimuli, including pain, cold, and chemicals such as mustard oils; in snakes they facilitate infrared sensing to detect prey.

...cones of male plants produce heat as night falls, with cones of female plants warming up 3 hours later.

The difference in timing of thermogenesis between male and female plants is intriguing, and Valencia-Montoya *et al*. suggest that it could be regulated by the internal 24-hour circadian clock. However, thermogenesis could also be directly regulated by daily light-dark and/or ambient temperature cycles. For example, in the sacred lotus (*Nelumbo nucifera*), which has rhythmic nocturnal heating, thermogenesis is a response to changing ambient temperature (*5*). Experiments in other cycad species, *Macrozamia lucida* and *Macrozamia macleayi*, in which the plants were kept in constant conditions or exposed to rhythmic temperature cycles, demonstrated that in those species, thermogenic activity occurs at a particular point in a ~24-hour cycle set by the circadian clock, but it is environmental signals that fix the clock to a precise 24-hour cycle and align it with the correct time of day (*6*).

If thermogenesis in cycad cones is directly regulated by the light-dark or temperature cycle, differences in sensitivity to these stimuli could result in female cones warming up 3 hours after those of the males. Alternatively, if thermogenesis is regulated by circadian clocks, this could be achieved by differences in the phasing of circadian rhythms between the male and female plants. Plant circadian clocks can be phased differently in different organs and tissues (*7*), as demonstrated by the circadian regulation of leaf movements, which can rely on the shrinking of certain cells and the swelling of other cells at the same point in the circadian cycle. Further work is needed to understand the mechanisms that drive these differences in phasing between tissues, including the cones of male and female cycads.

To explore whether color signaling might also be important in pollinator attraction to cycad cones, Valencia-Montoya *et al.* dissected the dichromatic color vision of *P. floridana* and demonstrated that cycad cones are achromatic to the beetle eye. Analyses of large-scale flower and cone-color datasets and the distribution of thermogenesis in a phylogenetic context revealed a negative correlation between heat production and color diversity, with the diversification of the angiosperms and their colorful flowers correlating with that of insect groups with trichromatic color vision, such as Hymenoptera and Lepidoptera. Taken together, these observations identify infrared as the pollinator-attracting signal in cycads, and not the colors that attract trichromatic insect groups to the flowering plants.

The rapid diversification of the angiosperms after their origin ~125 million years ago is attributed at least in part to the concomitant radiation of the insects (*8*). The angiosperm radiation was dramatic in speed and breadth, generating an extant 300,000 to 400,000 species (*9*). This is a marked contrast to the diversification rates of other plant groups, with the living cycads numbering ~375 species because of slower diversification through evolutionary time (*10*). Similarly, the Bennettitales, although present in the fossil record from 288 million to 65 million years ago, did not diversify beyond two families. How can the radiation of one plant group (the angiosperms) be a feature of an associated radiation of insect groups, whereas other plant groups (the cycads, the Bennettitales) established similar pollination relationships with inects but did not undergo adaptive radiation?

The discovery that cycad pollination is dependent on infrared perception for short- to mid-range signaling may provide the answer to this question. TRPA1 detects the presence of infrared radiation, which is a signal that can only vary in intensity. By contrast, the butterflies and bees that radiated with the angiosperms have trichromatic color vision: Color is perceived as the relative degree to which each of three photoreceptors is stimulated by the light reflected from a surface. This allows the perception of an almost infinite number of colors, according to the relative intensity of light of each wavelength reflected. And because the insect groups with which the angiosperms radiated can perceive an almost infinite number of colors, the niche space into which the angiosperms could radiate by varying the wavelengths reflected from their flowers was similarly vast.

Not only does color provide a greater diversity of signal niche space than infrared, it also opens up the opportunity for pollination by diurnal insects. Infrared is most easily detectable at night, largely limiting cycads to pollination by night-flying beetles. Angiosperms, by contrast, produce colors that are visible by sunlight and by moonlight, further increasing the temporal pollinator niche space available to them. Perhaps by evolving a signal only detectable by a single receptor carried by a nocturnal insect group, the insect-pollinated cycads limited their speciation opportunities—the moon dance between cycads and beetles may have destined the cycads for limited evolutionary radiation. □

REFERENCES AND NOTES

1. W. A. Valencia-Montoya *et al*., *Science* **390**, 1164 (2025).
2. D. Peris *et al*., *Nat. Plants* **10**, 1297 (2024).
3. C. Peña-Kairath *et al*., *Trends Ecol. Evol.* **38**, 749 (2023).
4. E. Peñalver *et al*., *Curr. Biol.* **25**, 1917 (2015).
5. R. Seymour, P. Schultze-Motel, I. Lamprecht, *J. Exp. Bot.* **49**, 1213 (1998).
6 R. B. Roemer, L. Irene Terry, D. T. Booth, G. H. Walter, *Am. J. Bot.* **109**, 151 (2022).
7. M. Endo, H. Shimizu, M. A. Nohales, T. Araki, S. A. Kay, *Nature* **515**, 7527 (2014).
8. D. Peris, F. L. Condamine, *Nat. Commun.* **15**, 552 (2024).
9. P. Soltis, R. Folk, D. Soltis, *Proc. R. Soc. London Ser. B* **286**, 20190099 (2019).
10. M. Coiro, L. J. Seyfullah, *Commun. Biol.* **7**, 328 (2024).

10.1126/science.aed3346

Department of Plant Sciences, University of Cambridge, Cambridge, UK.
Email: bjg26@cam.ac.uk; aarw2@cam.ac.uk

CANCER

Chromosome shattering in cancer

A protein that cuts double-stranded DNA contributes to chromosome scrambling in human cancer cells

Stanley Clarke and **Marcin Imieliński**

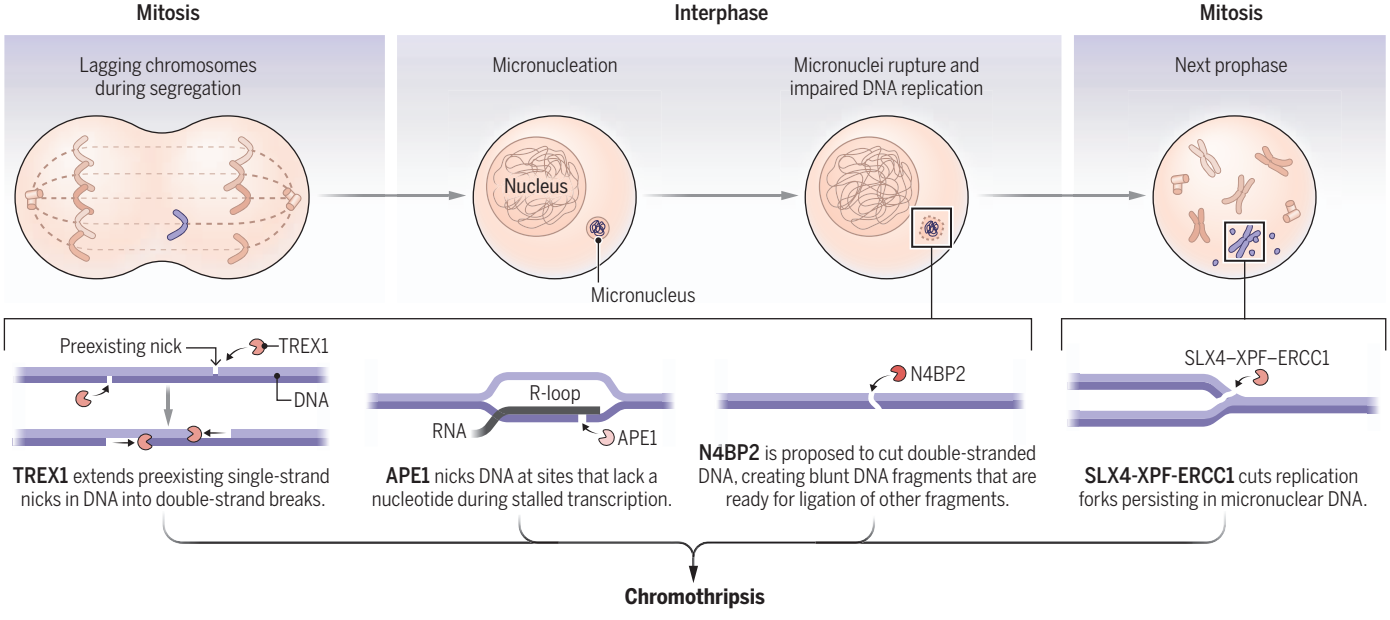
Cancer cells often contain an abnormal number of chromosomes as a result of incorrect chromosome segregation during cell division. These fragments of genetic material can be encapsulated by a membrane, forming small nucleus-like structures called micronuclei. These structures often rupture, exposing chromatin (DNA and associated proteins) to the harsh environment of the cytoplasm, which can lead to large-scale DNA damage in a process called chromothripsis, or chromosome shattering and scrambling. On page 1156 of this issue, Krupina *et al.* (*1*) report that the cytoplasmic protein NEDD4-binding protein 2 (N4BP2) may be responsible for chromothripsis.

Chromothripsis was identified through whole-genome sequencing (WGS) of human cancers in 2011 (*2*). Early studies of chronic lymphocytic leukemia (*2*) and pediatric brain cancer (*3*) revealed densely clustered rearrangements and variable copy numbers of genomic segments within single chromosomes. These observations implied that a catastrophic cellular event had created a massively scrambled chromosome in which tumor-suppressor gene losses or cancer-promoting gene fusions had taken place. For this to happen, tens to hundreds of double-strand breaks (DSBs) in DNA must have been generated, creating fragments that were then rearranged and rejoined by the DNA repair machinery of the cell. Later studies indicated that structures that form after abnormal cell division, either micronuclei (*4*) or chromatin bridges (*5*)—membranes that link daughter cells when chromosomes fuse—are implicated in this process.

A fundamental question since these discoveries has been to understand how chromosomes trapped in these aberrant cellular structures actually shatter (see the figure). Three-prime repair exonuclease 1 (TREX1), a cytoplasmic nuclease enzyme, accesses chromatin bridges or ruptured micronuclei and extends preexisting single-strand nicks in DNA into DSBs (*5*). A complementary mechanism involves the abnormal activity of the DNA repair enzyme DNA–(apurinic or apyrimidinic site) endonuclease 1 (APE1), which nicks DNA at abasic sites (DNA sites that lack a nucleotide base but where the sugar-phosphate

Slicing and dicing chromosomes

Chromosome fragments resulting from incorrect segregation during cell division (mitosis) in cancer cells can be encapsulated by a membrane, forming micronuclei. Between cell divisions, in the interphase period, micronuclei can rupture. Endonuclease enzymes in the cytoplasm cut DNA into fragments that can then ligate other fragments. This process of shattering and scrambling chromosomes, called chromothripsis, can cause cancer-promoting DNA rearrangements.



APE1, DNA-(apurinic or apyrimidinic site) endonuclease; N4BP2, NEDD4-binding protein 2; SLX4-XPF-ERCC1 complex, also called Fanconi–SLX4–XPF complex, formed by three proteins: structure-specific endonuclease subunit SLX4, DNA repair endonuclease XPF, and DNA excision repair protein ERCC-1; TREX1, three-prime repair exonuclease 1.

GRAPHIC: N. BURGESS/*SCIENCE*

backbone of DNA is still present) generated through defective transcription in micronuclei (*6*). Some chromothriptic breaks may not occur until the following cell division, when replication forks persisting in micronuclear DNA are cut by the SLX4–XPF–ERCC1 protein complex (also called Fanconi–SLX4–XPF complex, formed by three proteins: structure-specific endonuclease subunit SLX4, DNA repair endonuclease XPF, and DNA excision repair protein ERCC-1) (*7*).

Krupina *et al*. systematically inhibited the individual activity of hundreds of cytoplasmic nuclease enzymes for their role in micronuclear DNA damage using a human cancer cell line engineered to missegregate chromosome Y. Inhibition of the poorly characterized endonuclease N4BP2 greatly reduced the accumulation of histone γH2AX (a marker of DSBs) and Y-chromosome fragmentation in the cells. N4BP2 localized to ruptured micronuclei and chromatin bridges, and expression of N4BP2 in the nucleus, where the enzyme is not normally found, produced widespread DNA damage. Overexpression of N4BP2 caused chromothripsis-like genomic rearrangements, as detected by WGS of cells in which micronuclei had been created. The authors also made these observations in several nonengineered cancer cell lines.

...the hallmark of chromothripsis is a scrambled chromosome, which requires ligation of shattered DNA fragments...

How does N4BP2-mediated chromothripsis fit with previously proposed models? Earlier proposed mechanisms of chromothripsis all require additional events to shatter chromosomes, upstream and downstream of cytoplasmic endonuclease activity. These include preexisting DNA damage to create or extend single-strand DNA breaks (also known as nicks) or additional downstream steps to convert nicks into ligation-ready DSBs (for example, through collapse of DNA replication forks at nicks, which eliminates single-stranded overhangs at the ends of the DNA molecule). Notably, deletion of TREX1 or APE1 did not substantially affect DSB formation in the cells studied by Krupina *et al*. A cytoplasmic endonuclease that acts on undamaged DNA to create blunt DSBs, generating DNA fragments that are ready for ligation of other fragments in ruptured interphase micronuclei, is an attractively simple mechanism of chromosome shattering. Further biochemical characterization of N4BP2's substrates and products will be needed to determine whether N4BP2 indeed fits this role.

The most likely scenario is that there are multiple routes to chromosome shattering. Krupina *et al*.'s screen yielded numerous candidate proteins that could be involved in these processes in addition to N4BP2. Previous studies also showed residual chromosome fragmentation after deletion of TREX1, APE1, or SLX4–XPF–ERCC1 complex proteins (*5*–*7*), suggesting that multiple mechanisms may operate simultaneously. Furthermore, although Krupina *et al*. focused primarily on micronuclear DNA damage, the hallmark of chromothripsis is a scrambled chromosome, which requires ligation of shattered DNA fragments (*8*) to a centromere (the segment of a chromosome that allows it to be stably inherited in cells). Hence, the outcome of chromothripsis can only be rigorously verified by WGS. Understanding how these various pathways influence the frequency of WGS-confirmed chromothripsis in the same cellular system will help to define their interplay.

Which of the mechanisms that lead to chromosome shattering in experimental models are relevant for chromothripsis in human cancers is a key question. Krupina *et al*. analyzed thousands of human cancer genomes and found higher levels of N4BP2 expression in tumors with evidence of at least one chromothripsis event than in tumors without chromothripsis. This observation is striking, as WGS of tumor samples detects chromothripsis that occurred in the past, whereas transcript levels reflect a current cellular state. If high N4BP2 expression causes chromothripsis, these chromothripsis events may be much more widespread than the historical events detected by WGS. A mutational process that continuously shatters chromosomes in multiple generations of these cancer cells may be ongoing. N4BP2 is expressed at low levels across most human tissues (*9*), raising questions about its physiological role in normal cells and about the triggers that might increase its expression to levels that promote chromothripsis.

Ongoing chromothripsis may also be relevant to the formation of extrachromosomal circular DNA (ecDNA), which is implicated in gene amplification and drug resistance in cancer (*10*). DNA fragments generated by chromothripsis frequently circularize and become more numerous through random segregation and selection (*4*, *11*). Krupina *et al*. observed that N4BP2 (but not TREX1) promotes generation of ecDNA and formation of aggressive tumors in pluripotent stem cells genetically engineered to form gliomas in mice. This finding suggests that N4BP2 expression—and, more broadly, chromothripsis—may be evolutionarily selected to generate ecDNA that is oncogenic or promotes drug resistance.

Understanding how N4BP2 or other factors influence ongoing chromothripsis may require a deeper view of intratumoral genomic variation than is possible with current approaches. WGS of bulk tumor tissue can only detect chromothripsis events shared by a majority of cancer cells. However, chromosomes scrambled by ongoing chromothripsis may only be present in a few cells of the tumor. Mainstream single-cell WGS technologies still cannot reliably detect structural variants and copy-number changes of DNA at the level of detail required to routinely detect chromothripsis (*12*).

Making these links explicitly in human tumors may require approaches that combine scalable, high-resolution single-cell WGS with simultaneous gene and protein expression or epigenomic analyses. Recent order-of-magnitude drops in sequencing costs and innovations in the preparation of single-cell libraries have paved the way for cutting-edge technologies, including Smart-PTA (*13*) and dATAC (*14*), that can make these measurements across hundreds or thousands of human cancer cells. Such tools will be essential to rigorously assess the relevance of the mechanistic insights that are emerging from the chromosomal instability field for human cancer (*15*). These insights span the biology of mitotic aberrations, nuclear-envelope integrity, cytoplasmic DNA sensing, and ecDNA biogenesis, and have all been sparked by the discovery of chromothripsis over a decade ago. □

REFERENCES AND NOTES

1. K. Krupina *et al*., *Science* **390**, 1156 (2025).
2. P. J. Stephens *et al*., *Cell* **144**, 27 (2011).
3. T. Rausch *et al*., *Cell* **148**, 59 (2012).
4. C.-Z. Zhang *et al*., *Nature* **522**, 179 (2015).
5. J. Maciejowski, Y. Li, N. Bosco, P. J. Campbell, T. de Lange, *Cell* **163**, 1641 (2015).
6. S. Tang, E. Stokasimov, Y. Cui, D. Pellman, *Nature* **606**, 930 (2022).
7. J. L. Engel *et al*., *Cell* **187**, 6055 (2024).
8. Q. Hu *et al*., *Nat. Commun.* **15**, 5611 (2024).
9. GTEx Consortium, *Science* **369**, 1318 (2020).
10. X. Yan, P. Mischel, H. Chang, *Nat. Rev. Cancer* **24**, 261 (2024).
11. O. Shoshani *et al*., *Nature* **591**, 137 (2021).
12. D. D. Shao *et al*., *Nat. Rev. Genet.* **26**, 761 (2025).
13. T. Prieto *et al*., *bioRxiv* 10.1101/2025.10.11.681805 (2025).
14. M. Mossner *et al*., *bioRxiv* 10.1101/2025.04.15.648959v1 (2025).
15. X. Chen, A. S. Agustinus, J. Li, M. DiBona, S. F. Bakhoum, *Nat. Rev. Genet.* **26**, 31 (2025).

10.1126/science.aed1825

Perlmutter Cancer Center, NYU Langone Health, New York, NY, USA.
Email: marcin.imielinski@nyulangone.org

MATERIALS SCIENCE

Invisible heat insulators

A nanotube network with precisely engineered pores could replace insulating components in windows

Longnan Li and **Wei Li**

Windows are among the least energy-efficient components of a building. They occupy a small fraction of the exterior but leak nearly half of the heating and cooling energy from the interior (*1*). Conventional solutions such as double glazing and low-emissivity coatings are mechanically robust and optically transparent, yet their thermal insulation performance is limited (*2*). Modern technologies such as silica and cellulose aerogels (a porous material filled with gas) could achieve better heat insulation. However, their optical haze, fragility, and limited scalability continue to hinder widespread adoption (*3*, *4*). On page 1171 of this issue, Bhardwaj *et al.* (*5*) report an optically transparent heat insulator that is built from self-assembled polysiloxane nanotube networks. The material transmits >99% of visible light while conducting heat more poorly than the surrounding still air. This could be used to make clear windows with thermal insulation that is comparable with that of building walls.

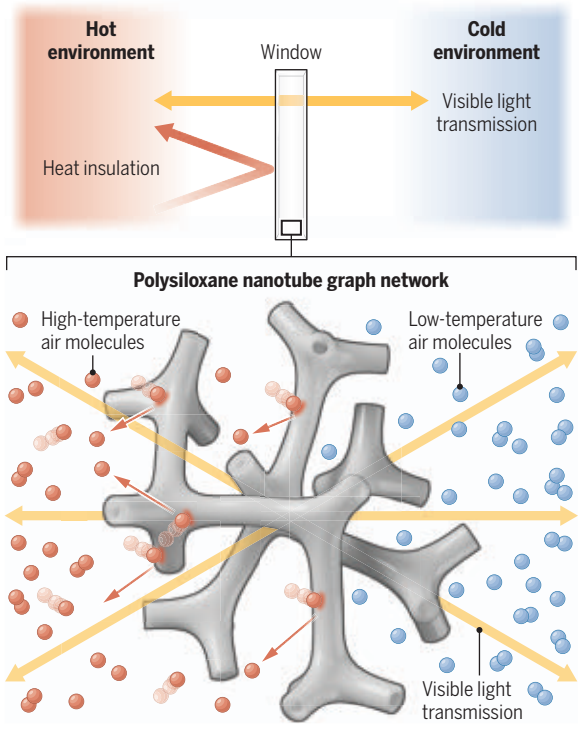
Heat insulation and optical transparency rarely coexist. Heat transport through a solid can be suppressed by scattering phonons (quasiparticles of vibrational energy in a crystal lattice), increasing thermal resistance at an interface, or introducing microscopic pores. However, these mechanisms often scatter visible light, resulting in haze (*4*, *6*). Aerogels were once considered a potential window material with light weight and low thermal conductivity (*7*). But the inherent large variations in pore size and morphology caused haze by scattering light in all directions as well as structural weakness. These effects prevented the large-scale integration of aerogels for window applications (*2*). Overcoming the fundamental coupling between optical and thermal transport requires precise control of the structure across length scales (from nanometers to centimeters) while maintaining chemical and mechanical stabilities under operating conditions.

Bhardwaj *et al.* used a self-templating approach in which surfactant molecules assemble into interconnected networks of cylindrical micelles (tiny clusters of molecules with both water-loving and water-repelling properties) and guide the formation of polysiloxane precursors. This produced a structure with two distinct, interpenetrating networks of polysiloxane tubes. All characteristic dimensions (nanotube diameter, wall thickness, and pore sizes) of the polysiloxane nanotubes were less than 50 nm, which is smaller than the wavelength of visible light and the mean free path (an average distance that a particle can travel without collision) of air molecules (see the figure). This architecture simultaneously suppressed scattering of light waves by spherical particles (Mie scattering) and heat conduction, enabling a visible light transparency that exceeds 99% and ultralow thermal conductivity (10 mW $m^{-1} K^{-1}$) less than that of still air. When used as a filler between two glass window panes, the material exhibited a thermal resistance of 2.64 $m^2 K W^{-1}$, which is comparable with that of wall insulation, but at a thickness that is thinner than conventional double-pane glass windows.

Beyond the exceptional performance and compatibility with existing windows, Bhardwaj *et al.* generated square-meter films and centimeter-thick slabs of the polysiloxane networks by carefully balancing solvent exchange and supercritical drying conditions to preserve the pore geometry and prevent structural collapse. Notably, the near-unity refractive index (n; the measurements of how much light bends when passing an interface) of the porous material ($n \approx 1.03$) in air eliminated loss of light from reflection (<0.02%). As a result, the polysiloxane slabs appear optically invisible even when the light hits them at very shallow angles. In contrast to conventional aerogels, multiple polysiloxane networks could be assembled into a large window panel without an optical discontinuity.

Mesoporous optically clear heat insulator

Interpenetrating networks of polysiloxane nanotubes create a structure with uniform pore size and geometry. All characteristic dimensions of nanotubes are smaller than the wavelength of visible light and the average distance that an air molecule can travel without collision. This allows >99% of visible light to transmit through the material while blocking heat transport from one side to another.



GRAPHIC: A. FISHER/*SCIENCE*

The concept presented by Bhardwaj *et al.* represents a transition from conventional aerogels with random pore structures to metamaterials that are engineered with ordered nanoscale structures and govern macroscale thermal and optical performance simultaneously. From an energy and economic standpoint, the potential impact of the polysiloxane metamaterial is substantial. Buildings consume nearly 40% of global energy and account for about one-third of global greenhouse gas emissions (*1*). A moderate improvement in window insulation can cut the global carbon dioxide emissions by hundreds of megatons each year (*1*). The observed mechanical and chemical stabilities of the polysiloxane networks over 20 years of exposure to heat and humidity cycling, which were determined with accelerated durability tests, suggest that the strategy of Bhardwaj *et al.* can match or exceed the lifetime of commercial insulating windows. In addition, the authors used technoeconomic modeling to show that large-scale production of the material could deliver 3-mm-thick sheets at roughly $25 per square meter and about $50 per square meter when used as a filler between two glass window panes. These costs are competitive

with high-performance systems such as silica aerogels, silanized cellulose aerogels, and vacuum-insulated glazes. Although the initial costs may exceed those of standard single-pane windows, simulations predicted $1000 to $4000 in annual household energy savings depending on climate, which could pay back the differential cost within a few years.

Equally compelling is the potential for functional integration. Because the refractive index of the polysiloxane networks nearly matches that of air, the material could host an optical or photovoltaic layer without unwanted light reflection. Combining with an additional layer such as a thermo-, mechano-, or electrochromic coating, liquid crystal films or switchable infrared films could enable smart windows that autonomously regulate daylight, transparency, and heat flow (*8*, *9*). Furthermore, the ability to trap infrared light while transmitting visible light opens a pathway to passive solar heating and energy-generating facades that reduce greenhouse gas emissions. The approach of Bhardwaj *et al*. may represent a new class of architectural material that actively manages energy instead of merely conserving it.

A key challenge is translating the self-assembly process into a scalable method such as ambient pressure drying or roll-to-roll manufacturing (*10*). This would enable mass production without sacrificing nanoscale precision. Extending similar structural control to other materials such as polymers, ceramics, and composites could further tune how much light and heat they transmit, reflect, or emit and improve mechanical resilience. Incorporating functional materials may also allow dynamic switching between different modes (heating and cooling), directional regulation of heat flow, and even simultaneous power generation with integrated high-power-density energy storage systems (*11*–*14*). In the coming decade, metamaterials may transform optically transparent planes (such as windows, skylights, and textiles) into intelligent, energy-managing surfaces and contribute to the low-carbon built environment. □

REFERENCES AND NOTES

1. C. Harris, "Pathway to zero energy windows," no. NREL/TP-5500-80171 (US Department of Energy, 2022).
2. K. Khaled, U. Berardi, *Energy Build.* **244**, 111022 (2021).
3. L. Zhao *et al*., *ACS Nano* **13**, 7508 (2019).
4. E. Abraham *et al*., *Nat. Energy* **8**, 381 (2023).
5. A. Bhardwaj *et al*., *Science* **390**, 1171 (2025)
6. R. Yalcin *et al*., *APL Photonics* **10**, 046103 (2025).
7. M. Wu *et al*., *Science* **382**, 1379 (2023).
8. S. Wang *et al*., *Science* **374**, 1501 (2021).
9. Y. Ke *et al*., *Adv. Energy Mater.* **9**, 1902066 (2019).
10. K. Lin *et al*., *eLight.* **3**, 22 (2023)
11. S. Fan, W. Li, *Nat. Photonics* **16**, 182 (2022).
12. F. Xie *et al*., *Science* **386**, 788 (2024).
13. Q. Zhang *et al*., *Adv. Energy Mater.* **11**, 2101213 (2021).
14. Y. Zhou *et al*., *Joule* **4**, 2458 (2020).

ACKNOWLEDGMENTS

The authors acknowledge support from the National Natural Science Foundation of China (grants T2525033, 62134009, 62121005, and 62475261) and the New Cornerstone Science Foundation through the XPLORER PRIZE.

10.1126/science.aed1907

GPL Photonics Laboratory, State Key Laboratory of Luminescence Science and Technology, Changchun Institute of Optics, Fine Mechanics and Physics, Chinese Academy of Sciences, Changchun, China. Email: weili1@ciomp.ac.cn

GEOCHEMISTRY

Deep mantle clues to Earth's watery beginning

Minerals in the lower mantle may store more water than previously estimated

Michael Walter

Earth's ocean makes the planet habitable by regulating the climate and sustaining the water and nutrient cycles that support life. This life-essential body of water is believed to have formed early, nearly 4.4 billion years ago. The mantle crystallized from a magma ocean, a mass of molten rock with dissolved water that covered the planet during its formation. The crystallization expelled most of the water to the surface, but a small fraction was held in the solidified mantle. The mineral bridgmanite is key for understanding early water distribution. On page 1177 of this issue, Lu *et al*. (*1*) report an increase in the partitioning of water into bridgmanite with increasing temperature, suggesting that the amount of water dissolved into the rock was more substantial when the hot magma ocean crystallized than previously thought (*2*). This finding is important for understanding the initial water distribution on early Earth.

Earth formed through the accretion of dust, pebbles, boulders, and planetesimals (small objects of dust, rock, and other materials) that accumulated under the influence of gravity. During this process, countless impacts among progressively larger objects deposited a large amount of kinetic energy on the planet, which converted into heat and triggered the melting of its mantle (the rocky silicate layer between the surface crust and the metallic core). It may be that late in the growth process, a Mars-sized object called Theia collided with Earth, promoting the widespread melting of rocks. These events created a global magma ocean that may have extended from Earth's surface to the base of the mantle.

Water is highly soluble in molten silicate rocks at high pressures and temperatures inside the mantle. As the hot magma ocean cooled from more than 5000 K to below 3000 K, water partitioned between the silicate melt and the crystallizing minerals, which largely determined the initial distribution of water between Earth's mantle and surface reservoirs. Bridgmanite, which is a magnesium-iron silicate mineral, is stable as a solid phase under the extreme conditions of the lower mantle (670 to 2890 km below Earth's surface) and makes up roughly 60% of the entire mantle. Measuring the water-holding capacity of bridgmanite in an environment that is similar to that of primordial Earth is important for understanding early water distribution. However, previous measurements of how water partitions into bridgmanite are highly variable.

Lu *et al*. measured the amount of water that bridgmanite can hold relative to silicate melt and calculated a partition coefficient, the ratio of water concentrations between the two phases at equilibrium. The authors recreated the intense conditions of a deep magma ocean by using a laser-heated diamond anvil cell, a small device that can compress samples to high pressures (up to about 700,000 atm in this study) under temperatures higher than 4000 K. Silicate glass containing various amounts of water was melted under these extreme conditions, then quenched to room temperature quickly. This created samples with a pocket of "frozen" silicate melt surrounded by solid bridgmanite crystals. Lu *et al*. performed nanoscale secondary ion mass spectrometry to probe the amount of water in solid bridgmanite and quenched silicate melt at submicron spatial resolution. Crystallized bridgmanite contained a few hun-

dred to nearly 2000 parts per million (ppm) of water. By contrast, the silicate melt contained several thousand to more than 60,000 ppm of water. The results confirmed that water in bridgmanite was genuinely part of the mineral's structure and not from micron-scale hydrous minerals or other contamination (*2*), which may have been a problem in some previous measurements.

The partitioning of water between bridgmanite and silicate melt did not depend on the applied pressure or the original water content. Rather, it varied substantially with temperature. At higher temperatures, bridgmanite incorporated progressively larger amounts of water relative to the melt. Lu *et al*. derived a mathematical relationship that describes the scaling of water partitioning with respect to temperature. Although this model matched some previous experimental results, much of the existing data do not follow the relationship. This highlights the large discrepancy in previous measurements, which has clouded the understanding of Earth's early water distribution.

...water solubility in bridgmanite and other mantle minerals... remains essential for assessing the deep-Earth water cycle.

Based on the new partitioning data, Lu *et al*. modeled how water may have been retained in the lower mantle during cooling and crystallization of the magma ocean. The authors considered a relatively wide range (1 to 12) of ocean masses of water on primordial Earth (1 ocean mass = 1.4×10^{21} kg of water). By making the reasonable assumption that rapid convection in the magma ocean maintains a homogeneous magma ocean, and ignoring the amount of water that escaped to the surface or partitioned into the core, two magma ocean crystallization scenarios were proposed: a bottom-up model in which the molten mantle crystallizes from the base layer to the top layer of mantle and a middle-out model where crystallization starts at an intermediate depth of the molten mantle and then expands outward.

The crystallization models of Lu *et al*. indicated that as the magma ocean cooled, water gradually became more concentrated in the silicate melt. At the same time, substantial amounts remained in the crystallizing bridgmanite. Owing to the higher temperatures at the base of the mantle and the potential segregation of dense melt to form a basal magma ocean with increasing water contents, Lu *et al*. suggested that bridgmanite crystallizing near the base of Earth's mantle may have held considerably more water than previously estimated (*2*), perhaps a hundred times more. The trapped water could potentially serve as an important long-term water reservoir after solidification.

Residual silicate melts at the top of the crystallizing mantle may have released water in hydrous gases, forming the earliest surface ocean. A rapidly convecting, hot mantle in the Hadean eon (more than 4 billion years ago) may also have facilitated expulsion of any remaining water-containing silicate melts to Earth's surface. Four billion years of subsequent mantle convection and plate tectonics have further reshaped both the amount and distribution of water in the mantle and at the surface (*3*). Nonetheless, some remnant of this deep, water-rich primordial reservoir at the base of the mantle may still exist today (*4*). This could contribute to the increased water content and the distinct hydrogen and helium isotope signatures in some present-day magmas that erupt on the ocean floor and tap the deepest, perhaps primordial, mantle sources such as ocean island basalts (*5*).

The solidified Hadean mantle was hotter than the modern mantle, possibly by more than 300 K. A previous study suggests that as the mantle cools, its solid minerals can contain increasing amounts of water before reaching the saturation point, which can lead to partial melting of the mantle (*6*). This implies that the present-day solid mantle has a greater capacity to store water than the primordial mantle. Theoretically, the Hadean mantle could hold a maximum of about 0.5 to 1.5 ocean masses, whereas the modern mantle may store as much as four or more ocean masses (*6*).

Although still debated, geochemical evidence indicates that the modern mantle holds about one ocean mass of water (*7*). Adding the amount of surface water gives roughly two ocean masses of water. If all water originated from the magma ocean, any water exceeding the Hadean mantle storage capacity would have been released to the surface after the mantle had fully solidified (*6*). This suggests that the present amount of surface water is approximately the same as that of the Archean eon (4 billion to 2.5 billion years ago), with a variance of half an ocean mass. The estimate aligns with the predicted steadiness of the average elevation of continental land above sea level since at least the Archean (*8*).

Earth's mantle is not static but has undergone dynamic overturn by convection since it solidified, and modern plate tectonics may have been active for at least 3 billion years (*9*). On the planetary surface, tectonic plates beneath the ocean become variably hydrated, and subduction (a process in which one tectonic plate submerges beneath another at the plate boundary) returns these plates to the mantle. Most of the subducted water returns to the surface through a shallow-water cycle, which involves mantle melting and volcanism that are the result of dehydration of the subducted plate. However, estimates suggest that some water is returned to the deep mantle by subduction at a rate of about one ocean mass every 4 billion years (*10*). If the mantle is undersaturated with water, as indicated by its present low water content and greater water storage capacity, then surface water is progressively being added to the mantle, potentially leading to desiccation of the surface in another 4 billion years—a slow conversion of a water world into a desert world.

A deeper understanding of water solubility in bridgmanite and other mantle minerals as a function of pressure, temperature, and composition remains essential for assessing the deep-Earth water cycle. Equally critical are establishing tight constraints on the present-day water content of the mantle and evaluating the amount of water dissolved in the core. This information is required to determine Earth's bulk water inventory, which remains largely unknown. The findings of Lu *et al.* add another vital piece to an intricate and multifaceted puzzle. Further experiments under the extreme conditions of the deep mantle on a range of mineral and melt compositions, complemented by theoretical simulations, are needed to understand and quantify the mechanisms by which water is incorporated into the deepest mantle minerals. □

REFERENCES AND NOTES

1. W. Lu *et al*., *Science* **390**, 1177 (2025).
2. W. R. Panero, J. S. Pigott, D. M. Reaman, J. E. Kabbes, Z. Liu, *J. Geophys. Res. Solid Earth* **120**, 894 (2015).
3. J. W. E. Drewitt, M. J. Walter, J. P. Brodholt, J. M. R. Muir, O. T. Lord, *Earth Planet. Sci. Lett.* **581**, 117408 (2022).
4. K. Chotalia, J. Brodholt, C. Lithgow-Bertelloni, *Geology* **51**, 890 (2023).
5. M. W. Loewen, D. W. Graham, I. N. Bindeman, J. E. Lupton, M. O. Garcia, *Earth Planet. Sci. Lett.* **508**, 62 (2019).
6. J. J. Dong *et al*., *AGU Adv.* **2**, e2020AV000323 (2021).
7. M. M. Hirschmann, *Earth Planet. Sci. Lett.* **502**, 262 (2018).
8. J. Korenaga, *Life* **11**, 1142 (2021).
9. R. M. Palin *et al*., *Earth Sci. Rev.* **207**, 103172 (2020).
10. P. E. van Keken *et al*., *J. Geophys. Res. Solid Earth* **116**, B01401 (2011).

10.1126/science.aed3351

Earth and Planets Laboratory, Carnegie Science, Washington, DC, USA.
Email: mwalter@carnegiescience.edu



BOOKS ET AL.

NEUROSCIENCE

Dealing with distressing dreams

A sleep scientist offers hope for nightmare sufferers **Jaime Herndon**



Michelle Carr
Henry Holt, 2025.
272 pp.

NIGHTMARE OBSCURA | Fewer than one-third of patients report nightmares to their clinicians, and most health care professionals never even ask patients about nightmares, much less know how to treat them. But chronic nightmares can have devastating effects on a person's mental and physical health. Dream researcher and sleep scientist Michelle Carr's new book, *Nightmare Obscura: A Dream Engineer's Guide Through the Sleeping Mind*, aims to help readers actively engage with their dreams, break free from nightmares, and develop more agency when it comes to the sleep experience.

Carr is the director of the Dream Engineering Laboratory at the Center for Advanced Research in Sleep Medicine in Montreal. While her goal for the book appears, at least in part, to be to make her own research accessible to the public, she covers a broad scope of sleep health. *Nightmare Obscura* focuses on the science behind nightmares and the available treatments for those who suffer from them as well as new interventions that aim to work with the sleeping brain to ease distressing dreams. It is broken down into four parts: the science of dreaming and the types of memories, emotions, and actions that play out in dream content; the experience of dreaming; how one can work with nightmares for better sleep; and what dreams can tell us about our sleep and mental health.

It is common knowledge now that sleep is important for good health, focus, and mental sharpness. But while there is a growing awareness of how nightmares can affect a person's health, the expertise required to treat them is not as widespread as it should be. "Most clinicians do not yet have the tools to help patients, given that there is a lack of sleep and nightmare training in medical school," writes Carr. "Such training would be highly valuable, since nightmares are linked to all manner of mental health disorders and to the severity of symptoms in these disorders, too."

Indeed, as Carr explains, nightmares are prevalent in people with posttraumatic stress disorder and are associated with anxiety, depression, and suicide risk. They have been found to predict increases in psychosis symptoms, and dream changes can precede suicidal thoughts and behavior. Physical health is not excluded either: Dreaming has been associated with physical health "during pregnancy, after physical trauma, in autoimmune disease, and even at the end of life," notes Carr.

Nightmare disorder, Carr reveals, originates from a recurring pattern of emotional dysregulation. People living with nightmare disorder often find it hard to control their negative thoughts and/or emotions, and so an important component of treating nightmares is to break the cycle of dysregulation. Carr outlines steps one can take to do so, including using waking imagination to rewrite nightmares and fostering favorable conditions for lucid dreaming. A third treatment—one she studies as part of her research program—is a technique she calls "dream engineering," which is "designed to modulate dreams by stimulating the sleeping brain and body." Building on the fact that when one dreams, the brain can react to outside stimuli such as a door slamming, this treatment uses sensory cues such as lights, sounds, touch, or vibration to cause sensations that Carr's team has found can help create better dreams.

Carr presents these treatments confidently, but it is ultimately not clear how accepted or successful they are, nor is it obvious what risks individuals might face while attempting to treat their own sleep disturbances. Research is still being conducted on many of the topics discussed in the book, and our scientific understanding of dreaming is fairly new and ever-evolving.

Nightmare Obscura is nonetheless a welcome conversation starter for those living with distressing dreams and those who care for them. And Carr makes a convincing argument that treating sleep disturbances, including nightmare disorder, is crucial to comprehensive health care. □

10.1126/science.aec5999

The reviewer is a freelance science writer based on the East Coast of the United States.
Email: jaime.rochelle@gmail.com

ILLUSTRATION: MALTE MUELLER VIA GETTY IMAGES

SOCIAL SCIENCE

The statusocratic dilemma

An organizational theorist probes the hidden drivers of social power

Sorin M. S. Krammer



Toby Stuart
Simon & Schuster, 2025. 288 pp.

ANOINTED | When Dogecoin, a cryptocurrency launched as a joke, soared to a market capitalization of tens of billions on the back of celebrity tweets and viral memes, it crystallized a truth about our "statusocratic" markets: Intrinsic value is far less important than who vouches for you. This, argues Toby Stuart in *Anointed*, is not an aberration but rather a fundamental principle of organizing contemporary societies.

Stuart builds his theory on what he dubs the "Other Uncertainty Principle": In a world saturated with choices, people lack time to evaluate quality directly. Instead, they use status shortcuts to make decisions about which schools to attend, which candidates to vote for, and which experts to believe. This substitution has the appeal of reducing cognitive loads and conflicts, but it also skews the distribution of opportunities and resources in ways that amplify entrenched inequalities.

The book's analytical architecture rests on three conceptual mechanisms. First, the "Big Shift" occurs when judgments pivot from intrinsic qualities to affiliative pedigree—we assess the wine by the château, the research by the university, the company by its venture backers. Second, categorization conflates competences: People quickly slot others into social groups and reflexively project group-level expectations onto them, thereby perpetuating systematic biases (*1*). Third, "anointers"—for example, critics, committees, pundits, influencers—translate ambiguity into legible signals, rerouting opportunities and importing their own prejudices into the resource allocation process.

Stuart documents these dynamics across various domains, demonstrating how status systems solve coordination problems: Fashion standards emerge when elite signals create shared awareness; deference norms make social interactions smoother, help allocate resources efficiently, and reduce conflicts in groups by designating specific roles to their members. Yet anointment also entrenches inequality, crowds out promising alternatives, and institutionalizes errors.

Anointers such as wine critics, academic prize committees, university ranking bodies, and celebrity endorsers all wield extraordinary power: A favorable review skyrockets sales, a prestigious award reshapes careers, an influential endorsement redirects capital (*2*). However, their authority is becoming more fragile and contentious in an increasingly fluid, competitive, and polarized world. Experts disagree, committees seek narrow interests, metrics invite gaming, and homophily limits which talent becomes prominent.

Initial leads, often small and arbitrary, become self-reinforcing over time...

Stuart pays special attention to cumulative advantage, commonly referred to as the Matthew effect (*3*). Initial leads, often small and arbitrary, become self-reinforcing over time: Status attracts more funds, larger audiences, and superior resources that genuinely improve quality while perversely legitimizing the early advantage. Network effects and digital platforms further amplify these effects and produce winner-take-most distributions across science, art, music, technology, and urban development (*4*–*6*).

Despite its ubiquitous benefits, status is frequently double-edged. The anointed gain resources and deference but face constrained experimentation and considerable pressure to protect their reputations rather than pursue riskier but higher-payoff innovations. Apex positions create perverse incentives (e.g., conformity, self-protection, lower accountability) that can stifle creativity and cause organizational failures (*7*).

Glossy narratives, curated proofs, and celebrity backers allow some to "fake it till they make it," fueling credibility arms races and porous competitions where style trumps substance. This raises barriers for talented outsiders lacking social capital and exposes systems to major waste when the bridge between real capabilities and allocation collapses. In science, this manifests in a multifaceted reward system where symbolic capital (e.g., networks and social media visibility) is increasingly shaping academic trajectories despite inherent limitations and often in contradiction to traditional research metrics (*8*).

Stuart's verdict is sober: Anointment is an efficient and likely unavoidable human adaptation that makes social life easier to navigate, but its benefits are inseparable from profound distributional harms. The book offers no easy solutions because none exist—but it highlights a hidden yet critical coordination mechanism of our society. In an era of digital platforms that amplify status-based rewards to unprecedented scale, a better understanding of these phenomena is essential. □

REFERENCES AND NOTES

1. D. Melamed *et al.*, *Am. Soc. Rev.* **84**, 1013 (2019).
2. T. E. Stuart, H. Hoang, R. C. Hybels, *Adm. Sci. Q.* **44**, 315 (1999).
3. R. K. Merton, *Science* **159**, 56 (1968).
4. W. Y. Lee, *Adm. Sci. Q.* **69**, 881 (2024).
5. S. M. S. Krammer, P. Dahlin, *Acad. Manag. Learn. Educ.* **23**, 214 (2024).
6. T. Yogev, *Socio-Econ. Rev.* **8**, 511 (2010).
7. C. M. Christensen, *The Innovator's Dilemma: When New Technologies Cause Great Firms to Fail* (Harvard Business Review Press, 1997).
8. N. Hall, *Genome Biol.* **15**, 424 (2014).

10.1126/science.aed3596

The reviewer is at the University of Southampton Business School, University of Southampton, Southampton, UK. Email: s.krammer@soton.ac.uk



The US Marine Mammal Protection Act and the Endangered Species Act have effectively protected marine life, including humpback whales, for 50 years.

PHOTO: MATTHEW LESLIE, *PANACETACEA*

Landmark marine mammal laws under threat

In the 1970s, the US Congress passed two landmark wildlife protection laws, the Marine Mammal Protection Act (MMPA) and the Endangered Species Act (ESA), with strong public support and bipartisan backing (*1*). For more than 50 years, the MMPA and the ESA have protected iconic species such as dolphins, whales, manatees, pinnipeds, sea otters, and polar bears by banning commercial hunting and mitigating threats from fishing, vessel strikes, and industrial activities. As of 2017, 91.3% of marine mammal populations listed under the ESA were either recovering (78.3%) or stable (13%) (*2*). However, recent US legislative and executive actions threaten the laws' success. Scientists should demand that the US Congress preserve the integrity of the MMPA and ESA.

Between 2023 and 2025, the 118th US Congress introduced multiple bills and amendments aimed at weakening core marine mammal protections. Proposed policies sought to block measures reducing vessel strikes on endangered whales (*3*), to delay or prevent critical habitat designations under the ESA (*4*), and to exempt industry from MMPA provisions that govern the management of harm to marine mammals (*5*). In 2025, the 119th Congress proposed multiple rollbacks, including programmatic amendments that weaken both statutes (*6*).

Recent administrative actions are further eroding marine mammal protections and essential scientific programs. Mass firings at the National Oceanic and Atmospheric Administration (NOAA) have removed experts nationwide (*7*). Staff with a cumulative 27,000 years of experience left the agency in April, choosing to take voluntary separation packages after threats of layoffs (*8*). Meanwhile, the Office of Management and Budget is proposing deep cuts to cooperative marine research programs between NOAA and universities (*8*). The Trump administration also recently proposed rules that substantially weaken the ESA, including allowing the inclusion of economic considerations into decisions to list endangered species and designate critical habitat for these species. ESA decisions should be based only on the best available science, as written in the Act (*9*).

These actions risk undoing decades of progress in US marine mammal conservation. That outcome becomes inevitable if the US Congress further weakens the MMPA and ESA. Whales and other marine mammals, sentient beings with complex societies and evidence of culture (*10*), sustain key marine ecosystems and ocean services (*11*). The MMPA and ESA ensure science-based decision-making that allows development to proceed while safeguarding vulnerable species. Weakening these laws would jeopardize recovery efforts and increase the risk of future endangerment and extinction, especially given the potentially devastating impacts of climate change on these species and their habitats (*12*). Removing protections also directly hinders the whale watch industry and ecosystem services that fuel the blue economy. Preventing Congress and the Trump administration from undermining the MMPA and ESA preserves ocean health, supports coastal communities and economies, and ensures effective stewardship of marine biodiversity.

Matthew S. Leslie[1], Joe Roman[2], Christian Sonne[3]

[1]Department of Biology, Ursinus College, Collegeville, PA, USA. [2]Gund Institute for Environment, University of Vermont, Burington, VT, USA. [3]Department of Ecoscience, Aarhus University, Roskilde, Denmark. Email: mleslie@ursinus.edu

REFERENCES AND NOTES

1. J. Roman *et al.*, *Ann. N. Y. Acad. Sci.* **1286**, 29 (2013).
2. A. Valdivia *et al.*, *PLOS ONE* **14**, e0210164 (2019).
3. 118th Congress, H.R.4323 (2023); https://www.congress.gov/bill/118th-congress/house-bill/4323/all-actions.
4. 118th Congress, H.R.6008 (2023); https://www.congress.gov/bill/118th-congress/house-bill/6008/text.
5. 118th Congress, H.R.1 (2023); https://www.congress.gov/bill/118th-congress/house-bill/1/text.
6. 119th Congress, Discussion draft (2025); https://docs.house.gov/meetings/II/II13/20250722/118447/BILLS-119pih-DiscussionDraft.pdf.
7. C. Flavelle, A. Gaffney, C. Baker, A. Swanson, "Mass Layoffs begin at NOAA, with hundreds said to be fired in one day," *The New York Times*, 27 February 2025.
8. "Trump's first 100 days, by the numbers," *E&E News by Politico*, 29 August 2025.
9. "Administration revises endangered species act regulations to strengthen certainty, reduce burdens and uphold the law," *US Department of the Interior*, 19 November 2025; https://www.doi.gov/pressreleases/administration-revises-endangered-species-act-regulations-strengthen-certainty.
10. H. Whitehead, L. Rendell, *The Cultural Lives of Whales and Dolphins* (Univ. of Chicago Press, 2014).
11. A. M. M. Sequeira, U. R. Sumaila, A. A. Rogers, *npj Ocean Sustain.* **3**, 38 (2024).
12. M. D. Lettrich *et al.*, *PLOS ONE* **18**, e0290643 (2023).

10.1126/science.aec4817

Communities can enforce China's national parks

China's National Parks Law (*1*), which will take effect on 1 January 2026, provides the legal foundation for a national park system planned to encompass about 50 sites that cover an area of about one-tenth of China's total territory (including land and water) (*1*, *2*). Effective governance and enforcement of the vast park system will be a challenge (*3*) that requires technological instruments and strengthened institutional capacity, including interagency coordination and landscape monitoring (*4*, *5*). To ensure effective protection and enforcement, China should engage the communities that live within the borders of the proposed parks.

China's parks encompass long-inhabited landscapes, where the livelihoods and cultures of residents are tightly interwoven with ecological systems (*2*, *6*). In recognition of these communities, the law emphasizes "public participation and community involvement" as pillars of governance (*1*). However, this approach requires a decisive shift from earlier models in which residents' roles in protected areas were confined to passive observation and informal reporting (*7*–*9*).

To realize the Law's ambition of "harmonious human-nature coexistence" through "participatory and shared approaches" (*1*), its implementation should operationalize these principles by embedding community-integrated enforcement within park management systems. For instance, regulations could authorize trained residents to safely remove immediate threats such as illegal snares, establish community-based restorative justice panels for minor infractions such as unauthorized subsistence herb collection, and streamline procedures for submitting local testimony as formal evidence (*10*).

Establishing such a system could help to transform local residents from passive subjects of regulation into active stewards. This approach would not only address the practical challenges of managing vast territories but also create a more legitimate and socially grounded conservation model—one capable of addressing the socioecological dynamics in China's national parks. By building a community-integrated enforcement regime, China can enhance not only conservation effectiveness but also social justice and resilience in its protected landscapes. Ultimately, the success of the National Parks Law depends on realizing its promises of participation and co-management, not merely in legal text but also in everyday practice.

Shuo Gao[1,2] and Qinglong Shao[3]

[1]School of Public Affairs, University of Science and Technology of China, Hefei, China. [2]Department of Biology, University of Oxford, Oxford, UK. [3]School of Ecology, Sun Yat-sen University, Shenzhen Campus, Shenzhen, China. Email: shuo.gao@foxmail.com; shaoqlong@mail.sysu.edu.cn

REFERENCES AND NOTES

1. National Forestry and Grassland Administration & National Park Administration, "National Parks Law of the People's Republic of China" (2025) [in Chinese]; https://www.forestry.gov.cn/lyj/1/lcdt/20250912/642163.html.
2. W. Zhao, *Nat. Sci. Rev.* **9**, nwac150 (2022).
3. T. Chen, X. Li, *Biodivers. Sci.* **31**, 22485 (2023) [In Chinese].
4. Z. Ouyang, X. Tang, A. Du, Z. Zang, W. Xu, *Nat. Park* **1**, 67 (2023) [In Chinese].
5. Z. Ouyang *et al. Nat. Park* **2**, 605 (2024) [In Chinese].
6. J. Brien, Y. Lin, *J. Environ. Law Policy* **3**, 106 (2023).
7. J. Zhang, Y. Zhang, *Biodivers. Sci.* **25,** 64 (2017) [In Chinese].
8. G. Huang *et al.*, *Nat. Sci. Rev.* **8**, nwab042 (2021).
9. W. Sharkey, "Understanding the contributions of local residents to protected area law enforcement," thesis, University of Edinburgh, Edinburgh, UK (2025).
10. W. Sharkey, E. J. Milner-Gulland, P. Sinovas, A. Keane, *Oryx* **58**, 746 (2024).

10.1126/science.aed0470

Arctic route demands advanced marine coatings

On 23 September, China launched the China-Europe Arctic Express, a new Arctic shipping route that shortens the Asia-Europe maritime journey to 18 days (12 to 15 days shorter than conventional routes) (*1*). This route will accelerate cargo transit, reduce carbon emissions, and provide an alternative to the congested Suez Canal (*2*). However, it also introduces environmental challenges that could make marine coating materials less effective, such as extreme polar conditions, substantial temperature fluctuations, and highly corrosive seawater (*3*). Furthermore, the Arctic's fragile ecosystem, which has a slow recovery rate, is extremely vulnerable to pollutants (*4*, *5*), including microplastics and toxic residues such as copper ions leached from conventional marine coatings (*6*). Addressing these challenges requires a breakthrough in advanced multifunctional marine coatings (*7*).

Researchers should prioritize materials that integrate the abilities to repel ice and resist abrasion with antifouling and anticorrosion capabilities. Hybrid organic-inorganic composites, coatings that dynamically modify their properties in response to external conditions, and nontoxic antifouling surfaces each have the potential to protect vessel integrity and the fragile Arctic ecosystem (*8*–*10*). Translating laboratory innovations into practical applications also requires the development of Arctic-specific testing protocols that accurately replicate the synergistic effects of mechanical (abrasion), thermal (alternating temperature differentials >80°C), and chemical (corrosion) stresses encountered on the Arctic route (*3*, *11*).

The development of such coatings is critical to the safety and sustainability of Arctic route operations. The current marine coating techniques could trigger environmental disasters and undermine the economic viability of the China-Europe Arctic Express. Urgent interdisciplinary collaboration is essential to create coatings that can withstand the extreme environmental conditions of the route (*12*), thereby protecting this delicate ecosystem.

Tao Zhang and Liping Wang

State Key Laboratory of Advanced Marine Materials, Ningbo Institute of Materials Technology and Engineering, Chinese Academy of Sciences, Ningbo, China. Email: tzhang@nimte.ac.cn

1. Y. Chen, "New express via Arctic to enhance ties with Europe," *China Daily*, 26 September 2025.
2. P. Zhao *et al.*, *Nat. Commun.* **16**, 8431 (2025).
3. W. Gao *et al.*, *Adv. Eng. Mater.* **27**, 2500149 (2025).
4. M. Lin *et al.*, *Environ. Sci. Pollut. Res.* **31**, 40419 (2024).
5. X. Qi *et al.*, *Ocean Coast. Manage.* **247**, 106936 (2024).
6. L. Yang, L., S. Li, R. Zhang, *Science* **389**, 6763 (2025).
7. J. Callow, M. Callow, *Nat. Commun.* **2**, 244 (2011).
8. Y. Wu *et al.*, *Adv. Mater.* **36**, 2312460 (2024).
9. H. Jin *et al.*, *Prog. Mater. Sci.* **124**, 100889 (2022).
10. R. Teijido *et al.*, *Prog. Mater. Sci.* **163**, 106684 (2022).
11. S. Sun *et al.*, *J. Chin. Soc. Corros. Prot.* **44**, 1177 (2024).
12. M. Zhang, T. Ding, C. Ding, *Transport. J.* **64**, e12019 (2025).

10.1126/science.aed1509

Science
JOURNALS AAAS



Publish your research in the *Science* family of journals

The *Science* family of journals (*Science, Science Advances*, *Science Immunology, Science Robotics, Science Signaling*, and *Science Translational Medicine)* are among the most highly-regarded journals in the world for quality and selectivity. Our peer-reviewed journals are committed to publishing cutting-edge research, incisive scientific commentary, and insights on what's important to the scientific world at the highest standards.

Submit your research today!

Learn more at **Science.org/journals**

POLICY ARTICLE

COMPUTATIONAL SOCIAL SCIENCE

Mapping the online manipulation economy

A market perspective on digital manipulation may help improve online trust and safety

A. Dek[1], Y. Kyrychenko[2], S. van der Linden[2], J. Roozenbeek[2]

The internet is awash with inauthentic activity. Although some of this activity is harmless, a substantial proportion can be classified as malicious, including bots designed to steal personal data, networks of inauthentic social media accounts promoting crypto scams, and coordinated political influence operations (*1*, *2*). To enhance security, online platforms have implemented measures to counter inauthentic activity, with most requiring users to confirm account authenticity via a one-time password sent through short message service (SMS). However, there exists a thriving market for buying and selling on-demand SMS verifications, which forms a cornerstone of the wider online manipulation economy. Despite its centrality in the digital manipulation ecosystem, this SMS verifications market has not been systematically studied. To address this knowledge gap, we developed the Cambridge Online Trust and Safety Index (COTSI; cotsi.org), which tracks the daily price of SMS verifications for 197 countries and >500 platforms.

Malicious inauthentic activity is common. For example, one study found that "social bots played a disproportionate role in spreading [news] articles from low-credibility sources" (*3*). Another investigation showed that, in 2024, "bad bots" made up 24% of all internet traffic (*4*). However, the problem extends beyond bots: Researchers distinguish between automation (to what extent online activity is governed by algorithms or code), inauthenticity (whether an account is truthful in its representation), and coordination (accounts working together to achieve certain goals) (*5*). Studies have elucidated the role of automated, inauthentic, and/or coordinated activity in the proliferation of disinformation campaigns, cryptocurrency scams on social media, and distributed denial of service attacks (*2*, *6*, *7*). With the rise of generative artificial intelligence, this type of content has become easy to produce and extremely difficult to detect (*8*). Yet, rather than cracking down on inauthentic activity, many online platforms have cut measures to curb it and have started paying users for creating engaging content, thus incentivizing a reliance on inauthentic engagement.

THE ONLINE MANIPULATION MARKETPLACE

To address these challenges, researchers have sought to understand how to detect digital manipulation efforts—for instance, by developing bot detection algorithms (*8*) [see supplementary materials (SM) S1.1]. However, with some exceptions (*9*), few studies have explicitly looked at inauthentic online activity through the lens of market economics. We argue that doing so is key for the study of financial crime and political influence operations, and for the design and implementation of interventions. The online manipulation marketplace is thriving: Inauthentic likes, comments, views, and followers are all readily available for purchase. Offers range from low-end fake likes and views used for vanity metrics inflation, to mid-end manipulations used by search engine optimization specialists to promote businesses, and even high-end influence campaigns (*6*, *9*). As a starting point, manipulation service providers purchase physical or virtual SIM (subscriber identity module) cards in bulk. These SIM cards are linked to phone numbers, which are then used to verify accounts via SMS for the purpose of mass account registration.

We conceptualize this online manipulation economy as a transnational gray market (*10*) (see SM S1.2). Providers of manipulation services operate worldwide, but outside of authorized distribution channels. For example, using an SMS verification service to register a social media account goes against most online platforms' terms of service. However, whether doing so is illegal is not clear. Providers may be held liable in some jurisdictions, depending on how their services are used (e.g., for fraud), though legal precedent is lacking (see SM S1.2.1). There are also several benign use cases for such services, including by open-source investigators and people in countries with internet restrictions.

Buyers of online manipulation services take on risks, both formal (e.g., detection by platforms) and informal (e.g., account registrations being unsuccessful, their data being leaked or hacked). Because manipulation service providers often operate as informal businesses based in hard-to-reach jurisdictions, buyers have limited legal recourse to offset losses. Products are differentiated (not homogeneous), as there is substantial variation in quality—for example, with respect to the success rate of account registrations.

It is often possible to register an account using an SMS verification from a country where it could be bought more cheaply, and later deploy or sell this account in a more expensive country—a phenomenon we refer to as arbitrage. However, most platforms have security measures in place to disincentivize such efforts. For example, a Facebook account registered in Vietnam pretending to be a US voter may be flagged by Facebook's fingerprinting system—a process for gathering user information, e.g., through their browser or device settings—and banned. Buyers are therefore incentivized to register accounts using local SIM cards and phone numbers (see SM S1.2). However, such arbitrage is not always feasible. For messenger apps (e.g., WhatsApp), accounts' phone numbers are readily visible to all users, thus revealing their country of origin. Facebook public page administrators are required to disclose their country of registration, and LinkedIn's (voluntary) account verification system also shows this information.

A few studies are available that shed light on how the digital manipulation market operates (*11*, *12*). For example, Shi *et al.* (*9*) investigated the market for fake likes and comments in the European Union. Fredheim *et al.* (*6*) found that, in 2023, a mere €10 could buy tens of thousands of views, thousands of likes, and hundreds of followers on several high-profile online platforms. The authors point out that very little has been done since 2021 to counteract these flaws and protect platforms' integrity (see SM S1.1).

THE SMS VERIFICATIONS MARKET

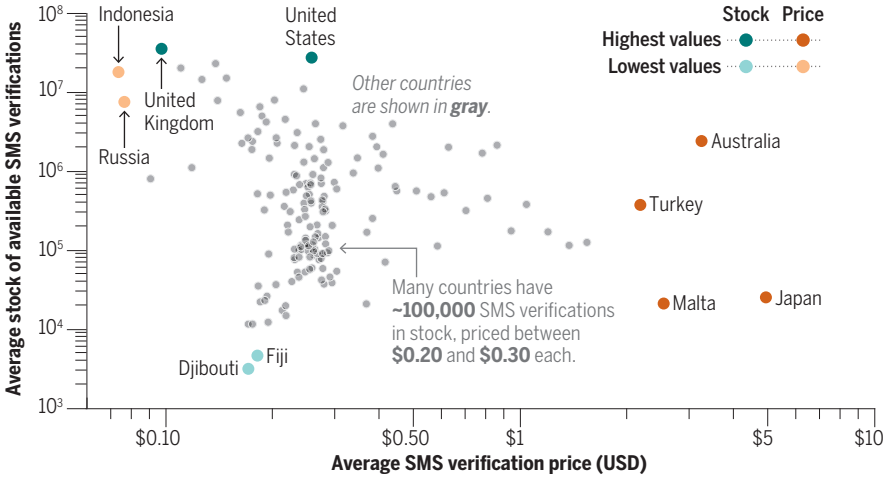
Few studies have investigated the underlying SMS verifications infrastructure that serves as a cornerstone of the online manipulation

economy. SMS verifications are an essential component for the registration of accounts on online platforms: Without them, downstream online manipulation services (account creation, programming bots to post or engage with content, etc.) become near-impossible. Studying the SMS verifications market is thus key to understanding how inauthentic content spreads, and to finding new ways of countering digital manipulation.

By our count, there are at least 17 providers offering on-demand SMS verifications (see SM S2.1). These providers operate worldwide but cater mainly to Russian- and, to a lesser extent, Chinese-speaking customers, as evidenced by their websites being available in grammatically correct Russian (but incorrect English), and offering payment through Russian payment platforms. Visitors can select both the platform for which they wish to verify an account and the country of the phone number to which the SMS will be sent. The site then lists the price and the number of verifications available for that country. Providers bulk-purchase SIM cards to deliver their services. Because a SIM card can be used to register for a given platform only once, prices and stocks of SMS verifications vary considerably. The range of platforms on offer is broad: not only social media platforms, but also messenger apps (e.g., WhatsApp, Telegram), financial services (e.g., Revolut), crypto exchanges (e.g., Coinbase, Binance), and marketplaces (e.g., Amazon) (see SM S1.3).

Price and stock of SMS verifications by country

Price and available stock of short message service (SMS) verifications from 25 July 2024 through 27 July 2025. Data are sums (stock) or stock-weighted averages (price) across platforms and providers, then averaged over days. Each point represents a country, and labels highlight some of the most extreme values for prices and stocks.



We developed the COTSI (cotsi.org) to enable accurate assessments of price fluctuations over time, and to monitor the implementation and evaluation of countermeasures. This free online platform tracks the daily price and availability of on-demand SMS verifications across 197 countries and >500 online platforms. To create the index, we first identified 17 providers of SMS verification services and sorted them by the web traffic they receive (see tables S1 and S20). These providers operate out in the open, with publicly accessible websites (some even keep blogs), and application programming interfaces (APIs) that allow visitors to extract data (e.g., on prices or stocks). From this list, we selected four providers to be included in the price index (SMSActivate, 5Sim, SMShub, and SMSPVA) on the basis of (i) their verification prices and stocks being freely available via API, preferably without login or paywall; and (ii) the website being distinctive and not a clone of another provider (some websites look identical and have the same prices and stocks listed) (see table S20). We then developed scripts that automatically collect data through the providers' APIs. COTSI data consist of the daily price (stock-weighted averages across providers) of SMS verifications, and the number of verifications available, for each combination of country and platform (see SM S2.1).

Predictors of SMS verifications prices

To understand what drives the cost of on-demand SMS verifications, we collected 1 year of COTSI data (25 July 2024 to 27 July 2025) and calculated the average price and stock of SMS verifications in each country per provider (see SM S3.1). We then linked these data with the Digital Society Project, a country-level dataset that consists of 37 variables divided into five categories: coordinated influence operations, digital media freedom, states' internet regulatory capacity and approach, online media polarization, and social cleavages (see SM S2.3 for details and tables S18 and S19 for an overview of item wordings and scale points used). Owing to conceptual and statistical complications of aggregating the variables according to these categories (see SM S2.3), we recoded the variables into the following categories: the presence of (i) domestic and (ii) foreign social media disinformation, (iii) internet censorship, (iv) internet governance, (v) online social media use, (vi) online media diversity, (vii) the use of social media for political action, and (viii) political polarization (all Cronbach's $\alpha > 0.70$). We also collected country-level statistics: minimum SIM card price, mobile data cost, country population, the number of phones per capita, and gross domestic product (GDP) per capita (see SM S3.1 for further details).

We noticed substantial variation in the success rate of SMS verifications, depending on the provider. For instance, 5Sim lists its success rate per country on its website. In late July 2025, it reported its success rate for registering a Facebook account in the US as being at most 21.43%. This may be due to the fact that some providers rely primarily on virtual SIM cards, which are of lower quality than physical ones. This is likely because platforms can identify the carrier associated with a phone number, and their security algorithms may treat numbers from virtual providers with increased suspicion. After experimenting with registering our own verifications, we concluded that SMSPVA has the highest success rate (>90%). In our analyses, we therefore look separately at the predictors of SMS verification prices for SMSPVA, to understand the differences between high-quality and lower-quality services. Finally, many of the 500 platforms in the COTSI are of minimal use in influence campaigns. We therefore also look separately at the predictors of SMS verification prices for social media and messaging platforms: Google (including YouTube and Gmail), Facebook, Instagram, Twitter/X, WhatsApp, TikTok, LinkedIn, VKontakte, Discord, Telegram, Line, WeChat, Snapchat, Weibo, and QQ. Because of nonlinearity in our data, we ran mixed-effects gamma regressions with log-transformed SMS verification price as the dependent variable, our aggregated Digital Society categories and country-level measures as independent variables, and providers and countries as random effects (see SM S3.2).

We find that account verifications via SMS are consistently most expensive in Japan ($4.93), Australia ($3.24), Turkey ($2.54), and Malta ($2.18). These prices are higher than for other countries including the US ($0.26), the UK ($0.10), and Russia ($0.08) (see the figure). This may be related to the price of (physical) SIM cards, which cost a minimum of $29.77 in Japan, $6.23 in Australia, and $10.37 in Malta. High SIM card prices may be partially a function of regulation: Japan requires proof of residency before buying a SIM card, and

CREDITS: (GRAPHIC) M. HERSHER/*SCIENCE*; (DATA) CAMBRIDGE ONLINE TRUST AND SAFETY INDEX

Australia requires photo identification (*13*). However, SIM card price does not tell the full story, as these cost ~$0.95 in Turkey. That said, registering a SIM card in Turkey is complex, as phone numbers are linked to passports.

We further find that the most important factors associated with the price of SMS verifications are the stock of available verifications in a given country for a given platform (b = 0.92 [0.92, 0.93; numbers in brackets are 95% confidence intervals], P < 0.001; lower stocks tend to increase the price), GDP per capita (b = 1.20 [1.08, 1.33], P = 0.001; higher GDP predicts higher price), and the number of phones per capita (b = 0.89 [0.81, 0.97], P = 0.007; fewer phones are linked to higher price). All other associations are nonsignificant at P > 0.067 (see table S11). When zooming in on the provider with the highest verification success rate (SMSPVA), we find that (in addition to GDP and phones per capita) a higher minimum price for a SIM card is also associated with an increase in the price of SMS verifications (b = 1.22 [1.06, 1.40], P = 0.004). Curiously, the effect for stocks is also significant but in the opposite direction (b = 1.05 [1.02, 1.07], P = 0.012; higher stocks instead increase price). All other P values > 0.055 (see table S14). We find that, with minor variations, all these associations are robust when only looking at social media and messaging platforms (see tables S13 and S15). Finally, we find no significant associations between our sociopolitical variables and SMS verification price. However, when looking at SMSPVA verifications only, we find marginally significant effects for (more) domestically produced disinformation on social media (b = 1.26 [0.99, 1.60], P = 0.063), and the (lower) use of social media for political action (b = 0.79 [0.63, 1.00], P = 0.055) (see table S14 and SM S3.3).

Influence operations during election campaigns

To understand how the online manipulation market might react to political events, we examined whether the price and availability of SMS verifications for eight social media platforms (Google/YouTube/Gmail, Facebook, Instagram, Twitter/X, WhatsApp, TikTok, LinkedIn, and Telegram) increase ahead of national elections. If confirmed, this may indicate increased demand for online manipulation services during contentious political moments, and a sign of influence operations. We conducted a cumulative average abnormal returns analysis to see whether SMS verifications prices and stocks yield abnormal returns in the 30 days leading up to 61 national elections held between July 2024 and June 2025, in countries with >1 million inhabitants. We find that for Telegram and WhatsApp (though with less statistical confidence for the latter), SMS verifications prices increase significantly ahead of national elections, indicating increased demand for such registrations during these periods. However, we do not find this to be the case for the other six platforms (see SM S3.4).

POLICY CONSIDERATIONS

Substantial progress can be made in our understanding of online influence operations and financial crime by investigating the thriving market that buttresses online manipulation. We developed the COTSI to help illuminate this underground market. The COTSI has many applications. For instance, it can be used to track changes in SMS verification prices and stocks ahead of elections, or to assess whether interventions affect the price or availability of manipulation services.

Drawing on 1 year of COTSI data, we examined what predicts the price of SMS verifications. On the basis of these analyses, we offer several considerations for policy-makers. First, the availability of cheap SIM cards in some countries may make it easier to mass-register accounts. Policy-makers may therefore investigate malicious actors' reliance on local infrastructure, e.g., SIM farms. In April 2025, the United Kingdom was the first country in Europe to pass legislation making SIM farms illegal (*14*). As this law comes into effect, the COTSI will allow us to see whether SMS verification prices in the UK indeed increase. As the price and availability of SIM cards are associated with high-quality SMS verification prices, policy-makers may consider making the purchase and registration of a SIM card more complex (without unduly sacrificing users' privacy). Shi *et al*. (*9*) also suggest making manipulation service providers harder to find on search engines, thus reducing their visibility.

Regarding the finding that SMS verifications prices increase significantly ahead of elections for Telegram and WhatsApp, but not other social media platforms, we offer several explanations (see SM S3.4). Most notably, arbitrage is more limited for messaging apps. It is easy to use a fake social media account registered in one country to post about events in another, because the account's country of registration is usually not visible to other users. Messaging apps, however, make it easy to see where an account is from, thus incentivizing the registration of local (inauthentic) accounts. Platforms may therefore consider making accounts' country of registration more transparent for all users.

Our study is not without limitations. We focus on the SMS verifications market, which we argue is a cornerstone of the wider online manipulation economy. However, although we posit a strong theoretical link between SMS verification prices and the cost of other services such as fake likes and comments (*9*), we are currently unable to trace these costs through the COTSI. Furthermore, there is a risk that the publication of this paper alerts SMS verification providers, who might then make access to their APIs more difficult, complicating future study. We also recognize that inauthentic behavior forms only one part of a wider set of challenges around digital information consumption and production. Nonetheless, we believe that our findings serve as a starting point for boosting trust and safety on online platforms. □

REFERENCES AND NOTES

1. Z. Lin, J. Cui, X. Liao, X. Wang, arXiv:2401.03315 (2024).
2. V. Chergarova *et al*., *Issues Inf. Syst.* **23**, 242 (2022).
3. C. Shao *et al*., *Nat. Commun.* **9**, 4787 (2018).
4. T. Richabadas, "Threat Spotlight: Bad bots are evolving to become more 'human'" (2024); https://blog.barracuda.com/2024/11/19/threat-spotlight-bad-bots-evolving-more-human.
5. L. Mannocci, M. Mazza, A. Monreale, M. Tesconi, S. Cresci, arXiv:2408.01257 (2024).
6. R. Fredheim, S. Bay, T. Haiduchyk, A. Dek, M. Stolze, "Social Media Manipulation 2022/2023: Assessing the Ability of Social Media Companies to Combat Platform Manipulation" (2023); https://stratcomcoe.org/publications/social-media-manipulation-20222023-assessing-the-ability-of-social-media-companies-to-combat-platform-manipulation/272.
7. J. Pastor-Galindo, P. Nespoli, J. A. Ruipérez-Valiente, D. Camacho, arXiv:2502.11827 (2025).
8. K. Yang, F. Menczer, *J. Quant. Descr. Digit. Media* **4**, 1 (2024).
9. L. Shi *et al*., "FAMOUS: Fake Activity Market Observation System of Unethical Services" (2025); https://drive.google.com/file/d/1ijSRgnvQmvAQN-UiILS1f-EGaUrUzJ0O/view.
10. L. P. Bucklin, *Int. J. Res. Mark.* **10**, 387 (1993).
11. M. Mazza, G. Cola, M. Tesconi, *Online Soc. Netw. Media* **31**, 100224 (2022).
12. T. Elmas, R. Overdorf, K. Aberer, *Proc. Int. AAAI Conf. Web Soc. Media* **16**, 171 (2022).
13. P. Bischoff, "Which governments impose SIM-card registration laws to collect data on their citizens? *Comparitech* (2025); https://www.comparitech.com/blog/vpn-privacy/sim-card-registration-laws/.
14. UK Home Office, "Major step for fraud prevention with landmark ban on SIM farms" (2025); https://www.gov.uk/government/news/major-step-for-fraud-prevention-with-landmark-ban-on-sim-farms.
15. A. Dek, Y. Kyrychenko, S. van der Linden, J. Roozenbeek, Data and code for "Mapping the online manipulation economy," *OSF* (2025); https://osf.io/t3xzg/.

ACKNOWLEDGMENTS

A.D. and J.R. contributed equally. The authors thank I. Dek (Centre for Information Resilience) and K. Manakhov (Trementum Analytics) for help with the COTSI. The authors acknowledge support from the UK Cabinet Office (IRIS Academic, # SCH-00001-3391). The funding source had no involvement in the study design, data collection, analysis, writing, or decision to submit. All information necessary to replicate our findings (data, code, and supplementary analyses) can be found at (*15*).

SUPPLEMENTARY MATERIALS

science.org/doi/10.1126/science.adw8154

10.1126/science.adw8154

[1]Judge Business School, University of Cambridge, Cambridge, UK. [2]Department of Psychology, University of Cambridge, Cambridge, UK. Email: jjr51@cam.ac.uk

RESEARCH

IN *SCIENCE* JOURNALS

Edited by **Michael Funk**



Emissions from fossil fuel extraction and refinement are a major source of methane, seen here being burned off in a gas flare.

PHOTO: CALLUM FRASER VIA ALAMY

METHANE EMISSIONS

Point by point

Methane emissions from oil, gas, and coal facilities are responsible for a large portion of global greenhouse gas emissions and are relatively simple to mitigate, but first those sources need to be identified. Jervis *et al.* determined estimates for methane emissions in 2023 from energy sector point sources using global high-resolution data from the GHGSat satellite constellation. These observations revealed the intermittent nature of many of the emissions, as well as the degree of spatial correlation of emissions with existing inventories, demonstrating the utility of high-resolution satellite observations and providing actionable information for targeted mitigation efforts. —Jesse Smith

Science p. 1151, 10.1126/science.adv3183

QUANTUM SIMULATION

Ultracold gases step up

In the Josephson effect, a current can flow through an insulating barrier between two superconductors without dissipation. For a high enough current, dissipation does occur, and if microwave radiation is also applied, a series of plateaus—the so-called Shapiro steps—appear in the current-voltage characteristic. Instead of using superconductors, Del Pace *et al*. and Bernhart *et al*. observed Shapiro steps in an atomic Josephson junction. The researchers moved a barrier through an ultracold gas at a speed that had a periodically modulated component to emulate microwave radiation. The height of the resulting Shapiro steps in the chemical potential difference was proportional to the frequency of the modulation. —Jelena Stajic

Science p. 1125, 10.1126/science.ads8885
p. 1130, 10.1126/science.ads9061

METABOLISM

Control of purine metabolism

Cells tightly regulate concentrations of purine nucleotides because they have important roles in cell proliferation, as components of synthesis of RNA and DNA, and in other cellular metabolic and signaling functions. Purines can be produced by de novo synthesis or by a salvage mechanism, and these pathways influence one another. In complementary work, Nguyen *et al*. and Wu *et al*. screened for gene products that influenced the de novo synthesis of purines and identified Nudix hydrolase 5 (NUDT5), a member of a superfamily or hydrolases that cleave nucleoside diphosphates. Characterization of NUDT5's roles revealed that such enzymatic activity was not required in this context. Rather, NUDT5 appears to have another function in scaffolding the oligomerization of phosphoribosyl pyrophosphate amidotransferase (PPAT), the rate-limiting enzyme in de novo purine biosynthesis, and decreasing its enzymatic activity. The findings help to explain the mechanisms that balance activity of the synthesis and salvage pathways and have implications for therapeutic strategies that use purine analogs to combat cancers and inflammatory diseases. —L. Bryan Ray

Science p. 1143, 10.1126/science.adv4257
p. 1134, 10.1126/science.adx9717

MINERAL PHYSICS

A deep mantle water trap

Where did all the water go when Earth's early magma oceans crystallized? For the deepest mantle, the answer has been elusive. To recreate lower-mantle temperature and pressure, Lu *et al*. applied laser heating to silicate glass in a diamond anvil cell (see the Perspective by Walter). Bridgmanite, the lower mantle's most common mineral, formed in equilibrium with silicate melt and strongly partitioned water as the

temperature increased. These experiments indicate that after magma ocean crystallization, bridgmanite may have stored an ocean's worth of water in the lower mantle. This deep reservoir would have affected the planet's water budget during subsequent mantle cooling and convection. —Angela Hessler

Science p. 1177 10.1126/science.adx5883; see also p. 1105 10.1126/science.aed3351

INFECTIOUS DISEASES

Reverse vaccinology in action

Two recent outbreaks of mpox, caused by monkeypox virus (MPXV), underscore the urgent need to develop and stockpile effective vaccines and therapeutics. Paciello *et al.* applied reverse vaccinology combined with AlphaFold3-based structural modeling to identify an MPXV protein targeted by human B cells to enable the development of antibody therapeutics and vaccines. The authors recombinantly expressed MPXV-neutralizing antibodies derived from B cells of individuals who had a history of MPXV infection or vaccination. They then used modeling and cryo–electron microscopy to identify the target of a subset of potent, broadly neutralizing antibodies as the protein encoded by the conserved orthopoxviral gene 153 (*OPG153*). Immunization of mice with an adjuvanted MPXV OPG153 vaccine elicited neutralizing antibodies, suggesting that OPG153 represents both a candidate vaccine antigen and a therapeutic antibody target. Together, these findings highlight the power of leveraging human immunity to design therapeutics and vaccines. —Courtney Malo

Sci. Transl. Med. (2025) 10.1126/scitranslmed.aeb3840

THYMUS

Thymus regeneration in salamanders

Although acute damage and age-related decline can lead to a loss of thymic and immune function, the adult mammalian thymus retains some limited regenerative capacity. Czarkwiani *et al.* found that juvenile axolotls can fully regenerate their thymus after its complete removal. Thymus regeneration was associated with restoration of morphological and transcriptional features. The key mammalian thymic transcription factor Foxn1 was dispensable for thymus regeneration, and single-cell transcriptomics identified the growth factor midkine as a possible driver. Future studies in axolotls could inform therapeutic approaches for promoting thymus regeneration. —Claire Olingy

Sci. Immunol. (2025) 10.1126/sciimmunol.adw9903

CHEMICAL PHYSICS

Exact quantum molecular dynamics

Exact molecular dynamics (MD) simulations must consider the quantum nature of both electrons and nuclei. Up to now, most MD simulations have used the Born-Oppenheimer approximation that treats electrons as quantum and nuclei as classical objects. Although many effects beyond this approximation are known, it has proven difficult to formulate an elegant and practical method for fully quantum MD simulations. Xie *et al.* formulated a new approach called quantum geometrical molecular dynamics that retains the elegance of the Born-Oppenheimer approximation yet enables fully quantum simulations. The researchers showed that the overlap matrix between many-electron states at different nuclear geometries encodes the intrinsic quantum geometry and accounts for all effects beyond the Born-Oppenheimer approximation, thus providing an exact framework for quantum dynamics. —Alexandre Tkatchenko

Sci. Adv. (2025) 10.1126/sciadv.adz3711

IN OTHER JOURNALS

Edited by **Corinne Simonti** and **Jesse Smith**

CELL BIOLOGY

Modulating context for cell migration

Integrins are heterodimeric cell surface glycoproteins that mediate cell adhesion and require glycosylation to function. Specificity for binding to otherwise common glycan structures is achieved by the glycan context. Shafaq-Zadah *et al.* showed that for $\alpha_5\beta_1$ integrin, such glycan context is generated in a tunable manner depending on the conformational state of the cell adhesion protein. Only one specific conformer can nucleate oligomerization of the glycan-binding protein galectin-3. This drives the endocytosis and subsequent polarized redistribution of the integrin to the leading edge of the cell during cell migration. Thus, glycan context and galectins respectively encode and decode binding selectivity, thereby driving plasma membrane nanodomain assembly and cellular responses. —Stella M. Hurtley

Nat. Commun. (2025) 10.1038/s41467-025-64523-7

BIOGEOGRAPHY

Mapping medicinal plants

Humans use tens of thousands of plant species for their medicinal properties. Shrestha *et al.* examined the global distribution of these species and how their diversity relates to environmental and social factors. Medicinal plant diversity is highly correlated with overall vascular plant diversity across regions, but it is also correlated with the length of time that regions have been occupied by humans. Patterns in the number of known medicinal plant species may also be influenced by long-standing systems of classifying and documenting their uses (e.g., Ayurveda and traditional Chinese medicine) and erosion of traditional knowledge caused by colonialism. —Bianca Lopez

Curr. Biol. (2025) 10.1016/j.cub.2025.09.050



PHOTO: VINCENT GRAFHORST VIA MINDEN PICTURES

OPTICS

Metalenses for the vacuum ultraviolet

The development of planar arrays of subwavelength nanostructures has enabled bulk optical components to be engineered as ultrathin devices. These metalenses have tended to operate, by design, at wavelengths of 300 nanometers and above, where fabrication tools and materials are readily available. For certain applications such as bioimaging, photolithography, and particle detectors, there is a desire to push the operation to shorter wavelengths such as ultraviolet and below. Martins *et al.* demonstrate a metalens based on



ANCIENT DNA

Heavy footfall of recent evolution

Hippopotami are assumed to have become extinct in Europe during the last interglacial about 115,000 years ago. Arnold *et al.* sequenced the genomes of ancient hippos from remains found in the Upper Rhine Rift in Germany from a mere 31,000 years ago, during a period of glacial advance. Surprisingly, they appeared to be genetically close to African hippos. This suggests that the range of *Hippopotamus amphibius* has become restricted to Africa relatively recently and that a small population of hippos and straight-tusked elephants survived in warmer refugia in glacial Europe. Populations of these animals successively expanded and retreated with the ice, along with woolly mammoths and rhinos. —Caroline Ash

Curr. Biol. (2025) 10.1016/j.cub.2025.09.035

Ancient hippos may have survived in warm refugia in Europe long after the last interglacial period.

engineered nanoposts formed in a fused silica substrate. Designed to operate at 175 nanometers, the demonstration illustrates that flat optics can be applied to the vacuum ultraviolet regime (and shorter wavelengths), opening opportunities for integrated optical applications. —Ian S. Osborne

Optica (2025) 10.1364/OPTICA.573503

BATTERY RECYCLING

Trace water aids recycling

The rapidly growing volume of research on rechargeable lithium metal batteries highlights the urgent need for efficient and sustainable recycling strategies for spent, highly reactive lithium metal anodes. Zhou *et al.* investigated the use of trace water–containing acetone as a medium for lithium metal recycling and lithium carbonate production. They found that subpercent levels of water enabled the controlled removal of lithium dendrites. The resulting lithium hydroxide initiated acetone aldol condensation, producing diacetone alcohol, which further reacted with the lithium metal anode. This approach successfully yields beyond-battery-grade lithium carbonate, which can be used to fabricate layered NMC cathodes with performance comparable to commercial counterparts. —Jack Huang

Joule (2025) 10.1016/j.joule.2025.102136

IMMUNOLOGY

Neutrophils retain memories of hypoxia

Acute respiratory distress syndrome (ARDS) is a life-threatening condition associated with inflammation, lung damage, and low blood oxygen levels. Sanchez-Garcia *et al.* found that for several months after patients recovered from ARDS, their neutrophils were abnormal, showing reduced antimicrobial effector functions, changes in metabolism, and loss of a histone modification that is critical for regulating gene expression. These changes resembled those observed in healthy individuals who had experienced lowered blood oxygen induced by altitude. In mice exposed to hypoxia, neutrophil precursors within the bone marrow exhibited an irreversible shortening of histone proteins, a process known as histone clipping, that resulted in the defective histone modifications observed in mature neutrophils. —Sarah H. Ross

Nat. Immunol. (2025) 10.1038/s41590-025-02301-9

STEM EDUCATION

What is a chemist?

Understanding what constitutes a "legitimate" group member is crucial for inclusion and respect within said group. In chemistry, identifying limiting beliefs about who can be a chemist and revealing whether current models of being a chemist inadvertently exclude individuals could help broaden participation in the discipline. Castano *et al.* interviewed chemistry professionals across academic, industry, and government sectors to examine how they describe a "chemistry person." Results show that perceptions of a "legitimate" chemist as someone who has a chemistry degree, conducts academic research, and does molecular-level work exclude members of groups such as chemical engineers and industrial chemists and reflect a limited chemistry identity that systematically marginalizes chemists who work across disciplinary lines. These exclusionary practices are difficult to challenge and lead to sustained obstacles underlying diversity and retention in chemistry. —Melissa McCartney

JACS Au. (2025) 10.1021/jacsau.5c00769

www.xsava.xyz

Edited by **Michael Funk**

PHOTOSYNTHESIS

Chlorophylls f in far-red photosystem I

Chlorophyll is the key pigment of oxygenic photosynthesis, and different chlorophyll variants have slightly different absorption spectra that enable expanded photosynthetic ranges for some organisms. Consoli *et al*. tackled the question of how the far-red absorbing pigment chlorophyll f is incorporated into cyanobacterial photosystem I using high-resolution cryo–electron microscopy and computational simulations. The authors were able to assign eight chlorophyll f molecules in the structure and thus propose that chlorophyll f serves as both a primary donor and a conduit for excitation energy sharing between subunits in the photosystem I trimer. —Michael A. Funk

Science p. 1118, 10.1126/science.ado6830

CELL BIOLOGY

Mechanosensitive enhancers of stiffness

Cells sense and respond to the stiffness of their surrounding environment, which can influence health or disease states such as fibrosis. Cosgrove *et al*. investigated how mechanical signals from the extracellular matrix (ECM) regulate gene activity through noncoding regions of DNA called mechanoenhancers. Using advanced genome editing and single-cell screening, the authors discovered that these DNA elements control cell behaviors such as growth, migration, and programmed cell death in response to ECM stiffness. Precise editing of mechanoenhancers can reprogram cell responses and may prevent disease-associated changes, highlighting their potential as therapeutic targets for mechanically driven diseases. —Di Jiang

Science p. 1119, 10.1126/science.adl1988

GENOMICS

Jay pangenomes reveal variant dynamics

Structural variants such as genomic deletions, insertions, and inversions have often received focus for their adaptive potential but are difficult to identify and study systematically without long-read sequencing. Edwards *et al.* assembled a pangenome for three species of North American jays with very different population histories. Contrary to other systems, they found that the species with the smallest population size also had the smallest genome and the fewest repeats. The researchers posit that this difference is due to stochastic loss of repeats after a large expansion in the ancestor of these three species. These data represent one of the first pangenomes for nonmodel organisms and give a better understanding of the dynamics influencing structural variants. —Corinne Simonti

Science p. 1120, 10.1126/science.adw1931

REPRODUCTION

Of mice and women

Mice are frequently used in biomedical research as a model of human biology and disease, but there are many differences between the two, and it is helpful to know what exactly those differences are when interpreting data from mouse models of disease. An atlas of ovarian aging compiled by Gaylord *et al*. facilitates this task and provides insights into both species by characterizing transcriptomic changes and physical structure and function of the ovaries at different ages and life stages. In addition to providing a resource with side-by-side species comparisons, the authors also identified neurons and glia within the ovaries and examined their role in folliculogenesis in mice, which may be relevant for human fertility as well. —Yevgeniya Nusinovich

Science p. 1121, 10.1126/science.adx0659

ORGANIC CHEMISTRY

Synthesis of gukulenin A

Gukulenin A, an organic compound isolated from a marine sponge, has attracted fundamental interest on account of the pair of seven-carbon tropolone ring motifs in its framework. Preliminary studies have also highlighted the compound's anticancer activity in mouse models. Gupta *et al*. report the synthesis of this compound in 24 steps, hinging in particular on the use of a tin reagent that was custom-developed to couple the two tropolone fragments in a manner that differentiates their subtly distinct substituents. The route also enabled the preparation of 15 analogs to study the structural factors underlying the previously reported cytotoxicity. —Jake S. Yeston

Science p. 1122, 10.1126/science.aea9310

IMMUNOLOGY

Tissue residency determinant

Tissue-resident memory T (T_{RM}) cells provide defense against recurring infections, but their dysfunction can lead to disease. Although transcriptional programs associated with the formation of $CD8^+$ T_{RM} cells have been defined, much less is known about the development of $CD4^+$ T_{RM} cells. Kiuchi *et al*. identified a transcription factor, hepatic leukemia factor (HLF), that promoted the differentiation of $CD4^+$ T_{RM} cells in the lungs of mice during chronic inflammation. Based on its DNA-binding profile, HLF coordinated the up-regulation of genes required for tissue residency and a pro-inflammatory phenotype while suppressing the expression of genes that are required for tissue egress. Mice that lacked HLF expression in $CD4^+$ T cells had less lung pathology during long-term exposure to a fungal antigen. —Sarah H. Ross

Science p. 1123, 10.1126/science.adp0714

NEUROSCIENCE

Long-range inputs shape computation

Discrimination and generalization are critical functions for recognizing and classifying objects and features and memory processing that relies on pattern separation and completion. We still do not fully understand the specific circuit mechanisms that provide neuronal ensembles a dynamic range to perform both pattern separation and completion according to external inputs and contextual demands. Robert *et al*. examined the specific roles of long-range circuit interactions between the entorhinal cortex and hippocampal area CA3 to find out how a single brain area can dynamically perform these fundamental information-processing operations. Lateral entorhinal cortex glutamatergic and GABAergic inputs independently and conjunctively shaped pattern separation and completion in CA3 by recruiting pathway- and compartment-specific feedforward inhibition and disinhibition, endowing CA3

with both novelty discrimination and context generalization functions. —Peter Stern

Science p. 1124, 10.1126/science.adn0623

MOLECULAR BIOLOGY

Nuclease drives chromothripsis in cancer

Massive genome rearrangements, or chromoanagenesis, are common in cancer and associated with poor prognosis. The most frequent form, chromothripsis, arises when one or more missegregated chromosomes form micronuclei that rupture, exposing their chromatin to the cytoplasm. Using an imaging-based small interfering RNA screen of human nucleases, Krupina *et al*. found that N4BP2, a previously uncharacterized cytoplasmic endonuclease, enters ruptured micronuclei and shatters chromosomes (see the Perspective by Clarke and Imieliński). N4BP2 was shown to promote the formation of extrachromosomal DNA and to enhance tumor growth in a human glioma model. Analysis of approximately 10,000 cancer genomes revealed that tumors with high N4BP2 expression were enriched for chromothripsis and copy number amplifications, implicating N4BP2 as a key driver of complex genome rearrangements. —Di Jiang

Science p. 1156, 10.1126/science.ado0977; see also p. 1102, 10.1126/science.aed1825

EVOLUTION

Thermal attraction

Plants have evolved an astonishing repertoire of signals to lure pollinators. Although color and scent are well-established pollination signals, some plants also produce heat. Valencia-Montoya *et al.* discovered that plant-produced heat is an early pollination signal and describe the molecular basis of both heat generation in cycads and heat sensing in beetle antennae (see the Perspective by Glover and Webb). By integrating detailed molecular analysis with field documentation of pollination, this study reveals an ancient sensory channel in plant-pollinator communication and contributes to elucidating the early evolution of pollination. —Mattia Maroso

Science p. 1164, 10.1126/science.adz1728; see also p. 1100, 10.1126/science.aed3346

THERMAL MANAGEMENT

A clear insulating coat for windows

Networks of mesoporous polysiloxane tubes that are optically transparent can be used as highly thermally insulating window coatings. Bhardwaj *et al*. solvent-exchanged polysiloxane hydrogels with ethanol and then replaced ethanol with carbon dioxide through supercritical drying to create highly porous, graph-like networks of thin, bicontinuous tubes (see the Perspective by Li and Li). The resulting films have greater than 99% visible-range optical transparency and low thermal conductivity and can be used in new and existing windows. —Phil Szuromi

Science p. 1171, 10.1126/science.adx5568; see also p. 1104, 10.1126/science.aed1907

NEUROSCIENCE

Better recall with dopamine and calcium

Dopamine signaling alters the strength of synaptic connections that underlie learning and memory. Man *et al*. found that dopamine receptors team up with calcium channels in the hippocampus to mediate working memory involved in problem-solving and decision-making. In cultured mouse neurons, activation of dopamine receptors induced the phosphorylation of nearby L-type calcium channels by cyclic adenosine 3′,5′-monophosphate–dependent protein kinase, which increased calcium influx. Spatial working memory was impaired in mice expressing mutant channels that could not be phosphorylated by this kinase. The findings provide deeper insight into how precisely dopamine promotes learning. —Leslie Ferrarelli

Sci. Signal. (2025) 10.1126/scisignal.adp7760

RESEARCH ARTICLE SUMMARY

PHOTOSYNTHESIS

Locating the missing chlorophylls f in far-red photosystem I

Giovanni Consoli†, Fiazall Tufail†, Ho Fong Leong†, Stefania Viola, Geoffry A. Davis, Nicholas Rew, Daniel Medranda, Michael Hofer, Paul Simpson, Marco Sandrin, Benoit Chachuat, Jenny Nelson, Thomas Renger, James W. Murray, Andrea Fantuzzi*, A. William Rutherford*

Full article and list of author affiliations: https://doi.org/10.1126/science.ado6830

INTRODUCTION: When shaded from visible light, some cyanobacteria can replace their chlorophyll a (Chl a)–based photosystems with far-red-light–absorbing paralogs. To do this, a small number of Chl a molecules are replaced with far-red–absorbing pigments, primarily Chl f. Initially, Chl f was considered to function exclusively as a light-harvesting pigment. However, when far-red photosystems were isolated, several lines of evidence indicated a photochemical role in both photosystems. This represents a second distinct low-energy paradigm for oxygenic photosynthesis, with potential importance for the quest for more efficient photosynthesis.

For photosystem II, long-wavelength photochemistry was confirmed both structurally and spectroscopically, but for photosystem I, uncertainty persisted. Structural studies disagreed on the locations of the Chl f molecules, key spectroscopic signatures have been debated, and sequence analyses reported no far-red–specific conserved amino acid changes around the primary donor sites. These uncertainties have left the photochemical role of Chl f in far-red photosystem I in doubt.

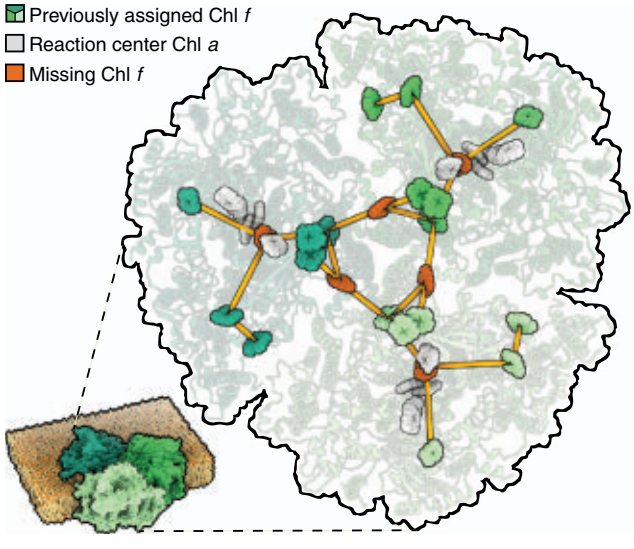
RATIONALE: Cryo–electron microscopy (cryo-EM) single-particle analysis has become a central tool in photosynthesis and bioenergetics, providing atomic-level structural insights into large membrane complexes. However, it poorly discriminates between Chl a and Chl f, which differ only by a C2 substituent: a formyl group in Chl f replacing the methyl group in Chl a. This subtle chemical difference is especially difficult to assign because of the electronegativity of the formyl oxygen that reduces its contribution to the measured electrostatic potential. To overcome this problem, we used a combination of high-resolution structural information, specific statistical approaches to simulate and quantify the electrostatic potential of chlorophyll substituents, and simulations of electrochromic shifts of far-red photosystem absorption spectra.

RESULTS: We report two cryo-EM structures of far-red photosystem I from *Chroococcidiopsis thermalis* PCC 7203 at resolutions of 2.01 and 1.89 Å, which allowed the quantitative assignment of eight Chl f molecules, including the photochemically active A_{-1B}. This Chl f lacks a stabilizing hydrogen bond to its formyl group but presents a distinctive structural motif involving a conserved phenylalanine and a far-red–specific cysteine, which likely influences its redox properties. In addition, our simulations of the electrochromic shifts indicate that the presence of Chl f at the A_{-1B} site is necessary to reproduce the experimental difference spectra.

A Chl f was also assigned in the far-red-light–specific subunit PsaL2, the subunit responsible for trimerization of far-red photosystem I. This site is located between the B07 Chl f molecules in adjacent monomers, forming a ring of six Chl f molecules spanning the three monomers at the core of the trimer. The other Chl f candidates—A21, A23, B07, B30, B37, and B38—were confirmed in the present model.

CONCLUSION: We present several lines of evidence for A_{-1B} being a Chl f and thus the primary electron donor, implying dominant B-side photochemistry. The cysteine-phenylalanine–Chl f formyl motif may influence binding and redox properties of the proposed A_{-1B} Chl f. The ring of six Chl f molecules in the trimer's core suggests a role for intermonomer excitation energy sharing. Site-energy assignments of some Chl f molecules are suggested. □

*Corresponding author. Email: a.rutherford@imperial.ac.uk (A.W.R.); a.fantuzzi@imperial.ac.uk (A.F.) †These authors contributed equally to this work. **Cite this article as G. Consoli *et al.*, *Science* 390, eado6830 (2025). DOI: 10.1126/science.ado6830**



Chl f locations in far-red photosystem I trimers. The far-red photosystem I trimer is viewed from the cytoplasmic side of the membrane. Chl f locations in each monomer are colored in different shades of green, previously unassigned Chl f in orange, and reaction-center Chl a molecules in white. Chl f closest neighbors are connected by yellow lines.

PHOTOSYNTHESIS

Locating the missing chlorophylls f in far-red photosystem I

Giovanni Consoli[1]†, Fiazall Tufail[1]†, Ho Fong Leong[1]†, Stefania Viola[1]‡, Geoffry A. Davis[1]§, Nicholas Rew[2], Daniel Medranda[2], Michael Hofer[3], Paul Simpson[4], Marco Sandrin[5], Benoit Chachuat[5], Jenny Nelson[2], Thomas Renger[3], James W. Murray[1], Andrea Fantuzzi[1]*, A. William Rutherford[1]*

The discovery of chlorophyll f–containing photosystems, with their long-wavelength photochemistry, represented a distinct, low-energy paradigm for oxygenic photosynthesis. Structural studies on chlorophyll f–containing photosystem I could identify some chlorophyll f sites, but none among the photochemically active pigments, and thus concluded that chlorophyll f plays no photochemical role. Here, we report two cryo–electron microscopy structures of far-red photosystem I from *Chroococcidiopsis thermalis* PCC 7203, allowing the assignment of eight chlorophyll f molecules, including the redox active A_{-1B}. Simulations of absorption difference spectra induced by charge separation indicated that the experimental spectra can be reproduced only by considering the presence of a chlorophyll f at the A_{-1B} site. The chlorophyll f locations, wavelength assignments, and conserved far-red–specific residues provide functional insights for efficient use of long-wavelength photons.

Chlorophyll f (Chl f) was discovered in a cyanobacterium isolated from stromatolites when grown under far-red (FR) light (*1*). The ability to produce Chl f is present in a small but diverse proportion of cyanobacterial species (*2*, *3*) and is associated with a ~21-gene cluster that codes for FR-light versions of the main chlorophyll-containing subunits of photosystems I and II (FR-PSI and FR-PSII), as well as other proteins needed for FR photosynthesis (*2*). In cells adapted to FR light, Chl a still dominates, with only seven or eight Chl f molecules present in FR-PSI and four Chl f and one Chl d in FR-PSII (*4*).

Originally, the long-wavelength pigments were thought to play only a light-harvesting role (*5*), with heat from the environment needed for the uphill transfer of excitation energy to the higher-energy, photochemically active Chl a primary donor. This view was contradicted by biophysical studies of the FR photosystems, which provided a range of evidence for long-wavelength primary electron donors in both FR photosystems, the most telling of which was the efficient FR-light–driven charge separation at cryogenic temperatures (*4*). Chl f–based photochemistry was a surprise and greeted with excitement as a low-energy and potentially more energy-efficient paradigm for oxygenic photosynthesis, one that resonated with the long-standing desire for more efficient crop production (*6*).

The primary donor in FR-PSII was proposed to be one of the five long-wavelength pigments and located in the Chl_{D1} position (*4*), and this was confirmed by cryo–electron microscopy (cryo-EM) to be the single Chl d (*7*). When cryo-EM structures of FR-PSI appeared, however, they showed no evidence of Chl f among the redox-active pigments (*8*–*11*), and it was argued that Chl f had no photochemical role in this photosystem. Subsequent spectroscopic studies based their interpretations on this conclusion (*12*–*14*).

The only chemical difference between Chl a and Chl f is the substituent at the C2 position: a methyl group in Chl a and a formyl group in Chl f (*1*). In cryo-EM, the atomic Coulomb potential, which arises from the negatively charged electron cloud and the positively charged nucleus, scatters the electron beam, resulting in a map of the electrostatic potential (ESP). Because the formyl oxygen of Chl f is negatively polarized, it contributes less to the signal than carbon, nitrogen, and sulfur atoms (*15*–*17*). This property is reflected in previous FR-PSI cryo-EM models (*8*–*11*), the most recent of which classify only five Chl f molecules as likely candidates from direct observation of additional ESP (*10*). Chl f assignments have also been influenced by consideration of conserved changes in FR-PSI proteins relative to their homologs in white-light–absorbing Chl a PSI (WL-PSI) and by the chemistry of Chl f, that is, the likely H-bond partners of its formyl group and its preference for a nonhistidine axial ligand to the Mg^{2+} (*4*, *18*).

Given the intrinsic difficulties in detecting Chl f by cryo-EM, higher-resolution structures are needed to solve the key mechanistic controversy over the presence of a Chl f among the redox-active pigments of FR-PSI. To address this question, we obtained two independent cryo-EM maps of FR-PSI from *Chroococcidiopsis thermalis* PCC 7203 (*C. thermalis*) at 1.89- and 2.01-Å resolution and introduced an improved statistical method to classify chlorophyll substituents (fig. S1). The ESP from the formyl group, FR-conserved amino acid changes, and electrochromic shifts induced by the stable, light-induced chlorophyll cation $P700^+$ on the nearby pigments all provide evidence for the presence of Chl f in the A_{-1B} site, a candidate as the primary electron donor in PSI (*4*, *19*–*21*).

Location of the Chl f sites in the cryo-EM structure of FR-PSI

The improved resolution of our structures allows the formyl groups to be detected in ESP maps for all eight Chl f molecules in *C. thermalis* FR-PSI: A_{-1B}, A21, A23, B07, B30, B37, B38, and L03 [Fig. 1, A and B, figs. S3 to S8, and supplementary text S1; chlorophyll nomenclature based on Jordan *et al.* (*22*)]. The previously published structures allowed the assignment of some of the expected eight Chl f molecules (*8*, *9*, *11*), some of which are in common with the candidates presented here (table S21). The presence of a C2 formyl H-bond in five of these cases (A21, A23, B07, B30, and B37) contributes to the ESP signal by fixing the possible orientations of the formyl group and by diminishing the charge on the negatively polarized formyl oxygen atom. Our assignments are supported by a new statistical analysis we developed here that is based on the cone-scan method from Gisriel *et al.* (*16*, *23*). The original cone-scan method analyzed variations in ESP around the putative formyl carbon at the precise distance corresponding to the length of a carbon-oxygen double bond. However, the maximum variations in ESP (positive and negative) do not necessarily occur at one fixed distance; therefore, the approach we used in this work quantifies the local ESP environment of chlorophyll substituents over a range of distances from their respective carbon atom, allowing a more thorough exploration of ESP maps and thus a more rigorous identification of the formyl groups (fig. S1).

Structural evidence for Chl f in the A_{-1B} site in the reaction center

We used the cryo-EM data to map the experimental ESP distribution over a conical surface of aperture 120° around the C2′ carbon of the A_{-1B} chlorophyll (Fig. 2A and fig. S1). A positive ESP feature (red), evident at a torsion angle of ~145° (Fig. 2B and see materials and methods), indicates the presence of a formyl group at the C2 position of the A_{-1B} chlorophyll and confirms the presence of Chl f among the six reaction-center chlorophylls (fig. S9), as originally suggested (*4*). A negative ESP feature (blue or blue-green) is present at ~270°, at the interface between

[1]Department of Life Sciences, Imperial College, London, UK. [2]Department of Physics, Imperial College, London, UK. [3]Institute for Theoretical Physics, Johannes Kepler University, Linz, Austria. [4]Centre for Structural Biology, Imperial College, London, UK. [5]Sargent Centre for Process Systems Engineering, Department of Chemical Engineering, Imperial College London, London, UK. ***Corresponding author. Email: a.rutherford@imperial.ac.uk (A.W.R.); a.fantuzzi@imperial.ac.uk (A.F.)** †These authors contributed equally to this work. ‡Present address: Aix Marseille Univ, CEA, CNRS, BIAM, UMR7265, Saint-Paul-Lez-Durance, France. §Present address: Department of Plant Biochemistry, Biology, Ludwig Maximilian University of Munich, Planegg-Martinsried, Germany.

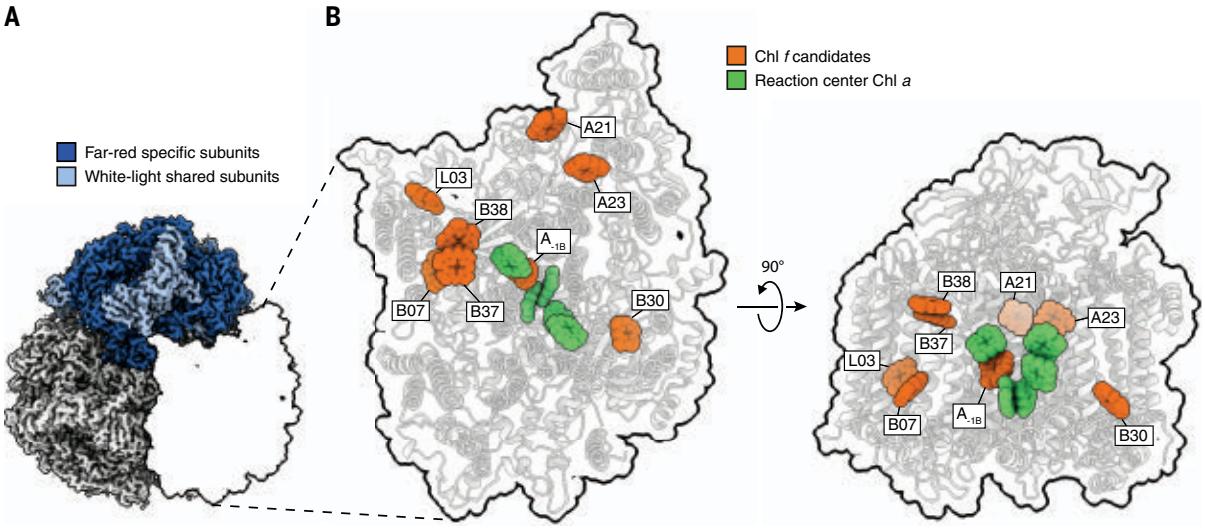


Fig. 1. Structure of trimeric FR-PSI and Chl f locations. (**A**) View of the trimeric FR-PSI map from the cytoplasmic side. The map presents clear ESPs for all the known PSI subunits: The six FR-light–specific subunits (PsaA2, PsaB2, PsaF2, PsaI2, PsaJ2, and PsaL2) are represented in dark blue, and the six subunits in common with WL-PSI (PsaC, PsaD, PsaE, PsaK, PsaM, and PsaX) are represented in light blue. (**B**) Location of the eight candidate Chl f molecules (in orange) in a FR-PSI monomer, as viewed from the cytosolic face and membrane plane. Reaction-center Chl a molecules are represented in green.

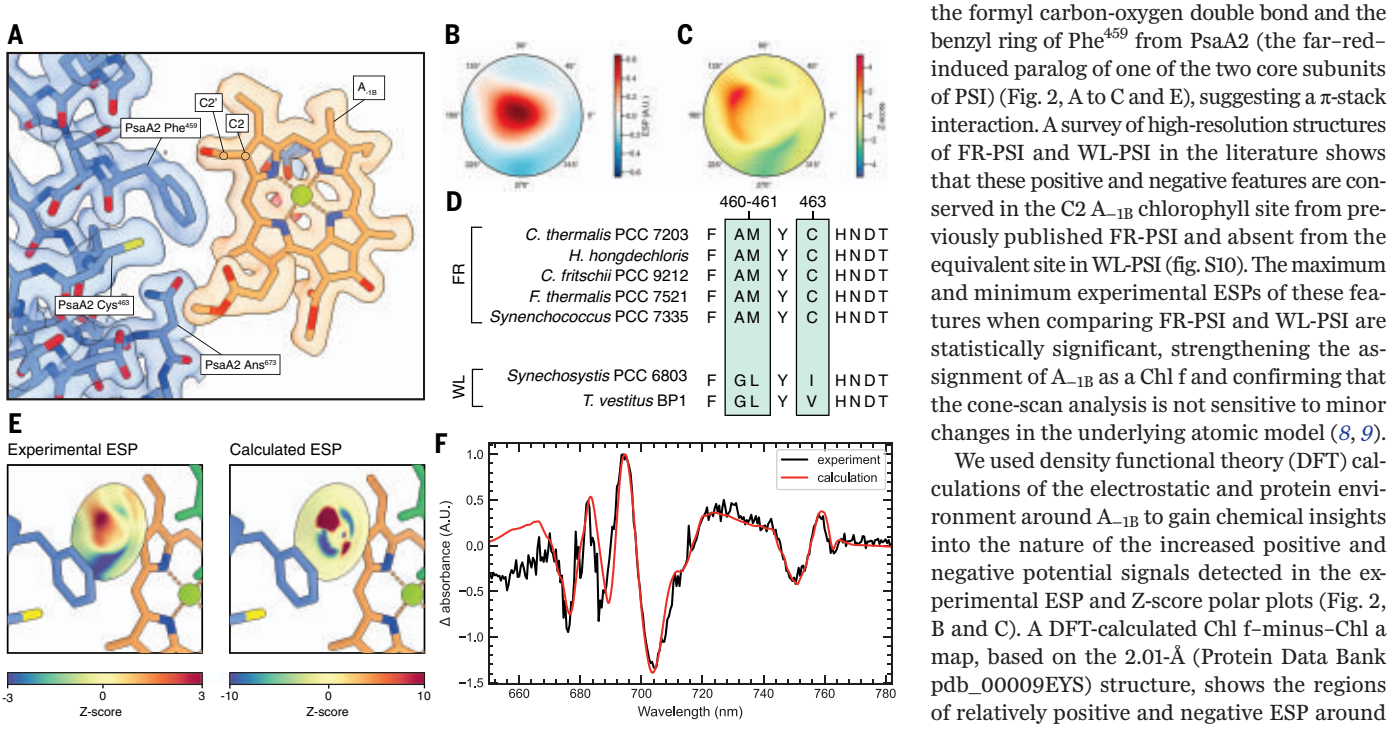


Fig. 2. Evidence for A_{-1B} being a Chl f. (**A**) The chemical environment of the A_{-1} chlorophyll on the B branch of the FR-PSI reaction center (pdb_00009I9L). The chlorophyll density is in orange, and the density of the amino acids from PsaA2 are in blue. (**B**) The ESP polar plot showing the presence of an increased positive potential at a 145° torsion angle around the C2 substituent. A.U., arbitrary units. (**C**) The Z-score polar plot highlighting the presence of statistically significant (table S21) increases in positive (145° torsion angle) and negative (270° torsion angle) ESP features around the C2 of the A_{-1B} chlorophyll relative to the averaged ESP environment around a methyl substituent (fig. S1). (**D**) Conserved amino acid differences near the A_{-1B} C2 substituent of FR and WL PsaA. A, Ala; C, Cys; D, Asp; F, Phe; G, Gly; H, His; I, Ile; L, Leu; M, Met; N, Asn; T, Thr; V, Val; Y, Tyr. (**E**) On the left, the data in (C) are presented in 3D together with Chl A_{-1B}, PsaA2 Phe^{459}, and PsaA2 Cys^{463}. On the right, the corresponding Z-score polar plot obtained from DFT-calculated ESP maps is also shown in 3D. The Z-scores are displayed on the surface of the cone with its axis extending from that of the C2-C2′ bond, with an aperture of 120°. (**F**) Comparison of the experimental $P700^{+}$-minus-P700 difference spectrum of FR-PSI (black) (*26*) and that calculated (red) with a Chl f in the A_{-1B} position (at a temperature of 1.8 K).

the formyl carbon-oxygen double bond and the benzyl ring of Phe^{459} from PsaA2 (the far–red–induced paralog of one of the two core subunits of PSI) (Fig. 2, A to C and E), suggesting a π-stack interaction. A survey of high-resolution structures of FR-PSI and WL-PSI in the literature shows that these positive and negative features are conserved in the C2 A_{-1B} chlorophyll site from previously published FR-PSI and absent from the equivalent site in WL-PSI (fig. S10). The maximum and minimum experimental ESPs of these features when comparing FR-PSI and WL-PSI are statistically significant, strengthening the assignment of A_{-1B} as a Chl f and confirming that the cone-scan analysis is not sensitive to minor changes in the underlying atomic model (*8*, *9*).

We used density functional theory (DFT) calculations of the electrostatic and protein environment around A_{-1B} to gain chemical insights into the nature of the increased positive and negative potential signals detected in the experimental ESP and Z-score polar plots (Fig. 2, B and C). A DFT-calculated Chl f–minus–Chl a map, based on the 2.01-Å (Protein Data Bank pdb_00009EYS) structure, shows the regions of relatively positive and negative ESP around the formyl group and in the vicinity of PsaA2 Phe^{459}, reflecting the expected rearrangement of negative ESP along the geometric Q_y axis of the chlorophyll (fig. S11). DFT-calculated absolute ESP contour plots comparing Chl a and Chl f in the A_{-1B} site show additional negative ESP regions between the A_{-1B} chlorophyll and PsaA2 Phe^{459} when the Chl f is present but not when it is replaced by Chl a (fig. S14). When the highest-resolution structural model (pdb_00009I9L) is used (fig. S14E), the additional negative region is located between the formyl and the benzyl ring of PsaA2 Phe^{459}.

We also converted the DFT-calculated ESP maps into a format comparable with the experimental cone scans of absolute ESP and Z-scores around the C2 substituent of the A_{-1} chlorophyll. We note that although the scattering phenomena probed in cryo-EM reflect the atomic potentials, the extracted ESP signal differs from the ESP calculated using DFT, and so the scaling and intensities of the features are not directly comparable. In the supplementary materials, we show DFT-calculated absolute ESP and Z-score cone scans of (i) A_{-1B} in three different structural models with Chl a and Chl f modeled into the site (fig. S15) and (ii) controls using "known" Chl f and Chl a in other sites in FR-PSI (figs. S12 and S13). The experimental Z-score cone scans for A_{-1B} are clearly more like those calculated with the formyl substituent (i.e., Chl f) in the A_{-1B} position than those with the methyl group (i.e., Chl a) (fig. S15). An example of a DFT-calculated Z-score cone scan is shown in Fig. 2E (right-hand panel). The dominant positive red ESP from the formyl oxygen is in a similar position to that in the experimental Z-score, whereas the smaller positive region from the formyl hydrogen is not detected experimentally. In the calculated cone scan, the two near-symmetrical negative arcs, the stronger one proximal to the benzyl ring, may be counterparts to those in experimental Z-scores. The latter are much more asymmetric in their intensities, with the more intense negative region spread out closer to the benzyl ring. The additional asymmetry in intensity and location of the negative ESP in the experimental case may be attributed to the intrinsic negativity of the FR-A_{-1B} site modulated and intensified by the presence of the formyl group from Chl f. Together, these computational results are consistent with Chl a being replaced by Chl f in the A_{-1B} site.

Conserved FR-specific residues around A_{-1B} and steric effects

The apparent absence of conserved amino acid changes near the A_{-1} sites in FR-PSI has been used as an argument against the presence of a Chl f at this location (*8*). However, a conserved change, from Ile, Leu, or Val (depending on the species) to PsaA2 Cys^{463}, is present only in FR-PSI (Fig. 2D). The conserved sulfhydryl group of PsaA2 Cys^{463} and the C2 formyl of Chl f A_{-1B} are separated by the benzyl ring of PsaA2 Phe^{459} (Fig. 2A). The SH-π-formyl motif is likely to influence Chl f binding and redox tuning. The negative ESP near A_{-1B} (Fig. 2, B, C, and E), which is modified by the presence of the Phe-Cys pair (see DFT calculations in figs. S14 and S15), would be expected to destabilize the lowest unoccupied molecular orbital of the Chl f and make its redox potential more negative (*24*). This may compensate for the intrinsically less-reducing excited state of Chl f compared with that of Chl a, thereby restoring the reducing power needed for the PSI primary donor (*24*, *25*). Other conserved changes are present near the A_{-1B} site, PsaA2 Ala^{460}, PsaA2 Met^{461}, and PsaA2 Asn^{673}, with possible functional importance (Fig. 2D and fig. S18).

Another argument against the presence of Chl f in the A_{-1} positions was lack of space for the formyl oxygen (*12*); nevertheless, no steric clashes are observed in any of the FR-PSI structures available. The possibility that the equivalent site on the other electron-transfer branch of FR-PSI (A_{-1A}) is a Chl f, as previously suggested (*4*), is excluded on the basis of the absence of an increased ESP in the cryo-EM maps and the lack of conserved changes around this site (*4*).

Simulation of the $P700^+$-induced electrochromic changes in the absorption spectrum

We obtained independent evidence locating Chl f in the FR-PSI reaction center by calculating the illuminated-minus-dark ($P700^+ F_A^-$–minus–P700 F_A) difference absorption spectra from FR-PSI (*26*) and comparing them with experimental spectra (*26*) (Fig. 2F). In the charge-separated state, the positive charge is primarily localized on the special-pair pigment P_B (*27*), and the negative charge is known to reside on the iron sulfur cluster, F_A (*26*, *28*). The negative charge leads only to very minor electrochromic shifts that can be neglected (*26*) (fig. S27 and tables S11 to S13), whereas the positive charge on P_B has a measurable effect on the local transition energies (site energies) of nearby chromophores, particularly those in the reaction center (tables S1 to S3). Figure 2F shows a calculated $P700^+$-minus-P700 difference spectrum, in which the ground and excited states of the Chl a and Chl f, as well as the oxidized Chl a at the P_B site, are represented by atomic partial charges obtained from a fit of the ESP of their respective charge densities obtained with (time-dependent) DFT. The electrochromic shifts are obtained by considering the long-range Coulomb interaction between the partial charges of the pigments in their excited or ground states with the charge density of P_B in its oxidized or neutral state, as appropriate (supplementary text S3).

The P_B^+-induced shifts on either Chl a or Chl f in the A_{-1B} site were found to be 9 and −50 cm^{-1}, respectively. This sign difference between the two types of chlorophyll has not been previously predicted (*4*, *26*). With Chl f in the A_{-1B} site and with a site energy at 747 nm (corresponding to an absorption at 755 nm, where the red shift results from the reorganization energy of the optical transition), the improved calculation gave a $P700^+$-minus-P700 difference spectrum that almost quantitatively reproduces all features of the experimental spectrum (Fig. 2F). The difference spectrum cannot be reproduced when the calculation is done with Chl f in the antenna chlorophyll locations only and not in the A_{-1B} position (figs. S21 and S22). When calculations were done with Chl f at the A_{-1A} position, a band shift could be generated in the FR region. This is not surprising, given its location symmetrical to A_{-1B}, but the calculated spectrum is quantitatively a less-good fit to the experimental spectrum (fig. S23).

An additional small but distinct negative peak around 762 nm in the experimental spectrum is interpreted as a band shift from a Chl f antenna pigment. We calculated the largest electrochromic shifts of the Chl f pigments in the antenna to originate from the B30 (8.5 cm^{-1}) and B07 (10.5 cm^{-1}) sites (table S4). Whereas B07 is excitonically coupled to L03, B30 is relatively isolated from the other Chl f pigments, and its assignment to 762 nm would thus be consistent with the lack of a circular dichroism signal from this feature (*4*). The calculated difference spectrum with B30 as the 762-nm absorbing pigment nicely reproduces the experimental spectrum (Fig. 2F), whereas that done with B07 (fig. S33) at this wavelength is a less-good fit. Thus, the more likely candidate for the small negative dip at 762 nm in the $P700^+$-minus-P700 difference spectrum is B30.

All major peaks in the visible region of the $P700^+$-minus-P700 difference spectrum can be explained by considering a minimal model that takes into account the reaction-center pigments plus three antenna Chl a pigments—A26, B39, and B24—which are close to the reaction center and experience the largest electrochromic shifts (fig. S28 and table S1). The site energies of the critical pigments were obtained from a fit of the difference spectrum. For Chl f at the A_{-1B} site, this assignment is straightforward because there is no other Chl f in the reaction center, and, therefore, its excited state is practically localized on that pigment (fig. S31). Concerning the site energies of the Chl a pigments in our minimal model, an assignment is more difficult, because the difference spectrum is strongly influenced by delocalization effects of the excited states of these pigments (fig. S31). Nevertheless, an obvious best fit is obtained within our model assumptions. The calculated difference spectrum is robust with respect to (i) the detailed charge distribution of the state $P700^+$ (fig. S26), (ii) the influence of high-frequency vibrational modes and taking into account more sophisticated line-shape theory (fig. S29), and (iii) the structural variations between different cryo-EM models (fig. S25). The resolutions of the present and earlier cryo-EM models are high enough for electrostatic calculations of site-energy shifts induced by P_B^+. A direct calculation of site-energy shifts induced by the local environments of the pigments would require more detailed information, including amino acid side-chain conformations (*29*) and (for some pigments) wave function overlap with neighboring pigments (*30*–*32*), which are less certain.

The reports of a weak (*4*) or absent (*9*) Chl f band shift in room-temperature difference spectra can be explained by the temperature dependence of the dielectric constant (fig. S24). At room temperature, local conformational dynamics of polar groups in the protein, which are frozen out at cryogenic temperatures, contribute to the screening of electrostatic interactions, resulting in a larger dielectric constant and a smaller electrochromic shift (*33*). Whereas the high-energy Chl a side of the difference spectrum is influenced by both the excitonic couplings and the electrochromic shifts in site energies, the low-energy Chl f region is dominated by electrochromic effects (figs. S31 and S32). This is due to the Chl f at A_{-1B} being off-resonant with the other reaction-center chlorophylls, as they are all Chl a (see supplementary text S3).

Consequences of Chl f in the A_{-1B} site

Figure 2 provides evidence of A_{-1B} being a Chl f and likely acting as the primary electron donor responsible for the previously reported long-wavelength photochemistry at cryogenic temperatures (*4*). Most of the antenna Chl f molecules are also located on the B side, closer to A_{-1B}, and this reflects the greater number of conserved amino acid differences in PsaB2 relative to PsaA2 (*4*). Excitation with FR light should thus result in charge separation mainly on the B side of the reaction center, and this should be more marked at low temperatures. As seen in ultrafast kinetic studies, when excited by visible light, the Chl a antenna rapidly transfers the excitation onto the Chl f pigments (*12*, *34*). However, visible light may also excite redox-active Chl a molecules (A_{-1A}, P_A, and P_B), especially when they are excited directly, and these species are potentially capable of charge separation on the A side (*4*, *12*, *34*) if primary electron transfer can compete with energy transfer to the low-energy Chl f at A_{-1B}. This predicted complex mixture of kinetic pathways may be unraveled by the appropriate use of excitation-wavelength selectivity.

No changes are seen in the vicinity of the A-side quinone, A_{1A}, but a specific FR conserved change around the lower-potential quinone A_{1B} is present—the substitution of PsaB2 Ser^{673} with Thr (*35*). The structure around the quinone appears to be unaffected by this Ser-to-Thr difference, and thus a change in the redox properties of the A_{1B} is not expected. However, PsaB2 Thr^{673} is involved in a steric interaction with Chl A_{0B}, and this could limit any potential dynamic changes associated with quinone reduction. As pointed out recently, the PsaB2 Ser^{673}-to-Thr^{673} change, together with two other FR conserved amino acid changes (PsaB Val^{666}, Ile^{666}, and Ser^{667}), contribute to a 5° rotation of Chl A_{0B}, changing its aromatic overlap with A_{-1B} and thus modifying their coupling (*35*). Our quantum chemical calculations show that the rotation of Chl A_{0B} leads to increased electronic coupling in the Chl f A_{-1B}–Chl a A_{0B} pair (see supplementary text S4 and fig. S34) that may well be important for charge separation between the two chlorophylls.

Assignment of absorption peaks to Chl f sites

A23 is assigned here as an H-bonded Chl f, in agreement with earlier work (*9*, *10*) (fig. S4). The conserved amino acid changes in FR-PSI around this site in *C. thermalis* and *Halomicronema hongdechloris* are present in a subclass of FR-PSI found in approximately half of FR species, whereas the other half lack these changes and have a Met instead of a Glu in PsaA2 position 365 (fig. S4). In the structures of FR-PSI from *Fischerella thermalis* PCC 7521 and *Synechococcus* sp. PCC 7335, where PsaA2 Met^{365} is present, A23 was assigned as a Chl a based on sequence analysis and structure (*11*). A comparison of the 77-K absorption spectra in the literature from these two types of FR-PSI shows several differences in the 740- to 760-nm region (*4*, *9*, *13*), corresponding to changes in contributions of some Chl f molecules to the absorption spectra (i.e., excitonic coupling, reorganization energy) and the loss of a Chl f in the A23 site. The complexity of the spectral differences does not allow a definitive interpretation, but it seems consistent with contributions from A23 to the absorption around 750 nm and an underlying absorption from A_{-1B} Chl f at 755 nm (see supplementary text S1).

The 77-K fluorescence spectra of FR-PSI show the presence of two terminal emitters, one at ~750 nm and the other at ~800 nm, with the exact wavelength depending on the species (*4*, *13*). The two terminal emitters are expected to be separated from each other, both spatially and by an energy barrier, such as by several Chl a molecules. Tros *et al.* (*36*) showed that the emitter at ~750 nm was insensitive to the presence of $P700^+$, whereas the emitter at ~800 nm was quenched by $P700^+$. The emission at ~800 nm originates from a coupled pair of Chl f molecules, B37 and B38 (*4*, *13*), with a distance from P_B^+ of 26 Å. In this pair, the interpigment distance is less than 4 Å, where short-range contributions to site-energy shifts (*32*) and difference-dipole moments (*37*) are expected to be substantial. In agreement with this assignment, we found that we needed to increase the difference-dipole moments of B37 and B38 by at least a factor of five to explain the order of magnitude of the experimental $P700^+$-minus-P700 difference signal around 800 nm (fig. S30). The quenching of the ~800-nm emitter by $P700^+$ seems likely to be protective in excess light.

The lack of quenching of the ~750-nm emitter likely reflects it being at a greater distance from $P700^+$ than the 800-nm emitter. From their locations (fig. S35), A21 and B30 are the most likely candidates to be the emitter at ~750 nm, as already suggested (*13*), because they are both far from $P700^+$ (34 and 28 Å, respectively) and seem relatively isolated from the central core of Chl f molecules. However, the wavelength assigned to B30 is 762 nm on the basis of its contribution to the band shifts in the difference spectrum (Fig. 2F). Therefore, A21 appears to be the more likely of the two candidates. Given the proximity of A21 to A23, for A21 to be the terminal emitter, A23 would have to absorb at a shorter wavelength within the range assigned to it above (i.e., 740 to 760 nm), otherwise A21 would transfer excitation energy to the lower-energy pigment (A23) rather than emit.

Although individual Chl f molecules can be tentatively assigned to specific absorptions in the spectrum (A_{-1B}, 755 nm, B37-B38 pair at 800 nm, B30 at 762 nm), there is insufficient evidence to assign the others. Now that they have all been localized, future work will focus on their physical and functional properties.

Functional importance of the trimerization on excitation-energy transfer

ESP polar plots of Chl L03 show a clear density for a formyl group in the C2 position that does not appear to be H-bonded (Fig. 3). A FR-specific conserved amino acid change is present, with PsaL2 Val^{81} replacing the Lys, Leu, or Ile of the WL PsaL, generating the space necessary for the formyl group. The increased ESP density is present at a polar angle that suggests a possible interaction with a diglyceride (LMG^{5007}) that is present both in WL-PSI and FR-PSI (Fig. 3, A to C).

FR-PSI exists as trimers in vivo, whereas WL-PSI is found as dimers or tetramers in *C. thermalis* (*38*). The Chl f sites identified here are mainly located on the PsaB2 side of the FR-PSI complex, and trimerization results in that side being close to the interface between individual PSI monomers. Thus, the formation of a FR-PSI trimer results in a core structure enriched in Chl f (fig. S35). PsaL2 mediates trimer formation, and the Chl f in the L03 site is between the B07 Chl f of the same complex and that of the neighboring one. Thus, the Chl f L03 likely plays an important role in the Chl f connectivity in FR-PSI trimers. Within this core, the distances between Chl f molecules could allow efficient excitation-energy transfer between the Chl f molecules and between the PSI monomers in the trimer (Fig. 3E). Excitation-energy sharing between the individual PSI complexes in the PSI trimer has been suggested to occur in WL-PSI via specific routes, one of which involves the chlorophylls of PsaL (*39*). Excitation-energy sharing among the Chl f molecules within the trimer would increase the chances of charge separation when one or both of other PSI monomers in the trimer are photochemically "closed."

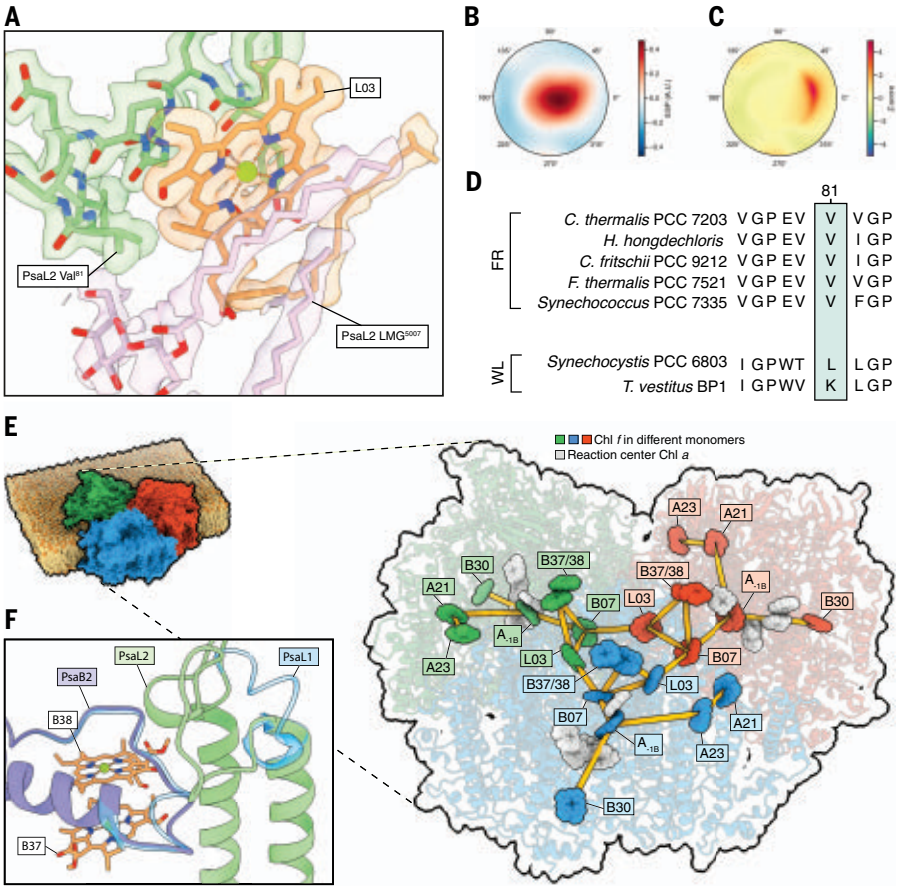


Fig. 3. The L03 Chl f site, a long-wavelength bridge between the monomers. (**A**) Chemical environment of the L03 chlorophyll. The chlorophyll density is in orange, the density of the amino acid residues from PsaL2 is in green, and the density of the diglyceride is in pink. (**B**) ESP polar plot indicating the presence of an increased potential around the C2 substituent. (**C**) Z-score polar plot indicating the presence of an increased potential around the C2 substituent. (**D**) Multiple sequence alignment of FR and WL PsaL, showing the FR-specific Val residue in position 81. E, Glu; K, Lys; P, Pro; W, Trp. (**E**) Position of the Chl f molecules in a FR-PSI trimer (right) as seen from the orientation on the left. Each monomer is colored in red, green, and blue; connections to the nearest Chl f neighbors are represented in yellow. L03 and B07 form a ring of Chl f pigments at the core of the trimer. Their distance within the same monomer is ~11 Å, and their distance between two monomers is ~15 Å. (**F**) The structures of WL-PSI PsaB and PsaL are represented in blue, Chl f in orange, PsaB2 in purple, and PsaL2 in green.

The present work also confirms that both positive and negative ESP signals can provide information on the electrostatic environment and the orientation of functional groups of cofactors and amino acid side chains, as discussed previously (*15*–*17*). Here, information obtained from this extra data provides additional mechanistic insights. When present, the H-bonds to the formyl oxygen not only stabilize the binding of the Chl f but also shift the redox properties of the chlorophylls, making them easier to reduce and harder to oxidize. This would not greatly affect the antenna function of chlorophylls (other than small changes in their absorption peaks), but it would be detrimental for Chl f when it comes to a redox role and, particularly, a role as the primary donor, which is thought to be the most reducing species in PSI, the low-potential photosystem. Therefore, a Chl f acting as a primary donor in PSI would be expected to lack an H-bond to its formyl group and thus be difficult to detect by cryo-EM. Both expectations were found to be the case for the Chl f in the A_{-1B} site. Indeed, the FR-A_{-1B} site appears to be specifically negatively charged (Fig. 2, B, C, and E), an indication of redox tuning.

The identification of Chl f at the L03 site in the core of the trimer and at the A_{-1B} site in the reaction center represents major advances in understanding how FR-PSI works. The L03 Chl f indicates excitation-energy sharing between the PSI monomers in the trimer, whereas the A_{-1B} Chl f indicates photochemistry with Chl f as the primary donor. The $P700^{+}$-minus-P700 difference spectrum cannot be explained without the presence of a Chl f in the reaction center. Previous spectroscopic studies of FR-PSI, which assumed no Chl f in the reaction center, and their resulting mechanistic models of excitation-energy transfer and charge separation should now be reassessed. FR-PSI is comparable to Chl d PSI in *Acaryochloris marina* [with the primary donor P740 (*40*)], in that they both use near-infrared photons for oxygenic photosynthesis, and thus they have broken the red photochemical energy limit. As seen with PSII (*4*, *41*), these two distinct low-energy paradigms have evolved different strategies to perform the same chemistry as in conventional Chl a photosynthesis but by using less energy. Comparisons of the two long-wavelength paradigms with each other and with Chl a photosystems will advance our understanding of the mechanisms of all three.

The importance of this intertrimer Chl f connectivity is also highlighted by another structural feature: the FR-specific B37-B38 loop of PsaB2, which has extensive interactions with a FR-specific loop of PsaL2 (Fig. 3F). These interactions could stabilize the B37-B38 Chl f dimer, favor the association of PsaB2-PsaL2, and prevent the formation of a chimeric WL-FR-PSI by obstructing PsaL1 and PsaB2 interactions.

Conclusions

The structural models presented here show the positions of all expected eight Chl f molecules in FR-PSI. H-bonds stabilize most of the antenna Chl f molecules—that is, A21, A23, B07, B30, and B37 (figs. S3 to S7)—making the formyl oxygens on Chl f more easily detectable by cryo-EM. When the formyl oxygens are not H-bonded—that is, A_{-1B}, L03, and B38 (Figs. 2A and 3A and fig. S8)—they are more difficult to detect because of their increased negative partial charge and because they may occupy a broader range of torsion angles. This class of formyl oxygens therefore required improved resolution and the development of more thorough statistical analysis to allow them to be detected in cryo-EM maps. This explains their apparent absence from earlier work.

Materials and methods are available in the supplementary materials.

REFERENCES AND NOTES

1. M. Chen *et al.*, A red-shifted chlorophyll. *Science* **329**, 1318–1319 (2010). doi: 10.1126/science.1191127; pmid: 20724585
2. F. Gan *et al.*, Extensive remodeling of a cyanobacterial photosynthetic apparatus in far-red light. *Science* **345**, 1312–1317 (2014). doi: 10.1126/science.1256963; pmid: 25214622
3. L. A. Antonaru, T. Cardona, A. W. D. Larkum, D. J. Nürnberg, Global distribution of a chlorophyll f cyanobacterial marker. *ISME J.* **14**, 2275–2287 (2020). doi: 10.1038/s41396-020-0670-y; pmid: 32457503
4. D. J. Nürnberg *et al.*, Photochemistry beyond the red limit in chlorophyll f-containing photosystems. *Science* **360**, 1210–1213 (2018). doi: 10.1126/science.aar8313; pmid: 29903971
5. S. I. Allakhverdiev *et al.*, Chlorophylls d and f and their role in primary photosynthetic processes of cyanobacteria. *Biochemistry* **81**, 201–212 (2016). doi: 10.1134/S0006297916030020; pmid: 27262189

6. M. Chen, R. E. Blankenship, Expanding the solar spectrum used by photosynthesis. *Trends Plant Sci.* **16**, 427–431 (2011). doi: 10.1016/j.tplants.2011.03.011; pmid: 21493120
7. C. J. Gisriel *et al.*, Structure of a dimeric photosystem II complex from a cyanobacterium acclimated to far-red light. *J. Biol. Chem.* **299**, 102815 (2023). doi: 10.1016/j.jbc.2022.102815; pmid: 36549647
8. C. Gisriel *et al.*, The structure of photosystem I acclimated to far-red light illuminates an ecologically important acclimation process in photosynthesis. *Sci. Adv.* **6**, eaay6415 (2020). doi: 10.1126/sciadv.aay6415; pmid: 32076649
9. K. Kato *et al.*, Structural basis for the adaptation and function of chlorophyll f in photosystem I. *Nat. Commun.* **11**, 238 (2020). doi: 10.1038/s41467-019-13898-5; pmid: 31932639
10. C. J. Gisriel *et al.*, Quantitative assessment of chlorophyll types in cryo-EM maps of photosystem I acclimated to far-red light. *BBA Adv.* **1**, 100019 (2021). doi: 10.1016/j.bbadva.2021.100019; pmid: 37082022
11. C. J. Gisriel *et al.*, Structure of a photosystem I-ferredoxin complex from a marine cyanobacterium provides insights into far-red light photoacclimation. *J. Biol. Chem.* **298**, 101408 (2022). doi: 10.1016/j.jbc.2021.101408; pmid: 34793839
12. D. A. Cherepanov *et al.*, Evidence that chlorophyll f functions solely as an antenna pigment in far-red-light photosystem I from *Fischerella thermalis* PCC 7521. *Biochim. Biophys. Acta Bioenerg.* **1861**, 148184 (2020). doi: 10.1016/j.bbabio.2020.148184; pmid: 32179058
13. M. Tros *et al.*, Breaking the red limit: Efficient trapping of long-wavelength excitations in chlorophyll-f-containing photosystem I. *Chem* **7**, 155–173 (2021). doi: 10.1016/j.chempr.2020.10.024
14. I. H. M. van Stokkum *et al.*, Energy transfer and trapping in photosystem I with and without chlorophyll-*f*. *iScience* **26**, 107650 (2023). doi: 10.1016/j.isci.2023.107650; pmid: 37680463
15. J. Wang, P. B. Moore, On the interpretation of electron microscopic maps of biological macromolecules. *Protein Sci.* **26**, 122–129 (2017). doi: 10.1002/pro.3060; pmid: 27706888
16. C. J. Gisriel, J. Wang, G. W. Brudvig, D. A. Bryant, Opportunities and challenges for assigning cofactors in cryo-EM density maps of chlorophyll-containing proteins. *Commun. Biol.* **3**, 408 (2020). doi: 10.1038/s42003-020-01139-1; pmid: 32733087
17. M. A. Marques, M. D. Purdy, M. Yeager, CryoEM maps are full of potential. *Curr. Opin. Struct. Biol.* **58**, 214–223 (2019). doi: 10.1016/j.sbi.2019.04.006; pmid: 31400843
18. J. K. Hoober, L. L. Eggink, M. Chen, Chlorophylls, ligands and assembly of light-harvesting complexes in chloroplasts. *Photosynth. Res.* **94**, 387–400 (2007). doi: 10.1007/s11120-007-9181-1; pmid: 17505910
19. H. Toporik, Z. Dobson, Y. Mazor, "The photosystem I complex of oxygenic photosynthesis" in *Encyclopedia of Biological Chemistry III*, vol. 2, J. Jez, Ed. (Elsevier, ed. 3, 2021), pp. 191–206.
20. M. G. Müller, J. Niklas, W. Lubitz, A. R. Holzwarth, Ultrafast transient absorption studies on photosystem I reaction centers from *Chlamydomonas reinhardtii*. 1. A new interpretation of the energy trapping and early electron transfer steps in photosystem I. *Biophys. J.* **85**, 3899–3922 (2003). doi: 10.1016/S0006-3495(03)74804-8; pmid: 14645079
21. M. G. Müller, C. Slavov, R. Luthra, K. E. Redding, A. R. Holzwarth, Independent initiation of primary electron transfer in the two branches of the photosystem I reaction center. *Proc. Natl. Acad. Sci. U.S.A.* **107**, 4123–4128 (2010). doi: 10.1073/pnas.0905407107; pmid: 20142514
22. P. Jordan *et al.*, Three-dimensional structure of cyanobacterial photosystem I at 2.5 Å resolution. *Nature* **411**, 909–917 (2001). doi: 10.1038/35082000; pmid: 11418848
23. C. J. Gisriel *et al.*, A quantitative assessment of (bacterio)chlorophyll assignments in the cryo-EM structure of the *Chloracidobacterium thermophilum* reaction center. *Photosynth. Res.* **162**, 187–196 (2024). doi: 10.1007/s11120-023-01047-5; pmid: 37749456
24. M. Kobayashi *et al.*, "Physicochemical properties of chlorophylls in oxygenic photosynthesis—succession of co-factors from anoxygenic to oxygenic photosynthesis" in *Photosynthesis*, Z. Dubinsky, Ed. (InTech Rijeka, 2013), pp. 47–90.
25. J. R. Diers *et al.*, A perspective on the redox properties of tetrapyrrole macrocycles. *Phys. Chem. Chem. Phys.* **23**, 19130–19140 (2021). doi: 10.1039/D1CP01943K; pmid: 34490865
26. J. Langley *et al.*, Simulating the low-temperature, metastable electrochromism of photosystem I: Applications to *Thermosynechococcus vulcanus* and *Chroococcidiopsis thermalis*. *J. Chem. Phys.* **157**, 125103 (2022). doi: 10.1063/5.0100431; pmid: 36182424
27. A. Petrenko *et al.*, A high-field EPR study of P700+ in wild-type and mutant photosystem I from *Chlamydomonas reinhardtii*. *Biochemistry* **43**, 1781–1786 (2004). doi: 10.1021/bi035466j; pmid: 14967019
28. I. R. Vassiliev, M. L. Antonkine, J. H. Golbeck, Iron–sulfur clusters in type I reaction centers. *Biochim. Biophys. Acta Bioenerg.* **1507**, 139–160 (2001). doi: 10.1016/S0005-2728(01)00197-9
29. J. Adolphs, F. Müh, Mel.-A. Madjet, T. Renger, Calculation of pigment transition energies in the FMO protein: From simplicity to complexity and back. *Photosynth. Res.* **95**, 197–209 (2008). doi: 10.1007/s11120-007-9248-z; pmid: 17917787
30. M. Gorka *et al.*, A dimeric chlorophyll electron acceptor differentiates type I from type II photosynthetic reaction centers. *iScience* **24**, 102719 (2021). doi: 10.1016/j.isci.2021.102719; pmid: 34278250
31. F. G. Gemeinhardt *et al.*, Short-range effects in the special pair of photosystem II reaction centers: The nonconservative nature of circular dichroism. *J. Phys. Chem. Lett.* **14**, 11758–11767 (2023). doi: 10.1021/acs.jpclett.3c02693; pmid: 38117270
32. Mel.-A. Madjet, F. Müh, T. Renger, Deciphering the influence of short-range electronic couplings on optical properties of molecular dimers: Application to "special pairs" in photosynthesis. *J. Phys. Chem. B* **113**, 12603–12614 (2009). doi: 10.1021/jp906009j; pmid: 19697949
33. G. Raszewski, B. A. Diner, E. Schlodder, T. Renger, Spectroscopic properties of reaction center pigments in photosystem II core complexes: Revision of the multimer model. *Biophys. J.* **95**, 105–119 (2008). doi: 10.1529/biophysj.107.123935; pmid: 18339736
34. M. Kaucikas, D. Nürnberg, G. Dorlhiac, A. W. Rutherford, J. J. van Thor, Femtosecond visible transient absorption spectroscopy of chlorophyll f-containing photosystem I. *Biophys. J.* **112**, 234–249 (2017). doi: 10.1016/j.bpj.2016.12.022; pmid: 28122212
35. C. J. Gisriel, D. A. Bryant, G. W. Brudvig, T. Cardona, Molecular diversity and evolution of far-red light-acclimated photosystem I. *Front. Plant Sci.* **14**, 1289199 (2023). doi: 10.3389/fpls.2023.1289199; pmid: 38053766
36. M. Tros *et al.*, Harvesting far-red light: Functional integration of chlorophyll f into photosystem I complexes of *Synechococcus* sp. PCC 7002. *Biochim. Biophys. Acta Bioenerg.* **1861**, 148206 (2020). doi: 10.1016/j.bbabio.2020.148206; pmid: 32305412
37. D. J. Lockhart, S. G. Boxer, Magnitude and direction of the change in dipole moment associated with excitation of the primary electron donor in *Rhodopseudomonas sphaeroides* reaction centers. *Biochemistry* **26**, 664–668 (1987). doi: 10.1021/bi00377a001
38. C. MacGregor-Chatwin *et al.*, Changes in supramolecular organization of cyanobacterial thylakoid membrane complexes in response to far-red light photoacclimation. *Sci. Adv.* **8**, eabj4437 (2022). doi: 10.1126/sciadv.abj4437; pmid: 35138895
39. M. K. Şener *et al.*, Excitation migration in trimeric cyanobacterial photosystem I. *J. Chem. Phys.* **120**, 11183–11195 (2004). doi: 10.1063/1.1739400; pmid: 15268148
40. A. A. Petrova *et al.*, Role of pheophytin a in the primary charge separation of photosystem I from *Acaryochloris marina*: Femtosecond optical studies of excitation energy and electron transfer reactions. *Biochim. Biophys. Acta Bioenerg.* **1864**, 148984 (2023). doi: 10.1016/j.bbabio.2023.148984; pmid: 37187220
41. S. Viola *et al.*, Impact of energy limitations on function and resilience in long-wavelength photosystem II. *eLife* **11**, e79890 (2022). doi: 10.7554/eLife.79890; pmid: 35852834
42. G. Consoli, M. Sandrin, J. W. Murray, chlorophyll-substituents-scan. Release v0.1.0. Zenodo (2025); https://doi.org/10.5281/zenodo.16927639.

ACKNOWLEDGMENTS

We thank K. Renard for the numerous discussions, J. Schuller for the insightful conversation and suggestion on grid preparation and data processing, D. Bubeck for useful suggestions on data processing, V. Kaila for helpful suggestions on the computational approaches, S. Islam for computation assistance, and D. Lindorfer and S. Egginger for support in the early stage of the calculation of optical difference spectra. We thank the Centre for Structural Biology at Imperial College for the training provided and for help with the early stages of sample screening and with data collection. We thank Diamond for access to and support from the cryo-EM facilities at the UK's national electron Bio-Imaging Centre (eBIC), proposal BI25127. This project made use the Computing Platform for Electron Microscopy at Imperial College funded by the Biotechnology and Biological Sciences Research Council (BBSRC) mid-range equipment initiative 22ALERT (BB/X019284/1). **Funding:** This work was funded by Marie Skłodowska-Curie grant agreement no. 955520 (G.C., M.S., A.W.R., A.F., B.C.); Biotechnology and Biological Sciences Research Council (BBSRC) grants BB/R001383/1 (A.W.R., A.F., S.V., G.A.D.), BB/V002015/1 (A.W.R,. A.F., J.W.M., S.V., D.M.), BB/R00921X (A.W.R., A.F., G.A.D.), and BB/M011178/1 (F.T.); Leverhulme Trust grant RPG-2022-203 (A.W.R., G.A.D., A.F.); UKRI, Frontier Research Guarantee "POTENtIAl," EP/Z533361/1 (J.N.); European Research Council, Advanced Grant CAPaCITy, grant agreement no. 742708 (J.N., D.M.); The Royal Society (Royal Society Research Professorship 2021) (J.N., N.R.); an Engineering and Physical Sciences Research Council Doctoral training award (N.R.); The Royal Society (Royal Society Research Professorship 2024) (A.W.R.); Austrian Science Fund (FWF) P33155-NBL (T.R.) and I-6313-N (T.R.); and Marie Skłodowska-Curie grant agreement no. 101119442 (T.R.). **Author contributions:** G.C., F.T., and H.F.L. initiated the study. S.V. grew and harvested *C. thermalis* PCC 7203. G.C., F.T., H.F.L., A.F., and A.W.R. conceived of the main experiments, collated results and interpretations, and wrote the article with input, edits, and approval from all authors. S.V. and G.A.D. developed and performed the isolation of the photosystems. G.C. and F.T. prepared the grids. G.C., F.T., and P.S. collected the micrographs. G.C. and F.T. processed the data to obtain the maps. G.C., F.T., and J.W.M. built the atomic models. H.F.L. and A.F. collected the sequences and performed the phylogenetic analysis. G.C., M.S., and J.W.M. developed and coded the local experimental ESP quantification method and its visualization. N.R., D.M., and J.N. performed DFT calculations, developed the method to calculate and visualize computational ESP and Z-score cone scans, calculated A_{0B}/A_{-1B} electronic coupling, and wrote the relevant sections in the main text and supplementary materials. M.H. and T.R. calculated the electrochromic shifts, simulated the $P700^{+}$-minus-P700 difference spectrum, performed the underlying electronic structure

calculations, and wrote the relevant sections in the main text and supplementary materials. G.C. and B.C. fitted the low-temperature absorption spectra. **Competing interests:** The authors declare that they have no competing interests. **Data and materials availability:** The atomic coordinates have been deposited in the Protein Data Bank under accession codes pdb_00009EYS (2.01 Å) and pdb_00009I9L (1.89 Å). Data and scripts used in data processing, analysis, and visualization are available on GitHub (https://github.com/giovanniconsoli/chlorophyll-substituents-scan) and are archived at Zenodo (*42*). **License information:** Copyright © 2025 the authors, some rights reserved; exclusive licensee American Association for the Advancement of Science. No claim to original US government works. https://www.science.org/about/science-licenses-journal-article-reuse. This research was funded in whole or in part by UKRI (BB/R001383/1, BB/V002015/1, BB/R00921X, BB/M011178/1, EP/Z533361/1), a cOAlition S organization, and by ERC (742708); as required, the author will make the Author Accepted Manuscript (AAM) version available under a CC BY public copyright license.

SUPPLEMENTARY MATERIALS

science.org/doi/10.1126/science.ado6830
Materials and Methods; Supplementary Text; Figs. S1 to S38; Tables S1 to S25; References (*43*–*81*)

Submitted 11 June 2024; resubmitted 27 February 2025; accepted 4 September 2025; published online 9 October 2025

10.1126/science.ado6830

Science
JOURNALS AAAS



Publish your research in the *Science* family of journals

The *Science* family of journals (*Science, Science Advances, Science Immunology, Science Robotics, Science Signaling*, and *Science Translational Medicine)* are among the most highly-regarded journals in the world for quality and selectivity. Our peer-reviewed journals are committed to publishing cutting-edge research, incisive scientific commentary, and insights on what's important to the scientific world at the highest standards.

Submit your research today!

Learn more at **Science.org/journals**

RESEARCH ARTICLE SUMMARY

CELL BIOLOGY

Mechanosensitive genomic enhancers potentiate the cellular response to matrix stiffness

Brian D. Cosgrove†, Lexi R. Bounds†, Carson Key Taylor†, Alan L. Su, Anthony J. Rizzo, Alejandro Barrera, Tongyu Sun, Alexias Safi, Lingyun Song, Thomas Whitlow, Aleksandra Tata, Nahid Iglesias, Yarui Diao, Purushothama Rao Tata, Brenton D. Hoffman*, Gregory E. Crawford*, Charles A. Gersbach*

Full article and list of author affiliations: https://doi.org/10.1126/science.adl1988

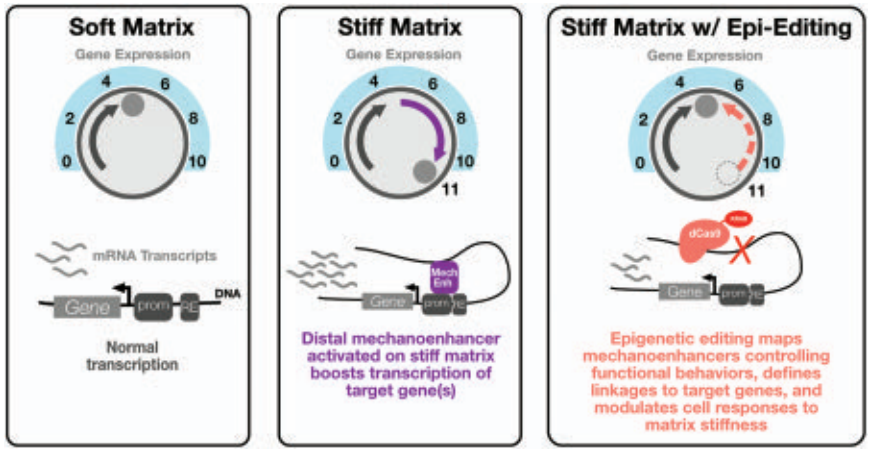
INTRODUCTION: Cellular behaviors are heavily influenced by the mechanical properties of their microenvironments, such as extracellular matrix stiffness and applied external forces. These mechanical stimuli are known to influence fundamental cellular functions such as growth, apoptosis, differentiation, and migration. Moreover, they play a key role in tissue development, regeneration, aging, and mechanically sensitive disease processes such as fibrosis, tumor growth, and atherosclerosis. Despite the role of mechanical inputs in these important functions, the influence of mechanical cues on the epigenome that regulates the downstream changes in gene expression that govern these behaviors remains largely unexplored.

RATIONALE: Understanding how and where mechanical cues shape gene expression and genome structure could reveal how cells adapt to different physical environments and provide insights into mechanisms driving diseases such as fibrosis and cancer, where altered tissue stiffness is implicated in disease progression. This study aimed to identify regulatory regions of the noncoding genome that respond to changes in the mechanical environment and influence transcription of nearby genes. We refer to these mechanically sensitive genomic regulatory elements as "mechanoenhancers." Using a combination of genome-wide chromatin accessibility profiling, epigenetic editing, high-throughput CRISPR screening on cell functions including growth and migration, and CRISPR-based epigenetic editing paired with single-cell RNA sequencing (RNA-seq), we investigated how cells sense mechanical cues and convert that information into changes in genome structure, gene expression, and behavior.

RESULTS: Human fibroblasts and A549 lung adenocarcinoma cells grown on soft (1 kPa) or stiff (50 kPa) hydrogels showed widespread differences in gene expression and chromatin accessibility by RNA-seq and ATAC-seq (assay for transposase-accessible chromatin with high-throughput sequencing). CRISPR interference (CRISPRi) was used to perturb differentially accessible regions surrounding stiffness-responsive genes such as *MYH9*, *BMF*, and *FZD2* and identify distal mechanoenhancers that influence gene expression. Functional high-throughput CRISPRi screening was performed to discover ~100 putative regulatory regions that influenced cell growth or migration. CRISPRi screening with single-cell RNA-seq identified 201 functional connections of these mechanoenhancers to their gene targets, including *CTGF*, *CYR61*, *NF2*, *RFLNB*, *RANGAP1*, *SKP2*, and others. Epigenetic editing of mechanoenhancers with CRISPRi in cells cultured on stiff substrates, including activated human donor–derived fibroblasts from healthy and idiopathic pulmonary fibrosis lung tissue, resulted in gene expression patterns similar to those observed on soft substrates. Epigenetic modulation of these mechanoenhancers also resulted in functional changes in mechanosensing, migration, growth, and apoptosis.

CONCLUSION: This study identifies mechanoenhancers as key regulators of how cells translate mechanical cues into gene activity and functional behaviors. Epigenetic repression of stiffness-activated mechanoenhancers resulted in marked reductions in target gene expression, even in the continued presence of strong mechanical cues. Epigenetic editing of these enhancers can reprogram the cellular response to material stiffness without disrupting normal gene function, highlighting mechanoenhancers as a promising potential therapeutic target in diseases characterized by abnormal tissue stiffness. □

*Corresponding author. Email: charles.gersbach@duke.edu (C.A.G.); greg.crawford@duke.edu (G.E.C.); brenton.hoffman@duke.edu (B.D.H.) †These authors contributed equally to this work. Cite this article as B. D. Cosgrove *et al.*, *Science* **390**, eadl1988 (2025). DOI: 10.1126/science.adl1988



Mechanoenhancers control gene expression responses in environments of pathological tissue stiffness. (Left) Soft tissue matrix representative of the normal physiologic microenvironment leads to moderate gene expression levels. (Middle) Stiff matrix typical of some pathogenic environments can activate distal mechanoenhancers that promote target gene expression. (Right) Epigenetic editing of mechanoenhancers on stiff matrix can block responses to these cues, thereby reverting transcription levels and cell functions to those seen on softer tissue. prom, promoter; RE, regulatory element; Mech Enh, mechanoenhancer.

CELL BIOLOGY

Mechanosensitive genomic enhancers potentiate the cellular response to matrix stiffness

Brian D. Cosgrove[1,2]†, Lexi R. Bounds[1,2]†, Carson Key Taylor[1,2]†, Alan L. Su[1,2], Anthony J. Rizzo[1,2], Alejandro Barrera[2,3], Tongyu Sun[4], Alexias Safi[2,5], Lingyun Song[2,5], Thomas Whitlow[4], Aleksandra Tata[4,6], Nahid Iglesias[1,2], Yarui Diao[2,4,7], Purushothama Rao Tata[2,4,7,8], Brenton D. Hoffman[1,4]*, Gregory E. Crawford[2,5]*, Charles A. Gersbach[1,2,4,6,7]*

Epigenetic control of gene expression and cellular phenotype is influenced by changes in the local microenvironment, yet how mechanical cues precisely influence epigenetic state to regulate transcription remains largely unmapped. In this study, we combined genome-wide epigenome profiling, epigenome editing, and phenotypic and single-cell RNA sequencing CRISPR screening to identify a class of genomic enhancers that responds to the mechanical microenvironment. These "mechanoenhancers" can be preferentially activated on either soft or stiff extracellular matrix contexts and regulate transcription to influence critical cell functions including apoptosis, adhesion, proliferation, and migration. Epigenetic editing of mechanoenhancers reprograms the cellular response to the mechanical microenvironment and modulates the activation of disease-related genes in lung fibroblasts from healthy and fibrotic donors. Epigenetic editing of mechanoenhancers holds potential for precise targeting of mechanically driven diseases.

The cellular microenvironment is a potent regulator of cellular behavior (*1*, *2*). Advances in epigenetic profiling and CRISPR screening have deepened our understanding of how chemical stimuli including hormones, cytokines, and pharmacologic interventions shape the epigenetic landscape (*3*–*6*). Mechanical stimuli from the microenvironment, such as stiffness of the extracellular matrix (ECM) or applied forces, are also potent regulators of many fundamental cell processes, including growth, death, differentiation, and migration, and play key roles in tissue development, regeneration, aging, and disease pathology such as fibrosis, tumor formation, and atherosclerosis (*7*–*10*). Mechanosensitive gene regulation occurs across a variety of pathways through nucleocytoplasmic shuttling of transcriptional co-regulators (*11*), including YAP and MRTF (*12*–*14*). These proteins shuttle to the nucleus through pathways responsive to mechanical cues, such as nuclear pore deformation (*15*) and filamentous/globular actin (F/G-actin) ratios (*16*–*18*). Mechanical force has additionally been shown to modulate epigenetic modifications (*19*–*22*) and directly deform chromatin (*23*, *24*), both of which can influence patterns of gene expression.

Traditionally, the binding of transcription factors and coactivators at promoter regions has been the classical mechanism for modulation of target gene expression. However, genome annotation efforts over the past two decades have described the critical role of noncoding gene regulatory regions that occur predominantly outside promoters (*25*). For instance, the mechanosensitive coactivators YAP/TAZ can bind to distal enhancers in cells cultured on rigid tissue culture plastic (*26*, *27*). Enhancers act across variable genomic distances to regulate transcription and are marked by a combination of chromatin accessibility, presence of active histone marks (e.g., H3K27ac), depletion of repressive histone marks (e.g., H3K9me3), transcription factor binding, and chromatin looping to distal target genes (*28*). The complex logic of gene regulation by these distal elements has been notoriously difficult to dissect, but advances in high-throughput CRISPR screening and single-cell genomics have transformed the capability to classify how and where these cis-regulatory elements modulate transcription across the genome (*4*, *5*, *29*, *30*).

Despite these recent developments, the impact of mechanical stimuli on the noncoding genome and the resulting transcriptional and phenotypic responses remain largely unmapped. In this study, we used genome-wide chromatin accessibility profiling, epigenetic editing, high-throughput CRISPR screening, and single-cell sequencing to characterize how ECM stiffness cues activate cis-regulatory elements to regulate gene expression. Through this work, we identified and validated a previously unknown set of cis-regulatory elements that are responsive to changes in the mechanical microenvironment. For simplicity, we term these regions as "mechanoenhancers" and show that they behave as key drivers for downstream mechanically driven behaviors in human cells. This work provides new insights into the regulation of gene expression by mechanical cues.

Results

Widespread changes in gene expression and chromatin accessibility result from short-term exposure to physiologically soft or stiff substrates

We first characterized the response of gene expression and chromatin structure to changes in ECM stiffness cues by culturing primary human neonatal foreskin fibroblasts (HFF cells) and A549 tumor-derived lung epithelial cells on substrate stiffness conditions mimicking a range of pericellular environments found in both healthy and diseased tissues. Fibroblasts were chosen because of their key role in ECM synthesis and their contribution to tissue fibrosis (*31*) and because they have been extensively profiled through functional genomics. Similarly, the A549 cell line responds to ECM stiffness (*32*), complements skin fibroblasts, and has extensive functional genomics data readily available (*33*–*35*). Cells were cultured for 20 hours on either soft (elastic modulus, $E = 1$ kPa, mimicking soft connective tissues) or stiff ($E = 50$ kPa, mimicking organized musculoskeletal tissues or fibrotic lesions) polyacrylamide hydrogels (*9*, *36*, *37*) as well as on tissue culture plastic (TCP; E = ~1 GPa). The 20-hour time point minimizes transcriptional feedback that could further complicate understanding the direct influence of ECM stiffness on epigenetic state. After 20 hours, cells were harvested to examine both transcriptional changes [RNA sequencing (RNA-seq)] and chromatin accessibility changes [assay for transposase-accessible chromatin with high-throughput sequencing (ATAC-seq)] in response to these ECM stiffness cues (Fig. 1A). We performed all sequencing experiments in at least duplicate per condition, and all RNA-seq and ATAC-seq data were highly reproducible and met appropriate quality control metrics (fig. S1 and table S1).

Transcriptomic analysis identified 4009 differentially expressed genes in HFFs and 221 differentially expressed genes in A549 cells [defined as false discovery rate (FDR) < 0.05 and absolute value($\log_2$ fold change) > 0.5] (Fig. 1, B and C, and tables S2 and S3). The disparity in the number of differentially expressed genes between the two cell types may reflect the difference in mechanical memory between primary cells and immortalized lines, with transcriptional adaptation potentially occurring after longer subculturing and increased mechanical memory in A549 cells (*38*). Notably, 76 genes were differentially expressed in both cell types, including canonical genes associated with YAP/TAZ

[1]Department of Biomedical Engineering, Duke University, Durham, NC, USA. [2]Center for Advanced Genomic Technologies, Duke University, Durham, NC, USA. [3]Department of Biostatistics and Bioinformatics, Duke University, Durham, NC, USA. [4]Department of Cell Biology, Duke University, Durham, NC, USA. [5]Department of Pediatrics, Duke University Medical Center, Durham, NC, USA. [6]Department of Surgery, Duke University Medical Center, Durham, NC, USA. [7]Duke Regeneration Center, Duke University, Durham, NC, USA. [8]Division of Pulmonary, Allergy, and Critical Care Medicine, Department of Medicine, Duke University School of Medicine, Durham, NC, USA. ***Corresponding author. Email: charles.gersbach@duke.edu (C.A.G.); greg.crawford@duke.edu (G.E.C.); brenton.hoffman@duke.edu (B.D.H.)**
†These authors contributed equally to this work.

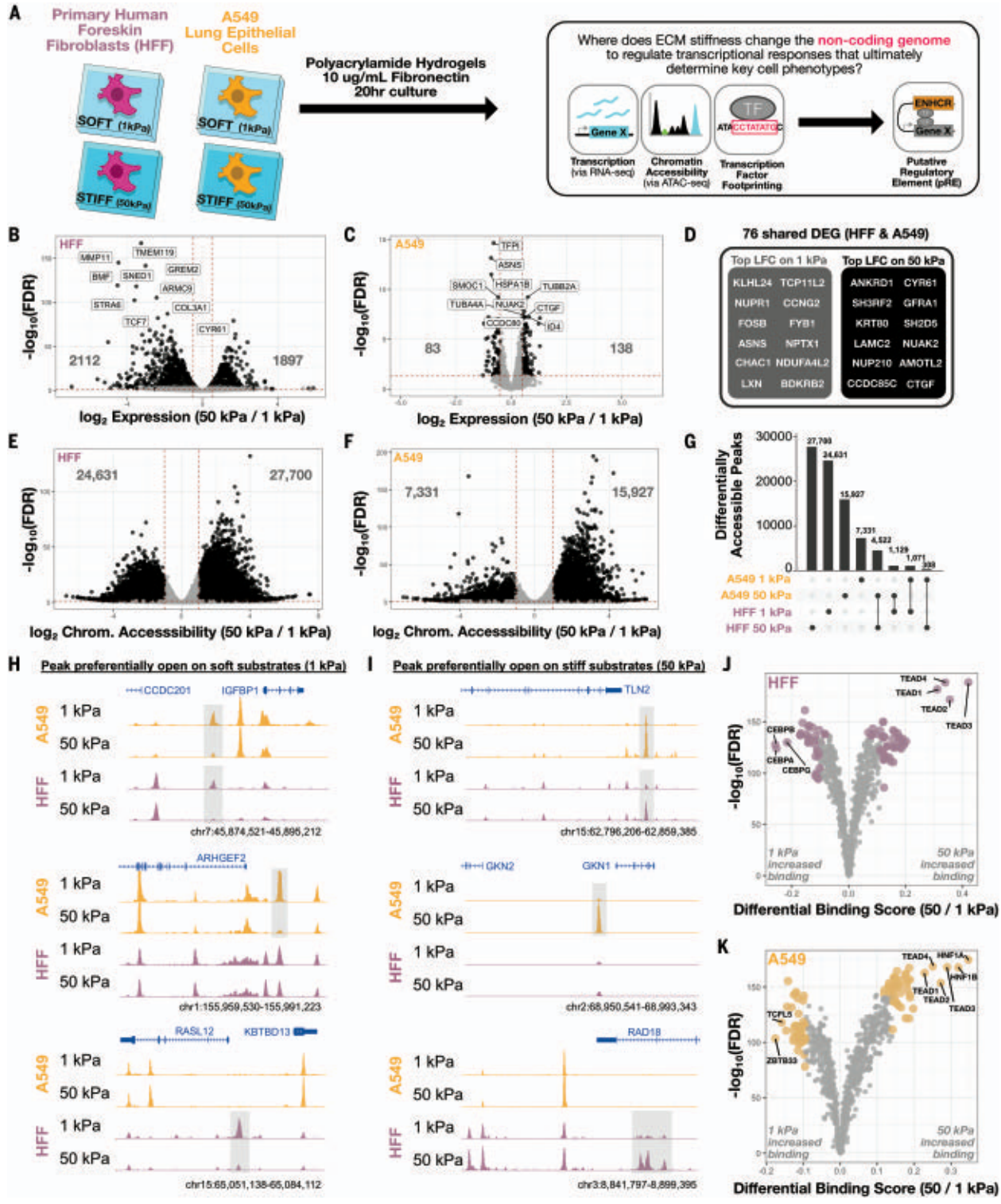


Fig. 1. Short-term culture on physiologically soft materials results in broad changes in gene expression and chromatin structure. (**A**) To assess how physiologically soft mechanical microenvironments affect the cellular epigenetic state, primary human neonatal foreskin fibroblasts (HFF cells) and A549 cells were cultured on soft (elastic modulus, $E = 1$ kPa) or stiff ($E = 50$ kPa) fibronectin-coated polyacrylamide hydrogels for 20 hours. (**B** to **D**) RNA-seq analysis revealed differentially expressed genes [FDR < 0.05, abs($\log_2$ fold change) > 0.5] in (B) HFF and (C) A459 cells, with overlapping differentially expressed genes shown in (D). (**E** to **G**) ATAC-seq analysis revealed differentially accessible chromatin regions [FDR < 0.01, abs($\log_2$ fold change) > 1] in HFF and A549 cells cultured on soft 1 kPa or stiff 50 kPa hydrogels [(E) and (F)], with overlap in accessibility between the two cell types displayed in (G). (**H** and **I**) ATAC-seq tracks showing representative regions with significantly higher accessibility (highlighted in gray) on soft 1 kPa hydrogels (e.g., near IGFBP1, ARHGEF2, RASL12) or on stiff 50 kPa hydrogels (e.g., near TLN2, GKN1, RAD18). The top two rows highlight peaks shared between both cell types, while the subsequent rows show cell type–specific peaks. (**J** and **K**) Transcription factor footprinting analysis using TOBIAS identified significantly enriched protein binding around key transcription factor motifs in differentially accessible regions on either 1 kPa or 50 kPa substrates in both HFF and A549 cells.

translocation (CYR61, CTGF, AMOTL2, ANKRD1, and NUAK2) upregulated on stiffer materials (Fig. 1D), consistent with previous studies (*39*, *40*).

We next compared changes in chromatin accessibility between the soft and stiff hydrogels by ATAC-seq. After 20 hours of culture, we observed widespread changes in chromatin accessibility in both cell types, with ~23% of identified accessible chromatin peaks showing significant [FDR < 0.01, abs($\log_2$ fold change) > 1] differential accessibility in HFF cells and ~15% in A549 cells between the two materials (Fig. 1, E and F, and tables S4 and S5). In both cell types, there was an equal distribution of peaks exhibiting increased accessibility on soft and stiff conditions. Both cell types shared only about 10% of peaks that were more accessible on soft hydrogels (N = 1071 peaks) or stiff hydrogels (N = 4522 peaks) (Fig. 1G). The main difference between substrate conditions was that more promoters were accessible on 50 kPa hydrogels (fig. S2). This highlights that while these regions are sometimes shared between cell types, the vast majority of these regions were cell type–specific (Fig. 1, H and I), in accordance with previous observations of cell type specificity of genomic enhancers (*41*). We then investigated the short-term reversibility of changes in chromatin accessibility in response to small-molecule inhibitors of intracellular actomyosin contractility (Y-27632) and key coactivator protein-protein interactions, verteporfin (TEAD-YAP interaction) and CCG-222740 (MRTF-A/CArG) (*42*, *43*) (supplementary text 1, figs. S5 and S6, and tables S6 and S31). HFFs cultured on 50 kPa hydrogels had 7131 differentially accessible peaks after 1-hour treatment with Y-27632. Treatment with verteporfin and CCG-222740 for 18 hours resulted in changes of similar magnitude in differentially accessible peaks, with newly closed peaks being enriched for TEAD and CArG/SRF motifs for each inhibitor, respectively. These results highlight the role of mechanical force and mechanosensitive signaling in altering the accessible chromatin landscape.

To further identify transcription factor modules that might be driving these accessibility changes, we performed de novo transcription factor motif analysis on the differentially accessible peaks for both material conditions and cell types, revealing enrichment for ATF, FOXF1, and CEBPA on soft hydrogels and TEAD, FOXA, HNF1B, and LEF motifs on stiff hydrogels (fig. S3). We additionally performed TOBIAS transcription factor footprinting analyses on the ATAC-seq data (*44*) to determine whether there were stiffness-mediated changes in protein-DNA engagement within these differentially accessible chromatin peaks across material stiffness conditions. Footprinting analysis showed more protein engagement around TEAD family motifs on 50 kPa hydrogels in HFF and A549 cells, and at HNF1 motifs in A549 cells on 50 kPa (Fig. 1, J and K; fig. S4; and tables S24 and S25). The enrichment of TEAD on stiff materials is consistent with the known role of TEAD in YAP/TAZ-mediated mechanotransduction (*26*, *45*–*47*). On soft 1 kPa hydrogels, CEBP family motifs and ZBTB motifs were the most preferentially bound in HFF and A549 cells, respectively (Fig. 1, J and K). Other motif families with differential engagement across 1 and 50 kPa hydrogels in both HFF and A549 cells included JUN/FOS (AP1), ATF, and ELK. In summary, both motif analysis and transcription factor footprinting identify TEAD, HNF, and CEBP as being the most differentially engaged transcription factor families across materials of differential stiffness in HFF and A549 cells.

Previous work suggests that chromatin looping can facilitate interactions between cis-regulatory elements and the genes they regulate. To investigate whether mechanical stimuli altered three-dimensional chromatin interactions, we performed HiCAR (Hi-C on accessible regulatory DNA) on HFF cells cultured on either soft (1 kPa) or stiff (50 kPa) hydrogels. Of the called loops (tables S7 and S8), ~12.5 to 12.8% were specific to a given stiffness condition, whereas ~43.5 to 46.7% of called loops had overlapping loop anchors for both materials (fig. S7, A and B). We next compared the chromatin loops and the differentially accessible ATAC-seq peaks for each ECM stiffness condition, and 42.4 to 42.9% of chromatin loop anchors overlapped at least one differentially accessible ATAC-seq peak. For both soft and stiff hydrogels, a larger proportion of ATAC-seq peaks that overlap loop anchors were substantially more accessible in the ECM stiffness condition for which the loop was called (fig. S7C). Specifically, 51.2% of differentially accessible ATAC-seq peaks that overlapped a chromatin loop in cells cultured on soft hydrogels were more accessible on soft hydrogels than on stiff hydrogels (fig. S7D). Similarly, 55.7% of differentially accessible ATAC-seq peaks that overlapped a chromatin loop in cells cultured on stiff hydrogels were more accessible on stiff hydrogels than on soft hydrogels (fig. S7D). These results indicate that long-range chromatin interactions, in part, may facilitate the observed changes in gene expression between cells cultured on soft or stiff hydrogels.

Mechanoenhancers increase gene expression on stiff materials

We next determined whether any stiffness-sensitive chromatin regions could harbor functional putative regulatory elements (pREs). We first noted that one of the most differentially accessible regions across 1 and 50 kPa hydrogels was an intergenic pRE located ~14 kb upstream of *FZD2* (fig. S13 and supplementary text 2). This region had exogenous enhancer activity in reporter constructs that responded to small-molecule perturbations in cell contractility. dCas9^{KRAB} repression of this upstream distal pRE was found to regulate FZD2 activity, confirming the role of this region as a mechanically responsive enhancer (or "mechanoenhancer") of FZD2 that becomes activated on stiffer materials.

Given that cell contractility is necessary to maintain the stiffness-dependent changes in chromatin accessibility observed on stiff hydrogels (fig. S5), we next investigated cis-regulatory mechanisms controlling the nonmuscle myosin genes *MYH9*, *MYH10*, and *MYH14*. These genes encode nonmuscle myosins IIA, IIB, and IIC, respectively, which are the primary drivers of cellular contractility in nonmuscle cells (*48*). In HFF cells, *MYH9* was the predominantly expressed nonmuscle myosin and the only one to exhibit ECM stiffness-dependent changes in expression, with a large absolute transcriptional shift between 1 and 50 kPa hydrogels (Fig. 2A). Our ATAC-seq analysis identified 14 stiffness-sensitive chromatin regions within 100 kb of the *MYH9* transcriptional start site (TSS), so we next tested whether any of these cis-regulatory regions might be regulatory elements that modulate *MYH9* expression in response to mechanical cues.

To perturb the epigenetic state at any specific genomic locus, we used CRISPR interference (CRISPRi) with the dCas9^{KRAB} epigenome editor. dCas9^{KRAB} induces epigenetic silencing by recruiting factors that catalyze the addition of repressive histone marks at the target site (e.g., H3K9me3), also leading to the removal of active histone marks (e.g., H3K4me3 or H3K27ac) and decreased chromatin accessibility (*49*, *50*). We first performed a CRISPRi screen with a guide RNA (gRNA) library tiling all ATAC-seq peaks in HFF cells within ±440 kb of the *MYH9* TSS regardless of whether they were mechanically sensitive (114 regions, 5192 gRNAs) (Fig. 2B). Cells were fixed, stained for *MYH9* (NMIIA), sorted into *MYH9*-high and *MYH9*-low expression bins, and compared for their distributions of gRNAs (supplementary text 3, fig. S8, tables S9 and S10, and methods). We identified five pREs as strong regulators of MYH9 protein expression, including two in the *MYH9* promoter/TSS region and three within a ~5 kb section of intron 3 of *MYH9* (Fig. 2, C and D). Of the three pREs in intron 3, only the first pRE was differentially accessible between soft and stiff hydrogels (Fig. 2E). Further analysis of H3K27ac across diverse ENCODE biosamples around the subregion of differential accessibility showed low H3K27ac signal in suspension (e.g., K562 cells) or weakly adherent cell lines, but greater H3K27ac signal across increasingly adherent and contractile cell lines (e.g., HUVEC/HSMM; Fig. 2F). Singleton validation of the screen hits confirmed the cis-regulatory role of all of three hit pRE regions (fig. S9). Targeting the stiffness-sensitive intron 3 pRE#1 reduced *MYH9* mRNA levels by as much as 54% compared with controls (Fig. 2G), to expression levels consistent with those seen on soft ECM (Fig. 2A). Targeting the *MYH9* promoter resulted in ~87% repression of *MYH9* transcript

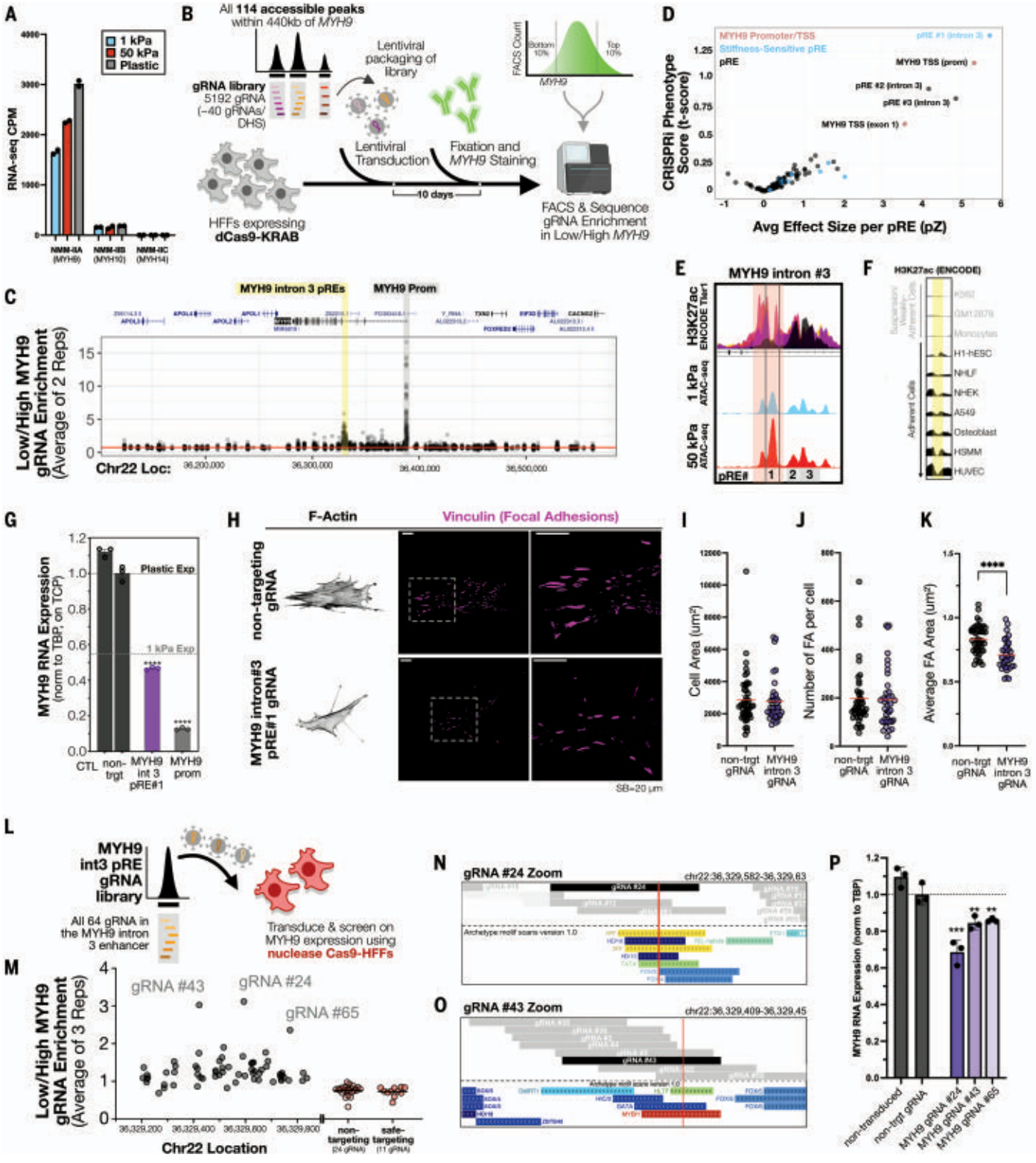


Fig. 2. CRISPRi screen reveals a mechanoenhancer in *MYH9* intron 3 that regulates MYH9 expression and cell contractility. (**A**) RNA-seq data showing expression of *MYH9* on soft 1 kPa hydrogels, stiff 50 kPa hydrogels, and TCP ($N = 2$ reps per group). (**B**) Schematic of CRISPRi screening procedure for finding genomic regulators of MYH9 protein expression. DHS, DNase I hypersensitive site; FACS, fluorescence-activated cell sorting. (**C**) Individual gRNA enrichment in low versus high MYH9 expression bins following the *MYH9* locus screen averaged across two replicates. (**D**) CRISPRi screening results across the *MYH9* locus as shown by MYH9 repression phenotype scores (t-score) and average effect size (z-score) as calculated for each DHS in the screen. Blue points indicate that DHS was differentially accessible in ATAC-seq data between soft and stiff hydrogel conditions across both screen replicates. (**E**) ATAC-seq signal in the *MYH9* intron 3 enhancer region, highlighting the force-sensitive pRE#1 subregion in yellow. (**F**) Normalized ENCODE H3K37ac signal around differentially accessible pRE#1 peak from *MYH9* intron 3 region, compared across nine available ENCODE tier 1 cell lines. (**G**) Relative *MYH9* RNA expression 10 days after lentiviral transduction with dCas9^{KRAB} and either a nontargeting gRNA, a *MYH9* intron 3 enhancer-targeting gRNA, or an *MYH9*

promoter-targeting gRNA. The control (CTL) group represents cells without transduction. (**H**) Representative immunostaining images of F-actin and vinculin FAs (SB, scale bars), with corresponding quantifications (**I** to **K**) of FA morphological parameters in HFF cells after transduction with either a nontargeting or a *MYH9* intron 3 enhancer-targeting gRNA ($N = 39$ to 45 FA per group, $^{**}P < 0.01$, $^{****}P < 0.0001$ by Student's t test). Red line indicates group means. (**L**) Schematic of Cas9 nuclease saturation indel screening performed across the MYH9 int3 enhancer region in HFF cells. (**M**) Results of the Cas9 screen, showing the ratio of gRNA enrichment in low versus high MYH9 expression bins across the *MYH9* intron 3 enhancer, compared with nontargeting gRNAs and ENCODE safe-targeting gRNAs. Data points represent averages across all three replicates. (**N** and **O**) gRNA positions of top hits relative to key motifs, including the core SRF CArG motif (gRNA#24) and HLTF motif (gRNA#43). (**P**) Relative *MYH9* expression in validation experiments for the top three gRNA hits from the screen, measured 6 days after transduction ($N = 3$ replicates per group).

levels (Fig. 2G). Immunostaining with flow cytometry analysis confirmed similar trends in *MYH9* protein levels 15 days after transduction of the gRNA along with dCas9^{KRAB} (fig. S10). Vinculin-containing focal adhesions (FAs) are key mechanoresponsive subcellular structures, and their size and shape are strongly dependent on myosin activity (*48*, *51*). Repression of the *MYH9* promoter on tissue culture plastic showed substantial changes in cell size and a near-complete loss of vinculin-containing FAs (fig. S11). However, repression of the pRE#1 mechanoenhancer on rigid tissue culture plastic resulted in significantly reduced FA size and altered actin organization (Fig. 2, H to K, and fig. S11), indicating a lower contractile state of these cells compared with cells that received the nontargeting control gRNA. Thus, the *MYH9* intron 3 pRE#1 functions as a mechanoenhancer and dictates *MYH9* expression in response to ECM stiffness cues.

Nuclease-active Cas9 and densely tiled saturating gRNA libraries can be used to determine key motifs involved in enhancer function by introducing a variety of disruptive small insertions and deletions (indels) through nonhomologous end joining (NHEJ)–based DNA repair (*52*). Sequence changes in cells with a loss of enhancer function are then used to identify key transcription factor motifs. We adapted this Cas9 screening approach to identify motifs in the *MYH9* intron 3 mechanoenhancer that control *MYH9* expression. Using a stable HFF-Cas9 cell line, we introduced all 64 potential gRNAs tiling across the *MYH9* intron 3 mechanoenhancer and sorted cells on the basis of MYH9 protein expression as the screen endpoint (Fig. 2L and table S11). We identified three gRNAs that substantially decreased *MYH9* expression on TCP relative to the other gRNAs across the mechanoenhancer (Fig. 2M). Of these gRNAs, gRNA #24 targeted regions overlapping an SRF/CArG motif, and gRNAs #43 and #65 both overlapped an HLTF (helicase-like transcription factor) motif (Fig. 2, N and O). Upon delivery of these individual gRNAs, *MYH9* mRNA expression was significantly decreased, with a maximum of ~30% repression by gRNA #24 (Fig. 2P). Cytosolic G-actin ratios regulate the mechanically responsive nuclear shuttling of MRTF-A, which then interacts with DNA-bound SRF to further regulate transcription (*17*). In further support of this SRF motif region being critical for MYH9 mechanoenhancer activity, the transcription factor footprinting analysis showed signals suggestive of enriched protein binding around this site that was increased on 50 kPa hydrogels (fig. S12). HLTF is a key member of the SWI/SNF complex, which has been implicated in actin-based YAP/TAZ release and subsequent DNA binding (*53*). Together, these results support that actin-associated mechanosensitive processes drive *MYH9* mechanoenhancer activity.

An intronic mechanoenhancer of *BMF* is more active on soft materials and is a key driver of the ECM stiffness–driven apoptotic response

Low substrate stiffness, reduced adhesion, and limited cell spreading have been shown to increase apoptosis or adipogenesis (*7*, *8*, *54*, *55*). Apoptosis triggered by loss of ECM engagement is called anoikis (*56*, *57*), and developing resistance to anoikis is a key step in cancer progression (*58*). From our RNA-seq analysis, we noted that *BMF* (the Bcl2 modifying factor gene), a key transcriptional effector of anoikis, was strongly up-regulated on soft substrates (Fig. 3A). We also identified a cluster of ATAC-seq peaks near *BMF* that were significantly more accessible on soft hydrogels (Fig. 3B). To examine whether these peaks function as regulatory elements of *BMF* transcription, we cloned the genomic DNA from the top three differentially accessible regions (pRE#1–pRE#3) into a luciferase reporter plasmid and transfected these reporter plasmids into HFF cells cultured on TCP. Luciferase activity was measured after 24 hours. Because *BMF* transcription was increased in the low contractility context of soft materials, we hypothesized that the addition of ROCKi Y-27632 would further increase luciferase activity. Only *BMF* pRE#1 in intron 4 demonstrated any basal enhancer reporter activity on TCP, which was significantly increased after treatment with 10 μM Y-27632 compared to dimethyl sulfoxide (DMSO), whereas other regions remained at basal levels (Fig. 3C). This indicates that pRE#1 enhancer activity is increased in low-contractility environments, further supporting the function of this region in driving increased *BMF* expression preferentially on soft substrates.

We next tested the ability of *BMF* pRE#1 to regulate *BMF* transcription and anoikis. Latrunculin-A (LatA) treatment is a canonical model system for anoikis that is used to depolymerize the actin cytoskeleton to induce loss of FAs and integrin engagement to mimic loss of adhesion to the ECM (*59*). We transduced HFF cells with dCas9^{KRAB} and either a nontargeting gRNA or a gRNA targeting *BMF* pRE#1 or the *BMF* promoter. After 8 days, we evaluated *BMF* mRNA levels. Treatment with LatA increased *BMF* expression ~60-fold in comparison to DMSO-treated cells (Fig. 3D). Epigenetic repression of *BMF* pRE#1 and the *BMF* promoter reduced this LatA-dependent increase in *BMF* expression by ~60 and ~85%, respectively (Fig. 3D). We then assessed changes in apoptosis by measuring caspase-3/7 activity using a luciferase reporter system 14 days after transduction (8 days +LatA). Repression of *BMF* pRE #1 reduced LatA-induced apoptosis by ~50%, whereas repression of the promoter completely prevented LatA-induced apoptosis relative to the DMSO-treated control condition (Fig. 3E). These observations were further supported by direct measures of cell number, wherein cells were seeded onto tissue culture plastic and 1 day later challenged with LatA for 3 days before fixation and cell counting. *BMF* promoter epigenetic repression was found to completely block LatA-induced changes in cell number, and BMF enhancer repression showed significantly reduced cell number compared with cells treated with a nontargeting gRNA (Fig. 3F), suggesting increased cell death or reduced proliferation. Collectively, these data show that *BMF* pRE#1 acts as a mechanoenhancer of *BMF*, becomes activated on softer ECM stiffness, and regulates the apoptotic cellular response in states of reduced cytoskeletal engagement and ECM attachment.

High-throughput CRISPR screening identifies key mechanoenhancers regulating cellular growth and migration

To identify cis-regulatory elements that contribute most strongly toward mechanosensitive cellular behaviors, we performed high-throughput CRISPRi screening with cellular growth and migration as the phenotypic readouts. We generated a library of 21,458 gRNAs targeting the top 1000 nonpromoter ATAC-seq peaks, ranked by their increased accessibility on stiff hydrogels (tables S4 and S8). We also included gRNAs targeting the promoters of 53 genes known to modulate migration (*60*) as positive controls and 1000 nontargeting gRNAs as negative controls. HFF cells were transduced with the library and then assessed for changes in growth or migration (Fig. 4A). For the growth screen, gRNA enrichment was determined on day 8 and day 29 or 30 (after ~14 population doublings). The migration screen involved two consecutive overnight transwell assays at 8 days after transduction, with gRNA enrichment compared between migrated and nonmigrated cells (methods).

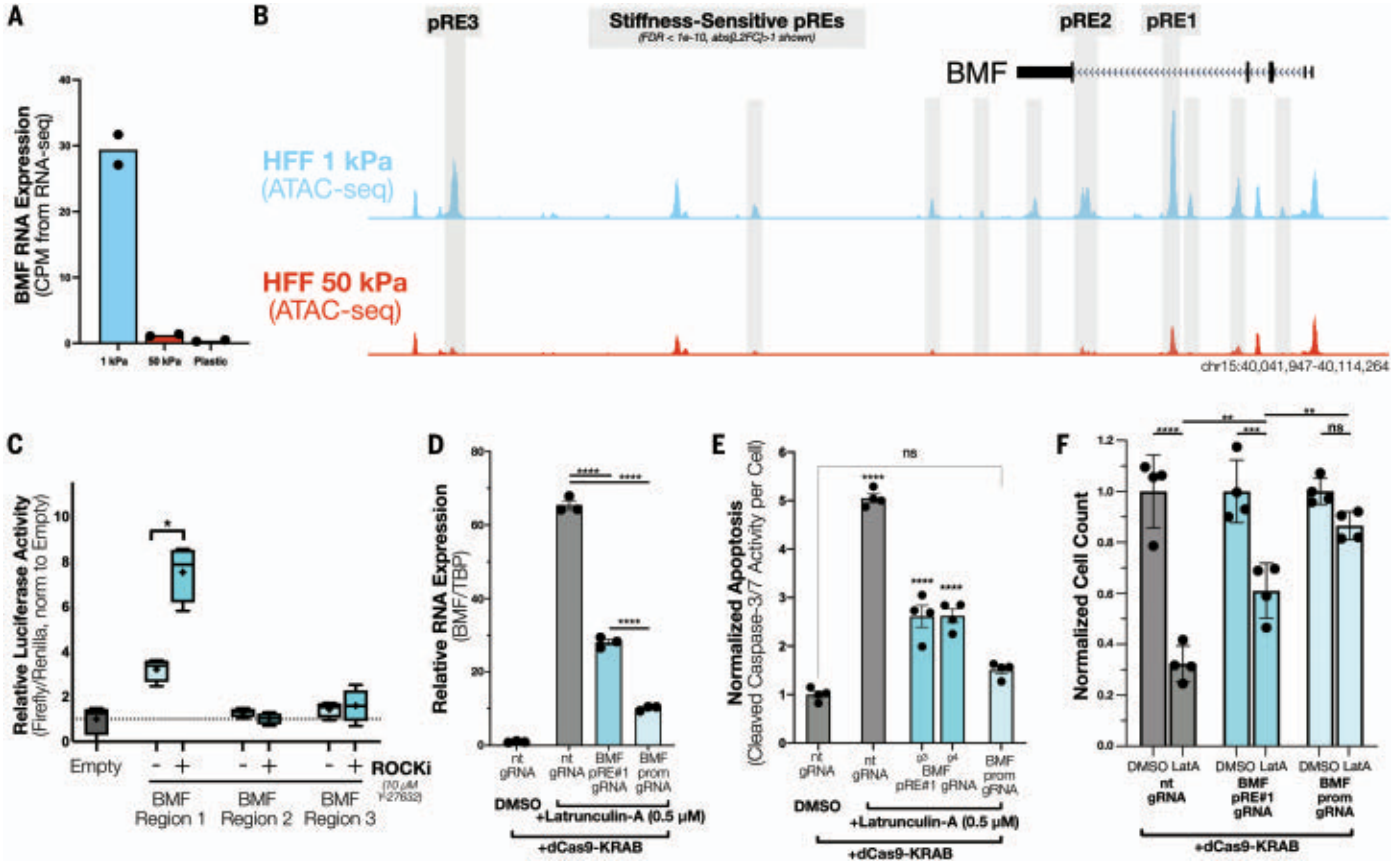


Fig. 3. *BMF* intron #4 mechanoenhancer has increased activity with reduced contractility and is a mediator of anoikis. (**A**) *BMF* RNA expression from RNA-seq in HFF cells cultured under different stiffness conditions ($N = 2$ replicates per stiffness condition). (**B**) Comparison of ATAC-seq data for HFF cells grown on soft and stiff hydrogels. Gray shading highlights regions of differential chromatin accessibility between the stiffness conditions. (**C**) Luciferase enhancer reporter readouts from three of the BMF regions with and without 24 hours of 10 μM Y-27632 treatment, showing relative firefly luciferase activity controlled by these enhancers normalized to a control cotransfected Renilla luciferase reporter. Box and whisker plots show median, plus indicates the group mean, and bars indicate the top and bottom 10% expression range ($N = 4$ replicates per group). (**D**) Relative *BMF* RNA expression ($N = 3$) and (**E**) normalized apoptosis as measured by cleaved caspase-3/7 activity ($N = 4$ replicates per group) in HFF cells either untreated or transduced with various gRNAs after 24 hours of 0.5 μM LatA treatment. (**F**) HFF cells transduced with dCas9^{KRAB} and either a nontargeting, BMF promoter, or BMF pRE#1 gRNA were seeded on TCP for 1 day in normal growth media, followed by treatment with either DMSO or 0.5 μM LatA added to the media for an additional 72 hours. After treatment, each HFF group was subjected to on-plate fixation followed by DAPI staining of cell nuclei and cell counting. All data shown were normalized to DMSO-treated wells for each gRNA condition. All data are presented as mean ± SEM and are representative of at least two independent experiments. ****$P < 0.0001$, *$P < 0.05$ by Student's *t* test. ns, not significant. Cleaved caspase-3/7 activity and luciferase assay statistics are shown compared with the DMSO control group, whereas RNA expression comparisons are shown with overlay bars. "nt gRNA" refers to nontargeting gRNA.

We observed strong negative effects on cell proliferation when targeting the promoters of the positive control DepMap essential genes (e.g., *GPKOW*, *EIF3E*, *ACTG1*, *CSNK1A1*, *PCYT1A*, *PTPN23*) (*61*, *62*) and genes related to proliferation (e.g., *ABL1*, *ITGB8*, *G3BP2*, *OTUD6B*) (*63*, *64*). In the migration screen, we found that promoter-targeted repression of key genes known to influence cell adhesion and force generation, including *ITGAV*, *ACTG1*, *CDC42*, and *TPM3* (*60*), led to decreased cell migration (fig. S14). Perturbation of mechanically sensitive pREs led to effects comparable to those observed in the positive control promoter targets (fig. S14). Z-score enrichment was found to be driven by a small fraction of the gRNAs across both screens (Fig. 4, B and C), consistent with previous reports on epigenetic editing of regulatory elements (*30*). In total, we identified 58 pREs regulating migration and 50 pREs affecting proliferation, with seven regions regulating both phenotypes (Fig. 4D, tables S12 and S13, and methods). Although ECM stiffness is known to influence both cell proliferation and migration (*65*, *66*), we found no correlation between the phenotypic scores across pREs regulating either or both phenotypes (fig. S15A). Furthermore, perturbations of pREs that regulated only migration or both phenotypes had greater effects on migration compared with pREs that regulated only growth (fig. S15B). There was no difference between the same groups for the growth phenotype. We next asked whether any of the pREs from the growth and migration screens were functional in other cell types and tissues by examining their overlap with accessible chromatin regions in 95 ENCODE biosamples (table S14, supplementary text 4, and fig. S16). pRE hits from functional screening had the greatest overlap with accessible chromatin regions for highly adherent cell types (e.g., skeletal muscle myoblast and fibroblast lineages, 96 to 99% of pREs in accessible chromatin) and the least overlap with suspension cell types (e.g., T cells and K562 cells with only 19% of pREs accessible). Together, these analyses show that the functional pREs that become activated on stiff ECM are shared across multiple cell types and can be active across many adherent cell types.

Single-cell CRISPRi screening identifies gene targets regulated by mechanoenhancers that drive cellular growth and migration

To identify gene targets regulated by the pREs identified in the proliferation and migration screens, we performed CRISPRi followed by

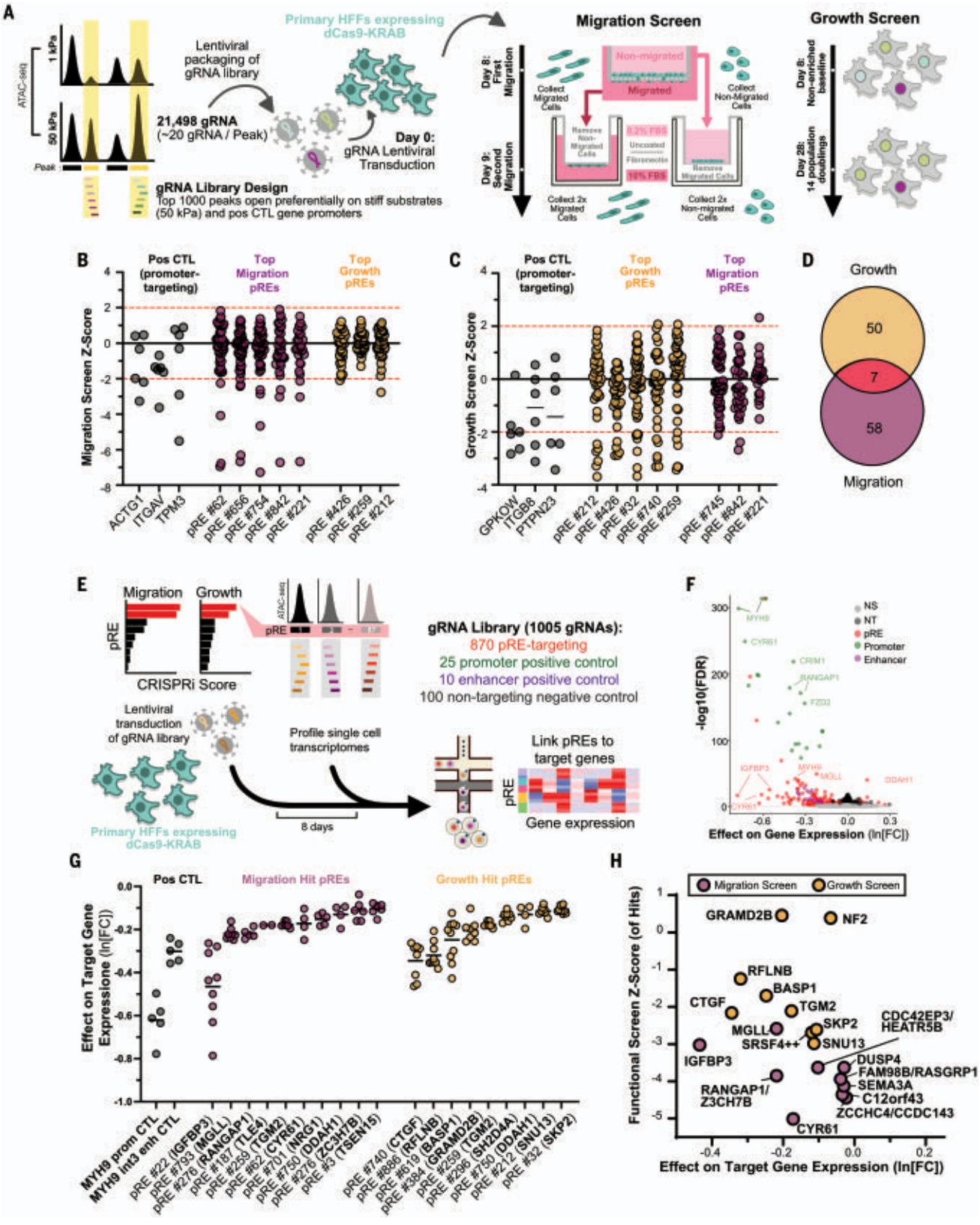


Fig. 4. Functional migration and growth screening paired with single-cell CRISPRi screening identifies mechanosensitive regulatory elements driving functional behaviors and their target genes. (**A**) Schematic of the experimental setup for the paired migration and cellular growth screens in HFF cells, transduced with a CRISPRi library containing 21,498 gRNAs targeting the top 1000 differentially accessible ATAC-seq peaks on stiff substrates. (**B** and **C**) Z-scores for migration (B) and growth (C) phenotypes, showing promoter-positive controls, the top five pREs with the highest Z-scores for each phenotype, and three representative pREs ranked among the highest Z-scores for the other phenotype. Each dot represents a gRNA targeting a given pRE. Red dashed line indicates a Z-score threshold of 2. (**D**) Venn diagram comparing the hit pREs regulating both phenotypes or only one. (**E**) Workflow overview of the single-cell CRISPRi screen. A gRNA library targeting pREs identified from migration and growth screens was delivered to

CRISPRi HFF cells, and single-cell transcriptomes were profiled 8 days later. (**F**) Volcano plot showing the change in target gene expression (ln[FC]; FC, fold change) versus significance [−log10(FDR)] for each gRNA-gene connection. Significant gRNA-gene connections are colored as follows: putative regulatory element ("pRE," red), previously identified enhancers ("Enhancer," purple), promoter regions ("Promoter," green), and nontargeting controls ("NT," black), with an FDR < 0.01. Nonsignificant ("NS") gRNA-gene connections are shown in light gray. (**G**) Average effect on target gene expression for *MYH9* promoter-targeting positive control gRNAs, intron 3 enhancer-targeting positive control gRNA (gray), and the top 10 pREs affecting migration (purple) and growth (yellow). Points represent individual gRNA-gene linkages, with all regions showing significant target gene reduction (FDR < 0.01). (**H**) Z-scores of hit gRNAs for each pRE from functional screening plotted versus the average effect on target gene expression from the same pRE in the single-cell screening. Points represent the top 10 pREs by Z-score from functional screening, along with the greatest absolute fold change of pRE-gene linkages from the single-cell RNA-seq screen.

single-cell RNA-seq. We designed a sublibrary of gRNAs targeting 87 pREs, selecting those with the largest effect sizes from the previous screens, with 10 gRNAs per pRE (methods). This library also included positive controls of promoter-targeting and known enhancer-targeting gRNAs as well as 100 nontargeting negative control gRNAs, resulting in a total of 1005 gRNAs (table S15). We transduced HFF cells expressing dCas9^{KRAB} cultured on TCP with this gRNA library at a multiplicity of infection (MOI) of 0.33, and 8 days after transduction, we profiled 103,440 quality single-cell transcriptomes (Fig. 4E). We recovered a median of one gRNA per cell and identified an average of 159 cells containing each gRNA (fig. S17, A and B). To link pREs to their gene targets, we compared the expression of all genes within ±1 Mb of each targeted pRE in cells that received the gRNA against those that did not receive the gRNA (Fig. 4F, table S16, and methods). This ±1 Mb window was chosen because previous studies suggest that most cis-regulatory interactions occur within this genomic distance (*29*, *67*–*69*).

In total, we identified 201 significant pRE-gene connections and connected 65 pREs to at least one gene (74.7%, 65/87), with a median of two genes linked to every pRE and one pRE to each gene with at least one connection (fig. S17, C to E, and methods). In contrast to the expectation that a cis-regulatory element targets its nearest gene, we found that a median of three and a mean of six and a half genes were "skipped" by pREs to regulate a more distant target gene. In fact, 37.1% of pRE-gene links skipped at least one other gene, and 21.8% skipped five or more genes (fig. S22, A and B, and supplementary text 5). One notable pRE had >10 gene linkages and was accessible in multiple ENCODE biosamples ("ubiquitous" cluster in fig. S16, fig. S18, and supplementary text 6). For the positive controls, we recovered 92% of expected promoter-targeting gRNA and 100% of enhancer-targeting gRNA connections with their target gene (fig. S19A), with all effects showing significant decreases in target gene expression, as expected (fig. S19, B to E). Notably, perturbation of the *MYH9* intron 3 enhancer (Fig. 2) reduced *MYH9* expression and also up-regulated two additional genes, *APOL2* (~90 kb downstream) and *RAC2* (~900 kb upstream) (table S16). Across the identified pRE-gene linkages, the magnitude of gene repression correlated positively with the basal expression level of the target gene, with more highly expressed genes showing stronger repression (fig. S20A). Gene expression changes diminished as the distance between the pRE and the target gene increased (fig. S20, B to D), consistent with previous work (*29*). To determine the taxonomy of the pREs, we intersected the pREs with predicted cis-regulatory elements in human cell types and tissues (*70*) and chromatin state annotations in HFF cells (*71*). The majority of pREs identified by both bulk and single-cell screening approaches overlapped distal enhancer-like signature (dELS) elements and genomic regions annotated as having "Enhancer"-like chromatin state (fig. S21, A to D).

Genes linked to mechanically regulated pREs play key roles in diverse cellular functions

Next we examined the downstream target genes regulated by pREs that showed strong functional significance in driving growth or migration in our screens. Initially, we examined the effects of perturbing the positive control *MYH9* promoter and its associated mechanoenhancer. We observed that targeting the *MYH9* intron 3 mechanoenhancer led to ~50% of the repression as targeting the *MYH9* promoter (Fig. 4G), in agreement with the previous singleton gRNA experiments (Fig. 2G). We compared the effect size of the top eight pRE-gene linkages from the growth and migration screens (ranked by phenotype Z-score) to the impact on target gene expression in the single-cell RNA-seq screen (Fig. 4, F and G). For comparison, we also included the top two pRE-gene linkages that most strongly influenced gene expression without any requirements for functional screen enrichment (Fig. 4F). Of note, pRE#62 showed the strongest combination of effects on gene expression and migration and was found to modulate the transcription of *CYR61*. Similarly, perturbation of pRE #740 led to strong effects on both *CTGF* expression and cellular growth (Fig. 4, F and G). Both *CYR61* and *CTGF* are canonical YAP/TAZ target genes, with *CYR61* being strongly linked to migratory phenotypes across many cell types (*72*) and *CTGF* playing key roles in cellular growth (*73*, *74*). Using this single-cell CRISPRi screening approach, we further identified pREs as strong drivers of cell migration that also changed the expression of genes known to function in mechanoresponsive and cell migration–related pathways (Fig. 4F). These genes include *CYR61* (*CCN1*; fig. S23), *DUSP4* (fig. S24, A and B), *FAM98B* and *RASGRP1* (fig. S25), and *RANGAP1* (fig. S26) (supplementary text 7). Similarly, perturbation of pREs driving cellular growth led to changes in expression of genes with known functions in cell proliferation, including *CTGF* (also known as *CCN2*; Fig. 5E), *NF2* (fig. S23, C and D), and *SKP2* (fig. S27), as well as in genes not previously linked to cell proliferation, including *RFLNB* (fig. S24, C and D) (supplementary text 8).

To validate the pRE-gene linkages identified in the single-cell RNA-seq CRISPRi screen, we selected 13 pRE-gene connections for singleton gRNA validations and validated 30 gRNAs across these connections in HFF cells. We delivered individual gRNAs to the same HFF CRISPRi cell line cultured on TCP and assayed for changes in gene expression by reverse transcription quantitative polymerase chain reaction (RT-qPCR) at 8 days after transduction. We confirmed 10 out of 13 pRE-gene connections, validating mechanoenhancers of *CTGF*, *RFLNB*, *SKP2*, and *NF2* (growth) and *CYR61*, *DUSP4*, *FAM98B*, *RASGRP1*, *RANGAP1*, and *ZC3H7B* (migration) (Fig. 4, F and G; figs. S23 to S27; and table S17). The changes in mRNA expression in the validations correlated with the gene expression changes observed in the single-cell screen (fig. S28). Collectively, these data demonstrate that many of the identified pREs are bona fide mechanoenhancers that regulate the expression of key genes and ultimately alter cell growth and migration in response to ECM stiffness cues.

Epigenetic repression of validated mechanoenhancers impairs cellular mechanosensitivity across cell types and ECM stiffness

Next, we selected three validated mechanoenhancers for additional analysis (*SKP2*, *CTGF*, and *MYH9*) on the basis of their responsiveness to both material stiffness and cell contractility inhibition as well as their implicated role in fibrosis (*13*, *75*–*77*). Specifically, we first tested the effect of epigenetic repression of these mechanoenhancers on transcription in HFFs and A549 cells cultured on the fibronectin-coated hydrogel system (1 and 50 kPa) as well as TCP on which the screens were performed. All three mechanoenhancers were accessible and responsive to CRISPRi under at least one condition in each cell type (Fig. 5). The *SKP2* mechanoenhancer (~4 kb downstream of the TSS; Fig. 5A) was responsive to CRISPRi on TCP but not on the hydrogels in HFF cells (Fig. 5B). However, in A549 cells, this *SKP2* mechanoenhancer was repressed by CRISPRi in all conditions and showed increased magnitude of

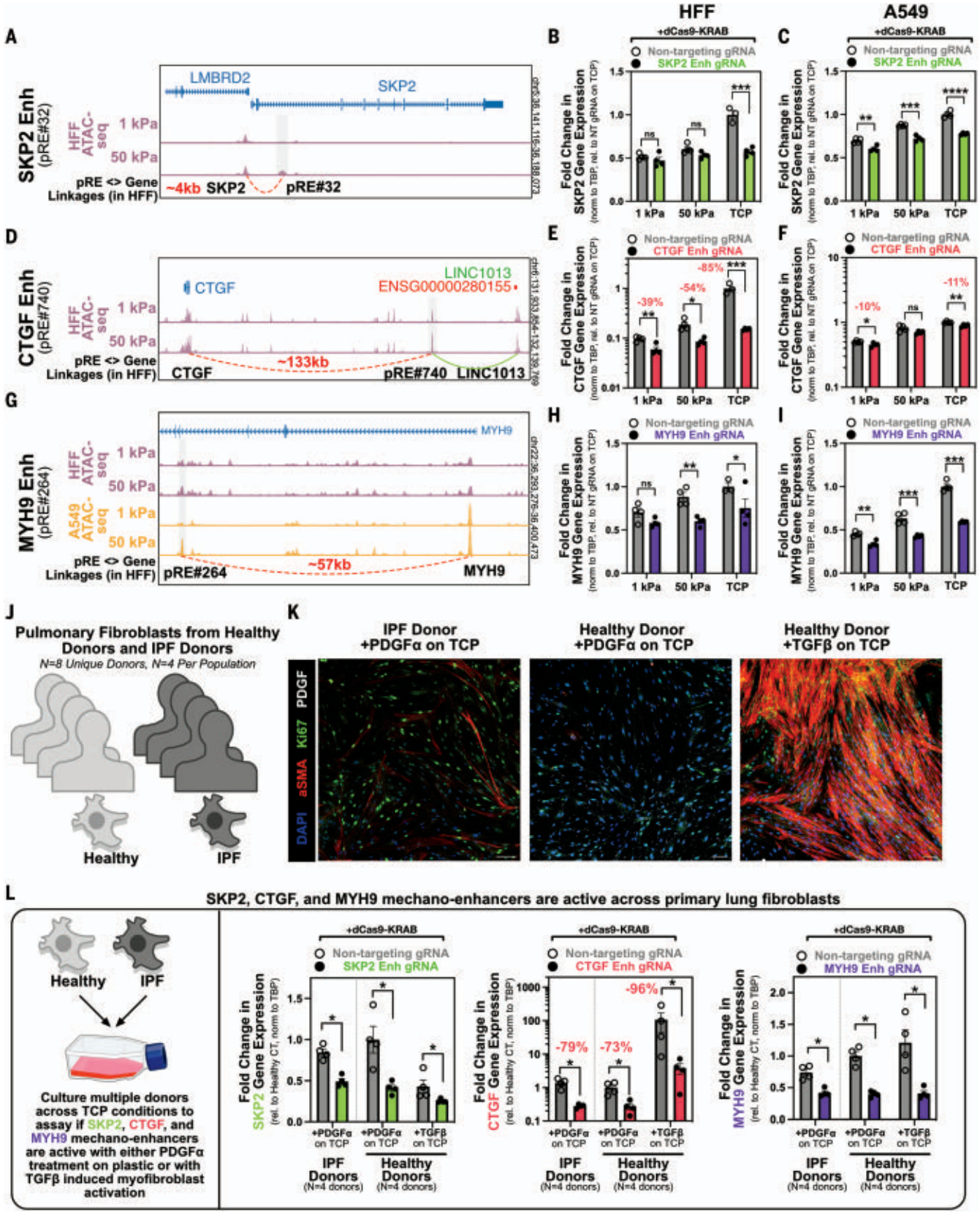


Fig. 5. Epigenetic repression of validated mechanoenhancers inhibits cellular mechanoresponses across cell lines and profibrotic disease contexts. (**A**) ATAC-seq and pRE-gene linkages in HFF cells showing *SKP2* regulation by the mechanoenhancer at pRE#32. (**B** and **C**) Singleton validations of dCas9^{KRAB}-induced mechanoenhancer *SKP2* repression in (B) HFF cells and (C) A549 cells. (**D**) ATAC-seq and pRE-gene linkages in HFF cells showing regulation of *CTGF* and *LINC1013* by the mechanoenhancer at pRE#740. (**E** and **F**) Singleton validations of dCas9^{KRAB}-induced *CTGF* mechanoenhancer repression in (E) HFF cells and (F) A549 cells. (**G**) ATAC-seq and pRE-gene linkages in HFF cells and A549 cells showing regulation of *MYH9* by the mechanoenhancer at pRE#264. (**H** and **I**) Singleton validations of dCas9^{KRAB}-induced *MYH9* mechanoenhancer repression

across (H) HFF cells and (I) A549 cells. Each dot represents an independent biological replicate for HFF and A549 cells. (**J**) Lung fibroblasts were isolated from four healthy donors and four IPF patients. The baseline response of healthy donor cells (treated with PDGFα on TCP) was compared with IPF cells in the same conditions. Further, healthy donor cells were activated with TGFβ on TCP, and this response was compared with control baseline conditions. (**K**) Representative images show differences in αSMA staining under these conditions. (**L**) Singleton validations of dCas9^{KRAB}-induced mechanoenhancer repression of the SKP2, CTGF, and MYH9 mechanoenhancers.

response with increasing stiffness (Fig. 5C). The intergenic *CTGF* mechanoenhancer (~133 kb upstream of the TSS; Fig. 5D) showed strongly increasing transcriptional contributions with increasing ECM stiffness in HFF cells (Fig. 5E). In contrast, the *CTGF* mechanoenhancer showed more modest activity and limited stiffness response in A549 cells (Fig. 5F). Finally, transcriptional contributions from the *MYH9* intron 3 mechanoenhancer (~57 kb downstream of the TSS; Fig. 5G) were strongly stiffness-dependent in both cell types (Fig. 5, H and I). Epigenetic repression of each mechanoenhancer nearly completely removed stiffness-driven increases in transcription, resulting in levels of transcription that were similarly low across all material conditions.

Tissue fibrosis is associated with changes to ECM composition and stiffening of local matrix mechanical properties that can provide positive feedback to pathological progression (*78*). Gene targets of our identified mechanoenhancers have been implicated in fibrotic disease, including *CTGF*, which is a hallmark of fibrosis across numerous tissues. CTGF expression is specifically found to be up-regulated in patients diagnosed with idiopathic pulmonary fibrosis (IPF) (*75*). To determine whether these validated mechanoenhancers are functional in cell types relevant to fibrotic disease, we characterized activity of these mechanoenhancers in primary human lung fibroblasts isolated from four control healthy donors and four donors with IPF (Fig. 5, J to L). Lung fibroblasts were harvested from tissue using a magnetic-activated cell sorting (MACS)–based enrichment approach, cultured, transduced with a lentivirus encoding dCas9^{KRAB}, and subsequently transduced with an additional lentivirus encoding a gRNA targeting either the *SKP2*, *CTGF*, or *MYH9* mechanoenhancers. First, we studied IPF and healthy donor fibroblasts stimulated with platelet-derived growth factor subunit alpha (PDGFα) as a baseline mitogen allowing for cell outgrowth (*79*, *80*). All primary fibroblasts were seeded on rigid TCP to induce strong baseline fibrogenic activation and assess mechanoenhancer activity. Immunostaining revealed modestly increased alpha smooth muscle actin (αSMA), a marker of fibroblast activation, in the IPF-derived fibroblasts relative to cells from healthy donors under these conditions (Fig. 5K). At baseline, the expression of CTGF, SKP2, and MYH9 was generally similar across healthy and IPF donor fibroblasts with PDGFα treatment alone (Fig. 5L). This similarity is potentially due to the rigid TCP culture conditions outweighing the effect of the disease state of the original donor in driving activity of these mechanoenhancers. We also compared the transcriptional responses between healthy lung fibroblasts activated in vitro with transforming growth factor–β1 (TGFβ1) to induce the fibroblast to myofibroblast transition implicated in fibrosis (*81*). Strongly increased immunostaining of αSMA confirmed that TGFβ1 treatment successfully activated healthy lung fibroblasts relative to the baseline PDGFα and TCP treatment (Fig. 5K). In cells treated with a nontargeting gRNA, TGFβ1 treatment reduced SKP2 expression by ~60%, increased CTGF by nearly 100-fold, and slightly increased MYH9 expression compared with the baseline PDGFα treatment (Fig. 5L).

We next used CRISPRi of the *SKP2*, *CTGF*, and *MYH9* mechanoenhancers to assess their specific transcriptional contributions across these eight donor-derived cell lines and two fibrotic model culture systems. Notably, repression of these mechanoenhancers reduced transcriptional activity of their target genes across all eight donor lines (Fig. 5L). This strong conservation across samples suggests a broad role of these mechanoenhancers in gene regulation. Moreover, epigenetic repression of the *CTGF* mechanoenhancer prevented 96% of the 100-fold increase in transcription induced by treatment of healthy donor fibroblasts cultured on TCP supplemented with TGFβ1. These findings highlight the critical, context-dependent role of these mechanoenhancers in regulating gene expression in response to mechanochemical stimuli, including ECM stiffness and procontractile soluble cues. Epigenetic editing of these mechanoenhancers effectively reduced ECM stiffness–mediated transcriptional responses and prevented the activation of genes known to be associated with the fibroblast-to-myofibroblast transition in isolated lung fibroblasts from healthy and IPF donors, including *CTGF* and *MYH9* (*75*, *82*).

Conclusions

Using complementary modern technologies for functional genomics, we identified a class of cis-regulatory elements that are responsive to changes in material stiffness, which we refer to as "mechanoenhancers." Mechanoenhancers could be more active on either soft or stiff substrates and were dependent on intracellular contractility. Functional screening revealed that some mechanoenhancers could act as key transcriptional drivers of fundamental cell processes, including ECM mechanosensing, apoptosis, cellular growth, and migration. Notably, these mechanoenhancers were active in lung fibroblasts isolated from healthy and IPF donors when cultured on tissue culture plastic (Fig. 5). The gene-to-mechanoenhancer connections identified through unbiased transcriptome-wide screening revealed that, unlike promoter-based regulation, mechanoenhancers often regulate multiple downstream gene targets, with a median of two linkages per mechanoenhancer, spanning large genomic distances (figs. S17 and S20). This provides one example of how mechanical and chemical cues, particularly those that regulate contractility, may combine to regulate mechanoenhancers. This work suggests that epigenome editing of mechanoenhancers can be an effective means of decoupling mechanically driven behaviors from the mechanical stimuli.

On stiff ECM conditions, we found that the activities of multiple mechanosensitive signaling pathways likely drive the activity of mechanoenhancers. We observed that mechanoenhancers were enriched with binding sites for canonical mechanosensitive transcription factors including TEAD and SRF/CArG (Figs. 1 and 2 and figs. S3 and S4) (*26*, *40*, *45*), in addition to motifs for protein families that have not previously been strongly associated with mechanosensing pathways (e.g., LEF, FOXA, HNF) (figs. S3 and S4). A key question for future work will be determining how multiple mechanosensitive proteins and pathways work in combination to regulate changes in gene expression at mechanoenhancers.

Whereas mechanosensitive signaling pathways that increase transcription on stiff ECM are well described, comparatively less is known about those that drive increased transcription preferably on soft ECM. Previous studies examining chromatin accessibility in soft hydrogel conditions with ATAC-seq did not find peaks with increased accessibility preferentially on soft materials (*45*, *47*). However, through the use of on-plate ATAC-seq processing that did not require de-adhesion of cells before collection, we identified a large subset of peaks that were more accessible on soft ECM (Fig. 1, E to G), with one region preferentially open on soft ECM found to function as a *BMF* mechanoenhancer. One potential mechanism driving this pattern of activity is stiffness-induced epigenetic repression. For instance, dynamic mechanical stretch can induce the H3K27me3 repressive histone mark and transcriptional down-regulation (*20*–*22*). YAP-based epigenetic repression around this *BMF* mechanoenhancer on TCP was previously noted in non–small cell lung cancer (NSCLC) treated with kinase inhibitors, further supporting a stiffness-induced epigenetic repression mechanism (*83*) (supplementary text 9). A key aspect of future work will be to determine whether stiffness-induced epigenetic repression is a common mechanism of mechanoenhancer regulation.

One common characteristic of mechanically induced disease states, including cancer and fibrosis, is the excessive activation of positive feedback loops that amplify mechanical signaling and drive disease progression (*78*, *84*–*87*). In this process, initial increases in ECM stiffness trigger gene expression changes that further sensitize cells to, or increase, ECM stiffness cues. This work identified mechanoenhancers that drive the activation of multiple genes likely contributing to these positive feedback loops, including *CTGF*, *CYR61*, *MYH9*, *RFLNB*, *RANGAP1*, *RASGRP1*, and *NF2*. For example, we found that the *MYH9* mechanoenhancer drives increased expression of *MYH9* in response to ECM stiffness, thereby initiating a possible mechanical signaling loop wherein enhanced contractility potentially further activates the mechanoenhancer, which sensitizes the cell to ECM stiffness changes (*87*). Another potential example of propagating mechanical feedback loops is through the mechanoenhancer for *RANGAP1*, a key factor in cytoplasmic-nuclear shuttling that promotes increased import into the nucleus (*15*, *88*). In this proposed positive feedback loop, mechanical forces activate the mechanoenhancer resulting in increased *RANGAP1* expression, which potentially promotes nuclear import and further increases the sensitivity of that cell to subsequent mechanical signals. This extends current models of how mechanical force can directly bias nuclear transport (*89*), by suggesting that this process may be further tuned by transcriptional feedback from mechanoenhancers of key nuclear transport machinery such as *RANGAP1*.

By epigenetic editing of mechanoenhancers activated by increased ECM stiffness, we could prevent increased expression of key genes (e.g., *CTGF*) associated with fibrotic disease. These effects are likely due to reduced activation of mechanosensitive positive feedback loops. Moving forward, epigenome editing of mechanoenhancers will be a powerful tool for precisely engineering cellular responses to the mechanical microenvironment and could have widespread applications in both cell engineering and gene therapy. Therapeutic modulation of known gene targets implicated in mechanically driven disease states such as cancer, atherosclerosis, fibrosis, and aging has historically proven to be challenging, as strong modulation of genes and their products can disrupt both pathogenic and essential functions. If therapeutic epigenome editing of key mechanoenhancers can modulate pathogenic positive feedback loops while leaving essential signaling functions intact, this approach may enable novel treatment strategies in mechanosensitive diseases.

Materials and methods

Cell culture for RNA/ATAC-seq

Primary human neonatal fibroblasts (HFF cells) were acquired from ATCC (CRL-2097) and cultured in Dulbecco's minimum essential medium (DMEM) with 10% fetal bovine serum (FBS), 1% AntiAnti, and 1% NEAA (Sigma) on TCP. A549 cells were cultured in F-12K Medium from ATCC (30-2004) with 10% FBS. All work was performed within 30 doublings from the initial passage of the vial.

RNA-seq and Omni-ATAC-seq

Cell culture and soft hydrogel processing: Polyacrylamide hydrogel 35 and 150 mm PetriSoft EasyCoat dishes (Matrigen) with an Elastic Modulus of 1 kPa ("soft") and 50 kPa ("stiff") were used for all NGS experiments. These dishes were incubated for 5 min with sterile PBS, rinsed two more times with sterile PBS, followed by addition of 10 μg/ml fibronectin (Sigma) for 30 min at room temperature. Fibronectin was then removed, and dishes were rinsed twice with sterile PBS, followed by a 20-min incubation with complete growth media while cells were passaged. Media was removed from the dishes, and cell suspensions were added and allowed to attach overnight.

Bulk RNA-seq: Forty thousand HFF cells were seeded on 35 mm 50 kPa dishes and TCP dishes, while 70,000 HFF cells were seeded on 1 kPa 35 mm dishes to achieve the same effective plating density owing to slightly reduced HFF attachment rates (and spreading) on 1 kPa hydrogels. Similarly, A549 cells were seeded on Matrigen T75 flasks (1 kPa and 50 kPa) at slightly variable densities to account for reduced cell attachment on softer substrates (2 million and 1.25 million cells for 1 and 50 kPa flasks, respectively). Twenty hours after seeding, cells were trypsinized spun down at 300*g* for 5 min, and then RNA was isolated from the cells using the Norgen Total RNA Purification Kit (#17250) according to the manufacturer's protocol, and samples were run on an RNA TapeStation (Agilent) to verify all samples had a RIN score of >8. cDNA Libraries were built from our RNA inputs using the TruSeq Stranded Library Prep Kit (Illumina #RS-122-2101) according to manufacturer's instructions. Quality control was performed by running the amplified libraries out on a High Sensitivity D1000 Tapestation (Agilent) to confirm expected size, and Qubit dsDNA HS assays were performed to determine a final concentration. Libraries were diluted to 10 nM and pooled together in equal volumes, followed by sequencing performed on an Illumina HiSeq 2500 using a 50 bp PE RapidRun kit. Resulting reads were subjected to adapter trimming using Trimmomatic v0.32 (*90*) and aligned to GRCh38 with the STAR v2.4 aligner (*91*), and counts were retrieved using featureCounts (*92*) from subread version 1.4.6p4 with Gencode v22 gene annotations used as reference. Differential expression analysis was performed using edgeR quasi-likelihood methodology (*93*), and data were visualized using Degust (*94*) and Rstudio. Genes with significant differential expression were determined using a threshold of FDR < 0.05 and absolute value of $\log_2(FC) > 0.5$.

Omni ATAC-seq: HFFs were seeded on 35 mm Matrigen dishes of varying stiffness (1, 12, 50 kPa elastic modulus) at slightly variable densities to account for reduced cell attachment on softer substrates (70,000, 45,000, and 40,000 HFF cells seeded per group) and allowed to culture for 20 hours. A549s were seeded in a similar fashion with Matrigen T75 flasks (1 and 50 kPa elastic modulus) seeded with either 2 million and 1.25 million cells per flask, respectively, and allowed to culture for 20 hours. For Y-27632 ROCKi experiments, the cells were seeded as normal, but 1 hour before harvest, 10 μM Y-27632 ROCKi (StemCell Tech) in growth media was added to the cells. For verteporfin (Sigma-Aldrich) and CCG-222740 (MedChemExpress) studies, these inhibitors were added 18 hours befre harvest and used at 0.7 and 20 μM, respectively. The Omni-ATAC-seq protocol was used to minimize mitochondrial reads from the preps (*95*), however no trypsinization was used, and, instead, on-plate disruption/removal of nuclei (using the digitonin present in the lysis buffer) was used to better preserve nuclear mechanical context and connectivity before transposition by the Tn5. After the final PCR, libraries were cleaned with a 0.5×/1.8× double-sided SPRI clean. Libraries were subjected to quality control by determining the number of cycles required to reach 25% of the peak threshold in the diagnostic PCR as well as running the amplified libraries out on a High Sensitivity D1000 Tapestation (Agilent) to confirm expected size, and Qubit dsDNA HS assays were performed to determine a final concentration. Libraries were individually diluted to 6 nM and then pooled at equal volumes before sequencing on an Illumina HiSeq 4000 using a single lane of 50 bp single end reads. FastQC (*96*) was used to identify read quality, and adapter reads were trimmed using Trimmomatic v0.32 (*90*) followed by Bowtie (*97*) alignment (v1.0) of the reads to the reference genome using the settings: -v 2 –best –strata -m 1 with duplicate reads removed using Picard MarkDuplicates (v1.13) and ENCODE hg38 blacklist reads removed using bedtools2 v2.25 (*98*). Peak calling was performed using MACS2 with narrowPeak settings and a threshold of FDR < 0.001 (*99*), and a master peak set was generated as the union set of all called peaks across every sample analyzed (224,906 unique regions total). Count matrices were made using featureCounts (*92*) and DEseq2 v1.36 was used for differential accessibility analysis (*100*). Annotation of genomic regions was performed using ChIPSeeker (*101*), interactive visualization of processed data was done using Degust (*94*) and Rstudio along with ggplot2 and tidyverse plugins were used

to generate data visualizations. Sequencing-depth normalized ATAC bigWig files were generated using deeptools bamCoverage v3.0.1 (*102*). All motif analysis was performed using the HOMER suite (*103*).

Footprinting: A TOBIAS-based footprinting analysis was performed to assess differential transcription factor (DTF) binding in A549 cells and HFF cells under distinct conditions (1 kPa versus 50 kPa). Replicates for each condition were merged using samtools (v1.21). The resulting BAM files were then sorted and indexed. To correct for Tn5 insertion bias, ATAC-seq BAM files and peak sets were processed by TOBIAS (version 0.17.1) ATACorrect with the hg38 reference genome (*44*), which generated corrected BigWig files for downstream analysis and visualization. TOBIAS FootprintScores were then applied to the corrected files and corresponding union peaks to generate footprint scores for each condition. DTF binding analysis was performed using TOBIAS BINDetect, with motif definitions from the JASPAR 2024 CORE vertebrates nonredundant database in MEME format. TOBIAS PlotTracks was used to visualize DTF footprints at specific genomic loci. ATAC-seq signal tracks and corresponding footprint scores from both 1 kPa and 50 kPa conditions were plotted across selected genomic regions defined in a custom BED file. High-confidence binding sites were overlaid as both sites and highlight tracks to emphasize regions of interest. Gene annotations were incorporated from the GENCODE v47 GTF file, and distinct color codes were applied to facilitate condition-specific comparison.

HiCAR: HFF cells were seeded on Matrigen T75 flasks (1 kPa and 50 kPa) at slightly variable densities to account for reduced cell attachment on softer substrates (2 million and 1.25 million). After 20 hours, HiCAR libraries were prepared as previously described, with the following modification: Glycine was added to a final concentration of 0.125 M and incubated at room temperature for 5 min to quench formaldehyde (*104*). This protocol included a rapid fixation step before Tn5 transposition. Two hundred thousand cross-linked cells were used for each replicate. Nuclei were isolated using NPB buffer [5% bovine serum albumin (BSA) in phosphate-buffered saline (PBS), 1 mM dithiothreitol (DTT), 0.2% IGEPAL, Protease Inhibitor] and incubated with assembled Tn5 transposase in 1X TB buffer (33 mM Tris-AC pH 7.8, 66 mM KCl-AC, 10 mM Mg-AC, 16% *N*,*N*′-dimethylformamide) at 37°C on a rotator for 1 hour. Chromatin digestion was performed with MseI, followed by in situ ligation with T4 DNA ligase and DNA purification. Purified genomic DNA was further digested with NlaIII and circularized with T4 DNA ligase, followed by DNA purification and PCR amplification. After size selection, the libraries were sequenced using the Illumina Novaseq X.

The analysis pipeline to process the HiCAR libraries can be found at https://nf-co.re/hicar/1.0.0 with the following parameters: --genome GrCh38, --profile singularity, --ensyme 'MseI', --restriction_sites '^TAA', --resample_pairs, --qval_thresh 0.01. Briefly, quality reads were determined using FASTQC (https://www.bioinformatics.babraham.ac.uk/projects/fastqc/), then adapters were trimmed using cutadapt (*105*). Reads were aligned to the reference genome using bwa mem (https://bio-bwa.sourceforge.net/bwa.shtml#12). Aligned reads were then processed using pairtools (*106*), and quality control was performed using pairsqc (https://github.com/4dn-dcic/pairsqc). MACS2 (*99*) was used to call peaks, and MAPS (*107*) was used to find genomic interaction loops. Differential analysis was performed using edgeR (*93*), and files for visualization were generated using Cooler (*108*) and Juicer (*109*). To compare the chromatin loops between ECM stiffness conditions, we used bedtools pairtopair with the -type parameter set to both, either, or neither (*110*). To compare the chromatin loops with the differentially accessible ATAC-seq peaks, we used bedtools pairtobed (*110*).

MYH9 locus screening

Library design and cloning: Using the ATAC-seq data, every open chromatin region that was within 440 kb of the MYH9 TSS was used as input to generate an oligo pool. For each ATAC-seq peak, we included any gRNA that had a GuideScan specificity score of >0.2, which has previously been shown to increase the quality of noncoding screens (*111*). This resulted in 114 peaks represented in the library, with an average of ~41 gRNA/peak. We also included 500 nontargeting gRNA as negative controls (*112*). This combined gRNA library of 5192 gRNA was synthesized as an oligo pool by Twist Biosciences with common overhangs for cloning into our lentiviral backbone.

This oligo pool was PCR amplified, and a hU6-driven lentiviral gRNA vector (pBDC119) was then digested with Esp3I, gel purified, and then ligated along with the amplified oligo pool by Gibson assembly. After a 1× SPRI cleaning, the Gibson assembly was transformed into Endura competent cells (Lucigen) according to the manufacturer's protocol and cultured overnight before maxi-prepping the gRNA-library plasmid. A PCR amplicon across the gRNA region of the resulting plasmid was sequenced to a depth of ~100,000 to 1 million read pairs on an Illumina miSeq to verify coverage across the entire gRNA library (fig. S29).

Lentiviral generation and functional titering of MYH9 locus library: gRNA library plasmid was cotransfected into ~18 million human embryonic kidney 293T (HEK293T) cells along with two lentiviral packaging plasmids using Lipofectamine 3000 (ThermoFisher). Twenty hours after transfection, the transfection media was removed and fresh growth media was added. Media containing viral particles was removed 1 day later, at 48 hours after transfection, and stored, replaced with fresh media, and collected 1 day later before being stored at 4°C. Combined media containing viral particles was filtered through 0.45 μm low-protein binding filters and then concentrated using Lenti-X Concentrator (Takara Bio) according to the manufacturer's protocol. Functional titering to determine MOI was performed by transducing HFF cells across a 50×–10,000× dilution range of the viral stock and then subjecting the cells to FACS-based cell sorting to identify what percent of the population was mCherry+ for each viral stock dilution.

CRISPRi locus screen: A stable HFF line was created using a lentiviral dCas9^{KRAB} construct [pLV-hUbC-dCas9-KRAB-2A-Blast (pJB289)], followed by the gRNA library being transduced at an MOI of ~0.33 and Puro selection for 4 days at 1 μg/ml. Cells were maintained for an additional 4 days, before trypsinization and fixation at day 10 after transduction. After trypsinization with 0.25% Trypsin-EDTA for 5 min at 37°C, trypsin was neutralized with 1× volumes of complete growth media followed by 300*g* for 5 min centrifugation and aspiration of the supernatant, one rinse with 1× volume PBS, followed by another centrifugation and aspiration leaving 200 μl of PBS above the pellet. The eBioScience ICC Fixation kit (ThermoFisher) was used to fix/permeabilize cells according to manufacturer's instructions, with both reagents being equilibrated to room temp before usage. Fixation was performed through the addition of 500 μl eBioSciences Fix/Perm Buffer (ThermoFisher) to the 200 μl PBS and pellet, and incubation at room temperature for 20 min. At the end of this incubation, 1X Permeabilization Buffer was added to 8 ml total volume, spun at 600*g* for 5 min, followed by an additional perm buffer rinse. After this step, HFF cells were counted, and ~2 million cells were removed to be used for unsorted controls, and ~500,000 cells were set aside to be control samples for single-channel compensation controls. Immunostaining of MYH9 was performed using a AlexaFluor-488 conjugated Rabbit monoclonal anti-NMMIIA antibody (clone EPR8965, Abcam, #ab204675) at a ratio of 0.5 μl antibody per 300,000 HFF cells per 100 μl of Perm Buffer, which was determined to be the ideal staining ratio using an antibody titration series. HFF cells were incubated for 30 min at room temperature in the dark on a nutating rocker, a 600*g* for 5 min spin, and two repeats of 3 ml 1X Perm Buffer rinse/spin cycles. After the last spin down, cells were resuspended in FACS Buffer [1X PBS supplemented w/ 1% BSA (Sigma) and 0.5mM EDTA (Sigma)] at density of ~9 million cells/ml and sorted. A SH800 Cell Sorter (Sony Biotechnologies)

was used to separate out the top/bottom-expressing MYH9 fractions after immunostaining. Compensation panels were set up using single channel–expressing cell populations including untreated cells, antibody-only cells, mCherry-only cells. The top 10% and lower 10% of the MYH9 population was sorted off and used for downstream gRNA-enrichment analysis and sequencing.

gDNA recovery and library preparation: Cells were counted after sorting to verify enrichment, followed by DNA recovery and extraction from fixed cells using the PicoPure DNA extraction kit (ThermoFisher) according to manufacturer's instructions. Recovery digests were performed for 20 hours at 65°C using up to 1.5M HFF cells per reaction volume. All gDNA was split between sample-indexed 100 μl Q5 PCR reactions (up to ~340 ng max input per 100 μl reaction) to amplify out the gRNA protospacer from HFF cells. These PCRs from gDNA were run as follows (98°C for 30s/25×: 98°C for 10 s, 60°C for 30 s, 72°C for 15 s/72°C for 2 min] with primers in table S19, followed by individual PCRs being pooled together and subjected to a double-sided 0.65X/1X SPRI clean-up. Quality control was performed by running the amplified libraries out on a High Sensitivity D1000 Tapestation (Agilent) to confirm expected size, and Qubit dsDNA HS assays were performed to determine a final concentration. All libraries were pooled to an effective concentration of 4 nM and combined in equal volumes before sequencing on an Illumina MiSeq, using a v2 50 cycle reagent kit with Read1 being 21 cycles (protospacer) and index read 1 being six reads (sample barcoding).

MYH9 locus library analysis: Resulting FASTQ files were aligned to a custom reference sequence corresponding to the given gRNA library using bowtie2, and all downstream analyses were performed in R. All gRNA were verified to be represented in the baseline untreated library at day 8 after transduction, and counts+1 for each gRNA were taken (to normalize for samples that dropped out in one condition) and normalized by sequencing depth for each library before downstream analysis [in counts per million reads sequenced (CPM)]. Given the highly apparent strand bias in the positive-strand when targeting the MYH9 gene body (supplementary text 1), we only included the nontargeting gRNA from the negative strand (2863 gRNA). A ratio was taken of the CPM for each gRNA of the low MYH9 expression group to high MYH9 expression group to identify whether the gRNA perturbation led to increases in enrichment in either expression bin. Next, for each screen replicate, the Z-score was calculated for each gRNA relative to the control nontargeting gRNA population using similar methodologies as previously described in (*6*). First, each sample's ratio was converted to a $\log_2$ fold enrichment, and population statistics for the negative control nontargeting gRNAs (median, standard deviation, gRNA number) were calculated. For each individual gRNA, the median of the negative control fold enrichment was subtracted from each individual gRNA's $\log_2$ fold enrichment value, and this value was further divided by the standard deviation of the negative control nontargeting gRNA population to get an individual Z-score relative to the negative control population. Raw Z-score values from both replicates were pooled to calculate pRE-wide effects. Phenotype scores (t-score based) were calculated as

$$Phenotype\ Score = U(pRE) - U\ CTL / \sqrt{\left(\frac{Svar}{Nexp} + \frac{Svar}{Nctl}\right)}$$

$$Svar = Var(pRE) * (N(pRE) - 1) + Var(CTL) * (Nctl - 1)$$

Individual gRNA validations: For gRNA validations of all five hit pRE across the MYH9 locus (including the two promoter/exon1 regions). Oligos containing protospacer sequences were chemically synthesized (Integrated DNA Technologies, IDT) and cloned into pLV_hU6-sgRNA_hUbC-GFP-P2A-PuroR (Addgene plasmid #162335). Sanger sequencing was used to confirm the identity of the gRNA. Lentivirus was generated as previously described (methods). dCas9^{KRAB} expressing HFF cells were seeded onto TCP and transduced on day 0. Twenty-four hours after transduction, lentivirus was removed and replaced with fresh growth media. Puromycin selection was applied as described for the bulk screen, and cells were harvested 9 days after transduction. mRNA was isolated using the Norgen Total RNA Purification Kit (#17250) according to the manufacturer's protocol. One hundred nanograms of mRNA was used as input for cDNA amplification using the Invitrogen SuperScript VILO cDNA Synthesis Kit. For RT-qPCR, each reaction contained 1 μl cDNA, 7 μl H_20, 1 μl Taqman probe for TBP, 1 μl Taqman probe for MYH9, and 10 μl Quantabio PerfeCTa FastMix II. Delta delta Ct analysis was performed in Microsoft Excel. Graphpad Prism was used to conduct one-way analysis of variance (ANOVA) tests followed by Tukey's post hoc test. Significance is reported in the figures as follows: $*P < 0.05$, $**P < 0.01$, $***P < 0.001$. Taqman probe information provided in table S20. A portion of the transduced cells for the MYH9-intron 3 pRE were propagated to day 15 and then subjected to MYH9 immunostaining and flow cytometry as described in the bulk screen section, with gain values held constant across all collections across samples. Populations were plotted to show shifts relative to transduction with the non-targeting gRNA. Noting high values of MYH9 promoter-targeting gRNA, we did a similar transduction and examined RNA expression at day 6 after transduction and saw markedly lower levels of MYH9 expression, supporting the idea that MYH9 deficiencies in cytokinesis led to a dropout of transduced cells over longer time frames (fig. S10).

Actin and vinculin labeling/immunostaining and focal adhesion imaging/analysis: HFF cells were seeded into 24-well plates while being transduced with lentiviruses encoding an all-in-one construct that expressed dCas9-KRAB/hU6-gRNA (Addgene plasmid #71236) with the gRNA being either a nontargeting control, a gRNA for the *MYH9* intron 3 enhancer, or a gRNA for the MYH9 promoter. Viral media was removed 20 hours later and replaced with complete growth media. Puromycin selection was started 2 days after transduction, wherein 1.5 μg/ml Puromycin was added to the growth media for 3 days before removal of the antibiotic selection and continued passaging of the cells for expansion. Six days after transduction, our transduced HFF cells were seeded at at ~5000 cells per well into μ-Slide 8 Well Glass Bottom (ibidi) chamber slides that were coated with 10 μg/ml fibronectin for 45 min at room temp and rinsed 1× with PBS before seeding. After an overnight culture, the media was removed on the chamber slide and 200 μL of 4% paraformaldehyde (PFA) was gently added to each well, and cells were fixed at room temp for 15 min, rinsed 2× with PBS, and then permeabilized with a permeabilizing solution (PBS supplemented with 0.5% TritonX-100, 10% w/v sucrose, 600 μM $MgCl_2$) for 10 min at 4°C. Permeabilizing solution was then removed from cells, followed by 2× PBS rinses, and blocked with a labeling solution [1% BSA (Sigma) in PBS] for 30 min at room temperature. Fresh labeling solution was added that contained a 1:300 dilution of a Rabbit monoclonal anti-Vinculin antibody (clone EPR8185, Abcam, #ab129002) and incubated in a nutating rocker in the dark overnight at 4°C. The next morning, the primary antibody was removed, rinsed 2× with labeling solution and then a secondary solution that contained a 1:200 dilution of AlexaFluor488 Goat anti-Rabbit secondary (Thermo #A-11008), a 1:100 dilution of AlexaFluor647-Phalloidin (Thermo #A22287) and a 1:5000 dilution of 4′,6-diamidino-2-phenylindole (DAPI) was added for 1 hour at room temperature on a nutating rocker in the dark. After three PBS rinses, chamber slide wells were mounted with Vectashield Antifade Mounting Media (Vector Laboratories, H-1000-10). All FA and actin imaging was performed using a 20×/0.8NA objective on a Zeiss AxioObserver 7 and a quad-bandpass filter. FA morphometric characteristics were quantified using vinculin images input to an online web tool, the Focal Adhesion Analysis Server (FAAS) (*113*). For this analysis the minimum adhesion size was set to 0.21 μm^2, and the stdev_thresh was set to 5.5. Each value is

reported as the average across an individual cell within the group, with $N = 39$ to 45 cells per group for either the control nontargeting gRNA or the *MYH9* intron 3 targeting gRNA.

MYH9 intron 3 saturation mutagenesis screening

Library design and cloning: For the *MYH9* intron 3 pRE saturation mutagenesis library, we included any gRNA that was within the hit pRE from the MYH9 locus library, which resulted in 64 gRNA across the library. We also included 25 nontargeting gRNA (*112*) and 11 safe-targeting gRNA (*114*) as negative controls. This combined gRNA library of 100 gRNA was synthesized as an oligo pool by Twist Biosciences with common overhangs for cloning into our lentiviral backbone. This oligo pool was PCR amplified, and pLV_hU6-sgRNA_hUbC-GFP-P2A-PuroR (Addgene plasmid #162335) was then digested with Esp3I, gel purified, and ligated along with the amplified oligo pool by Gibson assembly. After a 1× SPRI cleaning, the Gibson assembly was transformed into Endura competent cells (Lucigen) according to the manufacturer's protocol and cultured overnight before maxi-prepping the gRNA-library plasmid. A PCR amplicon across the gRNA region of the resulting plasmid was sequenced to a depth of ~100,000 to 1 million read pairs on an Illumina miSeq to verify coverage across the entire gRNA library (fig. S29).

Lentiviral generation and functional titering: gRNA library plasmid pool was cotransfected into ~7.8 million HEK293T cells along with two lentiviral packaging plasmids using Lipofectamine 3000 (ThermoFisher). Twenty hours after transfection, the transfection media was removed and fresh growth media was added. Media containing viral particles was removed 1 day later at 48 hours after transfection and stored, replaced with fresh media and collected 1 day later before being stored at 4°C. Combined media containing viral particles was filtered through 0.45 μm low-protein binding filters and then concentrated using Lenti-X Concentrator (Takara Bio) according to the manufacturer's protocol. Functional titering to determine MOI was performed by transducing HFF cells across a 0.75×–100x dilution range of the viral stock and then subjecting the cells to FACS-based cell sorting to identify what percent of the population was mCherry+ for each viral stock dilution.

MYH9 saturation mutagenesis screen: HFF cells were transduced with a lentiviral SpCas9 construct [FUGW-SpCas9-2A-HygroR (pVG54)], selected with 100 μg/ml hygromycin for 4 days with hygromycin in order to make a stable line. After four passages, the cells were frozen and used for subsequent screening experiments and validations. Six hundred thousand HFF cells were transduced with lentivirus encoding the *MYH9* intron 3 saturation pool. For screening, the same protocol was used as described above for the MYH9 CRISPRi locus screen, with 8 days of culture time before fixation, MYH9 immunostaining, FACS for the top/bottom 10% of cells, PicoPure gDNA recovery, and gRNA PCR and processing for enrichment across the low and high MYH9 expression bins.

Individual gRNA validations: For gRNA validations of all three hit gRNA that had significantly altered MYH9 expression and a nontargeting control gRNA, oligos containing protospacer sequences were synthesized by IDT and cloned into pLV_hU6-sgRNA_hUbC-GFP-P2A-PuroR (Addgene plasmid #162335). Sanger sequencing was used to confirm the identity of the gRNA. Lentivirus was generated as previously described above. Cas9 expressing HFF cells were seeded onto TCP and transduced on day 0. Twenty-four hours after transduction, lentivirus was removed and replaced with fresh growth media, cells were grown for 8 days (with 4 days of 1.5 μg/ml puromycin selection). And for harvest cells were split with 500,000 cells for gDNA harvested following FACS (as detailed below), and RNA was harvested from 500,000 cells using a Norgen Total RNA Purification Kit (#17250). qPCR for MYH9 expression was performed as described above for the MYH9 locus screen.

gRNA validation indel enrichment across MYH9 expression bins: Additionally, 500,000 cells were processed similarly to the *MYH9* locus screen that included cell fixation, MYH9 immunostaining, FACS for the top/bottom 10% of cells, PicoPure gDNA recovery. A *MYH9* intron 3 PCR was performed with an amplicon size of 666 bp. All gDNA was split between sample-indexed 100 μl Q5 PCR reactions (up to ~340 ng max input per 100 μl reaction) to amplify out the gRNA protospacer from HFF cells. These PCRs from gDNA were run as follows (98°C for 30 s/25×: 98°C for 10 s, 60°C for 30 s, 72°C for 15s/72°C for 2 min) with primers in table S15, followed by individual PCRs being pooled together and subjected to a double-sided 0.65X/1X SPRI clean-up. Quality control was performed by running the amplified libraries out on a High Sensitivity D1000 Tapestation (Agilent) to confirm expected size, and Qubit dsDNA HS assays were performed to determine a final concentration. All libraries were pooled to an effective concentration of 4 nM and combined in equal volumes before sequencing on an Illumina MiSeq, using a v2 50 cycle reagent kit with Read1 being 21 cycles (protospacer) and index read 1 being 6 reads (sample barcoding). FASTQ reads were run through Crispresso2 (*115*), and indel enrichment in the low MYH9 bin was used to examine any overlapping TF motifs on common indel sites.

BMF/FZD2 enhancer characterization

Luciferase enhancer reporter assays: BMF/FZD2/MYH9 regions with differential accessibility were identified, and primers were designed to amplify these regions from gDNA isolated from HFF cell-lines. Briefly, 2× 25 μl reactions were run wherein 30 ng gDNA was input with 2× KAPA HiFi Hot Start MM and 0.75 μl of 10uM PCR primers (table S21) for either Region #1/2/3 with an annealing temperature of 63°C. Sequences were confirmed through Sanger sequencing. These enhancer fragments were then assembled into an improved STARR-seq enhancer luciferase reporter vector (*116*) by Gibson assembly, and clones were sequenced by Sanger sequencing to confirm the fragment addition. To perform the luciferase assay, 15,000 HFF cells and 10,000 A549s were seeded per well into a 24-well plate 1 day before transfection, and the day of transfection, fresh media was added immediately before lipofection, with either DMSO only or blebbistatin (2, 10, 40 μM), Y-27632 (10 μM), nocodazole (10 μM) added. A Rho agonist, Rho Activator II #CN03 (Cytoskeleton Inc, #CN03) was also used at a final concentration of 1 μg/ml. Lipofectamine LTX (2.25 μl per well for HFF, 2.5 μl per well for A549) was used to transfect luciferase reporter plasmids (300 ng for HFF, 500 ng for A549) at a mass ratio of 90% experimental firefly luciferase plasmid to 10% Renilla luciferase pRL-CMV control plasmid (Promega) into cells. Cells were harvested 24 hours later, and the Promega DualGlo Luciferase Assay was performed according to manufacturer's instructions, with luciferase activity read on a Promega GloMax Discover instrument (0.3 s integration time). The average of four blank wells was then set as the background level and subtracted from all experimental values. Firefly luciferase values for each well were normalized to the Renilla luciferase values. Each experiment was further normalized to the performance of an empty luciferase reporter plasmid or FZD2 pRE reporter levels as baseline.

LatA induction experiment culture: Oligos containing protospacer sequences were synthesized by IDT and cloned into an all-in-one lentiviral vector expressing dCas9-KRAB-P2A-PuroR from an hUbC promoter and a gRNA from an hU6 promoter (Addgene plasmid #71236). All gRNA were selected as (-) strand gRNA to minimize the strand-bias artifact (supplementary text 1). gRNA protospacers selected for further use were BMF-pRE1-g3 ("CGTACATTCGTGACCGTCCC"), BMF-pRE1-g4 ("GGCCAGGCGCGGCCTGCAGT") and BMF-prom ("TCACGCCGAGGACTGACCAA"). Sanger sequencing was used to confirm the identity of the gRNA after cloning. Lentivirus was generated as described above for MYH9. HFF cells were transduced and seeded per well in a 24-well plate on day 0, by adding 25 μl of 20× concentrated virus along with 5000 cells and

growth media. Twenty-four hours after transduction, lentivirus was removed. Antibiotic selection was applied for 4 days, and cells were grown for 8 days after transduction. At 9 days after transduction cells were trypsinized, and were reseeded at 5000 HFF cells per well in a 24-well plate for RNA experiments or 20,000 HFF cells per well in a 12-well plate for cleaved caspase-3/7 experiments. To model detachment, on day 11 after transduction, the media was replaced with growth media containing either DMSO or 0.5 μM LatA. Cells were harvested for RNA or CaspaseGlo 3/7 analysis 1 day after the addition of LatA.

Transcriptional expression and cleaved caspase-3/7 activity assays: mRNA was isolated using the Norgen Total RNA Purification Kit (#17250) according to the manufacturer's protocol. One hundred nanograms of mRNA was used as input for cDNA amplification using the Invitrogen SuperScript VILO cDNA Synthesis Kit. For RT-qPCR, each reaction contained 1 μl cDNA, 7 μl H_20, 1 μl Taqman probe for TBP, 1 μl Taqman probe for BMF or FZD2, and 10 μl Quantabio PerfeCTa FastMix II. Delta delta Ct analysis was performed in Microsoft Excel. Graphpad Prism was used to conduct one-way ANOVA tests followed by Tukey's post hoc test. Significance is reported in the figures as follows: $*P < 0.05$, $**P < 0.01$, $***P < 0.001$. Taqman probe information provided in table S20. For caspase-3/7 activity assays, HFF cells were subjected to the CaspaseGlo 3/7 Assay (Promega) and Cell TiterGlo Assay (Promega) according to manufacturer's instructions with luciferase values read out on a Promega GloMax Discover instrument (0.3 s integration time). The average of two blank wells per assay was then set as the background level and subtracted from all experimental values. CaspaseGlo3/7 values per group were further normalized to cell counts per group determined from the CellTiterGlo data.

Bulk growth and migration functional CRISPRi screens

Library design and cloning: The top 1000 regions from the ATAC-seq data that were increasingly accessible on the stiff 50 kPa substrates as compared with the soft 1 kPa substrate were used as input to generate an oligo pool (BDC03 ATAC libraries). For each peak, we included any gRNA that had a GuideScan specificity score of >0.2, which has previously been shown to increase the quality of noncoding screens (*111*). This resulted in 969 peaks represented in the library, with an average of ~20 gRNA per peak. We also included 1000 nontargeting gRNA (*112*) and 249 promoter-targeting gRNA for 83 positive control genes that have previously been shown to be key modulators of transwell migration following RNAi screens (*60*), with 3 gRNA per gene taken from the Dolcetto library (*117*). This combined gRNA library of 21,458 gRNA was synthesized as an oligo pool by Twist Biosciences with common overhangs for cloning into our lentiviral backbone. This oligo pool was PCR amplified, pLV_hU6-sgRNA_hUbC-GFP-P2A-PuroR (Addgene plasmid #162335) was digested with Esp3I and gel purified, and then the oligo pool and digested vector were ligated by Gibson assembly. After a 1× SPRI cleaning, the Gibson assembly was transformed into Endura competent cells (Lucigen) according to the manufacturer's protocol and cultured overnight before maxi-prepping the gRNA-library plasmid. A PCR amplicon across the gRNA region of the resulting plasmid was sequenced to a depth of ~100,000 to 1 million read pairs on an Illumina miSeq to verify coverage across the entire gRNA library (fig. S29).

Lentiviral generation and functional titering: Concentrated lentivirus was generated by the Duke Viral Vector Core from this plasmid pool. Functional titering to determine MOI was performed by transducing HFF cells across a 50× to 10,000× dilution range of the viral stock, and then subjecting the cells to a qPCR-based titering protocol that has been previously described in detail (*118*).

Migration/growth pRE library screen: To perform screening, 600,000 HFF cells were transduced with the lentiviral library virus at 10.8 MOI to achieve a coverage of ~279 cells per gRNA. Twenty hours after transduction, the viral media was removed and replaced with fresh media, and starting 48 hours after transduction, HFF cells were selected with 1 μg/ml puromycin for 4 days. Puromycin selection media was then removed and HFF cells were grown out for two additional days until day 8. On day 8, ~11 million cells were counted and split between migration and growth screens. Coverage of at least 279 cells per gRNA was maintained for each group throughout the entire experiment.

Migration screening: On day 8, the bottoms of 8 μm transwell inserts for six-well plates were coated with 10 μg/ml fibronectin at room temp for 45 min and then rinsed 1× with PBS for 30 min before use. HFF cells were counted, placed into low serum conditions (0.2% FBS) and seeded at 240,000 cells per transwell insert across 18 inserts (~4.4 million cells total). These inserts were placed into 10% serum, and cells were allowed to migrate for 24 hours. After this first day of migration, each side of the membrane was separately trypsinized and counted, where 27% of the initial cells were recovered as migratory cells (~1.2 million cells), and nonmigrated cells were recovered from the top of the insert. These migratory and nonmigratory populations were re-seeded (separately by group) in the same way on new fibronectin-coated transwell inserts, with 4 to 5 inserts seeded at 240,000 cells per insert and allowed to migrate overnight. After these two rounds of migration, we trypsinized and collected the cells that either migrated twice or did not migrate twice (with a similar number of cells, 24%, being found to have migrated during this second round) and isolated gDNA using DNeasy kits (Qiagen).

Growth screening: HFF cells were counted on day 8 after -transduction, and gDNA from 2M HFF cells were harvested as the "Day 0" reference population using a DNeasy Blood and Tissue Kit (Qiagen). Around 1 million HFF cells were reseeded into 15 cm dishes for ongoing culture and then serially passaged as normal for 14 doublings (either 21 days after "Day0" for replicate 1 or 22 days after "day0" for replicate 2) while maintaining at least 1 million cells per dish during each passaging, before the final gDNA harvest using a DNeasy Blood and Tissue Kit (Qiagen).

Library preparation and sequencing: All gDNA was split between sample-indexed 100 μl Q5 PCR reactions (up to ~340 ng max input per 100 μl reaction) to amplify out the gRNA protospacer from HFF cells. These PCRs from gDNA were run as follows (98°C for 30s/25 ×: 98°C for 10 s, 60°C for 30 s, 72°C for 15 s/72°C for 2 min] with primers in table S19, followed by individual PCRs being pooled together and subjected to a double-sided 0.65X/1X SPRI clean-up. Quality control was performed by running the amplified libraries out on a High Sensitivity D1000 Tapestation (Agilent) to confirm expected size, and Qubit dsDNA HS assays were performed to determine a final concentration. All libraries were pooled to an effective concentration of 4 nM and combined in equal volumes before sequencing on an Illumina MiSeq, using a v2 50 cycle reagent kit with Read1 being 21 cycles (protospacer) and index read 1 being 6 reads (sample barcoding).

Screen analysis: Resulting FASTQ files were aligned to a custom reference sequence corresponding to the given gRNA library using bowtie2 and all downstream analyses were performed in R. All gRNA were verified to be represented in the baseline untreated library at day 8 after transduction, and counts+1 for each gRNA were taken (to normalize for samples that dropped out in one condition) and normalized by sequencing depth for each library before downstream analysis (in CPM). For migration screens: A ratio was taken of the CPM for each gRNA of the 2x migrated group to the 2x nonmigrated group to identify migratory or nonmigratory enrichment. For growth screens: A ratio was taken of the CPM of the day 0 population relative to the final day 21/22 population for each replicate. Next, for each screen replicate the Z-score was calculated for each gRNA relative to the control nontargeting gRNA population using similar methodologies as previously described (*6*). First, each sample's ratio was converted to a $\log_2$ fold enrichment, and population statistics for the negative control nontargeting gRNAs

(median, standard deviation, gRNA number) were calculated. For each individual gRNA, the median of the negative control fold enrichment was subtracted from each individual gRNA's $\log_2$ fold enrichment value, and this value was further divided by the standard deviation of the negative control nontargeting gRNA population to get an individual Z-score relative to the negative control population. Raw Z-score values from both replicates were pooled to calculate pRE-level effects. An individual gRNA was called as a "hit" if the Z-score was >2 or <−2. pRE-level stats were generated by performing a Fisher's exact text relative to the nontargeting gRNA population, and a pRE-level was labeled significant for follow-up if the pval was <0.1. To select pREs for validation in single cell RNA-seq, we further selected the pRE hits that had more than one gRNA as a "hit" and had at least 10 gRNA/DHS in order to enable higher-powered analysis of the downstream data.

Comparison of phenotype scores between regions regulating growth, migration, or both phenotypes: Each significant region was labeled for the phenotype it regulated (one of growth, migration, or both). The phenotype (pZ) scores were compared between the three groups using a one-way ANOVA test followed by Tukey's post hoc tests using the aov and TukeyHSD functions in R.

Analysis of chromatin accessibility across ENCODE biosamples: We obtained the union set of DNase peak calls across 95 ENCODE biosamples using the "Table Browser" utility on the UCSC Genome Browser (downloaded February 2023; "wgEncodeRegDnaseClustered"). The union DNase peak calls were intersected with all regions included in the bulk screen library using bedtools intersect. Next, each region significant in at least one of two screens was labeled as "1" or "0" if the region did or did not overlap an accessible region in at least one biosample, respectively. The region X biosample visualization was generated using the pheatmap package in R with the following parameters: scale = "none", cluster_cols = TRUE, cluster_rows = TRUE. To extract the clusters, we used the cutree_col function specifying h = 8. We then compared the phenotype scores between each cluster by performing one-way ANOVA tests followed by Tukey's post hoc tests using the aov and TukeyHSD functions in R.

To determine whether significant screen regions were enriched or depleted from accessible regions in specific biosamples, we performed Fisher's exact tests separately for each biosample comparing the number of significant and nonsignificant screen regions that overlapped or did not overlap an accessible region using the fisher.test function in R.

Single-cell RNA-seq screen

gRNA library design and cloning: After hit identification from the combined migration and growth screens (as described above), a library was designed that included the top 10 gRNA by pZ value across either screen for the 87 hit pRE (870 gRNA total). One hundred nontargeting control gRNA with similar sequence composition to the targeting gRNAs were included in the library, and 25 gRNA targeting the promoters of contractile genes including *MYH9*, *RANGAP1*, and *CRIM1* were included as well as the top gRNA from the *MYH9* intron 3 enhancer as positive controls. In total, our library contained 1005 gRNA sequences, which were synthesized as an oligo pool by Twist Biosciences with common overhangs for cloning into our lentiviral backbone. This oligo pool was PCR amplified, and a hU6-driven lentiviral gRNA CROP-seq vector (Addgene Plasmid #106280) was then digested with Esp3I, gel purified, and then ligated along with the amplified oligo pool by Gibson assembly. After a 1x SPRI cleaning, the Gibson assembly was transformed into Endura competent cells (Lucigen) according to the manufacturer's protocol and cultured overnight before maxi-prepping the gRNA-library plasmid. A PCR amplicon across the gRNA region of the resulting plasmid was sequenced to a depth of ~100,000 to 1 million read pairs on an Illumina miSeq to verify coverage across the entire gRNA library (fig. S29).

Lentiviral generation and functional titering: gRNA library plasmid was cotransfected into ~18 million HEK293T cells along with two lentiviral packaging plasmids using Lipofectamine 3000 (ThermoFisher). Twenty hours after transfection, the growth media was removed, and fresh growth media was added. Media containing viral particles was removed at 48 hours, replaced, and removed at 72 hours after lipofection before being stored at 4°C. Combined media containing viral particles was filtered through 0.45 μm low-protein binding filters and then concentrated using Lenti-X Concentrator (Takara Bio) according to the manufacturer's protocol. Functional titering to determine MOI was performed by transducing HFF cells across a 50× to 10,000× dilution range of the viral stock and then subjecting the cells to a qPCR-based titering protocol that has been previously described in detail (*118*).

Single-cell CRISPRi screen: To perform screening, 775,000 HFF cells stably expressing $dCas9^{KRAB}$ were transduced at 0.33 MOI with the CROP-seq lentivirus to maintain a coverage of at least 150 cells per gRNA. After 20 hours, viral media was removed and replaced with regular growth media, and 48 hours after transduction, the cells selected with puromycin (1.5 μg/ml) for 4 days. After puromycin selection, HFF cells were maintained until day 8, at which point cells were trypsinized, and 150,000 cells were moved on to library prep.

Single-cell RNA-seq library preparation: Cells were washed 3× with PBS and then resuspended to a final concentration of 1000 cells/μl. Approximately 20,000 cells were loaded onto each channel of a 10X Genomics' 3′ Gene Expression (GEX) v3.1 assay chip. Downstream processing was performed according to the manufacturer's protocol. To recover the protospacer sequences (gRNA libraries), a tri-nested PCR was performed separately for each GEX library using 10% of the purified cDNA as input to reaction 1 as previously described (*29*). Briefly, 4 ng cDNA was input into a 50 μl reaction with KAPA HiFi and PCR primers prLRB470 and prLRB471 (table S22). The reaction was amplified for 12 cycles and then purified using 25 μl of AMPure XP DNA beads and eluted in 25 μl H_20. One microliter of the purified sample was input into reaction 2 using PCR primers prLRB472 and prLRB473 (table S22). The reaction was amplified for 14 cycles and purified as described above. One microliter of the purified sample was input into reaction 3 using PCR primers prLRB473 and prLRB289-302 (table S22), amplifying each sample with a unique i7 sequencing index. The reaction was amplified for seven cycles, purified using 25 μl of AMPure XP DNA beads (Beckman Coulter #A63881), and eluted in 25 μl Buffer EB (Qiagen #19086). Quality control of final libraries was performed before sequencing using the Agilent 2200 TapeStation with High Sensitivity DNA 5000 reagents, Qubit High Sensitivity dsDNA reagents, and KAPA Library Quantification Kit for Illumina platforms.

Sequencing: GEX libraries were pooled and sequenced on a NovaSeq 6000 S4 flow cell using the parameters: 28x10x10x90. gRNA libraries were pooled and sequenced on a NovaSeq 6000 S1 flow cell using the parameters: 28x10x10x90.

Data processing: Cell Ranger: All data processing steps were performed using CellRanger v6.0.1 and the human reference genome ("refdata-gex-GRCh38-2020-A") was downloaded from 10X Genomics' software downloads webpage. Fastq files for each flow cell lane and sequencing run were generated from .bcl files using the cellranger mkfastq pipeline. The corresponding fastq files for each sample were then merged. The merged fastqs were then processed using the cellranger count pipeline with the number of expected cells specified (--expect-cells = 15,000). The gene expression libraries were then aggregated using the cellranger aggr pipeline. The gRNA libraries were aligned to a custom bowtie index containing all protospacer sequences included in the pooled gRNA library and the UMI counts corresponding to each gRNA-cell pair were obtained.

Seurat: The gene expression and gRNA UMI count data was imported into Seurat v3.1. A gRNA was defined as "observed in a cell" if the gRNA had at least 5 UMI counts and made up at least 0.5% of the total gRNA UMI counts in that cell. We then calculated the total percent of mitochondrial reads per cell and filtered for quality cells as follows:

```
cells[["percent.mt"]] <- PercentageFeatureSet(cells, pattern = "^MT-")
cells <- subset(cells, subset = nCount_RNA > 10000 & percent.mt < 20)
```

Differential expression analysis: Using the gRNA-cell assignments, differential expression testing was performed using the MAST framework (*119*) within Seurat v3.1 (*120*), comparing cells in which a given gRNA was observed versus all other cells with at least one gRNA observed excluding the given gRNA and testing all genes within ±1 Mb of the midpoint of the pRE in which the gRNA is located. Gene coordinates were obtained from the Ensembl Human Gene v104 reference file. *P* values were then FDR-corrected on an individual gRNA level for all tests. All genes within ±1 Mb of any targeting gRNA were used as input features for NT gRNA tests ($N = 1313$). Significant gRNA-gene and corresponding pRE-gene pairs are defined as FDR < 0.01.

Calculation of interaction distance (ep_length): The distance between the gRNA and the paired gene was calculated as follows: 1) the gRNA midpoint (gRNA_mid) was defined as (gRNA_start + gRNA_end)/2, the gene start coordinate (gene_start) was defined as the start coordinate for genes on the "+" plus strand, and end coordinate for genes on the "−" strand. "ep_length" was calculated as gRNA_mid - gene_start.

Effect size comparison between targeting and control gRNAs: For each gene with a TSS- or validated enhancer-targeting gRNA, we compared the avg_logFC of expression for the respective gene between TSS-control, enhancer-control, pRE-targeting, and NT-control gRNAs (FDR < 0.01) using a one-way ANOVA followed by Tukey's post hoc test with Bonferroni correction (adjusted *P* value). Significant differences in the change in gene expression were defined as adjusted $P < 0.05$.

Interaction distance versus effect size: Using all significant pRE-targeting gRNA gene pairs, the avg_logFC and effect size (avg_logFC*(1-FDR)) were plotted versus the log10-transformed ep_length (log10(abs(ep_length+1))). Spearman correlation R^2 values were calculated using the "stat_cor" function from the "ggpubr" R package.

Nearest gene prediction analysis: For each potential pRE-gene pair, we calculated the number of genes "skipped" by the element to regulate the gene as follows. First, for the significant pRE-gene connections, we defined the start and end coordinates for a given element and the start and end coordinates, and strand, for the paired gene. Next, we counted the number of genes detected in the gene expression dataset for which the entire gene body was contained within the region between the element and the connected gene. We repeated this for all significant pRE-gene connections.

Comparison to microC looping: We obtained chromatin contact data (table S19) and intersected all targeted pREs, TSS regions (±1 kb) of every gene and all genes for which a differential expression test was performed, separately extended by ±500 bp with anchor 1 and anchor 2, using bedtools window -w 500. We then quantified the number of pREs, TSSs, and genes with at least one chromatin contact, defined as at least one intersection with anchor 1 or anchor 2. Next, for all regions that intersected a region in the anchor 1 set, we quantified the number of pRE-gene pairs for which the corresponding contact in the anchor 2 set overlapped either the same TSS/gene or a different TSS/gene. We repeated this for pREs intersecting the anchor 2 set with comparison of contacts for TSSs/genes in the anchor 1 set.

Comparison to ENCODE candidate cis-regulatory elements (cCREs) and chromHMM annotations: We obtained cCRE annotations from all human tissues and chromHMM annotations in human foreskin fibroblast primary cells (table S23). The cCREs and annotated regions were intersected with all regions included in the bulk screen and single cell screen libraries using bedtools intersect. To determine whether significant screen regions were enriched or depleted from accessible regions in specific biosamples, we performed Fisher's exact tests comparing the number of significant and nonsignificant screen regions that overlapped or did not overlap an annotation using the fisher.test function in R.

Single-cell screen versus individual gRNA validations: For the 10 pRE-gene connections with at least one significant individual gRNA validation, we calculated the Spearman correlation (R^2) and *P* value between the change in mRNA expression measured via RT-qPCR (DDCt) versus the gene expression change observed in the single cell screen (avg_logFC of the most significant gRNA-gene connection per DHS) using the "stat_cor" function from the "ggpubr" R package.

Individual gRNA validations: HFF cells: Oligos containing protospacer sequences were synthesized by IDT and cloned into pLV_hU6-sgRNA_hUbC-GFP-P2A-PuroR (Addgene plasmid #162335). Sanger sequencing was used to confirm the identity of the gRNA. Lentivirus was generated as described above. dCas9^{KRAB} expressing HFF cells were seeded onto TCP and transduced on day 0. Twenty-four hours after transduction, lentivirus was removed. Antibiotic selection was applied, and cells were harvested 8 days after transduction. mRNA was isolated using the Norgen Total RNA Purification Kit (#17250) according to the manufacturer's protocol. One hundred nanograms of mRNA was used as input for cDNA amplification using the Invitrogen SuperScript VILO cDNA Synthesis Kit. For RT-qPCR, each reaction contained 1 μl cDNA, 7 μl H20, 1 μl Taqman probe for TBP, 1 μl Taqman probe for gene of interest, and 10 μl Quantabio PerfeCTa FastMix II. Delta delta Ct analysis was performed in Microsoft Excel. Graphpad Prism was used to conduct one-way ANOVA tests followed by Tukey's post hoc test. Significance is reported in the figures as follows: $*P < 0.05$, $**P < 0.01$, $***P < 0.001$. Taqman probe information is provided in table S16.

Individual gRNA validations: A549/HFF cells: Oligos containing protospacer sequences were synthesized by IDT and cloned into pLV_hU6-sgRNA_hUbC-GFP-P2A-PuroR (Addgene plasmid #162335). Sanger sequencing was used to confirm the identity of the gRNA. Lentivirus was generated as described above. dCas9^{KRAB} expressing A549/HFF cells were seeded onto TCP and transduced on day 0. Twenty-four hours after transduction, lentivirus was removed and replaced with fresh media. Two days after transduction, antibiotic selection was applied. Eight days after transduction, cells were seeded on 24-well Matrigen dishes of varying stiffness (1 or 50 kPa elastic modulus) or TCP at slightly variable densities to account for reduced cell attachment on softer substrates (20,000 on 1 kPa and 12,500 on 50 kPa/TCP for A549 and 30,000 on 1 kPa and 18,750 on 50 kPa/TCP for HFF) and allowed to culture for 20 hours overnight. mRNA was isolated using the Norgen Total RNA Purification Kit (#17250) according to the manufacturer's protocol. One hundred nanograms mRNA was used as input for cDNA amplification using the Invitrogen SuperScript VILO cDNA Synthesis Kit. For RT-qPCR, each reaction contained 1 μl cDNA, 7 μl H_20, 0.5 μl Taqman probe for TBP, 0.5 μl Taqman probe for gene of interest, and 10 μl Quantabio PerfeCTa FastMix II. Delta delta Ct analysis was performed in Microsoft Excel. Graphpad Prism was used to conduct one-way ANOVA tests followed by Tukey's post hoc test. Significance is reported in the figures as follows: $*P < 0.05$, $**P < 0.01$, $***P < 0.001$. Taqman probe information is provided in table S20.

Patient-derived lung fibroblast isolations and validations

Human lung tissue dissociation: Human lung dissociation was performed as described previously (*121*). Briefly, ~2 to 3 g of human lung tissue was washed with PBS containing 1% Antibiotic-Antimycotic followed

by removal of pleura, small airway and visible vasculature. Remaining tissue was cut into small pieces followed by incubation with enzyme mixture (Collagenase type I: 1.68 mg/ml, Dispase: 5 U/ml, DNase: 10 U/ml) at 37°C for 1 to 1.5 hours with rotation. The cells were filtered through a 100 μm strainer and rinsed with DMEM containing 10% FBS. Cell suspension was spun down at 450*g* for 10 min, and the cell pellet was resuspended in red blood cell lysis buffer for 5 min, washed with DMEM containing 10% FBS, and filtered through a 40 μm strainer. Total cells were centrifuged at 450*g* for 5 min at 4°C, and the cell pellet was used for isolation of fibroblasts.

Primary human fibroblasts enrichment by MACS: Fibroblast enrichment was done using magnetic activated cell sorting (MACS) as previously described (*122*). Briefly, after lung dissociation, cells were incubated in MACS buffer (1% BSA, 2 mM EDTA, antibiotic/antimycotic in PBS, pH 7.2) containing CD146 (Miltenyi Biotec 130-093-596, 1:50), CD45 (Miltenyi Biotec 130-045-801, 1:50), and CD326 (Miltenyi Biotec 130-061-101, 1:50) microbeads at 4°C for 1 hour with rotation. Cells were then washed and incubated with CD31 biotinylated antibody (Miltenyi Biotec, 130-110-805, 1:50) at 4°C for 10 min followed by washes and incubation with streptavidin microbeads (Miltenyi Biotec, 130-048-102, 1:10) at 4°C for 15 min. Magnetic separation of antibody bound cells was performed using Miltenyi Biotec LS columns (130-042-401). Fibroblasts collected from the flowthrough were resuspended in fibroblast growth media (advanced DMEM/F12, Antibiotic/Antimycotic (Gibco 15240062, 100X), HEPES (Thermo Fisher Scientific, 15630080), GlutaMAX (Thermo Fisher Scientific, 35050061), B27 supplement (Thermo Fisher Scientific, 17504044), N2 supplement (Thermo Fisher Scientific, 17502048), *N*-acetylcysteine (Sigma-Aldrich, A9165), and 10 ng/ml PDGFα (Biolegend 773708), plated cultured on 5% Matrigel (Corning 354230) coated dish. Media was changed every 2 to 3 days.

Primary human fibroblast culture and viral transduction: To facilitate gene loss of function, fibroblasts were first transduced with lentivirus (1:50) containing $dCas9^{KRAB}$. Medium was changed 24 hours after transduction followed treatment with 8 μg/ml blasticidin for 5 days. Blasticidin-selected fibroblasts were then grown in fibroblast growth media without blasticidin for 24 hours, trypsinized, and replated in a 24-well plate. Fibroblasts were then transduced with one of the following lentiviruses (1:100): Skp2 gRNA, CCN1 gRNA, CCN2 gRNA, MYH9 intron 3 gRNA, or nontargeting control. Medium was changed 24 hours after transduction, and fibroblasts were grown for 1 day in fibroblast growth media followed by treatment with 0.5 μg/ml puromycin for 3 days. After selection, the media was changed to either standard fibroblast growth media, or fibroblast growth media supplemented with 10 ng/ml hTGFβ1 (Biolegend 580702). Cells were collected for RNA isolation on day 5.

Immunofluorescence staining of primary human fibroblasts: Fibroblasts were fixed in 4% PFA for 15 min at room temperature. Samples were washed three times with PBS and permeabilized with PBST (0.1%Triton-X 100 in PBS), followed by blocking and incubation with primary antibodies: PDGFRA (R&D Systems, AF-307-SP, 1:500), Ki67 (eBioscience 14-5698-82, 1:500), and αSMA-cy3 (Sigma-Aldrich C6198, 1:500) overnight at 4°C with. Fibroblasts were washed three times with PBST and incubated with the following secondary antibodies: Donkey-anti-goat IgG Alexa Fluor 647 (Invitrogen A-21447, 1:500) and donkey-anti-rat IgG Alexa Fluor 488 (Invitrogen A-21208, 1:500) for one hour. Samples were then washed three times with PBST, once with PBST containing DAPI, followed by one wash in PBST. Confocal images were captured using Olympus FV3000 microscope with 10X objective.

REFERENCES AND NOTES

1. S. J. Morrison, A. C. Spradling, Stem cells and niches: Mechanisms that promote stem cell maintenance throughout life. *Cell* **132**, 598–611 (2008). doi: 10.1016/j.cell.2008.01.038; pmid: 18295578
2. D. L. Jones, A. J. Wagers, No place like home: Anatomy and function of the stem cell niche. *Nat. Rev. Mol. Cell Biol.* **9**, 11–21 (2008). doi: 10.1038/nrm2319; pmid: 18097443
3. P. Jiang *et al.*, Systematic investigation of cytokine signaling activity at the tissue and single-cell levels. *Nat. Methods* **18**, 1181–1191 (2021). doi: 10.1038/s41592-021-01274-5; pmid: 34594031
4. D. R. Simeonov *et al.*, Discovery of stimulation-responsive immune enhancers with CRISPR activation. *Nature* **549**, 111–115 (2017). doi: 10.1038/nature23875; pmid: 28854172
5. G. Korkmaz *et al.*, Functional genetic screens for enhancer elements in the human genome using CRISPR-Cas9. *Nat. Biotechnol.* **34**, 192–198 (2016). doi: 10.1038/nbt.3450; pmid: 26751173
6. K. Han *et al.*, CRISPR screens in cancer spheroids identify 3D growth-specific vulnerabilities. *Nature* **580**, 136–141 (2020). doi: 10.1038/s41586-020-2099-x; pmid: 32238925
7. R. McBeath, D. M. Pirone, C. M. Nelson, K. Bhadriraju, C. S. Chen, Cell shape, cytoskeletal tension, and RhoA regulate stem cell lineage commitment. *Dev. Cell* **6**, 483–495 (2004). doi: 10.1016/S1534-5807(04)00075-9; pmid: 15068789
8. C. S. Chen, M. Mrksich, S. Huang, G. M. Whitesides, D. E. Ingber, Geometric control of cell life and death. *Science* **276**, 1425–1428 (1997). doi: 10.1126/science.276.5317.1425; pmid: 9162012
9. A. J. Engler, S. Sen, H. L. Sweeney, D. E. Discher, Matrix elasticity directs stem cell lineage specification. *Cell* **126**, 677–689 (2006). doi: 10.1016/j.cell.2006.06.044; pmid: 16923388
10. R. J. Pelham Jr., Y. Wang, Cell locomotion and focal adhesions are regulated by substrate flexibility. *Proc. Natl. Acad. Sci. U.S.A.* **94**, 13661–13665 (1997). doi: 10.1073/pnas.94.25.13661; pmid: 9391082
11. S. Dupont, S. A. Wickström, Mechanical regulation of chromatin and transcription. *Nat. Rev. Genet.* **23**, 624–643 (2022). doi: 10.1038/s41576-022-00493-6; pmid: 35606569
12. S. Piccolo, S. Dupont, M. Cordenonsi, The biology of YAP/TAZ: Hippo signaling and beyond. *Physiol. Rev.* **94**, 1287–1312 (2014). doi: 10.1152/physrev.00005.2014; pmid: 25287865
13. S. Dupont *et al.*, Role of YAP/TAZ in mechanotransduction. *Nature* **474**, 179–183 (2011). doi: 10.1038/nature10137; pmid: 21654799
14. Z. Meng *et al.*, RAP2 mediates mechanoresponses of the Hippo pathway. *Nature* **560**, 655–660 (2018). doi: 10.1038/s41586-018-0444-0; pmid: 30135582
15. F. R. Bischoff, C. Klebe, J. Kretschmer, A. Wittinghofer, H. Ponstingl, RanGAP1 induces GTPase activity of nuclear Ras-related Ran. *Proc. Natl. Acad. Sci. U.S.A.* **91**, 2587–2591 (1994). doi: 10.1073/pnas.91.7.2587; pmid: 8146159
16. C. Y. Ho, D. E. Jaalouk, M. K. Vartiainen, J. Lammerding, Lamin A/C and emerin regulate MKL1–SRF activity by modulating actin dynamics. *Nature* **497**, 507–511 (2013). doi: 10.1038/nature12105; pmid: 23644458
17. M. K. Vartiainen, S. Guettler, B. Larijani, R. Treisman, Nuclear actin regulates dynamic subcellular localization and activity of the SRF cofactor MAL. *Science* **316**, 1749–1752 (2007). doi: 10.1126/science.1141084; pmid: 17588931
18. F. Miralles, G. Posern, A.-I. Zaromytidou, R. Treisman, Actin dynamics control SRF activity by regulation of its coactivator MAL. *Cell* **113**, 329–342 (2003). doi: 10.1016/S0092-8674(03)00278-2; pmid: 12732141
19. Y. A. Miroshnikova, M. M. Nava, S. A. Wickström, Emerging roles of mechanical forces in chromatin regulation. *J. Cell Sci.* **130**, 2243–2250 (2017). doi: 10.1242/jcs.202192; pmid: 28646093
20. H. Q. Le *et al.*, Mechanical regulation of transcription controls Polycomb-mediated gene silencing during lineage commitment. *Nat. Cell Biol.* **18**, 864–875 (2016). doi: 10.1038/ncb3387; pmid: 27398909
21. S.-J. Heo *et al.*, Differentiation alters stem cell nuclear architecture, mechanics, and mechano-sensitivity. *eLife* **5**, e18207 (2016). doi: 10.7554/eLife.18207; pmid: 27901466
22. M. M. Nava *et al.*, Heterochromatin-driven nuclear softening protects the genome against mechanical stress-induced damage. *Cell* **181**, 800–817.e22 (2020). doi: 10.1016/j.cell.2020.03.052; pmid: 32302590
23. A. Tajik *et al.*, Transcription upregulation via force-induced direct stretching of chromatin. *Nat. Mater.* **15**, 1287–1296 (2016). doi: 10.1038/nmat4729; pmid: 27548707
24. J. Sun, J. Chen, E. Mohagheghian, N. Wang, Force-induced gene up-regulation does not follow the weak power law but depends on H3K9 demethylation. *Sci. Adv.* **6**, eaay9095 (2020). doi: 10.1126/sciadv.aay9095; pmid: 32270037
25. ENCODE Project Consortium, An integrated encyclopedia of DNA elements in the human genome. *Nature* **489**, 57–74 (2012). doi: 10.1038/nature11247; pmid: 22955616
26. F. Zanconato *et al.*, Genome-wide association between YAP/TAZ/TEAD and AP-1 at enhancers drives oncogenic growth. *Nat. Cell Biol.* **17**, 1218–1227 (2015). doi: 10.1038/ncb3216; pmid: 26258633
27. G. G. Galli *et al.*, YAP drives growth by controlling transcriptional pause release from dynamic enhancers. *Mol. Cell* **60**, 328–337 (2015). doi: 10.1016/j.molcel.2015.09.001; pmid: 26439301
28. J. P. Noonan, A. S. McCallion, Genomics of long-range regulatory elements. *Annu. Rev. Genomics Hum. Genet.* **11**, 1–23 (2010). doi: 10.1146/annurev-genom-082509-141651; pmid: 20438361
29. M. Gasperini *et al.*, A genome-wide framework for mapping gene regulation via cellular genetic screens. *Cell* **176**, 377–390.e19 (2019). doi: 10.1016/j.cell.2018.11.029; pmid: 30612741

30. T. S. Klann *et al.*, CRISPR-Cas9 epigenome editing enables high-throughput screening for functional regulatory elements in the human genome. *Nat. Biotechnol.* **35**, 561–568 (2017). doi: 10.1038/nbt.3853; pmid: 28369033
31. M. V. Plikus *et al.*, Fibroblasts: Origins, definitions, and functions in health and disease. *Cell* **184**, 3852–3872 (2021). doi: 10.1016/j.cell.2021.06.024; pmid: 34297930
32. J. Swift *et al.*, Nuclear lamin-A scales with tissue stiffness and enhances matrix-directed differentiation. *Science* **341**, 1240104 (2013). doi: 10.1126/science.1240104; pmid: 23990565
33. P. Song *et al.*, β-catenin induces A549 alveolar epithelial cell mesenchymal transition during pulmonary fibrosis. *Mol. Med. Rep.* **11**, 2703–2710 (2015). doi: 10.3892/mmr.2014.3013; pmid: 25435076
34. D. Zhao *et al.*, Substrate stiffness regulated migration and angiogenesis potential of A549 cells and HUVECs. *J. Cell. Physiol.* **233**, 3407–3417 (2018). doi: 10.1002/jcp.26189; pmid: 28940499
35. I. C. McDowell *et al.*, Glucocorticoid receptor recruits to enhancers and drives activation by motif-directed binding. *Genome Res.* **28**, 1272–1284 (2018). doi: 10.1101/gr.233346.117; pmid: 30097539
36. V. F. Achterberg *et al.*, The nano-scale mechanical properties of the extracellular matrix regulate dermal fibroblast function. *J. Invest. Dermatol.* **134**, 1862–1872 (2014). doi: 10.1038/jid.2014.90; pmid: 24670384
37. K. Arda, N. Ciledag, E. Aktas, B. K. Aribas, K. Köse, Quantitative assessment of normal soft-tissue elasticity using shear-wave ultrasound elastography. *AJR Am. J. Roentgenol.* **197**, 532–536 (2011). doi: 10.2214/AJR.10.5449; pmid: 21862792
38. C. X. Li *et al.*, MicroRNA-21 preserves the fibrotic mechanical memory of mesenchymal stem cells. *Nat. Mater.* **16**, 379–389 (2017). doi: 10.1038/nmat4780; pmid: 27798620
39. M. Darnell, L. Gu, D. Mooney, RNA-seq reveals diverse effects of substrate stiffness on mesenchymal stem cells. *Biomaterials* **181**, 182–188 (2018). doi: 10.1016/j.biomaterials.2018.07.039; pmid: 30086447
40. D. L. Jones *et al.*, Mechanoepigenetic regulation of extracellular matrix homeostasis via Yap and Taz. *Proc. Natl. Acad. Sci. U.S.A.* **120**, e2211947120 (2023). doi: 10.1073/pnas.2211947120; pmid: 37216538
41. S. Heinz, C. E. Romanoski, C. Benner, C. K. Glass, The selection and function of cell type-specific enhancers. *Nat. Rev. Mol. Cell Biol.* **16**, 144–154 (2015). doi: 10.1038/nrm3949; pmid: 25650801
42. Y. Liu-Chittenden *et al.*, Genetic and pharmacological disruption of the TEAD-YAP complex suppresses the oncogenic activity of YAP. *Genes Dev.* **26**, 1300–1305 (2012). doi: 10.1101/gad.192856.112; pmid: 22677547
43. E. M. Lisabeth *et al.*, Identification of pirin as a molecular target of the CCG-1423/CCG-203971 series of antifibrotic and antimetastatic compounds. *ACS Pharmacol. Transl. Sci.* **2**, 92–100 (2019). doi: 10.1021/acsptsci.8b00048; pmid: 32039344
44. M. Bentsen *et al.*, ATAC-seq footprinting unravels kinetics of transcription factor binding during zygotic genome activation. *Nat. Commun.* **11**, 4267 (2020). doi: 10.1038/s41467-020-18035-1; pmid: 32848148
45. R. S. Stowers *et al.*, Matrix stiffness induces a tumorigenic phenotype in mammary epithelium through changes in chromatin accessibility. *Nat. Biomed. Eng.* **3**, 1009–1019 (2019). doi: 10.1038/s41551-019-0420-5; pmid: 31285581
46. J. M. Miano, Serum response factor: Toggling between disparate programs of gene expression. *J. Mol. Cell. Cardiol.* **35**, 577–593 (2003). doi: 10.1016/S0022-2828(03)00110-X; pmid: 12788374
47. D. L. Jones *et al.*, ZNF416 is a pivotal transcriptional regulator of fibroblast mechanoactivation. *J. Cell Biol.* **220**, e202007152 (2021). doi: 10.1083/jcb.202007152; pmid: 33625469
48. M. Vicente-Manzanares, X. Ma, R. S. Adelstein, A. R. Horwitz, Non-muscle myosin II takes centre stage in cell adhesion and migration. *Nat. Rev. Mol. Cell Biol.* **10**, 778–790 (2009). doi: 10.1038/nrm2786; pmid: 19851336
49. P. I. Thakore *et al.*, Highly specific epigenome editing by CRISPR-Cas9 repressors for silencing of distal regulatory elements. *Nat. Methods* **12**, 1143–1149 (2015). doi: 10.1038/nmeth.3630; pmid: 26501517
50. L. A. Gilbert *et al.*, CRISPR-mediated modular RNA-guided regulation of transcription in eukaryotes. *Cell* **154**, 442–451 (2013). doi: 10.1016/j.cell.2013.06.044; pmid: 23849981
51. B. D. Hoffman, C. Grashoff, M. A. Schwartz, Dynamic molecular processes mediate cellular mechanotransduction. *Nature* **475**, 316–323 (2011). doi: 10.1038/nature10316; pmid: 21776077
52. M. C. Canver *et al.*, *BCL11A* enhancer dissection by Cas9-mediated *in situ* saturating mutagenesis. *Nature* **527**, 192–197 (2015). doi: 10.1038/nature15521; pmid: 26375006
53. L. Chang *et al.*, The SWI/SNF complex is a mechanoregulated inhibitor of YAP and TAZ. *Nature* **563**, 265–269 (2018). doi: 10.1038/s41586-018-0658-1; pmid: 30401838
54. J. Oliver-De La Cruz *et al.*, Substrate mechanics controls adipogenesis through YAP phosphorylation by dictating cell spreading. *Biomaterials* **205**, 64–80 (2019). doi: 10.1016/j.biomaterials.2019.03.009; pmid: 30904599
55. J. L. Leight, M. A. Wozniak, S. Chen, M. L. Lynch, C. S. Chen, Matrix rigidity regulates a switch between TGF-β1–induced apoptosis and epithelial–mesenchymal transition. *Mol. Biol. Cell* **23**, 781–791 (2012). doi: 10.1091/mbc.e11-06-0537; pmid: 22238361
56. Z. Ma, Z. Liu, D. P. Myers, L. S. Terada, Mechanotransduction and anoikis: Death and the homeless cell. *Cell Cycle* **7**, 2462–2465 (2008). doi: 10.4161/cc.7.16.6463; pmid: 18719379
57. B. Zhao *et al.*, Cell detachment activates the Hippo pathway via cytoskeleton reorganization to induce anoikis. *Genes Dev.* **26**, 54–68 (2012). doi: 10.1101/gad.173435.111; pmid: 22215811
58. P. Paoli, E. Giannoni, P. Chiarugi, Anoikis molecular pathways and its role in cancer progression. *Biochim. Biophys. Acta* **1833**, 3481–3498 (2013). doi: 10.1016/j.bbamcr.2013.06.026; pmid: 23830918
59. T. Schmelzle *et al.*, Functional role and oncogene-regulated expression of the BH3-only factor Bmf in mammary epithelial anoikis and morphogenesis. *Proc. Natl. Acad. Sci. U.S.A.* **104**, 3787–3792 (2007). doi: 10.1073/pnas.0700115104; pmid: 17360431
60. M. Seo *et al.*, RNAi-based functional selection identifies novel cell migration determinants dependent on PI3K and AKT pathways. *Nat. Commun.* **5**, 5217 (2014). doi: 10.1038/ncomms6217; pmid: 25347953
61. R. M. Meyers *et al.*, Computational correction of copy number effect improves specificity of CRISPR-Cas9 essentiality screens in cancer cells. *Nat. Genet.* **49**, 1779–1784 (2017). doi: 10.1038/ng.3984; pmid: 29083409
62. F. M. Behan *et al.*, Prioritization of cancer therapeutic targets using CRISPR-Cas9 screens. *Nature* **568**, 511–516 (2019). doi: 10.1038/s41586-019-1103-9; pmid: 30971826
63. H. Zhang *et al.*, BAALC-AS1/G3BP2/c-Myc feedback loop promotes cell proliferation in esophageal squamous cell carcinoma. *Cancer Commun. (Lond.)* **41**, 240–257 (2021). doi: 10.1002/cac2.12127; pmid: 33476486
64. C. Paulmann *et al.*, The OTUD6B-LIN28B-MYC axis determines the proliferative state in multiple myeloma. *EMBO J.* **41**, e110871 (2022). doi: 10.15252/embj.2022110871; pmid: 36059274
65. M. Sun *et al.*, Effects of matrix stiffness on the morphology, adhesion, proliferation and osteogenic differentiation of mesenchymal stem cells. *Int. J. Med. Sci.* **15**, 257–268 (2018). doi: 10.7150/ijms.21620; pmid: 29483817
66. M. Ehrbar *et al.*, Elucidating the role of matrix stiffness in 3D cell migration and remodeling. *Biophys. J.* **100**, 284–293 (2011). doi: 10.1016/j.bpj.2010.11.082; pmid: 21244824
67. B. Mifsud *et al.*, Mapping long-range promoter contacts in human cells with high-resolution capture Hi-C. *Nat. Genet.* **47**, 598–606 (2015). doi: 10.1038/ng.3286; pmid: 25938943
68. A. Sanyal, B. R. Lajoie, G. Jain, J. Dekker, The long-range interaction landscape of gene promoters. *Nature* **489**, 109–113 (2012). doi: 10.1038/nature11279; pmid: 22955621
69. C. P. Fulco *et al.*, Activity-by-contact model of enhancer-promoter regulation from thousands of CRISPR perturbations. *Nat. Genet.* **51**, 1664–1669 (2019). doi: 10.1038/s41588-019-0538-0; pmid: 31784727
70. J. E. Moore *et al.*, Expanded encyclopaedias of DNA elements in the human and mouse genomes. *Nature* **583**, 699–710 (2020). doi: 10.1038/s41586-020-2493-4; pmid: 32728249
71. J. Ernst, M. Kellis, ChromHMM: Automating chromatin-state discovery and characterization. *Nat. Methods* **9**, 215–216 (2012). doi: 10.1038/nmeth.1906; pmid: 22373907
72. A. M. Babic, M. L. Kireeva, T. V. Kolesnikova, L. F. Lau, CYR61, a product of a growth factor-inducible immediate early gene, promotes angiogenesis and tumor growth. *Proc. Natl. Acad. Sci. U.S.A.* **95**, 6355–6360 (1998). doi: 10.1073/pnas.95.11.6355; pmid: 9600969
73. Z. Chen *et al.*, Connective Tissue growth factor: From molecular understandings to drug discovery. *Front. Cell Dev. Biol.* **8**, 593269 (2020). doi: 10.3389/fcell.2020.593269; pmid: 33195264
74. F. Zhang *et al.*, The matricellular protein Cyr61 is a key mediator of platelet-derived growth factor-induced cell migration. *J. Biol. Chem.* **290**, 8232–8242 (2015). doi: 10.1074/jbc.M114.623074; pmid: 25623072
75. W. I. Effendi, T. Nagano, Connective tissue growth factor in idiopathic pulmonary fibrosis: Breaking the bridge. *Int. J. Mol. Sci.* **23**, 6064 (2022). doi: 10.3390/ijms23116064; pmid: 35682743
76. M. Mikamo *et al.*, Inhibiting Skp2 E3 ligase suppresses bleomycin-induced pulmonary fibrosis. *Int. J. Mol. Sci.* **19**, 474 (2018). doi: 10.3390/ijms19020474; pmid: 29415439
77. X. Sun, M. Zhu, X. Chen, X. Jiang, MYH9 inhibition suppresses TGF-β1-stimulated lung fibroblast-to-myofibroblast differentiation. *Front. Pharmacol.* **11**, 573524 (2021). doi: 10.3389/fphar.2020.573524; pmid: 33519439
78. M. A. T. Freeberg *et al.*, Mechanical feed-forward loops contribute to idiopathic pulmonary fibrosis. *Am. J. Pathol.* **191**, 18–25 (2021). doi: 10.1016/j.ajpath.2020.09.008; pmid: 33031756
79. J. T. Allen, M. A. Spiteri, Growth factors in idiopathic pulmonary fibrosis: Relative roles. *Respir. Res.* **3**, 13 (2002). doi: 10.1186/rr162; pmid: 11806848
80. H. N. Antoniades *et al.*, Platelet-derived growth factor in idiopathic pulmonary fibrosis. *J. Clin. Invest.* **86**, 1055–1064 (1990). doi: 10.1172/JCI114808; pmid: 2170444
81. F. S. Younesi, A. E. Miller, T. H. Barker, F. M. V. Rossi, B. Hinz, Fibroblast and myofibroblast activation in normal tissue repair and fibrosis. *Nat. Rev. Mol. Cell Biol.* **25**, 617–638 (2024). doi: 10.1038/s41580-024-00716-0; pmid: 38589640
82. J. Sun *et al.*, Systematic analyses identify the anti-fibrotic role of lncRNA TP53TG1 in IPF. *Cell Death Dis.* **13**, 525 (2022). doi: 10.1038/s41419-022-04975-7; pmid: 35661695
83. K. J. Kurppa *et al.*, Treatment-induced tumor dormancy through YAP-mediated transcriptional reprogramming of the apoptotic pathway. *Cancer Cell* **37**, 104–122.e12 (2020). doi: 10.1016/j.ccell.2019.12.006; pmid: 31935369

84. V. F. Fiore *et al.*, Mechanics of a multilayer epithelium instruct tumour architecture and function. *Nature* **585**, 433–439 (2020). doi: 10.1038/s41586-020-2695-9; pmid: 32879493
85. M. J. Paszek *et al.*, Tensional homeostasis and the malignant phenotype. *Cancer Cell* **8**, 241–254 (2005). doi: 10.1016/j.ccr.2005.08.010; pmid: 16169468
86. J. Herrera, C. A. Henke, P. B. Bitterman, Extracellular matrix as a driver of progressive fibrosis. *J. Clin. Invest.* **128**, 45–53 (2018). doi: 10.1172/JCI93557; pmid: 29293088
87. J. D. Humphrey, E. R. Dufresne, M. A. Schwartz, Mechanotransduction and extracellular matrix homeostasis. *Nat. Rev. Mol. Cell Biol.* **15**, 802–812 (2014). doi: 10.1038/nrm3896; pmid: 25355505
88. T. Ritterhoff *et al.*, The RanBP2/RanGAP1*SUMO1/Ubc9 SUMO E3 ligase is a disassembly machine for Crm1-dependent nuclear export complexes. *Nat. Commun.* **7**, 11482 (2016). doi: 10.1038/ncomms11482; pmid: 27160050
89. I. Andreu *et al.*, Mechanical force application to the nucleus regulates nucleocytoplasmic transport. *Nat. Cell Biol.* **24**, 896–905 (2022). doi: 10.1038/s41556-022-00927-7; pmid: 35681009
90. A. M. Bolger, M. Lohse, B. Usadel, Trimmomatic: A flexible trimmer for Illumina sequence data. *Bioinformatics* **30**, 2114–2120 (2014). doi: 10.1093/bioinformatics/btu170; pmid: 24695404
91. A. Dobin *et al.*, STAR: Ultrafast universal RNA-seq aligner. *Bioinformatics* **29**, 15–21 (2013). doi: 10.1093/bioinformatics/bts635; pmid: 23104886
92. Y. Liao, G. K. Smyth, W. Shi, featureCounts: An efficient general purpose program for assigning sequence reads to genomic features. *Bioinformatics* **30**, 923–930 (2014). doi: 10.1093/bioinformatics/btt656; pmid: 24227677
93. M. D. Robinson, D. J. McCarthy, G. K. Smyth, edgeR: A Bioconductor package for differential expression analysis of digital gene expression data. *Bioinformatics* **26**, 139–140 (2010). doi: 10.1093/bioinformatics/btp616; pmid: 19910308
94. D. R. Powell, Degust: Interactive RNA-seq analysis, Zenodo (2019); https://doi.org/10.5281/zenodo.3258932.
95. M. R. Corces *et al.*, Omni-ATAC-seq: Improved ATAC-seq protocol, Protocol Exchange (2017); https://dx.doi.org/10.1038/protex.2017.096.
96. FastQC: A quality control tool for high throughput sequence data (Babraham Bioinformatics, Babraham Institute, 2010); https://www.bioinformatics.babraham.ac.uk/projects/fastqc/.
97. B. Langmead, Aligning short sequencing reads with Bowtie. *Curr. Protoc. Bioinformatics* **Chapter 11**, 7 (2010). doi: 10.1002/0471250953.bi1107s32; pmid: 21154709
98. A. R. Quinlan, BEDTools: The Swiss-army tool for genome feature analysis. *Curr. Protoc. Bioinformatics* **47**, 11.12.1–11.12.34 (2014). doi: 10.1002/0471250953.bi1112s47; pmid: 25199790
99. Y. Zhang *et al.*, Model-based analysis of ChIP-Seq (MACS). *Genome Biol.* **9**, R137 (2008). doi: 10.1186/gb-2008-9-9-r137; pmid: 18798982
100. M. I. Love, W. Huber, S. Anders, Moderated estimation of fold change and dispersion for RNA-seq data with DESeq2. *Genome Biol.* **15**, 550 (2014). doi: 10.1186/s13059-014-0550-8; pmid: 25516281
101. G. Yu, L.-G. Wang, Q.-Y. He, ChIPseeker: An R/Bioconductor package for ChIP peak annotation, comparison and visualization. *Bioinformatics* **31**, 2382–2383 (2015). doi: 10.1093/bioinformatics/btv145; pmid: 25765347
102. F. Ramírez, F. Dündar, S. Diehl, B. A. Grüning, T. Manke, deepTools: A flexible platform for exploring deep-sequencing data. *Nucleic Acids Res.* **42**, W187–W191 (2014). doi: 10.1093/nar/gku365; pmid: 24799436
103. S. Heinz *et al.*, Simple combinations of lineage-determining transcription factors prime cis-regulatory elements required for macrophage and B cell identities. *Mol. Cell* **38**, 576–589 (2010). doi: 10.1016/j.molcel.2010.05.004; pmid: 20513432
104. X. Wei *et al.*, HiCAR is a robust and sensitive method to analyze open-chromatin-associated genome organization. *Mol. Cell* **82**, 1225–1238.e6 (2022). doi: 10.1016/j.molcel.2022.01.023; pmid: 35196517
105. A. Kechin, U. Boyarskikh, A. Kel, M. Filipenko, cutPrimers: A new tool for accurate cutting of primers from reads of targeted next generation sequencing. *J. Comput. Biol.* **24**, 1138–1143 (2017). doi: 10.1089/cmb.2017.0096; pmid: 28715235
106. N. Abdennur *et al.*, Pairtools: From sequencing data to chromosome contacts. *PLOS Comput. Biol.* **20**, e1012164 (2024). doi: 10.1371/journal.pcbi.1012164; pmid: 38809952
107. I. Juric *et al.*, MAPS: Model-based analysis of long-range chromatin interactions from PLAC-seq and HiChIP experiments. *PLOS Comput. Biol.* **15**, e1006982 (2019). doi: 10.1371/journal.pcbi.1006982; pmid: 30986246
108. N. Abdennur, L. A. Mirny, Cooler: Scalable storage for Hi-C data and other genomically labeled arrays. *Bioinformatics* **36**, 311–316 (2020). doi: 10.1093/bioinformatics/btz540; pmid: 31290943
109. N. C. Durand *et al.*, Juicer provides a one-click system for analyzing loop-resolution Hi-C experiments. *Cell Syst.* **3**, 95–98 (2016). doi: 10.1016/j.cels.2016.07.002; pmid: 27467249
110. A. R. Quinlan, I. M. Hall, BEDTools: A flexible suite of utilities for comparing genomic features. *Bioinformatics* **26**, 841–842 (2010). doi: 10.1093/bioinformatics/btq033; pmid: 20110278
111. J. Tycko *et al.*, Mitigation of off-target toxicity in CRISPR-Cas9 screens for essential non-coding elements. *Nat. Commun.* **10**, 4063 (2019). doi: 10.1038/s41467-019-11955-7; pmid: 31492858
112. M. A. Horlbeck *et al.*, Compact and highly active next-generation libraries for CRISPR-mediated gene repression and activation. *eLife* **5**, e19760 (2016). doi: 10.7554/eLife.19760; pmid: 27661255
113. M. E. Berginski, S. M. Gomez, The Focal Adhesion Analysis Server: A web tool for analyzing focal adhesion dynamics. *F1000Res.* **2**, 68 (2013). doi: 10.12688/f1000research.2-68.v1; pmid: 24358855
114. D. Yao *et al.*, Multicenter integrated analysis of noncoding CRISPRi screens. *Nat. Methods* **21**, 723–734 (2024). doi: 10.1038/s41592-024-02216-7; pmid: 38504114
115. K. Clement *et al.*, CRISPResso2 provides accurate and rapid genome editing sequence analysis. *Nat. Biotechnol.* **37**, 224–226 (2019). doi: 10.1038/s41587-019-0032-3; pmid: 30809026
116. F. Muerdter *et al.*, Resolving systematic errors in widely used enhancer activity assays in human cells. *Nat. Methods* **15**, 141–149 (2018). doi: 10.1038/nmeth.4534; pmid: 29256496
117. K. R. Sanson *et al.*, Optimized libraries for CRISPR-Cas9 genetic screens with multiple modalities. *Nat. Commun.* **9**, 5416 (2018). doi: 10.1038/s41467-018-07901-8; pmid: 30575746
118. M. G. Gordon *et al.*, lentiMPRA and MPRAflow for high-throughput functional characterization of gene regulatory elements. *Nat. Protoc.* **15**, 2387–2412 (2020). doi: 10.1038/s41596-020-0333-5; pmid: 32641802
119. G. Finak *et al.*, MAST: A flexible statistical framework for assessing transcriptional changes and characterizing heterogeneity in single-cell RNA sequencing data. *Genome Biol.* **16**, 278 (2015). doi: 10.1186/s13059-015-0844-5; pmid: 26653891
120. T. Stuart *et al.*, Comprehensive integration of single-cell data. *Cell* **177**, 1888–1902.e21 (2019). doi: 10.1016/j.cell.2019.05.031; pmid: 31178118
121. H. Katsura *et al.*, Human lung stem cell-based alveolospheres provide insights into SARS-CoV-2-mediated interferon responses and pneumocyte dysfunction. *Cell Stem Cell* **27**, 890–904.e8 (2020). doi: 10.1016/j.stem.2020.10.005; pmid: 33128895
122. P. Kadur Lakshminarasimha Murthy *et al.*, Human distal lung maps and lineage hierarchies reveal a bipotent progenitor. *Nature* **604**, 111–119 (2022). doi: 10.1038/s41586-022-04541-3; pmid: 35355018
123. L. Bounds *et al.*, Mechanosensitive genomic enhancers potentiate the cellular response to matrix stiffness [software], version 1, Zenodo (2025); https://doi.org/10.5281/zenodo.17008807.doi: 10.5281/zenodo.17008807

ACKNOWLEDGMENTS

We thank the Duke Sequencing Core and the Duke Viral Vector Core for their help and guidance and members of the Gersbach and Crawford labs at Duke University who provided feedback throughout this project. We thank the BioRepository and Precision Pathology Center (BRPC), Research Support (SSCRS), and Duke Surgery for providing human tissues under Institutional Review Board oversight and Substrate Services Core. We also thank R. Rai for help with genomics data visualization and Z. Farino for suggestions. Figure panels containing images of sequencing machines were created with BioRender.com. **Funding:** National Institutes of Health grant UM1HG009428 (C.A.G., G.E.C.); National Institutes of Health grant UM1HG012053 (C.A.G., G.E.C.); National Institutes of Health grant U01AI146356 (C.A.G.); National Institutes of Health grant RM1HG011123 (C.A.G., G.E.C.); National Institutes of Health grant R01MH125236 (G.E.C., C.A.G.); National Institutes of Health grant R35GM156302 (B.D.H.); National Institutes of Health grant R01HL146557 (P.R.T.); National Institutes of Health grant R01HL160939 (P.R.T.); National Institutes of Health grant R01HL153375 (P.R.T.); National Institutes of Health PROSPER grant T32HL160494 (T.W.); National Science Foundation grant EFMA-1830957; Allen Distinguished Investigator Award from the Paul G. Allen Frontiers Group (C.A.G.); Open Philanthropy (C.A.G.); NSF-GRFP (NSF-GRFP DGE - 2139754) (L.R.B., C.K.T.); Regeneration Next Postdoctoral Fellowship (B.D.C.). **Author contributions:** Conceptualization: B.D.C., L.R.B., C.A.G., G.E.C., B.D.H.; Methodology: B.D.C., L.R.B., C.A.G., G.E.C., B.D.H., A.B.; Investigation: B.D.C., L.R.B., C.K.T., A.B., A.L.S., A.J.R., T.S., A.S., L.S., T.W., A.T.; Visualization: B.D.C., L.R.B., N.I.; Funding acquisition: C.A.G., G.E.C., B.D.H.; Project administration: B.D.C., L.R.B., C.A.G., G.E.C., B.D.H.; Supervision: C.A.G., G.E.C., B.D.H., Y.D., P.R.T.; Writing – original draft: B.D.C., L.R.B., N.I.; Writing – review & editing: B.D.C., L.R.B., C.K.T., C.A.G., G.E.C., B.D.H. **Competing interests:** C.A.G. is a cofounder of Tune Therapeutics and Locus Biosciences and an adviser to Tune Therapeutics and Sarepta Therapeutics. B.D.C., L.R.B., B.D.H., G.E.C., and C.A.G. are inventors on patent application PCT/US2024/057925 held and submitted by Duke University and related to this work. B.D.C. is an employee of Tune Therapeutics. L.R.B. is an employee of Xaira Therapeutics. The remaining authors have no conflicts of interest to declare. **Data and materials availability:** Public datasets used in this study are provided in table S23. All datasets generated in this study are available through the NCBI Gene Expression Omnibus (GEO) under accession number GSE243765 and the NIH IGVF Data Portal (https://data.igvf.org/) under reference file IGVFFI8553BTYV. All code used in this manuscript is available in the Zenodo online repository (*123*). Addgene catalog numbers for plasmids used in this study are noted in the methods. All materials used in this study will be made available upon request. Detailed protocols are available at https://www.protocols.io/workspaces/gersbach-lab. **License information:** Copyright © 2025 the authors, some rights reserved; exclusive licensee American Association for the Advancement of Science. No claim to original US government works. https://www.science.org/about/science-licenses-journal-article-reuse

SUPPLEMENTARY MATERIALS

science.org/doi/10.1126/science.adl1988
Supplementary Text; Figs. S1 to S29; Tables S1 to S32; References (*124*–*144*);
MDAR Reproducibility Checklist

Submitted 4 October 2023; resubmitted 6 December 2024; accepted 1 September 2025; published online 25 September 2025

10.1126/science.adl1988

RESEARCH ARTICLE SUMMARY

GENOMICS

Multispecies pangenomes reveal a pervasive influence of population size on structural variation

Scott V. Edwards*, Bohao Fang, Danielle Khost, George E. Kolyfetis, Rebecca G. Cheek, Devon A. DeRaad, Nancy Chen, John W. Fitzpatrick, John E. McCormack, W. Chris Funk, Cameron K. Ghalambor, Erik Garrison, Andrea Guarracino, Heng Li, Timothy B. Sackton

Full article and list of author affiliations: https://doi.org/10.1126/science.adw1931

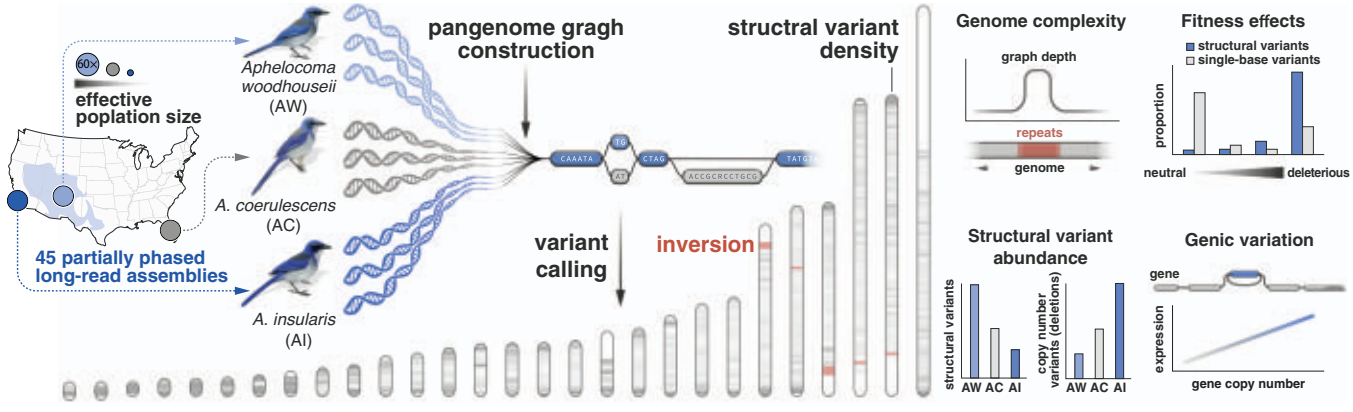
INTRODUCTION: Structural variants are a diverse class of mutations, including insertions, deletions, translocations, inversions, and other multinucleotide mutations. The number, chromosomal distribution, and fitness effects of structural variants as well as the effect of demographic events on their diversity and evolution make up a major frontier in evolutionary genomics. Yet what little we know about these issues is based on DNA sequencing and computational methods that cannot capture the full diversity of structural variants. Several recent studies have demonstrated that structural variants are often deleterious, but most of these studies have used DNA sequencing methods involving short reads and bioinformatics pipelines involving mapping variants to a single reference genome. Population-scale long-read datasets, involving sequencing and de novo assembly of multiple individuals within a species, are better at capturing the full spectrum of structural variants, but such datasets are rare outside of humans. Pangenome methods using all-versus-all approaches to genome alignment without designating a reference genome are also rarely applied in nonmodel species, but they allow better characterization of the full landscape of structural variants. Together, pangenomes based on population-scale long-read datasets provide opportunities for understanding the full diversity of structural variants and their evolutionary properties.

RATIONALE: We used population-scale long-read sequencing and pangenome methods to characterize diversity and evolution of structural variants in three species of North American scrub-jays (*Aphelocoma*) that exhibit a strong gradient in effective population sizes. Whereas the widespread Woodhouse's scrub-jay (*Aphelocoma woodhouseii*) has six times the variation found in humans, the island scrub-jay (*Aphelocoma insularis*) underwent a strong bottleneck and has one-tenth the variation of humans, resulting in an ~55-fold range in effective population size among the species. We sequenced 45 long-read genomes across three scrub-jay species, reasoning that these birds would provide a powerful setting for applying comparative population genomics to understand the evolutionary forces acting on structural variants in natural populations.

RESULTS: Our pangenome survey revealed unexpected differences in genome size between these closely related species; identified more than 3 million insertion-deletion polymorphisms and nearly 450,000 structural variants; facilitated visualizing the pangenomic signatures of these variants; and helped quantify their interaction with prominent repetitive features of avian genomes, such as the highly dynamic satellite landscape. Structural variants, including more than 300 inversions ranging in length up to ~3 megabases, were most abundant in *A. woodhouseii*, followed by *Aphelocoma coerulescens* and *A. insularis*. These variants were estimated to be, on average, more deleterious than single-nucleotide variants and potentially adaptive only in the species with large population size. Gene copy number variants, such as gene deletions, were widespread, yet occurred most frequently in *A. insularis*—the species with the smallest population size—suggesting even greater deleteriousness. Through transcriptomes, we show that gene copy number variation influences gene expression and therefore likely has detectable effects on organismal function.

CONCLUSION: Population-scale long-read sequencing and pangenome tools provided a high-resolution lens on the rapid evolution of genome architecture, repeat landscapes, and structural variant and gene copy number diversity in this trio of closely related species. The use of pangenome tools in natural populations will facilitate our understanding of the evolutionary drivers of structural variation. □

*Corresponding author. Email: sedwards@fas.harvard.edu Cite this article as S. V. Edwards *et al.*, *Science* **390**, eadw1931 (2025). DOI: 10.1126/science.adw1931



Pangenomes across a gradient of effective population sizes. Long-read sequencing and pangenome analysis of 45 scrub-jays (*Aphelocoma*) and outgroups reveal a dynamic repeat landscape. The abundance of most structural variants scales with effective population size. Gene copy number deletions show an inverse relationship with population size and drive variation in gene expression. Statistical analysis reveals that structural variants are, on average, more deleterious than single-nucleotide polymorphisms and only rarely are adaptive.

GENOMICS

Multispecies pangenomes reveal a pervasive influence of population size on structural variation

Scott V. Edwards[1,2]*, Bohao Fang[1,2], Danielle Khost[3], George E. Kolyfetis[1], Rebecca G. Cheek[4], Devon A. DeRaad[5], Nancy Chen[6], John W. Fitzpatrick[7], John E. McCormack[8], W. Chris Funk[4], Cameron K. Ghalambor[9], Erik Garrison[10], Andrea Guarracino[10], Heng Li[11], Timothy B. Sackton[3]

Structural variants (SVs) are widespread in vertebrate genomes, yet their evolutionary dynamics remain poorly understood. Using 45 long-read de novo genome assemblies and pangenome tools, we analyze SVs among three closely related species of North American jays (*Aphelocoma*, scrub-jays) displaying a 55-fold range in effective population size. We find rapid evolution of genome architecture, including ~100-megabase decreases in genome size driven by shifts in complex satellite landscapes. SVs exhibit slightly deleterious dynamics modulated by variant length and population size, with consistent evidence of adaptive fixation only in the largest population. Gene copy number variants exhibit an inverse relationship with population size, indicating strongly deleterious dynamics, with consequences for gene expression. Our long-read dataset and pangenome analysis demonstrate how population size shapes genome complexity.

A fundamental challenge of genome evolution is to understand how diverse demographic mechanisms affect genome architecture and the degree to which the observed variation is adaptive, neutral, or deleterious (*1*, *2*). Empirical studies using single-nucleotide polymorphisms (SNPs) have shown that smaller populations harbor more weakly deleterious segregating variation compared with large populations (*3*–*7*). Fewer studies have demonstrated these patterns for structural variants (SVs) (insertions, deletions, inversions, and other complex multinucleotide variants) and have mostly done so with short-read, reference-based methods, especially in nonhuman populations (*8*–*11*). Comparisons of SV abundance and dynamics among species are difficult given the biases induced by reference-based analyses with short-read sequencing data (*12*–*14*) and the heterogeneity of laboratory and bioinformatic pipelines between studies. These shortcomings have limited our understanding of the fitness consequences of these important classes of mutations, which often affect many more genomic bases than SNPs (*8*–*10*, *15*). Moreover, many studies of SV dynamics in natural populations, with a few exceptions (*8*, *11*, *16*, *17*), have focused primarily on the adaptive potential of selected SVs, such as inversions (*18*–*20*). Thus, unbiased and comprehensive genome-wide surveys of the number and distribution of SVs in natural populations are still rare outside of primates (*21*, *22*).

Pangenomes can capture the full spectrum of genetic variation, including SVs, among individuals of a species or among species (*23*–*25*). By comparing all de novo assemblies with one another in an unbiased, reference-free manner, pangenome approaches avoid many of the problems associated with reference-based variant calling methods. For example, SVs can be overlooked if query sequences contain genomic regions not found in the reference. Pangenomes have been a useful framework for understanding variation in gene, SV, and repeat content among individuals, species, and strains, particularly among bacteria and domesticated animals and plants (*26*–*31*). The Human Pangenome Consortium has shown how a draft pangenome, consisting of 47 long-read phased diploid assemblies, captures more SVs and provides better mapping rates and accuracies compared with protocols involving a single reference assembly (*32*). Pangenomes are more effective at capturing SVs when built with long-read genomes assembled de novo, yet we have few examples of datasets of the size and quality of the human draft pangenome. We also know little about the effectiveness of many pangenome tools among closely related vertebrate species (*33*).

Avian genomes are a good test case for the higher-resolution approaches afforded by population-scale long-read sequencing (*34*) and pangenome tools because they are thought to exhibit broad interchromosomal collinearity and a conservative mode of structural evolution compared with mammals and nonavian reptiles (*35*–*39*). Previous comparative genomic surveys have revealed that avian genomes exhibit a depauperate repeat landscape, with a few notable examples of expansions of transposable elements and long arrays of noncoding repeated sequences (satellites) emerging in specific lineages (*40*, *41*). Additionally, avian genomes are thought to harbor largely congruent gene content, with a few noteworthy examples of gene duplication and loss providing substrates for adaptive evolution (*42*, *43*).

In this work, we present a pangenome analysis of genomic variation among 45 long-read, partially phased diploid assemblies of North American scrub-jays in the genus *Aphelocoma* as well as additional related species. Scrub-jays are a model system for studies in biogeography, speciation, life history, ecology, and local adaptation and have been the subject of decades-long studies of social behavior (*44*–*49*). We chose these birds because their phylogeny, phylogeography, and levels of SNP diversity are well understood and provide a clear context for interpreting the evolution of SVs (*44*, *50*, *51*). We focus on the Florida [*Aphelocoma coerulescens* (AC)], island [*Aphelocoma insularis* (AI)], and Woodhouse's [*Aphelocoma woodhouseii* (AW)] scrub-jays, which together provide a comparative framework for understanding the effects of historical demography on patterns of structural variation (Fig. 1A). The AI birds on Santa Cruz Island are of particular interest, given the extreme and sustained bottleneck that has resulted in a very low number of genome-wide SNPs (*44*).

Study design and demographic background

Our study is based on multiple blood and tissue samples rapidly cryopreserved from AW in New Mexico ($n = 15$ individuals), AI from Santa Cruz Island ($n = 15$), and AC from Florida ($n = 14$) (Fig. 1A and table S1). An individual from another genus of New World jay, the Yucatán jay [*Cyanocorax yucatanicus* (CY), $n = 1$] served as an outgroup for polarizing variants. To better capture interspecific genomic patterns across New World jays generally, we added one California scrub-jay [*Aphelocoma californica* (AA) (*52*)] and one Steller's jay [*Cyanocitta cristata* (CS) (*53*)], all with a well-known phylogeny (*54*) (Fig. 1B). We sequenced each sample with PacBio-HiFi to 29.6X to 61.4X coverage (average 43.7X; table S2) and used hifiasm to generate 90 partially phased diploid assemblies (*55*), whose contig N50 ranged from 5.1 to 19 Mb (fig. S1 and table S2). We improved the assembly of an AW male and female with HiC (fig. S2), followed by chromosomal scaffolding into 29 autosomes, the Z, and the W, against the assemblies for AC (*56*) and the Hawaiian crow (*Corvus hawaiiensis*) (*57*). The AW female reference was annotated using TOGA

[1]Department of Organismic and Evolutionary Biology, Harvard University, Cambridge, MA, USA. [2]Museum of Comparative Zoology, Harvard University, Cambridge, MA, USA. [3]Informatics Group, Harvard University, Cambridge, MA, USA. [4]Department of Biology, Graduate Degree Program in Ecology, Colorado State University, Fort Collins, CO, USA. [5]Department of Ecology and Evolutionary Biology, University of California, Los Angeles, Los Angeles, CA, USA. [6]Department of Biology, University of Rochester, Rochester, NY, USA. [7]Cornell Lab of Ornithology, Cornell University, Ithaca, NY, USA. [8]Moore Laboratory of Zoology, Occidental College, Los Angeles, CA, USA. [9]Department of Biology, Norwegian University of Science and Technology, Trondheim, Norway. [10]Department of Genetics, Genomics and Informatics, University of Tennessee Health Science Center, Memphis, TN, USA. [11]Department of Data Science, Dana-Farber Cancer Institute, Boston, MA, USA. ***Corresponding author. Email: sedwards@fas.harvard.edu**

(*58*) projections from the chicken and zebra finch, which were collapsed into a single nonredundant annotation of high BUSCO completeness (97.2% overall). Karyotypes can help guide genome scaffolding, yet the karyotypes of most North American birds remain unknown (*59*). Karyotypes for multiple male and female AW birds were prepared at the San Diego Zoo Wildlife Alliance, revealing a diploid number of 80, with nine macrochromosomes and ~31 microchromosomes (fig. S2), which suggests that up to 10 microchromosomes remain as unplaced scaffolds in our assembly.

To confirm and refine the demographic history of this species complex (*44*), we focused on regions of high mapping quality (*60*), making up ~85% of the AW reference genome (fig. S3). Individuals of each species were confirmed to be mostly unrelated (fig. S4). Pairwise sequentially Markovian coalescent (PSMC) (*61*) and Bayesian phylogeography and phylogenetics (bpp) (*62*) confirmed the rank order of nucleotide diversity among *Aphelocoma* species as AW > AC > AI (Fig. 1, C and D, and fig. S5); AW birds have an effective population size ~55 times that of AI birds, assuming similar mutation rates ($N_{eAW}/N_{eAI} = \theta_{AW}/\theta_{AI} = 52.9$ to 56.8, estimated from the bpp results). AI birds exhibit longer runs of homozygosity (fig. S6), and nearly 70% of AI haplotype trees are monophyletic, as expected for a species that experienced a strong bottleneck (fig. S7 and table S3). We found no evidence for gene flow between AW and AC birds (*44*, *48*, *63*) (fig. S8), as expected given their wholly allopatric distributions today.

Rapid evolution of genome size and satellite landscapes

We were surprised to find significant differences in assembly sizes among species: The average haplotype assembly sizes of AI birds (1.20 Gb, SD = 0.02 Gb) and the CY outgroup (1.17, SD = 0.02) were ~88.9 Mb and ~112.8 Mb shorter, respectively, than that for AW (1.28 Gb, 0.032); AC assemblies (1.26, SD = 0.017) were also significantly shorter than AW assemblies (Fig. 2A and fig. S9). Theoretical predictions suggest that genome size should increase in small populations, driven by fixations of weakly deleterious transposable element insertions, yet our assemblies show the opposite trend, with the largest assembly sizes in the largest population (AW). Multiple lines of evidence suggest that variation in heterozygosity between the species is not the primary driver of assembly size differences in our data, as previously suggested (*64*, *65*). For instance, the assemblies show no significant differences in the size of the single copy fraction of the genome, which all fall between 955 Mb (AI) and 974 Mb (CY) (fig. S10). We therefore conducted a detailed investigation of the repeat landscape, annotating repeats using RepeatModeler2, RepeatMasker (*66*, *67*), and Satellite Repeat Finder (*68*) (fig. S11).

Repetitive DNA constituted up to 26% of the haplotype assemblies (28.9% of the primary assemblies), a high value for repeat abundances for birds (*69*, *70*). We found substantial variation in the abundance of long terminal repeats (LTRs), long interspersed nuclear elements

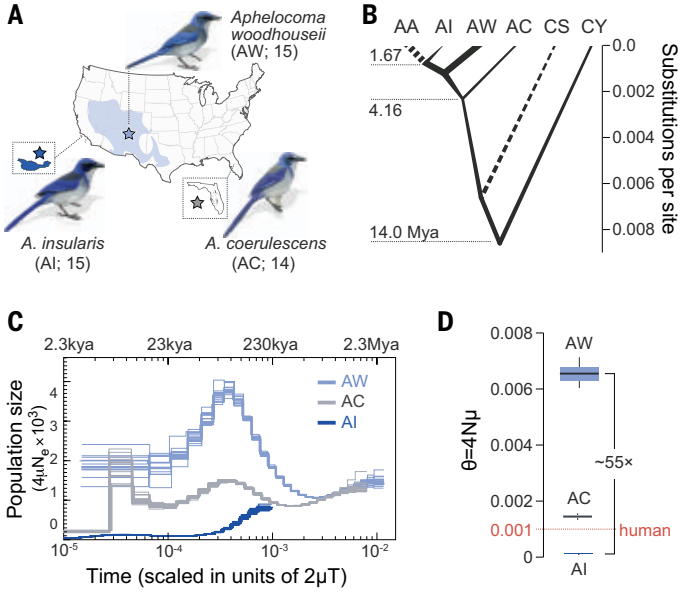


Fig. 1. Scrub-jays include a gradient of population sizes. (**A**) Distributions of Florida (*A. coerulescens*; AC), island (*A. insularis*; AI), and Woodhouse's (*A. woodhouseii*; AW) scrub-jays within the United States. Bird illustrations used with permission from Lynx Edicions. (**B**) Species tree with branch lengths and widths estimated with bpp, with approximate divergence times [in million years (Mya)]. (**C**) PSMC-inferred demographic histories for AI, AC, and AW individuals. kya, thousand years. (**D**) Genome-wide heterozygosity from bpp, with human shown in red as reference.

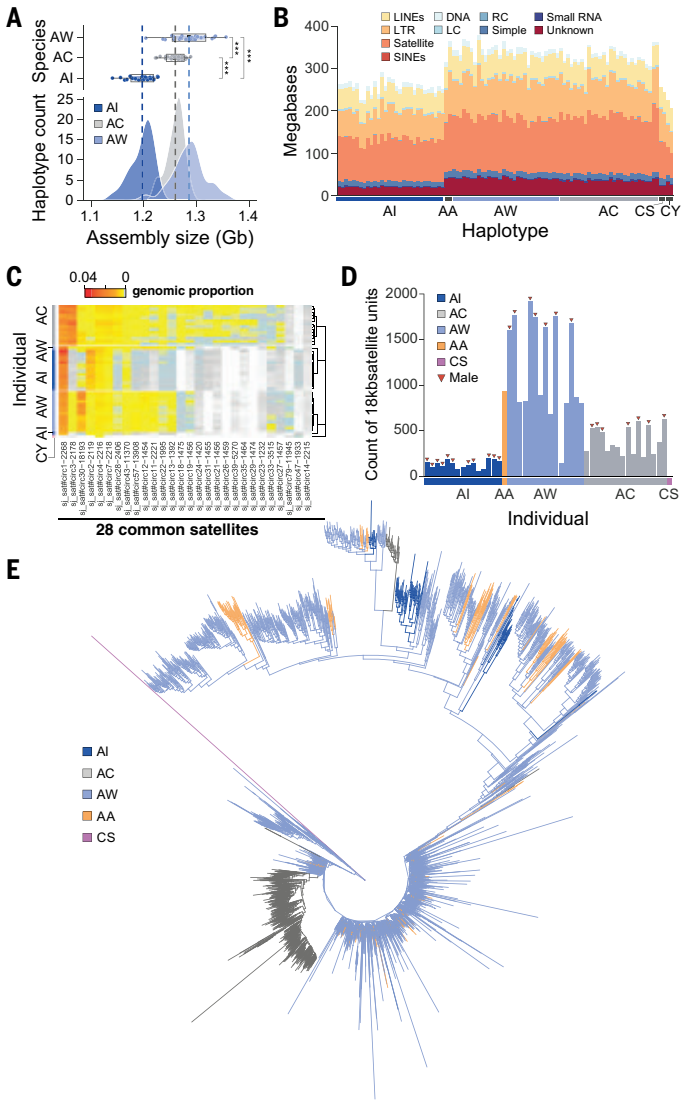


Fig. 2. Dynamic shifts in genome size and satellite landscapes. (**A**) Distribution of assembly sizes (gigabases) for the 90 haplotypes (45 diploid individuals). (**B**) Repeat content for the three species and two outgroups. CS, Steller's jay; CY, Yucatán jay. (**C**) Heatmap of the genomic proportions of 28 of the most abundant satellites across all haplotypes. Each satellite on the *x* axis has a distinct name; the circ(n) indicates a circular bubble in the srf-associated de Bruijn graph followed by an index number (n). The final number indicates the unit repeat length in base pairs. (**D**) Expansion of satellite sj_sat#circ30_18193 (18.2 kb unit repeats) on the Z chromosome of AW. (**E**) Neighbor-joining (*177*) tree of ~3500 proxies for ~27,000 18-kb satellite monomers showing partial homogenization.

(LINEs), and total satellites in AW and AC assemblies compared with AI, CY, and CS, consistent with differences in assembly size (Fig. 2B). Satellite DNA is the most common repeat type in these assemblies, making up between 37.1% (AW) and 41.5% (AC) of the total repeat landscape (Fig. 2, B and C, and table S4). Satellite DNA is difficult to assemble faithfully even when using HiFi reads (*71*, *72*), but we found a strong correlation between the abundance of individual satellites per bird in reads and assemblies (figs. S12 and S13). Satellite Repeat Finder (*68*) detected 28 core satellites with a per–base pair abundance of >0.001, with unit lengths ranging from 1232 base pairs (bp) to 18193 bp (four with units >10 kb; Fig. 2C and fig. S13). Scrub-jay satellites generally lacked higher-order internal structure like some human satellites (figs. S14 and S15) and exhibited rapid shifts in abundance between species (*72*). Fourteen of the 28 core satellites had >80% similarity to more-fragmented satellites found in other corvids, suggesting long-term persistence across at least 20 million years (table S5) (*73*).

The satellite sj_sat#circ30-18193 exhibited an unusual evolutionary history. sj_sat#circ30-18193 had a unit repeat length (>18 kb) that, to our knowledge, exceeded the lengths of other avian satellites studied thus far; we identified 27,083 full-length copies of this satellite across the 94 haplotypes of *Aphelocoma* and outgroups. Although there were no full-length copies of satellite sj_sat#circ30-18193 in CY and only a single full-length copy in CS, this satellite underwent a marked expansion in *Aphelocoma*, most pronounced on the Z chromosome of AW birds (Fig. 2D): Male AW birds harbor an average of 500 more copies compared with AW females. The phylogenetic relationships of the ~27,000 full-length 18-kb unit repeats (Fig. 2E and fig. S16) suggest that gene conversion among satellite unit repeats has not yet fully homogenized unit-repeat clades within species, as seen in some mammals (*74*–*76*). We also found subtle differences in GC content among species, attributable largely to differences in the abundance of specific satellite repeats (fig. S17).

Telomeres are a type of tandemly repeated DNA whose length shortens with increased stress and aging (*77*). Population genetics predicts shorter telomeres in species with smaller effective population sizes as a consequence of fixation of shorter, more deleterious telomere alleles (*78*). Consistent with this prediction, we found that AI birds have, on average, marginally lower telomere abundance than the other two species for both raw reads and haplotype assemblies and that the branch leading to AI is reconstructed to have experienced a sharp drop in telomere abundance (table S6 and fig. S18). However, we cannot entirely rule out that these patterns are driven by differences in average individual ages sampled across species.

Overall, the data suggest a scenario in which the abundances of multiple satellites and transposable elements exploded in the ancestor of *Aphelocoma* and then were differentially reduced by founder effects and drift in AI, shifting its genome-wide GC content and repeat composition. At least part of the wide variation in assembly size among AW birds (Fig. 2A) is likely real (*79*–*81*); some AW haplotypes are reconstructed as smaller than the largest AI haplotypes. Similarly large variation in AA birds, which exchange genes with AW (*44*), could provide a plausible scenario for the origin of small genome size in AI via founding of Santa Cruz Island by a small-genome AA lineage.

Pangenome graph construction and composition

To comprehensively survey SVs, we used the Pangenome Graph Builder (PGGB) (*82*) and minigraph (*33*) to build pangenome graphs (*63*) (fig. S19). PGGB first builds all-versus-all communities of related sequences, each typically representing a chromosome. By contrast, minigraph builds a pangenome graph sequentially, adding sequences from each haplotype in succession. The two methods have known differences in scalability, sensitivity, and ease of use by downstream applications (*83*): Whereas PGGB can align genomes and, with sufficient assembly contiguity, map SVs of any size with base pair resolution, minigraph's approximate mapping identifies SVs >50 bp. CY and CS were included as the outgroups in the PGGB graph and minigraph, respectively, owing to assembly availability at the time of graph construction. The sequence divergence between AW and AC, and that between AW and CY, is approximately half that between human and chimp and human and orangutan, respectively (figs. S20 and S21 and table S7), for which there is a recent multispecies pangenome (*84*). The lower sequence divergence, despite similar divergence times among these species pairs (*85*), reflects the expected slower substitution rate of birds compared with primates and other mammals (*39*, *86*).

Across all 90 haplotypes (including the CY outgroup) and the reference AW assembly, we input a total of 113,401,058,458 bp in 113,148 contigs into the PGGB pipeline (Fig. 3A). The main PGGB pangenome graph (Fig. 3A) incorporated 92,619,931,975 bp (81.7% of input) in 45,190 contigs across 30 communities, each corresponding to an AC chromosome (*56*). Another 13,238,463,357 bp (11.7%) in 56,813 contigs were incorporated into 18 additional communities with AW reference sequences but without chromosomal assignment. An additional 7,319,110,588 bp (6.5%) in 6856 contigs were incorporated into 946 additional communities without any reference assembly sequence. Graph compaction—the ratio of the length of the input sequences to the length of the graph (calculated as the sum of the lengths of all graph nodes)—was lowest for the highly repetitive W chromosome, whereas greater compaction was observed for chromosomes with less repetitive DNA (Fig. 3B).

The node depth in a pangenome graph records the number of times that a node is traversed by haplotypes in the graph (*87*). High-depth nodes (in our case depth > 90 haplotypes) indicate repetitive regions that are succinctly described by haplotypes traversing a node repeatedly, whereas nodes close to depth 90 (or 45 in the case of sex chromosomes in females) indicate single- or low-copy regions. All 90 haplotypes populated most (84.2%) regions in the 30 chromosome-level communities in the PGGB pangenome graph, whereas ~43% of chromosome 15; ~37% of chromosome 2; and 11 to 14% of chromosomes 1, 1A, and 5 had regions of depth less than 10, which suggests inadvertent loss of these regions during graph construction (Fig. 3A). We note that several of these missing regions are flanked on one side by large inversions, which may have challenged the PGGB pipeline (Fig. 3A).

We found that PGGB graphs of whole chromosomes exhibited a wide range of node depths that faithfully recorded major repetitive regions, telomeres, and putative centromeres within chromosomes (Fig. 3C). Ultrahigh-depth regions (generally >10,000 to >100,000) tended to begin and end abruptly, producing blocklike patterns sometimes exceeding 900 kb in length (fig. S22). High-depth regions (>1000), such as those tentatively assigned to centromeres, were generally dominated by single satellites or LTRs (fig. S23). The highest-depth regions of chromosomes 1, 1A, and 3 were all dominated by sj_sat_circ146–2809, whereas such regions on other chromosomes tended to be dominated by chromosome-specific satellites. Two-dimensional (2D) graph visualizations of many of the main communities revealed putative centromeres and telomeric sequences (Fig. 3C).

To understand how pangenome PGGB graph structure is influenced by effective population size, we quantified "core" sequence (present in >90% of haplotypes) versus "accessory" sequence (either haplotype specific or found in <10% of haplotypes) using the Panacus pipeline (*88*) (Fig. 3, D to F). The pangenome graphs of all three species implied a high percentage of the assemblies, including both coding and noncoding DNA, as being core (AW, 79.4%; AC, 84.7%; AI, 89.3%), whereas the accessory sequence was more variable among species—13.3 and 4.6% of the AW and AI graphs, respectively, was deemed accessory. Although some of this variation could result from variation in assembly length and quality between species, variation in the percent of accessory sequence between species is consistent with predictions from the relative amounts of diversity within them: AI birds on average share more sequence within species than AW and AC birds.

The scrub-jay pangenomes show notable similarities as well as differences from the few pangenome graphs available for other vertebrates. At similar sampling intensities, the human pangenome exhibits

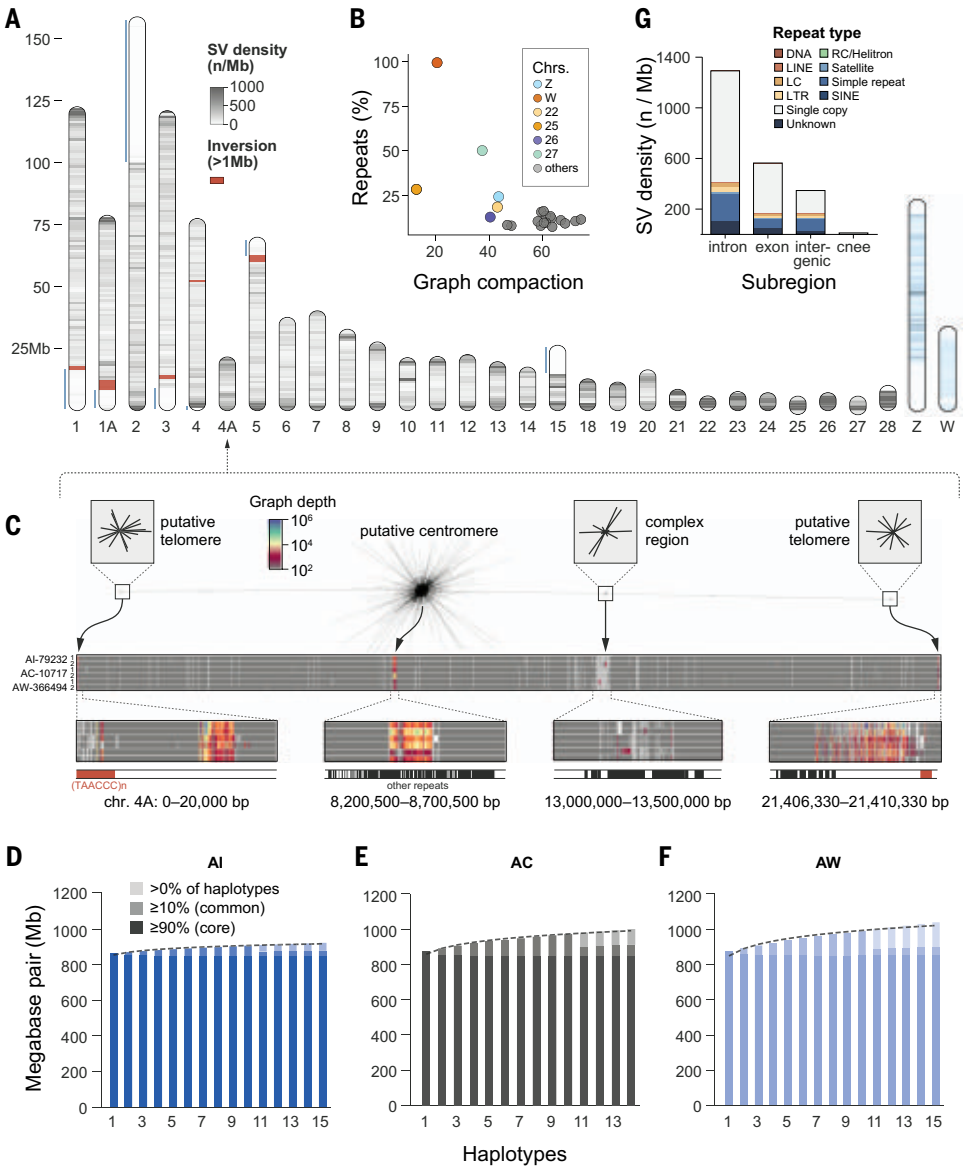


Fig. 3. Pangenome graph captures genome-wide SVs. (**A**) Chromosome-level schematic indicating overall SV density (n per megabase) and large inversions (>1 Mb). Light blue vertical lines indicate regions that failed PGGB graph construction. (**B**) Graph compaction (*x* axis) versus percent repeats (*y* axis) by chromosome, showing the highest compaction for chromosomes with lower repeat content. (**C**) Pangenome graph depth on chromosome 4A, revealing high-depth blocks in putative telomeric regions, centromeric regions, and other complex regions. (**D** to **F**) PGGB pangenome growth curves (*88*) show pangenome size (in megabases; *y* axis) added by each sample (*x* axis) to the graph for AI, AC, and AW, respectively. (**G**) SV density in different genomic compartments (*x* axis) and overlap with major repeat categories (stacked bars).

proportionally much less core sequence (56.2%) compared with our *Aphelocoma* pangenome, whereas a pangenome of inbred strains of chicken (*89*), constructed with methods broadly similar to those used in this work, exhibited a percent accessory sequence (5.0%) similar to that of the AI pangenome (fig. S24), suggesting a common effect of low genetic diversity. The lower core sequence in birds versus in humans could be driven in part by technical differences because each of the haplotypes in the human pangenome was more accurate and highly resolved compared with the haplotypes we studied (*32*).

SV diversity within and between species

We quantified the number and genomic distribution of SVs to ask how they are influenced by effective population size. To call SVs, we projected the PGGB pangenome graph to VCF (variant call format) format using vg deconstruct v1.40.0. The AW female reference assembly provided standardized coordinates for all haplotypes, the CY outgroup provided ancestral states, and we used a reproducible protocol for classifying multiallelic and complex SVs (*63*). Throughout, we refer to insertions and deletions <50 bp in length as insertion-deletion polymorphisms (indels) (INS and DEL) and those ≥50 bp as SVs (SVINS and SVDEL).

We found a total of 3,140,747 indels and 448,012 SVs in the 84% of the assembly lengths captured in the PGGB graph (fig. S25 and table S8). Whereas the modest indel bias (~1.29 to 1.50), also seen in genome-wide studies of other organisms (*17*, *90*), appears resistant to the reference genome used when projecting to the PGGB pangenome graph to the VCF, the SVDEL and SVINS bias is not only less pronounced when using the AW reference or across SV-detection methods (*33*, *91*) but also reduces to ~1 or <1 when using the smaller genomed CY or CS outgroups as references (table S9). This sensitivity likely points to the increased challenges of calling and polarizing SVs compared with indels, particularly complex SVs that may be driven by mutational dynamics challenging to capture by simple outgroup polarization (supplementary text).

The number of SVs identified by minigraph (*33*) and a reference-based method (*91*) are generally fewer than those identified with PGGB, but they exhibit similar trends within and across species (table S9). SVs were enriched toward chromosome ends (fig. S26) and positively associated with recombination rates across both macro- and microchromosomes (fig. S27) (*63*), resulting in higher densities on microchromosomes than on macrochromosomes (fig. S28). SVs were rarest in highly conserved nonexonic regions (CNEEs), which are known to influence gene regulation and to act as enhancers in birds (*92*) (Fig. 3G and fig. S25). We found that the density of SVs (SVs per megabase) was highest not in intergenic regions, which make up 59% of the reference genome, but in introns, which make up only 12.7% (Fig. 3G). Although the number of SVs in exons is much lower than in noncoding regions, the density per megabase is higher than even intergenic regions (521 per megabase in exons versus 328 per megabase in intergenic regions; Fig. 3G, fig. S25, and table S8). The high proportion of SVs in exons and introns may signal a relationship between SV formation and germline transcription, which would disproportionately affect exons and introns.

The rank order of the number of variants for SNPs, indels, and SVs in the PGGB graph was AW > AC > AI (Fig. 4, A and B). Biallelic SNPs were ~8.5 times as common as biallelic indels, which in turn were about 20 times as common as biallelic SVs (Fig. 4C). By contrast, multiallelic SVs were ~1.6 times as common as multiallelic SNPs, even

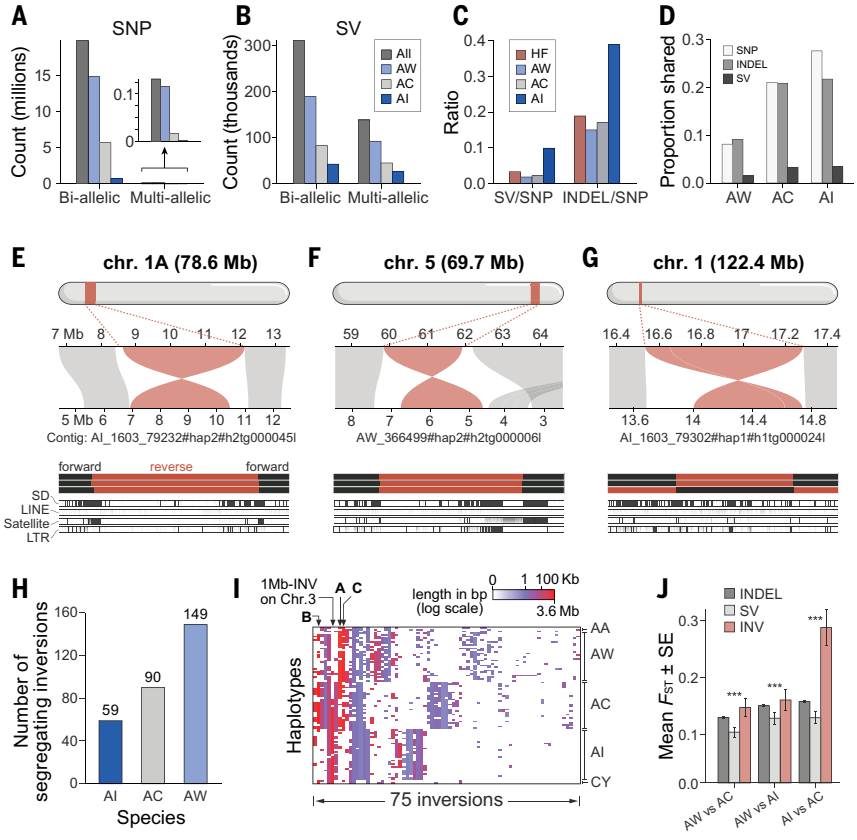


Fig. 4. Comparative analysis of SNPs, indels, and SVs. (**A** and **B**) Counts of biallelic and multiallelic SNPs (A) and SVs (B) across species. Inset in (A) shows expanded scale for multiallelic SNPs. (**C**) Ratios of indels/SNPs and SVs/SNPs for the three scrub-jays and house finch (HF) (*16*). (**D**) Proportion of variants shared among species. (**E** to **G**) The largest three large inversions detected by Syri (*93*) on chromosomes 1A, 5, and 1, respectively, with their approximate positions (in megabases) of inversion breakpoints. The bottom of each panel shows close-up views of strand flips across each inversion, visualized with *odgi viz* on the PGGB graph (*87*) and repeats [segmental duplications (SDs), satellite DNA, LINEs, and LTRs] near putative inversion breakpoints. (**H**) Count of segregating inversions in each species. (**I**) Heatmap showing presence (colored by log inversion length) or absence (white) of the most common 75 of 261 inversions (in columns) across 92 AW, AA, AI, AC, and CY haplotypes (in rows) detected by Syri. At top, columns corresponding to the three inversions in (E) to (G) as well as additional inversions >1 Mb are indicated. (I) Genetic differentiation (F_{st}) of indels, SVs, and inversions between species.

though the average number of multiallelic SV alleles (4.18) was on par with the maximum for SNPs (Fig. 4, A and B).

Interspecific variation in the ratio of SNPs to indels and SVs within each species can provide insight into the selective forces acting on SVs and indels and is robust to biases resulting from reference effects. The ratio of SVs and indels to SNPs varied from 0.019/0.150 in AW, to 0.022/0.171 in AC, and up to 0.099/0.389 in AI (Fig. 4C), consistent with the hypothesis that indels and SVs are more deleterious than SNPs and more easily purged in AW and AC versus AI, assuming neutrality of SNPs. These patterns hold when considering variants only in intergenic regions, where SNPs are more likely to meet the assumption of neutrality (AW, 0.016/0.147; AC, 0.019/0.169; AI, 0.087/0.369). In house finches [*Haemorhous mexicanus* (HF)], which have been surveyed for SVs using methods similar to those used in this work (*16*), the ratio of SVs or indels to SNPs is similar to that found in AW and AC, despite harboring nearly twice as many SNPs and SVs as in AW or AC, which highlights the extent to which AI is an outlier. The number of SVs shared between species and species-specific SVs also reflect these trends (Fig. 4D and fig. S29). Biallelic SNPs are 5.5 times as likely to be interspecifically shared by incomplete lineage sorting as SVs (6.8% of SNPs versus 1.2% of SVs), whereas indels and SNPs have similar proportions shared between species (7.45% indels shared)—patterns that hold for individual genomic compartments (fig. S30).

We comprehensively surveyed inversions using multiple pangenome-based, reference-based, and population-based principal components analysis (PCA)–sliding window approaches (*33*, *82*, *91*, *93*, *94*). We found a total of 382 inversions varying in length from 50 bp to 3.7 Mb (figs. S31 to S34), 95 of which were detectable by at least three methods (Fig. 4, E to G). Inversion flanking regions were enriched in repeats (Fig. 4, E to G, and fig. S35). The rank order of numbers of segregating inversions across species followed that of SVs and SNPs generally (Fig. 4H), but inversion frequencies showed substantial differentiation between species, as measured by fixation index (F_{st}), suggesting the possibility of adaptive differentiation (Fig. 4, I and J) (*95*). These patterns were exemplified by an ~1-Mb inversion on chromosome 3, detected by minigraph, that was polymorphic in AC, fixed in AI, and absent or near-absent in AW (Fig. 4I and fig. S36).

Distribution of fitness effects of SVs

The previous observations comparing the number and distribution of SNPs and SVs could imply that SVs are, on average, more deleterious than SNPs. To further test this hypothesis, we first estimated the distribution of the scaled selection coefficients of newly arising mutations (γ, the product of the effective population size and selection coefficient) across mutation types (SNPs, indels, and SVs). We used two maximum likelihood methods (*96*, *97*) that use the site frequency spectrum (SFS) of indels and SVs to estimate the distribution of fitness effects (DFEs) by comparing their SFSs (fig. S37) to those of putatively neutral SNPs, in our case intergenic SNPs. Both methods incorporate the possibility of misidentification of ancestral states and variation in mutation rate among site classes, factors that can compromise estimates of the DFEs if ignored (*98*–*100*). To allow for realistically variable mutation rates among intergenic SNPs and SVs, we constrained our maximum likelihood estimates of γ to be 0 or negative (supported by our estimates of α, the fraction of substitutions fixed by selection; see below). Across all genomic compartments, we found that estimates of γ for SVs tended to be more negative, and hence more deleterious, than for indels or SNPs (Fig. 5A and fig. S38). Estimates of the distribution of γ were broadly similar across species and methods, implying that the selection coefficients of variants segregating in AI birds are likely more negative than for AW and AC birds, given the smaller N_e for AI birds (Fig. 5A).

Estimates of γ necessarily rely on modeling assumptions (*96*–*98*, *100*). As a second line of evidence to estimate the fitness consequences of indels and SVs, we also examined interspecific differences in average indel and SV length, reasoning that any relationship between SV length and fitness effect should be apparent in length and frequency differences between species. The mean length of indels was longest in AI (6.59 bp) versus AW and AC (4.77 and 5.03 bp, respectively; figs. S39 and S40 and table S10), a trend that also held for bi- and multiallelic SVs but not for complex SVs (table S10). We then examined the relationship between SV length and derived allele frequency across the three focal species. Whereas neutral or adaptive variants can potentially fix and are thus plausibly found at any allele frequency, deleterious mutations (those with $N_e s$ approximately less than −1) are expected to rarely fix and be constrained

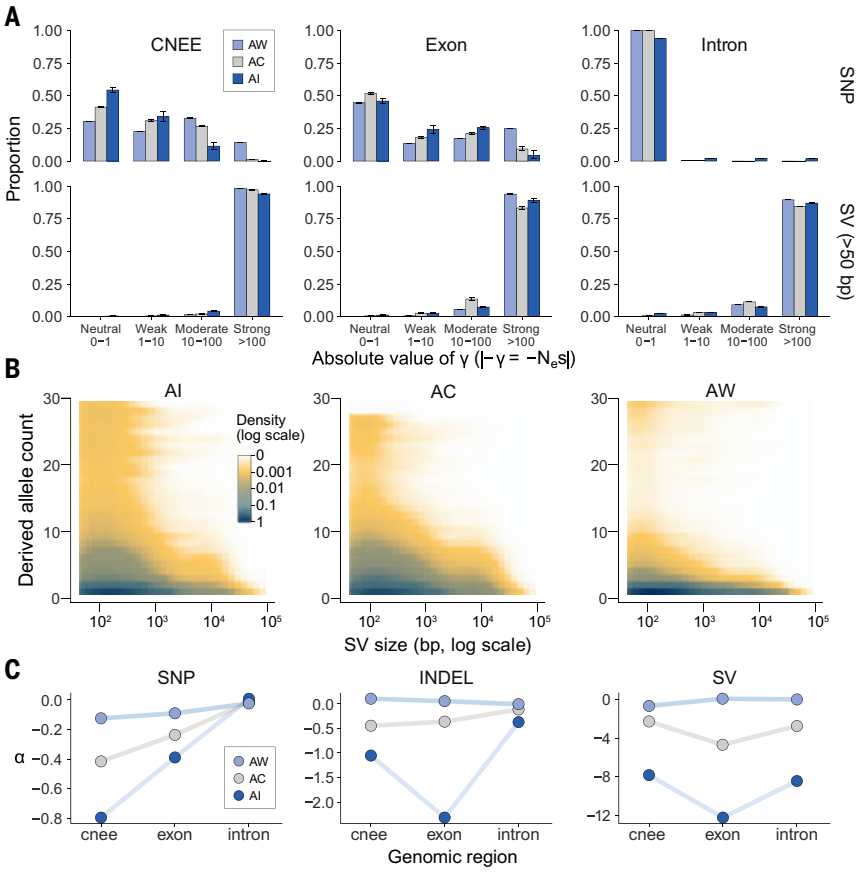


Fig. 5. DFEs of SVs. (**A**) DFEs in bins of population-scaled selection coefficient ($\gamma = N_e s$) estimated by fastDFE (*97*), reflecting variant deleteriousness, a function of the effective population size (N_e), and the selection coefficient (s). DFE was inferred from SFSs of different variant types residing in different genomic compartments. (**B**) 2D density plots (log scale) showing derived allele frequency (y axis) versus SV length (x axis) for three scrub-jay species. (**C**) Estimates of the fraction of variants fixed by selection (α) for SNPs, indels, and SVs across three genomic compartments: CNEEs, exons, and introns.

to low frequencies. We found that the number of large (>500 bp) SVs reaching high frequency in AI birds was greater than in AW or AC birds (Fig. 5B and fig. S41), consistent with drift driving frequencies of large and potentially deleterious SVs upward. Using fastDFE (*97*), we also found a detectable and predictable increase in estimated deleteriousness with length in base pairs of indels and SVs (fig. S42). Only the indel length class of 1 to 5 bp had an appreciable proportion of sites with $\gamma = 0$. As the length of indels increased to ~30 to 40 bp, the estimates of γ increased accordingly, until they leveled out above this length. As a result, estimated selection coefficients of indels (<50 bp) varied strongly with length, whereas SVs as a group yielded estimates of γ that were less influenced by length. These patterns held broadly across CNEEs, exons, and introns and are also evident in length differences for SVs in heterozygotes and homozygotes, especially with SVs >1 kb (fig. S43). Mean inversion lengths did not exhibit a clear difference in the homozygous compared with the heterozygous state (fig. S44), nor was there a clear relationship between inversion length and derived allele frequency within each species, except in AI birds (fig. S45).

Multiple lines of evidence therefore support the idea that SVs are, on average, more deleterious than SNPs. To test whether some proportion of SV substitutions may fix adaptively, we also estimated α, the fraction of substitutions between species fixed by positive selection (*101*, *102*). Classical tests of neutrality based on summary statistics comparing the numbers of synonymous and nonsynonymous polymorphisms and fixed differences in protein-coding genes (*101*, *102*) have also proven useful for the analysis of SVs (*96*). We first adapted an estimate of α, the fraction of nonsynonymous variants fixed between species by positive selection, to quantify the DFEs for SVs. Although α is usually calculated by comparing nonsynonymous and synonymous variants of protein-coding regions, in principle it can be applied to any class of sites, ideally closely linked (*103*). We therefore computed an α statistic based on comparing fixed and polymorphic intergenic SNPs with counts of fixed and polymorphic SVs overlapping different genomic compartments (CNEEs, exons, introns, and intergenic). In applying this approach, we filtered out variants below a frequency of 15% (derived allele count of ~4) so as not to dilute the estimate of α with slightly deleterious variants segregating at low frequency (*101*, *104*).

We found little evidence for adaptive fixations of either SVs or indels. In AI and AC birds, α was uniformly negative or 0 for all mutation types across genomic categories (Fig. 5C and table S11), indicating a predominance of segregating deleterious alleles, despite our filtering out the lowest-frequency variants. However, although SVs as a whole in AW are also estimated to be deleterious, a moderate (2 to 9%) fraction of SNPs and a potentially high (42 to 53%) fraction of indels and SVs in exons and intergenic regions of AW birds were estimated to be fixed adaptively (Fig. 5C and table S11). Estimates of the direction of selection, which is less biased by small sample sizes (*101*), reflect trends similar to α (table S11). These tests can potentially be affected by the choice of reference genome used when projecting the pangenome graph to the VCF (AW or CY; fig. S46), but we consistently observe AW having the highest (and often positive) α, consistent with AW alone experiencing appreciable adaptive fixation of indels and SVs.

Gene copy number variants and gene expression

An important component of the SV landscape is copy number variants (CNVs) of genes, yet we know little about how CNVs are influenced by N_e. We used miniprot (*105*) and pangene (*106*) to detect CNVs, estimate gene copy numbers per haplotype, and construct genome-wide pangene gene graphs for 96 haplotypes and 14,112 well-annotated genes (13,515 autosomal) across ingroups and outgroups (Fig. 6, A to C). Pangene aligns amino acid sequences to DNA contigs in the genome and requires well-annotated and highly complete haplotype assemblies. Moderately fragmented assemblies such as ours, as well as the difficulty of aligning noncontiguous protein sequences to DNA, increase the likelihood of false negatives, whereas false positives are less likely. Still, the overall trends in the dynamics of CNVs within and between species were robust to various filtering strategies. We found hundreds of cases of gene copy number variation (Fig. 6, A to C, and table S12). Consistent with estimates of rates of gene duplication and loss in model species (*107*–*111*), as well as estimates of the number of genes in humans exhibiting haplosufficiency (*112*), the proportion of genes experiencing CNVs in *Aphelocoma* is on the order of, if not higher than, the proportion of genomic sequences exhibiting SNPs. For example, whereas the proportion of the genome exhibiting SNPs within each species varies from ~0.01 in AW (≅15 million SNPs/1.3 Gb) to ~0.0005 in AI (table S8), the proportion of CNVs per species ranges from 0.066 in AW (=892 CNVs/13,515 autosomal genes surveyed) to 0.215 in AI (2905 CNVs/13515 genes surveyed) (table S13). Only under highly stringent filtering (table S13) does the proportion of genes experiencing CNVs within species decline to that of SNPs. In contrast to the distribution of SVs within species, AI birds harbored the most genes experiencing CNVs—more than twice

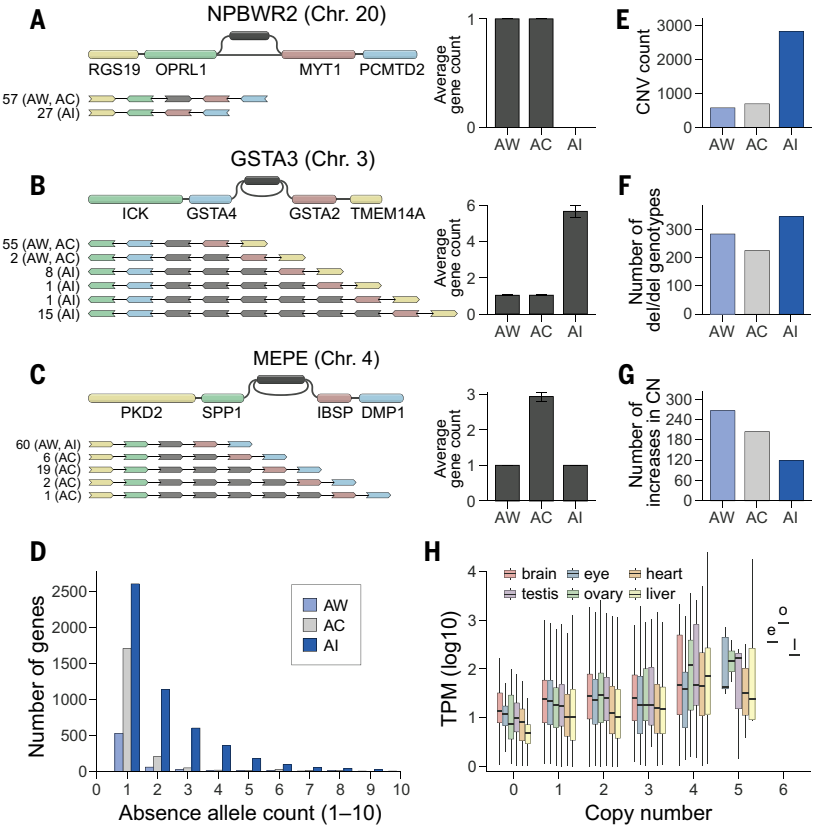


Fig. 6. Copy number variation and gene expression. (**A** to **C**) Three examples of gene presence-absence variation and copy number variation within the pangenome gene graph constructed using Pangene (left), and bar plots of average copy number per haplotype across species (right). Not all gene haplotypes are shown. (**D**) Number of genes (*y* axis) for which a given "absence allele count" (*x* axis) was detected per species. (**E**) Total number of CNVs per species, requiring at least two haplotypes to exhibit a CNV. (**F**) Number of genes with homozygous deletions per species. (**G**) Genes with copy number increases (multiplications) for each species. (**H**) Log_{10}-transformed TPM values in AW across tissues (brain, eye, heart, testes, gonad, and liver) by gene copy number, indicating that elevated expression is associated with higher gene copy number ($P = 0.048$).

as many as found in AC and AW across filtering strategies (Fig. 6, D and E). For CNVs found in at least two haplotypes, we detected 2839 in AI, 696 in AC, and 578 in AW (tables S12 and S13). Approximately 83.9% of CNVs in AI were AI specific, whereas this number was much lower in AC (37.3%) and AW (19.5%) (table S13). Across species, AI birds experienced the greatest number of genotypes homozygous for inferred deletion or truncation of genes, about 27 to 50% more than AC and AW (Fig. 6, D and F, and table S13), a result unlikely to be driven by variation in assembly quality (*63*). Whereas AI (Fig. 6A) and AC experienced complete loss of 14 and 15 autosomal genes, respectively, AW has lost only one (*EDMPN2*; table S13). Across loci within species, deletions of genes were between 2 and 68 times as common as multiplications (Fig. 6, F and G). In contrast to gene deletions, gene multiplications were less common in AI (119 genes) than in AC (204) or AW (266) (Fig. 6G, table S13, and figs. S47 and S48).

CNVs could have direct consequences for organismal or cellular phenotypes, such as gene expression. To detect the effect of CNVs on gene expression, we sequenced transcriptomes of five tissues across each of the 15 AW birds (brain, eye, liver, heart, and gonad) and blood for each of the 14 AC birds, for a total of 62 transcriptomes. We quantified gene expression across 15,870 genes, of which 10,671 both had expression levels greater than 1 transcript per million (TPM) in at least one tissue in AW birds and were included in the pangene analysis (fewer genes—7581—had TPM >1 in AC birds, as expected given our use of whole blood). A linear mixed model fit to autosomal genes with TPM as the response variable, copy number as the independent variable, and gene and tissue as random effects revealed a significant effect of AW gene copy number on TPM within and across tissues ($P = 0.048$; Fig. 6H) (*63*).

Discussion

Comparative population genomics has traditionally focused on SNPs as the primary metric of genomic diversity across species. Studies of indels and SVs are increasing, but few have comprehensively analyzed variation across the full spectrum of genomic changes, including inversions, across multiple species. In this study, we leveraged long-read sequencing at the population level and pangenome computational tools to investigate the dynamics of structural variation across three closely related avian species with notably different effective population sizes. Whereas human pangenome studies (*32*) benefit from exceptionally high-quality assemblies, they are limited to a single species with relatively low genetic diversity. By contrast, our pangenomes of 44 *Aphelocoma* jays span three species about half as diverged from each other as humans are from chimpanzees, with outgroups about half as diverged as the human-orangutan split (*84*). Advances in long-read sequencing and computational methods have now revealed that structural variation within humans and other species is far more widespread than previously appreciated, even in birds, whose mode of genome evolution is generally thought to be conservative (*11*, *113*). Our findings underscore the power of multispecies pangenome approaches to scale across the species boundary (*84*) and reveal how demographic processes influence genome architecture and diversification.

Our results provide a high-resolution lens on how genome size and architecture evolve between closely related species; significantly, the majority of the genomic events that we document in *Aphelocoma* can plausibly be ascribed to demographic processes, as opposed to mutational events (Fig. 7) (*81*, *114*–*116*). The smaller assembly size of island scrub-jays compared with close relatives contrasts with theoretical predictions that genetic drift associated with bottlenecks should lead to expansion of deleterious transposable elements, increasing genome size. Recent surveys in animals also reject this association (*117*); our data suggest that the relationship between population size and genome size in the short term is complex. We detected highly heterogeneous shifts in satellite abundance not predictable from population size alone but that instead suggest that both founder events and mutational processes—such as the burst of satellite abundance in the *Aphelocoma* ancestor—influence the distribution of satellites and genome size across species (Fig. 7). The discovery of unexpectedly long satellite repeat units (>10 kb) in *Aphelocoma* adds another layer of complexity to avian genome structure: Such long repeats may play roles in genome plasticity, with potential functional consequences (*118*, *119*) and roles in the evolution of complex traits (*115*).

SVs have played major roles in adaptive evolution across diverse taxa, especially inversions (*120*–*122*) and regulatory and dosage changes precipitated by indels and CNVs (*123*, *124*). Our findings indicate that most SVs behave as weakly deleterious variants and that adaptive variants are rare, consistently detected only in AW—the species with the largest N_e. This discrepancy likely reflects a bias in the literature, where inversions and other SVs with clear adaptive functions or phenotypic effects are more readily identified and studied, whereas the many inversions with neutral or deleterious effects remain underreported.

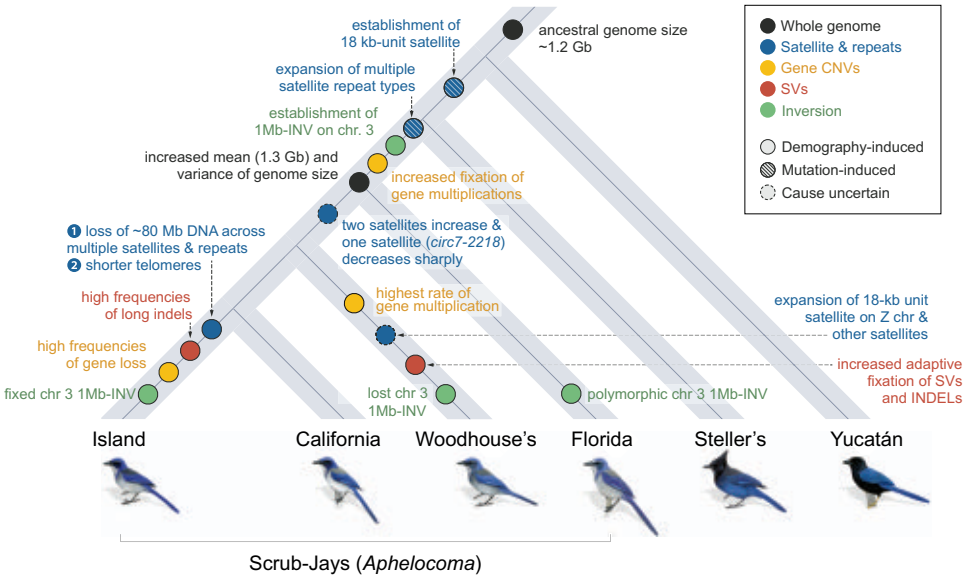


Fig. 7. Demography- and mutation-induced genomic changes across *Aphelocoma* and outgroups. Summary diagram indicating major findings of this study. Individual genomic events (indicated by circles) are categorized as induced by demography, mutation, or uncertain cause. Whole-genome traits are indicated in black, satellites and repeats in blue, gene copy number variants in yellow, SVs in red, and the 1-Mb inversion on chromosome 3 showing high differentiation between species in green. Genomic events were ascribed to demographic forces when plausible, otherwise to mutation or unknown sources. Bird illustrations used with permission from Lynx Edicions.

We also found multiple signatures of greater deleteriousness of SVs in AI birds, including a higher ratio of SVs and indels to SNPs and longer SVs rising to higher frequencies in AI compared with in other *Aphelocoma*.

Overall, we found that the number of SVs generally tracks effective population size. The one category of SVs that did not increase in number with N_e were CNV deletions, which showed a clear excess in AI birds, which have the smallest N_e. CNV deletions display the same inverse relationship to population size (AI > AC > AW) as amino acid substitutions in humans, which increase rather than decrease in populations that have undergone more serial bottlenecks and have incurred lower genome-wide SNP diversity (*125*). Patterns like this indicate that such variants, in our case CNV deletions, are strongly deleterious more often than other SVs, a pattern also found in model species under both experimental and natural conditions (*108*–*111*). By contrast, CNV multiplications were least common in AI birds and most common in AW birds, indicating a closer conformation to neutral or adaptive dynamics and potentially providing a path to adaptation with, on average, fewer deleterious consequences (*124*). Overall, the high incidence of CNVs found in this work agrees with high rates of CNVs found in model systems (*108*–*111*). For example, the accessory pangenome of natural isolates of baker's yeast (*Saccharomyces cerevisiae*) makes up 36% of 7796 genes, most of which are gene deletions (*126*). Moreover, our detection of a positive genome-wide relationship between gene copy number and gene expression shows that this type of SV has clear effects on downstream molecular processes. In humans, segmental duplications affect the copy numbers of more than 1000 (~5%) genes, with consequences for gene expression (*127*). Key tasks for the future of pangenome studies include improving standardization, validation, and transparency of SV calling pipelines at different phylogenetic scales and determining how the diversity of fitness effects of SVs affect adaptive processes in natural populations.

Materials and methods

Field methods

Field methods for island scrub-jays (*A. insularis*): The island scrub-jay is restricted to Santa Cruz Island, which is 32 km from the mainland of southern California, USA. The census population size is estimated to be between 1200 and 3000 individuals (*128*), and the effective population size (N_e) is estimated to be 346.8 with a 95% confidence interval of 327 to 368 based on a few thousand SNP loci (*129*). The 250-km^2 island has a Mediterranean climate characterized by cool, wet winters and hot, dry summers. The vegetation is composed of a mosaic of habitat dominated by island scrub oak and includes coastal sage scrub, oak woodlands, and oak chaparral (*130*, *131*). Juvenile and adult male and female island scrub-jays were captured using either mist nets or box traps from three large study plots from 2009 to 2011 [see Caldwell *et al.* (*132*) for detailed descriptions of the study plots]. Morphological measurements were collected from each captured individual using digital calipers to record (to ±0.01 mm): bill length measured from the anterior end of the nares to the tip of the bill; bill depth, measured at the anterior end of the nares; and tarsus length. Wing chord and tail length were measured with a ruler (to ±0.5 mm). We marked jays with a unique combination of up to five colored plastic leg bands and one numbered US Geological Survey band. Whole-blood samples were extracted from the brachial vein and preserved in Queen's lysis buffer (*133*). All work with living birds was approved by the Institutional Animal Care and Use Committees at Colorado State University (IACUC: #887) and the Smithsonian Institution.

Neutral population genetic analyses have shown that island scrub-jays exhibit isolation-by-distance across the east-west axis of the island which is likely driven by limited dispersal (*129*, *134*). Our criteria for selecting individuals for sequencing were that they be unrelated, have multiple blood samples taken between 2009 and 2011, and show limited spatial genetic structure. Based on these criteria, we selected eleven male and four female island scrub-jays for PacBio HiFi sequencing from our two study plots located in the central valley of Santa Cruz Island. We confirmed that all individuals were less than full siblings based on a kinship matrix calculated using the Genome-wide Efficient Mixed Model Association software toolkit (*129*, *135*).

Field methods for Woodhouse's scrub-jays (*A. woodhouseii*): Woodhouse's scrub-jay specimens were collected under permit 3704 from the New Mexico Department of Game and Fish and Federal US Fish and Wildlife permit no. MB155188-0. Field collection took place in October 2018 and June 2021 northwestern New Mexico in the vicinity of Turley, Navajo Dam City, Cedar Hill, and Blanco. Specimens for karyotyping were collected in May 2023. Specimens were collected by mist-net and shotgun. Birds were targeted for collection randomly upon encounter in the field. After sacrifice, tissues were immersed and minced in RNAlater in individual nunc tubes and stored at room temperature for 24 hours, after which they were immersed in liquid nitrogen or vapor for transport back to the Museum of Comparative Zoology (MCZ) at Harvard University. The *C. yucatanicus* sample from Yucatán, Mexico, was processed similarly to the AW samples. All specimens were prepared as vouchers and are retained in the MCZ. Full details on each specimen can be found in table S1 and at MCZbase (https://mczbase.mcz.harvard.edu/).

Field methods for Florida scrub-jays (*A. coerulescens*): The Florida scrub-jay is restricted to the xeric oak scrub habitats of Florida (*49*).

A population of individually banded Florida scrub-jays has been monitored at Archbold Biological Station in Venus, FL, since 1969, providing detailed information on individual life histories (*49*). Florida scrub-jays have very low rates of extra-pair paternity (*136*, *137*) allowing us to reconstruct fairly accurate pedigrees from field observations of breeding behavior, though we also confirmed pedigree relationships with genetic data for >15 years (*47*). For this project, we sampled mostly younger individuals (<3 years of age) out of convenience. We sampled birds with no known close relationships to each other (no parent-offspring, full sibling, or half sibling relationships). To minimize impacts on our study population, we focused on individuals who also needed a band replaced or were easily trappable. We captured individuals using Potter traps and collected whole blood from the brachial vein. Blood samples were stored in RNAlater at room temperature for 24 hours before transferring to a −80°C freezer and shipped on dry ice. All work was approved by the Institutional Animal Care and Use Committees at Cornell University (IACUC 2010-0015) and Archbold Biological Station (AUP-006-R), with permits from the US Fish and Wildlife Service (TE824723-8, TE-117769), the US Geological Survey (banding permits 07732, 23098), and the Florida Fish and Wildlife Conservation Commission (LSSC-10-00205).

In summary, most (67%) of the genomic resources for this work, including all AW and AC samples, were purpose-collected for this project, allowing us to maximize data quality and reproducibility.

Laboratory methods

DNA isolation and PacBio HiFi sequencing: All samples were sequenced at the Delaware Biotechnology Institute DNA Sequencing and Genotyping Center in Newark, Delaware. For AI or AC blood samples, 100ul of sample was pelleted and the pellet was processed with Qiagen's MagAttract HMW DNA extraction kit. Genomic DNA was isolated from the pellets using Qiagen's MagAttract HMW DNA extraction kit. Lysis was shortened to 30 min at 56°C and all shaking steps were replaced with rotation. Elution was performed overnight at room temperature. DNA isolation from the AW tissue samples was performed on cryo-pulverized material following the Qiagen MagAttract kit instructions. Lysis was shortened as much as possible until there was no visible tissue remaining (typically 30 to 60 min) and was conducted at 56°C. All shaking steps were converted to rotation and samples were eluted overnight at room temperature. Genomic DNA quality was assessed with a Femto instrument (Agilent). All samples were sheared using a Megaruptor 3 (Diagenode) instrument with target size 14 to 15 kb. All libraries were prepared using the PacBio SMRT Bell prep kit v3 (Pacbio). Sample libraries were size-selected for 6 to 8 kb fragments using a Blue Pippin instrument (Sage). Each sample was sequenced on 2 flow cells of a Sequel IIe instrument using sequencing kit v2 and Sequel II binding kit 2.2 and 30 hours of movie was recorded. PacBio HiFi reads were downloaded from the Delaware Center web site as BAM files for further processing.

HiC sequencing: HiC sequencing of the AW reference individual (number MCZ Orn 365336, female) and AW male individual MCZ Orn 365338 was performed by Arima Genomics in San Diego, CA. 359,457,888 read pairs were generated on an Illumina MiniSeq sequencer from AW 365336 and 352,068,517 were generated from MCZ 365338. Approximately 250,000 reads were generated from human control samples to evaluate quality of the library, which suggested 58.4 to 59.5% long-range cis interactions. Paired-end sequences were downloaded as fastq.gz files for genome assembly.

Karyotyping: Ten *A. woodhouseii* were collected in northwestern New Mexico in May 2023 and whole eyes and tracheal tissue were extracted with sterile dissecting equipment by immersing them in fresh medium [alpha minimum essential medium (MEM) + 10% fetal bovine serum (FBS), + 1% Glutamine/Pen-strep, + 1% fungizone] in biopsy vials. Tissues were shipped at room temperature overnight, or in some cases after 24 hours in at 4°C in a refrigerator, to the Frozen Zoo, Reproductive Sciences and Conservation Science, San Diego Zoo for processing. All samples were analyzed with standard (nonbanded) Giemsa staining. C- and G-banding was applied to one individual (female Lab#23907) sample. An example karyotype of is presented in fig. S1 and was found to have a diploid number of 80. Full details of the karyotype analysis will be published elsewhere.

RNA isolation and sequencing: RNA was isolated from ~12 µl of whole blood from *A. coerulescens* samples using Qiagen kits and the same methods as in (*138*). Cells were separated from RNAlater in the tube by centrifugation (20,800*g*). Cells were homogenized with Qiazol and zirconia/silica 1 mm beads (BioSpec Products) on a TissueLyser LT (Qiagen, Hilden, Germany) in the Harvard Bauer Core Facility. RNA was isolated from homogenized cells using the RNeasy Plus Universal mini kit protocol (Qiagen, Hilden, Germany). Libraries were prepared with KAPA mRNA Hyperprep kits by staff in the Bauer Core and sequenced on an Illumina NOVASeq SP platform with paired end reads of 150 bp length, yielding between 20 and 30 million reads per sample.

For tissues from *A. woodhouseii*, RNA was isolated from sample volumes of ~2 to 3 mm^2. Isolation followed instructions in the RNeasy Plus Universal mini kit protocol after homogenization with silica beads and the TissueLyser. Library preparation and sequencing was performed as for blood above.

Bioinformatics

Genome assembly: To automate assembly for our 46 individuals, we organized our workflow as a Snakemake pipeline, available at https://github.com/harvardinformatics/scrub-jay-genomics and on Zenodo (*139*). To summarize, we trimmed any remaining adapters from our reads using Cutadapt (*140*) and assembled using Hifiasm (*55*) using the option to partially phase each sample, which generates a primary assembly plus two partially phased haplotype assemblies per individual. We converted the GFA output from Hifiasm to FASTA and renamed the contigs to match the "PanSpec" naming convention to facilitate downstream analysis. Blood samples generally yielded more highly contiguous assemblies, whose N50 without scaffolding by HiC ranged from 5.1 to 19 Mb (fig. S2 and table S2).

For the samples for which we had paired-end HiC data (one male and one female *A. woodhouseii* and the outgroup *C. yucatanicus*) we integrated the reads into the Hifiasm assembly to better phase the output and improve contiguity. We first filtered the HiC reads using scripts from the Arima and Esrice pipelines (as modified at https://github.com/harvardinformatics/scrub-jay-genomics), then mapped each read pair against each draft genome individually using BWA (*141*). We then combined the individually mapped read pairs together and removed duplicates using samtools and converted the output to BED format using bedtools (*142*). The HiC BED file was then used for scaffolding with Yet Another HiC Scaffolding tool (YaHS) (*143*). We visualized the HiC alignment output from YaHS using JUICER (*144*).

Finally, for our reference *A. woodhouseii* female, to further improve contiguity and to assign chromosome names we performed reference-based scaffolding using RagTag (*145*) against a draft version of the Florida scrub-jay genome (*56*). Because the Florida scrub-jay assembly was generated from a male bird, we performed a second reference-based scaffolding against the Hawaiian crow genome to scaffold the W chromosome (*57*). Two contigs that were W-associated in the Hawaiian crow–scaffolded version were instead scaffolded as part of ch5 and chZ in the Florida scrub-jay–scaffolded assembly; we manually trimmed those contigs off the W, then added the W scaffold to the Florida scrub-jay–scaffolded genome to obtain our final assembly. In our final reference assembly (aphWoo1), chromosomes are named based on homology to the Florida scrub-jay reference (*56*).

Genomescope: We applied Genomescope (*146*) to the individual fastq files to estimate heterozygosity and genome size. Jellyfish (*147*) was used to count k-mers, using default parameters.

Dipcall: We used the program dipcall (*60*) to estimate heterozygous positions and confident bases in each individual, and to call small variants and long INDELs between haplotype assemblies of each individual. Dipcall works by aligning a diploid assembly (in this case, the two haplotypes from a particular individual) to a reference genome (in this case, aphWoo1) with minimap2 (*148*), and then identifying heterozygous positions (where one haplotype carries a nonreference allele). Confident bases are estimated based on alignment coverage, where confident bases are defined as bases that are covered by one ≥50 kb alignment with mapQ ≥5 from each parent and not covered by other ≥10 kb alignments in each parent. We built the variant call makefile with "make -j2" followed by "dipcall.kit/k8 and dipcall-aux.js vcfpair." The output comprised a phased VCF and a BED file of confident regions, which was then filtered with grep to remove sex chromosomes. Per-base heterozygosity for each individual was calculated as the number of heterozygous positions identified by dipcall, divided by the number of confident bases identified by dipcall.

PSMC and demographic analysis: To infer population size history with PSMC (*61*), we generated a diploid consensus sequence by (i) applying "seqtk mutfa" to the reference fasta assembly, modified with the Dipcall VCF (processed by "vcf2snp.pl"); (ii) masked using the BED file using "seqtk seq -cM"; and (iii) converted to PSMC input format with "fq2psmcfa." We then ran PSMC using the command "psmc -N25 -t15 -r5 -p "4+25*2+4+6" -o $SAMPLE.psmc $SAMPLE.psmcfa" and visualized the results with "psmc_plot.pl." No bootstrapping was performed. Each line in the PSMC plot in Fig. 1C represents a different individual.

Tests for gene flow between *A. coerulescens* and *A. woodhouseii*: Gene flow between species could influence the distribution of SNPs and SVs and could violate models for estimating the DFEs of variants, which usually assume single, isolated, and panmictic populations. To obtain a set of SNPs that overlapped between ingroup and outgroup and would satisfy the topology (((P1,P2),P3),Outgroup) that is required by Dsuite (*149*), we used bcftools (*150*) to intersect two vcf files, one containing all ingroup scrub-jay sample genotypes and one containing genotypes for the outgroup CY sample. We then merged the resulting intersected vcfs using bcftools (*150*) and thinned to 1 SNP per kb using vcftools (*151*) to generate a vcf with ~1 million SNP genotypes for the 45 samples (44 ingroup AI, AW, and AC) plus 1 Outgroup CY). We then removed the W and Z chromosome SNPs from that vcf and filtered to only biallelic genotypes (a Dsuite requirement).

Using this vcf as input for Dsuite, and treating missing sites as missing, we at first found a signature of significant gene flow between Florida and Woodhouse's scrub-jays, but with only a slight deviation from the null (D = 0.05). To test whether this signature would remain if the dataset was further filtered for linkage (to reduce the likely overpowered 1 million SNP analysis), we further filtered the dataset to one SNP per 50 kb, and found that the signature of significant gene flow disappeared. Regardless, the direction of the excess allele sharing remained between Woodhouse's and Florida scrub-jays. We believe that this consistent signal, that AI birds share few derived alleles with AC birds in all analyses, can be attributed to the fact that rates of lineage sorting were stronger in the AI lineage, which has undergone genetic bottlenecks and experienced repeated purging of broadly shared variants because of its evolutionary history on Santa Cruz Island. These demographic processes are likely strong enough to create a subtle deviation from the null expectation of D = 0 (*152*), which is considered significant when we use a large SNP dataset (~1 million SNPs), but disappears in datasets that are linkage-thinned in closer accordance to a realistic estimation of the number of independent linkage blocks present in the genome. We therefore attribute the significant ABBA/BABA results to unaccounted-for demographic processes in the AI birds and conclude that there is no significant gene flow between AW and AC in this dataset. This conclusion accords with previous findings in this system (*44*, *48*).

Bayesian phylogeography and phylogenetics: A bed file containing high-confidence regions generated by dipcall was parsed to identify 1-kb autosomal loci that did not occur within 10 kb of each other. This exercise generated ~2500 loci, which were retrieved from each haplotype using command-line blast (*153*). We attempted to extract the loci directly from the pangenome graph (*87*) but at the time of this work the odgi extract function was not working properly, and hence we used blast. The top-scoring and most complete blast hit was extracted from each haplotype. Loci were collated and aligned again using mafft v7.490 (*154*) and then formatted for input into bpp v4.7.0_linux_x86_64 (*155*), assigning each haplotype to its appropriate species. Before running bpp, the genealogy of each aligned locus was estimated using maximum likelihood using IQ-TREE (*156*, *157*) to detect possible aberrant orthologs or misalignments. Rates of monophyly of alleles within each species was counted using functions in the R package ape (*158*); the substitution model for each locus was estimated using ModelFinder (*159*).

In bpp, Model A00 was used, in which the species tree topology is provided and the program estimates branch lengths (in units of substitutions per site, $\mu\tau$, where μ = mutation rate and τ = divergence time in generations) and effective population sizes of extant and ancestral species ($\theta = 4N\mu$, where N is the effective population size). The results of the Markov Chain Monte Carlo (MCMC) run were summarized in Tracer v.1.7.1 (*160*). A substitution model for each locus (JC69, HKY, TN93) was assigned using the model closest to the results from ModelFinder.

Gene annotation: To generate a chain file for liftover, we aligned the final scaffolded *A. woodhouseii* reference genome (aphWoo1) against the *Gallus gallus* version 7b genome (GCF_016699485.2) from the National Center for Biotechnology Information (NCBI) using LASTZ (*161*), implemented as a Nextflow workflow at https://github.com/hillerlab/make_lastz_chains/tree/main. We first soft-masked repeats of the *A. woodhouseii* genome, as required for LASTZ alignment. Before performing liftover, we filtered the 80,621 chicken transcripts to remove noncoding RNA, resulting in 41,653 input transcripts. We then used the filtered transcripts and chain alignment file to annotate the *A. woodhouseii* reference using TOGA (*58*). For the query annotation, we removed any transcripts shorter than ten amino acids in length, and filtered to only retain Intact (I), Partially Intact (PI), or Uncertain Loss (UL) projections, resulting in a total of 41,563 transcripts annotated in *A. woodhouseii*.

To ensure our annotation was as complete as possible, we also aligned *A. woodhouseii* against the zebra finch genome v1.4 (GCF_003957565.2) (*162*), filtering the input transcripts similar to chicken (31,017 input transcripts with 48,058 isoforms). After performing liftover with TOGA we filtered the query annotation as above, resulting in a total of 42,730 annotated transcripts.

To produce our final combined, nonredundant annotation, we used gffcompare v0.12.6 (*163*) (https://github.com/gpertea/gffcompare) to merge annotations, using the zebra finch as the reference species and the -D option to remove duplicate intron chains. For the merged GTF file, we assigned unique gene labels to each transcript using the orthology relations generated by TOGA, with labels determined by the type of orthology relationship identified by TOGA. For orthologs identified as "one2one" (i.e., single copy in both reference and query species), we assigned the same gene ID as the reference species (with priority given to the zebra finch reference); for "one2many" orthologs (i.e., genes duplicated in *A. woodhouseii*), we append a number to each copy of the gene. Orthologs with a "many2one" relationship (i.e., multicopy in the reference species but single in *A. woodhouseii*) we append a "-like" suffix, and lastly for "many2many" orthologs (multicopy in both reference and query), we append a "-like-NUM" suffix for each copy. In total, after merging we identified 34,669 transcripts across 15,966 genes. We ran BUSCO (*164*) using the aves_odb10 dataset and obtained a score of 99.3%, indicating our annotation is highly complete.

PGGB pangenome graph: To construct our pangenome graph, we combined the two partially phased haplotype assemblies generated by hifiasm for each of our 44 individuals across the three species, plus the single CY outgroup and our reference *A. woodhouseii* individual for a total of 91 haplotypes, which comprises >113 Gbase across ~113,000 contigs. Because constructing an all-by-all graph from such a large dataset would be far too computationally intensive given our available computing resources, we first clustered our sequences into "communities" of related sequences, which we will then build into graphs individually. To partition into communities, we first performed an initial approximate all-by-all alignment of the sequences using wfmash [(*165*); https://github.com/waveygang/wfmash], with the parameter for minimum percent identity set as -p 94 based on expected divergence between the species and window size as -w 1024 to improve runtime. In total, wfmash partitioned the combined haplotypes into 994 communities. We split these communities into three classes. Thirty communities correspond to chromosomes, as identified by chromosomal scaffolds from the reference individual, which we refer to as chromosomal communities. These chromosomal communities together contain 92.6 Gbase of sequence (i.e., ~82% of the input sequence). Another 18 communities contain reference scaffolds that were not placed into chromosomal scaffolds, which we refer to as unplaced reference communities; these communities contain 13.2 Gbase of sequence, ~11% of the total. The remaining 946 communities we refer to as nonreference communities, which have zero reference sequence in them and comprise only 7.3 Gbase (~6.5% of the total). Most of these nonreference communities are quite small, with only a few contigs from a handful of individual haplotypes per community, and likely represent either spurious alignments between repeats or misassemblies or rare SVs present in only a few assemblies. Thus, we chose to omit them when constructing the graph.

For each of the chromosomal and unplaced reference communities, we constructed a pangenome graph of the sequences using PanGenome Graph Builder (PGGB) [(*82*); https://github.com/pangenome/pggb] using a minimum percent identity of -p 94 and a graph segment length of -s 100000. This produced a graph file in GFA format for each community containing indels, SVs and SNPs. Due to computational constraints, we were unable to construct graphs for 2 of the 48 input communities: one unplaced reference community and one corresponding to AC chromosome 17. These communities likely represent highly convoluted graphs that cannot be resolved by PGGB. In the end we were able to obtain graphs for 30 of the 34 currently known chromosomes from the high-quality AC reference assembly (*56*). All 46 successful chromosomal ($n = 29$) and unplaced ($n = 17$) communities have been deposited on Dryad (*166*).

In addition, we found segments of chromosomes 1, 1A, 2, 3, 5, and 15, often at the ends of chromosomes and flanked by large inversions, with aberrantly low graph depth. Investigation suggested that these segments represent regions of the reference genome where our initial community construction algorithm failed to correctly place haplotype sequence into the reference community, potentially because of complex repeat structures or rearrangements. To account for this in downstream analysis, we produced a bed file with regions of low graph depth indicated [available on Dryad (*166*)] and used this bed file as a filter for all downstream analyses.

SV calling: PGGB: We use the paths (contigs and haplotypes) in the graphs constructed by PGGB to call variants. For each community alignment, we take the GFA output and break it down into VCF file of individual variants using vg deconstruct v1.40.0 [(*167*); https://github.com/vgteam/vg], using the *A. woodhouseii* female reference (aphWoo1) as our base coordinates. To deal with overlapping and nested alleles in the graph, we ran vcfbub (*168*) on the deconstructed VCF files to keep only the top-level variant sites (i.e., "snarls") in the pangenome graph that are less than 100 kb in size. We then used vcfwave (*168*) to realign the reference and alternate alleles to the genome; this process splits nested alleles into individual entries and identifies inversions (>1 kb in size). Next we combined the VCF files from each community together using bcftools concat [(*150*); https://samtools.github.io/bcftools/bcftools.html] before concatenating, for any community with individuals missing (e.g., male samples for the W chromosome), we added in sample columns to those VCFs as missing data using bcftools query. For final cleanup, we used bcftools +fixploidy to set the same allele number for every site, bcftools +fill-tags to add allele count and allele frequency tags for each site and bcftools norm to split multiallelic records into biallelic.

Determination of ancestral states is critical to the designation of SVs as insertions, deletions, or the SV inversion status. To determine ancestral states in our study, we used an outgroup that was ~12–million years diverged from the ingroup species, and one that we learned in the process had a smaller assembly size than did the three ingroup species, resulting approximately half (51.3%) of SVs that could not be polarized, in part because the degree of divergence between the ingroup and outgroup species likely poses challenges to alignment and graph construction. It is difficult to distinguish the underlying causes of polarization failure. Many SVs likely could not be polarized because of the smaller assembly size of CY haplotypes, but in principle some could not be polarized because of assembly gaps in the CY outgroup for particular *Aphelocoma* SVs or because of difficulties in incorporating the diverged outgroup into the graph structure.

The use of a 12–million years diverged outgroup struck a balance between being relatively closely related to the ingroup, thereby ensuring confidence in ancestral states, yet being distant enough to the ingroup so as not to engage in allele sharing, whether by incomplete lineage sorting or hybridization. Additionally, multiallelic SVs proved challenging to count. What might be considered one multiallelic SV in one pipeline could be considered two or more biallelic SVs another pipeline. Simple deconvolution of multiallelic SVs into biallelic SVs is a solution, but may result in arbitrarily large numbers of SVs that may still be difficult to compare between species.

SV calling: Minigraph and other methods: We ran minigraph v. 0.20-r559 on a total of 94 haplotypes (AI, AC, AA, AW, CS, and CY) and the AW reference. We used the -j option (-j.05) to accommodate larger sequence divergence between species. The graph (in .gfa format) is available on Dryad (*166*). To call SVs, each haplotype is mapped back to the graph to produce a VCF-like file (*.gaf). The 93 *.gaf files were then merged to create a final VCF. The VCF contains insertions, deletions, and inversions relative to the AW reference. In the bed file generated by minigraph, when a bubble involves an inversion, column number 6 indicates a value of 1.

To run the SyRi pipeline, we generated 45 pseudo-chromosome-level assemblies using RagTag (*145*), a scaffolding tool that maps query scaffolds to a high-quality reference genome. The assemblies were aligned to the reference using minimap2 with the preset –eqx option, and the output was sorted into BAM files with samtools. Next, SyRI was executed on each BAM file to detect structural rearrangements. The inversions were extracted from the SyRI output using awk (awk '$11=="INV"').

Recombination: We used RELERNN (*169*) to estimate per–base pair recombination rates, only for the AW genomes, which had the most information and variability for estimating recombination rates. We used VCF files parsed by species and by chromosome and for biallelic sites with no missing data as input for RELERNN. We first used the SIMULATE function to train the algorithm, producing 13,000 training datasets, 2000 validation sets, and 100 for testing. We predicted recombination rates (rho) for each chromosome and conducted bias correction using the BSCORRECT module, using a mutation rate of 2.2×10^{-9} for noncoding DNA (*170*) and an upper limit for rho of 5.17. Recombination rates were plotted on a 1-Mb sliding window and averages

per chromosome. Correlations of SNP and SV density with recombination were conducted by counting the number variants per megabase from the PGGB VCF and plotting with recombination.

The density of SNPs, indels, and SVs each exhibit positive correlations with recombination rate in highly repeatable decreasing rank order (SNPs: $R^2 = 0.22$; indels: $R^2 = 0.12$; SVs: $R^2 = 0.03$) (fig. S26); as a consequence, all three types of variants exhibited the highest density on microchromosomes (fig. S27).

Kinship and runs of homozygosity: We used bcftools (roh command) to estimate runs of homozygosity, which uses the hidden markov model of Narasimhan *et al.* (*171*). We used PLINK2 (*172*) to estimate kinship coefficients using KING (*173*). The vcf file projected from the combined PGGB pangenome graph was parsed for biallelic autosomal SNPs. A table of relatedness was generated by PLINK2 within each species separately. Runs of homozygosity were estimated using default parameters.

RNA sequencing analysis: To evaluate transcript expression levels, we quantified transcript abundance for our sixty two samples from a variety of tissue types using kallisto (*174*). We indexed our merged TOGA transcriptome with kallisto index and used kallisto quant with 30 bootstrap replicates to estimate TPM and expected counts for each transcript in each sample.

Repeat annotation: RepatModeler2 (*67*) was run on the AW reference genome to generate a de novo repeat library. We also ran Satellite Repeat Finder (SRF) (*68*) on the reference assembly as well as on each haplotype assembly and individual sets of unassembled PacBio HiFi reads. The unit lengths of satellites detected by SRF were in general much longer than those detected in other corvids; for example, two previously detected satellites in birds-of-paradise had similar unit lengths to those found in jays, but otherwise the unit lengths of jay satellites were 15 to ~600 times as long as previously reported (table S5).

The SRF satellites were concatenated to the RepeatModeler library to obtain the full library used or annotation. In downstream analyses, satellites identified by RepeatModeler2 were removed from the library so as not to compete with the SRF satellites, which were generally longer and more diverse.

RepeatMasker was used to annotate each primary assembly, including the AW reference, as well as each haplotype assembly. For all analyses the out file produced by RepeatMasker was converted to *.bed format using rmsk2bed function of the bedops package (*175*) for downstream processing with custom R scripts.

Analysis of satellite landscapes: We used minimap2 to map the 300 satellites detected by SRF to PacBio HiFi reads. These outputs were then parsed with srfutils.js (available at https://github.com/lh3/srf) to produce *.len files consisting of columns designating the satellite; the total number of base pairs covered by the satellite in a given fastq.gz file; a rough measure of sequence divergence among the satellite copies; the proportion of read base pairs comprised of the satellite, excluding reads or contigs in which only one copy of the satellite repeat unit is found; and finally the number of base pairs comprised by the satellite including all reads or contigs in which only any number of copies of the satellite repeat unit is found. The *.len tables from individual birds were concatenated and the resulting tables parsed to examine the distribution of satellites across individuals and species.

Inspection of srf outputs and mapping of satellites by minimap2 indicated that satellite sj_sat_circ30_18193, which has a ~18 kb unit repeat, varied drastically between species and sexes. We mapped the distribution of this repeat to each haplotype using minimap2 and the command: minimap2 -c -N1000000 -f1000 -r100,100 18kb.fa ctg.fa > srf-aln.paf. The resulting .paf files were parsed for satellite unit copies that were at least 18 kb. There were 27,083 full-length unit copies of this satellite across AI, AA, AW, AC, CY, and CS haplotypes. These ~27,000 units were extracted from haplotype assemblies using a bed file and seqtk sample. They were then aligned with mafft, using the option –adjustdirectionalityaccurately. To reduce the number of sequences to be analyzed phylogenetically, we used cd-hit (*176*) to isolate 3500 unit sequences that were less than 0.999 similar to one another. We used the command line: cd-hit -i all_sj_haps_18kb_cat_pos_neg.fa -o all_sj_haps_18kb_cat_pos_neg_cdhit -T 4 -c 0.999 -M 100000 -n 5 -d 0.

These 3500 sequences were analyzed with the neighbor-joining method (*177*) as implemented in ape (*158*), using the Kimura 2-parameter distance (*178*). Negative branch lengths were adjusted by first setting them to 0, then reallocating the distance to the adjacent branch so that the distances between adjacent terminal nodes are not changed. The tree was depicted using functions in the R packages ape (*158*) and ggtree (*179*).

Telomeres: Telomeres were initially quantified using Satellite Repeat Finder and RepeatMasker. One of the ~300 satellites identified by SRF, sj_sat_circ86-113, corresponded to the canonical vertebrate telomere motif (TTAGGG)n, and was used either as baits in command-line blast searches (*153*) or quantified using SRF satellite distributions. During the analysis phase of this project, seqtk telo was added to the seqtk set of scripts (*180*) and subsequently was used for all telomere analyses. Seqtk telo counts telomeric sequences occurring at the ends of contigs or scaffolds. It currently ignores telomeric sequence not occurring at the ends of reads, contigs or scaffolds. Telomere abundances were calculated as the fraction of telomeric sequence divided by the total base pairs in the target, whether HiFi reads, haplotypes or primary assemblies.

Panacus plots: We estimated the pangenome growth curve and core size using panacus (*88*) on PGGB .gfa file. To compare growth curves among scrub-jays, humans, and chickens, we obtained a human pangenome graph [PGGB GFA; https://github.com/human-pangenomics/hpp_pangenome_resources; (*32*)] containing 44 samples from four populations [Punjabi from Lahore, Pakistan (PJL), East Asian (EAS), Admixed American (AMR)], as well as a chicken pangenome [PGGB GFA; https://zenodo.org/records/10018222; (*89*)] containing 18 samples. We then performed panacus analyses on both the human and chicken pangenomes.

Constructing SFSs for SNPs and SVs: We wrote a custom script (available at https://github.com/harvardinformatics/scrub-jay-genomics) to parse the PGGB VCF file into a tabular format facilitating plotting and tabulating. This table (available in the supplementary materials), in bed format with each row consisting of a single variant (SNP, indel, or SV), recorded the overlap of each SV with annotations, such as CNEEs, exons, introns, or intergenic regions, as well as overlaps with RepeatMasker repeats. The table also recorded the ancestral and alternative alleles as indicated in the outgroup (CY), as well as the type of variant (DEL, DEL_COMPLEX, INDEL_COMPLEX, INS, INS_Complex, SNP, SV_Complex, SVDEL, SVDEL_Complex, SVINS, SVINS_Complex). There are columns recording whether or not the variant represents an inversion; whether the variant is polarized; the ancestral and derived allele(s); the base and alternate allele length(s); maximum length of variants; and the allele count. Additionally, the derived allele count (DAC) was recorded for each species (AW, AC, and AI), as well as the number of haplotypes per species missing for a given variant, and the total number of alleles for the variant. We constructed SFSs for various classes of variation from this table. To compute unfolded (polarized) SFS, we first filtered to retain only biallelic variants (allele number = 2) that are polarized (polarized = TRUE). For most analysis, we also filter to only retain sites with no missing data. We then summarized counts of sites in each frequency bin (derived allele count, summarized separately for each of AC, AI, and AW) for SNPs (allele length = 1), INDELs (allele length > 1 and < 50), and SVs (allele length ≥ 50).

Estimating the DFEs: We used the maximum-likelihood programs fastDFE (*97*) and anavar (*96*) to estimate the DFEs for SNPs, INDELs, and SVs,

following the methods detailed by Fang and Edwards (*16*). Both methods use the SFS to infer the population-scaled mutation rate ($\theta = 4N_e\mu$, where N_e is the effective population size and μ is the per-site, per-generation mutation rate) and to fit shape and scale parameters of a gamma distribution for the population-scaled selection coefficients ($\gamma = 4N_e s$, with s being the selection coefficient). These approaches also control for demographic factors and polarization errors, following the method outlined by Eyre-Walker *et al.* (*181*).

We generated the unfolded SFS from the PGGB VCF for each species, targeting variants grouped by size class (SNPs, INDELs, SVs) and genomic region (CNEE, exon, intron) as described above. Only polarized, biallelic variants with complete data were included in the SFS and subsequent DFE analyses. In fastDFE, we fitted the SFS to the "GammaExpParametrization" model; in anavar, we fitted the SFS to "neutralSNP_vs_selectiveSNP" for SNP datasets and "neutralINDEL_vs_selectedINDEL" for INDEL and SV datasets, applying a continuous gamma distribution. Both programs used a putatively neutral reference SFS derived from intergenic variants to account for demography and polarization errors.

We report the gamma distributions as the proportion of variants within four bins of scaled selection coefficients (γ): neutral ($0 \leq -N_e s \leq 1$), weak ($1 < -N_e s \leq 10$), moderate ($10 < -N_e s \leq 100$), and strong ($-N_e s > 100$). In anavar, these bins are the default output; in fastDFE, we specified them as c(−Inf, −100, −10, −1, 0). All estimates of γ are negative, reflecting the deleterious nature of the mutations, based on the assumption that beneficial mutations are typically rare and subject to strong positive selection, leading to their rapid fixation in the population and minimal contribution to DFE (*7*, *182*) We derived 95% confidence intervals via parametric bootstrapping in fastDFE (using the inf.bootstrap function) and by gene permutation in anavar. Finally, using the same procedures, we also inferred DFEs for variants subdivided into size classes from 1 to 100 bp.

Detecting and quantifying inversions: We used PGGB (*183*), minigraph2 (*33*), SyRi (*93*), and svim-asm (*91*) to identify inversions across the three core *Aphelocoma* species. We also used lostruct (*94*) to identify large inversions. The PGGB vcf flags inversions when using recent versions of vcfwave (*168*), as of July 2023. The decomposed vcf produces a comment in the information column, "INV=YES," which was used to count inversions and retrieve their coordinates. Similarly, minigraph2 also lists inversions in the outputted vcf file. SyRi uses whole-genome alignment between a reference and a query genome to detect inversions. We broadly followed methods in (*16*).

To produce chromosome-scale inputs for SyRI, we first scaffolded our haplotype assemblies with RagTag (*145*); this will in principle normalize inversions between the haplotype and the reference when no contig in the haplotype assembly spans a breakpoint, but in these cases we have limited power to detect inversions in the first place. These scaffolded haplotype assemblies were aligned to the AW reference using minimap2 with the preset –eqx option, and the output was sorted into BAM files with samtools (*184*). Next, SyRI was applied to each BAM file to detect structural rearrangements, including inversions. The inversions were extracted from the SyRI output using awk (awk '$11=="INV"').

Svim-asm works with minimap to detect inversions and other SVs. We first mapped each haplotype to whichever reference was being used using minimap2; we used the AW reference for most analyses, but also used the CY outgroup and the recently published genome of *Cyanocitta stelleri* [Steller's jay; (*53*)]. The bam files produced by minimap2 were used as input for svim-asm in diploid mode; each run used the two bam files produced by the two haplotypes of each individual. The minimum variant size was set to 50 bp. Options --query_names and --symbolic_alleles were used to aid in vcf interpretation. Vcf files were parsed and inversions flagged as incomplete were retained and included in the final counts.

All of the above methods for detecting inversions are best at detecting small to moderately sized (50 to ~3 Mb) inversions, so we supplemented these approaches with genome-scanning methods, such as Lostruct (*94*). Lostruct uses multidimensional scaling (MDS) to infer subgroupings of haplotypes or individuals that diverge in their snp profiles, which may indicate an inversion. The main PGGB VCF was parsed by chromosome and by species, retaining only biallelic snps with no missing data. VCF files were loaded into R using the "read_vcf" function and eigenvalues were calculated for sliding windows of 5000 or 50,000 bp, depending on the SNP density in the VCF. Principal components were calculated with for each haplotype using "pc_dist." These PCs were then plotted on a 2D plot using the "cmdscale" function and saved. The coordinates of the resulting MDS plot were converted to genomic coordinates to aid in inversion location.

The resulting MDS plots each chromosome/species were visually inspected for abrupt shifts in the value of MDS1 that could indicate an inversion. Breakpoints in the MDS plots were estimated using the Bayesian breakpoint analysis tool mcp (*185*). MDS plots were visually inspected and the posterior distribution of the breakpoint(s) was manually shifted using strong priors when necessary. MCP alone often placed breakpoints earlier in the chromosome scan than expected given the major shift and number of potential shifts in MDS values across the chromosome. The mean position of each breakpoint was recorded and converted to a bed file for each chromosome.

The bed files were used to calculate principal components for each putative inversion genotype for each individual using SNPRelate (*186*). Heterozygosity for each putative inversion genotype was estimated using VCFtools [vcftools --het.; (*151*)].

To quantify the sharing of inversions between species, we used the 292 inversions identified by Syri to calculate allele frequency differences between species as well as Fst (*187*), using SNPRelate (*186*). These allele frequency spectra indicated that some inversions are fixed or nearly fixed between species, whereas some have more similar frequencies between species (fig. S39).

Pangene: Pangene (*106*) aligns protein sequences to genome assemblies to produce a graph of coding regions for a collection of genomes. We aligned annotated protein sequences from TOGA to each haplotype using miniprot (*105*), which creates a protein .paf file. This .paf file was used as input for pangene, which produces a .gfa file. The pangene-1.1-bin-sj.tar.bz2 file, shared on Dryad (*166*), contains instructions and data for building a local version of an interactive tool to explore the pangene results.

REFERENCES AND NOTES

1. T. Ohta, Near-neutrality in evolution of genes and gene regulation. *Proc. Natl. Acad. Sci. U.S.A.* **99**, 16134–16137 (2002). doi: 10.1073/pnas.252626899; pmid: 12461171
2. M. Lynch, *The Origins of Genome Architecture* (Sinauer Associates, 2007).
3. S. Mathur, A. J. Mason, G. S. Bradburd, H. L. Gibbs, Functional genomic diversity is correlated with neutral genomic diversity in populations of an endangered rattlesnake. *Proc. Natl. Acad. Sci. U.S.A.* **120**, e2303043120 (2023). doi: 10.1073/pnas.2303043120; pmid: 37844221
4. A. R. Hoelzel *et al.*, Genomics of post-bottleneck recovery in the northern elephant seal. *Nat. Ecol. Evol.* **8**, 686–694 (2024). doi: 10.1038/s41559-024-02337-4; pmid: 38383849
5. J. I. Hoffman *et al.*, Genomic and fitness consequences of a near-extinction event in the northern elephant seal. *Nat. Ecol. Evol.* **8**, 2309–2324 (2024). doi: 10.1038/s41559-024-02533-2; pmid: 39333394
6. S. Mathur, J. A. DeWoody, Genetic load has potential in large populations but is realized in small inbred populations. *Evol. Appl.* **14**, 1540–1557 (2021). doi: 10.1111/eva.13216; pmid: 34178103
7. J. Robinson, C. C. Kyriazis, S. C. Yuan, K. E. Lohmueller, Deleterious Variation in Natural Populations and Implications for Conservation Genetics. *Annu. Rev. Anim. Biosci.* **11**, 93–114 (2023). doi: 10.1146/annurev-animal-080522-093311; pmid: 36332644
8. T. Hämälä *et al.*, Genomic structural variants constrain and facilitate adaptation in natural populations of *Theobroma cacao*, the chocolate tree. *Proc. Natl. Acad. Sci. U.S.A.* **118**, e2102914118 (2021). doi: 10.1073/pnas.2102914118; pmid: 34408075

9. A. Catanach *et al.*, The genomic pool of standing structural variation outnumbers single nucleotide polymorphism by threefold in the marine teleost *Chrysophrys auratus*. *Mol. Ecol.* **28**, 1210–1223 (2019). doi: 10.1111/mec.15051; pmid: 30770610
10. 1000 Genomes Project Consortium, A global reference for human genetic variation. *Nature* **526**, 68–74 (2015). doi: 10.1038/nature15393; pmid: 26432245
11. K. E. Delmore *et al.*, Structural genomic variation and migratory behavior in a wild songbird. *Evol. Lett.* **7**, 401–412 (2023). doi: 10.1093/evlett/qrad040; pmid: 38045725
12. T. Günther, C. Nettelblad, The presence and impact of reference bias on population genomic studies of prehistoric human populations. *PLOS Genet.* **15**, e1008302 (2019). doi: 10.1371/journal.pgen.1008302; pmid: 31348818
13. M. J. Lin, S. Iyer, N. C. Chen, B. Langmead, Measuring, visualizing, and diagnosing reference bias with biastools. *Genome Biol.* **25**, 101 (2024). doi: 10.1186/s13059-024-03240-8; pmid: 38641647
14. R. Martiniano, E. Garrison, E. R. Jones, A. Manica, R. Durbin, Removing reference bias and improving indel calling in ancient DNA data analysis by mapping to a sequence variation graph. *Genome Biol.* **21**, 250 (2020). doi: 10.1186/s13059-020-02160-7; pmid: 32943086
15. P. Ebert *et al.*, Haplotype-resolved diverse human genomes and integrated analysis of structural variation. *Science* **372**, eabf7117 (2021). doi: 10.1126/science.abf7117; pmid: 33632895
16. B. Fang, S. V. Edwards, Fitness consequences of structural variation inferred from a House Finch pangenome. *Proc. Natl. Acad. Sci. U.S.A.* **121**, e2409943121 (2024). doi: 10.1073/pnas.2409943121; pmid: 39531493
17. H. J. Barton, K. Zeng, The Impact of Natural Selection on Short Insertion and Deletion Variation in the Great Tit Genome. *Genome Biol. Evol.* **11**, 1514–1524 (2019). doi: 10.1093/gbe/evz068; pmid: 30924871
18. U. Knief *et al.*, Evolution of Chromosomal Inversions across an Avian Radiation. *Mol. Biol. Evol.* **41**, msae092 (2024). doi: 10.1093/molbev/msae092; pmid: 38743589
19. E. R. Funk *et al.*, A supergene underlies linked variation in color and morphology in a Holarctic songbird. *Nat. Commun.* **12**, 6833 (2021). doi: 10.1038/s41467-021-27173-z; pmid: 34824228
20. U. Knief *et al.*, Fitness consequences of polymorphic inversions in the zebra finch genome. *Genome Biol.* **17**, 199 (2016). doi: 10.1186/s13059-016-1056-3; pmid: 27687629
21. J. L. Rocha, R. N. Lou, P. H. Sudmant, Structural variation in humans and our primate kin in the era of telomere-to-telomere genomes and pangenomics. *Curr. Opin. Genet. Dev.* **87**, 102233 (2024). doi: 10.1016/j.gde.2024.102233; pmid: 39042999
22. Y. Mao *et al.*, Structurally divergent and recurrently mutated regions of primate genomes. *Cell* **187**, 1547–1562.e13 (2024). doi: 10.1016/j.cell.2024.01.052; pmid: 38428424
23. J. M. Eizenga *et al.*, Pangenome Graphs. *Annu. Rev. Genomics Hum. Genet.* **21**, 139–162 (2020). doi: 10.1146/annurev-genom-120219-080406; pmid: 32453966
24. B. Paten, A. M. Novak, J. M. Eizenga, E. Garrison, Genome graphs and the evolution of genome inference. *Genome Res.* **27**, 665–676 (2017). doi: 10.1101/gr.214155.116; pmid: 28360232
25. S. Secomandi *et al.*, Pangenome graphs and their applications in biodiversity genomics. *Nat. Genet.* **57**, 13–26 (2025). doi: 10.1038/s41588-024-02029-6; pmid: 39779953
26. A. S. Leonard, D. Crysnanto, X. M. Mapel, M. Bhati, H. Pausch, Graph construction method impacts variation representation and analyses in a bovine super-pangenome. *Genome Biol.* **24**, 124 (2023). doi: 10.1186/s13059-023-02969-y; pmid: 37217946
27. J. Wang *et al.*, A pangenome analysis pipeline provides insights into functional gene identification in rice. *Genome Biol.* **24**, 19 (2023). doi: 10.1186/s13059-023-02861-9; pmid: 36703158
28. P. E. Bayer, A. A. Golicz, A. Scheben, J. Batley, D. Edwards, Plant pan-genomes are the new reference. *Nat. Plants* **6**, 914–920 (2020). doi: 10.1038/s41477-020-0733-0; pmid: 32690893
29. M. Schreiber, M. Jayakodi, N. Stein, M. Mascher, Plant pangenomes for crop improvement, biodiversity and evolution. *Nat. Rev. Genet.* **25**, 563–577 (2024). doi: 10.1038/s41576-024-00691-4; pmid: 38378816
30. F. Rosconi *et al.*, A bacterial pan-genome makes gene essentiality strain-dependent and evolvable. *Nat. Microbiol.* **7**, 1580–1592 (2022). doi: 10.1038/s41564-022-01208-7; pmid: 36097170
31. L. Rouli, V. Merhej, P. E. Fournier, D. Raoult, The bacterial pangenome as a new tool for analysing pathogenic bacteria. *New Microbes New Infect.* **7**, 72–85 (2015). doi: 10.1016/j.nmni.2015.06.005; pmid: 26442149
32. W. W. Liao *et al.*, A draft human pangenome reference. *Nature* **617**, 312–324 (2023). doi: 10.1038/s41586-023-05896-x; pmid: 37165242
33. H. Li, X. Feng, C. Chu, The design and construction of reference pangenome graphs with minigraph. *Genome Biol.* **21**, 265 (2020). doi: 10.1186/s13059-020-02168-z; pmid: 33066802
34. W. De Coster, M. H. Weissensteiner, F. J. Sedlazeck, Towards population-scale long-read sequencing. *Nat. Rev. Genet.* **22**, 572–587 (2021). doi: 10.1038/s41576-021-00367-3; pmid: 34050336
35. G. A. Bravo, C. J. Schmitt, S. V. Edwards, What Have We Learned from the First 500 Avian Genomes? *Annu. Rev. Ecol. Evol. Syst.* **52**, 611–639 (2021). doi: 10.1146/annurev-ecolsys-012121-085928
36. H. Ellegren, The Evolutionary Genomics of Birds. *Annu. Rev. Ecol. Evol. Syst.* **44**, 239–259 (2013). doi: 10.1146/annurev-ecolsys-110411-160327
37. J. D. Galbraith, R. D. Kortschak, A. Suh, D. L. Adelson, Genome Stability Is in the Eye of the Beholder: CR1 Retrotransposon Activity Varies Significantly across Avian Diversity. *Genome Biol. Evol.* **13**, evab259 (2021). doi: 10.1093/gbe/evab259; pmid: 34894225
38. D. K. Griffin *et al.*, Insights into avian molecular cytogenetics—with reptilian comparisons. *Mol. Cytogenet.* **17**, 24 (2024). doi: 10.1186/s13039-024-00696-y; pmid: 39482771
39. G. Zhang *et al.*, Comparative genomics reveals insights into avian genome evolution and adaptation. *Science* **346**, 1311–1320 (2014). doi: 10.1126/science.1251385; pmid: 25504712
40. J. Stiller, G. Zhang, Comparative Phylogenomics, a Stepping Stone for Bird Biodiversity Studies. *Diversity* **11**, 115 (2019). doi: 10.3390/d11070115
41. J. D. Manthey, R. G. Moyle, S. Boissinot, Multiple and Independent Phases of Transposable Element Amplification in the Genomes of Piciformes (Woodpeckers and Allies). *Genome Biol. Evol.* **10**, 1445–1456 (2018). doi: 10.1093/gbe/evy105; pmid: 29850797
42. T. Yuri, R. T. Kimball, E. L. Braun, M. J. Braun, Duplication of accelerated evolution and growth hormone gene in passerine birds. *Mol. Biol. Evol.* **25**, 352–361 (2008). doi: 10.1093/molbev/msm260; pmid: 18048401
43. S. Feng *et al.*, Dense sampling of bird diversity increases power of comparative genomics. *Nature* **587**, 252–257 (2020). doi: 10.1038/s41586-020-2873-9; pmid: 33177665
44. D. A. DeRaad, J. E. McCormack, N. Chen, A. T. Peterson, R. G. Moyle, Combining Species Delimitation, Species Trees, and Tests for Gene Flow Clarifies Complex Speciation in Scrub-Jays. *Syst. Biol.* **71**, 1453–1470 (2022). doi: 10.1093/sysbio/syac034; pmid: 35552760
45. N. Chen *et al.*, Allele frequency dynamics in a pedigreed natural population. *Proc. Natl. Acad. Sci. U.S.A.* **116**, 2158–2164 (2019). doi: 10.1073/pnas.1813852116; pmid: 30598449
46. S. M. Aguillon *et al.*, Deconstructing isolation-by-distance: The genomic consequences of limited dispersal. *PLOS Genet.* **13**, e1006911 (2017). doi: 10.1371/journal.pgen.1006911; pmid: 28771477
47. N. Chen, E. J. Cosgrove, R. Bowman, J. W. Fitzpatrick, A. G. Clark, Genomic Consequences of Population Decline in the Endangered Florida Scrub-Jay. *Curr. Biol.* **26**, 2974–2979 (2016). doi: 10.1016/j.cub.2016.08.062; pmid: 27746026
48. J. E. McCormack, J. Heled, K. S. Delaney, A. T. Peterson, L. L. Knowles, Calibrating divergence times on species trees versus gene trees: Implications for speciation history of *Aphelocoma* jays. *Evolution* **65**, 184–202 (2011). doi: 10.1111/j.1558-5646.2010.01097.x; pmid: 20681982
49. G. E. Woolfenden, J. W. Fitzpatrick, *The Florida Scrub Jay: Demography of a Cooperative-Breeding Bird* (Princeton Univ. Press, 1984).
50. J. L. Brown, S.-H. Li, Phylogeny of social behavior in *Aphelocoma* jays: A role for hybridization? *Auk* **112**, 464–472 (1995). doi: 10.2307/4088734
51. A. T. Peterson, Phylogeny and rates of molecular evolution in the *Aphelocoma* jays (Corvidae). *Auk* **109**, 133–147 (1992). doi: 10.2307/4088274
52. D. A. DeRaad *et al.*, De novo assembly of a chromosome-level reference genome for the California Scrub-Jay, *Aphelocoma californica*. *J. Hered.* **114**, 669–680 (2023). doi: 10.1093/jhered/esad047; pmid: 37589384
53. P. M. Benham *et al.*, A highly contiguous reference genome for the Steller's jay (*Cyanocitta stelleri*). *J. Hered.* **114**, 549–560 (2023). doi: 10.1093/jhered/esad042; pmid: 37395718
54. S. W. Fernando, A. T. Peterson, S.-H. Li, Reconstructing the geographic origin of the New World jays. *Neotrop. Biodivers.* **3**, 80–92 (2017). doi: 10.1080/23766808.2017.1296751
55. H. Cheng, G. T. Concepcion, X. Feng, H. Zhang, H. Li, Haplotype-resolved de novo assembly using phased assembly graphs with hifiasm. *Nat. Methods* **18**, 170–175 (2021). doi: 10.1038/s41592-020-01056-5; pmid: 33526886
56. R. M. H. Driscoll *et al.*, Allele frequency dynamics under sex-biased demography and sex-specific inheritance in a pedigreed jay population. *Genetics* **227**, iyae075 (2024). doi: 10.1093/genetics/iyae075; pmid: 38722645
57. J. T. Sutton *et al.*, A High-Quality, Long-Read *De Novo* Genome Assembly to Aid Conservation of Hawaii's Last Remaining Crow Species. *Genes* **9**, 393 (2018). doi: 10.3390/genes9080393; pmid: 30071683
58. B. M. Kirilenko *et al.*, Integrating gene annotation with orthology inference at scale. *Science* **380**, eabn3107 (2023). doi: 10.1126/science.abn3107; pmid: 37104600
59. T. M. Degrandi *et al.*, Introducing the Bird Chromosome Database: An Overview of Cytogenetic Studies in Birds. *Cytogenet. Genome Res.* **160**, 199–205 (2020). doi: 10.1159/000507768; pmid: 32369809
60. H. Li *et al.*, A synthetic-diploid benchmark for accurate variant-calling evaluation. *Nat. Methods* **15**, 595–597 (2018). doi: 10.1038/s41592-018-0054-7; pmid: 30013044
61. H. Li, R. Durbin, Inference of human population history from individual whole-genome sequences. *Nature* **475**, 493–496 (2011). doi: 10.1038/nature10231; pmid: 21753753
62. B. Rannala, Z. Yang, Efficient Bayesian species tree inference under the multispecies coalescent. *Syst. Biol.* **66**, 823–842 (2017). doi: 10.1093/sysbio/syw119; pmid: 28053140
63. Materials and methods are available at the end of this article.

64. J. D. Sigwart, D. R. Lindberg, C. Chen, J. Sun, Molluscan phylogenomics requires strategically selected genomes. *Phil. Trans. R. Soc. B* **376**, 20200161 (2021). doi: 10.1098/rstb.2020.0161; pmid: 33813889
65. A. Rhie *et al.*, Towards complete and error-free genome assemblies of all vertebrate species. *Nature* **592**, 737–746 (2021). doi: 10.1038/s41586-021-03451-0; pmid: 33911273
66. A. F. A. Smit, R. Hubley, P. Green, RepeatMasker Open-4.0 (2015); http://www.repeatmasker.org.
67. J. M. Flynn *et al.*, RepeatModeler2 for automated genomic discovery of transposable element families. *Proc. Natl. Acad. Sci. U.S.A.* **117**, 9451–9457 (2020). doi: 10.1073/pnas.1921046117; pmid: 32300014
68. Y. Zhang, J. Chu, H. Cheng, H. Li, De novo reconstruction of satellite repeat units from sequence data. *Genome Res.* **33**, 1994–2001 (2023). doi: 10.1101/gr.278005.123; pmid: 37918962
69. P. M. Benham *et al.*, Remarkably High Repeat Content in the Genomes of Sparrows: The Importance of Genome Assembly Completeness for Transposable Element Discovery. *Genome Biol. Evol.* **16**, evae067 (2024). doi: 10.1093/gbe/evae067; pmid: 38566597
70. H. T. Baalsrud *et al.*, Evolutionary new centromeres in the snowy owl genome putatively seeded from a transposable element. bioRxiv 2024.07.05.602039 [Preprint] (2024). doi: 10.1101/2024.07.05.602039
71. Z. Huang *et al.*, Evolutionary analysis of a complete chicken genome. *Proc. Natl. Acad. Sci. U.S.A.* **120**, e2216641120 (2023). doi: 10.1073/pnas.2216641120; pmid: 36780517
72. V. Peona, V. E. Kutschera, M. P. K. Blom, M. Irestedt, A. Suh, Satellite DNA evolution in Corvoidea inferred from short and long reads. *Mol. Ecol.* **32**, 1288–1305 (2023). doi: 10.1111/mec.16484; pmid: 35488497
73. K. A. Jønsson *et al.*, A supermatrix phylogeny of corvoid passerine birds (Aves: Corvides). *Mol. Phylogenet. Evol.* **94**, 87–94 (2016). doi: 10.1016/j.ympev.2015.08.020; pmid: 26327328
74. J. Thakur, J. Packiaraj, S. Henikoff, Sequence, Chromatin and Evolution of Satellite DNA. *Int. J. Mol. Sci.* **22**, 4309 (2021). doi: 10.3390/ijms22094309; pmid: 33919233
75. M. K. Rudd, G. A. Wray, H. F. Willard, The evolutionary dynamics of alpha-satellite. *Genome Res.* **16**, 88–96 (2006). doi: 10.1101/gr.3810906; pmid: 16344556
76. G. Dover, Molecular drive: A cohesive mode of species evolution. *Nature* **299**, 111–117 (1982). doi: 10.1038/299111a0; pmid: 7110332
77. G. M. Tricola *et al.*, The rate of telomere loss is related to maximum lifespan in birds. *Phil. Trans. R. Soc. B* **373**, 20160445 (2018). doi: 10.1098/rstb.2016.0445; pmid: 29335369
78. L. M. Brown, M. C. Elbon, A. Bharadwaj, G. Damle, J. Lachance, Does Effective Population Size Govern Evolutionary Differences in Telomere Length? *Genome Biol. Evol.* **16**, evae111 (2024). doi: 10.1093/gbe/evae111; pmid: 38771124
79. G. Bosco, P. Campbell, J. T. Leiva-Neto, T. A. Markow, Analysis of Drosophila species genome size and satellite DNA content reveals significant differences among strains as well as between species. *Genetics* **177**, 1277–1290 (2007). doi: 10.1534/genetics.107.075069; pmid: 18039867
80. C.-P. Stelzer, M. Pichler, A. Hatheuer, Linking genome size variation to population phenotypic variation within the rotifer, *Brachionus asplanchnoidis*. *Commun. Biol.* **4**, 596 (2021). doi: 10.1038/s42003-021-02131-z; pmid: 34011946
81. C. Biémont, Genome size evolution: Within-species variation in genome size. *Heredity* **101**, 297–298 (2008). doi: 10.1038/hdy.2008.80; pmid: 18665185
82. E. Garrison *et al.*, Building pangenome graphs. *Nat. Methods* **21**, 2008–2012 (2024). doi: 10.1038/s41592-024-02430-3; pmid: 39433878
83. F. Andreace, P. Lechat, Y. Dufresne, R. Chikhi, Comparing methods for constructing and representing human pangenome graphs. *Genome Biol.* **24**, 274 (2023). doi: 10.1186/s13059-023-03098-2; pmid: 38037131
84. D. Yoo *et al.*, Complete sequencing of ape genomes. *Nature* **641**, 401–418 (2025). doi: 10.1038/s41586-025-08816-3; pmid: 40205052
85. S. Kumar *et al.*, TimeTree 5: An Expanded Resource for Species Divergence Times. *Mol. Biol. Evol.* **39**, msac174 (2022). doi: 10.1093/molbev/msac174; pmid: 35932227
86. R. E. Green *et al.*, Three crocodilian genomes reveal ancestral patterns of evolution among archosaurs. *Science* **346**, 1254449 (2014). doi: 10.1126/science.1254449; pmid: 25504731
87. A. Guarracino, S. Heumos, S. Nahnsen, P. Prins, E. Garrison, ODGI: Understanding pangenome graphs. *Bioinformatics* **38**, 3319–3326 (2022). doi: 10.1093/bioinformatics/btac308; pmid: 35552372
88. L. Parmigiani, E. Garrison, J. Stoye, T. Marschall, D. Doerr, Panacus: Fast and exact pangenome growth and core size estimation. *Bioinformatics* **40**, btae720 (2024). doi: 10.1093/bioinformatics/btae720; pmid: 39626271
89. E. S. Rice *et al.*, A pangenome graph reference of 30 chicken genomes allows genotyping of large and complex structural variants. *BMC Biol.* **21**, 267 (2023). doi: 10.1186/s12915-023-01758-0; pmid: 37993882
90. K. Nam, H. Ellegren, Recombination drives vertebrate genome contraction. *PLOS Genet.* **8**, e1002680 (2012). doi: 10.1371/journal.pgen.1002680; pmid: 22570634
91. D. Heller, M. Vingron, SVIM-asm: Structural variant detection from haploid and diploid genome assemblies. *Bioinformatics* **36**, 5519–5521 (2020). doi: 10.1093/bioinformatics/btaa1034; pmid: 33346817
92. T. B. Sackton *et al.*, Convergent regulatory evolution and loss of flight in paleognathous birds. *Science* **364**, 74–78 (2019). doi: 10.1126/science.aat7244; pmid: 30948549
93. M. Goel, H. Sun, W.-B. Jiao, K. Schneeberger, SyRI: Finding genomic rearrangements and local sequence differences from whole-genome assemblies. *Genome Biol.* **20**, 277 (2019). doi: 10.1186/s13059-019-1911-0; pmid: 31842948
94. H. Li, P. Ralph, Local PCA Shows How the Effect of Population Structure Differs Along the Genome. *Genetics* **211**, 289–304 (2019). doi: 10.1534/genetics.118.301747; pmid: 30459280
95. S. M. Schaal, B. C. Haller, K. E. Lotterhos, Inversion invasions: When the genetic basis of local adaptation is concentrated within inversions in the face of gene flow. *Phil. Trans. R. Soc. B* **377**, 20210200 (2022). doi: 10.1098/rstb.2021.0200; pmid: 35694752
96. H. J. Barton, K. Zeng, New Methods for Inferring the Distribution of Fitness Effects for INDELs and SNPs. *Mol. Biol. Evol.* **35**, 1536–1546 (2018). doi: 10.1093/molbev/msy054; pmid: 29635416
97. J. Sendrowski, T. Bataillon, fastDFE: Fast and Flexible Inference of the Distribution of Fitness Effects. *Mol. Biol. Evol.* **41**, msae070 (2024). doi: 10.1093/molbev/msae070; pmid: 38577958
98. P. Tataru, M. Mollion, S. Glémin, T. Bataillon, Inference of Distribution of Fitness Effects and Proportion of Adaptive Substitutions from Polymorphism Data. *Genetics* **207**, 1103–1119 (2017). doi: 10.1534/genetics.117.300323; pmid: 28951530
99. S. Glémin *et al.*, Quantification of GC-biased gene conversion in the human genome. *Genome Res.* **25**, 1215–1228 (2015). doi: 10.1101/gr.185488.114; pmid: 25995268
100. E. M. Kvikstad, L. Duret, Strong heterogeneity in mutation rate causes misleading hallmarks of natural selection on indel mutations in the human genome. *Mol. Biol. Evol.* **31**, 23–36 (2014). doi: 10.1093/molbev/mst185; pmid: 24113537
101. N. Stoletzki, A. Eyre-Walker, Estimation of the neutrality index. *Mol. Biol. Evol.* **28**, 63–70 (2011). doi: 10.1093/molbev/msq249; pmid: 20837603
102. N. G. Smith, A. Eyre-Walker, Adaptive protein evolution in *Drosophila*. *Nature* **415**, 1022–1024 (2002). doi: 10.1038/4151022a; pmid: 11875568
103. P. Andolfatto, Adaptive evolution of non-coding DNA in *Drosophila*. *Nature* **437**, 1149–1152 (2005). doi: 10.1038/nature04107; pmid: 16237443
104. T. I. Gossmann *et al.*, Genome wide analyses reveal little evidence for adaptive evolution in many plant species. *Mol. Biol. Evol.* **27**, 1822–1832 (2010). doi: 10.1093/molbev/msq079; pmid: 20299543
105. H. Li, Protein-to-genome alignment with miniprot. *Bioinformatics* **39**, btad014 (2023). doi: 10.1093/bioinformatics/btad014; pmid: 36648328
106. H. Li, M. Marin, M. R. Farhat, Exploring gene content with pangene graphs. *Bioinformatics* **40**, btae456 (2024). doi: 10.1093/bioinformatics/btae456; pmid: 39041615
107. M. Lynch, J. S. Conery, The evolutionary fate and consequences of duplicate genes. *Science* **290**, 1151–1155 (2000). doi: 10.1126/science.290.5494.1151; pmid: 11073452
108. K. J. Lipinski *et al.*, High spontaneous rate of gene duplication in *Caenorhabditis elegans*. *Curr. Biol.* **21**, 306–310 (2011). doi: 10.1016/j.cub.2011.01.026; pmid: 21295484
109. N. Keith *et al.*, High mutational rates of large-scale duplication and deletion in *Daphnia pulex*. *Genome Res.* **26**, 60–69 (2016). doi: 10.1101/gr.191338.115; pmid: 26518480
110. D. R. Schrider, D. Houle, M. Lynch, M. W. Hahn, Rates and genomic consequences of spontaneous mutational events in *Drosophila melanogaster*. *Genetics* **194**, 937–954 (2013). doi: 10.1534/genetics.113.151670; pmid: 23733788
111. M. Lynch *et al.*, A genome-wide view of the spectrum of spontaneous mutations in yeast. *Proc. Natl. Acad. Sci. U.S.A.* **105**, 9272–9277 (2008). doi: 10.1073/pnas.0803466105; pmid: 18583475
112. R. L. Collins *et al.*, A cross-disorder dosage sensitivity map of the human genome. *Cell* **185**, 3041–3055.e25 (2022). doi: 10.1016/j.cell.2022.06.036; pmid: 35917817
113. R. L. Collins, M. E. Talkowski, Diversity and consequences of structural variation in the human genome. *Nat. Rev. Genet.* **26**, 443–462 (2025). doi: 10.1038/s41576-024-00808-9; pmid: 39838028
114. M. Naville *et al.*, Massive Changes of Genome Size Driven by Expansions of Non-autonomous Transposable Elements. *Curr. Biol.* **29**, 1161–1168.e6 (2019). doi: 10.1016/j.cub.2019.01.080; pmid: 30880010
115. M. Lamkin, M. Gymrek, The emerging role of tandem repeats in complex traits. *Nat. Rev. Genet.* **25**, 452–453 (2024). doi: 10.1038/s41576-024-00736-8; pmid: 38714860
116. F. Termignoni-Garcia, J. J. Kirchman, J. Clark, S. V. Edwards, Comparative Population Genomics of Cryptic Speciation and Adaptive Divergence in Bicknell's and Gray-Cheeked Thrushes (Aves: *Catharus bicknelli* and *Catharus minimus*). *Genome Biol. Evol.* **14**, evab255 (2022). doi: 10.1093/gbe/evab255; pmid: 34999784
117. A. Marino, G. Debaecker, A.-S. Fiston-Lavier, A. Haudry, B. Nabholz, Effective population size does not explain long-term variation in genome size and transposable element content in animals. *eLife* **13**, RP100574 (2024). doi: 10.7554/eLife.100574.2; pmid: 40679280
118. J. Stapley, A. W. Santure, S. R. Dennis, Transposable elements as agents of rapid adaptation may explain the genetic paradox of invasive species. *Mol. Ecol.* **24**, 2241–2252 (2015). doi: 10.1111/mec.13089; pmid: 25611725
119. L. Schrader, J. Schmitz, The impact of transposable elements in adaptive evolution. *Mol. Ecol.* **28**, 1537–1549 (2019). doi: 10.1111/mec.14794; pmid: 30003608
120. F. C. Jones *et al.*, The genomic basis of adaptive evolution in threespine sticklebacks. *Nature* **484**, 55–61 (2012). doi: 10.1038/nature10944; pmid: 22481358

121. J. L. Loveland *et al.*, A single gene orchestrates androgen variation underlying male mating morphs in ruffs. *Science* **387**, 406–412 (2025). doi: 10.1126/science.adp5936; pmid: 39847616
122. D. B. Lowry, J. H. Willis, A widespread chromosomal inversion polymorphism contributes to a major life-history transition, local adaptation, and reproductive isolation. *PLOS Biol.* **8**, e1000500 (2010). doi: 10.1371/journal.pbio.1000500; pmid: 20927411
123. K. T. Xie *et al.*, DNA fragility in the parallel evolution of pelvic reduction in stickleback fish. *Science* **363**, 81–84 (2019). doi: 10.1126/science.aan1425; pmid: 30606845
124. D. M. Klure, R. Greenhalgh, T. J. Orr, M. D. Shapiro, M. D. Dearing, Parallel gene expansions drive rapid dietary adaptation in herbivorous woodrats. *Science* **387**, 156–162 (2025). doi: 10.1126/science.adp7978; pmid: 39787210
125. B. M. Henn *et al.*, Distance from sub-Saharan Africa predicts mutational load in diverse human genomes. *Proc. Natl. Acad. Sci. U.S.A.* **113**, E440–E449 (2016). doi: 10.1073/pnas.1510805112; pmid: 26712023
126. J. Peter *et al.*, Genome evolution across 1,011 *Saccharomyces cerevisiae* isolates. *Nature* **556**, 339–344 (2018). doi: 10.1038/s41586-018-0030-5; pmid: 29643504
127. H. Jeong *et al.*, Structural polymorphism and diversity of human segmental duplications. *Nat. Genet.* **57**, 390–401 (2025). doi: 10.1038/s41588-024-02051-8; pmid: 39779957
128. T. S. Sillett, R. B. Chandler, J. A. Royle, M. Kéry, S. A. Morrison, Hierarchical distance-sampling models to estimate population size and habitat-specific abundance of an island endemic. *Ecol. Appl.* **22**, 1997–2006 (2012). doi: 10.1890/11-1400.1; pmid: 23210315
129. R. G. Cheek *et al.*, Habitat-linked genetic variation supports microgeographic adaptive divergence in an island-endemic bird species. *Mol. Ecol.* **31**, 2830–2846 (2022). doi: 10.1111/mec.16438; pmid: 35315161
130. S. Junak, *A Flora of Santa Cruz Island* (Santa Barbara Botanic Garden in collaboration with the California Native Plant Society, 1995).
131. D. T. Fischer, C. J. Still, A. P. Williams, Significance of summer fog and overcast for drought stress and ecological functioning of coastal California endemic plant species. *J. Biogeogr.* **36**, 783–799 (2009). doi: 10.1111/j.1365-2699.2008.02025.x
132. L. Caldwell *et al.*, Reproductive ecology of the island scrub-jay. *Condor* **115**, 603–613 (2013). doi: 10.1525/cond.2013.120028
133. G. Seutin, B. N. White, P. T. Boag, Preservation of avian blood and tissue samples for DNA analyses. *Can. J. Zool.* **69**, 82–90 (1991). doi: 10.1139/z91-013
134. K. M. Langin *et al.*, Islands within an island: Repeated adaptive divergence in a single population. *Evolution* **69**, 653–665 (2015). doi: 10.1111/evo.12610; pmid: 25645813
135. X. Zhou, M. Stephens, Genome-wide efficient mixed-model analysis for association studies. *Nat. Genet.* **44**, 821–824 (2012). doi: 10.1038/ng.2310; pmid: 22706312
136. J. S. Quinn, G. E. Woolfenden, J. W. Fitzpatrick, B. N. White, Multi-locus DNA fingerprinting supports genetic monogamy in Florida scrub-jays. *Behav. Ecol. Sociobiol.* **45**, 1–10 (1999). doi: 10.1007/s002650050534
137. A. K. Townsend, R. Bowman, J. W. Fitzpatrick, M. Dent, I. J. Lovette, Genetic monogamy across variable demographic landscapes in cooperatively breeding Florida scrub-jays. *Behav. Ecol.* **22**, 464–470 (2011). doi: 10.1093/beheco/arq227
138. N. Mejia, F. Termignoni-Garcia, J. Learned, J. Penniman, S. V. Edwards, Effects of plastic ingestion on blood chemistry, gene expression and body condition in wedge-tailed shearwaters (*Ardenna pacifica*). *PeerJ* **12**, e18566 (2024). doi: 10.7717/peerj.18566; pmid: 39619179
139. D. Khost, B. Fang, S. Edwards, T. Sackton, harvardinformatics/scrub-jay-genomics: v1.0.3, *Zenodo* (2025). doi: 10.5281/zenodo.16746467
140. M. Martin, Cutadapt removes adapter sequences from high-throughput sequencing reads. *EMBnet J.* **17**, 10–12 (2011). doi: 10.14806/ej.17.1.200
141. H. Li, R. Durbin, Fast and accurate short read alignment with Burrows-Wheeler transform. *Bioinformatics* **25**, 1754–1760 (2009). doi: 10.1093/bioinformatics/btp324; pmid: 19451168
142. A. R. Quinlan, I. M. Hall, BEDTools: A flexible suite of utilities for comparing genomic features. *Bioinformatics* **26**, 841–842 (2010). doi: 10.1093/bioinformatics/btq033; pmid: 20110278
143. C. Zhou, S. A. McCarthy, R. Durbin, YaHS: Yet another Hi-C scaffolding tool. *Bioinformatics* **39**, btac808 (2023). doi: 10.1093/bioinformatics/btac808; pmid: 36525368
144. N. C. Durand *et al.*, Juicer Provides a One-Click System for Analyzing Loop-Resolution Hi-C Experiments. *Cell Syst.* **3**, 95–98 (2016). doi: 10.1016/j.cels.2016.07.002; pmid: 27467249
145. M. Alonge *et al.*, Automated assembly scaffolding using RagTag elevates a new tomato system for high-throughput genome editing. *Genome Biol.* **23**, 258 (2022). doi: 10.1186/s13059-022-02823-7; pmid: 36522651
146. T. R. Ranallo-Benavidez, K. S. Jaron, M. C. Schatz, GenomeScope 2.0 and Smudgeplot for reference-free profiling of polyploid genomes. *Nat. Commun.* **11**, 1432 (2020). doi: 10.1038/s41467-020-14998-3; pmid: 32188846
147. G. Marçais, C. Kingsford, A fast, lock-free approach for efficient parallel counting of occurrences of *k*-mers. *Bioinformatics* **27**, 764–770 (2011). doi: 10.1093/bioinformatics/btr011; pmid: 21217122
148. H. Li, Minimap2: Pairwise alignment for nucleotide sequences. *Bioinformatics* **34**, 3094–3100 (2018). doi: 10.1093/bioinformatics/bty191; pmid: 29750242
149. M. Malinsky, M. Matschiner, H. Svardal, Dsuite - Fast *D*-statistics and related admixture evidence from VCF files. *Mol. Ecol. Resour.* **21**, 584–595 (2021). doi: 10.1111/1755-0998.13265; pmid: 33012121
150. P. Danecek *et al.*, Twelve years of SAMtools and BCFtools. *Gigascience* **10**, giab008 (2021). doi: 10.1093/gigascience/giab008; pmid: 33590861
151. P. Danecek *et al.*, The variant call format and VCFtools. *Bioinformatics* **27**, 2156–2158 (2011). doi: 10.1093/bioinformatics/btr330; pmid: 21653522
152. T. Koppetsch, M. Malinsky, M. Matschiner, Towards Reliable Detection of Introgression in the Presence of Among-Species Rate Variation. *Syst. Biol.* **73**, 769–788 (2024). doi: 10.1093/sysbio/syae028; pmid: 38912803
153. C. Camacho *et al.*, BLAST+: Architecture and applications. *BMC Bioinformatics* **10**, 421 (2009). doi: 10.1186/1471-2105-10-421; pmid: 20003500
154. K. Katoh, D. M. Standley, MAFFT multiple sequence alignment software version 7: Improvements in performance and usability. *Mol. Biol. Evol.* **30**, 772–780 (2013). doi: 10.1093/molbev/mst010; pmid: 23329690
155. T. Flouri, X. Jiao, B. Rannala, Z. Yang, Species Tree Inference with BPP Using Genomic Sequences and the Multispecies Coalescent. *Mol. Biol. Evol.* **35**, 2585–2593 (2018). doi: 10.1093/molbev/msy147; pmid: 30053098
156. L. T. Nguyen, H. A. Schmidt, A. von Haeseler, B. Q. Minh, IQ-TREE: A fast and effective stochastic algorithm for estimating maximum-likelihood phylogenies. *Mol. Biol. Evol.* **32**, 268–274 (2015). doi: 10.1093/molbev/msu300; pmid: 25371430
157. B. Q. Minh *et al.*, IQ-TREE 2: New Models and Efficient Methods for Phylogenetic Inference in the Genomic Era. *Mol. Biol. Evol.* **37**, 1530–1534 (2020). doi: 10.1093/molbev/msaa015; pmid: 32011700
158. E. Paradis, J. Claude, K. Strimmer, APE: Analyses of Phylogenetics and Evolution in R language. *Bioinformatics* **20**, 289–290 (2004). doi: 10.1093/bioinformatics/btg412; pmid: 14734327
159. S. Kalyaanamoorthy, B. Q. Minh, T. K. F. Wong, A. von Haeseler, L. S. Jermiin, ModelFinder: Fast model selection for accurate phylogenetic estimates. *Nat. Methods* **14**, 587–589 (2017). doi: 10.1038/nmeth.4285; pmid: 28481363
160. A. Rambaut, A. J. Drummond, D. Xie, G. Baele, M. A. Suchard, Posterior Summarization in Bayesian Phylogenetics Using Tracer 1.7. *Syst. Biol.* **67**, 901–904 (2018). doi: 10.1093/sysbio/syy032; pmid: 29718447
161. R. S. Harris, thesis, The Pennsylvania State University, University Park, PA (2007).
162. W. C. Warren *et al.*, The genome of a songbird. *Nature* **464**, 757–762 (2010). doi: 10.1038/nature08819; pmid: 20360741
163. G. Pertea, M. Pertea, GFF Utilities: GffRead and GffCompare. *F1000 Res.* **9**, 304 (2020). doi: 10.12688/f1000research.23297.1; pmid: 32489650
164. F. Tegenfeldt *et al.*, OrthoDB and BUSCO update: Annotation of orthologs with wider sampling of genomes. *Nucleic Acids Res.* **53**, D516–D522 (2025). doi: 10.1093/nar/gkae987; pmid: 39535043
165. A. Guarracino, N. Mwaniki, S. Marco-Sola, E. Garrison, wfmash: Whole-chromosome pairwise alignment using the hierarchical wavefront algorithm, GitHub (2021); https://github.com/waveygang/wfmash/tree/main.
166. S. Edwards, T. Sackton, D. Khost, B. Fang, Data from: Multispecies pangenomes reveal a pervasive influence of population size on structural variation, dataset, *Dryad* (2025). doi: 10.5061/dryad.8pk0p2p01
167. E. Garrison *et al.*, Variation graph toolkit improves read mapping by representing genetic variation in the reference. *Nat. Biotechnol.* **36**, 875–879 (2018). doi: 10.1038/nbt.4227; pmid: 30125266
168. E. Garrison, Z. N. Kronenberg, E. T. Dawson, B. S. Pedersen, P. Prins, A spectrum of free software tools for processing the VCF variant call format: Vcflib, bio-vcf, cyvcf2, hts-nim and slivar. *PLOS Comput. Biol.* **18**, e1009123 (2022). doi: 10.1371/journal.pcbi.1009123; pmid: 35639788
169. J. R. Adrion, J. G. Galloway, A. D. Kern, Predicting the Landscape of Recombination Using Deep Learning. *Mol. Biol. Evol.* **37**, 1790–1808 (2020). doi: 10.1093/molbev/msaa038; pmid: 32077950
170. K. Nam *et al.*, Molecular evolution of genes in avian genomes. *Genome Biol.* **11**, R68–R68 (2010). doi: 10.1186/gb-2010-11-6-r68; pmid: 20573239
171. V. Narasimhan *et al.*, BCFtools/RoH: A hidden Markov model approach for detecting autozygosity from next-generation sequencing data. *Bioinformatics* **32**, 1749–1751 (2016). doi: 10.1093/bioinformatics/btw044; pmid: 26826718
172. C. C. Chang *et al.*, Second-generation PLINK: Rising to the challenge of larger and richer datasets. *GigaScience* **4**, s13742-015-0047-8 (2015). doi: 10.1186/s13742-015-0047-8; pmid: 25722852
173. A. Manichaikul *et al.*, Robust relationship inference in genome-wide association studies. *Bioinformatics* **26**, 2867–2873 (2010). doi: 10.1093/bioinformatics/btq559; pmid: 20926424
174. N. L. Bray, H. Pimentel, P. Melsted, L. Pachter, Near-optimal probabilistic RNA-seq quantification. *Nat. Biotechnol.* **34**, 525–527 (2016). doi: 10.1038/nbt.3519; pmid: 27043002
175. S. Neph *et al.*, BEDOPS: High-performance genomic feature operations. *Bioinformatics* **28**, 1919–1920 (2012). doi: 10.1093/bioinformatics/bts277; pmid: 22576172
176. L. Fu, B. Niu, Z. Zhu, S. Wu, W. Li, CD-HIT: Accelerated for clustering the next-generation sequencing data. *Bioinformatics* **28**, 3150–3152 (2012). doi: 10.1093/bioinformatics/bts565; pmid: 23060610

177. N. Saitou, M. Nei, The neighbor-joining method: A new method for reconstructing phylogenetic trees. *Mol. Biol. Evol.* **4**, 406–425 (1987). doi: 10.1093/oxfordjournals.molbev.a040454; pmid: 3447015
178. M. Kimura, A simple method for estimating evolutionary rates of base substitutions through comparative studies of nucleotide sequences. *J. Mol. Evol.* **16**, 111–120 (1980). doi: 10.1007/BF01731581; pmid: 7463489
179. G. Yu, D. K. Smith, H. Zhu, Y. Guan, T. T.-Y. Lam, GGTREE: An R package for visualization and annotation of phylogenetic trees with their covariates and other associated data. *Methods Ecol. Evol.* **8**, 28–36 (2017). doi: 10.1111/2041-210X.12628
180. H. Li, Seqtk: A fast and lightweight tool for processing FASTA or FASTQ sequences, GitHub (2013); https://github.com/lh3/seqtk.
181. A. Eyre-Walker, M. Woolfit, T. Phelps, The distribution of fitness effects of new deleterious amino acid mutations in humans. *Genetics* **173**, 891–900 (2006). doi: 10.1534/genetics.106.057570; pmid: 16547091
182. T. R. Booker, Inferring Parameters of the Distribution of Fitness Effects of New Mutations When Beneficial Mutations Are Strongly Advantageous and Rare. *G3* **10**, 2317–2326 (2020). doi: 10.1534/g3.120.401052; pmid: 32371451
183. J. M. Eizenga *et al.*, Efficient dynamic variation graphs. *Bioinformatics* **36**, 5139–5144 (2020). doi: 10.1093/bioinformatics/btaa640; pmid: 33040146
184. H. Li *et al.*, The Sequence Alignment/Map format and SAMtools. *Bioinformatics* **25**, 2078–2079 (2009). doi: 10.1093/bioinformatics/btp352; pmid: 19505943
185. J. K. Lindeløv, mcp: An R Package for Regression With Multiple Change Points, *OSF Preprints* (2020). doi: 10.31219/osf.io/fzqxv
186. X. Zheng *et al.*, A high-performance computing toolset for relatedness and principal component analysis of SNP data. *Bioinformatics* **28**, 3326–3328 (2012). doi: 10.1093/bioinformatics/bts606; pmid: 23060615
187. B. S. Weir, C. C. Cockerham, Estimating *F*-Statistics for the Analysis of Population Structure. *Evolution* **38**, 1358–1370 (1984). doi: 10.2307/2408641; pmid: 28563791

ACKNOWLEDGMENTS

We thank G. Schmitt, D. Schmitt, F. T. Garcia, K. Näpflin, G. Kramer, and S. Shakya for assistance with fieldwork in New Mexico and the Yucatán and T. Bakley, R. Bowman, and other Archbold staff for collection of Florida samples. We thank O. Shevchenko, E. Bernberg, and B. Kingham from the University of Delaware Sequencing & Genotyping Center for their assistance with PacBio sequencing. J. Trimble and K. Eldridge of the MCZ Department of Ornithology facilitated access to specimens. N. Mejia isolated the RNA samples. A. Misuraca, J. Fronczek, K. Thomson, and M. Houck established cell lines and prepared and analyzed karyotypes. M. Hiller provided the human-chicken TOGA alignment, and E. Osipova produced the primate and jay alignments and the TOGA flowchart. A. Suh and V. Peona provided access to corvid satellite sequences. We thank C. Ané, P. Hohenlohe, G. David, J. Höglund, L. Gozashti, K. Lotterhos, E. Eichler, P. Sudmant, and R. Collins for helpful discussion and K. Lopez and T. Pegan for help with recombination and inversion analyses, respectively. Most of the computations in this article were performed on the Cannon cluster at Harvard University and supported by Harvard University Research Computing. **Funding:** S.V.E. and T.B.S. acknowledge support from Harvard University and from National Institutes of Health (NIH) grant R01HG011485. S.V.E. acknowledges support from the King XVI Carl Gustafs Professorship in Environmental Science at the University of Gothenburg, Sweden, in 2021, during which this project was conceived. E.G. and A.G. were funded by National Science Foundation (NSF) PPoSS award no. 2118709, NIH R01HG013618, NIH U01HG013760, NIH U01DA057530, NIH U41HG010972, and the Tennessee Center for Integrative and Translational Genomics. N.C. acknowledges NIH grant 1R35GM133412. **Author contributions:** S.V.E. conceived of the project, provided funding, conducted fieldwork, organized samples for sequencing, analyzed data, and wrote the manuscript. B.F. conducted fieldwork, analyzed data, assisted with project design and writing, and produced all main figures and many supplementary figures. T.B.S., D.K., and D.A.D. analyzed data and assisted with project design and with writing. G.E.K. analyzed data. R.G.C. and N.C. provided samples and assisted with writing. H.L. and A.G. analyzed data, provided project direction, and edited the paper. J.E.M., W.C.F., C.K.G., E.G., and J.W.F. assisted with interpretation, project design, and editing the manuscript. **Competing interests:** The authors declare that they have no competing interests. **Data and materials availability:** Sequence data for this work have been deposited in NCBI under Umbrella BioProject PRJNA1206191, the Scrub-Jay (*Aphelocoma*) Pangenome Project. Within this project, BioProject PRJNA1204306 contains the PacBio HiFi reads (with samples SAMN46016487 to SAMN46016457), whereas BioProjects PRJNA1204814 to PRJNA1204903 contain the haplotype assemblies. All scripts can be found at https://github.com/harvardinformatics/scrub-jay-genomics and at Zenodo (*139*). Pangene results can be viewed interactively at https://pangene.bioinweb.org/. Additional resources, including files necessary to set up the pangene results on a local web server, are available on Dryad (*166*).
License information: Copyright © 2025 the authors, some rights reserved; exclusive licensee American Association for the Advancement of Science. No claim to original US government works. https://www.science.org/about/science-licenses-journal-article-reuse

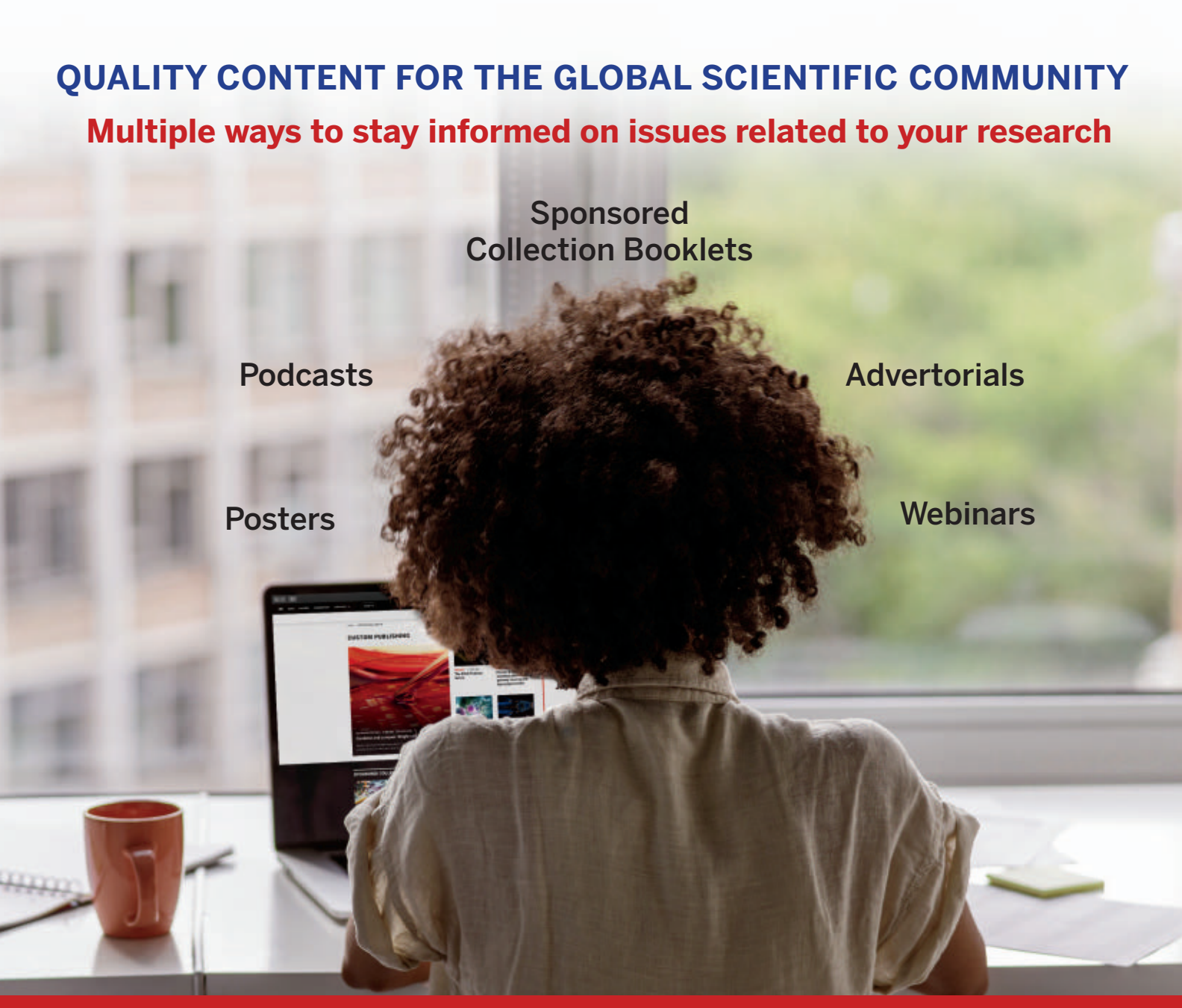
SUPPLEMENTARY MATERIALS

science.org/doi/10.1126/science.adw1931
Supplementary Text; Figs. S1 to S48; Tables S1 to S13; References (*188*–*191*); MDAR Reproducibility Checklist

Submitted 14 February 2025; resubmitted 21 April 2025; accepted 5 September 2025
10.1126/science.adw1931

QUALITY CONTENT FOR THE GLOBAL SCIENTIFIC COMMUNITY

Multiple ways to stay informed on issues related to your research



Science
AAAS

Scan the code and start exploring the latest advances in science and technology innovation!

Science.org/custom-publishing

Brought to you by the *Science*/AAAS Custom Publishing Office.

Posters **Podcasts** **Sponsored Collection Booklets** **Advertorials** **Webinars**

RESEARCH ARTICLE SUMMARY

REPRODUCTION

Comparative analysis of human and mouse ovaries across age

Eliza A. Gaylord†, Mariko H. Foecke†, Ryan M. Samuel†, Bikem Soygur, Angela M. Detweiler, Tara I. McIntyre, Leah C. Dorman, Michael Borja, Amy E. Laird, Ritwicq Arjyal, Juan Du, James M. Gardner, Norma Neff, Faranak Fattahi, Diana J. Laird*

Full article and list of author affiliations: https://doi.org/10.1126/science.adx0659

INTRODUCTION: The ovary governs fertility and reproductive aging by coordinating interactions between germline and somatic cells. In mammals, oocytes are formed before birth and do not renew; their decrease through ovulation and cell death determines the onset of menopause. Ovarian function declines long before age-related degeneration of all other organs, with pregnancy at 35 clinically considered "geriatric." Improved understanding of ovarian biology and hallmarks of ovarian aging is needed to devise therapies for prolonging fertility and delaying menopause.

RATIONALE: Laboratory mice share many reproductive features with humans and are widely used to study ovarian biology. However, their utility is limited by incomplete understanding of how cellular composition and molecular programs compare with those of human ovaries, especially during aging.

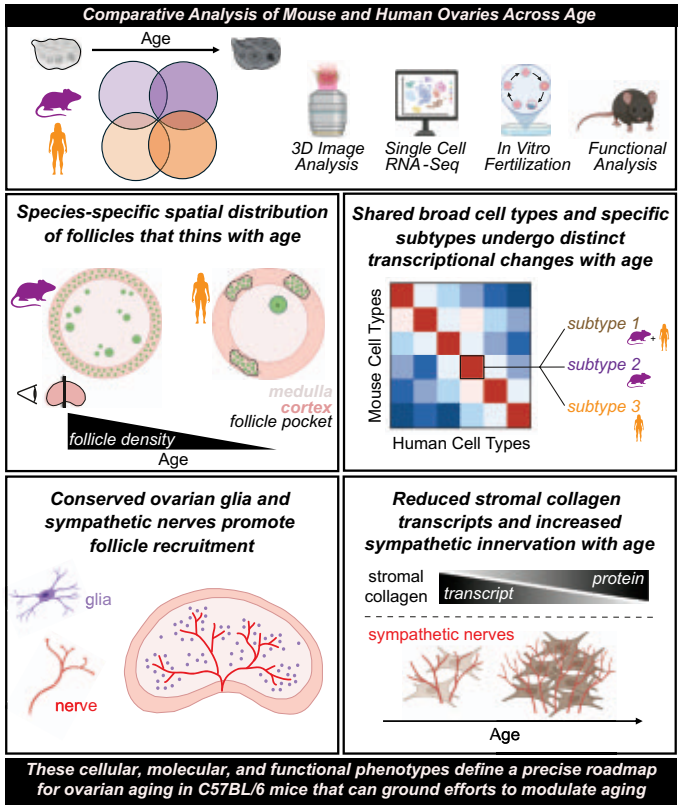
RESULTS: We performed a multimodal analysis of human and C57BL6/J mouse ovaries at young and advanced reproductive ages. We combined three-dimensional tissue imaging, single-cell RNA sequencing (scRNA-seq), and functional assays to define shared and species-specific features of oocyte follicle distribution, follicle growth and maturation, cellular composition and signaling, and age-associated changes.

High-resolution imaging of optically cleared intact mouse ovaries and human ovary fragments revealed discrete cortical "pockets" of human oocytes that shrink with age. Follicle density decreased with age in both species, and early decline of secondary-stage follicles in mice suggests vulnerability specific to stages of growth. scRNA-seq captured all major ovarian cell types and revealed both conserved and species-specific subtypes. Mature oocytes from both species shared enriched pathways, whereas immature oocytes diverged more substantially. Aging altered the transcriptome of oocytes in humans and mice more compared with that of surrounding granulosa cells, although early-stage oocytes were more changed in mice, and late-stage oocytes were more changed in humans.

Subtype analysis revealed that granulosa, fibroblast, and endothelial cells shared conserved transcriptional programs, whereas species-specific subtypes emerged in theca, pericyte, and epithelial compartments. Ovarian glial cells were identified in both species, frequently in association with sympathetic nerves. Innervation was implicated in the growth of follicles by genetically ablating sympathetic nerves in mice, and pericytes were shown as the major source of nerve growth factor. Networks of ovarian nerves became more dense with age in mouse and human samples. In ovarian fibroblasts, age-related transcriptional changes included down-regulation of collagen genes, despite increased deposition of collagen protein in aged human ovaries, suggesting a conserved compensatory mechanism for fibrosis.

Functionally, the competence and developmental potential of mouse oocytes declined markedly by 9 months of age, recapitulating the age dependence of human in vitro fertilization. Intercellular signaling between oocytes, granulosa, and theca cells was altered with age, revealing species-shared and -specific changes in pathways regulating oocyte support and maturation.

CONCLUSION: This work provides a comprehensive reference of ovarian aging across mouse and human populations, revealing conserved cellular specialization, including sympathetic nerves and glia, alongside species-specific dynamics of follicle depletion, oocyte maturation, and stromal remodeling. Our findings enhance the interpretability of mouse models for human reproductive aging and establish a foundational resource for cross-species analysis of ovarian function and decline. □



Schematic of whole-mount imaging, scRNA-seq, and functional assays used to compare human and mouse ovaries. Key findings include conserved and species-specific changes in follicle density and distribution, cellular composition, and innervation across reproductive aging in mouse and human ovaries. [Figure created with BioRender.com]

*Corresponding author. Email: diana.laird@ucsf.edu †These authors contributed equally to this work. Cite this article as E. A. Gaylord *et al.*, *Science* **390**, eadx0659 (2025). DOI: 10.1126/science.adx0659

REPRODUCTION

Comparative analysis of human and mouse ovaries across age

Eliza A. Gaylord[1,2,3]†, Mariko H. Foecke[1,2,3]†, Ryan M. Samuel[1,4]†, Bikem Soygur[1,2,5], Angela M. Detweiler[6], Tara I. McIntyre[1,2], Leah C. Dorman[6], Michael Borja[6], Amy E. Laird[7], Ritwicq Arjyal[6], Juan Du[8,9], James M. Gardner[8,9], Norma Neff[6], Faranak Fattahi[1,4,10], Diana J. Laird[1,2,3,11]*

The mouse is a tractable model for human ovarian biology; however, its utility is limited by incomplete understanding of how transcription and signaling differ interspecifically and with age. We compared ovaries between species using three-dimensional imaging, single-cell transcriptomics, and functional studies. In mice, we mapped declining follicle numbers and oocyte competence during aging; in human ovaries, we identified cortical follicle pockets and decreases in density. Oocytes had species-specific gene expression patterns during growth that converged toward maturity. Age-related transcriptional changes were greater in oocytes than in granulosa cells across species, although mature oocytes change more in humans. We identified ovarian sympathetic nerves and glia; axon density increased in aged ovaries and, when ablated in mice, perturbed folliculogenesis. This comparative atlas defines shared and species-specific hallmarks of ovarian biology.

The ovary orchestrates dynamic communication between germline and somatic cells (*1*) to generate mature oocytes and produce hormones that regulate fertility, pregnancy, and aging. In both humans and mice, the finite, nonrenewable oocyte pool forms before birth. Oocytes are then encapsulated by somatic cells to establish the primordial follicle reserve (*2*). During folliculogenesis, cohorts of quiescent primordial follicles "activate" and progress asynchronously through conserved stages: primary, secondary, tertiary or antral, and ovulatory (*3*–*5*). Granulosa and theca cells concurrently differentiate, secreting estrogen and androgen, respectively (*6*, *7*). From the tertiary stage, folliculogenesis is hormonally regulated and culminates in ovulation and corpus luteum (CL) formation (*8*). Despite broad similarities in cellular composition and function, folliculogenesis has diverged in scale between species; humans are mono-ovulatory, typically producing singleton pregnancies, whereas mice are multiovulatory, bearing litters of 2 to 12 pups depending on strain (*9*).

In both species, the decline in fertility precedes the age-related degeneration of all other organs (*10*); clinically, individuals aged ≥35 years (Y) are considered of advanced reproductive age (ARA) (*11*, *12*), and menopause occurs around 51Y, marking the cessation of cycling. Although mice do not undergo menopause, they recapitulate key aspects of human reproductive aging, including ceasing hormonal cycling and ovulation (*13*, *14*). Murine reproductive aging occurs on an accelerated timescale: Mice ~2 to 4 months (M) old approximate humans in their early 20s, whereas ~9M to 12M mice model human ovarian aging in the late 30s to mid-40s (fig. S1A). Direct mouse-human ovarian comparisons are needed to mobilize mouse models toward therapies for human fertility and ovarian aging. Existing single-species single-cell RNA sequencing (scRNA-seq) datasets have identified mechanisms of ovarian aging, including inflammation (*15*–*17*), senescence (*18*, *19*), fibrosis (*16*, *20*), and altered transcriptional signatures in the follicle (*18*, *19*, *21*–*23*). However, discrepancies between ovarian cell type annotations within and across species, particularly in the microenvironment, present challenges for comparing observations interspecifically (*20*, *21*, *24*).

To assess the capacity of the mouse to model human ovarian biology, we compared mouse and human ovaries across the reproductive window at the organ and single-cell levels. We selected C57BL/6 mice as the representative strain given their widespread use as a genetic background in biomedical research (*25*). Using three-dimensional (3D) quantitative imaging, we identified species differences in oocyte spatial distribution but conserved peripheral nervous system patterning. Genetic ablation in mice implicated peripheral nerves in the recruitment of follicles for growth. Our scRNA-seq pipeline captured diverse cell types from young and aged mouse and human ovaries, including an interspecific glial population. This work reveals species-shared and -specific ovarian programs spanning development to aging.

Results

3D imaging reveals species-specific follicle geographies

With each mouse estrous or human menstrual cycle, a mature, competent oocyte is ovulated. Unlike mono-ovulatory humans, mice sustain a large pool of growing follicles to support multiple ovulations and large litters (*26*, *27*). To map the asynchronous process of folliculogenesis in three dimensions, we developed a whole-mount immunostaining and clearing protocol for intact mouse ovaries (*28*) and adapted it for large human ovary pieces (Fig. 1A).

We imaged ovaries from estrous-staged C57BL/6 mice from 2M to 12M ($n \geq 4$ per group) (Fig. 1B and fig. S1, A and B). Follicles were classified by using newborn ovary homeobox protein (NOBOX; all oocytes), anti-Müllerian hormone (AMH) or steroidogenic acute regulatory (StAR) protein, and morphology (Movie 1 and fig. S2, A and B), enabling quantification of primordial, growing (primary, secondary, tertiary+), atretic (dying), and total follicles (Fig. 1, C to E; fig. S2, A to G; and table S1). AMH and StAR specifically marked growing follicles or CLs, respectively (fig. S2C). Primordial follicle numbers declined gradually until 6M, then steeply by 12M (Fig. 1C). Growing follicle numbers remained stable until 6M and declined at 9M (Fig. 1D and fig. S2, D to F) despite secondary follicle loss as early as 4M (fig. S2E), revealing more complex age-related dynamics than previously recognized. Oocyte density also decreased beginning at 4M (fig. S2, H to J). Atretic follicle dynamics echoed those of the growing pool (fig. S2G). Total follicle numbers remained unchanged by 6M ($P = 0.0559$) and decreased significantly by 9M ($P < 0.0001$) (Fig. 1E). Although the ratio of growing to primordial follicles remained stable between 2M and 9M (Fig. 1F), growing follicle decline accelerated after 9M (Fig. 1E). Together, these results (Fig. 1G) indicate a breakdown of follicular homeostasis by 9M.

Given the large size (~3 to 4 cm) and relative unavailability of human ovaries, we analyzed ≥1 cm^3 ovary pieces from donors of early reproductive age (ERA, 23Y and 30Y) and advanced reproductive age (ARA, 37Y and 58Y) (figs. S1, A to B, and S3A) with no history of hormonal interventions, fertility preservation, or reproductive tract cancer. Total oocytes were quantified by using *DEAD-box helicase 4* (*VASA*) (Movie 2). Newly growing follicles (arrowhead) were Laminin$^+$ and AMH$^-$ (Fig. 1,

[1]Eli and Edythe Broad Center for Regeneration Medicine and Stem Cell Research, University of California, San Francisco, San Francisco, CA, USA. [2]Center for Reproductive Sciences, Department of Obstetrics, Gynecology and Reproductive Science, University of California, San Francisco, San Francisco, CA, USA. [3]Bakar Aging Research Institute, University of California, San Francisco, San Francisco, CA, USA. [4]Department of Cellular and Molecular Pharmacology, University of California, San Francisco, San Francisco, CA, USA. [5]Reproductive Biology Hub, Center for Healthy Aging in Women, Buck Institute for Research on Aging, Novato, CA, USA. [6]Genomics and Computational Biology Platforms, Chan Zuckerberg Biohub San Francisco, San Francisco, CA, USA. [7]School of Public Health, Oregon Health and Science University – Portland State University, Portland, OR, USA. [8]Diabetes Center, University of California, San Francisco, San Francisco, CA, USA. [9]Department of Surgery, University of California, San Francisco, San Francisco, CA, USA. [10]Program in Craniofacial Biology, University of California, San Francisco, San Francisco, CA, USA. [11]Department of Anatomy, University of California, San Francisco, San Francisco, CA, USA. ***Corresponding author. Email: diana.laird@ucsf.edu** †These authors contributed equally to this work.

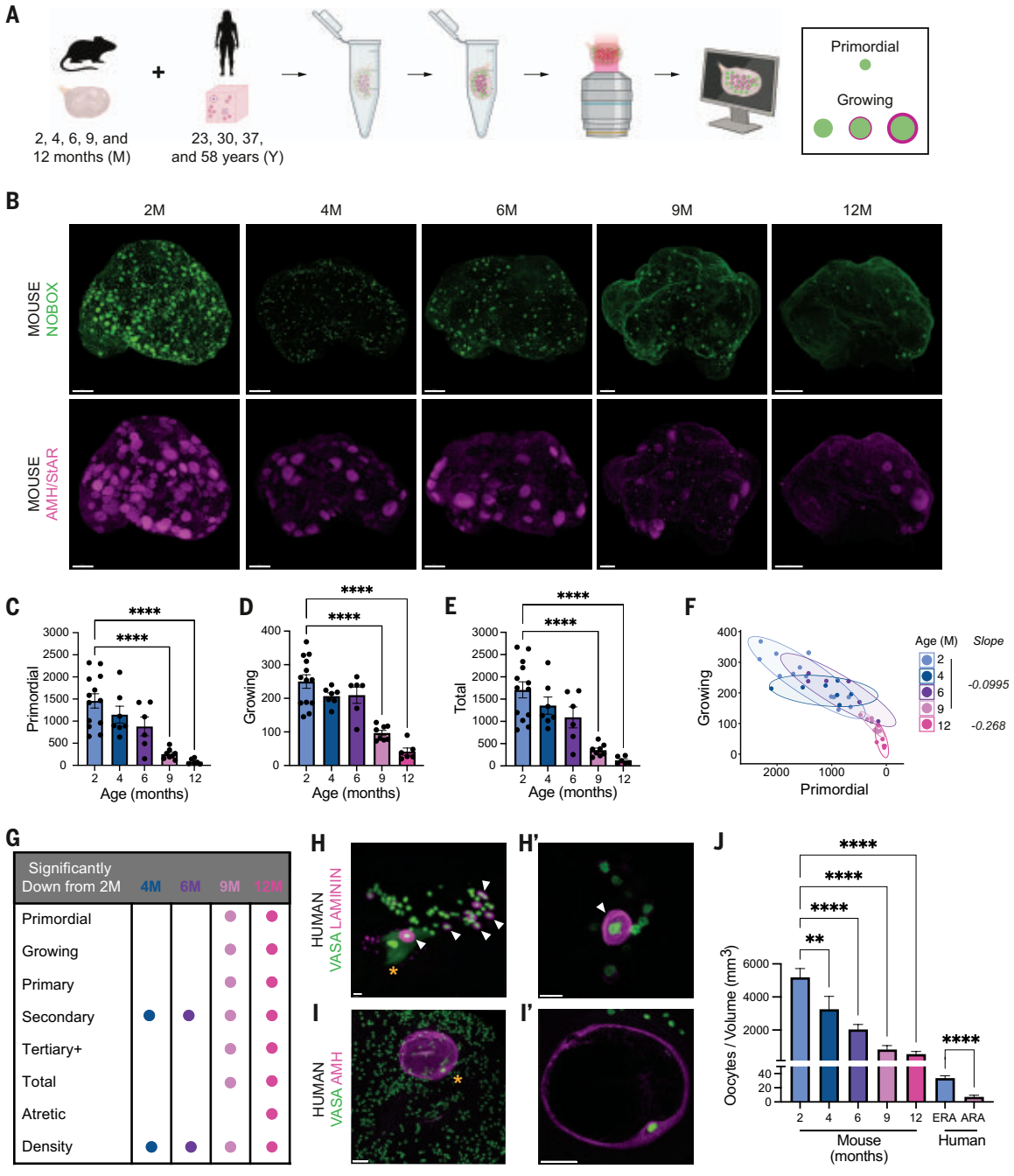
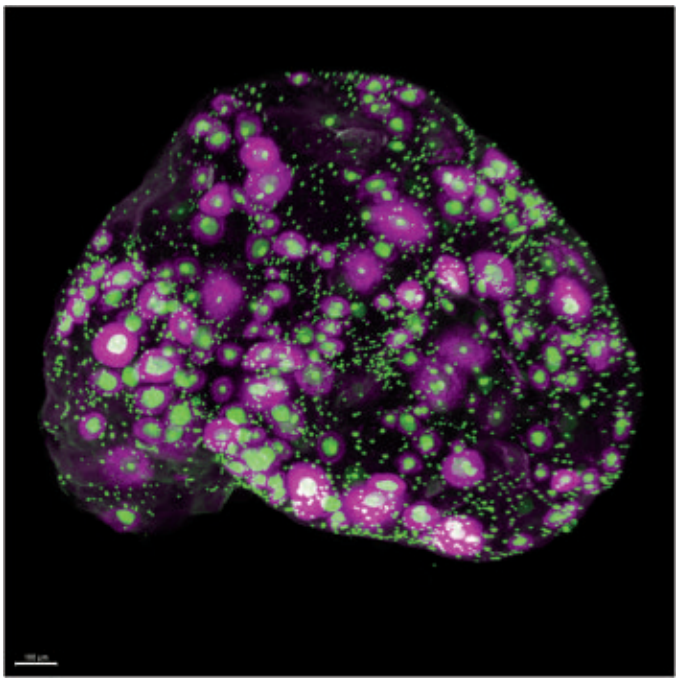
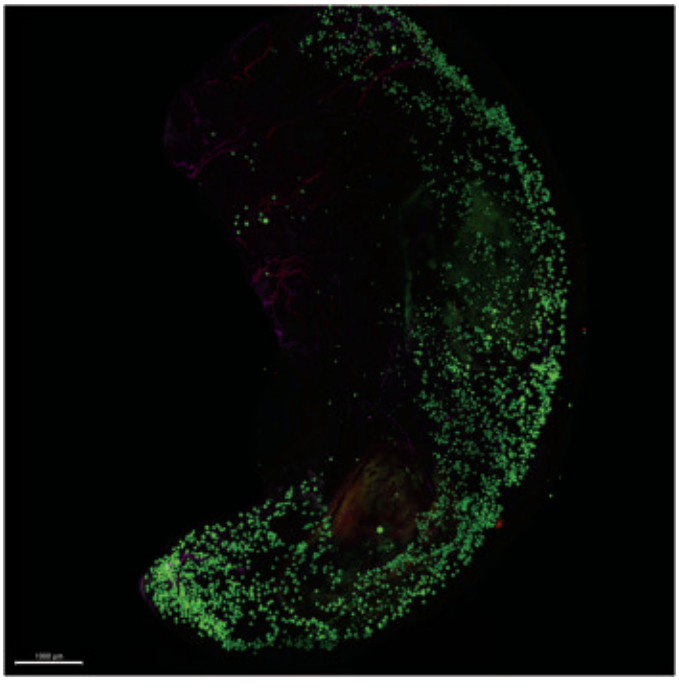


Fig. 1. Mapping of C57BL/6 mouse and human ovaries in 3D reveals species-specific oocyte distribution. (**A**) Schematic of whole-mount processing for 3D imaging and analysis of intact mouse ovaries and human ovary pieces. Murine ovaries were collected and analyzed at 2, 4, 6, 9, and 12M. Human ovaries from 23, 30, 37, and 58Y human donors were cut into ~1 cm^3 pieces before processing. (**B**) Representative 3D image stacks of whole-mount C57BL/6 ovaries at 2, 4, 6, 9, and 12M. Oocytes were marked by NOBOX (green), and growing follicles and corpora lutea were marked by AMH and StAR, respectively (magenta). Scale bars, 200 μm. (**C**) Quantification of primordial follicle oocytes, (**D**) growing oocytes, and (**E**) total oocytes from the whole-mount IF images at 2M ($n = 13$), 4M ($n = 7$), 6M ($n = 6$), 9M ($n = 8$), and 12M ($n = 6$). All data are represented as means ± SEM; $^{*}P < 0.05$; $^{**}P < 0.01$; $^{***}P < 0.001$; $^{****}P < 0.0001$; analysis of variance (ANOVA) test. (**F**) Density plot showing the relationship of primordial to growing follicles with age where the slope represents the rate of decline in oocyte number with age. (**G**) Schematic summarizing the timepoints at which each oocyte follicle pool was significantly decreased relative to the 2M reference group. Colored circles indicate statistically significant reductions in oocyte counts. ANOVA test was performed to determine significance. (**H**) Whole-mount IF images of an ERA human ovary piece with oocytes marked by VASA (green) and small growing follicles marked by laminin (magenta, arrowhead) at low and (**H′**) high magnification. Scale bars, 50 μm. (**I**) Similarly, large growing follicles marked by AMH (magenta, asterisk) and oocytes marked by VASA (green) at low and (**I′**) high magnification. Scale bars, 200 μm. (**J**) Quantification of oocyte density in mouse ovaries and human ovary pieces. All data represented as means ± SEM; $^{*}P < 0.05$; $^{**}P < 0.01$; $^{***}P < 0.001$; $^{****}P < 0.0001$; ANOVA test. Human data represented as means ± SEM; $^{*}P < 0.05$; $^{**}P < 0.01$; $^{***}P < 0.001$; $^{****}P < 0.0001$; Student's *t* test.



Movie 1. Classification of follicle maturation stages in C57BL/6 mice 3D projection and slice view of NOBOX+ oocytes (green) and AMH+ granulosa cells (magenta) from whole-mount ovary imaging permits quantification of the total follicle population. The spot view, merged with the IF signal, allows for detection and classification of primordial (green spot) and growing (magenta spot) follicles.



Movie 2. 3D projection of a cleared ERA human ovary piece shows a pocket of VASA+ oocytes (green) in the cortical region and TH+ sympathetic nerves (red) and S100β+ glia (magenta) permeating the medullary region.

H to I′, and fig. S3, B to B′), whereas larger follicles (*), sometimes exceeding 800 μm, were Laminin^{+} and AMH^{+} (Fig. 1, I to I′, and fig. S3B′′); staging criteria are outlined in fig. S3B′′′. 3D visualization revealed geographic differences across species: Mouse oocytes were distributed throughout the ovary across age, whereas human ovaries at ARA exhibited cortical oocyte "pockets" separated by follicle-free deserts (fig. S3, C and D), with relative pocket volume being significantly reduced with age (fig. S3E). Although mouse oocytes were more densely packed throughout the ovary, relative oocyte density declined with age in both species (Fig. 1J and fig. S3F). Together, our data show that although both species experience age-related oocyte loss, human ovaries retain isolated, oocyte-rich pockets, whereas follicles are maintained throughout the murine ovary.

Conserved cellular composition between mouse and human ovaries

We performed scRNA-seq at ERA (mouse, 2M; human, 26Y and 30Y) and ARA (mouse, 9M; human, 55Y and 56Y; fig. S1, A and B), combining 10X Genomics Chromium Single-Cell 3′ GEX (hereafter, 10X 3′ GEX) with Smart-seq2 to maximize capture of somatic cells and oocytes, respectively (*29*) (Fig. 2A). In mice, unbiased clustering and uniform manifold approximation and projection (UMAP) clustering of 43,316 cells identified 11 broad clusters: oocyte (170), granulosa (4594), luteal (1502), theca (10,547), fibroblast (14,620), smooth muscle (6283), pericyte (1701), epithelia (395), endothelia (1317), immune (2157), and glia (30) (Fig. 2, B and C), with all animals represented (fig. S4A). Module scoring using the Isola *et al.* (*15*) dataset revealed high correspondence with reference cell types (fig. S4B). Because our dataset lacked proestrus (fig. S1), we confirmed that cell type representation did not vary by estrous stage by integrating our dataset with published young (2M) and aged (9M) proestrus samples from Morris *et al.* (*30*) and Isola *et al.* (*15*) (fig. S4, C and D). Because all broad cell types were sufficiently represented across estrous stages, we proceeded with downstream analyses.

In parallel, 47,791 human cells formed 10 broad clusters: oocyte (97), granulosa (180), theca (577), fibroblast (36,358), smooth muscle (594), pericyte (4976), epithelia (651), endothelia (3739), immune (570), and glia (49) (Fig. 2, D and E). Module scoring using the Wu *et al.* (*18*) dataset confirmed matching human cell types (fig. S4E). Cross-species analysis confirmed that all broad cell types were most transcriptionally similar to their counterparts in the other species (Fig. 2F). Luteal cells, which produce progesterone after ovulation (*31*), were absent from human samples, likely owing to the menstrual stage or potential contraceptive use, both of which affect luteal differentiation.

Follicular cell types (fig. S4F), predominantly from ERA (fig. S4G), were underrepresented in the human dataset. Further, follicle-associated cell types, including ovulation-essential smooth muscle cells (*32*, *33*), were proportionally more represented in mice (fig. S4F), likely owing to higher follicle density (Fig. 1J). Both species shared conserved cell types, including ovarian glia, which can be annotated across datasets using the robust markers identified herein (table S2A).

Greater conservation of maturation gene patterns in more-mature oocytes

We suspected the maturity of sequenced oocytes was biased by method: Smart-seq2 selects for mature oocytes (≥40 μm), whereas 10X 3′ GEX captures immature oocytes (≤30 μm). To maximize representation of oocyte maturation stages, we integrated young (mouse, 3M; human, 18 to 30Y) and aged (mouse, 9M; human, 37 to 49Y) 10X oocyte subsets from mouse [Isola *et al.* (*15*)] and human [Wu *et al.* (*18*)] samples (Fig. 3, A to A′, and fig. S5, A to A′). After harmonizing by age to isolate maturation-related variation, six mouse and five human oocyte subclusters were aligned along a maturation trajectory using partition-based graph abstraction (PAGA) and visualized with forced atlas (FA; Fig. 3, B to B′, and fig. S5, B to B′). Subclusters formed linear trajectories separated by sequencing technology (fig. S5, A to A′ and C to C′),

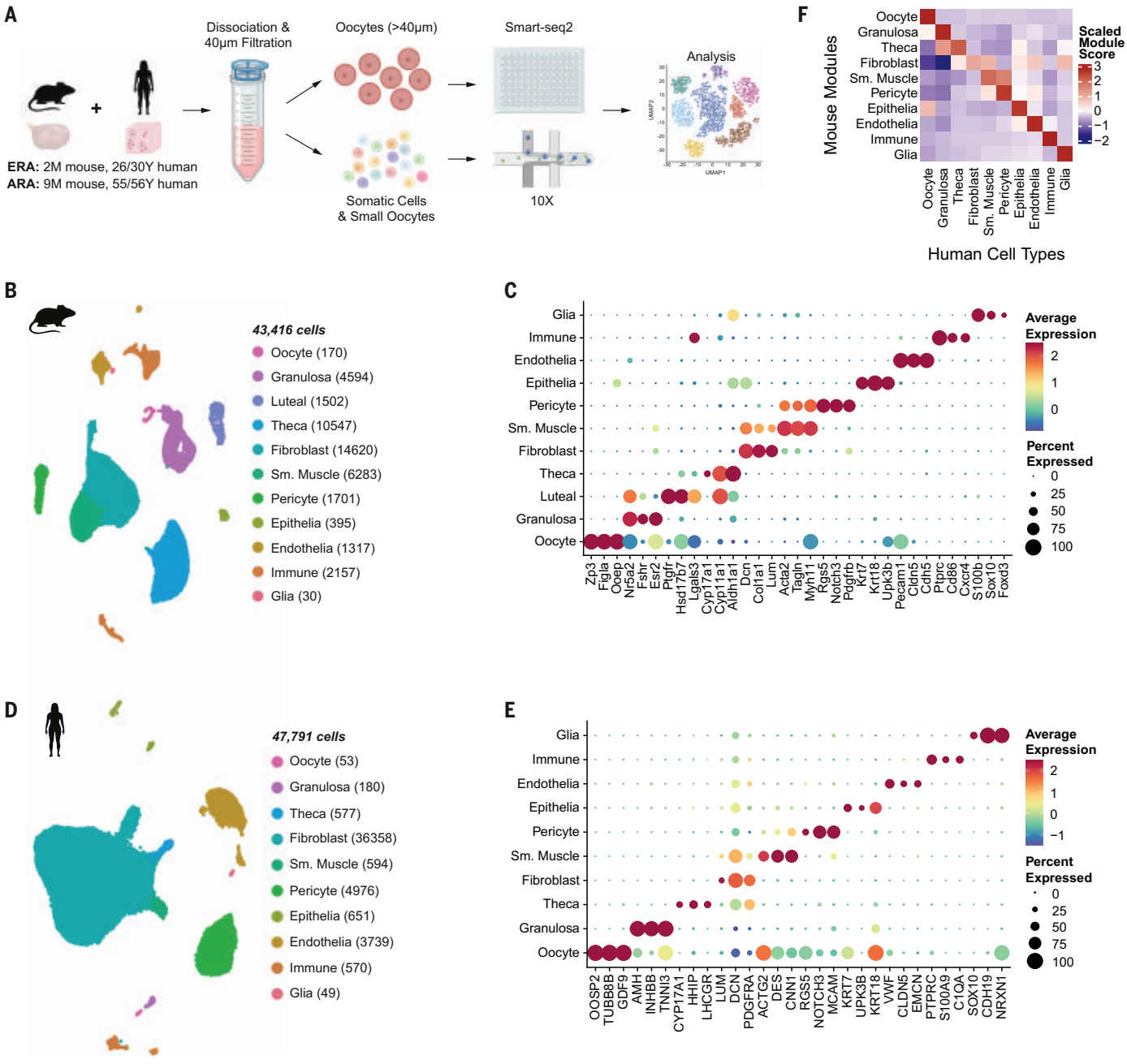


Fig. 2. Cellular composition is conserved between mouse and human ovaries. (**A**) Schematic of ovary processing for scRNA-seq. ERA samples included 2M mice and 26 and 30Y humans; ARA samples included 9M mice and 55 and 56Y humans. (**B**) UMAP plot of the 11 cell types captured in the mouse, including cell numbers, and (**C**) a dot plot of the scaled average expression of cell type marker genes used for annotation. (**D**) UMAP plot of the 10 cell types captured in the human, including cell numbers, and (**E**) a dot plot of the scaled average expression of cell type marker genes used for annotation. (**F**) Heatmap of the average scaled module score of the mouse cell type transcriptional signatures (top 100 DEGs) in the human cell types.

with growing oocyte markers, including *Gdf9*/*GDF9* (*34*), enriched in Smart-seq2 oocytes and absent in primordial-stage oocytes at the 10X trajectory root (fig. S5, D to D′), confirming directionality. Thus, the 10X end was selected as the root (*) (Fig. 3, B and B′).

We identified 15 mouse and 18 human gene expression patterns along the pseudotime trajectory (Fig. 3, C to C′), grouped into five stages: early, mid-early, mid, mid-late, and late. Pathway enrichment revealed greater cross-species similarity in mature oocytes (>24%) than immature oocytes (<14%) (Fig. 3D and fig. S5E). Late-stage oocytes showed conserved enrichment in chromatin and chromosome organization (Fig. 3, E to E′), with shared expression of meiosis regulator *Aurka*/*AURKA* (*35*) (fig. S5, F to F′). Mouse late-stage patterns included nuclear pore proteins *Nup37* (*36*), *Nup85*, and *Nup98* (fig. S5F), resembling *Drosophila* oocyte maturation (*37*). Human late-stage patterns featured genes related to meiosis, *TUBB8* (*38*), *ZAR1L* (*39*), and *SIRT7* (*40*); vesicle trafficking, *TRAPPC11* (*41*); and the PIWI-piRNA family, *PIWIL1*, *PIWIL2*, *TDRD9*, and *MOV10L1* (fig. S5F′).

To visualize gene-level conservation, we plotted homolog expression for each broad pattern along the pseudotime trajectory of the other species (Fig. 3F and fig. S5G). Several homologs peaked at

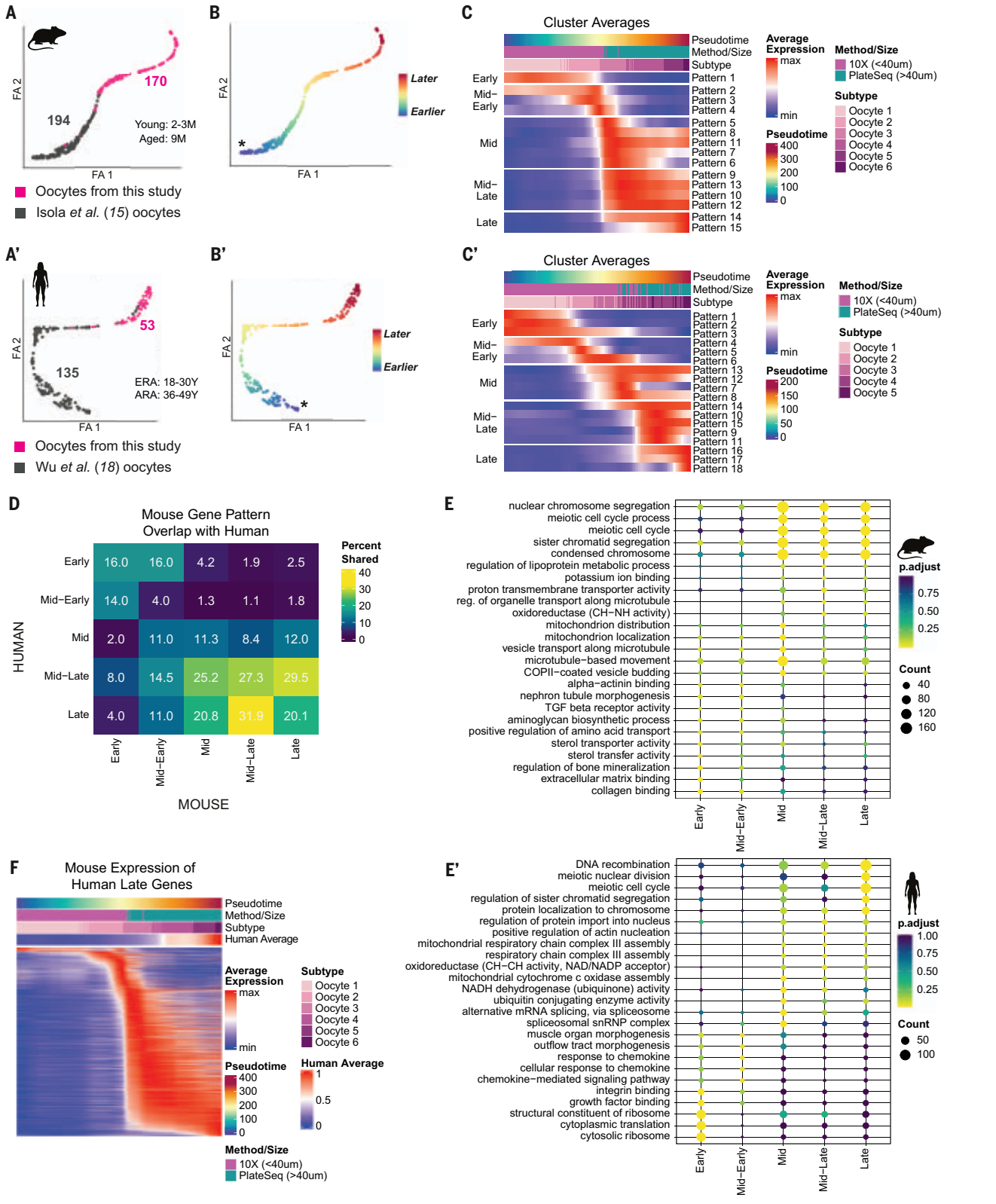


Fig. 3. Greater conservation of maturation gene patterns in more mature oocytes. (**A** and **A′**) Schematic illustrating integration of the oocytes from the (A) murine Isola *et al.* (*15*) and (A′) human Wu *et al.* (*18*) datasets with our subsetted mouse and human oocytes, respectively. The total number and age ranges of the oocytes from each study are listed. (**B** and **B′**) FA dimensionality reduction of the oocytes from (B) mouse and (B′) human datasets colored by pseudotime value with the root node indicated with an asterisk. (**C** and **C′**) Average fitted expression over pseudotime of genes in (C) 15 mouse and (C′) 18 human distinct expression patterns. (**D**) Heatmap displaying the percentage of shared human homologous genes across mouse broad pattern categories of oocyte maturation. Each value represents the percentage of genes within a given mouse category (columns) that have a human ortholog in the corresponding human gene category (rows). (**E** and **E′**) Dot plots of ontology pathways enriched in (E) mouse and (E′) human gene patterns. Select GSEA pathway names were abbreviated; see table S3 for the abbreviated pathways and the full name. p.adjust, adjusted *P* value. (**F**) The fitted expression of mouse homologous genes for Late patterns along the pseudotime trajectory of human oocyte maturation.

similar pseudotime points, indicating conserved timing and function, though they diverged outside the corresponding stage range. Roughly half of human early-pattern homologs peaked at the mid stage in mice (fig. S5G), whereas most late-pattern genes aligned between species (Fig. 3F). Consistent with prior reports of limited interspecific transcript overlap (*24*), our data suggest that early oocyte gene programs are more divergent, whereas later stages show increasing convergence.

Identification of species-specific subpopulations of theca, pericytes, and epithelia

To identify cell subtypes, each broad somatic cluster was subclustered to the highest resolution with distinct marker genes, producing mouse (m) and human (h) granulosa, immune, theca, fibroblast, pericyte, and endothelial subclusters (Fig. 4A). Granulosa and immune subtypes were annotated using reported markers, whereas all others were defined by distinctive markers (table S2, B and C) and inferred functions

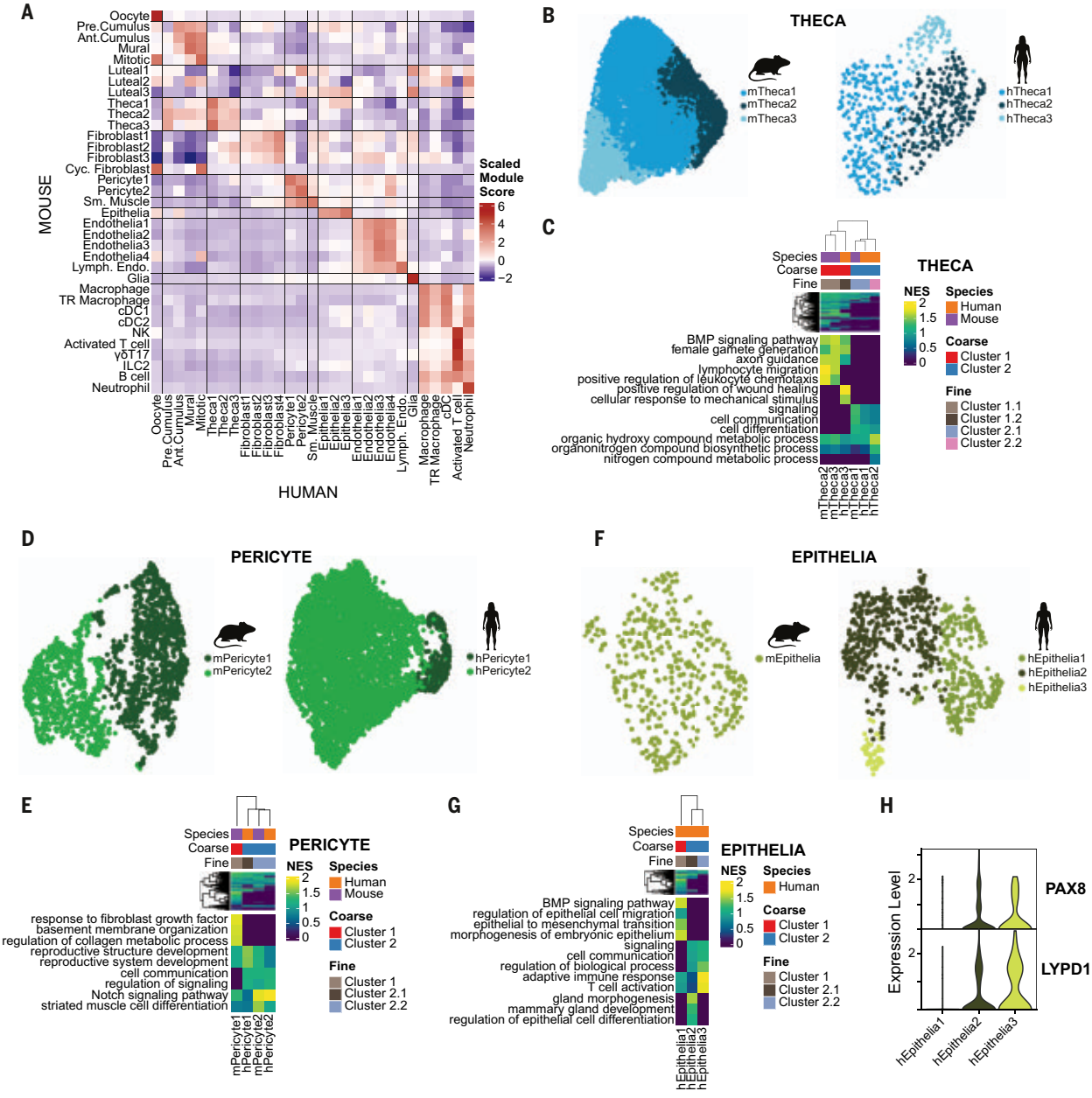


Fig. 4. Pathway analysis reveals species-specific theca, pericyte, and epithelia subtypes. (**A**) Heatmap showing the average scaled module scores of mouse subtype transcriptional signatures (defined by the top 100 differentially expressed genes) across human subtypes. (**B**) UMAP plots showing the three theca subtypes identified in the mouse and the human. (**C**) Heatmap of NESs for pathways enriched in DEGs for mouse and human theca subtypes. Pathways displayed are specific to or more highly enriched in hierarchical clusters, which were found by clustering based on NESs of all pathways (top heatmap body). (**D**) UMAP plots showing the two pericyte subtypes in mouse and human ovaries. (**E**) Heatmap of NESs for pathways enriched in DEGs for mouse and human pericyte subtypes. Pathways displayed are specific to or more highly enriched in hierarchical clusters, which were found by clustering based on NESs of all pathways (top heatmap body). (**F**) UMAP plot showing the three epithelia subtypes in human ovaries. (**G**) Heatmap of NESs for pathways enriched in DEGs for human epithelia subtypes. Pathways displayed are specific to or more highly enriched in hierarchical clusters which were found by clustering based on NESs of all pathways. (**H**) VlnPlots of rete ovarii genes PAX8 and LYPD1 across human epithelial subtypes.

using gene set enrichment analysis (GSEA). Species were compared by unsupervised hierarchical clustering of biological process pathway normalized enrichment scores (NESs) calculated by GSEA on subtype marker genes. The resulting dendrogram clusters were annotated at two levels of granularity indicating broadly shared (coarse) and subtype-specific (fine) gene ontology (GO) pathways. However, module scoring showed no consistent one-to-one subtype relationships across species, suggesting interspecific subtype heterogeneity (Fig. 4A). Granulosa, fibroblast, and endothelial subtypes were largely conserved, while species-specific subtypes emerged in the theca, pericyte, and epithelial compartments.

Granulosa cells formed four species-shared subtypes, augmented by data from Wu *et al.* (*18*) (ERA human, 18 to 30Y; ARA human, 37 to 39Y): Preantral-Cumulus, Antral-Cumulus, Mural, and Mitotic (fig. S6, A to C, and table S2B). A fifth, mouse-specific subtype was identified as Ghr+ (growth hormone receptor, *Ghr*), though sparse *GHR* transcripts in human granulosa (fig. S6D) suggest that it may be shared but undetected. Previous work (*15*, *16*) reported minimal estrous stage–dependent variation in ovarian subtype composition, though one study (*30*) noted enrichment of their granulosa Antral-Mural population in proestrus. We verified that our dataset included this population (fig. S4C) by comparing it to young and aged proestrus samples (*15*, *30*). All granulosa subtypes were present in our dataset, regardless of estrous stage (fig. S6E).

Although previously used to annotate atretic granulosa cells (*30*), GHR was implicated in follicle growth and protection from atresia (*42*–*44*). Given that (i) markers of this subtype (*Itih5*, *Pid1*) regulate growth in other organs (*45*, *46*) and (ii) the transcriptional similarity of the Ghr+ subtype to the mPreantral-Cumulus and mMural subtypes (fig. S6, A to C), we postulate that the Ghr+ subtype represents a transitory maturation state. To investigate Ghr+ granulosa dynamics, we analyzed the Mantri *et al.* (*47*) spatial transcriptomic time course of mouse ovaries before and after treatment with human chorionic gonadotropin (hCG) (fig. S6, F to K). Follicles were previously annotated (*47*) as Preantral, Antral, and Atretic, the latter enriched in cells scoring highly for markers of our Ghr+ cluster (Ghr score), which we relabeled as Ghr. Ghr+ granulosa cells were most abundant in untreated and 0-hour (pregnant mare serum gonadotropin–only) ovaries, depleted from 1 to 8 hours post-hCG (periovulatory window), and reappeared at 11 to 12 hours, forming a U-shaped temporal pattern (fig. S6F). Ghr score+ granulosa cells spanned a range of follicle sizes at baseline (fig. S6G) and late post-hCG timepoints (fig. S6H) but were absent during periovulation (fig. S6I). Follicular radius analysis adapted from Lan *et al.* (*48*) showed Ghr+ enrichment at the outer edge of preantral and Ghr follicles, whereas antral follicles contained few Ghr Score+ cells (fig. S6, J to K). The transcriptional proximity between Preantral, Ghr+, and Mural granulosa clusters (fig. S6A), along with their peripheral localization (fig. S6K), corroborates the Ghr+ subtype as a transient, hormonally responsive state rather than a degenerating population.

Ovarian immune cells support follicular development and postovulation remodeling (*17*). We identified species-shared subtypes: macrophage, tissue resident (TR) macrophage, neutrophil, activated T cell, and conventional dendritic (cDC) cell (fig. S6L). Whereas human cDCs were homogeneous, mice had distinct cDC1 (type 1) and cDC2 (type 2) subtypes. Four additional subtypes—natural killer (NK), double-negative interleukin-17+ γδ T cells (γδT17), type 2 innate lymphoid cells (ILC2), and B cells—were exclusive to mice (fig. S6L). These differences may reflect higher lymphocyte-to-neutrophil ratios in mouse blood (*49*).

Theca and fibroblast cells surround follicles, producing androgen and providing structural support, respectively (*6*, *50*). We identified three theca and four fibroblast subtypes in both species (Fig. 4, B and C, and fig. S7, A to C). Module scoring confirmed that *Cyp17a1*/*CYP17A1*+ theca subtypes (mTheca3, hTheca1) were steroidogenic (fig. S7A), yet these did not cluster together at coarse resolution, indicating species-specific steroidogenesis signatures (Fig. 4C). At coarse resolution, Theca Group1 (mTheca2, mTheca3, and hTheca3) was enriched for bone morphogenic protein (BMP) signaling and axon guidance pathways, suggesting a role in follicular innervation. Fine resolution revealed species-specific functions: mGroup1.1 (mTheca2 and mTheca3) was linked to immune migration-related pathways (Fig. 4C), which regulate steroidogenesis and proliferation (*51*, *52*); mTheca2 showed enrichment for extracellular matrix remodeling, whereas mTheca3 was enriched for hormone metabolism and vascular remodeling (table S3), implicating mGroup1.1 in immune signaling, remodeling, or early atresia. hGroup2.2 (hTheca2) was enriched for metabolism of hydroxy-containing compounds essential for androstenedione and testosterone synthesis. Despite shared steroidogenic roles, we identified subtypes with inferred species-specific functions.

Endothelial cells and pericytes form the ovarian vasculature, essential for hormone signaling (*53*). We identified four endothelial, one lymphatic, and two pericyte subtypes per species (Fig. 4D and fig. S7, D and E). Endothelial Group1 was interspecifically enriched for ovary-specific pathways, including female gamete generation and blastocyst development (fig. S7E); Group1.1 was enriched for nerve growth pathways, suggesting involvement in vascular innervation (*54*). Group2 pericytes, present in both species, were enriched for reproductive structure development, consistent with roles in follicle neovascularization (Fig. 4E) (*55*). mPericyte1, an outlier by coarse resolution, was solely enriched for fibroblast growth factor signaling, upstream of platelet-derived growth factor receptor β (PDGFRβ) signaling (*56*), indicating both species-shared and -specific vascular functions.

We identified three human epithelia and three mouse luteal subtypes (Fig. 4F and fig. S7, F to J). Cross-species analysis was limited owing to homogenous mouse epithelia (mEpithelia) and noncapture of human luteal cells. Group1 (hEpithelia1) was enriched for BMP signaling and epithelial morphogenesis, whereas Group2.1 (hEpithelia2) and Group2.2 (hEpithelia3) were enriched for glandular development and immune activation, respectively (Fig. 4G). Both expressed PAX8 and LYPD1, markers of the secretory rete ovarii (*57*, *58*) (Fig. 4H). Module scoring revealed that mEpithelia was most transcriptionally similar to hEpithelia1 and hEpithelia3 (fig. S7F). Human epithelial heterogeneity may reflect differences in organ size and epithelial thickness (*59*). Luteal Group1 (mLuteal1 and mLuteal2) was enriched for vasculogenesis and follicle development (fig. S7, G and H). Fine resolution revealed that mLuteal1 was associated with morphogenesis of progesterone-metabolizing organs (*60*, *61*), whereas mLuteal2 was enriched for cholesterol biosynthesis. mLuteal2 (*Parm1*/*Lhcgr*) and mLuteal1 (*Akr1c18*) correspond to early and late luteal cells identified by slide-seq (*62*); mLuteal3 was transitional, expressing both early (*Lhcgr*) and late (*Sfrp4*) markers but lacking *Akr1c18* (fig. S7I). CLs form and regress in a stage-dependent manner across the estrous cycle (*63*, *64*); mLuteal1 and mLuteal3 predominated in diestrus, whereas mLuteal2 derived solely from estrus-and metestrus-stage mice (fig. S7J), supporting a developmental progression.

As summarized in fig. S8, granulosa, fibroblast, and endothelial subtypes are conserved, whereas theca, pericyte, and epithelial compartments show species-specific subtype diversity, potentially reflecting organ-scale differences.

Sympathetic nerve loss perturbs first-wave folliculogenesis

Although peripheral nerves regulate organ-specific processes, their role in the ovary remains understudied. Sympathetic and sensory neurons were not detected in this or prior scRNA-seq studies, as their cell bodies reside in the celiac ganglion (*65*). However, we identified an interspecific population of glia, the supporting cells of neurons, using canonical markers [*S100b*/*S100*β (*66*) and *Sox10*/*SOX10* (*67*)].

Peripheral nerves regulate organ function by means of neurotransmitter signaling through target receptors (*68*, *69*), whereas local organ-derived cues maintain axons (*70*). Examining innervation cues and receptors in the ovary (Fig. 5, A and B, and fig. S9, A and B), we found low *Gabbr1*/*GABBR1* [a γ-aminobutyric acid (GABA) receptor] expression in theca cells of both species, whereas only human theca cells

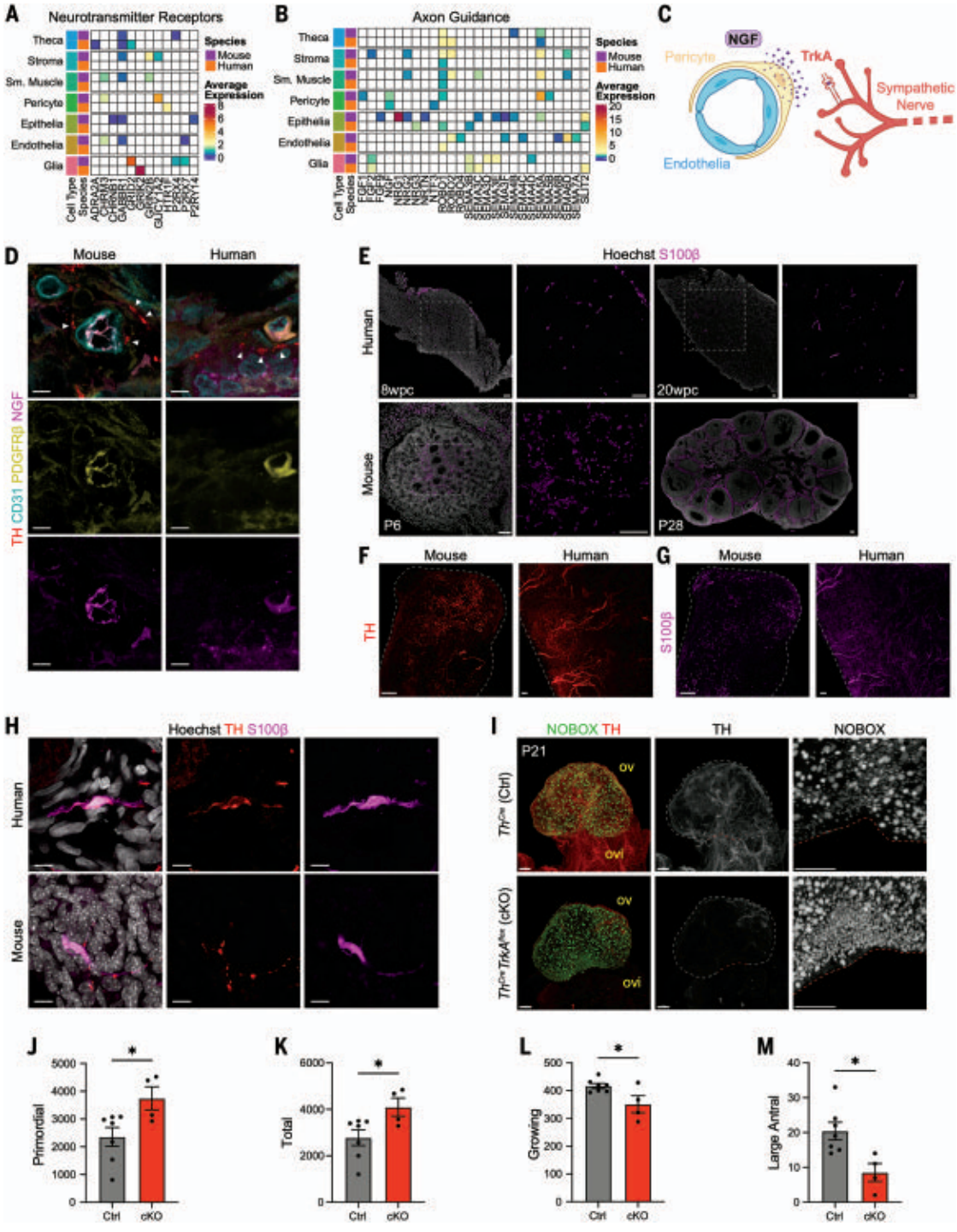
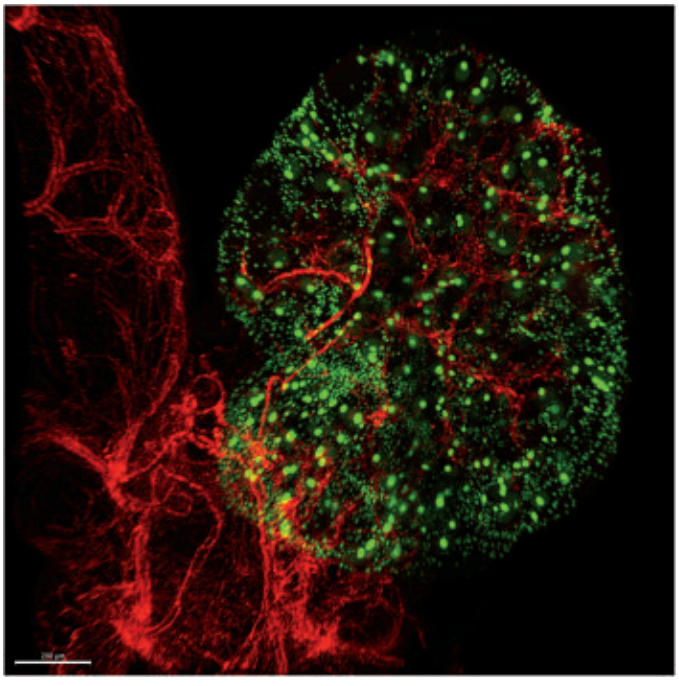


Fig. 5. Sympathetic nerve loss perturbs first wave folliculogenesis. (**A** and **B**) Heatmaps showing the average expression of neurotransmitter receptors (A) and axon guidance genes (B) across the broad cell types in the mouse and human ovary. (**C**) Schematic of neurovascular interactions in the ovary. (**D**) IF staining of mouse and human ovary sections for sympathetic nerves marked by TH (red), endothelial cells marked by CD31 (cyan), pericytes marked by PDGFRβ (yellow), and NGF (magenta). Arrows denote vasculature-associated sympathetic axons. Scale bars, 5 μm. (**E**) IF staining of nuclei marked by Hoechst (gray) and glia marked by S100β (magenta) during development at 8 and 20 wpc in the human ovary and P6 and P28 in the mouse ovary. Scale bars, 50 μm. (**F** and **G**) Whole-mount IF staining of sympathetic nerves marked by TH (red; F) and of glia marked by S100β (magenta; G) in 2M mouse and 23Y human ovaries. Scale bars, 100 μm. (**H**) IF staining of nuclei marked by Hoechst (gray), sympathetic nerves marked by TH (red), and glia marked by S100β (magenta) showing the presence of nerve-associating glia in the mouse and human ovary. (**I**) Whole-mount IF staining of $Th^{Cre/+}$ control and $Th^{Cre/+}TrkA^{fl/fl}$ cKO ovaries at P21, where NOBOX (green) marks all oocytes and TH (red) marks sympathetic nerves. Single-channel images of TH (gray) and NOBOX (gray) to show deletion of nerves and increase of primordial follicle oocytes, respectively. Scale bars, 100 μm. ov, ovary; ovi, oviduct. (**J** to **M**) Quantification of primordial (J), total (K), growing (L), and large antral oocytes (M) in $Th^{Cre/+}$ and $Th^{Cre/+}TrkA^{fl/fl}$ ovaries at P21. All data represented as means ± SEM; $^{*}P < 0.05$; $^{**}P < 0.01$; $^{***}P < 0.001$; Student's *t* test.

expressed *ADRA2A* (an adrenergic receptor) (Fig. 5A). The neuroprotective neuropeptide *Nampt*/*NAMPT* was broadly expressed, though higher in humans (fig. S9A). Both species expressed the axon guidance cue *Robo1*/*ROBO1* in theca cells (Fig. 5B), and glia robustly expressed *Sema3b*/*SEMA3B* (Fig. 5B); only human glia expressed *NRXN3*, a synaptic adhesion molecule (fig. S9B). Mouse and human pericytes expressed *Ngf*/*NGF* (nerve growth factor), essential for axon maintenance (Fig. 5B). Immunofluorescence (IF) confirmed that NGF+ pericytes (PDGFRβ+) were closely associated with sympathetic neurons [tyrosine hydroxylase (TH) +] and endothelial cells (CD31+) in both species, highlighting their role in neurovascular interactions (Fig. 5, C and D).

Peripheral nerves and glia emerge early in ovarian development, detectable by embryonic day (E) 16.5 in mice (*71*) and by 8 weeks postconception (wpc) in humans, expanding further by 20 wpc (Fig. 5E and fig. S9C). As E15 (Theiler stage 23) and 8 wpc (Carnegie stage 19 to 22) represent comparable developmental milestones (*72*), our findings suggest that ovarian innervation occurs within a conserved developmental window, albeit slightly earlier in humans. TH+ sympathetic nerves and S100β+ glia localized to the ovarian medulla during fetal and postnatal development (Fig. 5E and fig. S9, C to E) and later expanded to the theca and fibroblast compartments in adulthood (fig. S9F). 3D imaging revealed extensive innervation in both species, with large neuronal projections spanning medullary and cortical regions (Fig. 5F, fig. S9E, and Movies 2 to 3). Glia were abundant and largely nerve associated (Fig. 5, G and H). Costaining with TUBB3 (pan-neuronal) and TH (sympathetic) showed that most ovarian neurons are sympathetic (fig. S9G).

Sympathetic and sensory nerves influence folliculogenesis (*54*, *73*), particularly in polycystic ovarian syndrome (PCOS), where hypersympathetic activity correlates with increased antral follicles (*74*). However, studying this regulation is challenging owing to the nonspecific or lethal effects of existing tools for in vivo innervation-modulation. Similar to in other organs, ovarian peripheral innervation relies on NGF signaling to tropomyosin-related kinase A (TRKA) receptors on sympathetic nerves (*75*). We developmentally ablated sympathetic nerves by crossing Th^{Cre} (*76*) to $TrkA^{flox}$ mice (*77*, *78*) and analyzed ovarian follicle dynamics after the first wave of folliculogenesis at postnatal day (P) 21 using whole-mount imaging. $Th^{Cre/+}$;$TrkA^{fl/fl}$ (cKO) ovaries lacked sympathetic nerves in the ovary and oviduct (Fig. 5I), confirming successful ablation. cKO ovaries had increased primordial follicles (Fig. 5J) and a higher total follicle count (Fig. 5K) but significantly fewer growing follicles ($P = 0.0274$), especially large antral-staged follicles ($P = 0.0134$) (Fig. 5, L and M), compared with that of Th^{Cre} controls. To exclude oocyte-intrinsic effects, we examined *Th* and *TrkA* (*Ntrk1*) expression during murine ovarian development using ours and Niu and Spradling's (*79*) datasets. *Th* was expressed in oocytes from E11 through adulthood, whereas *TrkA* was not detected (fig. S9, H and I), suggesting that TrkA-dependent signaling is restricted to sympathetic nerves. These findings demonstrate the conserved emergence of sympathetic nerves and glia in ovarian development and reveal that, in mice, sympathetic innervation augments follicle recruitment and maturation during the first wave of folliculogenesis.



Movie 3. Whole-mount staining of NOBOX+ oocytes and TH+ sympathetic nerves in the postnatal C57BL/6 reproductive tract 3D projection and slice view of NOBOX+ oocytes (green) and TH+ sympathetic nerves (red) within the intact P21 ovary, oviduct, and uterus shows extensive innervation surrounding growing follicles in the medullary region of the ovary.

Sympathetic innervation increases with age in mouse and human ovaries

Age-related ovarian decline in both mice and humans is driven by microenvironmental changes, particularly increased fibrosis (*80*) and inflammation (*81*). In mice, several subtypes showed distinct young versus aged contributions (fig. S10, A to A′), whereas in humans, follicular cells came primarily from ERA donors (fig. S10, B to B′). Conversely, hEpithelia3, exclusive to ARA donors, was enriched for inflammatory pathways, suggesting that it represents an age-associated rete ovarii population (Fig. 4, G and H, and fig. S10B′). Mouse and human Endothelia2 subtypes, enriched for aging markers [*Fabp4* (*82*), *Edil3* (*83*), and *ACKR1* (*84*)], clustered together at fine resolution and were derived predominantly from aged ovaries (figs. S7E and S10, A′ to B′), consistent with reports linking vascular decline to murine reproductive aging (*85*).

To identify the microenvironmental compartments most affected by aging, we calculated transcriptional variance explained by age for each cell type using 50 principal components (PCs) and linear regression. In mice, theca cells exhibited the greatest age-related shifts, followed by fibroblasts and smooth muscle (Fig. 6A). In humans, fibroblasts and endothelia were most affected (Fig. 6A′). Immune cells remained largely stable with age in both species.

We grouped homologous genes by age-related fold change (Fig. 6, B and C, and fig. S10, C to F). In theca cells, neuro-repulsive *Sema5A*/*SEMA5A* and *Nexn*/*NEXN* increased with age in mice but decreased in ARA humans, whereas steroidogenic *Cyp11a1*/*CYP11A1* declined in both (Fig. 6B). Androgen receptor (*Ar*/*AR*) gene expression increased with age in epithelia from both species, whereas estrogen receptor (*ESR1*) increased in ARA human epithelia, consistent with estrogen-signaling shifts associated with fibrosis in aging ovaries (*20*) (Fig. 6C). Epithelial progenitor marker *Procr*/*PROCR*, critical for postovulatory repair (*86*), decreased with age in both species, specifically hEpithelia1 (fig. S10G). Fibroblasts showed increased aging markers *Lmna*/*LMNA* (*87*) and *Insr*/*INSR* (*88*) in both species (fig. S10C). Ovarian aging-associated *Foxp1*/*FOXP1* (*18*) and *Igf1r*/*IGF1R* (insulin-like growth factor 1R; *89*) increased in mouse but decreased in human smooth muscle (fig. S10D).

Pathway enrichment analysis of differentially expressed genes (DEGs) identified conserved and species-specific changes (Fig. 6, D and E, and fig. S10, H and I). In theca cells, cholesterol metabolism and steroidogenesis pathways declined (Fig. 6D), whereas proinflammatory p38 MAPK signaling increased with age (Fig. 6E). Only hTheca cells up-regulated mitochondrial inner membrane processes (*90*) (fig. S10H), whereas aged mTheca cells up-regulated axon extension repressors (fig. S10I). Fibroblasts, smooth muscle, and pericytes interspecifically

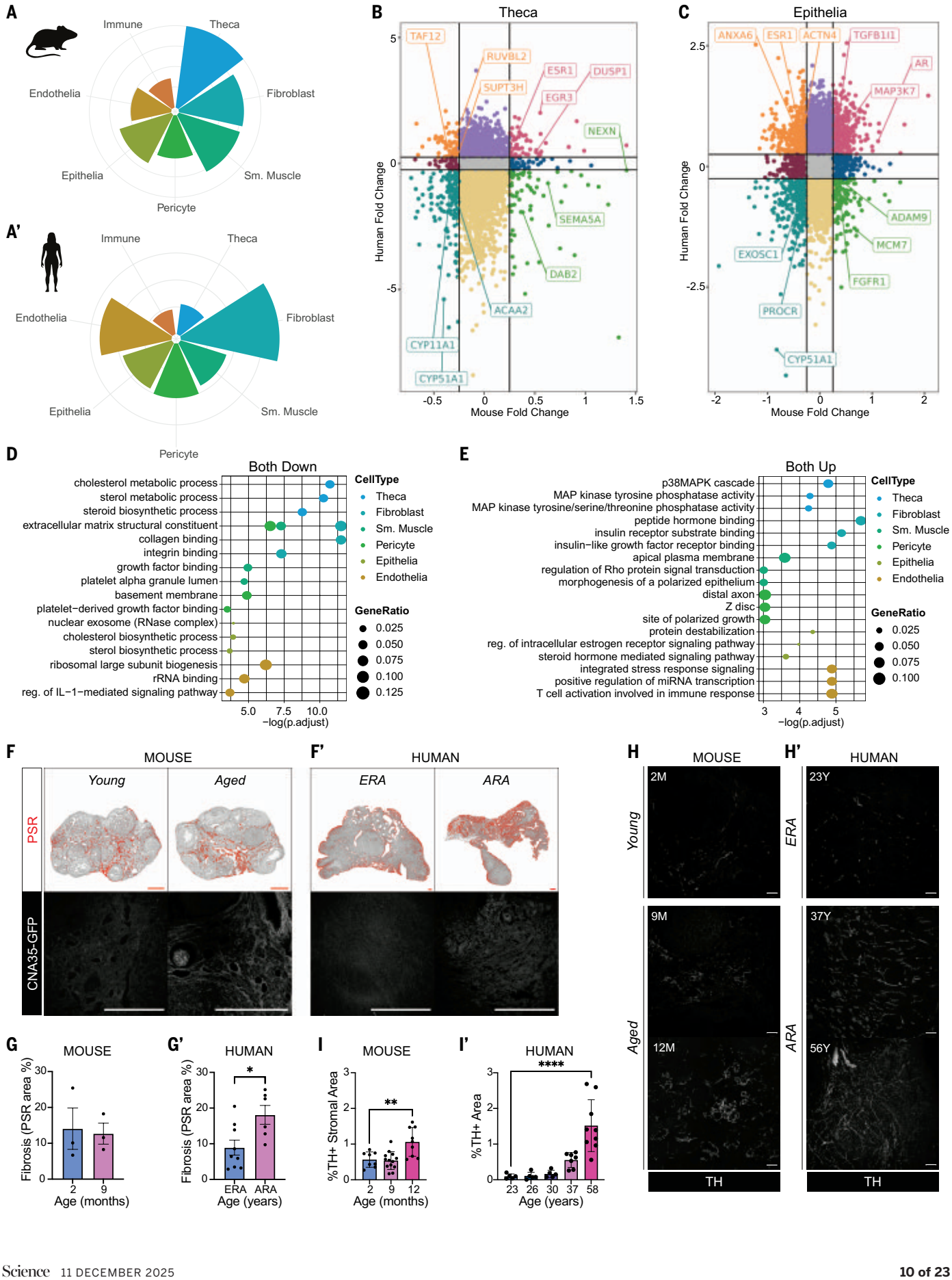

A
Immune
Theca
Fibroblast
Sm. Muscle
Pericyte
Epithelia
Endothelia
A'
Immune
Theca
Fibroblast
Sm. Muscle
Pericyte
Epithelia
Endothelia
B
Theca
TAF12
RUVBL2
SUPT3H
ESR1
DUSP1
EGR3
NEXN
SEMA5A
DAB2
ACAA2
CYP11A1
CYP51A1
Human Fold Change
Mouse Fold Change
C
Epithelia
ANXA6
ESR1
ACTN4
TGFB1I1
AR
MAP3K7
ADAM9
MCM7
FGFR1
EXOSC1
PROCR
CYP51A1
Human Fold Change
Mouse Fold Change
D
Both Down
cholesterol metabolic process
sterol metabolic process
steroid biosynthetic process
extracellular matrix structural constituent
collagen binding
integrin binding
growth factor binding
platelet alpha granule lumen
basement membrane
platelet−derived growth factor binding
nuclear exosome (RNase complex)
cholesterol biosynthetic process
sterol biosynthetic process
ribosomal large subunit biogenesis
rRNA binding
reg. of IL−1−mediated signaling pathway
−log(p.adjust)
CellType
Theca
Fibroblast
Sm. Muscle
Pericyte
Epithelia
Endothelia
GeneRatio
0.025
0.050
0.075
0.100
0.125
E
Both Up
p38MAPK cascade
MAP kinase tyrosine phosphatase activity
MAP kinase tyrosine/serine/threonine phosphatase activity
peptide hormone binding
insulin receptor substrate binding
insulin−like growth factor receptor binding
apical plasma membrane
regulation of Rho protein signal transduction
morphogenesis of a polarized epithelium
distal axon
Z disc
site of polarized growth
protein destabilization
reg. of intracellular estrogen receptor signaling pathway
steroid hormone mediated signaling pathway
integrated stress response signaling
positive regulation of miRNA transcription
T cell activation involved in immune response
−log(p.adjust)
CellType
Theca
Fibroblast
Sm. Muscle
Pericyte
Epithelia
Endothelia
GeneRatio
0.025
0.050
0.075
0.100
F
MOUSE
Young
Aged
PSR
CNA35-GFP
F'
HUMAN
ERA
ARA
G
MOUSE
Fibrosis (PSR area %)
Age (months)
G'
HUMAN
Fibrosis (PSR area %)
ERA
ARA
Age (years)
I
MOUSE
%TH+ Stromal Area
Age (months)
I'
HUMAN
%TH+ Area
Age (years)
H
MOUSE
Young
Aged
2M
9M
12M
TH
H'
HUMAN
ERA
ARA
23Y
37Y
56Y
TH

Fig. 6. Sympathetic innervation increases with age in mouse and human ovaries. (**A** and **A′**) Rose plots illustrating the magnitude of transcriptional variance explained by age across the broad cell types in mouse (A) and human ovaries (A′). (**B** and **C**) Comparative gene expression fold changes between young and aged theca (B) and epithelia (C) with genes colored by similar or diverging changes in expression with age between species. (**D** and **E**) Pathway enrichment analysis of the genes decreased (D) or increased (E) with age in both mouse and human cell types. Select GSEA pathway names were abbreviated in (D) and (E); see table S3 for the full names. (**F** and **F′**) Representative images of thresholded PSR staining in the young (2M) and aged (9M) mouse (F) and ERA (30Y) and ARA (55Y) human (F′) ovaries with high-magnification IF staining panels of fibrillar collagen marked by CNA35-GFP (gray). Scale bars, 300 μm. (**G** and **G′**) Quantification of the percentage of fibrotic tissue in the young and aged mouse (G) and human (G′) ovaries. Data represented as means ± SEM; $*P < 0.05$; Student's *t* test. (**H** and **H′**) IF staining of mouse (H) and human (H′) ovary for sympathetic nerves with TH (gray) at young and aged timepoints. Scale bars, 50 μm. (**I**) Quantification of the percentage of TH+ area within the stroma in young and aged mouse ovary sections. (**I′**) Quantification of the percentage of TH+ area in ERA and ARA human ovary sections. Data represented as means ± SEM; $*P < 0.05$; $**P < 0.01$; $***P < 0.001$; $****P < 0.0001$; ANOVA test.

down-regulated *Col1a2*/*COL1A2*, *Col3a1*/*COL3A1*, *Col4A1*/*COL4A1*, and *Col18a1*/*COL18A1* (fig. S10, C to E), refining previous unfractionated murine ovary data (*91*). Despite known age-related collagen accumulation, aged fibroblasts down-regulated collagen-binding and integrin-related pathways (Fig. 6D). Picrosirius red (PSR) staining (Fig. 6, F to F′) revealed stable collagen levels until 9M in mice (*80*), whereas human ARA ovaries showed significant fibrosis ($P = 0.0168$) (*92*) (Fig. 6, G to G′). Both species showed reactivity for collagen-binding marker CNA35–green fluorescent protein (GFP) (*93*) (Fig. 6, F to F′). This discrepancy between transcript and protein suggests a conserved compensatory response that slows fibrosis with age in multiple stromal cell types.

Given the role of sympathetic nerves in follicle recruitment, we examined age-related shifts in neuronal signaling (fig. S10, J and K). Theca cells in both species up-regulated *Gabbr1*/*GABBR1*, a receptor for hormone-sensitive GABA (*94*) (fig. S10J), potentially compensating for reduced perimenopausal GABAergic tone (*95*). Aging increased glial *Fgf2*/*FGF2*, pericyte *Ngf*/*NGF*, and theca *Robo1*/*ROBO1* and *ROBO2* expression, especially in humans (fig. S10K). Because FGF2 (*96*), NGF (*97*), and ROBO1/2 (*98*) regulate axonal growth, we quantified TH+ axon density in young and aged ovaries (Fig. 6, H to I′). Sympathetic axon density increased significantly by 12M in mice ($P = 0.0035$) (Fig. 6, H and I) and in ARA ovaries compared with that in ERA ovaries ($P < 0.0001$) (Fig. 6, H′ and I′). As estrogen dampens sympathetic innervation (*99*), this increase likely reflects postmenopausal estrogen decline.

Aging alters the transcriptome of oocytes more than that of granulosa cells

Despite age-related transcriptional changes in the soma, fertility decline is largely attributed to oocyte deterioration (*100*). To quantify oocyte competence, we performed in vitro fertilization (IVF) on C57BL/6 mice at 2, 4, 6, 9, and 12M ($n \geq 6$ per group). Gonadotropin-induced ovulation yield declined at 9M, consistent with reduced growing follicles (Fig. 7A), whereas maternal superovulation response rates remained stable until 12M (Fig. 7B), suggesting that oocyte availability declines before hormone responsiveness. Kaplan-Meier survival analysis, which weighs blastocyst formation probability per oocyte, revealed that developmental competence remained stable between 2 and 4M but declined by 6M, with the 2-cell (2C)–to-blastocyst transition being especially vulnerable to age (Fig. 7C). By 9 and 12M, survival to both the 2C (9M, $P = 0.0201$; 12M, $P = 0.0062$) and blastocyst (9M, $P = 0.0009$; 12M, $P = 0.0003$) stages significantly declined. Statistical modeling confirmed that sperm quality did not impact developmental success (table S4). Observed decline in C57BL/6 oocyte quantity and competence by 9M (Fig. 7D) echoes the reduced follicle numbers and embryo development rates in ARA humans (>35Y) (*101*).

Because follicles support oocyte maturation, we examined age-related transcriptional changes in granulosa cells and oocytes. Mouse and human oocyte and granulosa clusters were consolidated to maximize young versus aged comparisons. hPreantral- and hAntral-Cumulus clusters were merged into a single Cumulus cluster, and hMitotic cells, most similar to hMural, were combined into a Mural cluster (fig. S11A). For cross-species comparison, mCumulus or mMural and mMitotic granulosa clusters were merged (fig. S11B), whereas mGhr+ granulosa remained a species-specific cluster. Oocyte clusters (Fig. 3, A to A′) were divided into Early and Late milestones along pseudotime using scFates (fig. S11, A′ and B′). Variance-explained calculations revealed greater age-dependent transcriptional change in oocytes than granulosa cells. The most affected oocyte group differed by species: mEarly and hLate oocytes exhibited the largest age-related transcriptomic shifts (Fig. 7, E to E′). Among granulosa subtypes, Cumulus cells were most affected by age.

Age-associated DEGs were identified for each follicular cell type in both species. Differential expression was visualized using minus versus average (MA) plots, displaying gene expression levels versus age-related fold change. Cross-species similarity was assessed by mapping significant DEGs from one species onto the MA plots of the other [mouse: increased (red)/decreased (blue); human: increased (magenta)/decreased (cyan); source species (inlay)] (fig. S11, C to G). Only ARA hLate oocytes captured by 10X were included in DE analysis, as Smart-seq2 did not capture this population. Consistent with variance-explained results, mEarly and hLate oocytes showed the most age-related DEGs, though few overlapped, indicating species-specific oocyte aging (fig. S11, C, D, and H). Unlike in human oocytes, all zona pellucida transcripts (*Zp1*, *Zp2*, *Zp3*) declined with age in mEarly oocytes, suggesting compromised structure and sperm binding. In hLate oocytes, chromosome segregation genes [*FMN2* (*102*), *RANGAP1* (*103*), and *SMC1B*] decreased, wheras DNA damage response genes [*RAD50* and *MDC1* (*104*, *105*)] increased. Similar to oocytes, Cumulus granulosa subtypes had the most DEGs with largely species-specific changes.

To compare follicle aging processes, we performed pathway enrichment on age-related DEGs for each follicular subtype in both species (Fig. 7, F and G, and fig. S12, A to C). Pathways up-regulated with age were denoted as increased (mouse: red, human: magenta), and those enriched in young subtypes as decreased (mouse: blue, human: cyan). Young mCumulus DEGs were enriched for hormone secretion, while ERA hCumulus and hMural DEGs were enriched for vesicle trafficking, a potential oocyte-granulosa communication mechanism (*106*) (fig. S12, A and B). Young mEarly oocytes were enriched for cytoplasmic translation, whereas ERA hEarly oocytes were enriched for platelet alpha granule pathways, which include oocyte-relevant genes [*IGF1* (*107*), *HSPA1A* (*108*), *SMAD7* (*109*)] (Fig. 7F). With aging, mCumulus and hCumulus granulosa were enriched for inflammatory and reactive oxygen species pathways (fig. S12B), and aged Ghr+ were enriched for extracellular matrix binding (fig. S12C). Aged mEarly oocytes were enriched for protein ubiquitination and target of rapamycin (TOR) signaling, whereas ARA hEarly oocytes were enriched for DNA damage, aligning with declining oocyte quality and the efficacy of TOR inhibition through rapamycin (*110*). Unlike largely unchanged mLate oocytes, hLate oocytes were enriched for spindle organization at ERA and chromatin condensation pathways at ARA, both implicated in age-related aneuploidy (*111*) (Fig. 7G).

Follicles rely on coordinated cell-cell communication for successful maturation. Using CellChat, we identified species-shared (purple) and -specific (green) age-related signaling changes, assigning granulosa subtypes as senders (ligand expressing) and oocytes as receivers (receptor expressing). Less-mature granulosa subtypes (mPreantral-Cumulus and hCumulus) were paired with Early oocytes (Fig. 7H); more-mature granulosa subtypes (mAntral-Cumulus, mMitotic, mMural, hCumulus,

and hMural) were paired with Late oocytes (Fig. 7I). Given its putative transitory state, mGhr+ was included as a sender for both mEarly and mLate oocytes. KIT signaling (*112*) was detected between mPreantral-Cumulus granulosa and mEarly oocytes, and BMP signaling was detected between mGhr+ granulosa and mEarly oocytes (Fig. 7H). ERA hCumulus granulosa communicated with hEarly oocytes through macrophage migration inhibitory factor [MIF; (*113*)] and midkine [MK; (*114*)], pathways implicated in oocyte dynamics. Cyclophilin A (CypA) signaling, which regulates extracellular matrix proteins through transforming growth factor–β (TGF-β)/Smad3 (*115*), was conserved between granulosa and Early oocytes in both species. In aged mice, ANGPTL and IGF signaling to mLate oocytes decreased (Fig. 7I). In humans, CD99 and 27HC signaling, both implicated in ovarian cancer, increased between ARA hCumulus granulosa and hLate oocytes (*116*, *117*). CDH signaling, essential for follicle integrity, declined between ARA hMural granulosa and hLate oocytes, consistent with the role of N-cadherin in follicular structure and ovulatory capacity (*118*).

Theca cells support follicle growth, provide structural integrity, and drive granulosa estrogen synthesis via androgen secretion (*119*). Using CellChat, we identified age-related theca-to-granulosa signaling changes, designating theca subtypes as senders and Cumulus or Mural granulosa as receivers (fig. S12, D and E). In both species, testosterone signaling was present across all theca subtypes, whereas androstenedione signaling, a testosterone precursor, was restricted to mTheca1, mTheca3, and hTheca2. In mice, both signals remained stable with age, whereas in humans, they were specific to ERA hTheca. CypA signaling, present across all theca subtypes, was restricted to ERA human and Aged mouse follicles (fig. S12D). IGF signaling, which stimulates sex steroid production (*120*), was specific to ERA human theca-granulosa crosstalk, whereas age-related decreases in cholesterol signaling were conserved between species, reiterating aforementioned findings (Fig. 6D and fig. S12, D and E). These results reveal species-specific androgen signaling shifts with age; given the perimenopausal decline in testosterone (*121*), associated with aging-related issues such as cognitive decline and bone loss (*122*, *123*), this divergence highlights differential impacts of ovarian aging on follicular endocrine function.

Discussion

Across the reproductive window, we compared mouse and human ovaries at the functional, tissue, cellular, and transcriptional levels. Whole-organ imaging and 3D follicle mapping revealed age-related declines in follicle density in both species, including secondary follicle loss by 4M in mice. We identified interspecific spatiotemporal similarities in ovarian peripheral nervous system development and the presence of a glial population. Our dataset profiles oocytes across stages and species, uncovering divergent maturation gene patterns and species-specific age-related intrafollicular and microenvironmental changes. This study spans ovarian development, homeostasis, and aging, distinguishing species-shared or -specific ovarian features and defining the utility of the widely used C57BL/6 mouse strain as a model for humans.

The number of nonrenewing, primordial oocytes determines fertility and reproductive lifespan (*124*) but remains difficult to quantify. Clinically, antral follicle counts through ultrasound and circulating AMH serve as proxies for ovarian reserve (*125*, *126*), though their relationship to primordial follicle number remains unclear. With greater precision and throughput than previously possible, in C57BL/6 mice, we observed a linear relationship between primordial and growing follicles from 2 to 9M, followed by a sharp decline, suggesting that recruitment and attrition are steady until 9M. Secondary follicles were the most vulnerable with age, decreasing as early as 4M, alongside a drop in overall follicle density. Because the secondary stage is transient, this may reflect reduced survival or altered follicle growth dynamics. This is consistent with recently reported AMH decline by 6M in C57BL/6 mice, rescued by senolytics that increased primordial and early growing follicles, suggesting that endocrine changes reflect downstream consequences of early follicle depletion (*127*). Extending our whole-mount, cellular-resolution imaging to human ovaries, we identified species differences: Mouse oocytes were distributed throughout the ovary and become increasingly clustered by 6M (*128*), whereas human oocytes were confined to cortical "pockets" separated by follicle-depleted regions at ARA. Building on previous reports of regional heterogeneity in human cortical follicle density (*129*), our 3D spatial data enable cross-species comparison and highlight differences in oocyte distribution across the reproductive lifespan. The shift in the growing-to-primordial follicle ratio at 9M in mice likely models dysregulated human folliculogenesis during the fourth decade (*129*) and underscores the need for improved ovarian reserve biomarkers.

The gargantuan size of oocytes, expanding ~60 μm in mice (*130*) and ~90 μm in humans (*131*) during folliculogenesis, has limited their capture in droplet-based studies. By coupling 10X Genomics with well-based Smart-seq2, we broadly captured somatic cell types, except luteal cells and neurons, and oocytes across maturation stages from unstimulated mouse and human ovaries. Cross-dataset comparison revealed shared granulosa, fibroblast, and endothelial subtypes, whereas theca, pericyte, and epithelial compartments exhibited species-specific differences. Although we report the estrous stage for mouse data, consistent menstrual cycle metadata were unavailable for human donors, precluding direct cross-species comparisons of hormonal cycling. Mono-ovulation and possible hormonal contraceptive use in humans likely contributed to the underrepresentation of luteal cells. Accordingly, interspecies comparisons should be interpreted cautiously for cell types with abundance, function, or transcriptional profiles that vary with reproductive stage. Hormonal staging and broader sampling will enhance future understanding of cycle-dependent ovarian biology.

A population of ovarian glial cells present in both developing and adult mouse and human ovaries was identified by scRNA-seq and confirmed by IF. Despite their abundance by immunostaining, glia were likely underrepresented in previous ovarian scRNA-seq datasets owing to dissociation sensitivity. Single-nucleus RNA-seq may improve detection, although this approach may undercapture transcriptionally quiescent oocytes (*132*). Developmental patterning of ovarian glia and sympathetic nerves is similar between humans and mice (*71*). Based on localization and transcriptional identity, these glia likely support peripheral nerves, contributing to ovarian innervation integrity. Using a sympathetic neuron-specific conditional deletion model (*77*), we showed a functional role in the first wave of follicle recruitment and maturation. Absence of sympathetic nerves increased primordial but reduced large antral follicles, reinforcing their role in maturation and aligning with PCOS, where elevated sympathetic activity correlates with increased antral follicles (*74*); thus, sympathetic nerves may be targets for controlling precocious follicle maturation. The observed rise in sympathetic axon density in ARA ovaries, together with known age-related increases in ovarian nerve fibers (*133*) and adrenergic activity (*134*), suggests a complex regulatory shift beyond neuronal dysregulation. Future studies should assess whether expanded innervation compensates for declining follicle reserve and whether glial cells actively modulate neuro-ovarian signaling or fertility.

Age-related fertility decline is linked to decreased oocyte quality (*135*, *136*). Although we likely did not capture the terminal stage(s) of human oocyte maturation owing to mono-ovulation, hLate and mLate oocytes were similarly enriched for chromosome segregation pathways, a feature previously associated only with human preovulatory oocytes (*137*). mEarly oocytes exhibited greater age-related transcriptomic shifts than mLate oocytes, whereas hLate oocytes showed the opposite trend. A macaque scRNA-seq study reported more DEGs in mature oocytes with age (*19*), suggesting that primates undergo more pronounced transcriptional changes in late-stage oocytes. Modest pathway overlap at early stages indicates that Early oocytes follow

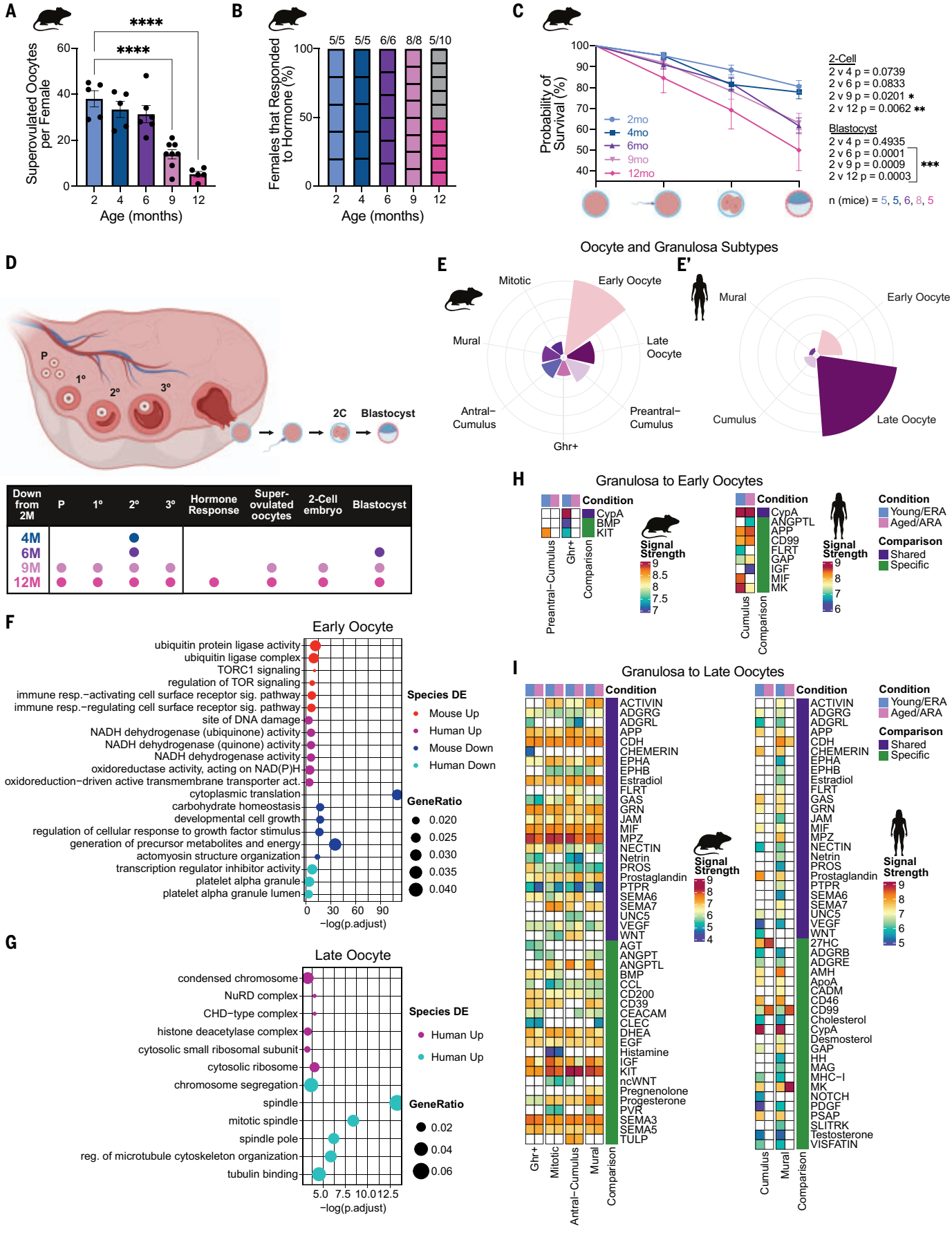

A
Superovulated Oocytes per Female
Age (months)
****
****
B
Females that Responded to Hormone (%)
5/5 5/5 6/6 8/8 5/10
Age (months)
C
Probability of Survival (%)
2mo
4mo
6mo
9mo
12mo
2-Cell
2 v 4 p = 0.0739
2 v 6 p = 0.0833
2 v 9 p = 0.0201 *
2 v 12 p = 0.0062 **
Blastocyst
2 v 4 p = 0.4935
2 v 6 p = 0.0001
2 v 9 p = 0.0009
2 v 12 p = 0.0003
***
n (mice) = 5, 5, 6, 8, 5
D
P
1°
2°
3°
2C
Blastocyst
Down from 2M
P
1°
2°
3°
Hormone Response
Super-ovulated oocytes
2-Cell embryo
Blastocyst
4M
6M
9M
12M
Oocyte and Granulosa Subtypes
E
Mitotic
Early Oocyte
Late Oocyte
Preantral–Cumulus
Ghr+
Antral–Cumulus
Mural
E'
Mural
Early Oocyte
Cumulus
Late Oocyte
H
Granulosa to Early Oocytes
Condition
CypA
BMP
KIT
Preantral–Cumulus
Ghr+
Comparison
Signal Strength
Condition
CypA
ANGPTL
APP
CD99
FLRT
GAP
IGF
MIF
MK
Cumulus
Comparison
Signal Strength
Condition
Young/ERA
Aged/ARA
Comparison
Shared
Specific
F
Early Oocyte
ubiquitin protein ligase activity
ubiquitin ligase complex
TORC1 signaling
regulation of TOR signaling
immune resp.−activating cell surface receptor sig. pathway
immune resp.−regulating cell surface receptor sig. pathway
site of DNA damage
NADH dehydrogenase (ubiquinone) activity
NADH dehydrogenase (quinone) activity
NADH dehydrogenase activity
oxidoreductase activity, acting on NAD(P)H
oxidoreduction−driven active transmembrane transporter act.
cytoplasmic translation
carbohydrate homeostasis
developmental cell growth
regulation of cellular response to growth factor stimulus
generation of precursor metabolites and energy
actomyosin structure organization
transcription regulator inhibitor activity
platelet alpha granule
platelet alpha granule lumen
−log(p.adjust)
Species DE
Mouse Up
Human Up
Mouse Down
Human Down
GeneRatio
0.020
0.025
0.030
0.035
0.040
G
Late Oocyte
condensed chromosome
NuRD complex
CHD−type complex
histone deacetylase complex
cytosolic small ribosomal subunit
cytosolic ribosome
chromosome segregation
spindle
mitotic spindle
spindle pole
reg. of microtubule cytoskeleton organization
tubulin binding
−log(p.adjust)
Species DE
Human Up
Human Up
GeneRatio
0.02
0.04
0.06
I
Granulosa to Late Oocytes
Condition
ACTIVIN
ADGRG
ADGRL
APP
CDH
CHEMERIN
EPHA
EPHB
Estradiol
FLRT
GAS
GRN
JAM
MIF
MPZ
NECTIN
Netrin
PROS
Prostaglandin
PTPR
SEMA6
SEMA7
UNC5
VEGF
WNT
AGT
ANGPT
ANGPTL
BMP
CCL
CD200
CD39
CEACAM
CLEC
DHEA
EGF
Histamine
IGF
KIT
ncWNT
Pregnenolone
Progesterone
PVR
SEMA3
SEMA5
TULP
Ghr+
Mitotic
Antral–Cumulus
Mural
Comparison
Signal Strength
Condition
ACTIVIN
ADGRG
ADGRL
APP
CDH
CHEMERIN
EPHA
EPHB
Estradiol
FLRT
GAS
GRN
JAM
MIF
MPZ
NECTIN
Netrin
PROS
Prostaglandin
PTPR
SEMA6
SEMA7
UNC5
VEGF
WNT
27HC
ADGRB
ADGRE
AMH
ApoA
CADM
CD46
CD99
Cholesterol
CypA
Desmosterol
GAP
HH
MAG
MHC−I
MK
NOTCH
PDGF
PSAP
SLITRK
Testosterone
VISFATIN
Cumulus
Mural
Comparison
Condition
Young/ERA
Aged/ARA
Comparison
Shared
Specific
Signal Strength

Fig. 7. Human and C57BL/6 oocytes have a larger magnitude of transcriptional change with age than granulosa cells. (**A**) Total number of oocytes retrieved at 2M ($n = 5$), 4M ($n = 7$), 6M ($n = 6$), 9M ($n = 8$), and 12M ($n = 5$) from superovulation. Data from females unresponsive to hormonal stimulation were excluded. Data represented as means ± SEM; *$P < 0.05$; **$P < 0.01$; ***$P < 0.001$; ****$P < 0.0001$; ANOVA test. (**B**) Percentage of mice at each age that ovulated in response to hormone priming. The numbers above each bar indicate the number of responding females out of the total injected. (**C**) Kaplan-Meier-style plot showing the percentage of superovulated oocytes that successfully progressed to the 2C and blastocyst stages following in vitro fertilization at 2M ($n = 5$), 4M ($n = 5$), 6M ($n = 5$), 9M ($n = 8$), and 12M ($n = 5$). Data are presented as Kaplan-Meier estimates ± SEM; Mantel-Cox test. Curves represent the proportion of oocytes that survived at each developmental stage, conditional on successful transfer. (**D**) Schematic of significant declines in fertility and oocyte quality in C57BL/6 ovaries relative to 2M of age. Colored circles indicate statistically significant reductions in oocyte quality; ANOVA and Mantel-Cox test. (**E** and **E′**) Rose plots illustrating the magnitude of transcriptional variance explained by age across the cell types of the follicle in the mouse (E) and human (E′) ovaries. (**F** and **G**) Pathways enriched in genes differentially expressed with age in the Early (F) and Late (G) oocytes in mouse (increased, red; decreased, blue) and human (increased, magenta; decreased, cyan) samples. Select GSEA pathway names were abbreviated in (F) and (G); see table S3 for the abbreviated pathways and the full name. (**H** and **I**) CellChat analysis between aged and young mPreantral-Cumulus and hCumulus subtypes as the sender with the Early oocytes as the receiver (H) and the mAntral-Cumulus, mMitotic, and mMural and hCumulus and hMural subtypes as the sender with the Late oocytes as the receiver (I). Pathways shared between species are indicated in purple; species-specific pathways are denoted in green.

species-specific programs, limiting the utility of C57BL/6 for studying early human oocytes. Understanding oocyte quality with age is crucial for improving assisted reproductive technology, as identifying signaling mediators may reveal therapeutic targets. Analysis of the most variable age-associated genes across maturation stages highlighted TOR signaling in mEarly oocytes, reinforcing previous findings that rapamycin delays murine ovarian aging and suggesting that global mTOR inhibition may improve oocyte quality (*89*, *110*). Detection of mouse ZP3 6M after metabolic labeling (*138*, *139*) suggested that oocytes may retain their ZP long-term. Thus, age-related decline of *Zp* transcript in mEarly oocytes may impair ZP integrity by reducing de novo translation or maintenance, accelerating degradation with age.

Recent studies identified aging hallmarks in the ovarian microenvironment (*140*); we found that fibroblast, smooth muscle, and epithelial compartments exhibited the greatest age-related transcriptional changes across species. Previous mouse studies detected fibrotic foci between 7 to 9M and significant fibrosis by 14 to 17M (*20*, *80*). Consistently, we observed no increase by 9M in mice but detected a significant fibrotic increase in ARA human ovaries. Murine stromal fibrosis is generally low at the onset of reproductive aging and strain dependent (*141*), preceding the extensive fibrosis observed after 22M (*80*), suggesting that C57BL/6 may be a suboptimal model for early fibrotic remodeling. Despite species differences, both showed age-related decreases in fibroblast collagen transcripts, suggesting a conserved compensatory down-regulation to delay fibrosis. These findings support early antifibrotic interventions to preserve ovarian function during reproductive aging (*142*, *143*).

This study provides a comprehensive comparison of species-shared and -specific facets of mammalian ovarian biology from development through aging but has limitations. We generated robust mouse and human ovary scRNA-seq datasets, capturing an interspecific ovarian glial population and overcoming previous difficulties in oocyte capture by integrating well-based and microfluidic technologies with published datasets. The number of high-quality human samples was limited by the difficulty of obtaining ovarian tissue from reproductively active individuals not undergoing cryopreservation, cancer treatment, or hormone therapy. Because our ARA samples for scRNA-seq were likely post-menopausal, we supplemented with oocytes and granulosa cells from 36- to 39-year-old donors from Wu *et al.* (*18*). We examined only one mouse strain, C57BL/6, selected for its widespread use and the availability of transgenic and knockout lines. Notably, our study leveraged both Smart-seq2 and 10X Genomics platforms, enabling us to capture rare and large cell types, such as non–hormone primed oocytes at all developmental stages alongside the full diversity of somatic cell types within the ovary. This combination of technologies yielded a comprehensive cellular and transcriptional atlas of ovarian aging across species. Future studies incorporating additional strains, expanded donor cohorts, and hormonal staging will further refine cross-species comparisons of ovarian aging. This work enhances our understanding of the mouse as a model for human ovarian biology and offers a valuable resource for future interspecific analyses.

Materials and Methods

Mice

All mouse work was performed under the University of California, San Francisco (UCSF) Institutional Animal Care and Use Committee guidelines in an approved facility of the Association for Assessment and Accreditation of Laboratory Animal Care International. All mice used in this study were on a C57BL/6J background. To ablate sympathetic nerves, $Th^{Cre/+}$ mice (MGI: 3056580) were crossed to $TrkA^{fl/fl}$ mice (MGI: 3583733) to generate $Th^{Cre/+}TrkA^{fl/fl}$ conditional knockout mice. $Th^{Cre/+}$ mice were used as a control as the *TrkA* floxed allele is a hypomorph (*77*, *78*).

Murine vaginal cytology

Primary cells were collected by rinsing the vaginal canal of virgin, wild type C57BL/6J mice with sterile saline. Cells were imaged using a Leica DMi8 Thunder with an N PLAN 5X/0.12 objective. Estrous cycle was staged as previously described (*144*) and corroborated with EstrousNet (*145*).

Human ovary samples

Human tissue was procured as previously described (*146*). Briefly, donated ovaries were procured at various hospital locations in Northern California through collaboration with Donor Network West (DNW, San Ramon, CA, USA), the UCSF Viable Tissue Acquisition Laboratory (VITAL) core, and UCSF Options Center. DNW is a not-for-profit, federally mandated organ procurement organization (OPO) for Northern California. Recovered ovaries were considered for research only after obtaining records of first-person authorization (donor's consent during DMV registrations) and/or consent from the family members of the donor. The Tabula Sapiens research protocol (STAN-19-104) was approved by the DNW internal ethics committee and the medical advisory board, as well as by the Institutional Review Board at Stanford University which determined that this project does not meet the definition of human subject research as defined in federal regulations 45 CFR 46.102 or 21 CFR 50.3. Ovaries were processed consistently across all donors. Each ovary was collected and transported in University of Wisconsin (UW) solution on ice to preserve cell viability. A private courier service was used to keep the time between ovary procurement and initial tissue preparation as short as possible. Tissue was obtained from otherwise healthy organ donors who experienced sudden, unexpected death. As a result, comprehensive longitudinal clinical data, including information on contraceptive use, were not available. This limitation may impact the interpretation of factors influencing ovarian cellular composition and transcriptional state.

Lysis plate preparation

Lysis plates were prepared by dispensing 4 μL of lysis buffer (0.02 5μl 10% Triton, 1.25 μl 10 mM dNTP mix, 0.125 μl 100 μM Oligo-dt30VN (IDT, 5′AAGCAGTGGTATCAACGCAGAGTACT30VN-3′), 0.125 μl of Recombinant RNase Inhibitor (RRI) (Takara Bio, 2313B), and 2.48 μl water) into 96-well hard-shell PCR plates using a SPT Labtech Dragonfly Discovery liquid handler. All plates were sealed with a clear microseal,

centrifuged for 1 min at 1000 rcf and immediately stored at -80°C until hand picking of oocytes.

Single-cell dissociation

Following dissection of murine or human ovaries to remove surrounding tissues (oviduct/fallopian tube, bursa, uterus, adipose), whole ovaries (murine) or ovary pieces (human) were gently chopped using a razor blade and then transferred to a Conical tube with 2 mg/mL collagenase type IV (Gibco, 17104019) in DMEM (Gibco, 11960044). Tubes were incubated at +37°C shaking at 250 rpm for 20 min then centrifuged at 250 x g for 5 min. The supernatant was aspirated and 0.25 % trypsin-EDTA (Gibco, 25200056) was added. Tubes were incubated at +37°C shaking at 250 rpm for 20 min then centrifuged at 250 x g for 5 min. The supernatant was aspirated, and the tissue was quenched with 10 % FBS (Gibco, 10438026) in DMEM. Using a P1000, tissue was gently triturated to generate a single cell suspension. The cell suspension was filtered using a reversible 37 μm sieve (STEMCELL Technologies, 27215) which was rinsed once with quench buffer (<37 μm filtered flow through for 10X), and then flipped and placed in a new tube for rinsing with quench buffer (>37 μm unfiltered suspension containing mature oocytes from which to handpick for Smart-seq2).

Smart-seq2 library preparation

Single oocytes were handpicked from the >37-μm unfiltered suspension using an EZ-Grip pipette with a 125 μm EZ-Tip, briefly washed in 0.04% BSA-PBS, and transferred into individual wells containing lysis buffer master mix. Lysed oocytes were snap-frozen on dry ice and stored at −80°C for further processing by the Genomics Platform at the Chan Zuckerberg Biohub SF.

Reverse transcription (RT) and complementary DNA (cDNA) synthesis were performed in 96-well plates using the Smart-seq2 protocol (*29*, *146*–*148*). To preserve RNA integrity, 2–4 lysis plates were thawed on ice and processed in a pre-PCR laboratory. RT master mix (6 μL per well in 96-well plates; 0.6 μL per well in 384-well plates) was prepared using the following components: 0.06 μL 1M $MgCl_2$, 2 μL 5X First-Strand Buffer (Takara Bio, 639538), 2 μL 5M Betaine, 0.5 μL 100 mM DTT, 0.1 μL 100 μM TSO (Exiqon, 5′ AAGCAGTGGTATCAACGCAGAGTGAATrGrGrG-3′), 0.25 μL RRI, 1 μL SmartScribe Reverse Transcriptase (Takara Bio, 639538), and 0.09 μL water. The RT master mix was dispensed into each well using an SPT Labtech Dragonfly Discovery liquid handler. Plates were sealed with a clear microseal, centrifuged at 1,000 rcf for 1 min, and incubated in a thermal cycler (Applied Biosystems ProFlex or Bio-Rad C1000 Touch Thermal Cycler) with the following conditions: 42°C for 90 min, followed by 70°C for 5 min.

cDNA amplification was performed by adding 15 μL of master mix per 96-well plate (1.5 μL per 384-well plate), containing 12.5 μL KAPA HiFi HotStart ReadyMix 2X (Kapa Biosystems, KK2602), 0.25 μL 10 μM IS PCR primer (IDT, 5′-AAGCAGTGGTATCAACGCAGAGT-3′), 0.113 μL Lambda Exonuclease (NEB, M0262L), and 2.14 μL water. The cDNA master mix was dispensed using an SPT Labtech Dragonfly Discovery, and the plates were sealed, centrifuged at 1,000 rcf for 1 min, and subjected to the following cycling conditions: 37°C for 30 min; 95°C for 3 min; 21 cycles of 98°C for 20 s, 67°C for 15 s, 72°C for 4 min; followed by a final extension at 72°C for 5 min.

cDNA quantity was spot-checked using a Quant-iT dsDNA High Sensitivity Kit (Thermo Fisher, Q33120) and fluorescence was measured using a SpectraMax M5 microplate reader (Molecular Devices). cDNA quality was assessed on an Agilent 5300 Fragment Analyzer. High-concentration cDNA samples were diluted 1:10 with nuclease-free water for optimal enzymatic fragmentation.

Library preparation was performed using Illumina's Nextera XT DNA Library Prep Kit (FC-131-1096), miniaturized for 384-well plates using an SPT Labtech Firefly liquid handler. Briefly, 0.4 μL cDNA (<1 ng) was stamped into each well of a 384-well plate, followed by 1.4 μL of tagmentation master mix (1 μL Tagment DNA buffer (TD) and 0.4 μL Amplicon Tagment Mix (ATM)). The plates were sealed, centrifuged at 2,000 rcf for 1 min, and incubated at 55°C for 5 min. Tagmentation was stopped by adding 0.4 μL of Neutralize Tagment Buffer (NT), followed by centrifugation at 2,000 rcf for 5 min.

Index PCR was performed by adding 1.2 μL of Nextera PCR Master Mix (NPM) and 0.8 μL of Nextera index adapters (0.4 μL of 5 μM i5 indexing primer, 0.4 μL of 5 μM i7 indexing primer, IDT). The thermal cycling program consisted of: 72°C for 3 min; 95°C for 30 s; 12 cycles of 95°C for 10 s, 55°C for 30 s, 72°C for 30 s; followed by a final extension at 72°C for 5 min.

Barcoded libraries were pooled using an SPT Labtech Mosquito LV, purified with two consecutive 0.7X AMPure XP bead clean-ups (Beckman Coulter, A63881), and eluted in 30 μL of nuclease-free water. Library fragment size was analyzed on an Agilent 4150 Tapestation System with D5000 ScreenTape (5067-5588) and quantified via qPCR (Bio-Rad CFX96 RT System) using the KAPA Library Quantification Kit (Kapa Biosystems, KK4923).

10X GEX library preparation

Filtered cell suspensions (<37 μm flow through) were counted and adjusted to 1,000 cells/μL in 0.04% BSA (Research Products International, A30075) in 1X PBS. Library preparation was performed by the UCSF Genomics CoLabs using the 10X Genomics Chromium Next GEM Single Cell 3′ Kit with dual indexing, following the manufacturer's protocol.

Sequencing and data processing

10X libraries were pooled and sequenced on NovaSeq S2 flow cells. Smart-seq2 libraries were pooled equimolar in sets of 4 to 16 384-well plates and sequenced on NextSeq 2000 P3 and NovaSeq S4 flow cells with the following cycling parameters: Read 1: 100 cycles, Index 1: 12 cycles, Index 2: 12 cycles, Read 2: 100 cycles. The target read depth was 1–2 million paired-end reads per sample for Smart-seq2 libraries and 20,000 reads per cell for 10X 3′ GEX libraries. Raw BCL files were converted to FASTQ format and demultiplexed using Illumina's bcl2fastq software (v2.20.0.422). For 10X Genomics libraries, FASTQ files were further processed and demultiplexed using CellRanger (v7.0.1).

Alignment and gene quantification

10X Genomics data were aligned using CellRanger (v7.0.1) with the mm10 (mouse) and GRCh38 (human) reference genomes. Smart-seq2 mouse reads were aligned to Gencode M31 (GRCm39) using STAR (v2.7.10a) with the following parameters:

```
"`
–outFilterMultimapNmax 20
–outSAMstrandField intronMotif
–outSAMtype BAM Unsorted
–outSAMattributes NH;HI;NM;MD
–outReadsUnmapped fastx
–alignIntronMin 20
–alignIntronMax 1000000
–alignMatesGapMax 1000000
–alignSJoverhangMin 8
–alignSJDBoverhangMin 1
"`
```

Gene counts were generated using HTSeq-count (v2.0.5) with stranded="no" and mode="intersection-nonempty". Human reads were aligned to Gencode Reference v41 (GRCh38) using STAR (v2.7.11b). Gene counts were produced using HTSeq (v2.0.5) with stranded="false" and mode="intersection-nonempty".

Single-cell analysis

Quality control and cell filtration: For all 10X libraries, initial quality control was performed separately for each sample. First, counts matrices were corrected for ambient RNA removal using the SoupX package (v1.6.2). Briefly, raw and filtered CellRanger output count matrices were read into R (v3.18) using the Seurat package (v5.1) Read10X function.

The soup object was created from the raw and filtered count matrices, while the filtered matrix was used to create a Seurat object using the CreateSeuratObject function. For two human samples, the filtered matrices were first adjusted to account for high background leading to improper cell calling estimations from CellRanger (See table S5). The Seurat analysis pipeline (NormalizeData, FindVariableFeatures, ScaleData, RunPCA, FindNeighbors, FindClusters, RunUMAP) was performed using default parameters and 30 PCA dimensions to provide clustering and dimensionality reduction information for the soup object using setClusters and SetDR. Ambient RNA counts were identified and removed using the autoEstCont and adjustCounts functions.

New Seurat objects were created using the adjusted count matrices. The PercenageFeatureSet function was used to calculate the percentage of reads mapping to mitochondrial transcripts and low-quality cells were removed based a max percentage of mitochondrial reads (percent.mt) and a minimum number of unique features per cell (nFeature_RNA) (table S5).

After filtration, the datasets were reprocessed using the Seurat pipeline to prepare for doublet detection and removal using the DoubletFinder package (v2.0.4). Seurat pipeline parameters were all default except FindNeighbors and RunUMAP were calculated based on all PCs with a standard deviation greater than 2, and a clustering resolution of 0.3 was used for FindClusters. To identify doublets the pK for each dataset was identified using the paramSweep, and find.pK functions. The pK for each dataset was set as the pK yielding the highest BCmetric. The nExp was estimated for each dataset based on cell recovery numbers (table S5). Finally, doublets were identified using the doubletFinder function, once again based on all PCs with a standard deviation greater than 2 and the previously identified pK and nExp values and subsequently removed.

For all Smart-seq2 libraries, percent.mt was calculated and low-quality cells were identified as having greater than 15% percent or nFeature_RNA less than 800 and were removed.

Dimensionality reduction, clustering, and annotation: Individual 10X and Smart-seq2 datasets from each animal or donor were merged to create a single Seurat object for each species to be analyzed independently using the Seurat pipeline with Harmony integration. Briefly, the RNA assay was split based on the individual dataset identifier using the split function. The count matrix was normalized, and variable features were identified using default parameters. Feature counts were scaled and the variables nFeature_RNA, nCount_RNA and percent.mt were regressed out using ScaleData. PCA was calculated using default parameters and subsequently used for integration using the IntegrateLayers function with the method set to HarmonyIntegration. Nearest neighbor graph construction and UMAP dimensionality reduction was calculated based on the harmony reduction, and broad cell type clusters were identified using Louvain clustering (**table S5**). Differentially expressed genes of each cluster were determined using the Wilcoxon Rank Sum test through the FindAllMarkers function. Clusters were assigned cell type identities based on significant differential expression of established cell-type markers.

Following annotation, each cell type for each species was sub clustered to identify subtypes. Following the creation of a new Seurat object consisting of a single cell type from a species, the above Seurat and Harmony integration workflow was repeated on the subset dataset. The clustering resolution was determined as the highest resolution resulting in all clusters with unique marker genes found by the FindAllMarkers function (pct.1 > 0.25, pct.2 < 0.25). See table S5 for the number of harmony dimensions and clustering resolution used for each cell type subset. Frequently, sub clustering resulted in the identification of additional low-quality (low nFeature) clusters which were additionally removed (table S5). If a low-quality cluster was removed, the workflow was repeated on the cell type subset until only high-quality clusters remained. For granulosa and immune subset datasets, subclusters were assigned annotations based on significant differential expression of established subtype markers.

Following sub clustering of each cell type, the sub cluster annotations were mapped back onto the full dataset. Cells that formed low-quality clusters in subset datasets were identified and removed from the full dataset. Finally, nearest neighbor graphs and UMAP dimensions were recalculated following cell removal.

Published dataset analysis: An analyzed and annotated Seurat object from the study of Isola *et al.* (*15*) was obtained from the authors (GEO GSE232309).

An analyzed and annotated Seurat object from the study of Morris *et al.* (*30*) was obtained from the Broad Institute Single Cell Portal (SCP1914).

Previously annotated scRNA-seq data from this study was integrated with proestrus samples from Morris *et al.* (*30*) and Isola *et al.* (*15*). For Morris *et al.* (*30*), proestrus cells (condition = "P") were selected excluding mouse "1C." For Isola *et al.* (*15*), cells from donor "5" were identified as proestrus.

Datasets were merged by individual mouse sample, and assay layers were restructured to ensure compatibility. Data were normalized (log normalization), highly variable features were identified, and expression values were scaled while regressing out nFeature_RNA, nCount_RNA, and percent.mt. Principal component analysis (PCA) was performed, and batch effects were corrected using Harmony integration on the first 30 principal components. Graph-based clustering was performed using Seurat FindNeighbors and FindClusters, and Uniform Manifold Approximation and Projection (UMAP) embeddings were generated from the Harmony components. Low-quality clusters were removed iteratively while retaining oocyte populations identified by at least one dataset's annotations. After removal, normalization, variable feature selection, scaling, PCA, Harmony integration, clustering, and UMAP embedding were repeated. Final cell type identities were assigned based on previous subtype annotations and marker gene expression, with a unified set of labels spanning oocyte, granulosa, luteal, theca, stroma, smooth muscle, pericyte, epithelia, endothelia, immune, and glia categories.

To examine granulosa cells specifically, granulosa populations were subset from our dataset and proestrus granulosa from Isola ("Granulosa A" and "Granulosa B") and Morris (Level0 = "Granulosa") datasets. Luteal cells from Morris (GC_CL_Active, GC_CL_Lytic, GC_Mural) were excluded to focus on non-luteinized granulosa. The subset was merged, layers were split by dataset, and data were normalized, variable features identified, and expression values scaled regressing out nFeature_RNA, nCount_RNA, and percent.mt. PCA was run, and Harmony integration was applied using the first 15 components. Neighbor finding, clustering, and UMAP embedding were performed, and granulosa clusters were annotated into Preantral-Cumulus, Ghr+, Antral-Cumulus, Mural, and Mitotic subtypes based on prior annotations and marker expression.

Sequencing data for the study of Wu *et al.* (*18*) were downloaded from the NCBI Gene Expression Omnibus under the accession number GSE255690. Individual donor samples were merged and analyzed using the same pipeline as above. Clusters were annotated using the same markers as described in the original publication.

Sequencing data for the study of Mantri *et al.* (*47*) were downloaded from figshare (*149*). Downloaded data were fully processed and annotated. The dataset was scored for the top 100 markers of the annotated Ghr+ granulosa cluster from this study using the AddModuleScore function. To quantify spatial trends across individual follicles, a radial binning strategy that normalized cell positions relative to each follicle's size and geometry was adapted from Lan *et al.* (*47*) and implemented. Spatial coordinates were extracted from the spatial reduction slot and assigned to each pre-annotated follicle. For each annotated follicle, the follicle centroid (the mean spatial coordinate (x, y) of all spots within that follicle) was calculated and the Euclidean distance of each spot from the follicle centroid was determined. This raw distance was then

scaled by the maximum observed distance within the follicle, producing a scaled radial distance ranging from 0 (centroid) to 1 (edge). Scaled radial distances were discretized into 20 equally spaced bins spanning the interval [0, 1] using a bin width of 0.05, corresponding to concentric radial zones of increasing distance from the follicle center and spots were annotated to a radial bin based on scaled distance. For visualization of the average Ghr score among granulosa cells per follicle radial bin, scores were clipped at a minimum value of zero. For percentage calculations, Ghr+ cells were defined as any cell with a nonzero count for Ghr or a Ghr score greater than 0.025.

Sequencing data for the study of Niu and Spradling (*79*) were downloaded from NCBI Gene Expression Omnibus under the accession number GSE136441. Individual timepoint analyzed individually using the same pipeline as above and subsequently merged for visualization. Clusters were annotated using the same markers as described in the original publication.

Cross-dataset cell-type signature module scoring: To identify transcriptionally similar cell populations between two datasets, differentially expressed (DE) genes of the reference dataset were first calculated using the FindAllMarkers function with the Wilcoxon Rank Sum test, retaining only genes with a positive fold change. The DEG lists were then filtered to exclude genes absent in the query dataset. For each cell cluster in the reference dataset, a transcriptional signature was generated by selecting the top 100 DEGs, ranked by increasing adjusted p-value. The query dataset was subsequently scored for each reference cluster's transcriptional signature using the AddModuleScore function. When comparing between a mouse and human dataset, genes were converted to the species ortholog using the ortholog gene table provided in the singleCellNet package (v0.1.0). Genes without species orthologs were excluded from transcriptional signatures in cross species analysis.

Oocyte maturation trajectory analysis: oocyte maturation pseudotime analysis was performed separately for each species. Oocytes were subset and merged with the oocyte datasets generated from the Isola *et al.* (*15*) and Wu *et al.* (*18*) studies for mouse and human, respectively. Due to oocyte numbers per sample limitations for downstream harmony integration, only Isola oocyte samples 2 and 5 were kept for merging. Additionally, the low-quality oocyte cluster described in the Wu *et al.* (*18*) study was removed prior to merging. After merging, drop-out counts were imputed using the RunALRA function from the SeuratWrappers package (v0.3.2) to pseudo-normalize the sequencing depth of the 10X sequenced and Smart-seq2 sequenced oocytes to be used later for differential gene expression testing and visualization only. Seurat objects were then converted into anndata files using the convertFormat function from the sceasy package (v0.0.7) for downstream analysis in Python using the reticulate package (v.1.39.0).

In Python, the scanpy package (v1.10.2) was used for dataset preprocessing. Raw counts were TPM log normalized using the normalize_total and log1p functions. 4000 variable features were identified using the highly_variable_genes function and were scaled for subsequent principal component analysis using default parameters. Oocyte datasets were harmonized based on the age condition to limit transcriptional variability due to maturation state using the harmony_integrate function from the scapny external package using the parameters theta = 2, sigma = 0.1 and lamb = 1. Nearest neighbor graph construction was performed on the harmony reduction using the neighbors function with specific n_neighbor and n_pcs parameters per species (table S5). UMAP dimensionality reduction was performed using the umap function and leiden clustering was performed to identify oocyte subtypes (table S5). Diffusion components and pseudotime were then calculated using the dpt function, with the root node set as the most distal cluster in UMAP space consisting of 10X sequenced oocytes. The first three diffusion components were then used to reconstruct the nearest neighbor graph. Partition-based Graph Abstraction (PAGA) was then performed on the reconstructed neighborhood graphs using the leiden clusters as the grouping observation. Finally, Force Atlas (FA) dimensionality reduction was performed using PAGA as the initialization to yield the final pseudotime maturation trajectory. The resulting trajectories were then analyzed with the scFates package (v1.0.8). Tree learning was performed using the curve function to identify and align cells along a single trajectory and identify transcriptionally significant milestones along the trajectory. All resulting metadata and reductions were mapped back on to the oocyte Seurat objects for downstream analysis.

As the resulting trajectories were a single line with no branching, genes changing in expression along the trajectory were found by performing differential gene expression using the FindAllMarkers function for the oocyte subtypes and oocyte milestones. For the oocyte subtype markers, any genes which were found as a marker in non-consecutive subtypes in the trajectory were dropped. To ensure the identification of robust gene expression changes, genes were also filtered based on a log2fold change greater than 2, detected in greater than half of the cells in the marker cluster, and have a normalized expression level greater than 0.5 in at least 5% of cells in the dataset. The resulting genes were then grouped semi-manually into groups of similar expression patterns. Briefly, each genes expression was fitted along pseudotime and smoothed using a rolling average calculation with a width of 10 cells. Genes showing more than one peak in expression along pseudotime were removed. The remaining gene expression patterns were then hierarchically clustered using a k means of 100 to group genes with similar expression patterns. Hierarchical clusters were then visualized based on the average expression patterns of all genes in a cluster and then collapsed into "patterns" if two or more clusters showed peak (>70% of max expression) expression in the same pseudotime range. To facilitate cross species comparison of gene expression patterns, granular patterns were further collapsed into five shared broad expression patterns for each species. Briefly, pseudotime ranges were fit to range 0 to 100 and granular patterns were assigned to a broad pattern based on the pseudotime start of average peak expression (Early: starts at pseudotime 0, Mid-Early: starts after 0 but before 45, Mid: starts between 45 and 55, Mid-Late: starts between 55 and 75, Late: starts after 75). To visualize the similarities and differences in oocyte maturation gene expression patterns across species, all genes belonging to one species gene cluster were converted to the species ortholog. The orthologous genes were then fitted and smoothed along the ortholog species pseudotime trajectory.

GO enrichment analysis: GO enrichment analysis was performed using the clusterProfiler package (v4.10.1). Gene lists were analyzed using the enrichGO function using the keyType as "SYMBOL", pAdjustMethod as "BH", qvalueCutoff as 0.05 and the org.Mm.eg.db (v3.18) or org.Hs.eg.db (v3.18) as the mouse and human OrgDb, respectively. The same analysis was repeated for each gene list using the biological pathway (BP), cellular component (CC) and molecular function (MF) gene sets and the results were concatenated.

GSEA hierarchical clustering: For each sub-clustered cell type dataset from both species, differentially expressed (DE) genes for each subtype were identified using the FindAllMarkers function. Gene set enrichment analysis (GSEA) was conducted for the genesets package (v0.2.7) GO sets on the up-regulated DEGs of each subtype (positive log2 fold change only), sorted in descending order by log2 fold change, using fgsea (v1.28). NESs were calculated for gene sets that contained at least 15 genes from the DEG list, with the scoreType parameter set to "positive." GSEA results for each subtype were filtered to retain only biological process gene sets, without applying a significance threshold, to avoid restricting the analysis to pathways enriched in the highest fold change genes. The filtered GSEA results for all subtypes were then combined, with pathways not detected in a given subtype assigned

a NES of 0. Hierarchical clustering was performed on the NES values to group both GO pathways and subtypes. Once coarse and fine cross species clusters were determined, pathways specific or enriched in each cluster were identified. A pathway was defined as enriched if the average NES of subtypes in the cluster was 0.5 greater than the average NES of subtypes not in the cluster. GSEA was selected over ortholog expression correlation or mutual nearest neighbors (MNN) for comparison across species as this approach is not limited by reduction of each gene to its 1:1 ortholog.

Gene set module scoring: Gene sets of interest were retrieved from the GO database using the getGO function from the genesets package for both mouse and human. Datasets were scored for gene set activity using the AddModuleScore function with default parameters.

Variance explained calculation: To calculate and compare the transcriptional variance explained by the age condition in each cell type, each cell type from each species was analyzed independently. For each cell type subset, all features were first scaled using ScaleData. PCA was then calculated for 50 PCs based on all features. The variance explained by the age condition was estimated by fitting linear models to each principal component's embeddings using the age condition as a predictor. The proportion of variance explained by each principal component was weighted by its contribution to the total variance, and the final variance explained by condition for each cell type was recorded.

Cross-species age-associated DEG comparison: To directly compare DEGs with age in a cell type specific manner across species in the ovarian microenvironment DEGs were identified on cell type subsets using the FindMarkers function using the default Wilcoxon Rank Sum test. The analysis was limited to genes with known species orthologs. Additionally, genes were dropped if they were detected in less than 25% of either the aged or young population of the cell type in either species. Genes were identified as increased or decreased with age in either species based on a fold change greater than 0.25.

To perform the same analysis on the follicular cell types consisting of merged datasets from different sequencing methods, the FindMarkers function was used with the MAST method to allow for latent variable regression on the dataset identifier and sequencing method when necessary. Imputed counts were used for DEG calculations for oocytes. Similarly, genes were dropped if they were detected in less than 25% of either the aged or young population of the cell type in either species. Genes were identified as increased or decreased with age in either species based on a fold change greater than 0.5 and adjusted p-value less than 0.05.

Ligand receptor interaction analysis: CellChat (v2.1.2) was run independently for each species dataset separated by age condition. Count matrices and metadata were extracted from the previously analyzed Seurat objects and used to generate CellChat objects with the createCellChat function. All ECM-receptor communication was excluded from the analysis. The subsetData function was applied to filter the imputed count matrix for genes involved in signaling. Using this filtered matrix, identifyOverExpressedGenes was used to detect ligands and receptors with elevated expression in each specified cell group, followed by identifyOverExpressedInteractions to identify overexpressed ligand-receptor interactions. The probability of communication between the specified cell groups was then estimated using computeCommunProb and overall signaling pathway communication probabilities were determined using computeCommunProbPathway, which aggregates individual ligand-receptor probabilities. The subsetCommunication function was used to retrieve the aggregated probabilities, which were subsequently transformed by scaling by 10^{10} followed by log normalization. Signaling probabilities were then visualized for each species and age condition between specified sender and receiver populations.

Whole-mount immunostaining

Whole-mount immunostaining was performed as previously described (*28*). Postnatal (P21) and adult (2, 4, 6, 9, 12M) mouse ovaries were removed and finely dissected in cold 1XPBS then transferred to 2mL Eppendorf tubes. All subsequent steps were carried out on a rocking shaker. Ovaries were fixed in 4% PFA (ThermoFisher Scientific, 043368-9M) for 4 hours at +4°C. After fixation, ovaries were washed three times in 1XPBS for 20 min each. Ovaries were dehydrated at room temperature using a MeOH:1XPBS series (25% to 50% to 75% to 100%) for 20 min each (100% twice) then incubated in 6% H_2O_2 (Sigma-Aldrich, H1009) in 100% MeOH (Sigma-Aldrich, 322415) overnight at +4°C. The following day, ovaries were rehydrated at room temperature using a MeOH:1XPBS series (100% to 75% to 50% to 25%) for 20 min each (100% twice) then washed twice in 1XPBS for 20 min each. Ovaries were blocked with 0.2% Gelatin (Ward's Science, 470301-134) and 2% Triton X-100 (Sigma-Aldrich, X100) in 1XPBS overnight at +4°C. Primary antibodies were diluted in 0.2% Gelatin and 2% Triton X-100 in 1XPBS and postnatal ovaries were incubated in primary antibodies for 7 nights at +37°C while adult ovaries were incubated in primary antibodies for 16 nights at +37°C. Primary antibodies used were NOBOX 1:1000 (A.Rajkovic), AMH 1:400 (Abcam, ab272221), StAR 1:200 (Cell Signaling Technology, 8449), and TH 1:400 (Sigma-Aldrich, AB1542; Abcam, ab76442). Ovaries were then washed 6 times with 0.2% Gelatin and 2% Triton X-100 in 1XPBS for 30 min each. Ovaries were incubated in Alexa-Fluor conjugated secondary antibodies diluted in 0.2% Gelatin and 2% Triton X-100 in 1XPBS for 3 nights at +37°C then an additional 5 nights at +4°C. Ovaries were then washed 6 times with 0.2% Gelatin and 2% Triton X-100 in 1XPBS for 30 min each. To dehydrate the ovaries, they were first incubated in 50% Tetrahydrofuran (THF, Sigma-Aldrich, 186562) in 1XPBS overnight at room temperature. The following day, the ovaries were incubated in 80% THF in 1XPBS for 1.5 hours, 100% THF for 1.5 hours, and Dichloromethane (DCM, Sigma-Aldrich, 270997) for 30 min at room temperature. Finally, the ovaries were cleared in Benzyl ether (DBE, Sigma-Aldrich, 108014) at room temperature for a minimum of 3 nights. Prior to imaging, the ovaries were transferred into 10mm glass cylinders (ACE Glass, 3865–10) mounted on coverslips (Fisherbrand, 12544E). The samples were imaged on a white-light Leica TCS SP8 inverted confocal microscope with a HC PL APO CS 10X/0.40 dry objective at a zoom of 0.75 and step size of either 2 or 3µm for postnatal and adult ovaries, respectively.

Human samples were removed from UW solution upon receipt, and the ovary was dissected to remove surrounding tissue then cut into ~1 cm^3 pieces. The incubation times for all the above steps was increased for human ovary pieces. Additional primary antibodies used were Laminin (Sigma-Aldrich, L9393) and VASA (R&D Systems, AF2030) (*150*). The human samples were imaged in ethyl cinnamate (ECi, Sigma-Aldrich, 112372) on the Miltenyi Blaze Ultra-Imaging 3D Light Sheet Microscope with the 1X objective.

Whole-mount quantifications

Quantitative image analysis was performed using Imaris v10 (Bitplane). Files were first opened in Surpass mode and channels were renamed appropriately. Where applicable, a surface was created manually on the ovary using the Surface module. Primordial and growing (primary, secondary, tertiary+, and atretic follicles) were quantified using the Spot module. For primordial quantifications, automated spots were generated in the NOBOX channel using 6µm × 12µm for spot dimensions. The quality score was adjusted to reflect accurate coverage, then using the edit tool, spots were removed or added to reflect an accurate count. For all growing categories, spots were added manually by visualization of follicle morphology, size, and expression patterns of NOBOX and AMH/StAR. In the process of generating automated NOBOX+ primordial spots, growing follicles were often also labeled, given they met the criteria of 6µm+. To remove double counted follicles (follicles with 'primordial' labeled spot and 'growing' labeled spot) to ensure numbers were accurate, the Imaris Spots Colocalize XTension (*151*) was used.

Screenshots were generated with 3500 dpi in 2048 × 2048-pixel dimension. For the human ovary quantitative image analysis, total ovary fragment as well as individual oocyte pockets were independently, manually segmented using the Surface module to measure piece and pocket volume, and oocytes were counted using automated spots that were generated in the VASA channel using 12μm × 20μm for spot dimensions. The quality score was adjusted to reflect accurate coverage, then using the edit tool, spots were removed or added to reflect an accurate count. Pocket size was normalized to piece size for comparing age-related decrease in pocket size. For mouse oocyte density, NOBOX+ spots were normalized to total ovary volume. For human oocyte density, VASA+ spots per pocket were normalized to total piece volume.

Tissue fixation and cryosectioning

Ovaries were removed and finely dissected in cold 1XPBS then transferred to 2 mL Eppendorf tubes. All subsequent steps were carried out on a rocking shaker. Ovaries were fixed in 4% PFA for 4 hours at +4°C. After fixation, ovaries were washed three times in 1XPBS for 20 min each. Ovaries were incubated in 10% sucrose (Research Products International, S24060) in 1XPBS then 30% sucrose in 1XPBS then 1:1 30% sucrose in 1XPBS:OCT for one night each at +4°C. Ovaries were embedded in OCT and stored at −80°C for subsequent cryosectioning on a Leica CM3050 S cryostat.

Tissue immunostaining

All following steps were conducted at room temperature. Ovary cryosections at 10-20μm thickness were washed twice in 1XPBS for 5 min then permeabilized with 0.4% TritonX in 1XPBS for 10 min. Slides were then incubated in a blocking buffer (0.1% TritonX, 5% Donkey Serum, 3% BSA in 1XPBS). Slides were incubated in primary antibodies diluted in blocking buffer overnight. Primary antibodies used were TH 1:400 (Sigma-Aldrich, AB1542; Abcam, ab76442), TUBB3 1:200 (BioLegend, 802001), S100B 1:200 (Cell Signaling Technology, 90393), NGF 1:200 (Sigma-Aldrich, N6655), CD31 1:200 (BD Biosciences, 557355), PDGRFβ 1:300 (R&D Systems, AF385), CNA35-eGFP 1:400 (K.Tharp), COLIII 1:300 (Abcam, ab7778) and Anti-Actin α-Smooth Muscle (α-SMA) - FITC 1:200 (Sigma-Aldrich, F3777). Following three 5- minute washes with 0.1% TritonX in 1XPBS, slides were incubated in Alexa-Fluor conjugated secondary antibodies diluted in blocking buffer for 1 hour. Slides were washed thrice with 0.1% TritonX in 1XPBS for 5 min each, then briefly washed with 1XPBS. For CNA35-GFP images, slides were incubated in TrueBlack Autofluorescence Quencher (Cell Signaling Technology, 92401S) for 30 s then washed three times with 1XPBS. Slides were mounted with Fluoromount G (SouthernBiotech, 0100-01) and sealed with #1.5 coverslips. Ovary sections were imaged on a white-light Leica TCS SP8 inverted confocal microscope.

Sympathetic innervation density quantifications

Ovary cryosections at 20μm thickness were collected from three distinct depths within the tissue, each separated by more than 200μm, for quantification in Fiji (ImageJ). Sections were stained for TH as described above. In mouse ovaries, co-staining with α-SMA and AMH/StAR was performed to delineate stromal regions. The stromal region of interest (ROI) was traced and used to define the total stromal area. TH+ area was quantified by applying the default thresholding settings. The percentage of TH+ stromal area was calculated from the total stromal area. In human ovaries, the entire section was used to quantify the total area. TH+ area was quantified by applying the default thresholding settings. The percentage of TH+ area was calculated from the total area.

Picrosirius red staining and quantifications

Ovary cryosections at 10 μm thickness were processed with minor modifications to a previously described protocol (*152*). Briefly, slides were washed with 1XPBS for 5 min to remove OCT and then stained with PSR staining solution by preparing Direct Red 80 (Sigma-Aldrich, 365548-5G) in 1.3% saturated aqueous solution of picric acid (Sigma-Aldrich, P6744-1GA) at 0.03% w/v for 10 min at room temperature. Slides were washed with 0.01 N HCl (Thermo Fisher, 035648.K7) for 2 min and then washed with 100% EtOH thrice for 30 s incubations each. Slides were cleared with Citrosolv (Decon Labs, Inc., 1601) for 5 min, then mounted with Cytoseal mounting media (Epredia, 8310-16) and #1.5 coverslips. Sections were imaged using a Keyence BZ-X710 Microscope. ImageJ was used to quantify the area of positive PSR staining above a threshold, which was determined based on the staining in the oldest sample for each species (mouse and human), as previously described (*153*). This threshold remained consistent across all images analyzed for each species.

In vitro fertilization

To stimulate follicle growth and ovulation, mice were injected intraperitoneally with 100 uL CARD HyperOva (Cosmo Bio Co., Ltd., KYD-010-06-EX) followed 48 hours later by intraperitoneal injection of 7.5IU hCG (Ilex Life Sciences, A225005). Oviducts were collected 14 hours after hCG administration and placed in mineral oil (EMD Millipore, ES-005-C) pre-warmed to 37°C. Cumulus oocyte complexes (COCs) were collected by puncturing the oviduct with a 30-gauge needle then allowed to capacitate for 40-50 min in a pre-warmed drop of CARD Medium (Cosmo Bio Co., Ltd., KYD-003-EX). 3 uL of sperm from a proven breeder that capacitated in a pre-warmed drop of CARD FERTIUP (Cosmo Bio Co., Ltd., KYD-002-05-EX) for 1 hour was then added to the drop of CARD Medium containing the COCs. Sperm from the same proven breeder was used for females from different experimental conditions on the day of the experiment. After 5 hours of fertilization time at 37°C and 5% CO_2, oocytes were washed in Continuous Single Culture-NX Complete (IrvineScientific, 90168) to remove excess sperm and cumulus cells. The oocytes viable after fertilization were then returned to the incubator and, 24 hours after fertilization, the embryos that successfully reached the 2-cell stage were counted and moved to a fresh drop of pre-warmed Continuous Single Culture-NX Complete. The 2-cell embryos were then returned to the incubators and, 96 hours after fertilization, the number of embryos that successfully reached the blastocyst stage were scored. Data were plotted in a Kaplan-Meier-style plot, where the curves represent proportions of oocytes that survived to each developmental stage, conditional on successful transfer.

Statistical analysis of male contribution to IVF success

To evaluate the role of male ID, we formulated a logistic regression model of oocyte success on female age (dichotomized as 12M vs 2-9M) and indicator of male ID. As expected, older female age is associated with a reduction in odds of oocyte success, adjusting for male ID (odds ratio 0.23 (0.06,0.82) for 12M vs 2-9M). Odds of oocyte success for each female age group varied across males, but there was no indication that any male performed better or worse than the others ($P = 0.12$, partial F-test).

REFERENCES AND NOTES

1. C. A. Doherty, F. Amargant, S. Y. Shvartsman, F. E. Duncan, E. R. Gavis, Bidirectional communication in oogenesis: A dynamic conversation in mice and Drosophila. *Trends Cell Biol.* **32**, 311–323 (2022). doi: 10.1016/j.tcb.2021.11.005; pmid: 34922803
2. K. J. Grive, R. N. Freiman, The developmental origins of the mammalian ovarian reserve. *Development* **142**, 2554–2563 (2015). doi: 10.1242/dev.125211; pmid: 26243868
3. A. N. Hirshfield, Development of follicles in the mammalian ovary. *Int. Rev. Cytol.* **124**, 43–101 (1991). doi: 10.1016/S0074-7696(08)61524-7; pmid: 2001918
4. E. A. McGee, A. J. W. Hsueh, Initial and cyclic recruitment of ovarian follicles. *Endocr. Rev.* **21**, 200–214 (2000). pmid: 10782364
5. A. Gougeon, Regulation of ovarian follicular development in primates: Facts and hypotheses. *Endocr. Rev.* **17**, 121–155 (1996). doi: 10.1210/edrv-17-2-121; pmid: 8706629
6. K. P. McNatty, A. Makris, C. DeGrazia, R. Osathanondh, K. J. Ryan, The production of progesterone, androgens, and estrogens by granulosa cells, thecal tissue, and stromal tissue from human ovaries in vitro. *J. Clin. Endocrinol. Metab.* **49**, 687–699 (1979). doi: 10.1210/jcem-49-5-687; pmid: 489711

7. M. K. Skinner, M. Schmidt, M. I. Savenkova, I. Sadler-Riggleman, E. E. Nilsson, Regulation of granulosa and theca cell transcriptomes during ovarian antral follicle development. *Mol. Reprod. Dev.* **75**, 1457–1472 (2008). doi: 10.1002/mrd.20883; pmid: 18288646
8. A. R. Baerwald, G. P. Adams, R. A. Pierson, Form and function of the corpus luteum during the human menstrual cycle. *Ultrasound Obstet. Gynecol.* **25**, 498–507 (2005). doi: 10.1002/uog.1891; pmid: 15846762
9. T. H. Roderick, J. B. Storer, Correlation between mean litter size and mean life span among 12 inbred strains of mice. *Science* **134**, 48–49 (1961). doi: 10.1126/science.134.3471.48; pmid: 13742527
10. F. E. Duncan, J. L. Gerton, Mammalian oogenesis and female reproductive aging. *Aging (Albany NY)* **10**, 162–163 (2018). doi: 10.18632/aging.101381; pmid: 29410392
11. E. Bornstein *et al.*, Advanced maternal age as a sole indication for genetic amniocentesis; risk-benefit analysis based on a large database reflecting the current common practice. *J. Perinat. Med.* **37**, 99–102 (2009). doi: 10.1515/JPM.2009.032; pmid: 18999912
12. C. K. Geiger, M. A. Clapp, J. L. Cohen, Association of Prenatal Care Services, Maternal Morbidity, and Perinatal Mortality With the Advanced Maternal Age Cutoff of 35 Years. *JAMA Health Forum* **2**, e214044 (2021). doi: 10.1001/jamahealthforum.2021.4044; pmid: 35977294
13. L. S. Felicio, J. F. Nelson, C. E. Finch, Prolongation and cessation of estrous cycles in aging C57BL/6J mice are differentially regulated events. *Biol. Reprod.* **34**, 849–858 (1986). doi: 10.1095/biolreprod34.5.849; pmid: 3730481
14. C. V. Mobbs, D. M. Gee, C. E. Finch, Reproductive senescence in female C57BL/6J mice: Ovarian impairments and neuroendocrine impairments that are partially reversible and delayable by ovariectomy. *Endocrinology* **115**, 1653–1662 (1984). doi: 10.1210/endo-115-5-1653; pmid: 6541567
15. J. V. V. Isola *et al.*, A single-cell atlas of the aging mouse ovary. *Nat. Aging* **4**, 145–162 (2024). doi: 10.1038/s43587-023-00552-5; pmid: 38200272
16. I. Winkler *et al.*, The cycling and aging mouse female reproductive tract at single-cell resolution. *Cell* **187**, 981–998.e25 (2024). doi: 10.1016/j.cell.2024.01.021; pmid: 38325365
17. T. Ben Yaakov, T. Wasserman, E. Aknin, Y. Savir, Single-cell analysis of the aged ovarian immune system reveals a shift towards adaptive immunity and attenuated cell function. *eLife* **12**, e74915 (2023). doi: 10.7554/eLife.74915; pmid: 37096871
18. M. Wu *et al.*, Spatiotemporal transcriptomic changes of human ovarian aging and the regulatory role of FOXP1. *Nat. Aging* **4**, 527–545 (2024). doi: 10.1038/s43587-024-00607-1; pmid: 38594460
19. S. Wang *et al.*, Single-Cell Transcriptomic Atlas of Primate Ovarian Aging. *Cell* **180**, 585–600.e19 (2020). doi: 10.1016/j.cell.2020.01.009; pmid: 32004457
20. Y. Wei *et al.*, Single-cell profiling of mouse and primate ovaries identifies high levels of *EGFR* for stromal cells in ovarian aging. *Mol. Ther. Nucleic Acids* **31**, 1–12 (2022). doi: 10.1016/j.omtn.2022.11.020; pmid: 36570672
21. W. Hu *et al.*, Single-cell transcriptome and translatome dual-omics reveals potential mechanisms of human oocyte maturation. *Nat. Commun.* **13**, 5114 (2022). doi: 10.1038/s41467-022-32791-2; pmid: 36042231
22. S. Llonch *et al.*, Single human oocyte transcriptome analysis reveals distinct maturation stage-dependent pathways impacted by age. *Aging Cell* **20**, e13360 (2021). doi: 10.1111/acel.13360; pmid: 33908703
23. L. Yuan *et al.*, Single-cell transcriptome analysis of human oocyte ageing. *J. Cell. Mol. Med.* **25**, 6289–6303 (2021). doi: 10.1111/jcmm.16594; pmid: 34037315
24. Z.-H. Zhao *et al.*, RNA-Seq transcriptome reveals different molecular responses during human and mouse oocyte maturation and fertilization. *BMC Genomics* **21**, 475 (2020). doi: 10.1186/s12864-020-06885-4; pmid: 32650721
25. D. A. Fontaine, D. B. Davis, Attention to Background Strain Is Essential for Metabolic Research: C57BL/6 and the International Knockout Mouse Consortium. *Diabetes* **65**, 25–33 (2016). doi: 10.2337/db15-0982; pmid: 26696638
26. S. A. Williams, P. Stanley, Mouse fertility is enhanced by oocyte-specific loss of core 1-derived O-glycans. *FASEB J.* **22**, 2273–2284 (2008). doi: 10.1096/fj.07-101709; pmid: 18276833
27. K. Wilsterman, A. I. Bautista, C. E. Butler, M. Y. Juergens, A. M. Larson, Evolution of Litter Size: Proximate and Ultimate Mechanisms. *Integr. Comp. Biol.* **64**, 1643–1660 (2024). doi: 10.1093/icb/icae052; pmid: 38802126
28. B. Soygur *et al.*, Germline Stem Cells, Methods and Protocols. *Methods Mol. Biol.* **2677**, 203–219 (2023). doi: 10.1007/978-1-0716-3259-8_12; pmid: 37464244
29. S. R. Quake, T. T. S. Consortium, Tabula Sapiens reveals transcription factor expression, senescence effects, and sex-specific features in cell types from 28 human organs and tissues. bioRxiv 2024.12.03.626516 [Preprint] (2024); https://doi.org/10.1101/2024.12.03.626516.
30. M. E. Morris *et al.*, A single-cell atlas of the cycling murine ovary. *eLife* **11**, e77239 (2022). doi: 10.7554/eLife.77239; pmid: 36205477
31. G. W. Corner, W. M. Allen, PHYSIOLOGY OF THE CORPUS LUTEUM. *Am. J. Physiol.* **88**, 326–339 (1929). doi: 10.1152/ajplegacy.1929.88.2.326
32. G. G. Martin, P. Talbot, Drugs that block smooth muscle contraction inhibit in vivo ovulation in hamsters. *J. Exp. Zool.* **216**, 483–491 (1981). doi: 10.1002/jez.1402160317; pmid: 7196941
33. G. G. Martin, P. Talbot, The role of follicular smooth muscle cells in hamster ovulation. *J. Exp. Zool.* **216**, 469–482 (1981). doi: 10.1002/jez.1402160316; pmid: 7276896
34. S. A. McGrath, A. F. Esquela, S. J. Lee, Oocyte-specific expression of growth/differentiation factor-9. *Mol. Endocrinol.* **9**, 131–136 (1995). pmid: 7760846
35. A. Castro, E. Mandart, T. Lorca, S. Galas, Involvement of Aurora A kinase during meiosis I-II transition in Xenopus oocytes. *J. Biol. Chem.* **278**, 2236–2241 (2003). doi: 10.1074/jbc.M207894200; pmid: 12426316
36. Q. Guo *et al.*, The function of Nucleoporin 37 on mouse oocyte maturation and preimplantation embryo development. *J. Assist. Reprod. Genet.* **39**, 107–116 (2022). doi: 10.1007/s10815-021-02330-x; pmid: 35022896
37. B. Hampoelz *et al.*, Nuclear Pores Assemble from Nucleoporin Condensates During Oogenesis. *Cell* **179**, 671–686.e17 (2019). doi: 10.1016/j.cell.2019.09.022; pmid: 31626769
38. R. Feng *et al.*, Mutations in TUBB8 and Human Oocyte Meiotic Arrest. *N. Engl. J. Med.* **374**, 223–232 (2016). doi: 10.1056/NEJMoa1510791; pmid: 26789871
39. A. Heim, M. L. Niedermeier, F. Stengel, T. U. Mayer, The translation regulator Zar1l controls timing of meiosis in Xenopus oocytes. *Development* **149**, dev200900 (2022). doi: 10.1242/dev.200900; pmid: 36278895
40. B. N. Vazquez, C. S. Blengini, Y. Hernandez, L. Serrano, K. Schindler, SIRT7 promotes chromosome synapsis during prophase I of female meiosis. *Chromosoma* **128**, 369–383 (2019). doi: 10.1007/s00412-019-00713-9; pmid: 31256246
41. P. J. Scrivens *et al.*, C4orf41 and TTC-15 are mammalian TRAPP components with a role at an early stage in ER-to-Golgi trafficking. *Mol. Biol. Cell* **22**, 2083–2093 (2011). doi: 10.1091/mbc.e10-11-0873; pmid: 21525244
42. K. A. Slot *et al.*, Reduced recruitment and survival of primordial and growing follicles in GH receptor-deficient mice. *Reproduction* **131**, 525–532 (2006). doi: 10.1530/rep.1.00946; pmid: 16514195
43. J. R. V. Silva, J. R. Figueiredo, R. van den Hurk, Involvement of growth hormone (GH) and insulin-like growth factor (IGF) system in ovarian folliculogenesis. *Theriogenology* **71**, 1193–1208 (2009). doi: 10.1016/j.theriogenology.2008.12.015; pmid: 19193432
44. A. Bachelot *et al.*, Growth hormone is required for ovarian follicular growth. *Endocrinology* **143**, 4104–4112 (2002). doi: 10.1210/en.2002-220087; pmid: 12239122
45. J. Veeck *et al.*, The extracellular matrix protein ITIH5 is a novel prognostic marker in invasive node-negative breast cancer and its aberrant expression is caused by promoter hypermethylation. *Oncogene* **27**, 865–876 (2008). doi: 10.1038/sj.onc.1210669; pmid: 17653090
46. B. Wang *et al.*, Identification and characterization of NYGGF4, a novel gene containing a phosphotyrosine-binding (PTB) domain that stimulates 3T3-L1 preadipocytes proliferation. *Gene* **379**, 132–140 (2006). doi: 10.1016/j.gene.2006.05.008; pmid: 16815647
47. M. Mantri, H. H. Zhang, E. Spanos, Y. A. Ren, I. De Vlaminck, A spatiotemporal molecular atlas of the ovulating mouse ovary. *Proc. Natl. Acad. Sci. U.S.A.* **121**, e2317418121 (2024). doi: 10.1073/pnas.2317418121; pmid: 38252830
48. T. C. T. Lan *et al.*, Aging disrupts spatiotemporal coordination in the cycling ovary. bioRxiv, 2024.12.15.628550 (2024).
49. J. Mestas, C. C. W. Hughes, Of mice and not men: Differences between mouse and human immunology. *J. Immunol.* **172**, 2731–2738 (2004). doi: 10.4049/jimmunol.172.5.2731; pmid: 14978070
50. G. Reeves, Specific stroma in the cortex and medulla of the ovary. Cell types and vascular supply in relation to follicular apparatus and ovulation. *Obstet. Gynecol.* **37**, 832–844 (1971). pmid: 4143757
51. J. S. Richards, Y. A. Ren, N. Candelaria, J. E. Adams, A. Rajkovic, Ovarian Follicular Theca Cell Recruitment, Differentiation, and Impact on Fertility: 2017 Update. *Endocr. Rev.* **39**, 1–20 (2018). doi: 10.1210/er.2017-00164; pmid: 29028960
52. D. H. Poole, J. L. Pate, Luteal microenvironment directs resident T lymphocyte function in cows. *Biol. Reprod.* **86**, 29 (2012). doi: 10.1095/biolreprod.111.092296; pmid: 21976598
53. R. C. Zimmermann, E. Xiao, P. Bohlen, M. Ferin, Administration of antivascular endothelial growth factor receptor 2 antibody in the early follicular phase delays follicular selection and development in the rhesus monkey. *Endocrinology* **143**, 2496–2502 (2002). doi: 10.1210/endo.143.7.8896; pmid: 12072380
54. X. Tong *et al.*, Ovarian Innervation Coupling With Vascularity: The Role of Electro-Acupuncture in Follicular Maturation in a Rat Model of Polycystic Ovary Syndrome. *Front. Physiol.* **11**, 474 (2020). doi: 10.3389/fphys.2020.00474; pmid: 32547407
55. F. Kizuka-Shibuya *et al.*, Locally existing endothelial cells and pericytes in ovarian stroma, but not bone marrow-derived vascular progenitor cells, play a central role in neovascularization during follicular development in mice. *J. Ovarian Res.* **7**, 10 (2014). doi: 10.1186/1757-2215-7-10; pmid: 24444000
56. K. Hosaka *et al.*, Dual roles of endothelial FGF-2-FGFR1-PDGF-BB and perivascular FGF-2-FGFR2-PDGFRβ signaling pathways in tumor vascular remodeling. *Cell Discov.* **4**, 3 (2018). doi: 10.1038/s41421-017-0002-1; pmid: 29423271
57. D. N. Anbarci, J. McKey, D. S. Levic, M. Bagnat, B. Capel, Rediscovering the *rete ovarii*, a secreting auxiliary structure to the ovary. *eLife* **13**, RP96662 (2025). doi: 10.7554/eLife.96662.3; pmid: 40105200

58. J. McKey *et al.*, Integration of mouse ovary morphogenesis with developmental dynamics of the oviduct, ovarian ligaments, and rete ovarii. *eLife* **11**, e81088 (2022). doi: 10.7554/eLife.81088; pmid: 36165446
59. A. S. K. Jones *et al.*, Cellular atlas of the human ovary using morphologically guided spatial transcriptomics and single-cell sequencing. *Sci. Adv.* **10**, eadm7506 (2024). doi: 10.1126/sciadv.adm7506; pmid: 38578993
60. R. Chen, Y. Yu, X. Dong, Progesterone receptor in the prostate: A potential suppressor for benign prostatic hyperplasia and prostate cancer. *J. Steroid Biochem. Mol. Biol.* **166**, 91–96 (2017). doi: 10.1016/j.jsbmb.2016.04.008; pmid: 27125450
61. M. Mori, B.-I. Tamaoki, In vitro metabolism of progesterone in the mammary tumor and the normal mammary gland of GRS/A strain of mice and dependency of some steroid-metabolizing enzyme activities upon ovarian function. *Eur. J. Cancer* **16**, 185–193 (1980). doi: 10.1016/0014-2964(80)90150-4; pmid: 6929251
62. T. C. T. Lan *et al.*, Aging disrupts spatiotemporal coordination in the cycling ovary. bioRxiv, 2024.12.15.628550 [Preprint] (2024); https://doi.org/10.1101/2024.12.15.628550.
63. H. H. Simmer, The first experiments to demonstrate an endocrine function of the corpus luteum. On the occasion of the 100th birthday of Ludwig Fraenkel (1870-1951). *Sudhoffs Arch. Z. Wissenschaftsgesch.* **55**, 392–417 (1971). pmid: 4261581
64. A. S. Teeli *et al.*, Possible Mechanisms for Maintenance and Regression of Corpus Luteum Through the Ubiquitin-Proteasome and Autophagy System Regulated by Transcriptional Factors. *Front. Endocrinol. (Lausanne)* **10**, 748 (2019). doi: 10.3389/fendo.2019.00748; pmid: 31803139
65. C. M. Klein, H. W. Burden, Anatomical localization of afferent and postganglionic sympathetic neurons innervating the rat ovary. *Neurosci. Lett.* **85**, 217–222 (1988). doi: 10.1016/0304-3940(88)90354-0; pmid: 3374837
66. V. Vives, G. Alonso, A. C. Solal, D. Joubert, C. Legraverend, Visualization of S100B-positive neurons and glia in the central nervous system of EGFP transgenic mice. *J. Comp. Neurol.* **457**, 404–419 (2003). doi: 10.1002/cne.10552; pmid: 12561079
67. K. Kuhlbrodt, B. Herbarth, E. Sock, I. Hermans-Borgmeyer, M. Wegner, Sox10, a novel transcriptional modulator in glial cells. *J. Neurosci.* **18**, 237–250 (1998). doi: 10.1523/JNEUROSCI.18-01-00237.1998; pmid: 9412504
68. J. N. Langley, On the stimulation and paralysis of nerve cells and nerve endings: Part II. Paralysis by curari, strychnine and brucine and its antagonism by nicotine. *J. Physiol.* **52**, 247–266 (1918). doi: 10.1113/jphysiol.1918.sp001828; pmid: 16993394
69. D. Lorton, D. L. Bellinger, Molecular mechanisms underlying β-adrenergic receptor-mediated cross-talk between sympathetic neurons and immune cells. *Int. J. Mol. Sci.* **16**, 5635–5665 (2015). doi: 10.3390/ijms16035635; pmid: 25768345
70. D. Bodmer, S. Levine-Wilkinson, A. Richmond, S. Hirsh, R. Kuruvilla, Wnt5a mediates nerve growth factor-dependent axonal branching and growth in developing sympathetic neurons. *J. Neurosci.* **29**, 7569–7581 (2009). doi: 10.1523/JNEUROSCI.1445-09.2009; pmid: 19515925
71. J. McKey, C. Bunce, I. S. Batchvarov, D. M. Ornitz, B. Capel, Neural crest-derived neurons invade the ovary but not the testis during mouse gonad development. *Proc. Natl. Acad. Sci. U.S.A.* **116**, 5570–5575 (2019). doi: 10.1073/pnas.1814930116; pmid: 30819894
72. L. Xue *et al.*, Global expression profiling reveals genetic programs underlying the developmental divergence between mouse and human embryogenesis. *BMC Genomics* **14**, 568 (2013). doi: 10.1186/1471-2164-14-568; pmid: 23961710
73. M. Del Campo, B. Piquer, J. Witherington, A. Sridhar, H. E. Lara, Effect of Superior Ovarian Nerve and Plexus Nerve Sympathetic Denervation on Ovarian-Derived Infertility Provoked by Estradiol Exposure to Rats. *Front. Physiol.* **10**, 349 (2019). doi: 10.3389/fphys.2019.00349; pmid: 31024331
74. G. A. Dissen *et al.*, Excessive ovarian production of nerve growth factor facilitates development of cystic ovarian morphology in mice and is a feature of polycystic ovarian syndrome in humans. *Endocrinology* **150**, 2906–2914 (2009). doi: 10.1210/en.2008-1575; pmid: 19264868
75. R. Kuruvilla *et al.*, A neurotrophin signaling cascade coordinates sympathetic neuron development through differential control of TrkA trafficking and retrograde signaling. *Cell* **118**, 243–255 (2004). doi: 10.1016/j.cell.2004.06.021; pmid: 15260993
76. J. Lindeberg *et al.*, Transgenic expression of Cre recombinase from the tyrosine hydroxylase locus. *Genesis* **40**, 67–73 (2004). doi: 10.1002/gene.20065; pmid: 15452869
77. T. Liu *et al.*, Local sympathetic innervations modulate the lung innate immune responses. *Sci. Adv.* **6**, eaay1497 (2020). doi: 10.1126/sciadv.aay1497; pmid: 32426489
78. X. Chen *et al.*, A chemical-genetic approach to studying neurotrophin signaling. *Neuron* **46**, 13–21 (2005). doi: 10.1016/j.neuron.2005.03.009; pmid: 15820690
79. W. Niu, A. C. Spradling, Two distinct pathways of pregranulosa cell differentiation support follicle formation in the mouse ovary. *Proc. Natl. Acad. Sci. U.S.A.* **117**, 20015–20026 (2020). doi: 10.1073/pnas.2005570117; pmid: 32759216
80. S. M. Briley *et al.*, Reproductive age-associated fibrosis in the stroma of the mammalian ovary. *Reproduction* **152**, 245–260 (2016). doi: 10.1530/REP-16-0129; pmid: 27491879
81. C. Lliberos, S. H. Liew, A. Mansell, K. J. Hutt, The Inflammasome Contributes to Depletion of the Ovarian Reserve During Aging in Mice. *Front. Cell Dev. Biol.* **8**, 628473 (2021). doi: 10.3389/fcell.2020.628473; pmid: 33644037
82. E. M. van der Ark-Vonk, M. V. Puijk, G. Pasterkamp, S. W. van der Laan, The Effects of FABP4 on Cardiovascular Disease in the Aging Population. *Curr. Atheroscler. Rep.* **26**, 163–175 (2024). doi: 10.1007/s11883-024-01196-5; pmid: 38698167
83. G. Hajishengallis, T. Chavakis, DEL-1-Regulated Immune Plasticity and Inflammatory Disorders. *Trends Mol. Med.* **25**, 444–459 (2019). doi: 10.1016/j.molmed.2019.02.010; pmid: 30885428
84. A. Barkaway *et al.*, Age-related changes in the local milieu of inflamed tissues cause aberrant neutrophil trafficking and subsequent remote organ damage. *Immunity* **54**, 1494–1510.e7 (2021). doi: 10.1016/j.immuni.2021.04.025; pmid: 34033752
85. L. Mu *et al.*, Physiological premature aging of ovarian blood vessels leads to decline in fertility in middle-aged mice. *Nat. Commun.* **16**, 72 (2025). doi: 10.1038/s41467-024-55509-y; pmid: 39747922
86. J. Wang, D. Wang, K. Chu, W. Li, Y. A. Zeng, Procr-expressing progenitor cells are responsible for murine ovulatory rupture repair of ovarian surface epithelium. *Nat. Commun.* **10**, 4966 (2019). doi: 10.1038/s41467-019-12935-7; pmid: 31672973
87. E. McPherson *et al.*, Ovarian failure and dilated cardiomyopathy due to a novel lamin mutation. *Am. J. Med. Genet. A.* **149A**, 567–572 (2009). doi: 10.1002/ajmg.a.32627; pmid: 19283854
88. K. D. Kimura, H. A. Tissenbaum, Y. Liu, G. Ruvkun, daf-2, an insulin receptor-like gene that regulates longevity and diapause in Caenorhabditis elegans. *Science* **277**, 942–946 (1997). doi: 10.1126/science.277.5328.942; pmid: 9252323
89. C. Jin *et al.*, Molecular and genetic insights into human ovarian aging from single-nuclei multi-omics analyses. *Nat. Aging* **5**, 275–290 (2025). doi: 10.1038/s43587-024-00762-5; pmid: 39578560
90. T. Brandt *et al.*, Changes of mitochondrial ultrastructure and function during ageing in mice and *Drosophila*. *eLife* **6**, e24662 (2017). doi: 10.7554/eLife.24662; pmid: 28699890
91. C. Lliberos *et al.*, Evaluation of inflammation and follicle depletion during ovarian ageing in mice. *Sci. Rep.* **11**, 278 (2021). doi: 10.1038/s41598-020-79488-4; pmid: 33432051
92. F. Amargant *et al.*, Ovarian stiffness increases with age in the mammalian ovary and depends on collagen and hyaluronan matrices. *Aging Cell* **19**, e13259 (2020). doi: 10.1111/acel.13259; pmid: 33079460
93. R. A. Boerboom *et al.*, High resolution imaging of collagen organisation and synthesis using a versatile collagen specific probe. *J. Struct. Biol.* **159**, 392–399 (2007). doi: 10.1016/j.jsb.2007.04.008; pmid: 17572104
94. G. MacKenzie, J. Maguire, The role of ovarian hormone-derived neurosteroids on the regulation of GABAA receptors in affective disorders. *Psychopharmacology* **231**, 3333–3342 (2014). doi: 10.1007/s00213-013-3423-z; pmid: 24402140
95. K. H. Tran *et al.*, Decreased GABA+ Levels in the Medial Prefrontal Cortex of Perimenopausal Women: A 3T 1H-MRS Study. *Int. J. Neuropsychopharmacol.* **26**, 32–41 (2023). doi: 10.1093/ijnp/pyac066; pmid: 36146906
96. R. Shirasaki, J. W. Lewcock, K. Lettieri, S. L. Pfaff, FGF as a target-derived chemoattractant for developing motor axons genetically programmed by the LIM code. *Neuron* **50**, 841–853 (2006). doi: 10.1016/j.neuron.2006.04.030; pmid: 16772167
97. R. W. Gundersen, J. N. Barrett, Characterization of the turning response of dorsal root neurites toward nerve growth factor. *J. Cell Biol.* **87**, 546–554 (1980). doi: 10.1083/jcb.87.3.546; pmid: 6257725
98. G. López-Bendito *et al.*, Robo1 and Robo2 cooperate to control the guidance of major axonal tracts in the mammalian forebrain. *J. Neurosci.* **27**, 3395–3407 (2007). doi: 10.1523/JNEUROSCI.4605-06.2007; pmid: 17392456
99. J. M. Marshall, Effects of ovarian steroids and pregnancy on adrenergic nerves of uterus and oviduct. *Am. J. Physiol.* **240**, C165–C174 (1981). doi: 10.1152/ajpcell.1981.240.5.C165; pmid: 7015875
100. J. P. Toner, D. A. Grainger, L. M. Frazier; the Registry and Research Committees of SART of ASRM, Birmingham, Alabama, Clinical outcomes among recipients of donated eggs: An analysis of the U.S. national experience, 1996–19981 1Reprints are not available. *Fertil. Steril.* **78**, 1038–1045 (2002). doi: 10.1016/S0015-0282(02)03371-X; pmid: 12413990
101. J. M. Franasiak *et al.*, The nature of aneuploidy with increasing age of the female partner: A review of 15,169 consecutive trophectoderm biopsies evaluated with comprehensive chromosomal screening. *Fertil. Steril.* **101**, 656–663.e1 (2014). doi: 10.1016/j.fertnstert.2013.11.004; pmid: 24355045
102. J. Dumont *et al.*, Formin-2 is required for spindle migration and for the late steps of cytokinesis in mouse oocytes. *Dev. Biol.* **301**, 254–265 (2007). doi: 10.1016/j.ydbio.2006.08.044; pmid: 16989804
103. J. Joseph, S.-T. Liu, S. A. Jablonski, T. J. Yen, M. Dasso, The RanGAP1-RanBP2 complex is essential for microtubule-kinetochore interactions in vivo. *Curr. Biol.* **14**, 611–617 (2004). doi: 10.1016/j.cub.2004.03.031; pmid: 15062103
104. L. Bian, Y. Meng, M. Zhang, D. Li, MRE11-RAD50-NBS1 complex alterations and DNA damage response: Implications for cancer treatment. *Mol. Cancer* **18**, 169 (2019). doi: 10.1186/s12943-019-1100-5; pmid: 31767017
105. Z. Lou *et al.*, MDC1 maintains genomic stability by participating in the amplification of ATM-dependent DNA damage signals. *Mol. Cell* **21**, 187–200 (2006). doi: 10.1016/j.molcel.2005.11.025; pmid: 16427009

106. C. A. Doherty, A. Tijani, S. C. Munger, D. J. Laird, Mammalian oocytes receive maternal-effect RNAs from granulosa cells. bioRxiv 2025.02.10.637575 [Preprint] (2025); https://doi.org/10.1101/2025.02.10.637575.
107. F. Scheffler *et al.*, Follicular GH and IGF1 Levels Are Associated With Oocyte Cohort Quality: A Pilot Study. *Front. Endocrinol. (Lausanne)* **12**, 793621 (2021). doi: 10.3389/fendo.2021.793621; pmid: 34925246
108. C. J. Mortensen *et al.*, Heat shock protein 70 gene expression in equine blastocysts after exposure of oocytes to high temperatures in vitro or in vivo after exercise of donor mares. *Theriogenology* **74**, 374–383 (2010). doi: 10.1016/j.theriogenology.2010.02.020; pmid: 20416934
109. X. Tian, A. N. Halfhill, F. J. Diaz, Localization of phosphorylated SMAD proteins in granulosa cells, oocytes and oviduct of female mice. *Gene Expr. Patterns* **10**, 105–112 (2010). doi: 10.1016/j.gep.2010.02.003; pmid: 20176141
110. D. N. Garcia *et al.*, Effect of caloric restriction and rapamycin on ovarian aging in mice. *Geroscience* **41**, 395–408 (2019). doi: 10.1007/s11357-019-00087-x; pmid: 31359237
111. E. E. Chatzidaki *et al.*, Ovulation suppression protects against chromosomal abnormalities in mouse eggs at advanced maternal age. *Curr. Biol.* **31**, 4038–4051.e7 (2021). doi: 10.1016/j.cub.2021.06.076; pmid: 34314679
112. B. Motro, A. Bernstein, Dynamic changes in ovarian c-kit and Steel expression during the estrous reproductive cycle. *Dev. Dyn.* **197**, 69–79 (1993). doi: 10.1002/aja.1001970107; pmid: 7691275
113. S. Wada, S. Fujimoto, Y. Mizue, J. Nishihira, Macrophage migration inhibitory factor in the human ovary: Presence in the follicular fluids and production by granulosa cells. *Biochem. Mol. Biol. Int.* **41**, 805–814 (1997). doi: 10.1080/15216549700201841; pmid: 9111941
114. S. Karino *et al.*, Regulation and localization of midkine in rat ovary. *FEBS Lett.* **362**, 147–150 (1995). doi: 10.1016/0014-5793(95)00231-W; pmid: 7720861
115. H. Hu *et al.*, CyPA interacts with SERPINH1 to promote extracellular matrix production and inhibit epithelial-mesenchymal transition of trophoblast via enhancing TGF-β/Smad3 pathway in preeclampsia. *Mol. Cell. Endocrinol.* **548**, 111614 (2022). doi: 10.1016/j.mce.2022.111614; pmid: 35304192
116. J. Wu, L. Zhang, H. Li, S. Wu, Z. Liu, Nrf2 induced cisplatin resistance in ovarian cancer by promoting CD99 expression. *Biochem. Biophys. Res. Commun.* **518**, 698–705 (2019). doi: 10.1016/j.bbrc.2019.08.113; pmid: 31472965
117. S. He *et al.*, Host CYP27A1 expression is essential for ovarian cancer progression. *Endocr. Relat. Cancer* **26**, 659–675 (2019). doi: 10.1530/ERC-18-0572; pmid: 31048561
118. A. Emery *et al.*, N-cadherin mechanosensing in ovarian follicles controls oocyte maturation and ovulation. *eLife* **13**, RP92068 (2025). doi: 10.7554/eLife.92068; pmid: 40728874
119. J. H. Dorrington, Y. S. Moon, D. T. Armstrong, Estradiol-17β biosynthesis in cultured granulosa cells from hypophysectomized immature rats; stimulation by follicle-stimulating hormone. *Endocrinology* **97**, 1328–1331 (1975). doi: 10.1210/endo-97-5-1328; pmid: 1183412
120. C. M. Foster, N. Hashimoto, J. F. Randolph Jr., I. Z. Beitins, Comparison of growth hormone and insulin-like growth factor-I regulation of estradiol and progesterone production in human luteinized granulosa cells. *Pediatr. Res.* **38**, 763–767 (1995). doi: 10.1203/00006450-199511000-00021; pmid: 8552446
121. B. Zumoff, G. W. Strain, L. K. Miller, W. Rosner, Twenty-four-hour mean plasma testosterone concentration declines with age in normal premenopausal women. *J. Clin. Endocrinol. Metab.* **80**, 1429–1430 (1995). pmid: 7714119
122. F. van der Made *et al.*, The influence of testosterone combined with a PDE5-inhibitor on cognitive, affective, and physiological sexual functioning in women suffering from sexual dysfunction. *J. Sex. Med.* **6**, 777–790 (2009). doi: 10.1111/j.1743-6109.2008.01142.x; pmid: 19207276
123. T. A. C. M. van Geel, P. P. Geusens, B. Winkens, J.-P. J. E. Sels, G.-J. Dinant, Measures of bioavailable serum testosterone and estradiol and their relationships with muscle mass, muscle strength and bone mineral density in postmenopausal women: A cross-sectional study. *Eur. J. Endocrinol.* **160**, 681–687 (2009). doi: 10.1530/EJE-08-0702; pmid: 19174532
124. J. K. Findlay, K. J. Hutt, M. Hickey, R. A. Anderson, How Is the Number of Primordial Follicles in the Ovarian Reserve Established?1. *Biol Reprod* **93**. *Article* **111**, 1–7 (2015).
125. I. A. J. van Rooij *et al.*, Serum anti-Müllerian hormone levels: A novel measure of ovarian reserve. *Hum. Reprod.* **17**, 3065–3071 (2002). doi: 10.1093/humrep/17.12.3065; pmid: 12456604
126. A. Bukman, M. J. Heineman, Ovarian reserve testing and the use of prognostic models in patients with subfertility. *Hum. Reprod. Update* **7**, 581–590 (2001). doi: 10.1093/humupd/7.6.581; pmid: 11727867
127. H. Yan *et al.*, Primary oocytes with cellular senescence features are involved in ovarian aging in mice. *Sci. Rep.* **14**, 13606 (2024). doi: 10.1038/s41598-024-64441-6; pmid: 38871781
128. M. Faire *et al.*, Follicle dynamics and global organization in the intact mouse ovary. *Dev. Biol.* **403**, 69–79 (2015). doi: 10.1016/j.ydbio.2015.04.006; pmid: 25889274
129. K. L. T. Schmidt, A. G. Byskov, A. Nyboe Andersen, J. Müller, C. Yding Andersen, Density and distribution of primordial follicles in single pieces of cortex from 21 patients and in individual pieces of cortex from three entire human ovaries. *Hum. Reprod.* **18**, 1158–1164 (2003). doi: 10.1093/humrep/deg246; pmid: 12773440
130. L. A. Chouinard, A light- and electron-microscope study of the nucleolus during growth of the oocyte in the prepubertal mouse. *J. Cell Sci.* **9**, 637–663 (1971). doi: 10.1242/jcs.9.3.637; pmid: 4112474
131. S. E. Pors *et al.*, Oocyte diameter predicts the maturation rate of human immature oocytes collected ex vivo. *J. Assist. Reprod. Genet.* **39**, 2209–2214 (2022). doi: 10.1007/s10815-022-02602-0; pmid: 36087150
132. H. An *et al.*, KAS-seq profiling captures transcription dynamics during oocyte maturation. *J. Ovarian Res.* **17**, 23 (2024). doi: 10.1186/s13048-023-01342-8; pmid: 38267939
133. U. Heider, I. Pedal, K. Spanel-Borowski, Increase in nerve fibers and loss of mast cells in polycystic and postmenopausal ovaries. *Fertil. Steril.* **75**, 1141–1147 (2001). doi: 10.1016/S0015-0282(01)01805-2; pmid: 11384640
134. Z. Merhi *et al.*, Ovarian kisspeptin expression is related to age and to monocyte chemoattractant protein-1. *J. Assist. Reprod. Genet.* **33**, 535–543 (2016). doi: 10.1007/s10815-016-0672-x; pmid: 26879207
135. A. Capalbo, E. R. Hoffmann, D. Cimadomo, F. M. Ubaldi, L. Rienzi, Human female meiosis revised: New insights into the mechanisms of chromosome segregation and aneuploidies from advanced genomics and time-lapse imaging. *Hum. Reprod. Update* **23**, 706–722 (2017). doi: 10.1093/humupd/dmx026; pmid: 28961822
136. T. Hassold, D. Chiu, Maternal age-specific rates of numerical chromosome abnormalities with special reference to trisomy. *Hum. Genet.* **70**, 11–17 (1985). doi: 10.1007/BF00389450; pmid: 3997148
137. Y. Zhang *et al.*, Transcriptome Landscape of Human Folliculogenesis Reveals Oocyte and Granulosa Cell Interactions. *Mol. Cell* **72**, 1021–1034.e4 (2018). doi: 10.1016/j.molcel.2018.10.029; pmid: 30472193
138. E. K. Bomba-Warczak *et al.*, Exceptional longevity of mammalian ovarian and oocyte macromolecules throughout the reproductive lifespan. *eLife* **13**, RP93172 (2024). doi: 10.7554/eLife.93172.3; pmid: 39480006
139. K. Harasimov *et al.*, The maintenance of oocytes in the mammalian ovary involves extreme protein longevity. *Nat. Cell Biol.* **26**, 1124–1138 (2024). doi: 10.1038/s41556-024-01442-7; pmid: 38902423
140. J. L. Balough, S. S. Dipali, K. Velez, T. R. Kumar, F. E. Duncan, Hallmarks of female reproductive aging in physiologic aging mice. *Nat. Aging* **4**, 1711–1730 (2024). doi: 10.1038/s43587-024-00769-y; pmid: 39672896
141. J. V. V. Isola *et al.*, Canagliflozin treatment prevents follicular exhaustion and attenuates hallmarks of ovarian aging in genetically heterogenous mice. *Geroscience* **47**, 3061–3076 (2025). doi: 10.1007/s11357-024-01465-w; pmid: 39672978
142. T. Umehara *et al.*, Female reproductive life span is extended by targeted removal of fibrotic collagen from the mouse ovary. *Sci. Adv.* **8**, eabn4564 (2022). doi: 10.1126/sciadv.abn4564; pmid: 35714185
143. D. A. Landry *et al.*, Metformin prevents age-associated ovarian fibrosis by modulating the immune landscape in female mice. *Sci. Adv.* **8**, eabq1475 (2022). doi: 10.1126/sciadv.abq1475; pmid: 36054356
144. M. C. Cora, L. Kooistra, G. Travlos, Vaginal Cytology of the Laboratory Rat and Mouse, Vaginal Cytology of the Laboratory Rat and Mouse: Review and Criteria for the Staging of the Estrous Cycle Using Stained Vaginal Smears. *Toxicol. Pathol.* **43**, 776–793 (2015). doi: 10.1177/0192623315570339; pmid: 25739587
145. N. S. Wolcott *et al.*, Automated classification of estrous stage in rodents using deep learning. *Sci. Rep.* **12**, 17685 (2022). doi: 10.1038/s41598-022-22392-w; pmid: 36271290
146. Tabula Sapiens Consortium, The Tabula Sapiens: A multiple-organ, single-cell transcriptomic atlas of humans. *Science* **376**, eabl4896 (2022). doi: 10.1126/science.abl4896; pmid: 35549404
147. Tabula Muris Consortium, Single-cell transcriptomics of 20 mouse organs creates a Tabula Muris. *Nature* **562**, 367–372 (2018). doi: 10.1038/s41586-018-0590-4; pmid: 30283141
148. S. Picelli *et al.*, Full-length RNA-seq from single cells using Smart-seq2. *Nat. Protoc.* **9**, 171–181 (2014). doi: 10.1038/nprot.2014.006; pmid: 24385147
149. M. Mantri, Mouse_ovulation, version 2, Figshare (2024); https://doi.org/10.6084/m9.figshare.c.6930214.
150. Z. Wang, C.-Y. Liu, Y. Zhao, J. Dean, FIGLA, LHX8 and SOHLH1 transcription factor networks regulate mouse oocyte growth and differentiation. *Nucleic Acids Res.* **48**, 3525–3541 (2020). doi: 10.1093/nar/gkaa101; pmid: 32086523
151. Bitplane Development, "Spots Colocalize," Imaris Learning Centre (Oxford Instruments, 2013); https://imaris.oxinst.com/open/view/spots-colocalize.
152. M. Akaiwa, E. Fukui, H. Matsumoto, Tubulointerstitial nephritis antigen-like 1 deficiency alleviates age-dependent depressed ovulation associated with ovarian collagen deposition in mice. *Reprod. Med. Biol.* **19**, 50–57 (2019). doi: 10.1002/rmb2.12301; pmid: 31956285
153. F. E. Duncan, M. T. Pritchard, Picrosirius Red (PSR) Staining and Quantification in Mouse Ovaries, protocols.io (2024); https://dx.doi.org/10.17504/protocols.io.4r3l295o4v1y/v1.
154. Tabula Sapiens data repositories; https://tabula-sapiens.sf.czbiohub.org/whereisthedata.
155. The Tabula Sapiens CELLxGENE Tool; https://cellxgene.cziscience.com/e/bb78adbb-1428-4468-bad0-63602bb974e9.cxg/.
156. Github LairdLabUCSF / Mouse_Human_Ovary_Aging_Comparison. https://github.com/LairdLabUCSF/Mouse_Human_Ovary_Aging_Comparison.

157. Laird Lab UCSF, LairdLabUCSF/Mouse_Human_Ovary_Aging_Comparison: Initial release for publication, Zenodo (2025); https://zenodo.org/records/15709407.
158. D. Laird, E. Gaylord, R. Samuel, M. Foecke, C57BL/6 Mouse Seurat Object (GSE290742), Figshare (2025); https://doi.org/10.6084/m9.figshare.30690137.v1.
159. D. Laird, E. Gaylord, R. Samuel, M. Foecke, Seurat Object of subsetted C57BL/6 Mouse Oocytes from this study (GSE290742) merged with those from Isola et al. 2024 (GEO GSE232309), Figshare (2025); https://doi.org/10.6084/m9.figshare.30690581.v1.
160. D. Laird, E. Gaylord, R. Samuel, M. Foecke, Seurat object of subsetted human granulosa cells from this study and from Wu et al. 2024 (GEO255690), Figshare (2025); https://doi.org/10.6084/m9.figshare.30690980.v1.
161. D. Laird, E. Gaylord, R. Samuel, M. Foecke, Seurat object of subsetted human oocytes from this study and from Wu et al. 2024 (GEO255690), Figshare (2025); https://doi.org/10.6084/m9.figshare.30690965.v1.
162. D. Laird, E. Gaylord, R. Samuel, M. Foecke, Human Seurat Object (GSE290743 and TSP27, TSP28, TSP30), Figshare (2025); https://doi.org/10.6084/m9.figshare.30691001.v1.

ACKNOWLEDGMENTS

We thank the families who consented to donate human ovaries for this study and R. Ponnusamy and A. Salehi with DNW for their assistance with VITAL core samples. In addition, we acknowledge the staff within the UCSF Genomics CoLab for their assistance with 10X library preparation; A. Edwards and the staff within the Biological Imaging Development CoLab (BIDC) at UCSF Parnassus Heights for their training and support in using the white-light Leica TCS SP8 inverted confocal microscope; R. Blandino at the Gladstone Institutes Histology and Light Microscopy Core (HLMC) for her training and support in using the Miltenyi Blaze; S. Paul, H. Mekonen, and A. Zhou from the Genomics group at CZ Biohub for their contributions; A. Rajkovic for kindly gifting the NOBOX antibody and K. Tharp and C. Minor for the CNA35-GFP; M. Stout, J. Isola, C. Hubbart, and the Stout Lab for sharing their data and insights; B. Jones, S. Crasta, and the Tabula Sapiens Consortium at Stanford University; J. McKey and K. Hutt for sharing raw data and helpful suggestions; G. Zaza and the Reproductive Biology Hub at the Buck Institute for Research on Aging for performing the PSR analysis; the Erlebacher Lab for assistance with antibody troubleshooting; L. La Follette for providing clinical insights on ovary morphology and N. Wolcott for assistance with EstrousNet; and members of the Laird lab (J. Zussman, E. Rojas, S. Cincotta, R. Dhada, and C. Doherty) for their help and thoughtful feedback on the manuscript. We thank our thesis committee members (S. Villeda, T. Nystul, M. Conti, and L. Jones) for their invaluable guidance throughout this work. Schematics were created with BioRender.com. **Funding:** National Institutes of Health grant 1F31HD108875 (E.A.G.); National Institutes of Health grant 1F31HD110208 (M.H.F.); UCSF Discovery Fellowship (E.A.G.); Hillblom/BARI Graduate Student Fellowship Award (E.A.G., M.H.F.); National Institutes of Health grant 1R01GM122902 (D.J.L.); National Institutes of Health grant 1R01ES023297 (D.J.L.); National Institutes of Health grant P30ES030284 (D.J.L.); CZ Biohub Investigator funds (D.J.L.); The Global Consortium for Reproductive Health through the Bia-Echo Foundation GCRLE-0123 (D.J.L.); The W. M. Keck Foundation (D.J.L.); The Simons Foundation International (D.J.L.); The Juno Fund (D.J.L.); Individual donors, including Mary Linda Laird (in honor of cancer researchers and survivors of ovarian and other cancers), Robert and Mary Laird, and Nikki J. Zapol (D.J.L.). Funding was also provided by the Chan Zuckerberg Initiative. **Author contributions:** Conceptualization: E.A.G., M.H.F., R.M.S., F.F., D.J.L.; Methodology: E.A.G., M.H.F., R.M.S., B.S., A.M.D., T.I.M., L.C.D., M.B., A.E.L., R.A.; Investigation: E.A.G., M.H.F., R.M.S., T.I.M.; Visualization: E.A.G., M.H.F., R.M.S., T.I.M., A.E.L.; Funding acquisition: E.A.G., M.H.F., N.N., D.J.L.; Project administration: E.A.G., M.H.F., R.M.S., D.J.L.; Supervision: D.J.L., F.F., N.N.; Writing – original draft: E.A.G., M.H.F., R.M.S.; Writing – review & editing: E.A.G., M.H.F., R.M.S., D.J.L., B.S., A.M.D., T.I.M., L.C.D., A.E.L., F.F. **Competing interests:** D.J.L. is on the scientific advisory board of Vitra, Inc. D.J.L. has served as a paid consultant in fields relevant to this study. M.H.F. is a scientist at Vitra, Inc. F.F. is an inventor on patent WO2017112901A1, held by Memorial Sloan Kettering Cancer Center, covering stem cell–derived enteric neural crest lineages for Hirschsprung's disease; on patent applications WO2018090002A1 and WO2018090002A1, held by Memorial Sloan Kettering Cancer Center and Weill Cornell Medicine, covering stem cell–derived Schwann cells and their application for drug discovery for diabetic peripheral neuropathy; on patent applications WO2020132701A1, WO2023130150A2, and WO2023130149A2, held by the Regents of the University of California, covering stem cell–derived enteric neurons and their use in treating gut motility disorders; and on patent application WO2024040123A1, held by the Regents of the University of California, covering stem cell–derived Schwann cells and their application for drug discovery for peripheral neuropathies. F.F. serves as a paid advisor for commercial entities including Cellanome and is a cofounder and advisor at EverTree Bio. All other authors declare that they have no competing interests. **Data and materials availability:** The mouse and human scRNA-seq data generated in this study have been deposited in Gene Expression Omnibus (GEO) under the accession codes GSE290742 and GSE290743. The raw fastq files for the human scRNA-seq data generated from the three human donors from Tabula Sapiens (TSP27, TSP28, and TSP30) are available for download from the Tabula Sapiens AWS repository (*154*) after signing the data use agreement. The Tabula Sapiens ovary dataset can also be explored online with the CELLxGENE tool (*155*). All other data needed to evaluate the conclusions in the paper are present in the paper or in the Supplementary Materials. All code used for data processing, analysis, and visualization are publicly available on Github (*156*) and archived in Zenodo (*157*). The fully analyzed Seurat objects generated from this study are available on Figshare (*158*–*162*). **License information:** Copyright © 2025 the authors, some rights reserved; exclusive licensee American Association for the Advancement of Science. No claim to original US government works. https://www.science.org/about/science-licenses-journal-article-reuse

SUPPLEMENTARY MATERIALS

science.org/doi/10.1126/science.adx0659
Figs. S1 to S12; Tables S1 to S5; Reproducibility Checklist

Submitted 27 February 2025; accepted 29 August 2025; published online 9 October 2025
10.1126/science.adx0659



AAAS.ORG/COMMUNITY







AAAS' Member Community is a one-stop destination for scientists and STEM enthusiasts alike. It's "Where Science Gets Social": a community where facts matter, ideas are big and there's always a reason to come hang out, share, discuss and explore.

Member COMMUNITY
AAAS

AMERICAN ASSOCIATION FOR THE ADVANCEMENT OF SCIENCE

RESEARCH ARTICLE SUMMARY

ORGANIC CHEMISTRY

Three-component assembly and structure-function relationships of (–)-gukulenin A

Vaani Gupta, Zechun Wang, Joshua B. Combs†, Timothy Wright†, Lei Chen, Boxu Lin, Ryan Holmes, Bo Qin, Joonseok Oh, Jason M. Crawford, Seth B. Herzon*

Full article and list of author affiliations: https://doi.org/10.1126/science.aea9310

INTRODUCTION: α-Tropolones are aromatic seven-membered rings that contain hydroxyl and carbonyl substituents in a 1,2-relationship. Their aromatic resonance stabilization energy has been estimated as ~47 kcal/mol, ~10 kcal/mol greater than more benzenoid systems. Separation of charge in the carbon-oxygen π bond enhances aromaticity. Consequently, α-tropolones possess a strong molecular dipole (3.71 *D*), affinity for divalent metals, ambiphilic reactivity, and an acidic hydroxyl residue [p*K*a (where K_a is the acid dissociation constant) = 6.7, H_2O]. α-Tropolones are found in many secondary metabolites, including a pseudodimeric metabolite known as (–)-gukulenin A that contains two substituted α-tropolone rings. (–)-Gukulenin A was isolated from the marine sponge *Phorbas gukulensis* and exhibited promise in a mouse model of ovarian cancer. However, the features of (–)-gukulenin A that drive its antitumor effects are unknown.

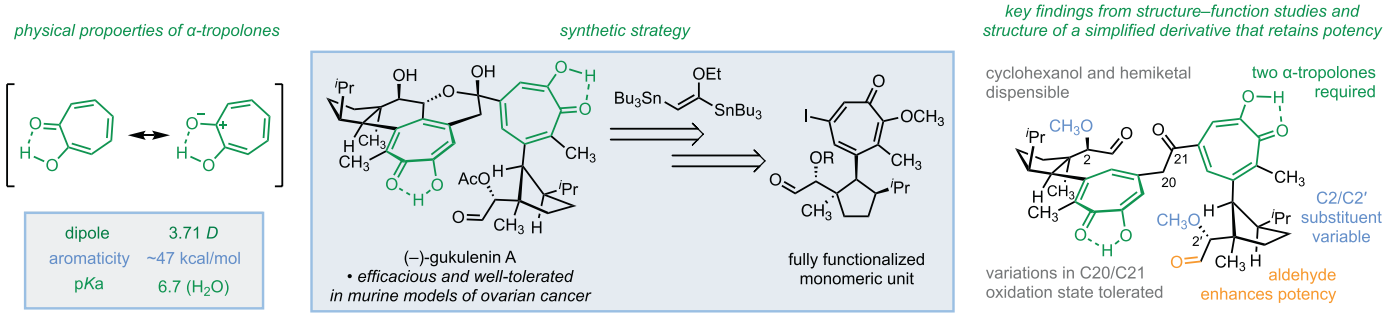
RATIONALE: We envisioned that a convergent, stereoselective synthesis of (–)-gukulenin A could serve as a platform to determine which structural elements in the isolate are necessary for antiproliferative activity. Such structure-function relationships would aid in identification of gukulenin's biological target, as well as designing simplified derivatives for preclinical evaluation. We modeled our synthetic strategy around the hypothesis that nature prepares (–)-gukulenin A by dimerization of two identical α-tropolone intermediates. Experimentally, we envisioned that this could be achieved by coupling of two monomeric methyl tropolone ethers and a suitably oxidized two-carbon linker, followed by a biomimetic cyclization to form the tetracycle of (–)-gukulenin A.

RESULTS: The cyclopentane rings of (–)-gukulenin A were derived from enantioenriched *exo*-(2*R*)-norbornylamine. After directed C–H arylation and further elaboration, a tandem Grob fragmentation–α-alkylation was implemented to reveal the cyclopentane rings of the target. We developed three methods to achieve the expansion of *ortho*-benzoquinone monoketals to α-tropolone methyl ethers, and the third method was ultimately used in the synthesis. The reagent (*E*)-1,2-di(tributylstannyl)-1-ethoxyethylene was designed, synthesized, and utilized in a twofold, site-selective cross-coupling reaction to access the carbon skeleton of (–)-gukulenin A. The cyclohexanol and hemiketal rings were introduced in one step by a thermal carbonyl-ene reaction. After deprotection, (–)-gukulenin A was obtained.

We applied this chemistry to the synthesis of 15 derivatives, each of which was designed to probe a specific structure-function relationship. By this approach, we established that the dimeric, α-tropolone structure is necessary for potent cytotoxicity, that variation in the C2/C2′ substituents and two-carbon linker (C20, C21) is tolerated, and that the aldehyde residue enhances the cytotoxicity of dimeric (but not monomeric) derivatives.

CONCLUSION: The synthetic strategy that we developed provides access to (–)-gukulenin A in 24 steps and 2.5% yield from commercial reagents. Our structure-function studies define the features of gukulenin that are critical for potent cytotoxic effects. Collectively, this work provides a foundation for target identification studies and the preclinical evaluation of simplified derivatives in single-agent and combinatorial chemotherapies. □

*Corresponding author. Email: seth.herzon@yale.edu †These authors contributed equally to this work. Cite this article as V. Gupta *et al.*, *Science* 390, eaea9310 (2025). DOI: 10.1126/science.aea9310



Properties of α-tropolones (left), our synthetic approach to (–)-gukulenin A (center), and key findings from structure-function studies (right).

ORGANIC CHEMISTRY

Three-component assembly and structure-function relationships of (–)-gukulenin A

Vaani Gupta[1], Zechun Wang[1], Joshua B. Combs[1]†‡, Timothy Wright[1]†§, Lei Chen[1]¶, Boxu Lin[1]#, Ryan Holmes[1]**, Bo Qin[1]††, Joonseok Oh[1,2]‡‡, Jason M. Crawford[1,2,3], Seth B. Herzon[1,4]*

α-Tropolones comprise an unsaturated seven-membered ring bearing a hydroxyl substituent adjacent to a polarized carbon-oxygen π bond. This polarization imparts a permanent molecular dipole and aromatic stabilization to the ring, resulting in distinct physical properties, including affinity for divalent metals and ambiphilic reactivity. Among secondary metabolites that contain α-tropolones, the pseudodimeric isolate (–)-gukulenin A (**7**) stands out for its complexity and has shown promise in treating mouse models of ovarian cancer. In this study, we describe an enantioselective synthesis of (–)-gukulenin A (**7**). Key steps include a directed C–H arylation, a tandem Grob fragmentation–alkylation, an innovative synthesis of methyl tropolone ethers, a multicomponent cross-coupling, and a thermal carbonyl-ene reaction. Structure-function studies establish the dimeric tropolone and aldehyde substructures as drivers of cytotoxicity.

The existence of a seven-membered aromatic ring was first posited by Dewar in 1950 to account for the physical properties of the natural product stipitatic acid (**1**) (Fig. 1A) (*1*). Dewar named this unconventional ring an α-tropolone and estimated its aromatic stabilization energy to be ~47 kcal/mol, which is considerably greater than that of benzenoid systems, such as phenol (**3**; 36 kcal/mol). This aromatic character is enhanced by separation of charge in the carbon-oxygen π bond. Consequently, α-tropolones present a strong molecular dipole (3.71 *D* for **2**) (*2*) and increased acidity of the hydroxyl residue [p*K*a (where K_a is the acid dissociation constant) = 6.7 (H_2O)] (*3*). Tropolone rings have been identified in other secondary metabolites, such as hinokitiol (**4**), colchicine (**5**), rubrolone A (**6**) (Fig. 1B), and (–)-gukulenins A and B (**7** and **8**, respectively, Fig. 1C) (*4*). (–)-Gukulenins A (**7**) and (**B**) were first isolated from a sample of the marine sponge *Phorbas gukulensis* found off the coast of Gageodo Island, South Korea, and are the most structurally complex tropolone natural products discovered to date (*5*). The pseudodimeric structure of (–)-gukulenin A (**7**) comprises two α-tropolone residues (green, Fig. 1C), 10 asymmetric stereocenters (two of which are quaternary and nine of which are contiguous with adjacent stereocenters), densely functionalized cyclopentane fragments, a labile hemiketal (blue, Fig. 1C), and an electrophilic α-acetoxy aldehyde (orange, Fig. 1C) (*4*). (–)-Gukulenin B (**8**) is identical to (–)-gukulenin A (**7**) save for the presence of a primary alcohol in place of the aldehyde substituent. Additional gukulenins arising from nucleophilic addition to the aldehyde within **7**, or opening of the hemiketal, have also been discovered (fig. S1) (*6*).

The biological effects of α-tropolones often derive from the physical properties of the ring (*7*). Owing to their strong dipole and acidity, α-tropolones chelate divalent metals with high affinity (*8*), as exemplified by hinokitiol (**4**), which restores homeostasis in models of iron deficiency (*9*). Alternatively, colchicine (**5**) is a noncovalent inhibitor of tubulin dynamics (*10*, *11*), whereas biosynthetic precursors to rubrolone A (**6**) are thought to serve a bacterial defense role (*12*). (–)-Gukulenin A (**7**) is a cytotoxin with half-maximal inhibitory potencies (IC_{50}s) in the 50- to 130-nM range against a panel of cultured human cancer cell lines. Whereas secondary metabolites are commonly pancytotoxic, metabolites that display selective toxicity toward cancer cells are rare. Thus, it is promising that moderate doses (3 mg/kg) of (–)-gukulenin A (**7**) were well tolerated and reduced tumor burden by >92% in a mouse model of ovarian cancer (*13*). Additionally, (–)-gukulenin A (**7**) exhibited synergy with poly(adenosine diphosphate-ribose) polymerase inhibitors (PARPis) (*14*), suggesting its use in single-agent or combinatorial chemotherapy regimens. However, the structural features underlying this activity [so-called structure-function relationships (*15*)] are unknown. Aldehydes are often reactive toward lysine residues (*16*), and the increased potency of (–)-gukulenin A (**7**) relative to (–)-gukulenin B (**8**) (*5*) points to a role for this functional group in biological activity. It is also not known whether the entire carbon skeleton and one or both α-tropolones are necessary for activity. A synthesis of (–)-gukulenin B (**8**) was reported by Nicolaou and co-workers in 2022 (Fig. 1D) (*17*). The tricyclic and bicyclic tropolone ethers **9** and **10**, respectively, prepared from β-bromotropolone methyl ether (not shown), were united in a palladium-catalyzed cross-coupling to provide the pseudodimeric structure **11** (43%), which was advanced to (–)-gukulenin B (**8**) in five steps (15%). However, no structure-function studies were reported, and the synthesis of (–)-gukulenin A (**7**), which is the most potent gukulenin isolate and the only one with validated in vivo anticancer activity (*13*), remains an outstanding challenge (*18*, *19*).

We developed a convergent enantioselective synthesis of (–)-gukulenin A (**7**) and adapted this route to the synthesis of 15 derivatives to elucidate structure-function relationships. Our route was based on the biosynthetic hypothesis depicted in Fig. 1E. We envisioned that oxidative dimerization (*20*, *21*) and C–H oxidation might proceed biochemically to form a dimeric ketone such as **14**. Formal 1,2-addition of the more electron-rich tropolone to the C1 aldehyde (C1–C14 bond formation), followed by restoration of aromaticity, would provide the pentacycle **15**. Selective removal of the C2 acetate and hemiketal formation would generate (–)-gukulenin A (**7**). Although this hypothesis is appealing from the perspectives of convergence and expected reactivity, the near C_2-symmetry of **14** introduces a subtle yet critical synthetic challenge, namely late-stage differentiation of the pairwise peripheral functional groups within **14** that are, strictly speaking, chemically inequivalent (owing to the presence of the C21 ketone).

Nonetheless, we envisioned implementation of this approach by the convergent coupling of two monomeric methyl tropolone ethers with a nonsymmetrical two-carbon linchpin reagent (see structure **17**) containing a synthetic handle for the C21 ketone in **14**. Extensive efforts led us to the reagent, (*E*)-1,2-di(tributylstannyl)-1-ethoxyethylene (**18**), to meet this goal (Fig. 1F). Construction of the α-tropolone and cyclopentane rings were recognized as two additional challenges. Most existing methods for tropolone synthesis are not compatible with the substitution pattern and functional groups in (–)-gukulenin A (**7**) (*22*), which led us to develop three methods for tropolone synthesis based on the one-carbon ring expansion of *ortho*-benzoquinone monoketal

[1]Department of Chemistry, Yale University, New Haven, CT, USA. [2]Institute of Biomolecular Design and Discovery, Yale University, West Haven, CT, USA. [3]Department of Microbial Pathogenesis, Yale School of Medicine, New Haven, CT, USA. [4]Departments of Pharmacology and Therapeutic Radiology, Yale School of Medicine, New Haven, CT, USA. ***Corresponding author. Email: seth.herzon@yale.edu** †These authors contributed equally to this work. ‡Present address: Department of Cellular and Molecular Pharmacology, University of California, San Francisco, San Francisco, CA, USA. §Present address: Innovation, Science and Economic Development Canada, Government of Canada, Gatineau, QC, Canada. ¶Present address: Sinomune Pharmaceutical, Xibei Town, Xishan District, Wuxi, Jiangsu, China. #Present address: Key Laboratory of Bioorganic Chemistry and Molecular Engineering, Ministry of Education, Beijing National Laboratory for Molecular Science, College of Chemistry and Molecular Engineering, Peking University, Haidian District, Beijing, China. **Present address: Prelude Therapeutics, Wilmington, DE, USA. ††Present address: Department of Chemistry, New York University, New York, NY, USA. ‡‡Present address: Amgen, Cambridge, MA, USA.

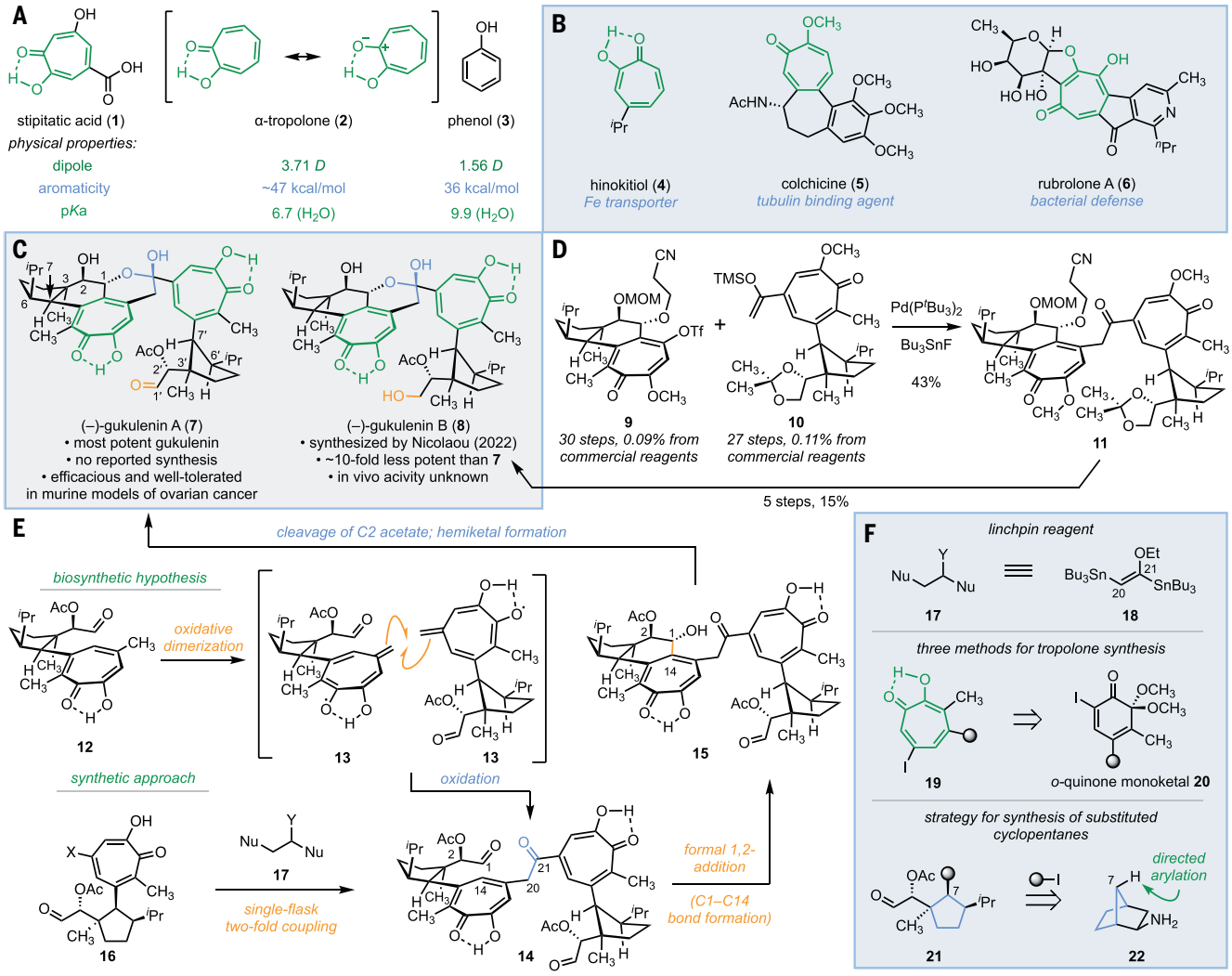


Fig. 1. Overview of α-tropolones and the gukulenins. (**A**) Structure of stipitatic acid (**1**) and physical properties of α-tropolone (**2**). The corresponding properties of phenol (**3**) are shown for comparison. (**B**) Representative secondary metabolites that contain a tropolone ring. (**C**) Structures of (−)-gukulenins A (**7**) and B (**8**). (**D**) Synthetic intermediates and fragment coupling in the synthesis of (−)-gukulenin B (**8**) by Nicolaou and co-workers (*17*). (**E**) Biosynthetic hypothesis (top) and synthetic approach (bottom) to (−)-gukulenin A (**7**). (**F**) Key challenges to the synthesis of (−)-gukulenin A (**7**), and overview of the solutions developed herein.

intermediates (see **19** and **20**). Chiral-substituted cyclopentane residues are most commonly derived from commercially available, scalemic terpene precursors (*23*). We instead leveraged the bicyclic structure of enantioenriched *exo*-2-norbornylamine (**22**) to control the relative and absolute stereochemistry of the cyclopentane rings and, subsequently, that of the isolates themselves.

Development of the synthesis

The picolinamide **23** was prepared by acylation of enantioenriched [>99% enantiomeric excess (ee)] *exo*-(2*R*)-norbornylamine with picolinic acid (92%; Fig. 2A). *Exo*-(2*R*)-norbornylamine has been used as a starting material in the production of a clinical drug candidate and is readily available on kilogram scales (*24*). On the basis of studies from Daugulis (*25*), Chen (*26*, *27*) and Sheppard (*28*), we evaluated the directed arylation of **23** using various arenes (see table S1). We anticipated that this would be a challenging arylation because the requisite arene contains two electron-donating oxygen substituents and is *ortho*-substituted. To the best of our knowledge, there are only two examples of arylation of related bicyclic substrates using *ortho*-substituted arenes (*28*). After extensive optimization, we found that heating a mixture of **23**, palladium acetate (0.10 equiv), silver carbonate (1.0 equiv), dibenzyl phosphate (0.20 equiv), and the iodoarene **24** (2.0 equiv; prepared in three steps and >99% yield from 2-bromo-6-methylanisole; see supplementary materials) to 105°C for 24 hours provided the arylation product **25** (67%, 10-g scale). The addition of dibenzyl phosphate was critical to obtain high conversion of **23** when the electron-rich halide **24** was used (*29*).

The picolinamide was cleaved by treatment with excess zinc and aqueous hydrochloric acid (*30*). Oxidative deamination of the unpurified product (not shown) by 3,5-di-*tert*-butyl-*ortho*-benzoquinone (*31*) provided the ketone **26** (52%, 2 steps, 11-g scale). Heating mixtures of **26** and potassium hydride (4.0 equiv) in dimethylcarbonate formed a β-ketoester (not shown). The addition of iodomethane (2.0 equiv) then provided the α-methyl-β-ketoester **27** in a single operation [>99%, >19:1 diastereomeric ratio (dr), proton nuclear magnetic resonance (^{1}H NMR) analysis]. Attempts to effect *C*-acylation by using other electrophiles [such as Mander's reagent (*32*), the Heller–Sarpong reagent (*33*), or alkyl chloroformates] provided *O*-acylation products or recovery of starting material. Nuclear Overhauser effect (NOE) analysis of the sulfonate **28** (vide infra) revealed that the methyl substituent was introduced to the *exo*-position, potentially as the result of a halogen

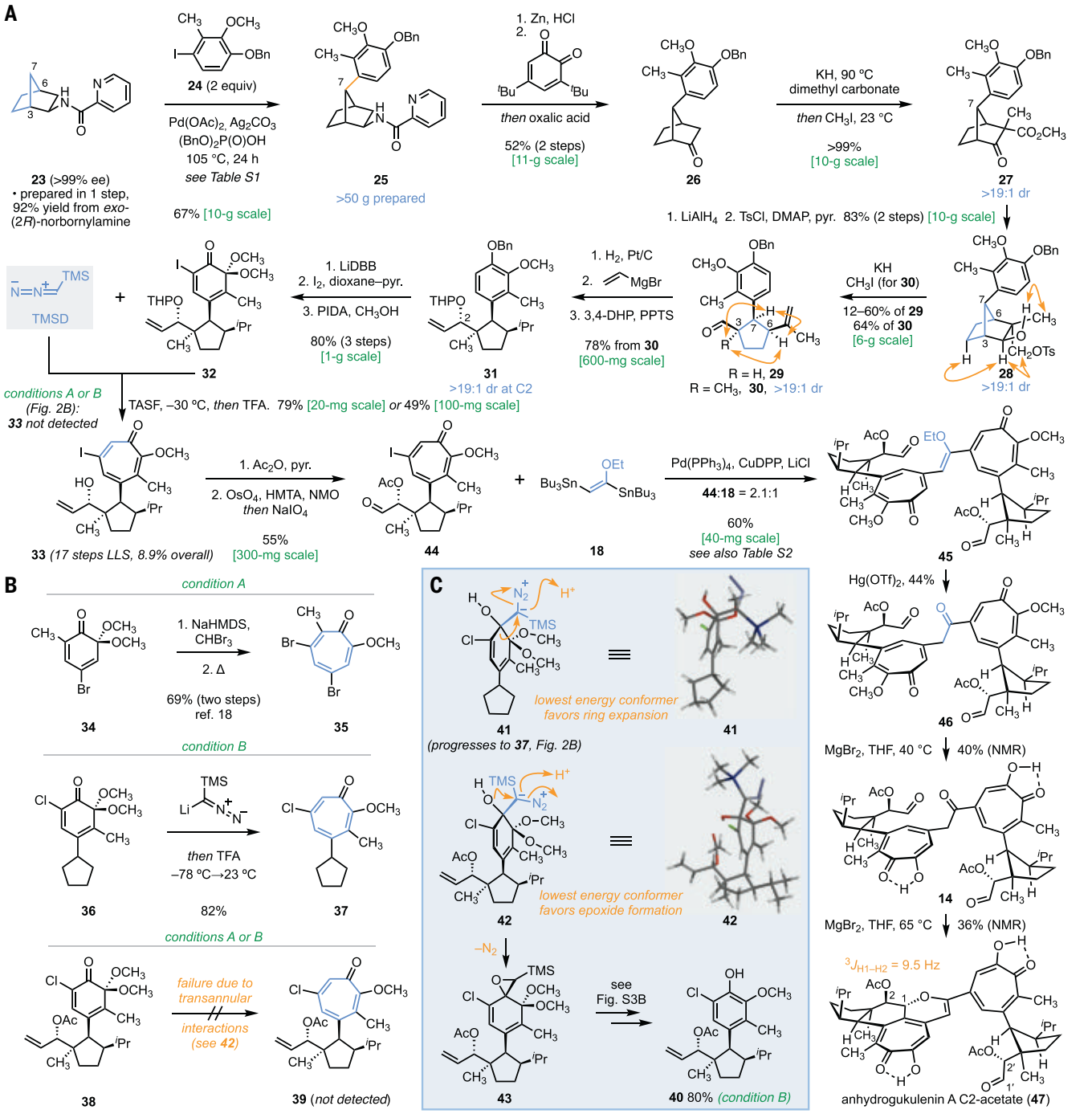


Fig. 2. Synthesis of the monomeric methyl tropolone ether 33 and the twofold Stille coupling product 45, elaboration of the two-fold Stille coupling product 45 to anhydrogukulenin A C2-acetate (47), and approaches and mechanistic analysis of the ring expansion. (**A**) Synthesis of the monomeric methyl tropolone ether **33** and the twofold Stille coupling product **45**. Orange arrows in **28** and **30** depict diagnostic NOE enhancements. (**B**) Strategies evaluated to form the methyl tropolone ether **33**. (**C**) Mechanistic analysis of the ring expansion (condition B) and rationalization for the disparate reactivity of **36** and **38**.

bonding interaction between iodomethane and the aromatic ring (*34*). Reduction of **27** (lithium aluminum hydride) followed by selective sulfonylation of the primary neopentylic alcohol [*p*-toluenesulfonyl chloride (TsCl), 4-(dimethylamino)pyridine (DMAP), pyridine] provided the hydroxysulfonate **28** [83% from **27**, >19:1 dr (^{1}H NMR analysis), 10-g scale].

We envisioned opening the bicyclic ring system within **28** by a Grob fragmentation (*35*) to establish the cyclopentane of the targets. The C3-desmethyl cyclopentane **29** (R = H) was rapidly formed upon exposure of hydroxysulfonate **28** to strong bases (e.g., potassium *tert*-butoxide, potassium hydride, or potassium hexamethyldisilazide), but the isolated yields were low and variable (12 to 60%). We hypothesized that the aldehyde within **29** was undergoing enolization and decomposition (*36*) and that we could leverage this reactivity to install the C3 methyl substituent in situ. In the event, the α-methylated Grob fragmentation product **30** was obtained in 64% yield and >19:1 dr (^{1}H NMR

analysis) on a 6-g scale upon treatment of **28** with potassium hydride (3.0 equiv) and methyl iodide (1.5 equiv) in tetrahydrofuran at 23°C. The relative configuration depicted was established by NOE analysis (see orange arrows, Fig. 2A). This approach made strategic use of the constrained bicyclic skeleton of picolinamide **23** to establish the congested and contiguous C3/C3′, C6/C6′, and C7/C7′ stereocenters in the target (compare structures **23**, **30**, and **7**).

The allylic ether **31** was prepared by a three-step sequence comprising alkene reduction (dihydrogen, platinum on carbon), addition of vinylmagnesium bromide (>19:1 dr, ^{1}H NMR analysis), and protection of the resulting allylic alcohol as the corresponding 2-tetrahydropyranyl (THP) ether [3,4-dihydropyran (DHP), pyridinium *para*-toluenesulfonate (PPTS); 78% from **30**, 600-mg scale]. A magnesium-substrate complex accounting for the diastereoselectivity is shown in fig. S2A, and the (2*S*) configuration depicted was supported by crystallographic analysis of a related synthetic intermediate (see fig. S2B). Removal of the benzyl ether [lithium di-*tert*-butylbiphenylide (LiDBB)] (*37*), *ortho*-iodination of the resulting phenol (iodine, pyridine), and oxidative dearomatization [diacetoxyiodobenzene (PIDA), methanol] provided the *ortho*-quinone monoketal **32** (80% from **31**, 1-g scale).

We previously developed a one-carbon ring expansion of *ortho*-quinone monoketals to access methyl tropolone ethers bearing the substitution pattern of the gukulenins (see "condition A," **34**→**35**, Fig. 2B) (*18*). These conditions failed to provide the methyl tropolone ether **33** when applied to ketal **32**. Accordingly, a ring expansion based on a Tiffeneau-Demjanov–like pathway was developed (*38*). Adapting conditions reported by Lee and co-workers for the expansion of simple cycloalkanones (*39*), we found that sequential addition of 1-lithio trimethylsilyldiazomethane (TMSD) and trifluoroacetic acid (TFA) to the model substrate **36** provided the methyl tropolone ether **37** ("condition B," 82%). This reaction likely proceeds by 1,2-addition of 1-lithio TMSD to **36**, *C*-protonation, 1,2-bond migration with loss of dinitrogen (see **41**, Fig. 2C), and formal 1,6-elimination of trimethylsilyl methyl ether. However the phenol **40** (Fig. 2C) was the only detectable product (80%) when these conditions were applied to the *ortho*-quinone monoketal **38**, which bears the fully functionalized cyclopentane of the targets. Molecular dynamics simulations were carried out (*40*) to gain insight into the disparate reactivity of **36** and **38**. The lowest-energy conformation of the TMSD addition product **41**, derived from **36**, was preorganized for ring expansion by positioning the trimethylsilyl substituent over the cyclohexyl ring. By comparison, the lowest-energy conformation of the TMSD addition product **42** (derived from **38**) adopted a conformation that would favor α-silyl epoxide **43** by positioning the trimethylsilyl substituent away from the cyclohexane ring, potentially to minimize transannular interactions. Space-filling models of the lowest-energy conformations of the addition products are shown in fig. S3A and support the hypothesis that the cyclopentane substituents within **42** influence the orientation of the trimethylsilyl residue. Epoxide formation is frequently a competitive pathway in Tiffeneau-Demjanov rearrangements (*38*). Further reaction of **43** yielded the phenol **40** (fig. S3B).

We reasoned that removal of the silyl substituent might restore the desired reactivity. However, the *ortho*-quinone monoketal **38** was unreactive toward diazomethane, likely because of the steric hindrance about the carbonyl substituent, and lithio diazomethane is not a viable reagent (*41*). Therefore, we developed a desilylative addition of TMSD to **32** (*42*). The desired ring expansion product **33** was obtained when tris(dimethylamino)sulfonium trimethyldifluorosilicate (TASF, 1.4 equiv) was added to a solution of **32** and TMSD (1.4 equiv) at −30°C, followed by excess TFA (6.5 equiv) and warming to 23°C. The yields of this transformation diminished with scale (79 versus 49% on 20- and 100-mg scales, respectively). We believe that the 1,2-addition may be promoted by formation of a nucleophilic fluorosilicate derived from TMSD. Addition of excess TFA promoted the ring expansion, 1,6-elimination of methanol, and cleavage of the THP ether protecting group in a single step (see fig. S3C). The aldehyde **44** was obtained by acetylation of the alcohol (acetic anhydride, pyridine) and oxidative cleavage of the alkene [osmium tetroxide, hexamethylenetetramine (HMTA), *N*-methylmorpholine-*N*-oxide (NMO), then sodium periodate] (*43*, *44*) (55% from **33**, 300-mg scale).

To implement the three-component assembly strategy, it became necessary to identify a two-carbon synthon to elaborate **44**. We eventually synthesized the distannane (*E*)-1,2-di(tributylstannyl)-1-ethoxyethylene (**18**) to meet this goal (see supplementary materials) (*45*, *46*). The reagent **18** was, notably, unknown, but *trans*-1,2-di(tributylstannyl)ethylene itself has found use as a linchpin reagent in synthesis (*47*). After extensive optimization of the twofold coupling (see table S2), the enol ether **45** was obtained in 60% yield by treatment of the distannane **18** (1.0 equiv) and the iodotropolone ether **44** (2.1 equiv) with tetrakis(triphenylphosphine)palladium(0), copper diphenylphosphinate (CuDPP), and lithium chloride (40-mg scale).

The ketone **46**, which constitutes the last intermediate in the sequence that is amenable to normal-phase purification, was prepared by mercury-mediated hydrolysis (*48*) of the enol ether (mercuric trifluoromethanesulfonate) (44%). Demethylation of the tropolone rings (magnesium bromide) provided the putative biosynthetic precursor **14** (40%, quantitative ^{1}H NMR analysis; see also Fig. 1E). Further heating of solutions of **14** and magnesium bromide in tetrahydrofuran to 65°C formed anhydrogukulenin A C2-acetate [**47**; 36% (quantitative ^{1}H NMR analysis), >19:1 dr at C1 (^{1}H NMR analysis)]. The structure of **47** was rigorously established by multidimensional NMR analysis (fig. S4). The vicinal coupling constant between H1 and H2 in **47** ($^3J_{H1–H2}$ = 9.5 Hz) was similar to that of (−)-gukulenin A (**7**; $^3J_{H1–H2}$ = 9.3 Hz) (*5*) and is consistent with a *trans* diaxial arrangement of these protons. Structure determination of oxidized compounds such as **47** can be challenging (*49*); accordingly, the assignment of **47** was corroborated by density functional theory NMR calculations (table S3) (*40*, *50*). Unfortunately, attempts to remove the C2 acetate under basic conditions were confounded by preferential cleavage of the C2′ acetate, followed by decomposition (table S4). We suspect that hydrolysis of the C2′ acetate occurs by a discrete mechanism initiated by nucleophilic addition to the C1′ aldehyde (fig. S5).

As discussed above, although this approach is convergent, the near C_2-symmetry of **45**, **46**, and **14** rendered differentiation of the acetate esters challenging. Accordingly, we considered introducing a tropolone monomer with an orthogonal C2 protecting group in the cross-coupling step. This approach, however, required selective reactivity of the α- and β-tributylstannyl substituents within the coupling reagent **18**, and it was not clear at the outset which stannyl substituent had a greater propensity for transmetalation. However, we detected (by ^{1}H NMR analysis) the α-arylation product **48** when **18** and **44** were used in equimolar quantities in the Stille coupling (Fig. 3A). The connectivity of **48** was supported by chemical shift (H22, δ 5.58) and coupling constant ($^2J_{H22–Sn}$ = 22 Hz) analysis. Attempted purification of **48** resulted in protodestannylation and formation of the terminal alkene **50**. The chemical shifts and coupling constants between the vinylic protons (H22, δ 3.96, 4.52; $^2J_{H22A–H22B}$ = 3.0 Hz) are consistent with a 2,2-disubstituted enol ether. Furthermore, the addition of iodobenzene to solutions of the α-arylation intermediate **48** provided the three-component coupling product **49** (48%). The observation of four-bond coupling between the *ortho*-phenyl protons and H22, as well as NOE enhancements between H29 and H12, and H29 and H14 (see orange arrows, Fig. 3A), further supported the connectivity depicted. In aggregate, these data indicated that a selective twofold cross-coupling using differentially protected tropolone monomers is possible, thereby allowing us to distinguish the remote C2/C2′ substituents while maintaining the convergence of the approach.

Extensive analysis and optimization led us to synthesize the *para*-methoxybenzyl (PMB) ether **52** by alkylation of the allylic alcohol **33** [alkynyl benzoate **51**, (triphenylphosphine)gold(I) chloride, silver

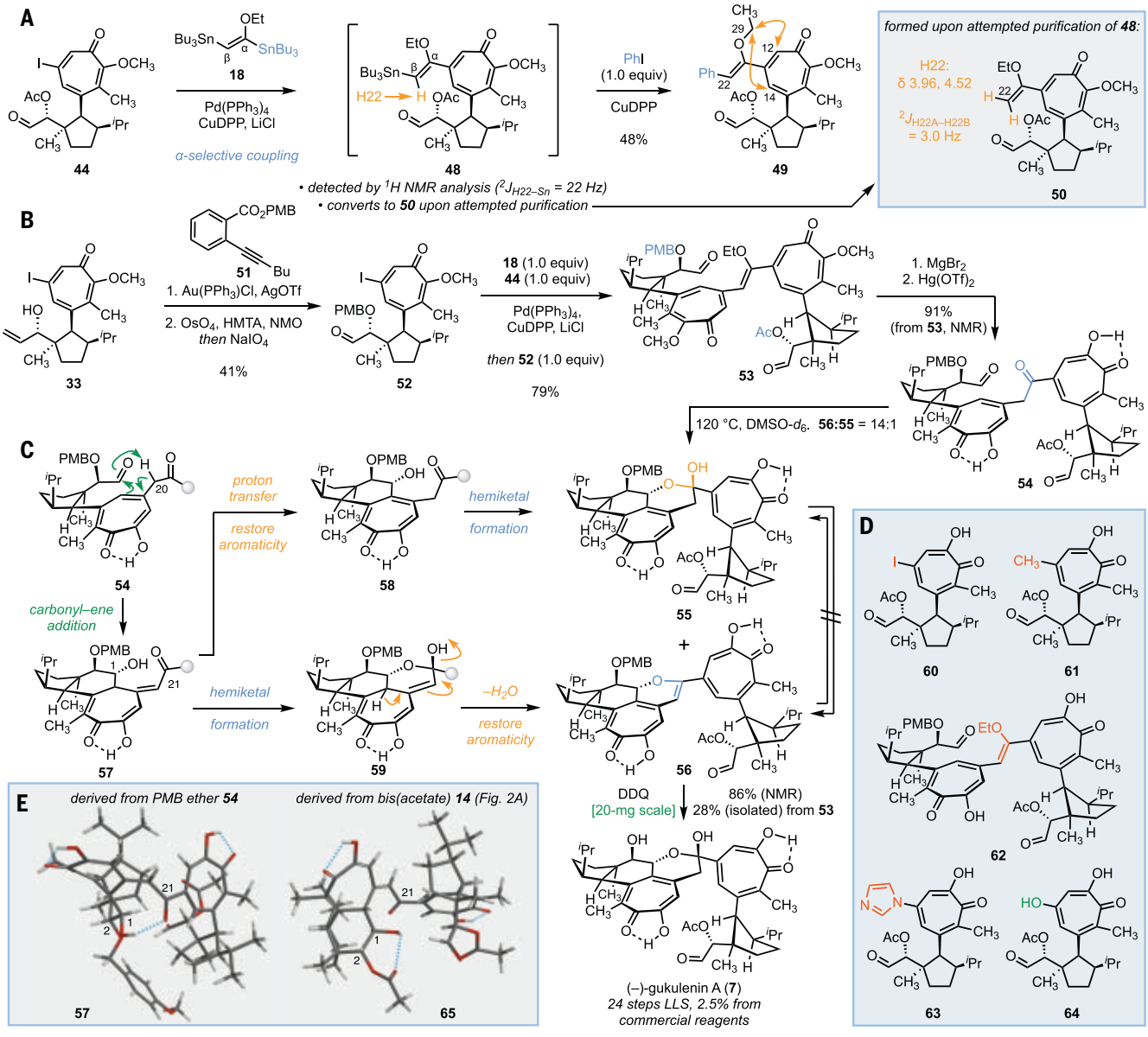


Fig. 3. Development of a heterodimerization strategy, synthesis of (−)-gukulenin A (7), potential mechanism of the cyclization, and substrates that inform the mechanistic model. (**A**) Site-selective cross-coupling of **18** to establish the feasibility of the approach. (**B**) Synthesis of (−)-gukulenin A (**7**). (**C**) Proposed mechanism of the cyclization (**54**→**55**, **56**). (**D**) Substrates used in the study of the cyclization step. (**E**) Conformational analysis of the cyclization intermediates **57** and **65** [**65** is derived from the homodimerization product **14** (Fig. 2A)].

trifluoromethanesulfonate] (*51*), followed by oxidative cleavage of the alkene (osmium tetroxide, HMTA, NMO, then sodium periodate; 41% from ***33***; Fig. 3B). The three-component coupling was further optimized by using a model system (table S5), and the desired product ***53*** was obtained by sequential coupling of the acetate ***44*** and the distannane ***18*** (1.0 equiv each), followed by addition of the PMB ether ***52*** (1.0 equiv; 79%). We attempted sequential enol ether hydrolysis and tropolone demethylation (as in Fig. 2A); however, this approach was low-yielding. Fortunately, by reversing the order of steps, we were able to obtain the ketone ***54*** in 91% yield (quantitative ^{1}H NMR analysis) from ***53***. Because α-tropolone intermediates such as ***54*** have poor mobility and stability on silica gel, on preparative scales, intermediates derived from ***53*** were advanced without purification.

Attempted cyclization of ***54*** (see ***14***→***47***, Fig. 2A) by using magnesium bromide as promoter led to decomposition. However, in an exploratory experiment, heating ***54*** to 120°C in deuterated dimethyl sulfoxide provided a 1:1 mixture of the hemiketal ***55*** and the enol ether ***56***. We were able to enhance this ratio to 14:1 after optimization (table S6). We reasoned that ***55*** and ***56*** could be interconverting, but all attempts to hydrate ***56*** or dehydrate ***55*** led to decomposition, suggesting that they arise from competing mechanistic pathways. On the basis of these and other data (vide infra), we believe this transformation is initiated by a thermal carbonyl-ene addition to form the alcohol ***57*** (Fig. 3C). Restoration of aromaticity by proton transfer would form ***58***, and hemiketalization would provide ***55***. Alternatively, hemiketal formation from ***57*** would generate the dihydropyran ***59***, which could undergo dehydration to ***56***. We initially anticipated that this reaction would proceed by nucleophilic 1,2-addition of the tropolone to the aldehyde (fig. S6A), but the substrates ***60*** to ***63*** failed to provide any cyclization products under thermal conditions, suggesting that an acidic proton

exocyclic to the tropolone is required (Fig. 3D). The γ-hydroxy-α-tropolone **64** did undergo cyclization, but this is not surprising given the increased electron density of the tropolone ring. We also considered a [4 + 2] cycloaddition pathway (fig. S6B), but the failure of the enol ether **62** to cyclize under similar conditions suggests that this mechanism is not operative.

The formation of the hemiketal **55** was unexpected because the magnesium-promoted cyclization of **14** yielded the enol ether **47** exclusively (Fig. 2A). The change in selectivity could be arising from either the change in reaction conditions or the substrate. To probe this, the homodimer **14** (Fig. 2A) was heated under optimized thermal conditions, which provided anhydrogukulenin A C2-acetate (**47**) and the corresponding hemiketal (not shown) in a 1:3 ratio, suggesting that thermal conditions favor hemiketal formation. Conformational analysis (*40*) provided insight into the higher selectivity of **54**, relative to **14**, for the hemiketal product. This study revealed a hydrogen bonding interaction between the C1 alcohol and the C21 ketone in the intermediate **57** (derived from the PMB ether **54**; Fig. 3E; see fig. S7 for computational details). This hydrogen bonding interaction would be expected to promote tautomerization (rearomatization). By comparison, the corresponding intermediate **65**, derived from the homodimer **14** (Fig. 2A), adopted a conformation wherein the C1 hydroxyl was hydrogen-bonded to the C2 acetate. This interaction may decrease the rate of rearomatization relative to hemiketalization. Thus, the C2 protecting group appeared to play a major and unexpected role in the product distribution of the carbonyl-ene addition. Treatment of the mixture of hemiketal **55** and enol ether **56** (14:1) with 2,3-dichloro-5,6-dicyano-1,4-benzoquinone (DDQ) provided (–)-gukulenin A [**7**; 86% from **53** by quantitative ^{1}H NMR analysis; 28% after purification by reversed-phase high-performance liquid chromatography, 20-mg scale; 24 steps (longest linear sequence), 2.5% overall yield from commercial reagents]. Synthetic (–)-gukulenin A (**7**) was identical to natural material by NMR analysis (table S7) and liquid chromatography–mass spectrometry co-injection with a natural sample (fig. S8).

Structure-function studies

The development of the three-component assembly strategy above allowed us to probe the structure-function relationships of (–)-gukulenin A (**7**) with atomic precision (Fig. 4). Fifteen discrete monomeric and dimeric gukulenin derivatives were designed and synthesized to evaluate the effects of dimerization, the α-tropolone residues, the cyclohexanol and hemiketal rings, the linker composition, and the aldehyde on cytotoxicity (see supplementary materials for syntheses). Their cytotoxicity was evaluated in short-term growth delay assays, using human pharynx cancer (FaDu), colon cancer (HCT116), and leukemia (K562) cell lines—which were used in the isolation reports (*5*, *6*)—and the A2780 human ovarian cancer cell line that was used in the in vivo study of (–)-gukulenin A (**7**) (*13*). For clarity, the IC_{50}s measured in the A2780 cell line are shown in Fig. 4, but the structure-function trends

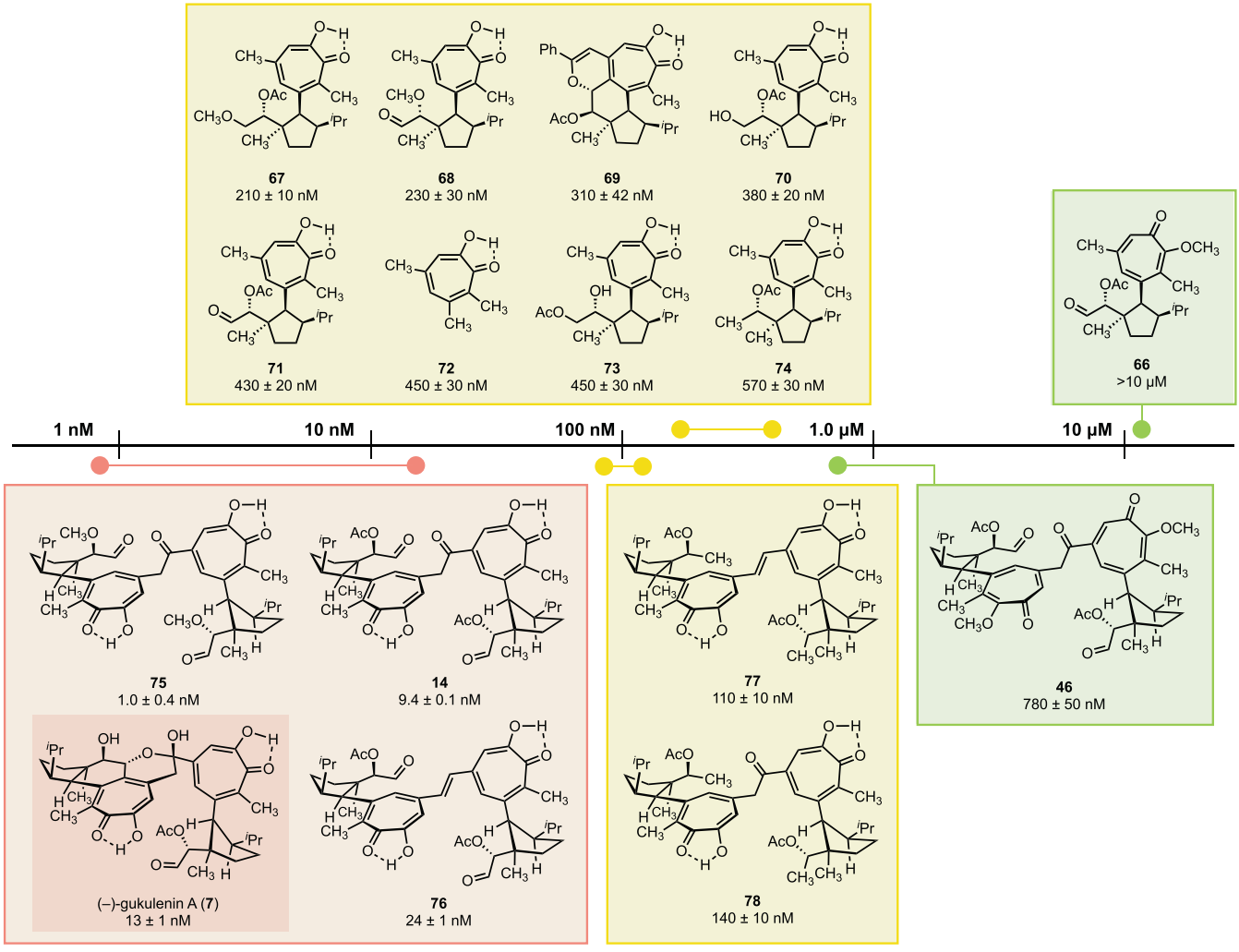


Fig. 4. IC_{50} values (A2780 cell line) of (–)-gukulenin A (7) and derivatives designed to probe structure-function relationships.

were qualitatively consistent across all four cell lines (see fig. S9 and table S8). Four clear relationships emerged from this study. First, the α-tropolone is a strong driver of cytotoxicity. The monomeric, methyl tropolone ether **66** was essentially inactive (IC_{50} >10 μM), whereas the corresponding (demethylated) α-tropolone **71** had an IC_{50} of 430 nM, and the related monomeric α-tropolones **67** to **70** and **72** to **74** had potencies in the 210- to 570-nM range. In the dimeric series, the methyl methyl tropolone ether **46** had an IC_{50} of 780 nM, but the corresponding dimeric demethylated α-tropolone derivatives **14** and **75** to **78** were up to ~780-fold more potent (IC_{50} = 1.0 to 140 nM). Second, these studies made clear that the cyclohexanol and hemiketal rings in (–)-gukulenin A (**7**) are dispensable. The dimeric derivatives **14** and **76** lacking these rings retained the potency of (–)-gukulenin A (**7**), and **75** was >10-fold more potent than (–)-gukulenin A (**7**) itself. Third, these studies established that changes in the oxidation state of the two-carbon linker between the α-tropolone residues do not markedly influence potency. Thus, the derivative **76**, which contains a simple ethylene-based linker, was only ~2.5-fold less potent than corresponding ketone **14**, whereas the ethylene derivative **77** displayed slightly greater potency (IC_{50} = 110 ± 10 nM) than the corresponding the ketone **78** (IC_{50} = 140 ± 10 nM). Fourth, these studies make clear that dimeric α-tropolones are at least an order of magnitude more potent than monomeric α-tropolones, with the difference >200-fold in certain cases (compare the dimeric structure **75** and the monomeric structure **68**). Lastly, these studies also indicate that the α-oxygenated aldehyde may contribute to cytotoxicity in dimeric—but not monomeric—structures. The dimeric derivatives **77** and **78**, which lack an aldehyde, were 10-fold less potent than (–)-gukulenin A (**7**) and were less potent than the related dimeric structures **14**, **75**, and **76**, which all contain an aldehyde residue. This trend is consistent with the decreased potency of (–)-gukulenin B (**8**) relative to (–)-gukulenin A (**7**) [~10-fold, see (*5*)]. However, in the monomeric series, the α-tropolones **67**, **69**, **70**, **72**, **73**, and **74**, which lack an aldehyde substituent, had comparable potency to those bearing an aldehyde (**68** and **71**). These findings raise the possibility that the mechanism of action of dimeric and monomeric gukulenin derivatives are distinct and that the aldehyde in (–)-gukulenin A (**7**) and dimeric derivatives may engage a biological nucleophile.

Discussion

The synthetic strategy we developed has provided an enantioselective route to (–)-gukulenin A (**7**). Our approach was inspired by a biosynthetic hypothesis (Fig. 1E) and implemented experimentally by a three-component assembly, using the linchpin reagent (*E*)-1,2-di(tributylstannyl)-1-ethoxyethylene (**18**). Although this route maximized convergence, it also presented challenges because the C2 acetate substituent in anhydrogukulenin A C2-acetate (**47**) could not be successfully removed in the presence of the C2′ acetate residue. To circumvent this, we exploited the relative rates of transmetalation of the α- and β-tributylstannyl substituents in **18** to achieve a high-yielding, three-component coupling reaction that provides the dimeric methyl tropolone ether **53** (Fig. 3B), which contains differentially protected C2/C2′ oxygen substituents. The development of three methods for the synthesis of methyl tropolone ethers from *ortho*-benzophenone monoketals, a strategy for the synthesis of highly substituted cyclopentanes, and the discovery of a thermal carbonyl-ene reaction formed the foundation of our successful approach and may find use in other contexts.

The flexibility of our synthetic approach enabled us to carry out structure-function studies of (–)-gukulenin A (**7**). These studies indicate that a dimeric α-tropolone substructure is critical for potent cytotoxicity. Given the established affinity of α-tropolones toward divalent metals (*8*, *9*), this finding raises the intriguing possibility that (–)-gukulenin A (**7**) may bind two discrete metalloproteins, thereby templating a native or neomorphic protein–protein interaction. Such "molecular glues" are an area of intensive research (*52*), but molecular glues derived from α-tropolones are, to the best of our knowledge, unknown. Additionally, our studies indicate that fully C_2-symmetric tropolone dimers, such as **76** (Fig. 4), and structures lacking the cyclohexanol and hemiketal rings (e.g., **75** and **14**), have potencies comparable to the natural isolate. These structures are more readily prepared and can be used to streamline target identification studies. The importance of the aldehyde residue in the biological activity of these dimeric tropolone structures is somewhat ambiguous. Although this residue is fully dispensable in the monomeric series, dimeric tropolones lacking this residue displayed decreased potency relative to (–)-gukulenin A (**7**), suggesting that this residue may engage the biological target in the dimeric series. Collectively, these studies set the stage for target identification of (–)-gukulenin A (**7**) as well as the preclinical evaluation of fully synthetic derivatives as monotherapy and combinatorial anticancer agents.

Materials and methods are available in the supplementary materials.

REFERENCES AND NOTES

1. M. J. S. Dewar, Tropolone. *Nature* **166**, 790–791 (1950). doi: 10.1038/166790a0; pmid: 14780257
2. Y. Kurita, M. Kubo, The Dipole Moments and Molecular Structures of Some Substituted Tropones. *Bull. Chem. Soc. Jpn.* **27**, 364–367 (1954). doi: 10.1246/bcsj.27.364
3. W. E. Doering, L. H. Knox, Tropolone. *J. Am. Chem. Soc.* **73**, 828–838 (1951). doi: 10.1021/ja01146a101
4. H. Guo, D. Roman, C. Beemelmanns, Tropolone natural products. *Nat. Prod. Rep.* **36**, 1137–1155 (2019). doi: 10.1039/C8NP00078F; pmid: 30556819
5. S. Y. Park, H. Choi, H. Hwang, H. Kang, J.-R. Rho, Gukulenins A and B, cytotoxic tetraterpenoids from the marine sponge *Phorbas gukulensis*. *J. Nat. Prod.* **73**, 734–737 (2010). doi: 10.1021/np900606h; pmid: 20232859
6. J. E. Jeon *et al.*, Cytotoxic diterpenoid pseudodimers from the Korean sponge *Phorbas gukhulensis*. *J. Nat. Prod.* **76**, 1679–1685 (2013). doi: 10.1021/np400389c; pmid: 24025124
7. J. Zhao, Plant troponoids: Chemistry, biological activity, and biosynthesis. *Curr. Med. Chem.* **14**, 2597–2621 (2007). doi: 10.2174/092986707782023253; pmid: 17979713
8. J. Li *et al.*, Novel α-substituted tropolones promote potent and selective caspase-dependent leukemia cell apoptosis. *Pharmacol. Res.* **113**, 438–448 (2016). doi: 10.1016/j.phrs.2016.09.020; pmid: 27663262
9. A. S. Grillo *et al.*, Restored iron transport by a small molecule promotes absorption and hemoglobinization in animals. *Science* **356**, 608–616 (2017). doi: 10.1126/science.aah3862; pmid: 28495746
10. R. Bai *et al.*, Mapping the binding site of colchicinoids on β -tubulin. 2-Chloroacetyl-2-demethylthiocolchicine covalently reacts predominantly with cysteine 239 and secondarily with cysteine 354. *J. Biol. Chem.* **275**, 40443–40452 (2000). doi: 10.1074/jbc.M005299200; pmid: 11005811
11. T. Graening, H.-G. Schmalz, Total syntheses of colchicine in comparison: A journey through 50 years of synthetic organic chemistry. *Angew. Chem. Int. Ed.* **43**, 3230–3256 (2004). doi: 10.1002/anie.200300615; pmid: 15213947
12. S. Moureu *et al.*, Rubrolone production by *Dactylosporangium vinaceum*: Biosynthesis, modulation and possible biological function. *Appl. Microbiol. Biotechnol.* **105**, 5541–5551 (2021). doi: 10.1007/s00253-021-11404-w; pmid: 34189614
13. J. H. Ahn, J. H. Woo, J. R. Rho, J. H. Choi, Anticancer Activity of Gukulenin A Isolated from the Marine Sponge *Phorbas gukhulensis* In Vitro and In Vivo. *Mar. Drugs* **17**, 126 (2019). doi: 10.3390/md17020126; pmid: 30795557
14. J.-H. Kim, J.-R. Rho, J.-H. Choi, Marine Sponge-Derived Gukulenin A Sensitizes Ovarian Cancer Cells to PARP Inhibition via Ferroptosis Induction. *Mar. Drugs* **23**, 138 (2025). doi: 10.3390/md23040138; pmid: 40278259
15. P. A. Wender, V. A. Verma, T. J. Paxton, T. H. Pillow, Function-oriented synthesis, step economy, and drug design. *Acc. Chem. Res.* **41**, 40–49 (2008). doi: 10.1021/ar700155p; pmid: 18159936
16. C. Gampe, V. A. Verma, Curse or Cure? A Perspective on the Developability of Aldehydes as Active Pharmaceutical Ingredients. *J. Med. Chem.* **63**, 14357–14381 (2020). doi: 10.1021/acs.jmedchem.0c01177; pmid: 32916044
17. K. C. Nicolaou, R. Yu, Z. Lu, F. G. Alvarez, Total Synthesis of Gukulenin B via Sequential Tropolone Functionalizations. *J. Am. Chem. Soc.* **144**, 5190–5196 (2022). doi: 10.1021/jacs.2c01305; pmid: 35275627
18. R. Kats-Kagan, S. B. Herzon, The discovery of a novel route to highly substituted α-tropolones enables expedient entry to the core of the gukulenins. *Org. Lett.* **17**, 2030–2033 (2015). doi: 10.1021/acs.orglett.5b00841; pmid: 25839211
19. D. Tymann, U. Bednarzick, L. Iovkova-Berends, M. Hiersemann, Progress toward the Total Synthesis of Gukulenin A: Photochemically Triggered Two-Carbon Ring Expansion Key to α-Tropolonic Ether Synthesis. *Org. Lett.* **20**, 4072–4076 (2018). doi: 10.1021/acs.orglett.8b01629; pmid: 29920109

20. M.-C. Tang, Y. Zou, K. Watanabe, C. T. Walsh, Y. Tang, Oxidative Cyclization in Natural Product Biosynthesis. *Chem. Rev.* **117**, 5226–5333 (2017). doi: 10.1021/acs.chemrev.6b00478; pmid: 27936626
21. W. Hüttel, M. Müller, Regio- and stereoselective intermolecular phenol coupling enzymes in secondary metabolite biosynthesis. *Nat. Prod. Rep.* **38**, 1011–1043 (2021). doi: 10.1039/D0NP00010H; pmid: 33196733
22. N. Liu, W. Song, C. M. Schienebeck, M. Zhang, W. Tang, Synthesis of Naturally Occurring Tropones and Tropolones. *Tetrahedron* **70**, 9281–9305 (2014). doi: 10.1016/j.tet.2014.07.065; pmid: 25400298
23. Z. G. Brill, M. L. Condakes, C. P. Ting, T. J. Maimone, Navigating the Chiral Pool in the Total Synthesis of Complex Terpene Natural Products. *Chem. Rev.* **117**, 11753–11795 (2017). doi: 10.1021/acs.chemrev.6b00834; pmid: 28293944
24. S. Caille *et al.*, Comparison of Large-Scale Routes to Manufacture Chiral *exo*-2-Norbornyl Thiourea. *Org. Process Res. Dev.* **14**, 133–141 (2010). doi: 10.1021/op9002328
25. V. G. Zaitsev, D. Shabashov, O. Daugulis, Highly regioselective arylation of sp^3 C-H bonds catalyzed by palladium acetate. *J. Am. Chem. Soc.* **127**, 13154–13155 (2005). doi: 10.1021/ja054549f; pmid: 16173737
26. G. He, G. Chen, A practical strategy for the structural diversification of aliphatic scaffolds through the palladium-catalyzed picolinamide-directed remote functionalization of unactivated C(sp3)-H bonds. *Angew. Chem. Int. Ed.* **50**, 5192–5196 (2011). doi: 10.1002/anie.201100984; pmid: 21538752
27. W. A. Nack, X. Wang, B. Wang, G. He, G. Chen, Palladium-catalyzed picolinamide-directed iodination of remote *ortho*-C-H bonds of arenes: Synthesis of tetrahydroquinolines. *Beilstein J. Org. Chem.* **12**, 1243–1249 (2016). doi: 10.3762/bjoc.12.119; pmid: 27559375
28. C. E. Coomber *et al.*, Silver-Free Palladium-Catalyzed C(sp^3)-H Arylation of Saturated Bicyclic Amine Scaffolds. *J. Org. Chem.* **83**, 2495–2503 (2018). doi: 10.1021/acs.joc.7b02665; pmid: 29241011
29. S.-Y. Zhang *et al.*, Palladium-catalyzed picolinamide-directed alkylation of unactivated C(sp3)-H bonds with alkyl iodides. *J. Am. Chem. Soc.* **135**, 2124–2127 (2013). doi: 10.1021/ja312277g; pmid: 23350845
30. D. H. O' Donovan, C. De Fusco, D. R. Spring, The Reductive Cleavage of Picolinic Amides. *Tetrahedron Lett.* **57**, 2962–2964 (2016). doi: 10.1016/j.tetlet.2016.05.068
31. E. J. Corey, K. Achiwa, Oxidation of Primary Amines to Ketones. *J. Am. Chem. Soc.* **91**, 1429–1432 (1969). doi: 10.1021/ja01034a027
32. L. N. Mander, S. P. Sethi, Regioselective Synthesis of β-Ketoesters from Lithium Enolates and Methyl Cyanoformate. *Tetrahedron Lett.* **24**, 5425–5428 (1983). doi: 10.1016/S0040-4039(00)87886-7
33. S. T. Heller, R. Sarpong, Chemoselective esterification and amidation of carboxylic acids with imidazole carbamates and ureas. *Org. Lett.* **12**, 4572–4575 (2010). doi: 10.1021/ol1018882; pmid: 20857922
34. G. Cavallo *et al.*, The Halogen Bond. *Chem. Rev.* **116**, 2478–2601 (2016). doi: 10.1021/acs.chemrev.5b00484; pmid: 26812185
35. K. Prantz, J. Mulzer, Synthetic applications of the carbonyl generating Grob fragmentation. *Chem. Rev.* **110**, 3741–3766 (2010). doi: 10.1021/cr900386h; pmid: 20163188
36. D. M. Hodgson, A. Charlton, Methods for Direct Generation Of α-Alkyl-Substituted Aldehydes. *Tetrahedron* **70**, 2207–2236 (2014). doi: 10.1016/j.tet.2013.11.046
37. R. R. Hill, S. D. Rychnovsky, Generation, Stability, and Utility of Lithium 4,4′-Di-*tert*-butylbiphenylide (LiDBB). *J. Org. Chem.* **81**, 10707–10714 (2016). doi: 10.1021/acs.joc.6b01748; pmid: 27786473
38. P. A. S. Smith, D. R. Baer, "The Demjanov and Tiffeneau-Demjanov Ring Expansions" in *Organic Reactions*, S. E. Denmark, L. E. Overman, Eds. (Wiley and Sons, 2011); https://doi.org/10.1002/0471264180.or011.02.
39. H. Liu, C. Sun, N.-K. Lee, R. F. Henry, D. Lee, New methylene homologation method for cyclic ketones. *Chemistry* **18**, 11889–11893 (2012). doi: 10.1002/chem.201201346; pmid: 22893575
40. Wavefunction, Spartan 24 (Wavefunction, Inc., 2024); https://www.wavefun.com/spartan.
41. G. Boche, J. C. W. Lohrenz, F. Schubert, Lithio-Diazomethane and Lithio-(trimethylsilyl) diazomethane: Theoretical and Experimental Studies of Their Structures, Reactions and Reaction Products. *Tetrahedron* **50**, 5889–5902 (1994). doi: 10.1016/S0040-4020(01)90444-2
42. H. Liu, M. J. O'Connor, C. Sun, D. J. Wink, D. Lee, Sequential reactions of trimethylsilyldiazomethane with 4-alkenyl ketones and aldehydes catalyzed by Lewis bases. *Org. Lett.* **15**, 2974–2977 (2013). doi: 10.1021/ol401124t; pmid: 23721259
43. R. Pappo, J. D. Allen Jr., R. Lemieux, W. Johnson, Osmium Tetroxide-Catalyzed Periodate Oxidation of Olefinic Bonds. *J. Org. Chem.* **21**, 478–479 (1956). doi: 10.1021/jo01110a606
44. W. Yu, Y. Mei, Y. Kang, Z. Hua, Z. Jin, Improved procedure for the oxidative cleavage of olefins by OsO_4-$NaIO_4$. *Org. Lett.* **6**, 3217–3219 (2004). doi: 10.1021/ol0400342; pmid: 15355016
45. M. Murakami, H. Amii, N. Takizawa, Y. Ito, Synthesis of Acylsilanes via Silastannation of Alkynes by a Palladium-Isocyanide Catalyst. *Organometallics* **12**, 4223–4227 (1993). doi: 10.1021/om00034a072
46. J. Mancuso, M. Lautens, Mild procedure for the catalytic bis(stannylation) of alkynes with hexaalkylditins. *Org. Lett.* **5**, 1653–1655 (2003). doi: 10.1021/ol034284e; pmid: 12735744
47. K. C. Nicolaou, T. K. Chakraborty, A. D. Piscopio, N. Minowa, P. Bertinato, Total synthesis of Rapamycin. *J. Am. Chem. Soc.* **115**, 4419–4420 (1993). doi: 10.1021/ja00063a093
48. M. Nishizawa, M. Skwarczynski, H. Imagawa, T. Sugihara, Mercuric Triflate-TMU Catalyzed Hydration of Terminal Alkyne to give Methyl Ketone Under Mild Conditions. *Chem. Lett.* **31**, 12–13 (2002). doi: 10.1246/cl.2002.12
49. M. DiBello, A. R. Healy, H. Nikolayevskiy, Z. Xu, S. B. Herzon, Structure Elucidation of Secondary Metabolites: Current Frontiers and Lingering Pitfalls. *Acc. Chem. Res.* **56**, 1656–1668 (2023). doi: 10.1021/acs.accounts.3c00183; pmid: 37220079
50. W. Hehre *et al.*, Efficient Protocol for Accurately Calculating ^{13}C Chemical Shifts of Conformationally Flexible Natural Products: Scope, Assessment, and Limitations. *J. Nat. Prod.* **82**, 2299–2306 (2019). doi: 10.1021/acs.jnatprod.9b00603; pmid: 31322872
51. H. Aikawa, S. Tago, K. Umetsu, N. Haginiwa, N. Asao, Gold-catalyzed Substitution Reaction with *Ortho*-alkynylbenzoic Acid Alkyl Ester as an Efficient Alkylating Agent. *Tetrahedron* **65**, 1774–1784 (2009). doi: 10.1016/j.tet.2008.12.033
52. M. Konstantinidou, M. R. Arkin, Molecular glues for protein-protein interactions: Progressing toward a new dream. *Cell Chem. Biol.* **31**, 1064–1088 (2024). doi: 10.1016/j.chembiol.2024.04.002; pmid: 38701786

ACKNOWLEDGMENTS

We thank J.-R. Rho (Department of Oceanography, Kunsan National University, Jeonbuk, South Korea) for a gift of natural (−)-gukulenin A (**7**) and J. Hill (Yale University) for assistance in editing the manuscript. We thank Y. Surovtseva and N. Dhingra of the Yale Center for Molecular Discovery for their assistance with CellTiter Glo viability assays. **Funding:** Financial support from the NIH (R35-GM131913 to S.B.H., RM1-GM141649 to J.M.C.) and Yale University (Wasserman Fellowship to V.G.) is gratefully acknowledged. The Yale Center for Molecular Discovery is supported in part by an NCI Cancer Center Support Grant (P30 CA016359). **Author contributions:** V.G., Z.W., J.B.C., T.W., L.C., B.L., R.H., and B.Q. carried out the experimental work; J.O. and J.M.C. carried out the structure elucidation of anhydrogukulenin A C2-acetate (**47**); V.G., Z.W., J.B.C., T.W., B.L., R.H., B.Q., J.M.C., and S.B.H. contributed to the writing of the manuscript; and S.B.H. directed the study. **Competing interests:** A provisional US patent application covering this work has been filed by Yale University (co-inventors: S.B.H., V.G., and Z.W.). **Data and materials availability:** Crystallographic data for **S45** and **S70** are available free of charge from the Cambridge Crystallographic Data Centre (CCDC nos. 2248440 and 2468738, respectively). All other spectral and characterization data, as well as details for synthesizing all reported compounds, are contained in the supplementary materials. **License information:** Copyright © 2025 the authors, some rights reserved; exclusive licensee American Association for the Advancement of Science. No claim to original US government works. https://www.science.org/about/science-licenses-journal-article-reuse

SUPPLEMENTARY MATERIALS

science.org/doi/10.1126/science.aea9310
Materials and Methods; Figs. S1 to S9; Tables S1 to S9; NMR Spectra; References (*53*–*63*)

Submitted 25 July 2025; accepted 16 September 202513 November 2025;
published online 13 November 2025

10.1126/science.aea9310

RESEARCH ARTICLE SUMMARY

IMMUNOLOGY

Hepatic leukemia factor directs tissue residency of proinflammatory memory CD4$^+$ T cells

Masahiro Kiuchi *et al.*

Full article and list of author affiliations: https://doi.org/10.1126/science.adp0714

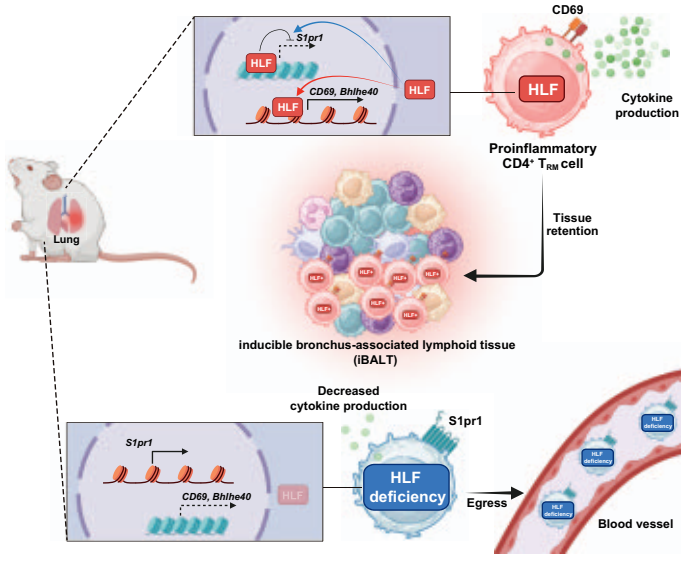
INTRODUCTION: Tissue-resident memory T (T_{RM}) cells residing in nonlymphoid barrier organs play crucial roles in host defense against pathogens and contribute to the pathogenesis of chronic inflammatory diseases. T_{RM} cells are characterized by the up-regulation of tissue retention molecules such as CD69 and CD103 and the down-regulation of lymphoid homing molecules such as Ccr7 and S1pr1. Recent research has revealed distinct transcriptional programs underlying CD8$^+$ T_{RM} cell development, with factors such as Blimp1, Hobit, and Runx3 orchestrating their formation. However, molecules regulating CD4$^+$ T_{RM} cell development and functional heterogeneity remain poorly understood.

RATIONALE: Understanding the molecular mechanisms controlling CD4$^+$ T_{RM} cells is crucial for elucidating the pathogenesis of various chronic inflammatory diseases across multiple organ systems. Chronic airway inflammatory diseases represent a major global health burden, and severe cases are often resistant to conventional therapies, thus necessitating the identification of potential therapeutic targets. This study aimed to identify transcription factors controlling CD4$^+$ T_{RM} cell tissue residency and function using an *Aspergillus fumigatus* antigen–induced chronic airway inflammation model.

RESULTS: Single-cell RNA sequencing of murine lung tissue revealed that *hepatic leukemia factor* (*Hlf*), a member of the bZIP transcription factor family, showed the highest differential expression between tissue-resident versus circulating CD4$^+$ T cells. In a mouse model of chronic airway inflammation, *Hlf*-deficient mice exhibited reduced numbers of lung CD4$^+$ T_{RM} cells and ameliorated airway inflammation, accompanied by decreased fibrotic responses. Chromatin immunoprecipitation sequencing analysis revealed that HLF directly bound to and repressed tissue egress genes, including *S1pr1*, *Klf2*, and *Tcf7*, while directly promoting the expression of tissue retention molecules, including *CD69* and the transcription factor *Bhlhe40*. *Hlf*-deficient CD4$^+$ T_{RM} cells exhibited increased S1pr1 and decreased CD69 expression, indicating impaired tissue retention. *Hlf*-deficient T_{RM} cells produced fewer inflammatory cytokines such as interleukin-5 (IL-5), IL-13, IL-17, and interferon-γ (IFN-γ). In patients with eosinophilic chronic rhinosinusitis, HLF$^+$ CD4$^+$ T_{RM} cells in nasal polyps showed enhanced tissue residency signatures and inflammatory cytokine expression compared with HLF$^-$ cells.

CONCLUSION: This study identifies HLF as a transcriptional regulator of CD4$^+$ T_{RM} cell tissue residency and proinflammatory function, acting through coordinated enhancement of tissue retention programs and suppression of egress mechanisms. This regulatory circuit appeared to be conserved across species and multiple inflammatory diseases. HLF represents a potential driver of pathogenic CD4$^+$ T_{RM} cell subsets in chronic inflammation. These findings provide molecular insights into tissue-specific immunity and identify HLF as a potential therapeutic target for treating intractable chronic inflammatory diseases. □

*Corresponding author. Email: hiraharak@chiba-u.jp Cite this article as M. Kiuchi *et al.*, *Science* **390**, eadp0714 (2025). DOI: 10.1126/science.adp0714



HLF regulates CD4$^+$ T_{RM} cell retention and inflammation in the lung. HLF promotes the expression of *CD69* and *Bhlhe40* and suppresses the expression of *S1pr1*, thereby facilitating CD4$^+$ T_{RM} cell retention within inducible bronchus-associated lymphoid tissue (iBALT) and enhancing proinflammatory cytokine production in the lung. By contrast, HLF deficiency reduces *CD69* and *Bhlhe40*, increases *S1pr1*, leads to enhanced egress of CD4$^+$ T cells from the lung, and results in attenuated local inflammation. [Figure created with BioRender.com]

IMMUNOLOGY

Hepatic leukemia factor directs tissue residency of proinflammatory memory CD4$^+$ T cells

Masahiro Kiuchi[1]†, Masahiro Nemoto[1]†, Hiroyuki Yagyu[1,2]†, Ami Aoki[3], Chiaki Iwamura[1,4], Hikaru Sugimoto[5], Yuki Masuo[6,7], Hajime Morita[6], Shuhe Ma[6,8], Yukiko Okuno[7,9], Takahisa Hishiya[1], Kaori Tsuji[1], Atsushi Sasaki[1,10], Kota Kokubo[1], Kanae Ohishi[1], Rie Shinmi[1,11], Yuri Sonobe[1,11], Tomohisa Iinuma[11], Syuji Yonekura[11], Tomomasa Yokomizo[12], Norio Komatsu[13], Atsushi Onodera[1,14,15], Shinya Okumura[16], Takashi Ito[16], Etsuro Hatano[16], Tatsuaki Tsuruyama[17], Yosuke Kurashima[4,14,18], Naoko Mato[19], Takuji Suzuki[4,10], Motoko Yagi Kimura[4,20], Shinichiro Motohashi[21], Eiryo Kawakami[5,22], Hideki Ueno[6,7,8], Damon J Tumes[23,24], Toyoyuki Hanazawa[11], Toshinori Nakayama[1,25]‡, Kiyoshi Hirahara[1,4,25]*

CD4$^+$ tissue-resident memory T (T_{RM}) cells contribute to host defense and to the pathogenesis of chronic inflammatory diseases, but the molecules that direct their differentiation are unknown. We found that the transcription factor hepatic leukemia factor (HLF) could direct the tissue residency program and function of CD4$^+$ T_{RM} cells. HLF simultaneously up-regulated tissue retention receptors, down-regulated tissue egress receptors, and promoted proinflammatory CD4$^+$ T_{RM} cells by inducing *Bhlhe40*, and all of these processes were associated with changes in chromatin accessibility. Genetic deletion of *Hlf* inhibited CD4$^+$ T_{RM} cell generation and ameliorated airway tissue inflammation in vivo. HLF$^+$ CD4$^+$ T_{RM} cells isolated from inflamed airway tissue in humans had a tissue residency signature and expressed inflammatory cytokines. We conclude that HLF may act as a central regulator of proinflammatory CD4$^+$ T_{RM} cell development and function.

Memory T cells are central to host protection against the invasion of pathogens, but they are also crucial for shaping the pathogenesis of various chronic inflammatory diseases (*1*, *2*). Circulating memory T cells comprise effector memory T (T_{EM}) cells, which surveil blood and tissues for rapid pathogen detection (*3*), and central memory T (T_{CM}) cells, which home to secondary lymphatic tissues and show enhanced recall responses and persistence (*4*). By contrast, tissue-resident memory T (T_{RM}) cells permanently reside in nonlymphoid barrier organs (*5*, *6*), including the respiratory, gastrointestinal, and reproductive tracts, as well as in the skin, and provide a rapid, localized frontline defense against reinvasion of harmful pathogens (*5*, *7*, *8*). Although T_{RM} cells play a protective role during infection, in cancer, and after vaccination, they can also exacerbate chronic inflammatory diseases (*9*, *10*). Thus, it is important to understand the differentiation of T_{RM} cell subpopulations that contribute to chronic inflammatory diseases (*11*).

T_{RM} cells are characterized by the up-regulation of cell adhesion molecules such as CD69 and CD103, accompanied by the down-regulation of lymphoid-homing molecules including Ccr7, S1pr1, and CD62L, which are crucial for tissue retention (*8*, *12*, *13*). Other molecules found on the surface of T_{RM} cells differ substantially across and within tissues (*8*). Many studies have characterized the phenotypic and functional heterogeneity of CD8$^+$ T_{RM} cells together with the transcription factors responsible for orchestrating their development (*14*–*17*). However, our knowledge about the molecules regulating CD4$^+$ T_{RM} cell development, heterogeneity, and function remains limited (*18*). We herein examined the ontology and heterogeneity of CD4$^+$ T_{RM} cells during chronic airway inflammation and define hepatic leukemia factor (HLF) as a transcriptional regulator of CD4$^+$ T_{RM} cells.

RESULTS

Lung-resident CD4$^+$ T_{RM} cells have high expression of *Hlf* during chronic airway inflammation

We used a fungus-associated chronic airway inflammation model in which mice were repeatedly exposed intranasally to *Aspergillus fumigatus* antigen for 7 weeks to induce CD4$^+$ T_{RM} cells in the lung (*19*) (fig. S1A). Repeated antigen exposure resulted in the formation of inducible bronchus-associated lymphoid tissue (iBALT) in the inflamed lung (fig. S1B).

After 7 weeks of *A. fumigatus* antigen exposure, we used in vivo labeling with anti-CD4 antibody to differentiate between CD4$^+$ T cells within the lung tissue and those that were circulating within blood vessels (*13*, *19*, *20*) (fig. S1A). We performed single-cell RNA sequencing (scRNA-seq) on the CD4$^+$ T cells within the lung and identified four subpopulations, naïve, memory, regulatory, and proliferating T cells, on the basis of their gene expression profiles (Fig. 1, A and B, and fig. S1C). Tissue CD4$^+$ T cells had higher expression of *Cd69* compared with CD4$^+$ T cells that were in the circulation, and also had heterogeneous expression of *Itgae*, which encodes CD103 in cell surface molecules (fig. S1D). In the inflamed lung, most tissue CD4$^+$ T cells were *Cd44*$^+$*Sell*$^-$ memory CD4$^+$ T cells, whereas circulating CD4$^+$ T cells formed a distinct cluster (Fig. 1, A and B, and fig. S1, E and F). Tissue CD4$^+$ T cells also had higher expression of *Bhlhe40*, a gene important for T_{RM} cell formation, and lower expression of the genes required for tissue egress and the migration and development of circulating memory T cells such as *Klf2*, *S1pr1*, *Ccr7*, *Tcf7*, and *Il7r* (*17*, *19*, *21*–*23*) (Fig. 1C and table S1). On the basis of this gene expression profile, we refer to these cells as CD4$^+$ T_{RM} cells.

One of the genes that had the highest expression in CD4$^+$ T_{RM} cells compared with circulating CD4 T cells was *Hlf*, which encodes HLF, a bZIP transcription factor family member (*24*, *25*) (Fig. 1C). *Hlf* was selectively expressed in CD4$^+$ T_{RM} cells that were protected from intravascular labeling by CD4 and was largely restricted to differentiated

[1]Department of Immunology, Graduate School of Medicine, Chiba University, Chuo-ku, Chiba, Japan. [2]Department of Pulmonology, Graduate School of Medicine, Yokohama City University, Yokohama, Japan. [3]Department of Respiratory Medicine and Infectious Diseases, Graduate School of Medical and Dental Sciences, Niigata University, Chuo-ku, Niigata, Japan. [4]Synergy Institute for Futuristic Mucosal Vaccine Research and Development, Chiba University, Chiba, Japan. [5]Predictive Medicine Special Project (PMSP), RIKEN Center for Integrative Medical Sciences (IMS), RIKEN, Yokohama, Kanagawa, Japan. [6]Department of Immunology, Graduate School of Medicine, Kyoto University, Kyoto, Japan. [7]Kyoto University Immunomonitoring Center (KIC), Kyoto University, Kyoto, Japan. [8]ASHBi Institute for the Advanced Study of Human Biology, Kyoto University, Kyoto, Japan. [9]Medical Research Support Center, Graduate School of Medicine, Kyoto University, Kyoto, Japan. [10]Department of Respirology, Graduate School of Medicine, Chiba University, Chuo-ku, Chiba, Japan. [11]Department of Otorhinolaryngology, Head and Neck Surgery, Graduate School of Medicine, Chiba University, Chuo-ku, Chiba, Japan. [12]Microscopic and Developmental Anatomy, Tokyo Women's Medical University, Tokyo, Japan. [13]Department of Hematology, Juntendo University Graduate School of Medicine, Juntendo University, Bunkyo-ku, Tokyo, Japan. [14]Institute for Advanced Academic Research, Chiba University, Chuo-ku, Chiba, Japan. [15]Research Institute of Disaster Medicine, Chiba University, Chuo-ku, Chiba, Japan. [16]D ivision of Hepato-Biliary-Pancreatic Surgery and Transplantation, Department of Surgery, Graduate School of Medicine, Kyoto University, Kyoto, Japan. [17]Department of Drug Discovery Medicine, Kyoto University Graduate School of Medicine, Kyoto, Japan. [18]Department of Innovative Medicine, Graduate School of Medicine, Chiba University, 1-8-1 Inohana, Chuo-ku, Chiba, Japan. [19]Division of Pulmonary Medicine, Department of Medicine, Jichi Medical University, Tochigi, Japan. [20]Department of Experimental Immunology, Graduate School of Medicine, Chiba University, Chuo-ku, Chiba, Japan. [21]Department of Medical Immunology, Graduate School of Medicine, Chiba University, Chuo-ku, Chiba, Japan. [22]Department of Artificial Intelligence Medicine, Graduate School of Medicine, Chiba University, Chuo-ku, Chiba, Japan. [23]Centre for Cancer Biology, University of South Australia and SA Pathology, Adelaide, Australia. [24]Adelaide University, Adelaide, Australia. [25]AMED-CREST, AMED, Chuo-ku, Chiba, Japan. ***Corresponding author. Email: hiraharak@chiba-u.jp** †These authors contributed equally to this work. ‡Deceased.

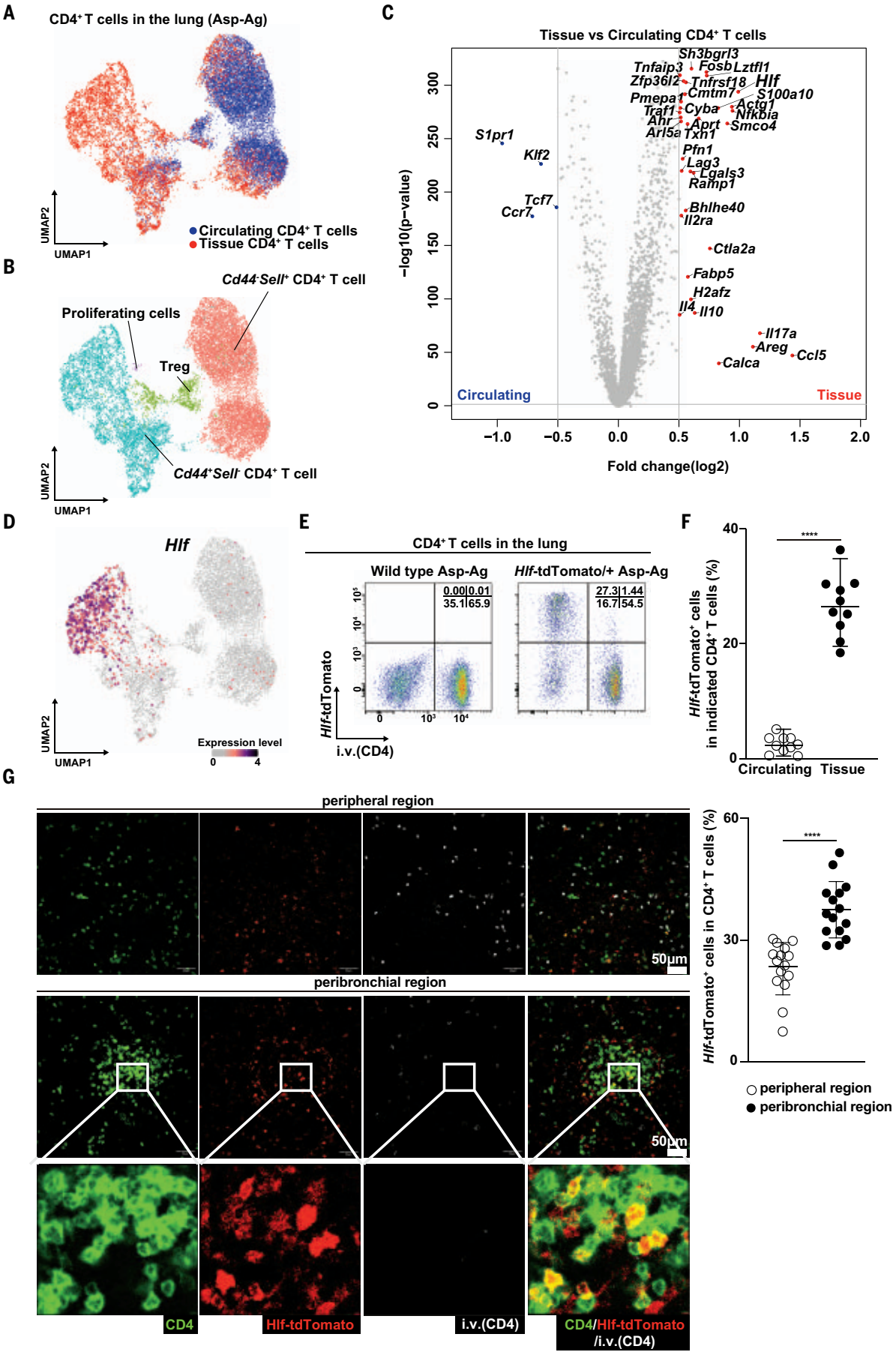

A
CD4+ T cells in the lung (Asp-Ag)
UMAP2
UMAP1
Circulating CD4+ T cells
Tissue CD4+ T cells
B
Cd44-Sell+ CD4+ T cell
Proliferating cells
Treg
Cd44+Sell- CD4+ T cell
UMAP2
UMAP1
C
Tissue vs Circulating CD4+ T cells
−log10(p−value)
Fold change(log2)
Circulating
Tissue
Sh3bgrl3
Tnfaip3
Fosb
Lztfl1
Zfp36l2
Tnfrsf18
Hlf
Pmepa1
Cmtm7
S100a10
Traf1
Cyba
Actg1
Ahr
Aprt
Nfkbia
Arl5a
Txn1
Smco4
S1pr1
Klf2
Pfn1
Lag3
Lgals3
Ramp1
Tcf7
Ccr7
Bhlhe40
Il2ra
Ctla2a
Fabp5
H2afz
Il4
Il10
Il17a
Areg
Ccl5
Calca
D
Hlf
UMAP2
UMAP1
Expression level
0
4
E
CD4+ T cells in the lung
Wild type Asp-Ag
Hlf-tdTomato/+ Asp-Ag
0.00 0.01
35.1 65.9
27.3 1.44
16.7 54.5
Hlf-tdTomato
i.v.(CD4)
F
Hlf-tdTomato+ cells in indicated CD4+ T cells (%)
****
Circulating
Tissue
G
peripheral region
peribronchial region
50 μm
Hlf-tdTomato+ cells in CD4+ T cells (%)
****
peripheral region
peribronchial region
CD4
Hlf-tdTomato
i.v.(CD4)
CD4/Hlf-tdTomato /i.v.(CD4)

Fig. 1. Lung-resident CD4$^+$ T_{RM} cells show high expression of *Hlf* during chronic airway inflammation. (**A** to **G**) Wild-type or *Hlf*-tdTomato reporter mice were repeatedly exposed to *A. fumigatus* antigen (Asp-Ag) for 7 weeks, as indicated in fig. S1A. (A) Circulating and tissue CD4$^+$ T cells in the lung from mice with repetitive exposure to Asp-Ag were isolated by fluorescence-activated cell sorting (FACS) from the lungs of wild type mice ($n = 10$) using intravascular staining of anti-CD4 antibody and analyzed by scRNA-seq ($n = 5$ mice pooled as $n = 2$ samples, 53,409 cells). Data were pooled from two independent experiments. Circulating (blue) and tissue (red) CD4$^+$ T cells separated by intravenous injection of anti-CD4 antibody projected onto a UMAP are shown. (B) Four CD4$^+$ T subsets projected onto a UMAP. (C) Volcano plot depicting differential gene expression between circulating and tissue CD4$^+$ T cells in the Asp-Ag–sensitized inflamed lungs. (D) Expression of *Hlf* projected onto a UMAP. (E) Representative cell staining profiles of *Hlf*-tdTomato and intravascular CD4 staining in CD4$^+$ T cells in the lung of Asp-Ag wild-type and Asp-Ag *Hlf*-tdTomato reporter mice. i.v., intravenous injection (gated as in fig. S18). (F) Percentage of *Hlf*-tdTomato$^+$ CD4$^+$ T cells in circulating and tissue CD4$^+$ T cells in the lungs of Asp-Ag *Hlf*-tdTomato reporter mice ($n = 10$). Data were pooled from four independent experiments. (G) Representative immunostaining of the lung stained with anti-CD4 (green), anti-tdTomato (red), and anti-CD4 i.v. (white) in peripheral or peribronchial regions of Asp-Ag *Hlf*-tdTomato reporter mice (left panel). Percentage of *Hlf*-tdTomato$^+$ CD4$^+$ T cells in peripheral or peribronchial region of Asp-Ag *Hlf*-tdTomato reporter mice ($n = 15$). Data were pooled from two independent experiments (right panel). Peripheral and peribronchial regions were defined as subpleural areas containing alveoli and a bronchovascular bundle region containing iBALT, respectively. Scale bars, 50 μm. Data are shown as the mean ± SD. Each dot represents a single mouse. *P* values were calculated by a two-tailed Welch's *t* test (F and G). ****$P < 0.0001$. See also figs. S1 to S3.

memory cells (Fig. 1D). Analysis of *Hlf*-tdTomato reporter mice (*26*) found that *Hlf*-tdTomato was predominantly expressed in CD4$^+$ T_{RM} cells that accumulated within iBALT in the inflamed lung (Fig. 1, E to G, and fig. S1G). Moreover, 7 weeks after the final antigen exposure, *Hlf*-expressing CD4$^+$ T_{RM} cells were preferentially maintained within iBALT in the lung (fig. S2, A to F).

To investigate *Hlf* expression in other inflammatory contexts, we analyzed published scRNA-seq datasets (*27*–*30*). In helminth-infected murine lungs, *Hlf* was specifically expressed in CD4$^+$ T cells with a high T_{RM} cell gene signature score (*27*) (fig. S2, G to J). In a mouse model of food allergy, *Hlf* was expressed in most CD4$^+$ T_{RM} cells from the intestinal tissues (*28*) (fig. S3, A to D). In influenza A virus–infected murine lungs, *Hlf* was specifically expressed in T helper 17 (T_H17)–type T_{RM} cells but not in T_H1-type T_{RM} cells (*29*) (fig. S3, E to I). In an experimental autoimmune encephalomyelitis (EAE) model, *Hlf*-expressing T_{RM} cells were detected in the inflamed brain (*30*) (fig. S3, J to M). In each dataset, *Hlf* expression was strongest in T_H2 and T_H17 CD4$^+$ T_{RM} cells. Therefore, *Hlf* emerged as a distinctive gene in CD4$^+$ T_{RM} cells during chronic airway inflammation, with its expression conserved in T_{RM} cells across various inflammatory contexts.

HLF is central to the development of proinflammatory CD4$^+$ T_{RM} cells that exacerbate chronic airway inflammation in vivo

We investigated the function of HLF in lung CD4$^+$ T_{RM} cells using single-cell assay for transposase-accessible chromatin sequencing (scATAC-seq). CD4$^+$ T_{RM} cells exhibited increased chromatin accessibility at the *Hlf* locus, including the promoter region, compared with circulating CD4$^+$ T cells (fig. S4, A to C). To evaluate the impact of *Hlf* deficiency on CD4$^+$ T_{RM} cell identity, we performed perturbation modeling using CellOracle (*31*) based on integrated scRNA-seq and scATAC-seq profiles (fig. S4D). This analysis predicted broad changes in gene expression patterns after *Hlf* deletion and indicated that *Hlf* depletion would induce transcriptional changes in CD4$^+$ T cells from tissue-resident toward circulating phenotypes (Fig. 2A). We concluded that *Hlf* regulates transcriptional programs critical for maintaining CD4$^+$ T_{RM} cell identity.

To determine whether HLF plays a functional role in the formation of lung CD4$^+$ T_{RM} cells in vivo during chronic lung inflammation, we analyzed *Hlf*-deficient mice (*32*). *Hlf*-deficient mice repetitively exposed to *A. fumigatus* antigen for 7 weeks had a reduced number of CD4$^+$ T_{RM} cells in the inflamed lung compared with wild-type mice (Fig. 2, B and C). By contrast, the number of CD4$^+$ lung circulating memory T cells was only mildly decreased (fig. S5A).

We isolated CD4$^+$ T cells and stimulated their differentiation in vitro. We found that the proliferation and apoptosis of *Hlf*-deficient CD4$^+$ T cells were similar to those of wild-type CD4$^+$ T cells (fig. S6, A to D). Histological analyses of the inflamed lung showed that CD4$^+$ T_{RM} cells were decreased in and adjacent to iBALT in *Hlf*-deficient mice (Fig. 2D and fig. S7A). We used *Hlf*-tdTomato reporter mice to examine the expression of HLF protein and found that it increased in tissue CD4$^+$ T cells over the first 3 weeks of *A. fumigatus* antigen exposure and was sustained through 7 weeks (fig. S8, A and B).

At 1 and 3 weeks of *A. fumigatus* antigen exposure, the frequencies of naive or effector CD4$^+$ T cells in the spleen, mediastinal lymph nodes, and peripheral blood, as well as their effector cytokine production, were comparable between *Hlf*-sufficient and *Hlf*-deficient mice (fig. S8, C and D), suggesting that HLF deficiency did not affect the generation of effector T cells. However, at this time, there was a decrease in CD4$^+$ T cells in the inflamed lungs in *Hlf*-deficient mice, and this was accompanied by a corresponding increase in circulating CD4$^+$ T cells (fig. S9A). Furthermore, *Hlf*-deficient tissue CD4$^+$ T cells exhibited increased expression of S1pr1 and decreased expression of CD69 compared with *Hlf*-sufficient tissue CD4$^+$ T cells (fig. S9, B and C). These findings suggested that HLF facilitates tissue retention of CD4$^+$ T cells by regulating genes involved in tissue residency and egress, such as *CD69* and *S1pr1*.

Hlf-deficient lung CD4$^+$ T_{RM} cells produced lower levels of inflammatory cytokines [interleukin 5 (IL-5), IL-13, IL-17, and interferon-γ (IFN-γ)] (Fig. 2E). Consistent with these results, *Hlf*-deficient mice had ameliorated eosinophilic airway inflammation together with a decreased fibrotic response (Fig. 2, F to H, and fig. S9D). This correlated with our previous finding that fibrosis is dependent on CD4$^+$ T_{RM} cells (*19*). The innate counterpart of tissue-resident lymphocytes, group 2 innate lymphoid cells (ILC2s), also express *Hlf* (*33*, *34*). However, in contrast to the dependency of CD4$^+$ T_{RM} cells on HLF, the number of ILC2s remained unchanged in *Hlf*-deficient mice after 7 weeks of *A. fumigatus* exposure (fig. S10, A and B). Similarly, *Hlf* deficiency did not alter the number of ILC2s in a papain-induced airway inflammation model (*35*) (fig. S10, C to E). Thus, we concluded that HLF contributes to the development and effector functions of CD4$^+$ T_{RM} cells and facilitates the development of chronic airway inflammation and airway remodeling.

T cell–intrinsic HLF promotes proinflammatory CD4$^+$ T_{RM} cell formation

To investigate the T cell–intrinsic role of HLF, we generated $Hlf^{+/+}$ or $Hlf^{-/-}$ T_H2 cells specific for the model antigen ovalbumin (OVA) by activating OT-II CD4$^+$ T cells in vitro and transferring them intravenously into congenic host mice. We then exposed the host mice to OVA intranasally twice, followed by a 4-week resting phase, which allowed us to examine the fate of antigen-specific CD4$^+$ T cells in vivo (fig. S11A). The number of tissue-resident CD4$^+$ T cells was decreased in mice that received *Hlf*-deficient OT-II T_H2 cells compared with mice that received *Hlf*-sufficient OT-II T_H2 cells regardless of antigen reexposure (Fig. 3A). Circulating CD4$^+$ T cells were increased in mice that received *Hlf*-deficient OT-II T_H2 cells compared with those that received *Hlf*-sufficient OT-II T_H2 cells (Fig. 3A). We concluded that *Hlf*-deficient CD4$^+$ T cells were impaired in their ability to enter or be retained in tissues. Consistent with this, *Hlf*-deficient OT-II T_H2 cells exhibited increased expression of S1pr1 and decreased expression of CD69 compared with *Hlf*-sufficient OT-II T_H2 cells (Fig. 3, B and C).

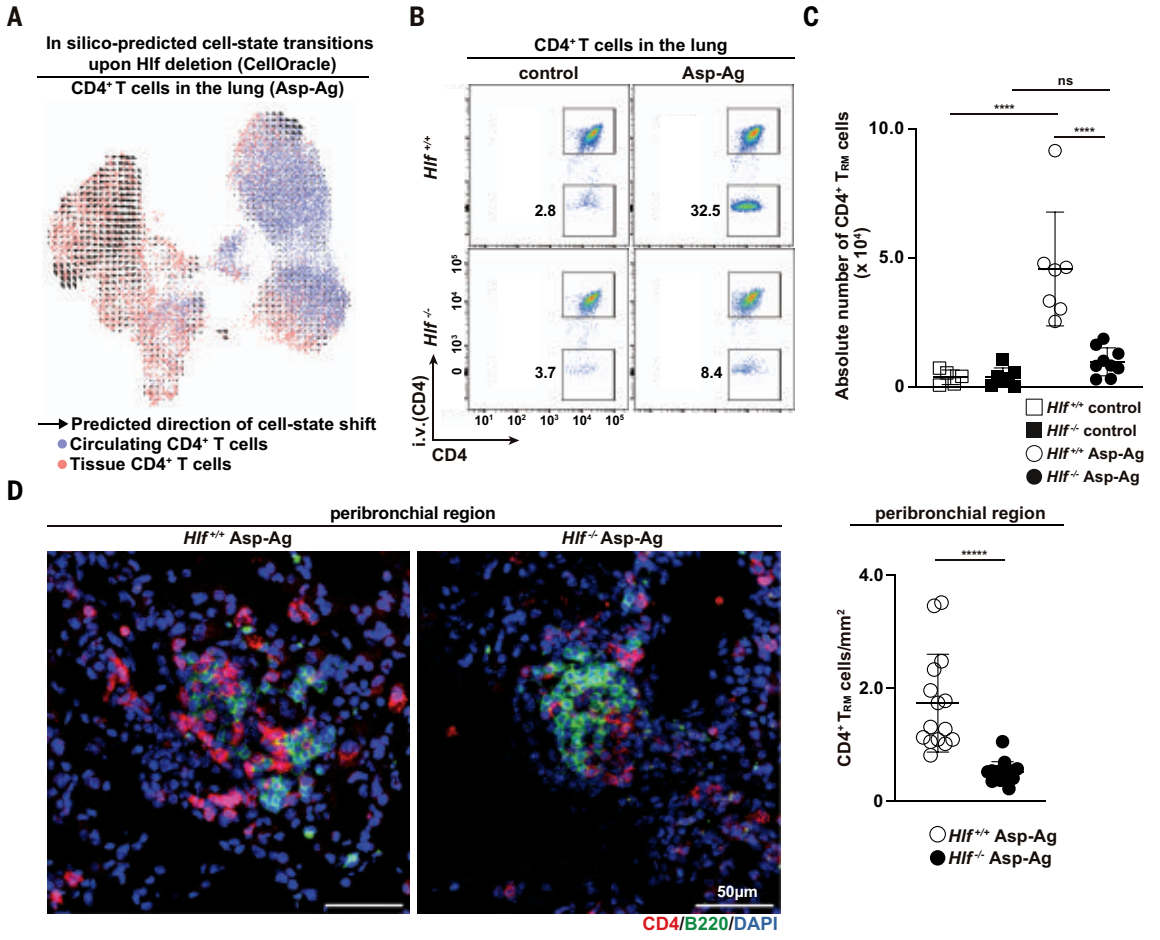

A
In silico-predicted cell-state transitions upon Hlf deletion (CellOracle)
CD4+ T cells in the lung (Asp-Ag)
Predicted direction of cell-state shift
Circulating CD4+ T cells
Tissue CD4+ T cells
B
CD4+ T cells in the lung
control
Asp-Ag
Hlf+/+
Hlf-/-
2.8
32.5
3.7
8.4
i.v.(CD4)
CD4
C
Absolute number of CD4+ TRM cells (x 10⁴)
ns
****
Hlf+/+ control
Hlf-/- control
Hlf+/+ Asp-Ag
Hlf-/- Asp-Ag
D
peribronchial region
Hlf+/+ Asp-Ag
Hlf-/- Asp-Ag
50μm
CD4/B220/DAPI
CD4+ TRM cells/mm²
*****
E
Cytokine-producing cells in CD4+TRM cells (%)
ns
***
IL-4
IL-5
IL-13
IL-17A
IFNγ
F
100μm
G
Histological score
Induced Sirius Red (μm²/μm)
*
H
BAL fluid
Absolute cell number (x10⁵)
Eos
Neut
Lymph
Mac
Total

Fig. 2. HLF is central to CD4$^+$ T_{RM} cell development and exacerbates chronic inflammation in vivo. (**A**) In silico perturbation of *Hlf* using CellOracle based on scRNA-seq–derived ($n = 5$ mice pooled as $n = 1$ sample, 53,409 cells) and scATAC-seq–derived ($n = 5$ mice pooled as $n = 1$ sample, 15,335 cells) gene-regulatory networks in circulating CD4$^+$ T cells and CD4$^+$ T_{RM} cells in the lungs of mice with repetitive exposure to Asp-Ag. Vector field plot shows the predicted cell-state transitions upon *Hlf* deletion. Each arrow indicates the direction and magnitude of the transcriptional shift for individual cells. (**B** to **H**) *Hlf*$^{+/+}$ and *Hlf*$^{-/-}$ mice were repeatedly exposed to *A. fumigatus* antigen for 7 weeks, as indicated in fig. S8A. (**B**) Representative cell-staining profiles of CD4$^+$ T_{RM} cells in the lungs of *Hlf*$^{+/+}$ and *Hlf*$^{-/-}$ mice (gated as in fig. S19). (C) Absolute numbers of CD4$^+$ T_{RM} cells in the lungs of *Hlf*$^{+/+}$ (control; $n = 5$, Asp-Ag; $n = 7$) and *Hlf*$^{-/-}$ mice (control; $n = 7$, Asp-Ag; $n = 9$). Data are representative of three independent experiments performed with similar results. (D) Representative immunostaining of the lungs stained with DAPI (blue), anti-CD4 (red), and anti-B220 (green) in the peribronchial region of Asp-Ag *Hlf*$^{+/+}$ and Asp-Ag *Hlf*$^{-/-}$ mice (left). Absolute numbers of CD4$^+$ T_{RM} cells in peribronchial region of *Hlf*$^{+/+}$ (Asp-Ag; $n = 5$ mice) and *Hlf*$^{-/-}$ mice (Asp-Ag; $n = 5$ mice) were pooled from three independent experiments (right). Scale bars, 50 μm. Peripheral and peribronchial regions were defined as subpleural areas containing alveoli and a bronchovascular bundle region containing iBALT, respectively. (E) Percentage of the indicated cytokine-producing CD4$^+$ T_{RM} cells in the lungs of Asp-Ag *Hlf*$^{+/+}$ mice ($n = 6$) and Asp-Ag *Hlf*$^{-/-}$ mice ($n = 6$). Data were pooled from two independent experiments. (F) Representative hematoxylin and eosin (H&E) staining (top panels) and Sirius red staining (bottom panels) of lungs from Asp-Ag *Hlf*$^{+/+}$ and Asp-Ag *Hlf*$^{-/-}$ mice. Scale bars, 100 μm. (G) Histological scores based on H&E staining (left) and ratios of areas of randomly selected regions stained with Sirius red surrounding bronchi versus the areas of associated basement membranes (right) of the lungs from *Hlf*$^{+/+}$ (Asp-Ag; $n = 5$ mice) and *Hlf*$^{-/-}$ mice (Asp-Ag; $n = 5$ mice) from three independent experiments. (H) Absolute numbers of total cells (Total), macrophages (Mac), lymphocytes (Lymph), neutrophils (Neut), and eosinophils (Eos) in the bronchoalveolar lavage (BAL) fluid of wild-type (control; $n = 7$, Asp-Ag; $n = 7$) and *Hlf*-deficient mice (control; $n = 7$, Asp-Ag; $n = 8$). Data are representative of three independent experiments performed with similar results and are shown as the mean ± SD. Each dot represents a single mouse. *P* values were calculated by a two-tailed Welch's *t* test [(D) and (G)] and one-way ANOVA [(C), (E), and (H)]. ns, not significant, $*P < 0.05$, $***P < 0.001$, ****, $P < 0.0001$. See also figs. S4 to S10.

Rechallenge of OVA decreased the number of eosinophils in the bronchoalveolar lavage (BAL) fluid (BALF) from mice that had received *Hlf*-deficient OT-II T cells compared with those into which *Hlf*-sufficient OT-II T cells had been transferred (Fig. 3D). The production of the inflammatory cytokines IL-4, IL-5, and IL-13 by OT-II T cells in the lung was decreased in mice with *Hlf*-deficient OT-II T_{RM} cells (Fig. 3, E and F).

To determine whether HLF was intrinsically required for CD4$^+$ T_{RM} cell formation, we generated bone marrow chimera mice by transplanting bone marrow from *Hlf*$^{+/+}$ and *Hlf*$^{-/-}$ mice at a 1:1 ratio into either C57BL/6 or *TCRβδ*-deficient mice (fig. S11B). After repeated exposure to *A. fumigatus* antigen for 7 weeks, bone marrow chimera mice showed approximately equal proportions of *Hlf*-sufficient Ly5.1$^+$ and *Hlf*-deficient Ly5.2$^+$ CD4$^+$ T cells in the inflamed lung (fig. S11, C and D, top panels). However, when considering the lung tissue–resident CD4$^+$ T cells, the frequency of *Hlf*-deficient cells was decreased compared with the *Hlf*-sufficient cells (fig. S11, C and D, bottom panels, and E and F). We concluded that there is a cell-intrinsic requirement for HLF to promote the formation of proinflammatory CD4$^+$ T_{RM} cells.

HLF orchestrates tissue-residency and inflammatory programs in CD4$^+$ T_{RM} cells

To explore the molecular mechanisms through which HLF regulates the development and effector functions of CD4$^+$ T_{RM} cells, we compared the global transcriptomes of *Hlf*$^+$ and *Hlf*$^-$ CD4$^+$ T_{RM} cells using conventional RNA-seq (fig. S12A). Genes encoding proinflammatory cytokines, including *Il5*, *Il13*, *Ifng*, and *Il17a*, were up-regulated, whereas genes related to T cell memory, such as *S1pr1*, *Ccr7*, *Klf2*, and *Tcf7*, were down-regulated in *Hlf*$^+$ CD4$^+$ T_{RM} cells (Fig. 4A). There was also an enrichment of genes associated with effector function and diminished migratory function in *Hlf*$^+$ CD4$^+$ T_{RM} cells (Fig. 4B), and *Hlf*$^+$ CD4$^+$ T_{RM} cells produced more effector cytokines, including IL-5, IL-13, IFN-γ, and IL-17A, compared with *Hlf*$^-$ CD4$^+$ T_{RM} cells (Fig. 4C and fig. S12B). Thus, we concluded that HLF regulates the molecules associated with tissue-residency and effector functions in CD4$^+$ T_{RM} cells.

To elucidate whether HLF has a direct role in regulating the transcriptional programs related to tissue residency and inflammation, we performed chromatin immunoprecipiation sequencing (ChIP-seq) to identify the genome-wide binding sites for HLF, in parallel with evaluating DNA accessibility with ATAC-seq, which we could then compare with gene expression changes established by bulk RNA-seq (fig. S12, C to E). HLF bound 29.9% of the genes down-regulated in *Hlf*-expressing CD4$^+$ T_{RM} cells (Fig. 4D, left panel) and directly bound to gene loci for *S1pr1*, *Klf2*, *Ccr7*, and *Tcf7*, genes that had lower expression in Hlf-expressing CD4 T cells and are linked to promoting the egress of CD4 T cells from tissues (*36*). Each of these loci had differentially accessible regions (DARs) that were closed in *Hlf*$^+$ CD4$^+$ T_{RM} cells (Fig. 4D and fig. S13A). These data indicated that HLF directly represses the tissue egress program.

Among the 106 genes with higher expression in *Hlf*$^+$ CD4$^+$ T_{RM} cells, HLF bound 41, including the tissue retention molecules *Cd69*, *Fosb*, *Rbpj*, *Rora*, *Bhlhe40*, and *Il10*. These genes were all associated with open chromatin in *Hlf*-expressing cells (Fig. 4E, left panel, and fig. S13B). The gene locus of *Bhlhe40*, a transcription factor that regulates inflammatory responses in CD4$^+$ T cells (*22*), was more accessible in *Hlf*$^+$ CD4$^+$ T_{RM} cells (Fig. 4E, right panel). Thus, we concluded that HLF shapes the functional attributes of CD4$^+$ T_{RM} cells by enhancing their tissue retention and inflammatory responses while concurrently suppressing tissue egress.

HLF is associated with tissue-resident transcriptional programs and chronic inflammation in human chronic inflammatory diseases

To determine whether the observed mechanisms were relevant to human CD4$^+$ T_{RM} cells in the inflamed airway, we analyzed tissue from patients with eosinophilic chronic rhinosinusitis (ECRS), a chronic upper airway inflammatory disease characterized by the formation of nasal polyps (*1*). The nasal polyps of patients with ECRS showed infiltration of CD4$^+$ T cells that expressed both CD45RO, a marker for memory T cells, and CD69, and thus exhibited characteristics of CD4$^+$ T_{RM} cells (Fig. 5A and fig. S14A). CD69$^+$ CD4$^+$ T_{RM} cells from nasal polyps also expressed HLF, but those from the healthy nasal submucosa showed negligible HLF expression (Fig. 5, A and B). Consistent with these results, CD45RO$^+$ memory-type CD4$^+$ T cells from inflamed nasal polyps showed enhanced chromatin accessibility in both the promoter and enhancer regions of the *HLF* gene locus compared with CD45RO$^+$ memory-type CD4$^+$ T cells from circulating peripheral blood mononuclear cells (PBMCs) (Fig. 5C).

Single-cell transcriptome analyses using CD45$^+$ cells from patients with ECRS showed that *HLF* was specifically expressed in a subpopulation of CD4$^+$ T cells (fig. S14, B to D). In CD8$^+$ T_{RM} cells, transcription factors such as Blimp1, Hobit, and Runx3 facilitate the expression of tissue-resident signature genes, simultaneously repressing circulating T cell signature genes (*12*, *15*). *HOBIT* was specifically expressed in polyp-infiltrating CD8$^+$ T cells in patients with ECRS (fig. S14D, right panel), suggesting that there is a different regulatory transcriptional mechanism between CD4$^+$ and CD8$^+$ T_{RM} cells.

Targeted analysis of CD4$^+$ T cells found that *HLF* exhibited specific expression with enhanced activity in memory-type CD4$^+$ T cell subsets among three distinct subpopulations from nasal polyps of ECRS patients (fig. S14, E to J). *HLF* expression was enriched in T_H2 and T_H17 subsets (fig. S14K). *HLF*-expressing CD4$^+$ T cells showed very strong enrichment of tissue-resident T cell transcriptome signatures (*37*)

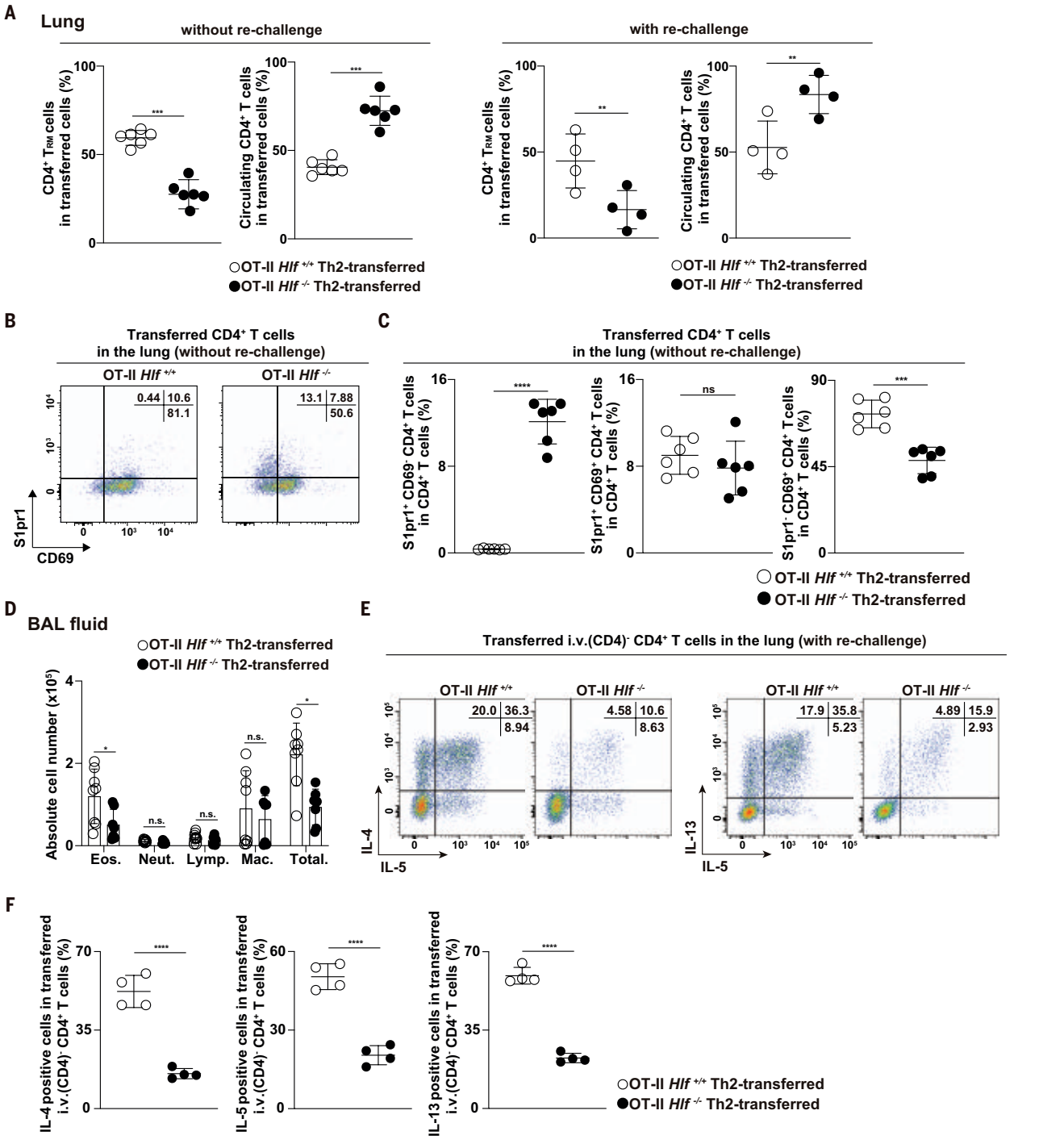


Fig. 3. HLF-deficient T_H2 cells show impaired $CD4^+$ T_{RM} formation and effector function in vivo. (**A** to **F**) OT-II *Hlf*$^{+/+}$ or OT-II *Hlf*$^{-/-}$ TH2 cells were adoptively transferred into C57BL/6 mice, followed by intranasal OVA administration on days 1 and 3 and rechallenge on day 27, as indicated in fig. S11A. (A) Percentages of CD4(iv)$^-$ $CD4^+$ T_{RM} cells or CD4(iv)$^+$ circulating $CD4^+$ T cells in transferred OT-II$^+$ TH2 cells infiltrating the lungs of mice adoptively transferred with OT-II *Hlf*$^{+/+}$ or OT-II *Hlf*$^{-/-}$ TH2 cells with or without OVA rechallenge. (B and C) Representative staining profiles of S1pr1 and CD69 in transferred OT-II$^+$ TH2 cells infiltrating the lungs (B) and percentages of S1pr1$^+$CD69$^-$, S1pr1$^+$CD69$^+$, and S1pr1$^-$CD69$^+$ cells in transferred OT-II$^+$ TH2 cells infiltrating the lungs (gated as in fig. S20A) (C) of mice adoptively transferred with OT-II *Hlf*$^{+/+}$ ($n = 6$) or OT-II *Hlf*$^{-/-}$ TH2 cells ($n = 6$) without OVA rechallenge. Data are representative of two independent experiments performed with similar results. (D) Absolute numbers of total cells (Total), macrophages (Mac), lymphocytes (Lymph), neutrophils (Neut), and eosinophils (Eos) in the BAL fluid from OVA-rechallenged mice adoptively transferred with OT-II *Hlf*$^{+/+}$ ($n = 8$) or OT-II *Hlf*$^{-/-}$ TH2 ($n = 7$) cells. Data are representative of two independent experiments performed with similar results. (E) Representative cytokine staining profiles of CD4(iv)$^-$ $CD4^+$ T_{RM} cells in the lungs of OVA-rechallenged mice adoptively transferred with OT-II *Hlf*$^{+/+}$ or OT-II *Hlf*$^{-/-}$ TH2 cells (gated as in fig. S20B). Data are representative of two independent experiments performed with similar results. (F) Percentages of the indicated cytokine-producing $CD4^+$ T_{RM} cells in the lungs of OVA-rechallenged mice that were adoptively transferred with OT-II *Hlf*$^{+/+}$ or OT-II *Hlf*$^{-/-}$ TH2 cells ($n = 4$). Data are representative of two independent experiments performed with similar results and are shown as the mean ± SD. Each dot represents a single mouse. *P* values were calculated by a two-tailed Welch's *t* test [(A), (C), and (F)] and two-way ANOVA (D). ns, not significant, $*P < 0.05$, $**P < 0.01$, $***P < 0.001$, ****, $P < 0.0001$. See also fig. S11.

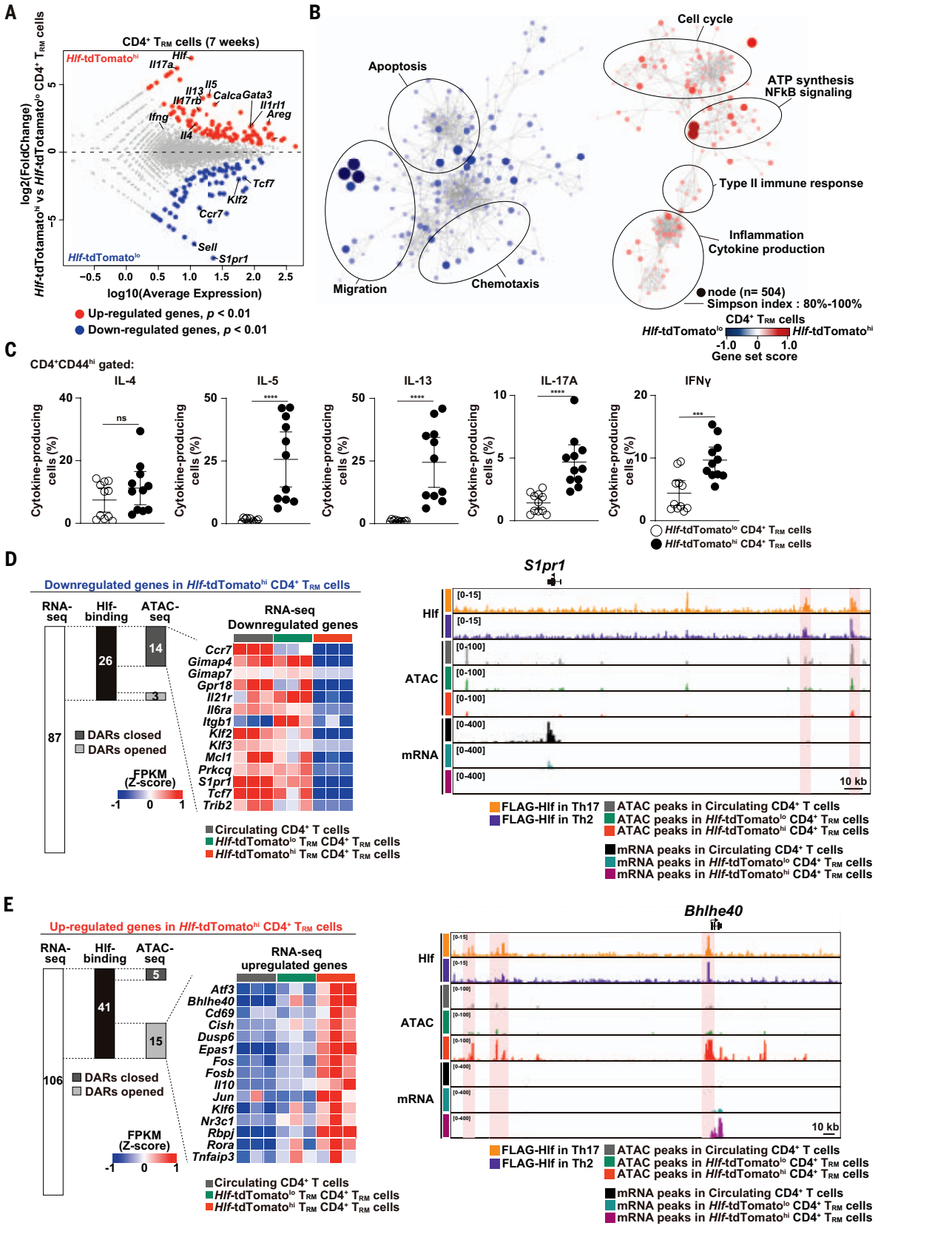


Fig. 4. HLF orchestrates tissue-resident and inflammatory programs of CD4$^+$ T_{RM} cells. (**A** to **E**) *Hlf*-tdTomato reporter mice were repeatedly exposed to Asp-Ag for 7 weeks, and bulk RNA-seq and ATAC-seq were conducted on day 50 using lung CD4(iv)$^+$ circulating CD4$^+$, *Hlf*-tdTomato^{lo} CD4(iv)$^-$ CD4$^+$, and *Hlf*-tdTomato^{hi} CD4(iv)$^-$ CD4$^+$ T cells, as indicated in fig. S12A. (A) Mean average plot (log ratio versus mean average expression) analysis of bulk RNA-seq showing differentially expressed genes between *Hlf*-tdTomato^{hi} and *Hlf*-tdTomato^{lo} CD4$^+$ T_{RM} cells in the lungs of Asp-Ag *Hlf*-tdTomato reporter mice ($n = 3$). (B) Gene Ontology (GO) enrichment network analysis depicting

pathways enriched in *Hlf*-tdTomato^{hi} compared with *Hlf*-tdTomato^{lo} CD4$^+$ T_{RM} cells. Node colors indicate GO terms that were significantly up-regulated (red) or down-regulated (blue) in *Hlf*-tdTomato^{hi} compared with *Hlf*-tdtomato^{lo} CD4$^+$ T_{RM} cells. Node sizes represent enrichment scores for each GO term. Node connections were determined using overlap of the elemental gene products in the GO terms (Simpson coefficient $R = 0.8$). (C) Percentage of indicated cytokine-producing cells in *Hlf*-tdTomato^{hi} and *Hlf*-tdTomato^{lo} CD4$^+$ T_{RM} cells in the lungs of Asp-Ag *Hlf*-tdTomato reporter mice ($n = 11$). Three independent experiments were performed with similar results. (D and E), left, heatmap showing *Z*-scored FPKM indicating mRNA expression levels of the selected differentially expressed genes (DEGs) identified in Fig. 4A. HLF-bound genes with DARs are selected. Numbers of genes with DARs closed (dark gray) and DARs opened (gray) in *Hlf*-tdTomato^{hi} compared with *Hlf*-tdTomato^{lo} CD4$^+$ T_{RM} cells are shown. (D and E), right, Genetrack views of the *S1pr1* (D) and *Bhlhe40* (E) gene loci showing HLF ChIP-seq signals in 3xFlag-HLF–transfected T_H2 and T_H17 cells and ATAC-seq and RNA-seq signals in circulating, *Hlf*-tdTomato^{lo} and *Hlf*-tdTomato^{hi} CD4$^+$ T_{RM} cells. HLF-bound regions with DAR(s) are highlighted. Data are shown as the mean ± SD. Each dot represents a single mouse. *P* values were calculated by a Wald test (A) and an unpaired *t* test (C). ***$P < 0.001$, ****, $P < 0.0001$. See also figs. S12 and S13.

compared with HLF$^-$ CD4$^+$ T cells (Fig. 5D, left panel, and table S2). Circulating T cell transcriptome signatures (*37*) were enriched in *HLF*$^-$ CD4$^+$ T cells (Fig. 5D, right panel, and table S2).

HLF-expressing CD4$^+$ T cells had increased expression of *CD69*, *IL5*, *IL13*, and *GATA3*, together with decreased expression of *KLF2* and *TCF7*, consistent with gene expression related to immune activation (fig. S15, A and B). Indeed, *HLF*-expressing CD4$^+$ T cells in the nasal polyps exhibited decreased expression of tissue egress–related genes, including *S1PR1*, and other transcription factors such as *KLF2* and *TCF7* (Fig. 5E). By contrast, *CD69* and *BHLHE40* had higher expression in *HLF*-expressing CD4$^+$ T cells compared with *HLF*$^-$ CD4$^+$ T cells in the nasal polyps (Fig. 5F). Furthermore, *HLF*-expressing CD4$^+$ T cells showed enhanced expression of effector cytokines including *IL5* and *IL13* compared with *HLF*$^-$ CD4$^+$ T cells (Fig. 5F).

We also examined published sequencing data from patients with idiopathic pulmonary fibrosis (IPF) (*38*) and detected *HLF*-expressing CD4$^+$ T cells with high *CD69* and *IL13* expression in the lungs (fig. S16, A to F). In CD4$^+$ T_{RM} cells from the intestinal tissues of inflammatory bowel disease (IBD) patients (*39*), *HLF* expression was observed in both the T_H2-type and T_H17-type T_{RM} subsets (fig. S16, G to L). In T cells isolated from giant papillae of patients with severe allergic conjunctivitis (*40*), *HLF* was expressed in T_H2-type T_{RM} cells but not in other T cell subsets (fig. S17, A to E). Furthermore, in patients with primary sclerosing cholangitis (PSC), HLF-expressing CD69$^+$CD4$^+$ T cells were detected around the intrahepatic bile duct (fig. S17, F and G). Thus, these data suggested that HLF may potentially play a role in shaping the proinflammatory CD4$^+$ T_{RM} cells in human chronic inflammatory diseases, warranting further functional investigation.

Discussion

An increasing number of studies have highlighted the transcriptional programs underlying CD8$^+$ T_{RM} cell development; however, there has been a lack of understanding of the transcriptional programs that regulate the formation of CD4$^+$ T_{RM} cells. Blimp1 and the related transcription factor Hobit cooperate to regulate the retention and differentiation of CD8$^+$ T_{RM} cells through suppression of tissue egress genes such as *Klf2*, *S1pr1*, and *Ccr7* (*15*). Runx3 promotes the expression of tissue residency molecules in CD8$^+$ T_{RM} cells, including CD69 and CD103 (*12*). Notch and Bhlhe40 are also known to be important in the differentiation of CD8$^+$ T_{RM} cells (*22*, *41*, *42*). Based on the results of our study, we propose that the transcription factor HLF programs proinflammatory CD4$^+$ T cell residency.

HLF was originally identified as a fusion protein with E2A, which causes pediatric acute B-lineage leukemia (*43*). In a high-risk group of acute myeloid leukemia patients, HLF promoted self-renewal of leukemic stem cells (*44*). HLF also regulates the quiescence of hematopoietic stem cells and modulates lineage fate during early hematopoiesis (*24*, *25*, *45*). In lymphocytes, HLF is expressed in ILC2s in the intestine and skin (*33*, *34*); however, the roles of HLF in T cells, especially CD4$^+$ T_{RM} cells, have remained uncertain. Our findings suggest that HLF may serve as a marker and regulator of tissue residency and may shape the functional attributes of CD4$^+$ T_{RM} cell subsets in both human and mouse inflamed respiratory organs. Because it is expressed in CD4$^+$ T_{RM} cells isolated from patients, HLF may function across various physiological and inflammatory contexts, including allergy, viral and helminth infections, autoimmune diseases, and fibrosis.

Various molecules, such as Klf2, S1pr1, Ccr7, and Tcf7, are involved in tissue egress of lymphocytes. For example, the transcription factor Klf2 drives the expression of S1pr1, which binds its ligand, S1P, and promotes lymphocyte egress from tissue (*46*), and Ccr7, which facilitates the tissue egress of lymphocytes (*47*). *Tcf7*, which encodes T cell factor 1 (TCF-1), promotes circulating memory CD8$^+$ T cell differentiation and suppresses CD103$^+$CD8$^+$ T_{RM} cell development simultaneously (*23*, *48*). Thus, the down-regulation of these molecules is crucial for T_{RM} cell formation (*17*, *48*). Our data indicate that HLF may simultaneously bind to and suppress *Klf2*, *S1pr1*, *Ccr7*, and *Tcf7* expression while directly inducing the key tissue residency molecule CD69 (*49*). Thus, we propose that HLF induces the formation of CD4$^+$ T_{RM} cells by inhibiting the transcriptional programs required for tissue egress and by promoting gene expression that promotes tissue residency.

T_{RM} cells need to adapt to the tissue environment where they are located during their development and for long-term survival and proper function, shaping functional and transcriptional diversity across tissues (*18*, *50*–*52*). Blimp1, Hobit, and Runx3 drive CD8$^+$ T_{RM} cell formation and function across multiple tissues, including skin, gut, liver, and kidney, by suppressing the expression of tissue egress genes (*12*, *15*). Bhlhe40 regulates the formation of lung CD8$^+$ T_{RM} cells (*22*), and the T-box transcription factor Eomes is required for the maintenance of small intestine CD8$^+$ T_{RM} cells (*14*). In CD4$^+$ T_{RM} cells, Blimp-1, Id2, and Bcl6 are required for CD4$^+$ T_{RM} formation and development in the small intestine during acute viral infection (*53*), and genetic deletion of both Hobit and Blimp-1 ameliorates experimental colitis by impairing cytokine and chemokine production in CD4$^+$ T_{RM} cells (*54*). We detected high expression of HLF in T_H2 and T_H17 CD4$^+$ T_{RM} cells across multiple inflammatory diseases and in CD4$^+$ T_{RM} cells during influenza A infection. In CD4$^+$ T_{RM} cells, HLF directly targeted genes encoding several transcription factors, including *Bhlhe40*, a known regulator of cytokine secretion, cell proliferation, and metabolism in both human and mouse T cells (*29*, *55*–*57*). Other HLF targets that may play a role in T_{RM} regulation include *Nr3c1* (*58*), *Rbpj* (*59*), and RORα (*60*), indicating that HLF orchestrates tissue residency and T_{RM} cell function through multiple pathways, including Bhlhe40-driven cytokine production and metabolic and hormonal regulation. Understanding the additional molecular mechanisms through which proinflammatory CD4$^+$ T_{RM} cells differentiate during immune responses will help in the development of therapeutic strategies for immune diseases.

Materials and methods

Mice

The animals used in this study were backcrossed to BALB/c or C57BL/6 mice >10 times. *Hlf*$^{-/-}$ mice were purchased from The European Mouse Mutant Archive. *Hlf*-tdTomato reporter mice were provided by T. Yokomizo (Tokyo Women's Medical University) and N. Komatsu (Juntendo University) (*26*). BALB/c and C57BL/6 mice were purchased from CLEA Japan (Tokyo, Japan). OT-II TCR transgenic (Tg) mice (stock no. 004194) and TCRβ$^{-/-}$ TCRδ$^{-/-}$ mice (stock no. 002122) were purchased from The Jackson Laboratory (Bar Harbor, ME, USA). Ly5.1$^+$ mice were purchased from the Sankyo Laboratory (Tokyo, Japan). All mice

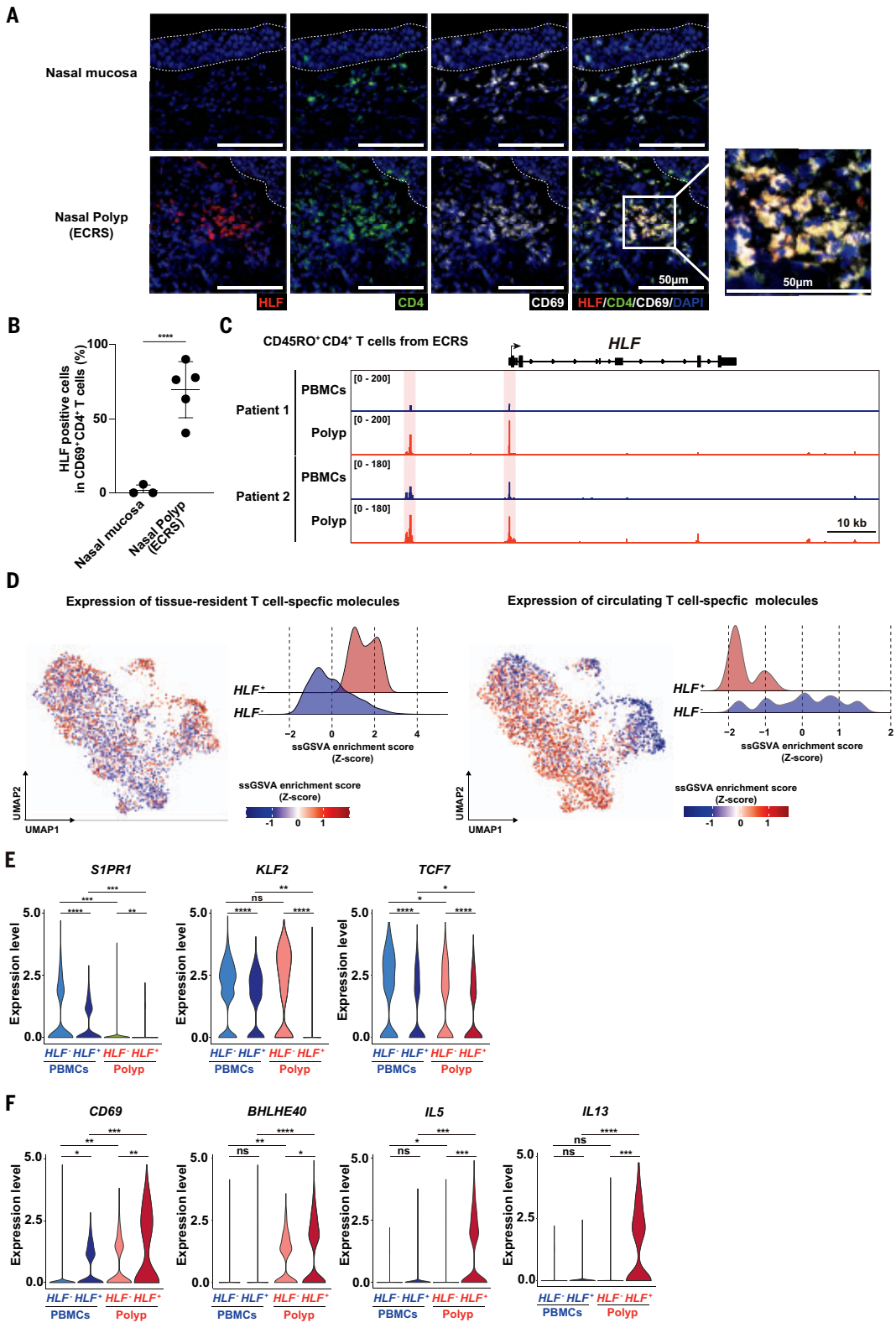


Fig. 5. HLF drives tissue-resident transcriptional programs and amplifies chronic airway inflammation in human ECRS nasal polyps. (**A**) Representative immunostaining of anti-HLF (red), anti-CD4 (green), anti-CD69 (white), and DAPI (blue) staining in nasal mucosa or nasal polyps from ECRS patients. Scale bars, 50 μm. (**B**) Percentage of $HLF^{+}CD69^{+}CD4^{+}$ T cells in nasal mucosa ($n = 3$) or nasal polyps from ECRS patients ($n = 5$). (**C**) Genetrack views of ATAC-Seq signals in $CD45RO^{+}CD4^{+}$ T cells from PBMCs or nasal polyps in the *Hlf* gene locus. (**D** to **F**) scRNA-seq using $CD4^{+}$ T cells in nasal polyps and PBMCs from ECRS patients ($n = 4$ patients pooled, 27,473 cells). (**D**) Enrichment analysis by ssGSVA of expression of tissue-resident T cell–specific (left) and circulating T cell–specific (right) cell surface molecules projected onto a UMAP. (**E** and **F**) Violin plot showing a comparison of the indicated genes in HLF^{-} and HLF^{+} $CD4^{+}$ T cells between PBMCs (blue) and nasal polyps (red) from ECRS patients. Data are shown as the mean ± SD. Each dot represents a single subject. *P* values were calculated by an unpaired *t* test (B) and quasi-likelihood F test [(E) and (F)]. ns, not significant, $*P < 0.05$, $**P < 0.01$, $***P < 0.001$, ****, $P < 0.0001$. See also figs. S14 to S17.

were used at 6 to 8 weeks of age and were maintained under specific-pathogen-free conditions. Sex-matched littermates were randomly assigned to experimental groups for comparisons between $Hlf^{+/+}$ and $Hlf^{-/-}$ mice. Both male and female mice were used in the experiments. The researchers conducting the mouse experiments were blinded to treatment group assignments. An independent individual not involved in the experiment randomly assigned numbers to the mice, and the researchers performing the experiments were only aware of these assigned numbers, not the treatment conditions or genetic backgrounds. All experimental protocols involving mice were approved by the animal committee of Chiba University. All animal care was performed in accordance with the guidelines of Chiba University (registration no. A7-158).

Human samples

This research was reviewed and approved by the ethics committee of Chiba University (registration nos. 2016127 and 3361), and informed consent was obtained from all participants. The diagnoses of all participants with ECRS were based on the diagnostic criteria for ECRS prescribed by the Ministry of Health, Labor, and Welfare, Japan. Human liver samples were obtained from liver transplantation donors who had undergone surgery at the Department of Hepato-Biliary-Pancreatic Surgery and Transplantation, Kyoto University Hospital. The patients included in this study provided informed consent, and the research protocol was approved by the ethics committee of Kyoto University Hospital (registration no. G1240-12).

Induction of chronic lung inflammation by repeated intranasal administration of *A. fumigatus* antigen

A. fumigatus antigen (Greer, Lenoir, NC, USA) was administered intranasally for 7 weeks in a protocol based on a previous study (*19*). For the first 3 weeks, 50 μg of antigen was administered once a week. For the following 4 weeks, 20 μg of antigen was administered twice a week. Assays were performed 24 h after the last antigen administration. In some experiments, mice were analyzed on days 0, 8, 22, and 36 of antigen administration or 7 weeks after the last antigen administration.

Intravenous staining of $CD4^+$ T cells localized in the vasculature of the lung

For intravascular cell staining of $CD4^+$ cells, mice were intravenously injected with 0.5 μg of anti-CD4 antibody (RM4-4; BioLegend, San Diego, CA, USA) diluted in 100 μl of phosphate buffered saline (PBS) 3 min before sampling.

Isolation of single-cell suspensions from blood and tissues

After euthanasia, mice were perfused with 5 ml of cold PBS through the left and right ventricle. In some experiments, blood was collected by cardiac puncture before PBS perfusion. Lungs were dissociated in a C tube (Miltenyi Biotec, Bergisch Gladbach, Germany) in digestion buffer containing RPMI 1640 supplemented with collagenase type III (200 U/ml; Worthington, NJ, USA) and DNase I (200 μg/ml; Sigma-Aldrich, St. Louis, MO, USA) using a gentleMACS tissue dissociator (Miltenyi Biotec). After 30 min at 37 °C, samples were treated with final dissociation with gentleMACS. Cell suspensions were filtered through a 70-μm cell strainer (Greiner Bio-One, Kremsmunster, Austria). Lung mononuclear cells were separated using a Percoll solution (GE Healthcare, Chicago, IL, USA). PBMCs were isolated by density centrifugation using Ficoll-Paque PLUS (Cytiva, Marlborough, MA, USA). Spleens and lymph nodes were mechanically dissociated and filtered through a 70-μm cell strainer (Greiner Bio-One).

Flow cytometry, cell staining, and sorting

Single-cell suspensions from the lungs, PBMCs, spleen, and mediastinal lymph nodes were incubated for 90 min with anti-mouse S1PR1 antibody (713412, R&D Systems, Minneapolis, MN, USA), followed by 45 min of staining with anti-rat IgG-biotin $F(ab')_2$ (2340649, Jackson ImmunoResearch), and then stained with streptavidin-conjugated allophycocyanin (APC) together with the following surface antibodies for 30 min at 4°C: anti-CD4 (RM4-5), anti-CD44 (IM7), anti-CD62L (MEL-14), anti-CD69 (H1.2F3), anti-CD45.1 (A20), and anti-CD45.2 (104) (BioLegend). For the detection of lung ILC2s, an anti-mouse lineage cocktail with isotype control, anti-IL-33Ralpha (DIH9), and anti-IL7Ralpha (A7R34) antibodies were used (BioLegend). For intracellular staining of cytokines, cells were restimulated with phorbol 12-myristate 13-acetate (50 ng/ml) and ionomycin (500 nM) for 4 hours at 37°C in the presence of 2 μM monensin (Sigma-Aldrich). After restimulation, the cells were fixed with 4% paraformaldehyde, permeabilized with 0.5% Triton X-100 in PBS, and blocked with 3% bovine serum albumin in PBS. Cells were stained for 30 min at 4°C with anti–IFN-γ (XMG1.2), anti–IL-4 (11B11), anti–IL-5 (TRFK5), and anti–IL-17A (TC11-18H10.1) (BioLegend) and anti–IL-13 (eBio13A) antibody (Thermo Fisher Scientific, MA, USA). All cells were incubated with anti-CD16/CD32 (2.4G2; BD Biosciences) to block Fc receptors before staining with the target antibodies. Fixable Viability Dye eFluor 780 (0.1%, Thermo Fisher Scientific) was used to exclude dead cells. The samples were analyzed on a BD FACSCanto II or LSRFortessa X-20 flow cytometer (BD Biosciences), and the resulting data were analyzed using FlowJo software (FlowJo, LLC, Ashland, OR, USA). Cell sorting was performed using a FACSAria III Cell Sorter (BD Biosciences) or a Cell Sorter SH800S (SONY, Tokyo, Japan).

Preparation of single-cell suspensions from human samples

Freshly obtained nasal polyps were immediately minced and incubated in RPMI 1640 medium containing 1 mg/ml collagenase III (Sigma-Aldrich), 0.5 mg/ml hyaluronidase, and 0.2 mg/ml DNase I (Sigma-Aldrich). After incubation, nasal polyp mononuclear cells were purified by density gradient centrifugation using Percoll solution (GE Healthcare). PBMCs were isolated from peripheral blood using Ficoll-Paque Plus solution (GE Healthcare). Cell suspensions were passed through a 70-μm nylon mesh sheet.

scRNA-seq

$CD4(iv)^-$ tissue $CD4^+$ T cells and $CD4(iv)^+$ circulating $CD4^+$ T cells from murine lungs and $CD45^+$ cells from human ECRS patients were freshly isolated from single-cell suspensions using a BD FACSAria III (10,000 cells per sample, cell viability >98%). Single-cell libraries from 10,000 cells per sample were prepared using the Chromium Single Cell 3′ Reagent Kits v3.1 with dual indexing (10x Genomics) following the manufacturer's protocol.

The generated scRNA-seq libraries were sequenced on a NovaSeq 6000 Sequencing System (Illumina) with paired-end, dual indexing. Sequencing was performed at a depth of at least 20,000 read pairs per cell. The recommended number of sequencing cycles was applied: 28 cycles for read 1, 10 cycles for the i7 index, 10 cycles for the i5 index, and 90 cycles for read 2.

The generated scRNA-seq libraries were sequenced on a NovaSeq 6000 Sequencing System (Illumina) with paired-end, dual indexing. Sequencing was performed at a depth of at least 20,000 read pairs per cell. The recommended number of sequencing cycles was applied: 26 cycles for Read 1, 10 cycles for the i7 index, 10 cycles for the i5 index, and 90 cycles for Read 2.

scATAC-seq

$CD4(iv)^-$ tissue $CD4^+$ T cells and $CD4(iv)^+$ circulating $CD4^+$ T cells were freshly isolated from lung single-cell suspensions using BD FACSAria III (10,000 cells each, cell viability >98%). Single-cell ATAC libraries from 10,000 cells per sample were prepared using Chromium Next GEM Single Cell ATAC Reagent Kits v1.1 (10x Genomics) following the manufacturer's protocol.

The generated scATAC-seq libraries were sequenced on a NovaSeq 6000 Sequencing System (Illumina) with the following run parameters: paired-end, dual indexing, with a sequencing depth of 25,000 read pairs per nucleus (25,000 reads for read 1N; 25,000 reads for read 2N). The number of sequencing cycles was: 50 cycles for read 1, 8 cycles for the i7 index, 16 cycles for the i5 index, and 50 cycles for read 2.

Histology and immunofluorescence

Pathological changes were evaluated by H&E staining, Sirius red staining, and immunofluorescence, as described previously (*61*). The lungs were harvested from mice with 10% formalin (Wako, Osaka, Japan) and fixed overnight, then embedded in paraffin, and sectioned at 5 μm as described previously. Lung sections were stained with H&E reagent. The samples were sectioned and stained with H&E, and the pathological changes were examined under a light microscope (BZ-X 710;

KEYENCE, Osaka, Japan). Histological scores for H&E staining were determined in a blinded manner based on the presence of the following criteria, as described previously (*61*): perivascular eosinophils (scored as 0 to 2); alveolar eosinophils (scored as 0 to 2); perivascular mononuclear cells (scored as 0 to 2); alveolar mononuclear cells (0 to 2); and epithelial desquamation (scored as: normal = 0; elongation/distortion = 1; elongation, infolding, and narrowing = 2; loss of cells with broken airways = 3). For quantification of Hlf-tdTomato$^+$ CD4(iv)$^-$ CD4$^+$ T cells in lung sections, peripheraland peribronchial regions were defined as subpleural alveolar regions and bronchovascular bundle areas, respectively. The numbers of Hlf-tdTomato$^+$ CD4(iv)$^-$ cells, and total CD4$^+$ T cells were counted within each defined area.

For Sirius red staining, the peribronchial area was outlined and quantified in a blinded manner using a light microscope (BZ-X 710, Keyence) attached to an image-analysis system (Photoshop; Adobe Systems Inc., San Jose, CA, USA). Results are expressed as the area of Sirius red staining per micrometer length of the basement membrane of bronchioles with an internal diameter of 100 μm. At least five bronchioles were analyzed per slide. Basement membrane thickening was assessed by calculating the basement membrane area per micrometer length of bronchial epithelium, as described previously (*62*).

For fluorescence staining, cryostat sections (thickness, 10 μm) of lung were stained and mounted with fluorescent mounting medium (DakoCytomation, Santa Clara, CA, USA). Monoclonal antibodies against CD4 (RM4-5; BioLegend) and anti-B220 (RA3-6B2; Thermo Fisher Scientific) were used for staining. 4′,6-Diamidino-2-phenylindole (DAPI) (Thermo Fisher Scientific) was used at the end of the procedure, in accordance with the manufacturer's protocol. A fluorescence microscope (BZ-X 710, Keyence), confocal microscope (LSM710, Carl Zeiss, Oberkochen, Germany), and A1 inverted confocal microscope (Nikon, Tokyo, Japan) were used, and the images were analyzed with ImageJ software (National Institutes of Health, Bethesda, MD, USA).

In vitro TH cell differentiation cultures

Splenic naïve CD4 T cells (CD44^{lo}CD62L^{hi}) from wild-type, *Hlf*$^{-/-}$, OT-II *Hlf*$^{+/+}$, and OT-II *Hlf*$^{-/-}$ mice were purified using an autoMACS magnetic cell sorter (Miltenyi Biotec). TH cell cultures were performed as described previously (*63*). In brief, naïve CD4 T cells were stimulated with anti–T-cell receptor β chain (TCRβ) mAb, IL-2 (25 U/ml), IL-12 (10 U/ml), anti–IL-4 mAb, and CD28 mAb (1 μg/ml) for TH1 cell differentiation. For TH2 cells, naïve CD4 T cells were cultured with IL-2 (25 U/ml), IL-4 (100 U/ml), anti–IFN-γ mAb, and CD28 mAb in the presence of anti-TCRβ mAb. For TH17 cell differentiation, naïve CD4 T cells were cultured with IL-6 (50 U/ml), transforming growth factor-β1 (TGF-β1, 5 ng/ml), anti–IFN-γ mAb, anti–IL-4 mAb, and CD28 mAb (1 μg/ml) in the presence of TCRβ mAb. For iTreg cell differentiation, naïve CD4 T cells were cultured with IL-2 (50 U/ml), TGF-β1 (10 ng/ml), anti–IFN-γ mAb, anti–IL-4 mAb, and CD28 mAb (1 μg/ml) in the presence of TCRβ mAb. The following antibodies were used for cell culture: anti-TCRβ mAb (H57-597; made in-house; Chiba University, Chiba, Japan), anti-CD28 mAb (37.51; BioLegend), anti–IL-4 mAb (11B11; made in-house), and anti–IFN-γ mAb (R46A2; made in-house). Mouse IL-12 was purchased from BD Pharmingen (San Diego, CA, USA); recombinant mouse IL-4, IL-6, IL-1β, and recombinant human TGF-β1 were purchased from PeproTech (Cranbury, NJ, USA).

BAL and analyses

BALF was collected 24 hours after the last antigen challenge, as described previously (*63*). BAL was performed by intratracheal administration of 1 ml of saline and lavage was collected. All viable cells in the BALF were cytocentrifuged onto glass slides using Cytospin 4 (Thermo Electron, Waltham, MA, USA) and stained with a Diff-Quik Stain Kit (Sysmex, Hyogo, Japan). A total of 200 BAL cells were counted on each slide. The cell types were determined using morphological criteria.

Apoptosis assays

Apoptotic cells were stained with anti–Annexin V antibody (BD Biosciences) dissolved in Annexin V binding buffer (BD Biosciences) for 15 min at room temperature and then analyzed by flow cytometry.

Adoptive transfer of TH2 cells into mice and OVA challenge

A total of 3×10^6 cultured OT-II Tg *Hlf*$^{+/+}$, OT-II Tg *Hlf*$^{-/-}$ TH2 cells were transferred intravenously into C57BL/6 recipient mice, followed by 100 μg of intranasal OVA administration on days 1 and 3 and rechallenge on day 17. Assays were performed 24 h after the last antigen administration.

A. fumigatus antigen challenge on bone marrow chimera mice

Recipient C57BL/6 or TCRβ$^{-/-}$ TCRδ$^{-/-}$ mice were irradiated (9.5 Gy). A total of 5×10^6 cells consisting of 1:1 mixture of bone marrow cells from *Hlf*$^{+/+}$ Ly5.1$^+$ and *Hlf*$^{-/-}$ Ly5.2$^+$ host mice were transferred intravenously into irradiated recipient mice. After 8 weeks of reconstitution, bone marrow chimera mice were subjected to intranasal administration of *A. fumigatus* antigen. For the first 3 weeks, 50 μg of antigen was administered once a week. For the following 4 weeks, 20 μg of antigen was administered twice a week. Assays were performed 24 h after the last antigen administration.

Retroviral infection

A retrovirus vector, the pMX-IRES-human nerve growth factor receptor plasmid, was generated as described previously (*63*). The pMX-IRES 3xFlag-HLF plasmid was purchased from VectorBuilder (Chicago, IL, USA). After 3 days of culture with antigen-presenting cells, effector TH2 cells were infected with the retrovirus. The infected TH2 cells were then enriched with antihuman nerve growth factor receptor antibody (BD Pharmingen) 2 days after infection. After an additional 2 days of culture, the infected TH2 cells were subjected to ChIP-seq.

RNA-seq

RNA-seq was performed as described previously (*63*). Total cellular RNA was extracted with TRIzol reagent (Invitrogen, Carlsbad, CA, USA). For cDNA library construction, we used a TruSeq RNA Sample Prep Kit v2 (Illumina) in accordance with the manufacturer's protocol. Sequencing of library fragments was performed on an Illumina NextSeq500 System. For the data analyses, read sequences (50 bp) were aligned to the mouse GRCm38 reference genome using the Bowtie 2 and TopHat (v1.3.2) software programs. Fragments per kilobase of exon per million mapped reads for each gene were calculated using the Cufflinks (v2.0.2) software programs.

ChIP-seq

ChIP experiments for 3xFlag-Hlf were performed using Dynabeads (Invitrogen) as described previously (*63*). In brief, 1 to 10×10^7 cells were fixed with 1% paraformaldehyde at 37°C for 10 min. Cells were sedimented, washed, and lysed with SDS lysis buffer of the iDeal ChIP-seq kit for transcription factors (Diagenode Diagnostics, Marlborough, MA, USA). The lysates were sonicated to reduce the DNA lengths to between 200 and 1000 bp. The soluble fraction was diluted in ChIP dilution buffer (Diagenode Diagnostics) and incubated with Ab conjugated with Dynabeads proteins A and G (Beckman Coulter, Brea, CA, USA) overnight at 4°C. The immune complexes were then captured using a magnet and washed with wash buffer 1 to 4 (Diagenode Diagnostics). Enriched chromatin fragments were eluted with elution buffer (0.1 M $NaHCO_3$ containing 1% SDS). The eluted material was incubated at 65°C for 6 hours to reverse the formaldehyde cross-links and treated with RNase A (10 mg/ml) and proteinase K (40 mg/ml) (Diagenode Diagnostics). DNA was extracted with a QIAquick PCR purification kit (Qiagen, Hilden, Germany). The total input DNA (cellular DNA without immunoprecipitation) was purified in parallel. Ab-specific immunoprecipitates and total input DNA samples were prepared using a NEBNext Ultra II DNA Library Prep Kit for Illumina (NEB, Ipswich, Massachusetts, USA). Adapter-ligated DNA was recovered using AMPure XP Beads (Beckman Coulter). This DNA was then amplified by 15 to 20

polymerase chain reaction (PCR) cycles and again recovered using AMPure XP Beads. The libraries were sequenced for 76 cycles (single-end reads) on an Illumina NextSeq500 (Illumina).

ATAC-seq

ATAC-seq was performed as described previously with minor modification (*64*). 50,000 cells were pelleted and washed with 50 μl of 1× PBS, followed by treatment with 50 μl of lysis buffer. The nuclei were resuspended in 40 μl of tagmented DNA enzyme buffer with 2 μl of Tn5 transposase (Illumina) to tag and fragmentize the accessible chromatin. The reaction was incubated at 37°C with shaking at 300 revolutions per minute for 30 min. The fragmentized DNAs were purified using a Qiagen MinElute kit and amplified with 11 or 12 PCR cycles based on the amplification curve. The libraries were sequenced for 76 cycles (single-end reads) on an Illumina NextSeq500.

Human samples for histochemistry and immunofluorescence

Cryostat-generated frozen sections (10 μm thickness) of nasal polyps from patients with ECRS were fixed with 4% paraformaldehyde, permeabilized with 0.4% Triton X-100 in PBS for 10 min, and blocked with 10% normal goat serum (abcam, Cambridge, UK) in PBS. Monoclonal antibodies anti-CD4 (OKT4), anti-CD45RO (UCHL1), and anti-CD69 (FN50) (BioLegend); and anti-HLF (HPA068156) (Sigma-Aldrich) were used as the primary antibodies. For the staining of CD69, goat anti-mouse IgG Alexa Fluor 488 (Thermo Fisher Scientific) was used as the secondary antibody. For the staining of HLF, goat anti-rabbit IgG Alexa Fluor 647 (Thermo Fisher Scientific) was used as the secondary antibody. DAPI (Thermo Fisher Scientific) was used at the end of the procedure according to the manufacturer's protocol. A confocal microscope Nikon A1 (Nikon, Tokyo, Japan) was used for image acquisition. Micrographs were analyzed using ImageJ software.

Formalin-fixed paraffin-embedded liver tissue sections from a patient with end-stage PSC were permeabilized with 0.4% Triton X-100 in PBS for 10 min and blocked with 10% normal goat serum (abcam, Cambridge, UK) in PBS. Anti-CD69 (EPR25398-81) (abcam) and anti-HLF (1F12-1C4) (Sigma-Aldrich) were used for the primary antibodies. Donkey anti-rabbit IgG Alexa Fluor 488 (Thermo Fisher Scientific) and donkey anti-mouse IgG Alexa Fluor 555 (Thermo Fisher Scientific) were used as the secondary antibodies for the staining of CD69 and HLF, respectively. Additionally, APC-conjugated anti-CD4 (PRA-T4) antibody (BioLegend) was used for the staining of CD4. DAPI (Thermo Fisher Scientific) was used at the end of the procedure according to the manufacturer's protocol. Micrographs were obtained using BZ-X800 (KEYENCE) and TCS SP8 (Leica Microsystems, Wetzlar, Germany).

Analysis of scRNA-seq data

Sequenced reads from all samples were processed and aggregated using the Cell Ranger (v4.3.2 and 7.0.1) pipeline, with GRCm38 (for mice) or GRCh38 (for humans) as a reference. The count matrix files of published dataset were downloaded from the Gene Expression Omnibus (GEO) with accession numbers GSE125788 (murine helminth infection), GSE124880 (murine OVA-induced food allergy), GSE153422 (murine influenza A infection), GSE130119 (murine EAE model), GSE214695 (human IBD), and GSE203217 (human severe allergic conjunctivitis). For reanalysis of the human IPF scRNA-seq dataset, the Seurat (*65*)-processed and cluster-annotated R dataset was downloaded from the GEO (accession number GSE135893).

The aggregated data were further analyzed using Seurat (v5.2.1) (*65*). Ambient RNA contamination was corrected using the SoupX (v1.6.2) (*66*). Low-quality cells were removed based on nFeature_RNA and the percentage of reads mapping to mitochondrial genes (percent.mt) was determined using median absolute deviation–based filtering. The data were normalized using SCTransform of Seurat, regressing out percent.mt, and doublets were identified and excluded using scDblFinder (v1.18.0) (*67*). Genes associated with mitochondrial, ribosomal, and noninformative categories were removed before downstream analysis. Principal component analysis (PCA) was performed using the top variable genes, and the following PCA dimensions were used for clustering and uniform manifold approximation and projection (UMAP): PCA dimensions of 1 to 10 (mouse lung $CD4^+$ T cells), 1 to 50 (human ECRS), 1 to 30 (murine helminth infection), 1 to 50 (murine OVA-induced food allergy), 1 to 50 (murine influenza A infection), 1 to 50 (murine EAE model), 1 to 50 (human IBD), and 1 to 23 (human severe allergic conjunctivitis) were used to find clusters using UMAP, and marker genes for these clusters were identified. Single-cell gene expression was visualized as UMAP overlays, marker gene heatmaps, and violin plots using the Seurat software program. The single-cell gene expression and gene module scoring were also visualized as density plots using the Nebulosa R software package (v1.0.1) algorithm. Module scores of T_{RM} signature and HLF target gene expression were generated using the AddModuleScore of Seurat based on identified tissue $CD4^+$ T cell–up-regulated genes (Fig. 1C) and identified HLF target genes by ChIP-seq (Fig. 4E). Statistical comparisons between groups shown in the violin plots were performed using edgeR (v4.4.2) with a quasi-likelihood F test on pseudobulk expression values aggregated per patient sample (*68*).

For visualization of the coregulation network, the 350 genes that showed gene expression variation among each cell according to the FindVariableFeatures of Seurat based on the vst method were subjected to analyses. The similarities among the genes were calculated by Simpson's coefficient, and correlated genes with a value >0.8 were defined as neighbor genes. The network graph of 350 genes was visualized with Radial plot in yFiles Layout Algorithms (v1.1.2) using Cytoscape (*69*) (v3.7.1). Enrichment of tissue-resident and circulating T cell surface markers (*37*) was assessed by ssGSVA (GSVA v0.0.23, https://github.com/guokai8/scGSVA) using curated gene sets, and scores were projected onto UMAP and ridge plot.

Analysis of scATAC-seq data

Sequenced reads from all samples were processed and aggregated using the Cell Ranger ATAC pipeline (10x Genomics; v2.1.0) with alignment to the mouse reference genome mm10. The resulting peak-barcode count matrices and fragment files were imported into R and analyzed using the Signac (v1.14.0) (*70*) and Seurat packages. Chromatin accessibility assays were created using the CreateChromatinAssay function, and gene annotations were retrieved from EnsDb.Mmusculus.v79 using GetGRangesFromEnsDb, followed by the assignment of appropriate genome and chromosome prefixes.

For quality control, cells were filtered based on multiple metrics to remove low-quality or artifactual data. Specifically, we retained cells with >3000 and <100,000 peak region fragments, a fraction of reads in peaks >40%, a blacklist region ratio <0.025, a nucleosome signal <4, and a TSS enrichment score >2. After filtering, term frequency–inverse document frequency normalization and singular value decomposition were performed to reduce dimensionality. UMAP embedding was then applied using Latent semantic indexing components 2 through 30, and unsupervised clustering was conducted using the Louvain algorithm with a resolution parameter of 1.2. Cells were annotated based on experimental condition, distinguishing circulating from tissue-resident $CD4^+$ T cells, and visualized on UMAP plots.

To infer gene activity from accessible chromatin regions, gene activity scores were computed using the GeneActivity function and stored as a separate assay. These scores were used to visualize the chromatin-based expression pattern of specific genes using UMAP overlays generated in Seurat.

To further investigate chromatin accessibility at specific genomic loci, we generated pseudobulk coverage plots using the CoveragePlot function in Signac.

To predict transcriptional consequences of *Hlf* deletion, gene-regulatory network inference and in silico transcription factor perturbation were performed using CellOracle (*31*) and Cicero (*71*). Gene-regulatory networks were constructed from scATAC-seq and

scRNA-seq data using promoter-based motif scanning and coaccessibility analysis with the default parameters of Cicero. In silico deletion of *Hlf* was simulated, and vector field plots were generated to visualize the predicted direction and magnitude of cell-state transitions in $CD4^+$ T_{RM} cells.

Analysis and graphic display of RNA-seq data

A total of 10,899 genes in which the maximum fragments per kilobase of feature per million mapped reads (FPKM) value of each gene was ≥1.0 were included in further analyses. A MA plot was constructed using the R software program. On the basis of the results of RNA-seq, differentially expressed genes were identified using the DESeq2 package (v1.10.1) with a Wald test on pseudobulk expression values aggregated per sample (*72*). Genes with a log2 (fold change) >1 or <−1 and a P value < 0.01 were defined as differentially expressed genes.

For the visualization of the coregulation network, the 350 genes that showed gene expression variation among each cell according to the FindVariableFeatures algorithm of Seurat based on the vst method were subjected to analyses. The similarities of the genes were calculated by Simpson's coefficient, and correlated genes with a value >0.8 were defined as neighbor genes. The network graph of 350 genes was visualized with Radial plot in yFiles Layout Algorithms (v1.1.2) using Cytoscape (*69*) (v3.7.1).

For the analysis of published RNA-seq dataset from murine influenza A infection model, FPKM values were downloaded from the GEO (accession number GSE153226).

The analysis and graphic display of ChIP-seq and ATAC-seq data

The ATAC-seq and ChIP-seq data were mapped to the mouse genome build GRCm38 using Hisat2 (*73*) (v2.2.1). MACS2 (*74*) was used for peak calling and binding visualization; ChIP-seq parameters were set to window_size = 300, gap_size = 300, and false discovery rate (FDR) = 0.01. ATAC-seq parameters were window_size = 100, gap_size = 100, and FDR = 0.01. HOMER tag directories, which were created by the HOMER platform (*75*) (makeTagDirectory) from the aligned sequence alignment map (SAM) formats using SAMtools (*76*). Called peaks were annotated using the annotatePeaks.pl function in HOMER. Peaks commonly observed in ATAC-seq and ChIP-seq for 3xFlag-Hlf were called and subjected to downstream analyses using the mergePeaks function in HOMER. DARs were identified by using HOMER getDifferentialPeaks. BigWig files were generated from the aligned SAM or browser extensible data (BED) file formats using SAMtools, BEDtools (*77*), and deepTools 2.0 (*78*). The Integrative Genomics Viewer software program (*79*) was used for the visualization of BiGWig files. A motif enrichment analysis was performed with the findMotifsGenome.pl function in the HOMER package using a 200-bp window.

In Fig. 4 and fig. S12, genes with DARs closed or opened were defined as genes with at least one annotated DAR where any HLF-binding peak was detected.

Statistical analyses

Statistical parameters are reported in the figures and figure legends. Data were analyzed with GraphPad Prism 9 and the R platform. P values <0.05 were considered to indicate statistical significance. Comparisons between the two groups were performed using an unpaired t test, a one-way analysis of variance (ANOVA) with Tukey's multiple-comparisons test, or a two-way ANOVA with Tukey's multiple-comparisons test. In the case of pseudobulk transcriptomic data, statistical comparisons were performed using edgeR (scRNA-seq) with a quasi-likelihood F test or DESeq2 (RNA-seq) with a Wald test.

REFERENCES AND NOTES

1. T. Nakayama *et al.*, Th2 cells in health and disease. *Annu. Rev. Immunol.* **35**, 53–84 (2017). doi: 10.1146/annurev-immunol-051116-052350; pmid: 27912316
2. M. Ruterbusch, K. B. Pruner, L. Shehata, M. Pepper, In vivo CD4+ T cell differentiation and function: Revisiting the Th1/Th2 paradigm. *Annu. Rev. Immunol.* **38**, 705–725 (2020). doi: 10.1146/annurev-immunol-103019-085803; pmid: 32340571
3. S. C. Jameson, D. Masopust, Understanding subset diversity in T cell memory. *Immunity* **48**, 214–226 (2018). doi: 10.1016/j.immuni.2018.02.010; pmid: 29466754
4. J. T. Chang, E. J. Wherry, A. W. Goldrath, Molecular regulation of effector and memory T cell differentiation. *Nat. Immunol.* **15**, 1104–1115 (2014). doi: 10.1038/ni.3031; pmid: 25396352
5. D. Masopust, A. G. Soerens, Tissue-resident cells and other resident leukocytes. *Annu. Rev. Immunol.* **37**, 521–546 (2019). doi: 10.1146/annurev-immunol-042617-053214; pmid: 30726153
6. S. N. Mueller, L. K. Mackay, Tissue-resident memory T cells: Local specialists in immune defence. *Nat. Rev. Immunol.* **16**, 79–89 (2016). doi: 10.1038/nri.2015.3; pmid: 26688350
7. J. I. Gray, D. L. Farber, Tissue-resident immune cells in humans. *Annu. Rev. Immunol.* **40**, 195–220 (2022). doi: 10.1146/annurev-immunol-093019-112809; pmid: 35044795
8. M. Heeg, A. W. Goldrath, Insights into phenotypic and functional $CD8^+$ T_{RM} heterogeneity. *Immunol. Rev.* **316**, 8–22 (2023). doi: 10.1111/imr.13218; pmid: 37191051
9. B. D. Hondowicz *et al.*, Interleukin-2-dependent allergen-specific tissue-resident memory cells drive asthma. *Immunity* **44**, 155–166 (2016). doi: 10.1016/j.immuni.2015.11.004; pmid: 26750312
10. T. Yokoi *et al.*, Identification of a unique subset of tissue-resident memory $CD4^+$ T cells in Crohn's disease. *Proc. Natl. Acad. Sci. U.S.A.* **120**, e2204269120 (2023). doi: 10.1073/pnas.2204269120; pmid: 36574662
11. C. Porsbjerg, E. Melén, L. Lehtimäki, D. Shaw, Asthma. *Lancet* **401**, 858–873 (2023). doi: 10.1016/S0140-6736(22)02125-0; pmid: 36682372
12. J. J. Milner *et al.*, Runx3 programs $CD8^+$ T cell residency in non-lymphoid tissues and tumours. *Nature* **552**, 253–257 (2017). doi: 10.1038/nature24993; pmid: 29211713
13. J. T. Crowl *et al.*, Tissue-resident memory $CD8^+$ T cells possess unique transcriptional, epigenetic and functional adaptations to different tissue environments. *Nat. Immunol.* **23**, 1121–1131 (2022). doi: 10.1038/s41590-022-01229-8; pmid: 35761084
14. Y. H. Lin *et al.*, Small intestine and colon tissue-resident memory $CD8^+$ T cells exhibit molecular heterogeneity and differential dependence on Eomes. *Immunity* **56**, 207–223.e8 (2023). doi: 10.1016/j.immuni.2022.12.007; pmid: 36580919
15. L. K. Mackay *et al.*, Hobit and Blimp1 instruct a universal transcriptional program of tissue residency in lymphocytes. *Science* **352**, 459–463 (2016). doi: 10.1126/science.aad2035; pmid: 27102484
16. J. J. Milner *et al.*, Heterogenous populations of tissue-resident $CD8^+$ T cells are generated in response to infection and malignancy. *Immunity* **52**, 808–824.e7 (2020). doi: 10.1016/j.immuni.2020.04.007; pmid: 32433949
17. C. N. Skon *et al.*, Transcriptional downregulation of S1pr1 is required for the establishment of resident memory CD8+ T cells. *Nat. Immunol.* **14**, 1285–1293 (2013). doi: 10.1038/ni.2745; pmid: 24162775
18. P. A. Szabo, Axes of heterogeneity in human tissue-resident memory T cells. *Immunol. Rev.* **316**, 23–37 (2023). doi: 10.1111/imr.13210; pmid: 37211646
19. T. Ichikawa *et al.*, $CD103^{hi}$ T_{reg} cells constrain lung fibrosis induced by $CD103^{lo}$ tissue-resident pathogenic CD4 T cells. *Nat. Immunol.* **20**, 1469–1480 (2019). doi: 10.1038/s41590-019-0494-y; pmid: 31591568
20. K. G. Anderson *et al.*, Cutting edge: Intravascular staining redefines lung CD8 T cell responses. *J. Immunol.* **189**, 2702–2706 (2012). doi: 10.4049/jimmunol.1201682; pmid: 22896631
21. P. A. Szabo, M. Miron, D. L. Farber, Location, location, location: Tissue resident memory T cells in mice and humans. *Sci. Immunol.* **4**, eaas9673 (2019). doi: 10.1126/sciimmunol.aas9673; pmid: 30952804
22. C. Li *et al.*, The transcription factor Bhlhe40 programs mitochondrial regulation of resident CD8+ T cell fitness and functionality. *Immunity* **51**, 491–507.e7 (2019). doi: 10.1016/j.immuni.2019.08.013; pmid: 31533057
23. X. Zhou *et al.*, Differentiation and persistence of memory CD8(+) T cells depend on T cell factor 1. *Immunity* **33**, 229–240 (2010). doi: 10.1016/j.immuni.2010.08.002; pmid: 20727791
24. K. Komorowska *et al.*, Hepatic leukemia factor maintains quiescence of hematopoietic stem cells and protects the stem cell pool during regeneration. *Cell Rep.* **21**, 3514–3523 (2017). doi: 10.1016/j.celrep.2017.11.084; pmid: 29262330
25. M. Wahlestedt *et al.*, Critical modulation of hematopoietic lineage fate by hepatic leukemia factor. *Cell Rep.* **21**, 2251–2263 (2017). doi: 10.1016/j.celrep.2017.10.112; pmid: 29166614
26. T. Yokomizo *et al.*, Hlf marks the developmental pathway for hematopoietic stem cells but not for erythro-myeloid progenitors. *J. Exp. Med.* **216**, 1599–1614 (2019). doi: 10.1084/jem.20181399; pmid: 31076455
27. I. K. Brown *et al.*, Single cell analysis of host response to helminth infection reveals the clonal breadth, heterogeneity, and tissue-specific programming of the responding CD4+ T cell repertoire. *PLOS Pathog.* **17**, e1009602 (2021). doi: 10.1371/journal.ppat.1009602; pmid: 34106992
28. H. Xu *et al.*, Transcriptional atlas of intestinal immune cells reveals that neuropeptide α-CGRP modulates group 2 innate lymphoid cell responses. *Immunity* **51**, 696–708.e9 (2019). doi: 10.1016/j.immuni.2019.09.004; pmid: 31618654
29. Y. M. Son *et al.*, Tissue-resident $CD4^+$ T helper cells assist the development of protective respiratory B and $CD8^+$ T cell memory responses. *Sci. Immunol.* **6**, eabb6852 (2021). doi: 10.1126/sciimmunol.abb6852; pmid: 33419791

30. M. A. Wheeler *et al.*, MAFG-driven astrocytes promote CNS inflammation. *Nature* **578**, 593–599 (2020). doi: 10.1038/s41586-020-1999-0; pmid: 32051591
31. K. Kamimoto *et al.*, Dissecting cell identity via network inference and in silico gene perturbation. *Nature* **614**, 742–751 (2023). doi: 10.1038/s41586-022-05688-9; pmid: 36755098
32. F. Gachon *et al.*, The loss of circadian PAR bZip transcription factors results in epilepsy. *Genes Dev.* **18**, 1397–1412 (2004). doi: 10.1101/gad.301404; pmid: 15175240
33. M. Gury-BenAri *et al.*, The spectrum and regulatory landscape of intestinal innate lymphoid cells are shaped by the microbiome. *Cell* **166**, 1231–1246.e13 (2016). doi: 10.1016/j.cell.2016.07.043; pmid: 27545347
34. T. Kobayashi *et al.*, Homeostatic control of sebaceous glands by innate lymphoid cells regulates commensal bacteria equilibrium. *Cell* **176**, 982–997.e16 (2019). doi: 10.1016/j.cell.2018.12.031; pmid: 30712873
35. T. Y. F. Halim *et al.*, Group 2 innate lymphoid cells are critical for the initiation of adaptive T helper 2 cell-mediated allergic lung inflammation. *Immunity* **40**, 425–435 (2014). doi: 10.1016/j.immuni.2014.01.011; pmid: 24613091
36. M. Matloubian *et al.*, Lymphocyte egress from thymus and peripheral lymphoid organs is dependent on S1P receptor 1. *Nature* **427**, 355–360 (2004). doi: 10.1038/nature02284; pmid: 14737169
37. B. V. Kumar *et al.*, Human tissue-resident memory T cells are defined by core transcriptional and functional signatures in lymphoid and mucosal sites. *Cell Rep.* **20**, 2921–2934 (2017). doi: 10.1016/j.celrep.2017.08.078; pmid: 28930685
38. A. C. Habermann *et al.*, Single-cell RNA sequencing reveals profibrotic roles of distinct epithelial and mesenchymal lineages in pulmonary fibrosis. *Sci. Adv.* **6**, eaba1972 (2020). doi: 10.1126/sciadv.aba1972; pmid: 32832598
39. A. Garrido-Trigo *et al.*, Macrophage and neutrophil heterogeneity at single-cell spatial resolution in human inflammatory bowel disease. *Nat. Commun.* **14**, 4506 (2023). doi: 10.1038/s41467-023-40156-6; pmid: 37495570
40. M. Okano *et al.*, Interleukin-33-activated neuropeptide CGRP-producing memory Th2 cells cooperate with somatosensory neurons to induce conjunctival itch. *Immunity* **55**, 2352–2368.e7 (2022). doi: 10.1016/j.immuni.2022.09.016; pmid: 36272417
41. A. Zaid *et al.*, Persistence of skin-resident memory T cells within an epidermal niche. *Proc. Natl. Acad. Sci. U.S.A.* **111**, 5307–5312 (2014). doi: 10.1073/pnas.1322292111; pmid: 24706879
42. P. Hombrink *et al.*, Programs for the persistence, vigilance and control of human $CD8^+$ lung-resident memory T cells. *Nat. Immunol.* **17**, 1467–1478 (2016). doi: 10.1038/ni.3589; pmid: 27776108
43. T. Inaba *et al.*, Fusion of the leucine zipper gene HLF to the E2A gene in human acute B-lineage leukemia. *Science* **257**, 531–534 (1992). doi: 10.1126/science.1386162; pmid: 1386162
44. S. Garg *et al.*, Hepatic leukemia factor is a novel leukemic stem cell regulator in DNMT3A, NPM1, and FLT3-ITD triple-mutated AML. *Blood* **134**, 263–276 (2019). doi: 10.1182/blood.2018862383; pmid: 31076446
45. R. Gazit *et al.*, Transcriptome analysis identifies regulators of hematopoietic stem and progenitor cells. *Stem Cell Reports* **1**, 266–280 (2013). doi: 10.1016/j.stemcr.2013.07.004; pmid: 24319662
46. J. G. Cyster, S. R. Schwab, Sphingosine-1-phosphate and lymphocyte egress from lymphoid organs. *Annu. Rev. Immunol.* **30**, 69–94 (2012). doi: 10.1146/annurev-immunol-020711-075011; pmid: 22149932
47. S. K. Bromley, S. Y. Thomas, A. D. Luster, Chemokine receptor CCR7 guides T cell exit from peripheral tissues and entry into afferent lymphatics. *Nat. Immunol.* **6**, 895–901 (2005). doi: 10.1038/ni1240; pmid: 16116469
48. J. Wu *et al.*, T cell factor 1 suppresses CD103+ lung tissue-resident memory T cell development. *Cell Rep.* **31**, 107484 (2020). doi: 10.1016/j.celrep.2020.03.048; pmid: 32268106
49. L. K. Mackay *et al.*, Cutting edge: CD69 interference with sphingosine-1-phosphate receptor function regulates peripheral T cell retention. *J. Immunol.* **194**, 2059–2063 (2015). doi: 10.4049/jimmunol.1402256; pmid: 25624457
50. L. Kok, D. Masopust, T. N. Schumacher, The precursors of $CD8^+$ tissue resident memory T cells: From lymphoid organs to infected tissues. *Nat. Rev. Immunol.* **22**, 283–293 (2022). doi: 10.1038/s41577-021-00590-3; pmid: 34480118
51. M. M. L. Poon *et al.*, Tissue adaptation and clonal segregation of human memory T cells in barrier sites. *Nat. Immunol.* **24**, 309–319 (2023). doi: 10.1038/s41590-022-01395-9; pmid: 36658238
52. M. Reina-Campos *et al.*, Metabolic programs of T cell tissue residency empower tumour immunity. *Nature* **621**, 179–187 (2023). doi: 10.1038/s41586-023-06483-w; pmid: 37648857
53. Q. P. Nguyen *et al.*, Transcriptional programming of $CD4^+$ T_{RM} differentiation in viral infection balances effector- and memory-associated gene expression. *Sci. Immunol.* **8**, eabq7486 (2023). doi: 10.1126/sciimmunol.abq7486; pmid: 37172104
54. S. Zundler *et al.*, Hobit- and Blimp-1-driven $CD4^+$ tissue-resident memory T cells control chronic intestinal inflammation. *Nat. Immunol.* **20**, 288–300 (2019). doi: 10.1038/s41590-018-0298-5; pmid: 30692620
55. C.-C. Lin *et al.*, IL-1-induced Bhlhe40 identifies pathogenic T helper cells in a model of autoimmune neuroinflammation. *J. Exp. Med.* **213**, 251–271 (2016). doi: 10.1084/jem.20150568; pmid: 26834156
56. M. E. Cook, N. N. Jarjour, C.-C. Lin, B. T. Edelson, Transcription factor Bhlhe40 in immunity and autoimmunity. *Trends Immunol.* **41**, 1023–1036 (2020). doi: 10.1016/j.it.2020.09.002; pmid: 33039338
57. J. Henriksson *et al.*, Genome-wide CRISPR screens in T helper cells reveal pervasive crosstalk between activation and differentiation. *Cell* **176**, 882–896.e18 (2019). doi: 10.1016/j.cell.2018.11.044; pmid: 30639098
58. A. Shimba *et al.*, Glucocorticoids drive diurnal oscillations in T cell distribution and responses by inducing interleukin-7 receptor and CXCR4. *Immunity* **48**, 286–298.e6 (2018). doi: 10.1016/j.immuni.2018.01.004; pmid: 29396162
59. Y. Maekawa *et al.*, Notch controls the survival of memory CD4+ T cells by regulating glucose uptake. *Nat. Med.* **21**, 55–61 (2015). doi: 10.1038/nm.3758; pmid: 25501905
60. X. Chi *et al.*, RORα is critical for mTORC1 activity in T cell-mediated colitis. *Cell Rep.* **36**, 109682 (2021). doi: 10.1016/j.celrep.2021.109682; pmid: 34525365
61. Y. Morimoto *et al.*, Amphiregulin-producing pathogenic memory T helper 2 cells instruct eosinophils to secrete osteopontin and facilitate airway fibrosis. *Immunity* **49**, 134–150.e6 (2018). doi: 10.1016/j.immuni.2018.04.023; pmid: 29958800
62. A. C. Valladao, C. W. Frevert, L. K. Koch, D. J. Campbell, S. F. Ziegler, STAT6 regulates the development of eosinophilic versus neutrophilic asthma in response to *Alternaria alternata*. *J. Immunol.* **197**, 4541–4551 (2016). doi: 10.4049/jimmunol.1600007; pmid: 27815425
63. M. Kiuchi *et al.*, The Cxxc1 subunit of the Trithorax complex directs epigenetic licensing of CD4+ T cell differentiation. *J. Exp. Med.* **218**, e20201690 (2021). doi: 10.1084/jem.20201690; pmid: 33433611
64. K. Kokubo *et al.*, Thioredoxin-interacting protein is essential for memory T cell formation via the regulation of the redox metabolism. *Proc. Natl. Acad. Sci. U.S.A.* **120**, e2218345120 (2023). doi: 10.1073/pnas.2218345120; pmid: 36595680
65. Y. Hao *et al.*, Dictionary learning for integrative, multimodal and scalable single-cell analysis. *Nat. Biotechnol.* **42**, 293–304 (2024). doi: 10.1038/s41587-023-01767-y; pmid: 37231261
66. M. D. Young, S. Behjati, SoupX removes ambient RNA contamination from droplet-based single-cell RNA sequencing data. *Gigascience* **9**, giaa151 (2020). doi: 10.1093/gigascience/giaa151; pmid: 33367645
67. P. L. Germain, A. Lun, C. Garcia Meixide, W. Macnair, M. D. Robinson, Doublet identification in single-cell sequencing data using *scDblFinder*. *F1000 Res.* **10**, 979 (2021). doi: 10.12688/f1000research.73600.1; pmid: 35814628
68. Y. Chen, L. Chen, A. T. L. Lun, P. L. Baldoni, G. K. Smyth, edgeR v4: Powerful differential analysis of sequencing data with expanded functionality and improved support for small counts and larger datasets. *Nucleic Acids Res.* **53**, gkaf018 (2025). doi: 10.1093/nar/gkaf018; pmid: 39844453
69. P. Shannon *et al.*, Cytoscape: A software environment for integrated models of biomolecular interaction networks. *Genome Res.* **13**, 2498–2504 (2003). doi: 10.1101/gr.1239303; pmid: 14597658
70. T. Stuart, A. Srivastava, S. Madad, C. A. Lareau, R. Satija, Single-cell chromatin state analysis with Signac. *Nat. Methods* **18**, 1333–1341 (2021). doi: 10.1038/s41592-021-01282-5; pmid: 34725479
71. H. A. Pliner *et al.*, Cicero predicts cis-regulatory DNA interactions from single-cell chromatin accessibility data. *Mol. Cell* **71**, 858–871.e8 (2018). doi: 10.1016/j.molcel.2018.06.044; pmid: 30078726
72. M. I. Love, W. Huber, S. Anders, Moderated estimation of fold change and dispersion for RNA-seq data with DESeq2. *Genome Biol.* **15**, 550 (2014). doi: 10.1186/s13059-014-0550-8; pmid: 25516281
73. D. Kim, J. M. Paggi, C. Park, C. Bennett, S. L. Salzberg, Graph-based genome alignment and genotyping with HISAT2 and HISAT-genotype. *Nat. Biotechnol.* **37**, 907–915 (2019). doi: 10.1038/s41587-019-0201-4; pmid: 31375807
74. T. Liu, Use model-based Analysis of ChIP-Seq (MACS) to analyze short reads generated by sequencing protein-DNA interactions in embryonic stem cells. *Methods Mol. Biol.* **1150**, 81–95 (2014). doi: 10.1007/978-1-4939-0512-6_4; pmid: 24743991
75. S. Heinz *et al.*, Simple combinations of lineage-determining transcription factors prime cis-regulatory elements required for macrophage and B cell identities. *Mol. Cell* **38**, 576–589 (2010). doi: 10.1016/j.molcel.2010.05.004; pmid: 20513432
76. P. Danecek *et al.*, Twelve years of SAMtools and BCFtools. *Gigascience* **10**, giab008 (2021). doi: 10.1093/gigascience/giab008; pmid: 33590861
77. A. R. Quinlan, I. M. Hall, BEDTools: A flexible suite of utilities for comparing genomic features. *Bioinformatics* **26**, 841–842 (2010). doi: 10.1093/bioinformatics/btq033; pmid: 20110278
78. F. Ramírez *et al.*, deepTools2: A next generation web server for deep-sequencing data analysis. *Nucleic Acids Res.* **44**, W160–W165 (2016). doi: 10.1093/nar/gkw257; pmid: 27079975
79. S. Mingrino, G. Salar, M. Scanarini, Long-term results of non-operative management of ruptured intracranial aneurysms. *J. Neurosurg. Sci.* **19**, 54–58 (1975). pmid: 1221095
80. M. Kiuchi *et al.*, Code for: Hepatic leukemia factor directs tissue residency of proinflammatory memory $CD4^+$ T cells, Dryad (2025); https://doi.org/10.5061/dryad.6djh9w1f8.

ACKNOWLEDGMENTS

We thank K. Sugaya for technical assistance. **Funding:** This work was supported by the Ministry of Education, Culture, Sports, Science, and Technology (MEXT Japan) [Grant-in-Aid for Scientific Research (S) JP19H05650 to T.N.; (B) JP20H03685 and JP23H02916 to K.H.; Grants-in-Aid for Young Scientists JP19K16683 and JP22K15485 to M.K.; and Transformative Research Areas (B) JP21H05120 and JP21H05121 to K.H.]; the Japan Agency for Medical Research and Development (AMED) [Practical Research Project for Allergic Diseases and Immunology (Research on Allergic Diseases and Immunology) JP21ek0410060 to T.N.; JP19ek0410045, JP22ek0410082, and JP24ek0410092 to K.H.; AMED-PRIME JP20g6110005 to K.H.; AMED-CREST JP23g1210003 to T.N.; JP24g1810009 to K.H.; AMED-SCARDA Synergy Institute for Futuristic Mucosal Vaccine Research and Development (cSIMVa) JP223fa627003 to K.H.; AMED-LEAP (Leading Advanced Projects for Medical Innovation) JP24 g0010011 to K.H.; Research Program on Emerging and Re-emerging Infectious Diseases JP23fk0210134 to H.U.; and Vaccine Development Support Program JP243fa627009 to H.U.]; the Mochida Memorial Foundation for Medical and Pharmaceutical Research (K.H.); MSD Life Science Foundation (K.H.); the Naito Foundation (K.H.), Takeda Science Foundation (K.H.); Chiba University Future Medicine Education and Research Organization (Early-Stage Medical and Pharmaceutical Research grant to M.K.); the Future Medicine Grant Program, Chiba University Future Medicine Fund (M.K.); and the Japan Science and Technology Agency (JST) JPMJFR200R to K.H. **Author contributions:** M.K., M.N., H.Y., T.N. and K.H. designed the experiments. M.K., M.N., H.Y., A.A., C.I., Y.M., H.M., S.Ma., Y.O., T.Hi., K.T., A.S., K.K., K.O., Y.K., H.U., and K.H. performed the experiments. Y.M., H.M., S.Ma., Y.O., R.S., Y.S., T.I., S.Y., S.O., T.I., E.H., T.T., T.S., H.U., and T.Ha. provided human samples. T.Y. and N.K. provided mice. M.K., M.N., H.Y., A.A., C.I., H.S., Y.M., H.M., S.Mo., Y.O., A.O., E.K., H.U., and K.H. analyzed and interpreted the data. A.O., Y.K., N.M., M.Y.K., S.Mo., and D.J.T. contributed through discussions. M.K., M.N., H.Y., H.S., D.J.T., T.N., and K.H. wrote the manuscript. T.N. and K.H. supervised the project. **Competing interests:** The authors declare no competing interests. **Data and materials availability:** All data needed to evaluate the conclusions in the paper are present in the main text or the supplementary materials. Sequencing data reported in this paper have been deposited at the Gene Expression Omnibus (GEO) with the accession numbers GSE295436 and GSE295553. The code generated to support the findings of this study have been deposited in Dryad (*80*). *Hlf-tdTomato* reporter mice are available from the CARD Mouse Bank at the Institute of Resource Development and Analysis, Kumamoto University (CARD ID: 3261). **License information:** Copyright © 2025 the authors, some rights reserved; exclusive licensee American Association for the Advancement of Science. No claim to original US government works. https://www.science.org/about/science-licenses-journal-article-reuse

SUPPLEMENTARY MATERIALS

science.org/doi/10.1126/science.adp0714
Figs. S1 to S20; Tables S1 and S2; MDAR Reproducibility Checklist

Submitted 6 March 2024; resubmitted 17 April 2025; accepted 2 September 2025
10.1126/science.adp0714

Your Legacy to Science

AN ESTATE GIFT TO THE
AMERICAN ASSOCIATION FOR THE ADVANCEMENT OF SCIENCE





Since 1848, our founding year, the American Association for the Advancement of Science (AAAS) has been deeply committed to advancing science, engineering and innovation around the world for the benefit of all people.

By making AAAS a beneficiary of your will, trust, retirement plan or life insurance policy, you become a member of our 1848 Society, joining Thomas Edison, Alexander Graham Bell and the many distinguished individuals whose vision led to the creation of AAAS and our world-renowned journal, *Science*, so many years ago.

Unlike many of its peers, *Science* is not for-profit. Your estate gift would provide long-term financial stability and durable annual income that will support operations and competitive innovation for years to come. **This support is vital.**

"As a teacher and instructor, I bear responsibility for the younger generations. If you have extra resources, concentrate them on organizations, like AAAS, that are doing work for all."

—Prof. Elisabeth Ervin-Blankenheim, 1848 Society member

If you intend to include AAAS in your estate plans, provide this information to your lawyer or financial adviser:

Legal Name: American Association for the Advancement of Science
Federal Tax ID Number: 53-0196568
Address: 1200 New York Avenue, NW, Washington, DC 20005

If you would like more information on making an estate gift to AAAS, cut out and return the form below or send an email to philanthropy@aaas.org. Additional details are also available online at **www.aaas.org/1848Society**.

1848 SOCIETY AAAS

cut here

Yes, I would like more information about joining the AAAS 1848 Society.

PLEASE CONTACT ME AT:

Name: _____

Address: _____

City: _____ State: _____ Zip code: _____ Country: _____

Email: _____ Phone: _____

RETURN THIS FORM TO:
AAAS Office of Philanthropy and Strategic Partnerships • 1200 New York Avenue, NW • Washington, DC 20005 USA

RESEARCH ARTICLE SUMMARY

NEUROSCIENCE

Cortical glutamatergic and GABAergic inputs support learning-driven hippocampal stability

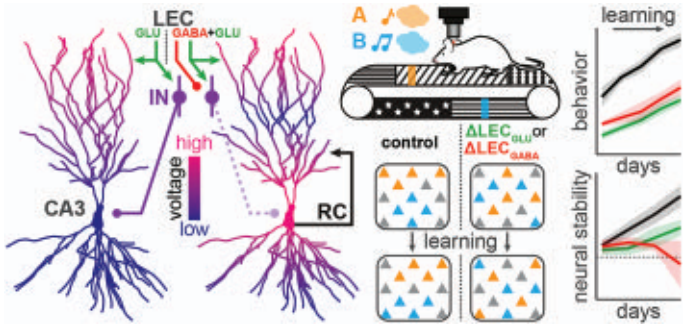
Vincent Robert, Keelin O'Neil, Jason J. Moore, Shannon K. Rashid, Cara D. Johnson, Rodrigo G. De La Torre, Boris V. Zemelman, Claudia Clopath, Jayeeta Basu*

Full article and list of author affiliations: https://doi.org/10.1126/science.adn0623

INTRODUCTION: The brain encodes memories through the activation of specific ensembles of neurons. Memory formation and recall require both flexibility and stability of neuronal ensembles. How do long-range connections interact with local circuits to form flexible yet stable ensembles? Projections across brain regions are chemically diverse, notably comprising both glutamatergic and γ-aminobutyric acid–ergic (GABAergic) neurons in memory circuits, such as those between the entorhinal cortex (EC) and hippocampus. Hippocampal pyramidal neurons (PNs) integrate sensory information from EC to form internal representations of the environment. These place-cell ensembles display both flexibility and stability of their spatial tuning depending on environmental variability, allowing for adaptive learned behaviors and memory recall from partial cues. Recurrent connections within the CA3 hippocampal subregion are well suited to form and reactivate neuronal ensembles during learning and recall. However, the influence of long-range EC inputs on the function of the CA3 local circuit remains underexplored. Therefore, we examined the role of lateral EC (LEC) glutamatergic (LEC_{GLU}) and GABAergic (LEC_{GABA}) inputs on driving CA3 activity and learning-associated ensemble coding.

RATIONALE: CA3 neuronal ensembles display context-dependent place-map dynamics, but their mnemonic contributions and underlying circuit mechanisms are not sufficiently understood. We hypothesized that LEC, which conveys contextual information to the hippocampus, may shape CA3 ensemble activity to support learning. Recent research described the role of LEC inputs to hippocampal area CA1 in modulating dendritic excitability, synaptic plasticity, and contextual memory. However, the conjunctive roles of LEC_{GLU} and LEC_{GABA} inputs to the hippocampus remain to be explored, and their interactions with CA3 recurrent connections and ensemble dynamics are unknown. Here, we leveraged multiplexed optogenetic and chemogenetic approaches to manipulate LEC_{GLU} and LEC_{GABA} inputs to CA3 simultaneously and decipher their impact on single-neuron and ensemble activity with compartment-specific ex vivo electrophysiology and in vivo two-photon imaging during a spatial-contextual learning behavior in mice.

RESULTS: Using dual-color optogenetics combined with intracellular somatic and dendritic recordings, we mapped the functional connectivity from LEC_{GLU} and LEC_{GABA} inputs to CA3. LEC_{GLU} drove excitation in CA3 PNs but also substantial feedforward inhibition that prevented somatic and dendritic spikes. LEC_{GABA} exclusively inhibited a subset of soma-targeting local CA3 inhibitory neurons recruited by LEC_{GLU}, thereby reducing feedforward inhibition onto CA3 PNs. This LEC_{GABA}-mediated disinhibition selectively increased CA3 PN somatic, but not dendritic, spiking in response to integrated LEC_{GLU} and CA3 feedback but not DG feedforward inputs. Using dual-chemogenetic silencing of CA3-projecting LEC_{GLU} or LEC_{GABA} and two-photon calcium imaging of CA3 PN somas and dendrites, we tested how this circuit supports memory-related ensemble activity and behavior. Head-fixed mice were trained in a goal-oriented learning task that required spatial-contextual associations in different environments with graded degrees of similarity. Behavioral task performance was impaired with either LEC_{GLU} or LEC_{GABA} silencing during learning but not during recall. In control conditions, CA3 somatic and dendritic ensembles differentially remapped between distinct environments and became more correlated within each environment with learning. Silencing of either LEC_{GLU} or LEC_{GABA} destabilized CA3 place maps, thereby reducing the contrast in spatial representations of different environments and preventing their stabilization associated with learning. Computational modeling of CA3 assembly formation showed that both LEC_{GLU} and LEC_{GABA} silencing could impair reactivation despite their differences in circuit organization.



Cortical inputs support hippocampal stability. On the left, LEC_{GLU} input excites hippocampal CA3 dendrites and inhibitory neurons (INs) that prevent somatic activity. LEC_{GABA} input relieves CA3 somas from inhibition, allowing recurrent circuit (RC) activity. On the right, chemogenetic silencing (Δ) reveals that both LEC inputs contribute to stabilizing CA3 neuronal ensembles as mice learn to navigate in different environments (A versus B) based on spatial-contextual associations.

CONCLUSION: LEC_{GLU} and LEC_{GABA} long-range inputs synergistically drive CA3 local excitatory, inhibitory, and disinhibitory circuit dynamics in a pathway- and compartment-specific manner. The resultant boost in CA3 recurrent activity helps stabilize CA3 place maps, supporting discrimination between environments and learning of spatial-contextual associations. □

*Corresponding author. Email: jayeeta.basu@nyulangone.org Cite this article as V. Robert *et al.*, *Science* **390**, eadn0623 (2025). DOI: 10.1126/science.adn0623

NEUROSCIENCE

Cortical glutamatergic and GABAergic inputs support learning-driven hippocampal stability

Vincent Robert[1], Keelin O'Neil[1], Jason J. Moore[1], Shannon K. Rashid[1], Cara D. Johnson[1], Rodrigo G. De La Torre[1], Boris V. Zemelman[2], Claudia Clopath[3], Jayeeta Basu[1,4,5]*

Flexibility and stability of neuronal ensembles are crucial features of brain function. Little is known about how these properties of local circuits are influenced by long-range inputs. We show, in mice, that lateral entorhinal cortex glutamatergic (LEC_{GLU}) and γ-aminobutyric acid (GABA)–ergic (LEC_{GABA}) projections to CA3 recruit specific microcircuits that conjunctively provide stability to neuronal ensembles, thereby supporting learning. LEC_{GLU} drives excitation in CA3 but also substantial feedforward inhibition that prevents somatic and dendritic spikes. Conversely, LEC_{GABA} suppresses this local inhibition to disinhibit CA3 activity with compartment and pathway specificity by selectively boosting somatic output to integrated LEC_{GLU} and CA3 recurrent inputs. This synergy allows the stabilization of spatial representations relevant to learning, as both LEC_{GLU} and LEC_{GABA} control the formation and maintenance of CA3 place cells across contexts and over time.

The brain encodes memories through the activation of specific ensembles of neurons to support behaviors critical for survival. Formation and recall of these representations require both flexibility and stability of ensembles. Within the hippocampus, place-cell ensembles can rapidly change their spatial tuning in response to differences in the environment (*1*–*4*). This phenomenon, known as remapping, allows for adaptive learned behaviors (*5*–*8*). Conversely, reliable navigation and memory recall from partial cues require that hippocampal place maps remain stable, withstanding some degree of environmental change (*9*–*13*). Principal neurons in the hippocampus integrate multimodal inputs from the entorhinal cortex (EC) to form these internal representations of the environment. However, it remains unclear how the organization and function of this long-range circuit support the dynamic interplay between flexibility and stability of representations.

Aside from canonical glutamatergic inputs, EC sends direct long-range γ-aminobutyric acid–ergic (GABAergic) projections to the hippocampus (*14*, *15*). Long-range GABAergic connections play key roles in dendritic excitability, oscillatory synchronization, synaptic plasticity, context discrimination, and top-down control (*14*–*20*). Specifically, the lateral EC (LEC) encodes information about contextual features such as objects, odors, novelty, and salient rewards or punishments to support goal-directed behaviors (*14*, *21*–*30*). Perturbations of LEC activity disrupt learning (*31*–*33*) and impair rate remapping of hippocampal area CA3 (*34*). CA3 pyramidal neurons (PNs) receive stratified dendritic input from many different sources. These include (i) the direct inputs to distal dendrites from EC that convey multisensory contextual, spatial, and cognitive information; (ii) the feedforward processed inputs from the dentate gyrus (DG) to proximal dendrites thought to provide orthogonalized information (*35*–*47*); and (iii) the feedback inputs from within CA3/2 through recurrent collaterals (RCs) upon medial and basal dendrites implicated in attractor dynamics (*35*, *38*, *45*, *48*–*54*). Even with the convergence of multiple inputs, CA3 PNs do not readily display spike output, in part owing to their intrinsic properties (*55*). How long-range glutamatergic and GABAergic inputs interact with local circuitry to support network-wide computations remains an open question. Mechanistically, how are the various inputs to CA3 gated to modulate output and information transfer?

To answer this, we examined LEC long-range glutamatergic (LEC_{GLU}) and GABAergic (LEC_{GABA}) inputs to CA3 and their interactions with local circuits at the single-cell and subcellular levels in mice, with dendritic and somatic patch-clamp electrophysiology and dual-color optogenetics. To link this circuit organization to behaviorally relevant CA3 activity, we examined the independent influence of LEC_{GLU} and LEC_{GABA} inputs on neuronal ensemble dynamics during learning and recall. For this, we used in vivo two-photon calcium imaging during a goal-oriented learning (GOL) behavioral task with cell type–specific chemogenetic manipulations. Lastly, based on our experimental findings, we present a computational model of how long-range LEC_{GLU} and LEC_{GABA} and local CA3 circuit interactions shape learning-driven stabilization in the recurrent network.

LEC_{GLU} and LEC_{GABA} drive excitation and inhibition in CA3 pyramidal cells and interneurons

LEC sends LEC_{GLU} and LEC_{GABA} projections to the hippocampus, but their synaptic targets in area CA3 are unknown. To map LEC inputs to CA3, we expressed CaMKII-driven-Chronos-GFP [(*56*); GFP, green fluorescent protein] in LEC_{GLU} and Syn-driven-flexed-ChrimsonR-tdTomato (*56*) in LEC_{GABA} by stereotaxic injection of viral vectors into LEC of GAD2-Cre mice (Fig. 1A). LEC_{GLU} (GFP^+) and LEC_{GABA} ($TdTomato^+$) axons projected to the distal dendritic layer [stratum lacunosum moleculare (SLM)] of area CA3 (Fig. 1B). Most experiments used this dual-optogenetic approach with appropriate parameters (fig. S1) within the same animals, and similar innervation patterns were observed with independent mapping of ChR2-eYFP–expressing (*57*) LEC_{GLU} and LEC_{GABA} in separate animals [fig. S2, A and B; eYFP, enhanced yellow fluorescent protein]. LEC_{GLU} innervation was denser than its LEC_{GABA} counterpart across the hippocampus (fig. S2C). To establish functional connectivity from LEC to CA3, we optogenetically stimulated LEC_{GLU} and LEC_{GABA} while performing patch-clamp recordings from CA3 neurons ex vivo (Fig. 1A). LEC_{GLU} stimulation elicited excitatory and inhibitory postsynaptic currents (EPSCs and IPSCs) in CA3 PNs (Fig. 1C). Application of tetrodotoxin (TTX) and 4-aminopyridine (4-AP) (*58*) spared EPSCs but abolished IPSCs, revealing that LEC_{GLU} drives direct monosynaptic excitation and feedforward polysynaptic inhibition in CA3 PNs (Fig. 1C and fig. S2D). Application of 2,3-dihydroxy-6-nitro-7-sulfamoyl-1,4-benzo[f]quinoxaline (NBQX) and 2-amino-5-phosphonovaleric acid (APV) abolished both LEC_{GLU}-driven EPSCs and IPSCs, confirming glutamatergic transmission (Fig. 1C and fig. S2E) and feedforward inhibition. By contrast, LEC_{GABA} stimulation failed to elicit postsynaptic responses in CA3 PNs, as probed by somatic and dendritic patch-clamp recordings (Fig. 1, C to E, and fig. S2, F and G) as well as dendritic extracellular local field potentials (fig. S2H). However, we found that a subset of CA3 interneurons (INs) with somatic location in SLM received convergent input from both LEC_{GLU} and LEC_{GABA} (Fig. 1, F and G, and fig. S2I). LEC_{GLU}-evoked EPSCs in CA3 INs were glutamatergic, as they were blocked by NBQX and APV (Fig. 1F). Application of the $GABA_AR$ (GABA type A receptor) and $GABA_BR$ (GABA type B receptor) antagonists SR95531 (SR) and CGP55845 (CGP) abolished LEC_{GABA}-evoked IPSCs in CA3 INs, confirming their GABAergic nature (Fig. 1G and fig. S2J). Whereas LEC_{GLU} targeted most CA3 PNs and INs (Fig. 1, E and H), LEC_{GABA} connected with only a fraction of CA3 INs (Fig. 1H) with

[1]Neuroscience Institute, Department of Neuroscience, New York University Grossman School of Medicine, New York, NY, USA. [2]Center for Learning and Memory, The University of Texas at Austin, Austin, TX, USA. [3]Department of Bioengineering, Imperial College London, London, UK. [4]Department of Psychiatry, New York University Grossman School of Medicine, New York, NY, USA. [5]Center for Neural Science, New York University, New York, NY, USA. *Corresponding author. Email: jayeeta.basu@nyulangone.org

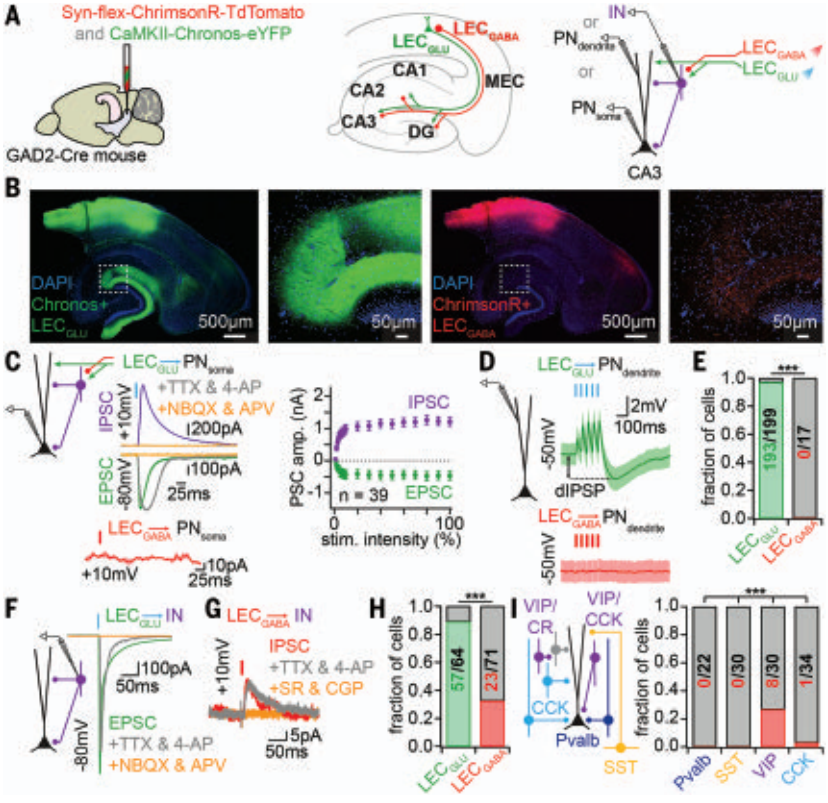


Fig. 1. LEC_{GLU} and LEC_{GABA} connectivity to area CA3. (**A**) Adeno-associated virus (AAV) injection of CaMKII-driven and Syn-driven-flexed opsins into LEC of GAD2-Cre mice (left) allows expression of Chronos-GFP in LEC_{GLU} and ChrimsonR-tdTomato in LEC_{GABA} projections to the hippocampus (middle), enabling input-specific dual-optogenetic circuit mapping in area CA3 with ex vivo patch-clamp electrophysiology (right). (**B**) Sample confocal fluorescence images with injection site of AAVs targeting LEC_{GLU} (left; Chronos-GFP, green) and LEC_{GABA} (right; ChrimsonR-tdTomato, red) neurons and their projections to CA3 SLM (expanded views of area demarcated by white dashed outline), with 4′,6-diamidino-2-phenylindole (DAPI) staining (blue). (**C**) At the top left are sample traces of LEC_{GLU}-driven CA3 PN postsynaptic responses in ACSF (EPSC, green; IPSC, purple), TTX and 4-AP (gray), and NBQX and APV (orange). At the bottom left are sample traces of CA3 PN somas under voltage clamp at +10 mV upon LEC_{GABA} stimulation. At the right are input-output curves of LEC_{GLU}-evoked CA3 PN EPSC (green) and IPSC (purple) amplitudes (amp.) with increasing stimulation (stim.) intensity. (**D**) Sample traces of CA3 PN dendrites held at −50 mV under current clamp upon LEC_{GLU} stimulation (top; dIPSP, dendritic inhibitory postsynaptic potential) and LEC_{GABA} stimulation (bottom). (**E**) Fraction of CA3 PNs receiving LEC_{GLU} and LEC_{GABA} inputs (χ^2 test, $p < 0.001$). (**F**) Sample traces of LEC_{GLU}-evoked CA3 IN EPSCs in ACSF (green), TTX and 4-AP (gray), and NBQX and APV (orange). (**G**) Sample traces of LEC_{GABA}-evoked CA3 IN IPSCs in ACSF (red), TTX and 4-AP (gray), and SR and GCP (orange). (**H**) Fraction of CA3 INs receiving LEC_{GLU} and LEC_{GABA} inputs. (**I**) Fraction of Pvalb (navy blue), SST (yellow), VIP (purple), and CCK (cyan blue) INs receiving LEC_{GABA} input (χ^2 test, $p < 0.001$). For applicable panels, error bars and shaded regions around plot lines represent SEM. ***$p < 0.001$.

a somatic location in SLM, which we further characterized as vasoactive intestinal peptide (VIP)– and putatively cholecystokinin (CCK)–expressing (Fig. 1I and fig. S3). VIP- and CCK-coexpressing INs in CA1 and cortex are a subpopulation of basket cells with somatic location in distal dendritic layers and perisomatic axonal projections (*59*–*64*), suggesting that LEC_{GABA} may selectively disinhibit the somatic compartment of CA3 PNs.

Inhibition gates the recruitment of CA3 PNs by LEC_{GLU}

CA3 PNs are leaky integrators that require high levels of input to reach the firing threshold (*55*) and are embedded in a complex microcircuit that involves DG mossy fibers (MFs) and CA2/3 RCs. Therefore, the influence of LEC_{GLU}-driven distal dendritic excitation and substantial feedforward inhibition on their input-output transformation is not trivial. To examine the contributions of LEC inputs to CA3 output, we monitored CA3 PN postsynaptic potentials (PSPs) in response to LEC_{GLU} optogenetic stimulation, as well as electrical stimulations of local DG (DCG-IV sensitive; fig. S4A) and RC inputs. Although PSP amplitude increased with input strength, CA3 PNs did not fire action potentials in response to any given input single-pulse stimulation (Fig. 2A and fig. S4B). However, blocking GABA receptors allowed LEC_{GLU} input to evoke CA3 PN action potential firing (Fig. 2A). This could stem from relieving CA3 PNs from LEC_{GLU}-driven feedforward inhibition and recruiting additional excitation in the hippocampal network. We therefore examined CA3 PN EPSC input-output curves in response to LEC_{GLU} stimulation in baseline [artificial cerebrospinal fluid (ACSF)], inhibition-blocked (SR and CGP), and monosynaptic-only (TTX and 4-AP) conditions (Fig. 2B and fig. S4, C to E). Increasing LEC_{GLU} input strength yielded multipeaked EPSCs, which further extended with GABAergic transmission blocked (Fig. 2B), indicating that inhibition indeed curtails LEC_{GLU}-driven excitation onto CA3. Such multipeaked EPSCs could be evoked with optogenetic stimulation of LEC_{GLU} above 3% (0.21 mW/mm^2) light-emitting diode (LED) intensity in regular ACSF, thus suggesting that strong LEC_{GLU} drive can recruit polysynaptic excitation from DG and/or CA3/2. Conversely, monosynaptic LEC_{GLU} input could be probed with 2% LED power (0.14 mW/mm^2) in our experimental conditions (Fig. 2B). We confirmed this by testing low and high LEC_{GLU} stimulation intensity while probing extracellular population spikes in DG and CA3, summation of repeated LEC_{GLU} activation, and occlusion of CA3 PN output in response to combined LEC_{GLU} and MF or RC input stimulation (figs. S4 and S5 and supplementary text S1).

LEC_{GABA} decreases feedforward inhibition in CA3 PNs

We next asked whether LEC_{GABA} modulates feedforward inhibition in CA3. Indeed, LEC_{GABA} disinhibits PN dendritic excitability in CA1 (*14*). Thus, we monitored CA3 SLM IN spike output to stimulation of LEC_{GLU} alone or with LEC_{GABA} and found that LEC_{GABA} decreased CA3 IN action potential firing to LEC_{GLU} input (Fig. 2C). This suggests that LEC_{GABA} likely disinhibits CA3 PNs. We tested this by recording LEC_{GLU}-evoked IPSCs in CA3 PNs alone or with coincident activation of LEC_{GABA}. LEC_{GABA} indeed decreased LEC_{GLU}-driven feedforward inhibition onto CA3 PNs (Fig. 2D). Although LEC_{GABA}-connected CA3 SLM INs received strong RC but weak DG excitation (fig. S6A), both DG- and RC-driven inhibition were unaffected by LEC_{GABA} stimulation (fig. S6, B and C). These results suggest that LEC_{GABA} may disinhibit CA3 PNs by selectively reducing LEC_{GLU}-driven feedforward inhibition. To test whether LEC_{GABA}-mediated disinhibition promotes CA3 PN compartment-specific excitation, we recorded CA3 PN somas or dendrites and repeatedly activated LEC_{GLU} monosynaptic input either alone or combined with LEC_{GABA} (Fig. 2, E and F). Surprisingly, we found no significant difference in PSP amplitude and spike probability in response to LEC_{GLU} alone or with LEC_{GABA} in both somas and dendrites (Fig. 2, E and F).

LEC_{GABA} selectively boosts CA3 PN somatic output through input-specific disinhibition

As LEC_{GLU} may require excitatory input summation combined with relief from inhibition to drive CA3 PN output, we asked whether LEC_{GABA}-mediated disinhibition would promote the integration of

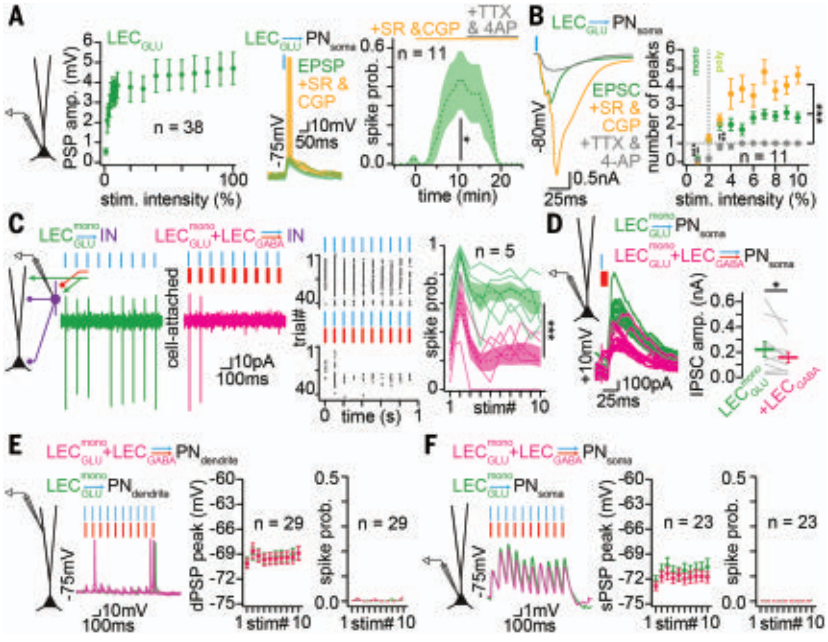


Fig. 2. Input-output transformation of LEC_{GLU} and LEC_{GABA} projections to CA3. (**A**) Input-output curve of LEC_{GLU}-evoked CA3 PN PSP amplitudes (left), sample traces of LEC_{GLU}-evoked CA3 PN PSPs and spikes in ACSF (green) and SR and CGP (orange) (middle), and the time course of LEC_{GLU}-evoked CA3 PN spike probability (spike probability in SR and CGP: $n = 11$, one-sample t test versus hypothetical mean of zero, $p = 0.024$) (right). (**B**) On the left are sample traces of LEC_{GLU}-evoked CA3 PN EPSCs in ACSF (green), SR and CGP (orange), and TTX and 4-AP (gray). On the right are input-output curves of the number of peaks in the LEC_{GLU}-evoked CA3 PN EPSC waveform in ACSF, SR and CGP, and TTX and 4-AP [number of EPSC peaks: $n = 11$, two-way analysis of variance (ANOVA): treatment, $p < 0.001$; power, $p < 0.001$; treatment x power, $p < 0.001$. Number of EPSC peaks against LED power: $n = 11$, one-sample t tests versus hypothetical mean of one: 1%, 0.07 mW/mm^2, $p < 0.001$; 2%, 0.14 mW/mm^2, $p = 0.167$; 3%, 0.21 mW/mm^2, $p = 0.008$]. (**C**) Sample traces of CA3 IN action potential firing evoked by stimulation of LEC_{GLU} alone (green) or with LEC_{GABA} (magenta) (left), sample raster plot (trials were interleaved during recordings but grouped here for visualization) (middle), and spike probability of CA3 INs evoked by stimulation of LEC_{GLU} alone or with LEC_{GABA} ($n = 5$, two-way ANOVA: input combination, $p < 0.001$; pulse number, $p < 0.001$; input combination x pulse number, $p = 0.982$) (right). (**D**) Sample traces (left) and amplitude (right) of LEC_{GLU}-evoked CA3 PN IPSCs with (magenta) or without (green) LEC_{GABA} stimulation ($n = 11$, paired t test, $p = 0.042$). (**E**) Sample traces (left), postsynaptic potential (PSP) peak (middle), and spike probability (right) of CA3 PN dendrites to repeated stimulation of LEC_{GLU} alone (green) or with LEC_{GABA} (magenta) inputs at 10 Hz [dendritic PSP (dPSP) peak: $n = 29$, two-way ANOVA: input combination, $p = 0.578$; pulse number, $p = 0.893$; input combination x pulse number, $p > 0.999$. Spike probability: $n = 29$, two-way ANOVA: input combination, $p = 0.670$; pulse number, $p = 0.081$; input combination x pulse number, $p = 0.947$]. (**F**) Same as (E) but with CA3 PN somas [somatic PSP (sPSP) peak: $n = 23$, two-way ANOVA: input combination, $p = 0.120$; pulse number, $p = 0.759$; input combination x pulse number, $p > 0.999$. Spike probability: $n = 23$, two-way ANOVA: input combination, $p = 0.318$; pulse number, $p = 0.439$; input combination x pulse number, $p = 0.439$]. For applicable panels, error bars and shaded regions around plot lines represent SEM. *$p < 0.05$; ***$p < 0.001$.

multiple inputs to yield CA3 PN output. For this, we tested whether coincident activation of LEC_{GABA} with LEC_{GLU} monosynaptic input and combinations of DG or RC inputs would supralinearly increase PSPs and spike output in CA3 PN somas or dendrites (Fig. 3A). We compared PSP peak and spike probability evoked by repeatedly stimulating LEC_{GLU}, DG, and RC either alone or combined with one another, with or without additional LEC_{GABA} activation. Combined stimulations of LEC_{GABA} with LEC_{GLU} and RC together yielded more action potential firing in CA3 PN somas than expected by the linear summation of LEC_{GLU} plus RC (Fig. 3B). By contrast, pairings of LEC_{GLU} and DG with added stimulation of LEC_{GABA} did not show such a supralinear increase in somatic action potential firing compared with their linear sum (Fig. 3C). Because nonlinearities in input integration can stem from dendritic spikes that help depolarizations from distal inputs such as LEC_{GLU} reach the soma, we assessed postsynaptic responses to LEC_{GABA} pairing with LEC_{GLU} and DG or LEC_{GLU} and RC with dendritic recordings. Surprisingly, although LEC_{GLU} and RC pairing sometimes elicited dendritic spikes, additional stimulation of LEC_{GABA} did not significantly change dendritic spike probability (Fig. 3D). LEC_{GLU} and DG inputs did not sum efficiently in CA3 PN dendrites, thus virtually never yielding dendritic spikes, and LEC_{GABA} had no further effect (Fig. 3E).

LEC_{GLU} and LEC_{GABA} inputs to CA3 contribute to behavioral learning

Because LEC_{GLU} and LEC_{GABA} synergistically drove CA3 activity ex vivo, we asked whether LEC inputs would have complementary roles in shaping behavioral learning and hippocampal representations in vivo. We examined the contributions of LEC_{GLU} and LEC_{GABA} inputs to CA3 at the behavioral and neural-coding levels during an operant GOL paradigm. Mice were first trained to run head-fixed for water rewards on multitextured belts (Fig. 4A). Once habituated to randomly forage (Fig. 4B), mice were subjected to the GOL task (*65*, *66*), which required navigating to specific reward zones in three different contexts (A, A′, and B) defined by combinations of sensory cues with graded similarity. Environments A and A′ had high similarity, as they retained the same tactile cues but differed in their olfactory and auditory cues. By contrast, A and B had low similarity, as they differed in all tactile, olfactory, and auditory cues. Thus, mice needed to associate spatial and nonspatial cues from each environment to find the reward zone in each context. A two-sided Möbius belt design with distinct textures on each side enabled rapid switching between tactile cues without dismounting the mice (*67*, *68*) to capture neural dynamics instantaneously from the first laps in every environment.

LEC should be engaged in this task because it conveys multimodal sensory information to the hippocampus (*14*, *21*–*30*). To test the role of LEC inputs to CA3 in this paradigm, we bilaterally injected a retrograde Cre virus into CA3 and Cre-dependent inhibitory chemogenetic constructs into LEC of C57BL/6J mice (Fig. 4, A and C). Most experiments targeted CA3-projecting LEC inputs with dual chemogenetics by expressing CaMKII-driven-flexed-hM4D(Gi)-mCitrine (*69*) in LEC_{GLU} and Dlx-driven-flexed-PSAM [(*70*); PSAM, pharmacologically selective actuator module] in LEC_{GABA} of the same animals. A separate subset of animals had silencing of either LEC_{GLU} (as above) or LEC_{GABA} with Dlx-driven-flexed-hM4D(Gi)-mCherry. Mice were injected intraperitoneally daily with clozapine-*N*-oxide (CNO) or pharmacologically selective effector molecule (PSEM) before running in environments A, A′, A again (A2), and B for 10-min sessions each. As a control, mice lacking expression of the chemogenetic receptors received randomized intraperitoneal injections of CNO or PSEM (fig. S7, A and B). These control mice readily increased their licking in the reward zones and showed daily improvement of their performance (Fig. 4, D and E, and fig. S7, C and E). By contrast, chemogenetic silencing of either LEC_{GLU} (ΔLEC_{GLU}) or LEC_{GABA} (ΔLEC_{GABA}) decreased performance throughout the task (Fig. 4, D and E, Table 1, and fig. S7, C and E). Such impairments indicate that both LEC_{GLU} and LEC_{GABA} inputs to CA3 contribute to GOL, although we note that CA3-projecting LEC inputs may collaterize to DG and that local circuit interactions in LEC enable cross-talk between LEC_{GLU} and LEC_{GABA} (fig. S8). Finally, silencing of

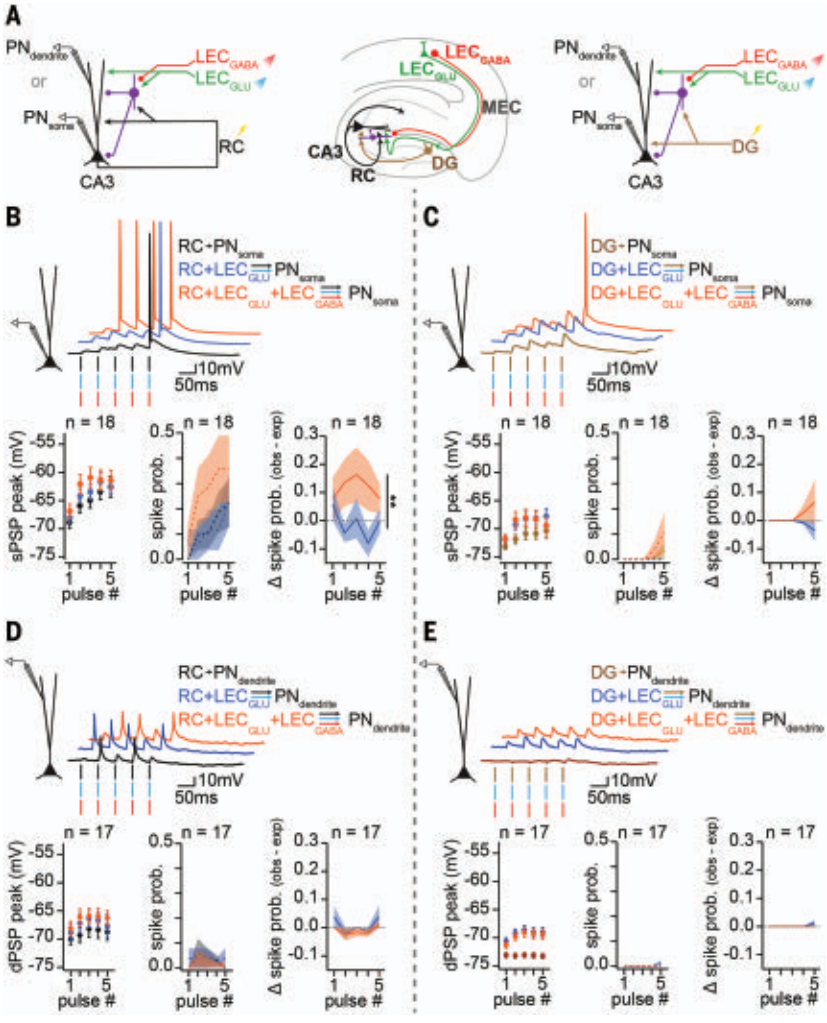


Fig. 3. Input- and compartment-specific disinhibition of CA3 PN output by LEC_{GABA}. (**A**) Dual-optogenetic activation of LEC_{GLU} and LEC_{GABA} combined with electrical stimulation of local RC (left) and DG (right) allows probing of CA3 output in response to specific input integration. (**B**) Sample traces (top), PSP peak and spike probability (bottom left) of RC-evoked (black), RC-and-LEC_{GLU}–evoked (blue), and RC-and-LEC_{GLU}-and-LEC_{GABA}–evoked (orange) CA3 PN somatic responses and delta spike probability (bottom right) between observed RC-and-LEC_{GLU} with or without LEC_{GABA} stimulation versus that expected from the linear sum of these inputs (difference between observed versus expected spike probability: $n = 18$, two-way ANOVA: input combination, $p = 0.007$; pulse number, $p = 0.841$; input combination x pulse number, $p = 0.549$). (**C**) Same as (B) with DG stimulation (brown) instead of RC (difference between observed versus expected spike probability: $n = 18$, two-way ANOVA: input combination, $p = 0.115$; pulse number, $p = 0.993$; input combination x pulse number, $p = 0.258$). (**D**) Same as (B) but in CA3 PN dendrites (difference between observed versus expected spike probability: $n = 17$, two-way ANOVA: input combination, $p = 0.173$; pulse number, $p = 0.111$; input combination x pulse number, $p = 0.925$). (**E**) Same as (C) but in CA3 PN dendrites (difference between observed versus expected spike probability: $n = 17$, two-way ANOVA: input combination, $p = 0.319$; pulse number, $p = 0.409$; input combination x pulse number, $p = 0.409$). For applicable panels, error bars and shaded regions around plot lines represent SEM. $^{**}p < 0.01$.

LEC_{GLU} or LEC_{GABA} after mice had learned the task had no effect on recall performance (Fig. 4, F and G, Table 1, and fig. S7, D and F), suggesting that LEC inputs are required for learning but not during memory recall once the task is successfully learned.

LEC_{GLU} and LEC_{GABA} support context-dependent remapping of CA3 ensembles

To resolve the neuronal dynamics underlying LEC_{GLU} and LEC_{GABA} contributions to GOL, we virally expressed CaMKII-driven-GCaMP6f or GCaMP8f in CA3 PNs to monitor their somatic and dendritic activity longitudinally with two-photon calcium imaging (Figs. 4A and 5, A and B, and figs. S9 to S12). We identified spatially tuned CA3 PN somas and dendrites in session A and compared their remapping in sessions A′, A2, and B using population vector (PV) and tuning curve (TC) correlations (Fig. 5, C to K, and figs. S13 and S14). In control conditions, PV and TC correlations between the A and B environments were lower than between the A and A′ environments (Fig. 5, C and F to K, Table 2, fig. S14, and table S1), indicating more remapping from A to B than from A to A′, which is consistent with B being more different from A than A′. By contrast, both ΔLEC_{GLU} and ΔLEC_{GABA} conditions showed substantial remapping between A and A′ (Fig. 5, D to K, Table 2, fig. S14, and table S1), thereby reducing the contrast in neural representation of similar (A-A′) versus different (A-B) environments. Analysis of same-environment remapping using spatial correlations either between A and A2 sessions (Fig. 5, C to K, Table 2, fig. S14, and table S1) or across first versus second halves within a session (fig. S15 and table S2) revealed decreased baseline stability in both ΔLEC_{GLU} and ΔLEC_{GABA} conditions compared with control conditions. This instability was not due to basic differences in activity (figs. S10 and S11) or decreased encoding of spatial features, because the fraction of spatially tuned regions of interest (ROIs) or the width of their place fields in ΔLEC_{GLU} and ΔLEC_{GABA} conditions were not different from that in control conditions (fig. S12). Rather, ΔLEC_{GLU} and ΔLEC_{GABA} conditions had degraded ensemble coding of space across time. This suggests that both LEC_{GLU} and LEC_{GABA} inputs support the stability of CA3 place maps, allowing context-dependent spatial coding by distinct ensembles.

Imaging both somas and dendrites simultaneously enabled us to explore links between the effects of LEC input silencing on behaviorally driven in vivo neural dynamics and the ex vivo circuit-mapping results that show compartment-specific disinhibition. Of note, analysis of dendritic tuning revealed lower stability in dendrites than in somas in control conditions but not in ΔLEC_{GLU} or ΔLEC_{GABA} conditions (Fig. 5, F to K, Table 2, fig. S14, and table S1). Although LEC input silencing decreased spatial correlations between most environments in both CA3 somas and dendrites, the higher stability of CA3 somas than dendrites in control conditions is consistent with the preferential boosting of CA3 PN somatic activity in response to combined LEC_{GLU}, LEC_{GABA}, and RC inputs (Fig. 3B) through perisomatic disinhibition from local CA3 basket cells (Figs. 1I and 2C).

LEC_{GLU} and LEC_{GABA} enable stability of CA3 place maps associated with learning

Next, we examined the neural correlates of behavioral performance in the GOL task and how they were influenced by LEC_{GLU} and LEC_{GABA}. Tracking place-cell ensembles across days (Fig. 6 and fig. S16) revealed a progressive increase in their correlation with day 5 over the course of learning in control mice (Fig. 6A). This suggests that neural representations relevant to spatial navigation in the GOL task stabilize with learning. By contrast, cross-day correlations remained low in ΔLEC_{GLU} and ΔLEC_{GABA} conditions (Fig. 6, B and C), indicating that LEC input-driven stabilization of spatial coding contributes to shaping CA3 ensembles during learning. Specifically, somatic PV correlations between days 1 to 4 and day 5 were significantly higher in control than in ΔLEC_{GLU} for environments

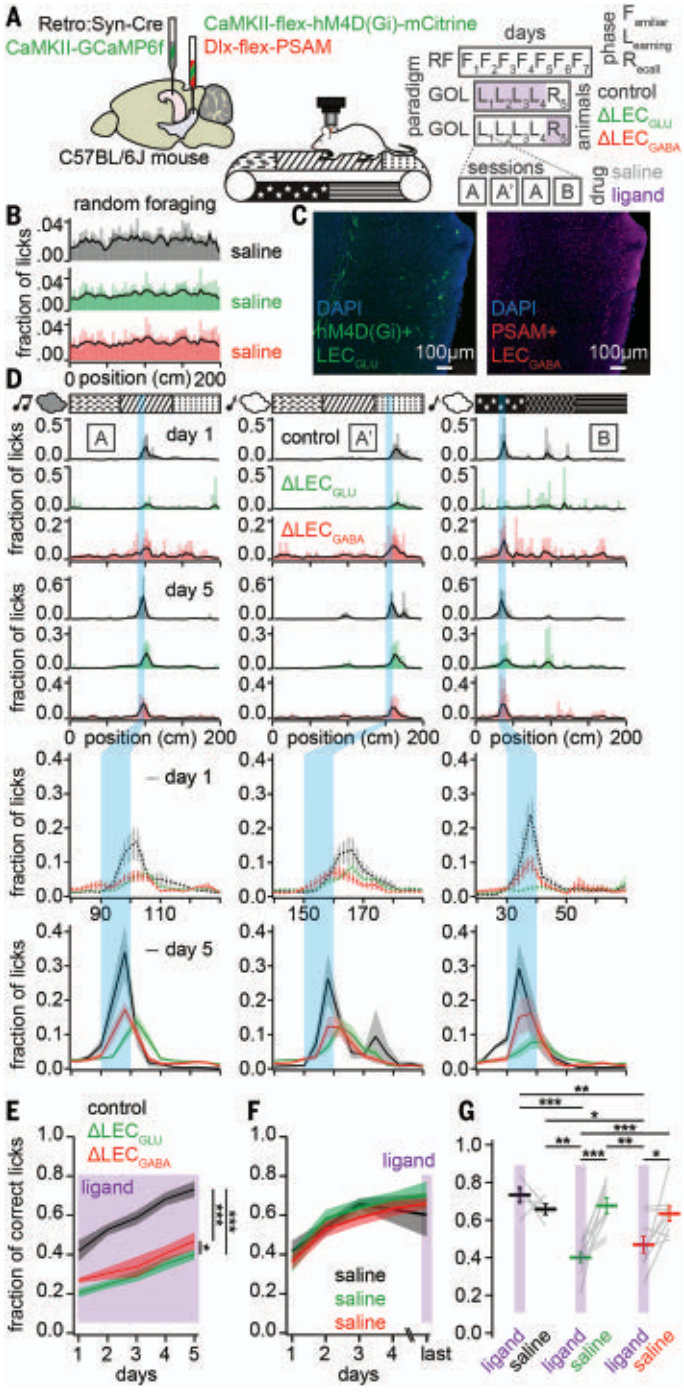


Fig. 4. Contributions of CA3-projecting LEC_{GLU} and LEC_{GABA} to GOL. (**A**) AAV injection of Syn-driven Cre-recombinase with retrograde tropism into CA3 and CaMKII-driven-flexed and Dlx-driven-flexed chemogenetic receptors into LEC of C57BL/6J mice allows expression of hM4D(Gi)-mCitrine in LEC_{GLU} and PSAM in LEC_{GABA}, enabling input-specific dual-chemogenetic perturbation of CA3-projecting LEC neurons in vivo. Further AAV injection of CaMKII-driven GCaMP6f into CA3 allows two-photon calcium imaging of CA3 PNs through a cranial window on head-fixed mice running for water rewards on multitextured belts in different paradigms. (**B**) Fraction-of-licks spatial distribution in random foraging for control (black, $n = 6$), ΔLEC_{GLU} (green, $n = 10$), and ΔLEC_{GABA} (red, $n = 9$) mice injected with saline. (**C**) Sample confocal fluorescence images with injection site of AAVs targeting CA3-projecting LEC_{GLU} [left; hM4D(Gi)-mCitrine, green] and LEC_{GABA} (right; α-bungarotoxin-stained PSAM, red) neurons, with DAPI staining (blue). (**D**) Fraction-of-licks spatial distribution in GOL environments A (left), A′ (middle), and B (right) on day 1 (top) and day 5 (middle) and expanded views of reward zones (bottom) for control (black, $n = 6$), ΔLEC_{GLU} (green, $n = 10$), and ΔLEC_{GABA} (red, $n = 9$) mice. Cross-hatched patterns indicate belt textures A and B; music notes indicate tones A and B; and cloud symbols indicate odors A and B. (**E**) Fraction of licks in reward zones across days with ligand injections (control, $n = 6$; ΔLEC_{GLU}, $n = 10$; ΔLEC_{GABA}, $n = 9$; two-way ANOVA: treatment, $p < 0.001$; days, $p < 0.001$; treatment x days, $p = 0.795$; Tukey post hoc test: control versus ΔLEC_{GLU}, $p < 0.001$; control versus ΔLEC_{GABA}; $p < 0.001$; ΔLEC_{GLU} versus ΔLEC_{GABA}, $p = 0.014$). (**F**) Fraction of licks in reward zones across days with saline injections (control, $n = 6$; ΔLEC_{GLU}, $n = 10$; ΔLEC_{GABA}, $n = 9$; two-way ANOVA: treatment, $p = 0.873$; days, $p < 0.001$; treatment x days, $p = 0.996$). (**G**) Fraction of licks in reward zone with or without silencing (control, $n = 6$; ΔLEC_{GLU}, $n = 10$; ΔLEC_{GABA}, $n = 9$; one-way ANOVA: $p < 0.001$; Tukey post hoc test: Table 1). For applicable panels, error bars and shaded regions around plot lines represent SEM. $^*p < 0.05$; $^{**}p < 0.01$; $^{***}p < 0.001$.

A′ and B and higher than in ΔLEC_{GABA} for environments A and A′ (Fig. 6, D to G, Table 3, fig. S17, and table S3). Accounting for time-related drift using pairwise day-day comparisons also showed increased somatic PV correlations in control compared with ΔLEC_{GLU} for environments A and B and with ΔLEC_{GABA} for all environments (Fig. 6, H to K, Table 4, fig. S17, and table S4). Restricting such analysis to place cells using TC correlations showed decreased differences between groups (fig. S17 and tables S3 and S4), perhaps because of the conserved tuning quality of individual cells (fig. S12). Altogether, these data implicate both LEC_{GLU} and LEC_{GABA} in providing stability to CA3 spatial representations associated with learning. Again, dendritic spatial ensembles were less stable than somatic ones in control conditions but not in ΔLEC_{GLU} or ΔLEC_{GABA} conditions (Fig. 6, D to K, and fig. S17). Hence, it is possible that LEC inputs promote stability in CA3 in vivo by facilitating its recurrent activity through somatic disinhibition, as seen with pairing LEC_{GLU}, LEC_{GABA}, and RC recurrent inputs ex vivo. Finally, we tested whether the decreased stability of CA3 somatic place-cell ensembles observed with LEC manipulations would affect the precision of spatial coding. We used the activity of CA3 PN somas to decode position across sessions in each given context during learning. Silencing of either LEC_{GLU} or LEC_{GABA} impaired position decoding compared with control (figs. S18 and S19A), consistent with reduced performance in GOL.

Lastly, to test how LEC_{GLU} and LEC_{GABA} inputs can influence encoding and recall in CA3 ensembles, we simulated the formation of a neuronal assembly in a recurrent network model parameterized by

Table 1. *p* values for comparison of fraction of licks in reward zones (Tukey post hoc tests).

Condition	Control ligand	Control saline	ΔLEC_{GABA} ligand	ΔLEC_{GABA} saline	ΔLEC_{GLU} ligand
Control saline	0.882	–	–	–	–
ΔLEC_{GABA} ligand	0.001*	0.042*	–	–	–
ΔLEC_{GABA} saline	0.590	0.999	0.032*	–	–
ΔLEC_{GLU} ligand	<0.001*	0.002*	0.757	<0.001*	–
ΔLEC_{GLU} saline	0.937	>0.999	0.003*	0.963	<0.001*

*Statistically significant values.

our deciphered circuit organization (fig. S19B). The model consisted of excitatory neurons with recurrent connections, where synaptic weights are plastic under a simple Hebbian learning rule. These neurons also received lateral inhibition as well as constant inputs from LEC_{GLU} and LEC_{GABA}. Because our optogenetic mapping work shows that LEC_{GLU} drives both excitation and feedforward inhibition, we assumed that LEC_{GLU} provides input to a subset of neurons that will form an assembly during the encoding phase. Based on our ex vivo findings that LEC_{GABA} drives disinhibition of CA3 recurrent activity, we modeled LEC_{GABA} as a general disinhibitory input to all neurons. At the end of the encoding phase, the recurrent weights within the assembly were strengthened. To assess performance, we tested recall with a pattern completion protocol stimulating 70% of the assembly and recording the activity of the remaining 30% to quantify reactivation. In control conditions, the reactivation performance was high. To mimic the experimental manipulations, we perturbed LEC_{GLU} or LEC_{GABA} inputs during encoding or recall. For ΔLEC_{GLU}, we degraded the input to the neuronal subset forming the assembly, assuming that disrupted sensory information would dilute the recruitment of specific postsynaptic CA3 PN ensembles. For ΔLEC_{GABA}, we reduced the constant disinhibitory input to the neuronal network. Both ΔLEC_{GLU} and ΔLEC_{GABA} perturbations impaired reactivation performance if applied during encoding but not recall (fig. S19C). This was because, after encoding, the strong recurrent weights within CA3 could promote reactivation of assemblies on their own. Consistent with the behavioral impairment (Fig. 4, E to G) and decreased stability of CA3 ensembles (Fig. 6, D to K) observed experimentally, both ΔLEC_{GLU} and ΔLEC_{GABA} perturbations during encoding similarly impaired reactivation performance despite being modeled differently based on our functional circuit mapping. Beyond our experimental findings, the model predicted that different mechanisms underlie reactivation deficits because the variability of activity in the assembly was increased during encoding with ΔLEC_{GLU} but not ΔLEC_{GABA} (fig. S19D). ΔLEC_{GABA} was abstracted as a global reduction of activity in the recurrent network, thus making the threshold for potentiating connections harder to reach, which resulted in a quantitatively weakened but qualitatively preserved assembly. By contrast, the net amounts of excitation and inhibition were conserved with ΔLEC_{GLU}. Instead, the distribution of neurons receiving input was broadened, yielding less specificity to the composition of the assembly.

Discussion

Flexibility and stability are critical features of memory formation and recall in many brain regions across species (*46*, *54*, *71*–*74*). Yet little is known of the circuit mechanisms that influence the flexibility versus stability of neuronal ensembles. Our study examined the specific roles of long-range glutamatergic and GABAergic circuit interactions between EC and hippocampal area CA3 to resolve how they orchestrate activity related to neuronal representation dynamics. Using multifaceted approaches, we found that LEC_{GLU} and LEC_{GABA} inputs synergistically support stability in CA3 by recruiting pathway- and compartment-specific excitation, feedforward inhibition, and disinhibition to promote recurrent circuit activity. This functionally endows CA3 with graded stabilization of its internal representations, supporting learning of spatial-contextual associations.

Long-range GABAergic projections form disinhibitory circuit motifs throughout the brain (*14*–*17*, *19*, *20*). However, depending on their targets, the disinhibition affects compartment-specific activity differentially. Our somatic and dendritic recordings validate the purely disinhibitory nature of LEC_{GABA} in CA3, wherein it exclusively targets local GABAergic INs but not PN somas or dendrites. Among the IN targets, LEC_{GABA} inhibits SLM VIP^+ and CCK^+ INs (Fig. 1I and fig. S3), including putative VIP^+-CCK^+ soma-targeting basket cells (*59*–*64*) to disinhibit CA3 PN somas. Consequently, coactivation of LEC_{GLU} and RC inputs aided by perisomatic disinhibition from LEC_{GABA} facilitates CA3 PN somatic firing without affecting dendritic spikes (Fig. 3, B and D) (*75*–*78*). Accordingly, our in vivo two-photon imaging shows baseline remapping differences between somas and dendrites in control in our GOL task, with LEC silencing-induced instability in both compartments leveling these differences (Figs. 5, F to K, and 6, D to K). In CA1 however, whereas LEC and MEC long-range GABAergic projections also target local INs and seemingly avoid PN somas (*14*, *15*), LEC-mediated disinhibition gates dendritic spike output. This is because, in CA1, LEC_{GLU} recruits inhibitory CCK^+ INs alongside disinhibitory VIP^+ INs to control dendritic excitability (*62*), and LEC_{GABA} suppresses dendrite-targeting SR-SLM CCK^+ INs to disinhibit timing-dependent dendritic spikes and associated plasticity without affecting somatic output (*14*). More generally, compartment-specific activity dynamics may arise from differences in circuitry and behavior (*67*, *79*–*82*).

LEC_{GABA} mediates pathway-specific disinhibition to preferentially boost RC output over DG, when coincident with LEC_{GLU}. Disinhibitory routing of LEC input through the CA3 recurrent network substantially amplifies its output, making the otherwise sparse LEC_{GABA} input quite impactful. This convergence may drive the similar effects of silencing LEC_{GLU} versus LEC_{GABA} on behavioral performance and CA3 neural dynamics, although interconnectivity within LEC may also contribute. Also consistent with converging effects, our model simulates ensemble activation by specific context-laden excitatory input (LEC_{GLU}) boosted by decreased local inhibition owing to LEC_{GABA} and amplified by the CA3 RC attractor network. This predicts a role for LEC in stabilizing spatial representations formed and stored within the autoassociative CA3 subregion. CA3 place cells can remap in novel or morphed environments, as well as reactivate complete representations from partial inputs, thus performing both pattern separation and completion computations (*35*, *36*, *38*, *42*–*49*, *52*–*54*). LEC neurons show weak spatial selectivity but strong context-dependent responses to a range of sensory and behaviorally salient stimuli (*14*, *21*–*28*). However, the tuning of LEC neurons and their CA1 projections to navigational goals (*30*), their relevance to GOL behavior in CA1 (*29*) as well as rate remapping in CA3 (*34*), and our present findings of stabilizing CA3 place-cell ensembles suggest a more direct role for LEC in hippocampal spatial coding functions.

Beyond their fundamental disinhibitory function of elevating excitation, long-range GABAergic projection circuits are poised to have a widespread impact on behaviorally relevant brain activity. By targeting local inhibitory neurons that coordinate network oscillations (*83*), long-range GABAergic projections can help synchronize distant brain areas (*16*) across several oscillation patterns (*15*, *18*, *84*–*89*). Long-range GABAergic neurons strongly respond to salient sensory stimuli across modalities (*14*, *90*), supporting association of multimodal inputs and novelty detection. Indeed, during encoding, silencing of LEC_{GABA} projections to CA1 (*14*) impairs learning of fear contexts and novel objects, whereas silencing the CA3-projecting LEC_{GABA} neurons impairs goal-oriented spatio-contextual learning. Our study provides a circuit mechanism whereby

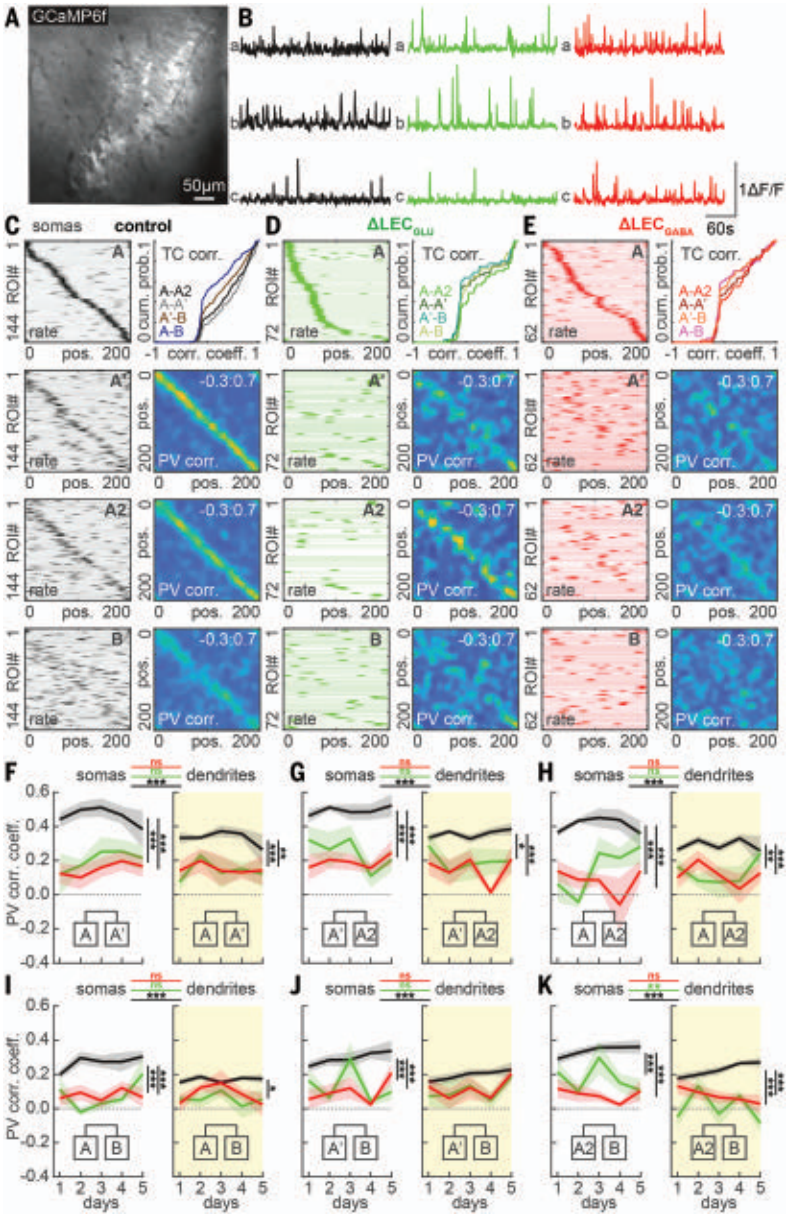


Fig. 5. Roles of LEC_{GLU} and LEC_{GABA} in CA3 context-dependent remapping. (**A**) Sample CA3 field of view. (**B**) Sample relative fluorescence intensity (ΔF/F) traces from three ROIs (a, b, and c) in control (black), ΔLEC_{GLU} (green), and ΔLEC_{GABA} (red) conditions. (**C** to **E**) Shown on the left are sample normalized rate maps of spatially tuned CA3 somas in the A (first row), A′ (second row), A2 (third row), and B (fourth row) environments sorted according to their place-field location in the A session. Shown on the right are sample spatial correlations reported as cumulative distribution of TC correlation coefficients between A-A2, A-A′, A′-B, and A-B sessions (first row) and population vector (PV) correlation matrix of A-A′ (second row), A-A2 (third row), and A-B (fourth row) sessions. The control is shown in (C), ΔLEC_{GLU} in (D), and ΔLEC_{GABA} in (E). (**F** to **K**) Somatic (left) and dendritic (right) PV correlation coefficients across days (control, $n = 6$; ΔLEC_{GLU}, $n = 9$; ΔLEC_{GABA}, $n = 8$; two-way ANOVAs, Tukey post hoc tests: Table 2). A-A′ is shown in (F), A′-A2 in (G), A-A2 in (H), A-B in (I), A′-B in (J), and A2-B in (K). For applicable panels, shaded regions around plot lines represent SEM. $^*p < 0.05$; $^{**}p < 0.01$; $^{***}p < 0.001$; ns is not significant.

LEC_{GLU} and LEC_{GABA} conjunctively modulate compartment- and pathway-specific excitation, inhibition, and disinhibition to support hippocampal place-cell stability for context-dependent learning. Beyond this, LEC_{GLU} versus LEC_{GABA} may differentially or synergistically shape synaptic plasticity (*91*, *92*) and ensemble dynamics, depending on brain state, neuromodulation, and task demands.

Materials and methods

Animals

All experiments were conducted in accordance with the National Institute of Health guidelines and with the approval of the New York University Grossman School of Medicine Institutional Animal Care and Use Committee (IACUC). Mice were obtained from Jackson Laboratory and subsequent breeding was established in-house. Acute slice electrophysiology experiments used GAD2-Cre, Pvalb-Cre, SST-Cre, CCK-Cre, VIP-Cre, Ai9, and Ai14 transgenic mice from both sexes, 8 weeks to 6 months old, with a C57BL/6J genetic background. In vivo two-photon calcium imaging experiments used C57BL/6J mice from both sexes, 3 to 6 months old.

Virus preparation

An adeno-associated virus encoding an inhibitory neuron promoter h56D (*93*), channelrhodopsin2 (H134R)-sfGFP, woodchuck hepatitis virus posttranscriptional regulatory element (WPRE) and SV40 polyadenylation signal was assembled using a modified helper-free system (Stratagene) as a serotype 2/7 (rep/cap genes) AAV and harvested and purified over sequential cesium chloride gradients as previously described (*94*). The codon-optimized channerhodopsin2 fusion protein included an EAGAVSGGVY linker between the protein domains and C-terminal Golgi and endoplasmic reticulum export signals (*95*, *96*) to aid membrane expression.

Stereotaxic surgery

Animals (>4 weeks old) were anaesthetized with isofluorane (1.5 to 3%, inhaled) and buprenorphine (0.1 mg/kg, injected intraperitoneally). Mice were placed in a stereotaxic apparatus (Stoelting), a small incision (~0.5-cm length) was made in the skin to expose the skull, and the skull was leveled flat according to bregma and lambda. A small craniotomy (~0.5-mm diameter) was drilled in the skull above the injection sites and 276 to 414 nl of virus was injected (Drummond Scientific Nanoject II) into the brain at the following coordinates: anterior–posterior relative to bregma: 3.2 and 3.0 mm for LEC, 1.5 to 1.9 mm for CA3; medial-lateral relative to midline: 4.5 and 4.7 mm for LEC, 1.7 to 2.2 mm for CA3; dorsal-ventral relative to the surface of the brain: 2.5, 2.8 and 3.0 mm for LEC, 1.8, 2.0 and 2.2 mm for CA3. The injection pipette was slowly lowered into the brain up to 0.2 mm deeper than the deepest targeted coordinate, left at this location for 1 min, retracted to the actual coordinate and held there for 30 s prior to injection. 46 to 69 nl of virus was injected in 23 nl increments spaced by 15 s at each z coordinate, with an additional 2 min pause between z coordinates and a final 10 min incubation at the last (shallowest) z coordinate of each injection site before slowly retracting the injection pipette out of the brain. Mice were sutured, given neosporin topically on the incision site, injected with 1 ml of sterile saline subcutaneously, monitored until full recovery from anesthesia was observed, and given analgesic postoperative care (buprenorphine, 0.1 mg/kg, injected intraperitoneally) for 3 days. Infection sites were confirmed to be specific post hoc for all experiments.

The adeno-associated virus (AAV) AAV2/5:EF1α-DIO-hChR2(H134R)-eYFP-WPRE-HGHpA (Addgene no. 20298) was used at 7.7×10^{12} to 1×10^{13} vg/ml, AAV2/5:CaMKIIa-hChR2(H134R)-eYFP (Addgene no. 26969) was used at 1.5×10^{13} vg/ml, AAV2/5:CaMKII-Chronos-GFP (Neurophotonics no. 319) was used at 1.3×10^{13} vg/ml, AAV2/5:Syn-flex-ChrimsonR-tdTomato (Addgene no. 62723) was used at 4.74×10^{12} to 2×10^{13} vg/ml, AAV2/7:h56D-ChR2-sfGFP (kindly provided by Boris Zemelman) was used at 2×10^{13} vg/ml, AAV2/1:CaMKII-GCaMP6f-WPRE-SV40 (Addgene no. 100834) was used

Table 2. *p* values for comparison of PV correlations across contexts (two-way ANOVAs, Tukey post hoc tests).

Sample	Factor	A-A′	A-A2	A-B	A′-A2	A′-B	A2-B
Somas	Time	0.760	0.580	0.647	0.748	0.256	0.678
	Treatment	<0.001*	<0.001*	<0.001*	<0.001*	<0.001*	<0.001*
	Time x treatment	0.987	0.301	0.585	0.859	0.279	0.617
	Control versus ΔLEC_{GLU}	<0.001*	<0.001*	<0.001*	<0.001*	<0.001*	<0.001*
	Control versus ΔLEC_{GABA}	<0.001*	<0.001*	<0.001*	<0.001*	<0.001*	<0.001*
	ΔLEC_{GLU} versus ΔLEC_{GABA}	0.626	0.414	0.999	0.575	0.707	0.068
Dendrites	Time	0.771	0.804	0.798	0.761	0.261	0.425
	Treatment	<0.001*	<0.001*	0.013*	<0.001*	0.045*	<0.001*
	Time x treatment	0.986	0.651	0.932	0.870	0.974	0.239
	Control versus ΔLEC_{GLU}	<0.001*	0.004*	0.021*	0.010*	0.061	<0.001*
	Control versus ΔLEC_{GABA}	0.001*	<0.001*	0.053	<0.001*	0.105	<0.001*
	ΔLEC_{GLU} versus ΔLEC_{GABA}	0.980	0.965	0.809	0.638	0.958	0.159
Control	Time	0.381	0.387	0.235	0.591	0.248	0.038*
	Compartment	<0.001*	<0.001*	<0.001*	<0.001*	<0.001*	<0.001*
	Time x compartment	0.983	0.932	0.702	0.988	0.983	0.925
ΔLEC_{GLU}	Time	0.807	0.234	0.707	0.718	0.274	0.564
	Compartment	0.369	0.728	0.754	0.516	0.578	0.004*
	Time x compartment	0.946	0.535	0.736	0.835	0.524	0.260
ΔLEC_{GABA}	Time	0.998	0.481	0.747	0.627	0.197	0.671
	Compartment	0.985	0.519	0.914	0.439	0.720	0.877
	Time x compartment	0.922	0.904	0.769	0.895	0.942	0.915

Factor	Somas			Dendrites		
	Control	ΔLEC_{GLU}	ΔLEC_{GABA}	Control	ΔLEC_{GLU}	ΔLEC_{GABA}
Time	0.123	0.162	0.547	0.130	0.979	0.588
Context	<0.001*	0.169	0.101	<0.001*	0.031*	0.550
Time x context	0.991	0.789	0.993	0.836	0.888	0.984
A-A′ versus A-A2	0.550	0.964	0.674	0.320	>0.999	0.984
A-A′ versus A-B	<0.001*	0.390	0.677	<0.001*	0.745	0.760
A-A′ versus A′-A2	0.886	0.982	0.956	0.861	0.922	>0.999
A-A′ versus A′-B	<0.001*	0.865	0.913	<0.001*	0.987	0.983
A-A′ versus A2-B	0.001*	0.998	0.730	<0.001*	0.198	0.656
A-A2 versus A-B	<0.001*	0.860	>0.999	<0.001*	0.841	0.983
A-A2 versus A′-A2	0.063	0.663	0.169	0.018*	0.829	0.988
A-A2 versus A′-B	0.003*	>0.999	0.998	<0.001*	0.998	>0.999
A-A2 versus A2-B	0.188	0.999	>0.999	0.042*	0.277	0.958
A-B versus A′-A2	<0.001*	0.112	0.175	<0.001*	0.217	0.784
A-B versus A′-B	0.958	0.960	0.998	0.820	0.969	0.986
A-B versus A2-B	0.203	0.704	>0.999	0.073	0.971	>0.999
A′-A2 versus A′-B	<0.001*	0.458	0.420	<0.001*	0.578	0.987
A′-A2 versus A2-B	<0.001*	0.882	0.215	<0.001*	0.018*	0.684
A′-B versus A2-B	0.728	0.986	0.999	0.701	0.534	0.964

*Statistically significant values.

at 1×10^{13} vg/ml, AAV2/1:CaMKII-GCaMP8f-WPRE (Addgene no. 176750) was used at 1.7×10^{13} vg/ml, AAV2/5:CaMKII-DIO-hM4D(Gi)-IRES-mCitrine (Neurophotonics no. 810) was used at 1.3×10^{13} vg/ml, AAV2/5:hDlx-flex-PSAM (custom construct from Neurophotonics) was used at 6.8×10^{12} vg/ml, AAV2/5:Dlx-DIO-hM4D(Gi)-mCherry (construct from Yingxi Lin laboratory, packaged by Boston Children's Harvard Viral Core) was used at 5.04×10^{13} vg/ml, AAV2/9:Dlx-flex-TdTomato (Addgene no. 83894) was used at 7×10^{12} vg/ml, AAVretro:Syn-Cre (Neurophotonics no. 1299) was used at 1.4×10^{13} vg/ml, AAV2/5:Dlx-Flex-ChR2-mCherry (custom construct from Neurophotonics) was used at 6.8×10^{12} vg/ml, AAV2/9:CaMKII-DIO-Chronos-eGFP (Neurophotonics no. 1830) was used at 1×10^{13} vg/ml.

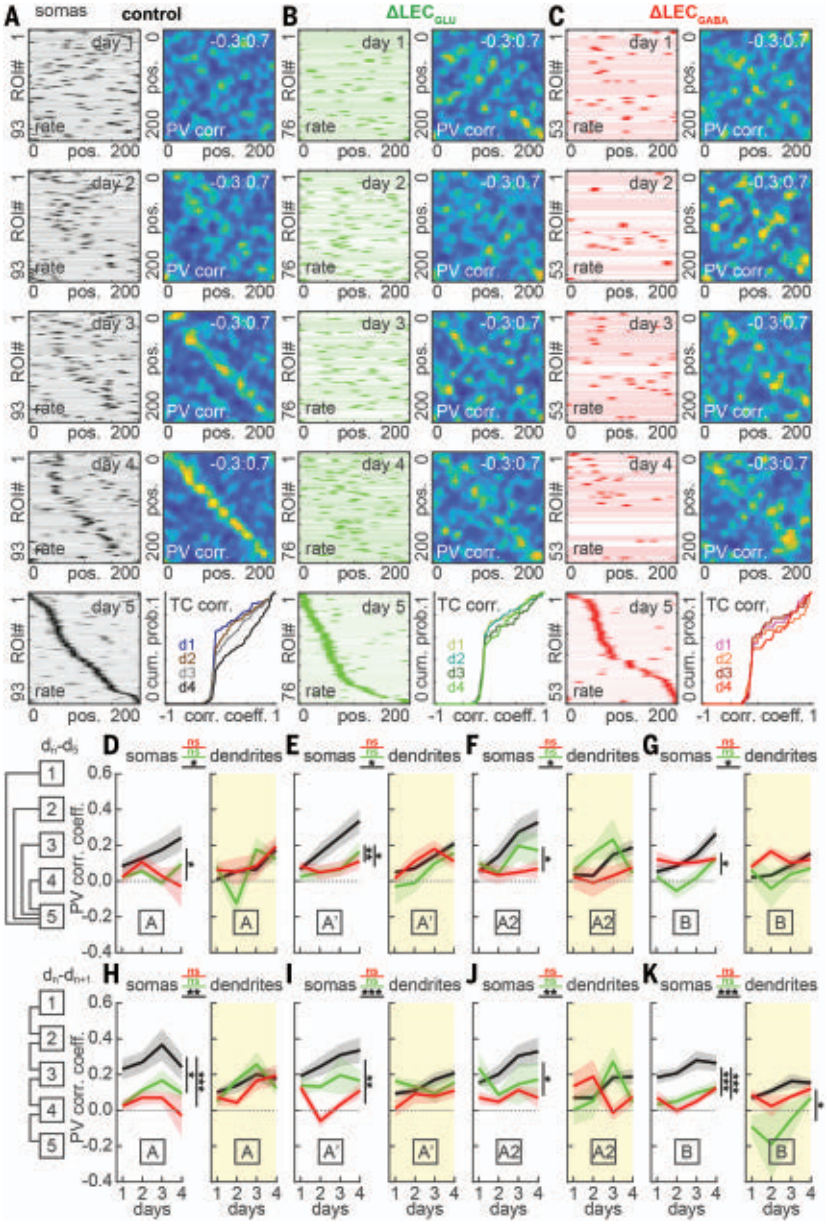


Fig. 6. Involvement of LEC_{GLU} and LEC_{GABA} in learning-associated CA3 spatial coding. (**A** to **C**) Shown on the left are sample normalized rate maps of spatially tuned CA3 somas in the A′ environment across days 1 to 5 sorted according to their place-field location from day 5. Shown on the right are sample spatial correlations across days 1 to 4 against day 5 reported as PV correlation matrix and cumulative distribution of TC correlation coefficients. The control is shown in (A), ΔLEC_{GLU} in (B), and ΔLEC_{GABA} in (C). (**D** to **G**) Somatic (left) and dendritic (right) PV correlation coefficients across days relative to day 5 (control, $n = 6$; ΔLEC_{GLU}, $n = 9$; ΔLEC_{GABA}, $n = 8$; two-way ANOVAs, Tukey post hoc tests: Table 3). A is shown in (D), A′ in (E), A2 in (F), and B in (G). (**H** to **K**) Somatic (left) and dendritic (right) PV correlation coefficients across days between pairs of days (control, $n = 6$; ΔLEC_{GLU}, $n = 9$; ΔLEC_{GABA}, $n = 8$; two-way ANOVAs, Tukey post hoc tests: Table 4). A is shown in (H), A′ in (I), A2 in (J), and B in (K). For applicable panels, shaded regions around plot lines represent SEM. $*p < 0.05$; $**p < 0.01$; $***p < 0.001$; ns is not significant.

Electrophysiology

Artificial cerebrospinal fluid (ACSF) and protective dissection ACSF (dACSF) were oxygenated with a 95% O_2 and 5% CO_2 mixture at all times. Mice were deeply anaesthetized with isoflurane (5% for 5 min, inhaled) and perfused transcardially with ~20 ml of ice-cold NMDG-based dACSF (*97*) containing (in mM): NMDG 93, KCl 2.5, NaH_2PO_4 1.25, $NaHCO_3$ 30, HEPES 20, glucose 25, thiourea 2, Na-ascorbate 5, Na-pyruvate 3, $CaCl_2$ 0.5, $MgCl_2$ 10. Brains were then rapidly removed, cortico-hippocampal complexes were dissected out and placed upright into a custom-made agar mold in ice-cold dACSF. Then, 400-µm-thick transverse slices were cut (vibratome, Leica VT1200S) at low speed (0.04 mm/s) and blade vibration amplitude (0.5 mm) in ice-cold dACSF. Slices were transferred to an immersed-type holding chamber and maintained in ACSF containing the following (in mM): NaCl 125, KCl 2.5, NaH_2PO_4 1.25, $NaHCO_3$ 25, glucose 22.5, Na-ascorbate 1, Na-pyruvate 3, $CaCl_2$ 2, $MgCl_2$ 1. Slices were incubated at 32°C for ~20 min and then maintained at room temperature for at least 30 min prior to recordings.

Individual slices were transferred to a recording chamber perfused with ACSF at 3 to 5 ml/min (peristaltic pump, Watson Marlow) at 30°C (in-line heater, Warner Instruments TC-324B). Tissue was visualized under an upright microscope (Zeiss Examiner A1 or Olympus BX51WI) equipped with DIC or Dodt gradient contrast at 5x to 40x magnification with additional zoom optics 1 to 2.5x, and captured by a video camera (Hamamatsu ORCA-spark or ORCA-flash4.0). The headstages connected to the recording electrodes were mounted on motorized micromanipulators (Luigs and Neumann GmbH). Patch-clamp recordings were performed with potassium- or cesium-based intracellular solution containing the following (in mM): K- or Cs-methyl sulfonate 135, KCl 5, EGTA-KOH 0.1, HEPES 10, NaCl 2, MgATP 5, Na2GTP 0.4, Na2-phosphocreatine 10, and either Alexa 594 (50 to 100 µM) or biocytin (4 mg/ml). Gigaohm seals were formed and whole-cell recordings were obtained from CA3 pyramidal neurons soma (blind patch) or dendrites (blind patch) and interneurons (visual patch). Somatic patch pipette resistances were 2 to 5 megaohms, series resistances were 8 to 20 megaohms. Dendritic patch pipette resistances were 13 to 17 megaohms, series resistances were 40 to 60 megaohms. Series resistance was compensated 0 to 50% to amount to an 8 to 10 megaohms actual resistance in voltage-clamp (somatic recordings). Bridge-balance was applied in current-clamp. Unless stated otherwise, the membrane potential was held at −70 mV in current-clamp. The liquid junction potential was <10 mV and not corrected for.

ChR2-, Chronos-, or ChrimsonR-expressing LEC inputs were stimulated optically with 1- to 10-ms-long 470- or 625-nm light pulses of intensity 0 to 100% (0.0 to 4.47 mW/mm^2). Dual-color optogenetic experiments were performed with Chronos- and ChrimsonR-expressed in LEC_{GLU} and LEC_{GABA}, respectively stimulated with 1-ms 1 to 2% (0.07 to 0.14 mW/mm^2) 470-nm and 10-ms 100% (4.47 mW/mm^2) 625-nm light pulses that were empirically determined to allow spectral separation (intensity below cross-talk threshold of ChrimsonR activation by 470-nm light). Monosynaptic transmission from ChR2- or Chronos-expressing LEC_{GLU} was probed with 1-ms 1 to 2% (0.07 to 0.14 mW/mm^2) 470-nm light pulses that were empirically determined to elicit monophasic and TTX and 4-AP resistant EPSCs in CA3 PNs, as well as below population spike initiation threshold from LFP recordings in DG GC and CA3 SP layers. Conversely, polysynaptic transmission from ChR2- or Chronos-expressing LEC_{GLU} was probed with 100% (3.76 mW/mm^2) 470-nm light pulses that were empirically determined to elicit polyphasic

Table 3. *p* values for comparison of PV correlations across each day to last (two-way ANOVA, Tukey post hoc test).

Sample	Factor	A	A′	A2	B
Somas	Time	0.700	0.020*	0.113	0.019*
	Treatment	0.034*	0.006*	0.034*	0.009*
	Time x treatment	0.567	0.585	0.582	0.481
	Control versus ΔLEC_{GLU}	0.080	0.009*	0.396	0.011*
	Control versus ΔLEC_{GABA}	0.042*	0.017*	0.026*	0.800
	ΔLEC_{GLU} versus ΔLEC_{GABA}	0.984	0.998	0.334	0.050
Dendrites	Time	0.036*	0.073	0.482	0.728
	Treatment	0.803	0.438	0.271	0.287
	Time x treatment	0.475	0.952	0.636	0.817
	Control versus ΔLEC_{GLU}	0.974	0.455	0.924	0.732
	Control versus ΔLEC_{GABA}	0.903	0.970	0.467	0.709
	ΔLEC_{GLU} versus ΔLEC_{GABA}	0.791	0.615	0.269	0.255
Control	Time	0.028*	0.001*	0.001*	<0.001*
	Compartment	0.042*	0.024*	0.017*	0.023*
	Time x compartment	0.981	0.713	0.653	0.747
ΔLEC_{GLU}	Time	0.188	0.079	0.526	0.376
	Compartment	0.617	0.663	0.937	0.950
	Time x compartment	0.083	0.910	0.656	0.949
ΔLEC_{GABA}	Time	0.959	0.592	0.889	0.871
	Compartment	0.291	0.549	0.644	0.906
	Time x compartment	0.428	0.445	0.986	0.643

Factor	Somas			Dendrites		
	Control	ΔLEC_{GLU}	ΔLEC_{GABA}	Control	ΔLEC_{GLU}	ΔLEC_{GABA}
Time	<0.001*	0.053	0.996	<0.001*	0.214	0.511
Context	0.412	0.119	0.391	0.181	0.626	0.358
Time x context	0.986	0.869	0.959	0.949	0.689	0.920
A versus A′	0.756	0.847	0.762	0.263	0.999	>0.999
A versus A2	0.759	0.216	0.959	0.653	0.840	0.565
A versus B	0.972	0.994	0.341	>0.999	0.971	0.986
A′ versus A2	>0.999	0.594	0.965	0.883	0.753	0.539
A′ versus B	0.524	0.690	0.902	0.252	0.991	0.996
A2 versus B	0.518	0.121	0.654	0.622	0.592	0.366

*Statistically significant values.

and TTX and 4-AP sensitive EPSCs in CA3 PNs, as well as above population spike initiation threshold from LFP recordings in DG GC and CA3 SP layers. The medial CA3 recurrent input and proximal dentate gyrus mossy fiber input were stimulated electrically with ACSF-filled pipettes mounted on manual micromanipulators (Siskiyou) and placed in CA1 stratum radiatum (SR) to antidromatically activate CA3 and in the hilus near the border of the upper blade granule cell layer to directly activate DG axons, respectively. Postsynaptic responses were evoked with constant current stimulation units (Digitimer Ltd.) delivering 0.1-ms-long 25 to 200-μA current pulses through monopolar electrodes.

Pharmacological agents were added to ACSF at the following concentrations (in μM): 10 NBQX and 50 D-APV to block AMPA and NMDA receptors, 1-2 SR95531 and 2 CGP55845 to block $GABA_A$ and $GABA_B$ receptors, 10 clozapine *N*-oxide (CNO) to activate hM4D(Gi) DREADDs, 0.2-1 tetrodotoxin (TTX) to prevent sodic action potential generation, 100 4-aminopyridine (4-AP) to block KV1 potassium channels, 1-10 (2S,2'R,3′R)-2-(2',3′-dicarboxycyclopropyl)-glycine (DCG-IV) to inhibit glutamate release from mossy fiber terminals by activating mGluR2/3.

Data was obtained using a Multiclamp 700B amplifier (Molecular Devices), sampled at 10 kHz, digitized using a Digidata 1550B AD/DA board (Molecular Devices), and acquired with the pClamp 10 software (Molecular Devices). Data analysis was performed in IgorPro (Wavemetrics) with custom-written code.

Two-photon calcium imaging

All anesthesia, analgesia, and presurgical procedures were performed as described above (see stereotaxic injections). C57BL/6J mice were first bilaterally injected with AAV2/1:CaMKII-GCaMP6f or AAV2/1:CaMKII-GCaMP8f and AAVretro:Syn-Cre in CA3, and AAV2/5:CaMKII-DIO-hM4D(Gi)-IRES-mCitrine and/or AAV2/5:hDlx-flex-PSAM or AAV2/5:Dlx-DIO-hM4D(Gi)-mCherry in LEC. Then, a unilateral circular 3-mm-diameter craniotomy was made centered on the CA3 imaging coordinates (anterior–posterior relative to bregma: 1.4 mm; medial-lateral

Table 4. *p* values for comparison of PV correlations across pairs of days (two-way ANOVA, Tukey post hoc test).

Sample	Factor	A	A′	A2	B
Somas	Time	0.339	0.475	0.641	0.092
	Treatment	<0.001*	0.002*	0.025*	<0.001*
	Time x treatment	0.986	0.758	0.798	0.836
	Control versus ΔLEC_{GLU}	0.014*	0.083	0.317	<0.001*
	Control versus ΔLEC_{GABA}	<0.001*	0.001*	0.019*	<0.001*
	ΔLEC_{GLU} versus ΔLEC_{GABA}	0.494	0.151	0.341	0.875
Dendrites	Time	0.057	0.483	0.735	0.292
	Treatment	0.667	0.169	0.817	0.017*
	Time x treatment	0.722	0.721	0.183	0.914
	Control versus ΔLEC_{GLU}	0.997	0.965	0.835	0.014*
	Control versus ΔLEC_{GABA}	0.685	0.172	0.863	0.698
	ΔLEC_{GLU} versus ΔLEC_{GABA}	0.752	0.264	0.997	0.089
Control	Time	0.287	0.039*	0.009*	0.045*
	Compartment	0.008*	<0.001*	0.002*	<0.001*
	Time x compartment	0.885	0.965	0.944	0.993
ΔLEC_{GLU}	Time	0.123	0.987	0.706	0.520
	Compartment	0.344	0.712	0.427	0.117
	Time x compartment	0.954	0.866	0.498	0.896
ΔLEC_{GABA}	Time	0.848	0.547	0.817	0.175
	Compartment	0.150	0.665	0.692	0.645
	Time x compartment	0.433	0.213	0.377	0.990

Factor	Somas			Dendrites		
	Control	ΔLEC_{GLU}	ΔLEC_{GABA}	Control	ΔLEC_{GLU}	ΔLEC_{GABA}
Time	0.016*	0.832	0.521	<0.001*	0.431	0.803
Context	0.730	0.522	0.822	0.531	0.044*	0.843
Time x context	0.960	0.984	0.619	0.978	0.712	0.575
A versus A′	0.999	0.826	0.976	0.987	0.997	0.865
A versus A2	0.903	0.818	0.789	0.693	0.860	0.977
A versus B	0.753	0.989	0.926	0.581	0.049*	0.871
A′ versus A2	0.949	>0.999	0.969	0.869	0.923	0.975
A′ versus B	0.829	0.622	0.999	0.780	0.060	>0.999
A2 versus B	0.990	0.617	0.989	0.998	0.217	0.982

*Statistically significant values.

relative to midline: 1.6 mm). The skull fragment was removed, and a vacuum system was used to gently aspirate the overlying cortex and external capsule. Ice-cold ACSF was used to irrigate the area throughout the duration of the procedure. A cranial window (3-mm-diameter, 1.7-mm-length stainless steel cannula attached to 3-mm-diameter glass coverslip) was then implanted over the area. The window was sealed to the skull (Vetbond), and a custom-designed 3D-printed plastic headpost was cemented over the skull. Mice were allowed to recover for 3 to 5 days before being placed under water restriction after which their weight was monitored daily to ensure it remained at least 80% of baseline.

Mice were head-fixed under the two-photon microscope on a treadmill belt (200 cm) and trained to run for 5% sucrose water as described previously (*65*, *66*). In vivo two-photon imaging was performed using a dual galvanometric and resonant laser scanning two-photon microscope (Ultima, Bruker), coupled to a tunable Ti:Sapphire laser (MaiTai eHP DeepSee, Spectraphysics) pulsed at a 80 MHz repetition rate and <70-fs pulse width along with dispersion compensation. GCaMP fluorophore was excited at 920 nm, using a resonant scanning X-galvanometer (8 kHz) paired with a 6-mm standard scanning Y-galvanometer. The scanning system was mounted on a movable objective microscope (Ultima), equipped with an orbital nosepiece coupled to a 16 X, 0.8 NA, 3-mm water immersion objective (Nikon). Imaging was performed at a scan speed of 29 fps, using 512 × 512 frame size (1.085 μm/pixel resolution). Fluorescence signal was detected using high-sensitivity GaAsP photomultiplier tubes (7422PA-40 PMTs, Hamamatsu). GCaMP-based calcium signals from CA3 PN somas and apical dendrites were imaged simultaneously on a single stable field of view in each mouse throughout the experiments.

Mice were first imaged for a single 10-min-long session daily as they ran on the same textured belt (familiar) for water rewards delivered at random positions on the belt (random foraging, RF) for 7 days. On days 8 to 10, mice were subjected to a 10-min RF imaging session on

the familiar belt and allowed to rest for 1 hour before another 10-min session on the familiar belt immediately followed by a final 10 min session on a novel belt (a new belt was used for each day). Mice were injected with either saline, CNO (5 mg/kg, ip), or PSEM308 (3 mg/kg, ip) 30 min into the 1-hour rest period between the familiar sessions. Thereafter, mice were trained in a series of goal-oriented learning (GOL) paradigms comprising different sessions defined by a combination of physical textures with olfactory and auditory cues (interleaved and pulsed for 1 s at 0.25 Hz) for 5 to 8 days. Each GOL block consisted of an A session with textures A, odor A (e.g., 10% pentyl acetate in mineral oil), sound A (e.g., 4 kHz), and reward location A (e.g., 90 to 100 cm); an A′ session with textures A, odor B [e.g., 10% (+)-α-pinene in mineral oil], sound B (e.g., 10 kHz), and reward location A′ (e.g., 150 to 160 cm); a repeat of the A session (A2); and a B session with textures B, odor B, sound B and reward location B (e.g., 30 to 40 cm). The order of sessions sequence was interleaved across daily blocks (as in A-A′-A2-B versus A′-A-B-A2 versus B-A-A′-A2). Textures, odors, sounds, and reward locations assigned to A, A′, and B were changed for each GOL training. Mice were injected with either saline, CNO (5 mg/kg, ip), or PSEM308 (3 mg/kg, ip) 30 min before imaging. ΔLEC_{GLU} and ΔLEC_{GABA} mice were trained in one GOL with daily ip injection of the cognate ligand, and in another GOL with daily ip injections of saline. Control mice were trained in one GOL with daily ip injections of CNO or PSEM308, and in another GOL with daily ip injections of saline. As described previously (*66*), odor delivery and scavenging were achieved by routing odor-charged air through a nose cone under constant 1 liter/min air flow and vacuum. Steady-state odor concentrations were verified using a photoionization detector (200B miniPID, Aurora Scientific). Environmental stimuli delivery and behavioral data recording were performed with custom-designed Arduino hardware. Imaging data was acquired with the PrairieView software (Bruker) and synchronized with the Arduino inputs and outputs.

For each mouse, image sequences from all sessions were concatenated and processed by suite2p (*98*) for motion correction and ROI detection. ROI sets were thereafter manually curated and annotated using ImageJ (*99*). All subsequent analyses were performed in MATLAB (MathWorks) with custom-written code. For each ROI (spatial component), the activity trace (time component) was obtained by averaging across all pixels within the ROI at each time point (frame) and normalized to baseline fluorescence. Calcium transients were detected and demixed from overlapping ROIs using the fitness algorithm of the d-NMF package (*67*). Briefly, activity traces were detrended and z-scored to detect putative events as positive peaks overshooting a threshold of two standard deviations from baseline. Putative events were then screened using a correlation threshold of 0.27 between the spatial component of the ROI and the actual spatial footprint of the ROI in the movie frame at the time of the event. Events with offset within 200 ms of another event's onset were merged, and events with rise time <200 ms, or width <200 ms were excluded from analysis. Subsequent analysis was performed on these curated events, with further behavioral restriction to run epochs as defined by a speed of the animal >2 cm/s. Spatially resolved activity rates were computed by smoothing and dividing the event counts by the occupancy within 5-cm-wide bins. For each session, spatial information content (*100*) was computed for each ROI as:

$$spatial\ information = \sum_{i=1}^{N} P_i R_i \log_2(R_i)$$

where P_i is the normalized occupancy in the ith spatial bin such that the sum across all $P_i = 1$, and R_i is the normalized value of the activity rate in the ith spatial bin such that the sum across all $R_i = 1$. Statistical significance of spatial tuning was determined for each ROI within each session by shifting event times from −250 to 250 time bins and normalizing the spatial information content at zero shift to that of the 99th percentile at nonzero shift. ROIs meeting criteria of a normalized spatial information content >1 and a number of events >4 were considered as significantly spatially tuned.

Spatial tuning curves were parametrized by circularly smoothing rate maps with a sigma of 15 cm and fitting the resulting smoothed curve with multiple Von Mises functions increasing in number until the residuals fell below 25% of the maximal value of the original rate map. Place field width was defined as the full width at half maximum of the fitted tuning curve component. Tuning curve (TC) correlations were computed as the correlation coefficient between tuning curves for each ROI active in both sessions and significantly tuned in at least one of the two sessions. Population vector (PV) correlations were computed by taking the correlation coefficient between spatial rate vectors constructed from ROIs active in both sessions and averaging across all matching spatial bins (main diagonal of the PV correlation matrix). PV decoding of animal position was performed by taking the index of the maximal correlation value at each timepoint between spatial and time rate vectors constructed from tuned ROIs. Time points with no activity across all relevant ROIs were assigned the latest previously decoded position. Decoding error was computed as the circular distance between the real and the decoded positions.

Computational modeling

We model a recurrent rate-based network in CA3 consisting of $N = 50$ excitatory neurons. The total current x_i in each neuron i is modeled as

$$\tau \frac{d}{dt} x_i = -x_i + \sum_j w_{ij} z_j + I_E - I_I - I_{I_lat} + I_{noise}$$

where $\tau = 10$[a.u.] is the neuronal time constant. The firing rate z_i of the neuron i is the current x_i rectified at 0 with a saturation at 1. The neurons receive LEC_{GLU} current I_E, LEC_{GABA} current I_I, a noisy current I_{noise} and lateral inhibition I_{I_lat}. The noisy current is modeled as filtered noise, initialized at 0, with time constant $\tau_noise = 10$[a.u.]

$$\tau_{noise} \frac{d}{dt} I_{noise} = -I_{noise} + \eta$$

where η is drawn from a uniform distribution between −1 and 1. The lateral inhibition is modeled as

$$I_{I_lat} = \gamma \sum_j z_j$$

with $\gamma = 8$. The recurrent weights w_{ij} are plastic following a standard Hebbian learning rule

$$\Delta w_{ij} = \alpha \left(z_i z_j - \theta \right)$$

where $\alpha = 1$ is the learning rate and $\theta = 0.04$ is a threshold. There are no self-connections. All the incoming weights to a given neuron are normalized to have a L1 norm of 1.5. All the weights have a hard lower bound at 0 and an upper bound at 0.3. We initialized the weights at 0. We first simulate an encoding phase and then a testing phase. During the encoding phase, we stimulate an assembly of size 10 (neuron 1 to 10) with a I_E of 0.4 and $I_I = 0$. We initialize the neural activity at 0 and we simulate the network for $T = 200$ time steps, with a dt = 1. We then simulate a testing phase, where we probe our network with a pattern completion protocol. We stimulate the first 70% of the assembly and record the average activity of the remaining 30% of the neurons, averaged over the last 10 time steps. We simulate a total of 100 trials. To compute the variability of the representation, we compute the standard deviation of the neural activity, averaged across neurons. To mimic the silencing of LEC_{GLU} or LEC_{GABA}, we respectively perturb I_E or I_I either during the encoding phase or during the testing phase. To perturb LEC_{GLU}, we assume that the input information content is degraded. Thus, at each time point we stimulate a random subset of 4 out of 10 neurons within the assembly, and stimulate another six neurons as a random subset of the neurons

outside the assembly, each with a current of 0.4. To perturb I_I, we set $I_I = 0.17$ as LEC_{GABA} is disinhibitory.

Histology

Mice were deeply anaesthetized with isoflurane (5% for 5 min, inhaled) and perfused transcardially with ~20 ml of phosphate-buffered saline (PBS) followed by ~20 ml of 4% paraformaldehyde (PFA) in PBS. Brains were removed and fixed in 4% PFA in PBS at 4°C for at least 24 hours. Brains were washed in 0.3 M Glycine in PBS for 15 min followed by three 15-min washes in PBS. Then, 50- to 100-µm-thick coronal slices were cut (vibratome, Leica VT1000S) and stored in PBS at 4°C. Similarly, samples recovered from ex vivo electrophysiology (400-µm-thick transverse slices) were fixed in 4% PFA in PBS at 4°C for at least 24 hours, washed in 0.3 M Glycine in PBS for 15 min followed by three 15-min washes in PBS, and stored in PBS at 4°C. Tissue was permeabilized with 0.5% Triton in PBS (PBST) for twice for 20 min, blocked with 10% NGS in 0.5% PBST for 4 hours, and incubated with primary antibodies in 3% NGS 0.1% PBST overnight at 4°C. Tissue was then washed with 0.2% PBST for 15 min followed by three 30-min washes in PBS before being incubated with secondary antibodies and Streptavidin where applicable in 3% NGS 0.1% PBST for 24 hours (100-µm slices) or 48 hours (400-µm slices) at 4°C. Lastly, slices were washed five times for 15 min in PBS and mounted in Vectashield Hard Set Mounting Medium with DAPI (Vector Laboratories). Tissue stained for α-bungarotoxin underwent similar processing, except substituting PBS for Tris-buffered saline (TBS) pH-buffered at 7.4.

Primary antibodies were rabbit anti-GFP (1:1000, ThermoFisher no. A6455), chicken anti-GFP (1:1000, Abcam no. 13970). All secondary antibodies and dyes were purchased from ThermoFisher: Alexa Fluor 488-conjugated goat anti-rabbit (1:1000, no. A11008), Alexa Fluor 488-conjugated donkey anti-chicken (1:1000, no. A78948), Alexa Fluor 488-conjugated goat anti-chicken (1:1000, no. A11039), Alexa Fluor 555-conjugated streptavidin (1:500, no. S11227), Alexa Fluor 594-conjugated streptavidin (1:500, no. S21381), Alexa Fluor 647-conjugated streptavidin (1:500, no. S21374), Alexa Fluor 455-conjugated Neurotrace (1:200, no. N21479); except Alexa Fluor 555-conjugated α-bungarotoxin (1:3000, Invitrogen) and Alexa Fluor 647-conjugated α-bungarotoxin (1:3000, Invitrogen).

Samples were screened by epifluorescence imaging (Olympus VS200). Relevant samples were imaged with an inverted Zeiss Axio Observer Z1 confocal microscope using 10x (air, 0.3 NA), 20x (air, 0.8 NA) or 40x (oil, 1.3 NA) objectives (Zeiss) and 405-, 488-, 594-, and 647-nm lasers for fluorophore excitation. Images were acquired as 1024 × 1024 pixels 16 bits Z-stacks with a 5-µm (10x, 20x) or 1-µm (40x) Z-step size and tiled in X and Y as needed to cover the samples, and thereafter stitched using the Zen Microscopy software (Zeiss). Further processing of confocal or epifluorescence images was done in ImageJ (*99*).

Statistics

Results are reported ±SEM. Normality was tested with the Shapiro-Wilk and Jarque-Bera tests, and homoscedasticity was tested using Barlett's test to choose between parametric and nonparametric statistical analysis. Statistical significance was assessed using the χ^2 test, Student's t test, Mann-Whitney U test, paired Student's t test, Wilcoxon signed-rank test, one-way ANOVA, Kruskal-Wallis ANOVA, repeated-measures ANOVA, Friedman ANOVA, Tukey post hoc test, Nemenyi post hoc test, Dunn-Holland-Wolfe post hoc test, or two-way ANOVA where appropriate. The symbols *, **, and *** denote p values of <0.05, <0.01, and <0.001, respectively.

REFERENCES AND NOTES

1. J. O'Keefe, J. Dostrovsky, The hippocampus as a spatial map. Preliminary evidence from unit activity in the freely-moving rat. *Brain Res.* **34**, 171–175 (1971). doi: 10.1016/0006-8993(71)90358-1; pmid: 5124915
2. E. Bostock, R. U. Muller, J. L. Kubie, Experience-dependent modifications of hippocampal place cell firing. *Hippocampus* **1**, 193–205 (1991). doi: 10.1002/hipo.450010207; pmid: 1669293
3. R. U. Muller, J. L. Kubie, The effects of changes in the environment on the spatial firing of hippocampal complex-spike cells. *J. Neurosci.* **7**, 1951–1968 (1987). doi: 10.1523/JNEUROSCI.07-07-01951.1987; pmid: 3612226
4. J. K. Leutgeb *et al.*, Progressive transformation of hippocampal neuronal representations in "morphed" environments. *Neuron* **48**, 345–358 (2005). doi: 10.1016/j.neuron.2005.09.007; pmid: 16242413
5. D. Dupret, J. O'Neill, B. Pleydell-Bouverie, J. Csicsvari, The reorganization and reactivation of hippocampal maps predict spatial memory performance. *Nat. Neurosci.* **13**, 995–1002 (2010). doi: 10.1038/nn.2599; pmid: 20639874
6. K. J. Jeffery, Place cells, grid cells, attractors, and remapping. *Neural Plast.* **2011**, 182602 (2011). doi: 10.1155/2011/182602; pmid: 22135756
7. J. Basu, K. Nagel, Neural circuits for goal-directed navigation across species. *Trends Neurosci.* **47**, 904–917 (2024). doi: 10.1016/j.tins.2024.09.005; pmid: 39393938
8. L. L. Colgin, E. I. Moser, M.-B. Moser, Understanding memory through hippocampal remapping. *Trends Neurosci.* **31**, 469–477 (2008). doi: 10.1016/j.tins.2008.06.008; pmid: 18687478
9. C. G. Kentros, N. T. Agnihotri, S. Streater, R. D. Hawkins, E. R. Kandel, Increased attention to spatial context increases both place field stability and spatial memory. *Neuron* **42**, 283–295 (2004). doi: 10.1016/S0896-6273(04)00192-8; pmid: 15091343
10. G. Buzsáki, E. I. Moser, Memory, navigation and theta rhythm in the hippocampal-entorhinal system. *Nat. Neurosci.* **16**, 130–138 (2013). doi: 10.1038/nn.3304; pmid: 23354386
11. N. T. M. Robinson *et al.*, Targeted activation of hippocampal place cells drives memory-guided spatial behavior. *Cell* **183**, 2041–2042 (2020). doi: 10.1016/j.cell.2020.12.010; pmid: 33357402
12. T. D. Goode, K. Z. Tanaka, A. Sahay, T. J. McHugh, An integrated index: Engrams, place cells, and hippocampal memory. *Neuron* **107**, 805–820 (2020). doi: 10.1016/j.neuron.2020.07.011; pmid: 32763146
13. J. Lisman *et al.*, Viewpoints: How the hippocampus contributes to memory, navigation and cognition. *Nat. Neurosci.* **20**, 1434–1447 (2017). doi: 10.1038/nn.4661; pmid: 29073641
14. J. Basu *et al.*, Gating of hippocampal activity, plasticity, and memory by entorhinal cortex long-range inhibition. *Science* **351**, aaa5694 (2016). doi: 10.1126/science.aaa5694; pmid: 26744409
15. S. Melzer *et al.*, Long-range-projecting GABAergic neurons modulate inhibition in hippocampus and entorhinal cortex. *Science* **335**, 1506–1510 (2012). doi: 10.1126/science.1217139; pmid: 22442486
16. A. Caputi, S. Melzer, M. Michael, H. Monyer, The long and short of GABAergic neurons. *Curr. Opin. Neurobiol.* **23**, 179–186 (2013). doi: 10.1016/j.conb.2013.01.021; pmid: 23394773
17. S. Melzer, H. Monyer, Diversity and function of corticopetal and corticofugal GABAergic projection neurons. *Nat. Rev. Neurosci.* **21**, 499–515 (2020). doi: 10.1038/s41583-020-0344-9; pmid: 32747763
18. R. Malik, Y. Li, S. Schamiloglu, V. S. Sohal, Top-down control of hippocampal signal-to-noise by prefrontal long-range inhibition. *Cell* **185**, 1602–1617.e17 (2022). doi: 10.1016/j.cell.2022.04.001; pmid: 35487191
19. J. Urrutia-Piñones, C. Morales-Moraga, N. Sanguinetti-González, A. P. Escobar, C. Q. Chiu, Long-range GABAergic projections of cortical origin in brain function. *Front. Syst. Neurosci.* **16**, 841869 (2022). doi: 10.3389/fnsys.2022.841869; pmid: 35392440
20. M. Hernández-Frausto, O. M. Bilash, A. V. Masurkar, J. Basu, Local and long-range GABAergic circuits in hippocampal area CA1 and their link to Alzheimer's disease. *Front. Neural Circuits* **17**, 1223891 (2023). doi: 10.3389/fncir.2023.1223891; pmid: 37841892
21. E. L. Hargreaves, G. Rao, I. Lee, J. J. Knierim, Major dissociation between medial and lateral entorhinal input to dorsal hippocampus. *Science* **308**, 1792–1794 (2005). doi: 10.1126/science.1110449; pmid: 15961670
22. S. S. Deshmukh, J. J. Knierim, Representation of non-spatial and spatial information in the lateral entorhinal cortex. *Front. Behav. Neurosci.* **5**, 69 (2011). doi: 10.3389/fnbeh.2011.00069; pmid: 22065409
23. A. Tsao, M.-B. Moser, E. I. Moser, Traces of experience in the lateral entorhinal cortex. *Curr. Biol.* **23**, 399–405 (2013). doi: 10.1016/j.cub.2013.01.036; pmid: 23434282
24. C. S. Keene *et al.*, Complementary functional organization of neuronal activity patterns in the perirhinal, lateral entorhinal, and medial entorhinal cortices. *J. Neurosci.* **36**, 3660–3675 (2016). doi: 10.1523/JNEUROSCI.4368-15.2016; pmid: 27030753
25. C. Wang *et al.*, Egocentric coding of external items in the lateral entorhinal cortex. *Science* **362**, 945–949 (2018). doi: 10.1126/science.aau4940; pmid: 30467169
26. W. Xu, D. A. Wilson, Odor-evoked activity in the mouse lateral entorhinal cortex. *Neuroscience* **223**, 12–20 (2012). doi: 10.1016/j.neuroscience.2012.07.067; pmid: 22871522
27. F. C. Leitner *et al.*, Spatially segregated feedforward and feedback neurons support differential odor processing in the lateral entorhinal cortex. *Nat. Neurosci.* **19**, 935–944 (2016). doi: 10.1038/nn.4303; pmid: 27182817
28. J. Y. Lee *et al.*, Dopamine facilitates associative memory encoding in the entorhinal cortex. *Nature* **598**, 321–326 (2021). doi: 10.1038/s41586-021-03948-8; pmid: 34552245

29. J. B. Issa, B. A. Radvansky, F. Xuan, D. A. Dombeck, Lateral entorhinal cortex subpopulations represent experiential epochs surrounding reward. *Nat. Neurosci.* **27**, 536–546 (2024). doi: 10.1038/s41593-023-01557-4; pmid: 38272968
30. J. C. Bowler, A. Losonczy, Direct cortical inputs to hippocampal area CA1 transmit complementary signals for goal-directed navigation. *Neuron* **111**, 4071–4085.e6 (2023). doi: 10.1016/j.neuron.2023.09.013; pmid: 37816349
31. T. Van Cauter *et al.*, Distinct roles of medial and lateral entorhinal cortex in spatial cognition. *Cereb. Cortex* **23**, 451–459 (2013). doi: 10.1093/cercor/bhs033; pmid: 22357665
32. D. I. G. Wilson *et al.*, Lateral entorhinal cortex is critical for novel object-context recognition. *Hippocampus* **23**, 352–366 (2013). doi: 10.1002/hipo.22095; pmid: 23389958
33. M. V. Kuruvilla, J. A. Ainge, Lateral entorhinal cortex lesions impair local spatial frameworks. *Front. Syst. Neurosci.* **11**, 30 (2017). doi: 10.3389/fnsys.2017.00030; pmid: 28567006
34. L. Lu *et al.*, Impaired hippocampal rate coding after lesions of the lateral entorhinal cortex. *Nat. Neurosci.* **16**, 1085–1093 (2013). doi: 10.1038/nn.3462; pmid: 23852116
35. D. L. Schacter, E. Tulving, Eds., *Memory Systems 1994* (The MIT Press, 1994). doi: 10.7551/mitpress/4545.001.0001
36. J. K. Leutgeb, S. Leutgeb, M.-B. Moser, E. I. Moser, Pattern separation in the dentate gyrus and CA3 of the hippocampus. *Science* **315**, 961–966 (2007). doi: 10.1126/science.1135801; pmid: 17303747
37. T. J. McHugh *et al.*, Dentate gyrus NMDA receptors mediate rapid pattern separation in the hippocampal network. *Science* **317**, 94–99 (2007). doi: 10.1126/science.1140263; pmid: 17556551
38. J. P. Neunuebel, J. J. Knierim, CA3 retrieves coherent representations from degraded input: Direct evidence for CA3 pattern completion and dentate gyrus pattern separation. *Neuron* **81**, 416–427 (2014). doi: 10.1016/j.neuron.2013.11.017; pmid: 24462102
39. M. W. Jung, B. L. McNaughton, Spatial selectivity of unit activity in the hippocampal granular layer. *Hippocampus* **3**, 165–182 (1993). doi: 10.1002/hipo.450030209; pmid: 8353604
40. D. GoodSmith *et al.*, Spatial representations of granule cells and mossy cells of the dentate gyrus. *Neuron* **93**, 677–690.e5 (2017). doi: 10.1016/j.neuron.2016.12.026; pmid: 28132828
41. M. Allegra, L. Posani, R. Gómez-Ocádiz, C. Schmidt-Hieber, Differential relation between neuronal and behavioral discrimination during hippocampal memory encoding. *Neuron* **108**, 1103–1112.e6 (2020). doi: 10.1016/j.neuron.2020.09.032; pmid: 33068531
42. A. D. Madar, L. A. Ewell, M. V. Jones, Pattern separation of spiketrains in hippocampal neurons. *Sci. Rep.* **9**, 5282 (2019). doi: 10.1038/s41598-019-41503-8; pmid: 30918288
43. A. D. Madar, L. A. Ewell, M. V. Jones, Temporal pattern separation in hippocampal neurons through multiplexed neural codes. *PLOS Comput. Biol.* **15**, e1006932 (2019). doi: 10.1371/journal.pcbi.1006932; pmid: 31009459
44. M. A. Yassa, C. E. L. Stark, Pattern separation in the hippocampus. *Trends Neurosci.* **34**, 515–525 (2011). doi: 10.1016/j.tins.2011.06.006; pmid: 21788086
45. H. Lee, D. GoodSmith, J. J. Knierim, Parallel processing streams in the hippocampus. *Curr. Opin. Neurobiol.* **64**, 127–134 (2020). doi: 10.1016/j.conb.2020.03.004; pmid: 32502734
46. S. Leutgeb, J. K. Leutgeb, A. Treves, M.-B. Moser, E. I. Moser, Distinct ensemble codes in hippocampal areas CA3 and CA1. *Science* **305**, 1295–1298 (2004). doi: 10.1126/science.1100265; pmid: 15272123
47. S. Leutgeb *et al.*, Independent codes for spatial and episodic memory in hippocampal neuronal ensembles. *Science* **309**, 619–623 (2005). doi: 10.1126/science.1114037; pmid: 16040709
48. D. Marr, Simple memory: A theory for archicortex. *Philos. Trans. R. Soc. London Ser. B* **262**, 23–81 (1971). doi: 10.1098/rstb.1971.0078; pmid: 4399412
49. A. Treves, E. T. Rolls, Computational constraints suggest the need for two distinct input systems to the hippocampal CA3 network. *Hippocampus* **2**, 189–199 (1992). doi: 10.1002/hipo.450020209; pmid: 1308182
50. K. Nakazawa *et al.*, Requirement for hippocampal CA3 NMDA receptors in associative memory recall. *Science* **297**, 211–218 (2002). doi: 10.1126/science.1071795; pmid: 12040087
51. A. E. Gold, R. P. Kesner, The role of the CA3 subregion of the dorsal hippocampus in spatial pattern completion in the rat. *Hippocampus* **15**, 808–814 (2005). doi: 10.1002/hipo.20103; pmid: 16010664
52. S. J. Guzman, A. Schlögl, M. Frotscher, P. Jonas, Synaptic mechanisms of pattern completion in the hippocampal CA3 network. *Science* **353**, 1117–1123 (2016). doi: 10.1126/science.aaf1836; pmid: 27609885
53. E. T. Rolls, An attractor network in the hippocampus: Theory and neurophysiology. *Learn. Mem.* **14**, 714–731 (2007). doi: 10.1101/lm.631207; pmid: 18007016
54. I. Lee, D. Yoganarasimha, G. Rao, J. J. Knierim, Comparison of population coherence of place cells in hippocampal subfields CA1 and CA3. *Nature* **430**, 456–459 (2004). doi: 10.1038/nature02739; pmid: 15229614
55. Q. Sun *et al.*, Proximodistal heterogeneity of hippocampal CA3 pyramidal neuron intrinsic properties, connectivity, and reactivation during memory recall. *Neuron* **95**, 656–672.e3 (2017). doi: 10.1016/j.neuron.2017.07.012; pmid: 28772124
56. N. C. Klapoetke *et al.*, Independent optical excitation of distinct neural populations. *Nat. Methods* **11**, 338–346 (2014). doi: 10.1038/nmeth.2836; pmid: 24509633
57. E. S. Boyden, F. Zhang, E. Bamberg, G. Nagel, K. Deisseroth, Millisecond-timescale, genetically targeted optical control of neural activity. *Nat. Neurosci.* **8**, 1263–1268 (2005). doi: 10.1038/nn1525; pmid: 16116447
58. L. Petreanu, T. Mao, S. M. Sternson, K. Svoboda, The subcellular organization of neocortical excitatory connections. *Nature* **457**, 1142–1145 (2009). doi: 10.1038/nature07709; pmid: 19151697
59. P. Somogyi, T. Klausberger, Defined types of cortical interneurone structure space and spike timing in the hippocampus. *J. Physiol.* **562**, 9–26 (2005). doi: 10.1113/jphysiol.2004.078915; pmid: 15539390
60. T. Klausberger, P. Somogyi, Neuronal diversity and temporal dynamics: The unity of hippocampal circuit operations. *Science* **321**, 53–57 (2008). doi: 10.1126/science.1149381; pmid: 18599766
61. Y. Kawaguchi, S. Kondo, Parvalbumin, somatostatin and cholecystokinin as chemical markers for specific GABAergic interneuron types in the rat frontal cortex. *J. Neurocytol.* **31**, 277–287 (2002). doi: 10.1023/A:1024126110356; pmid: 12815247
62. O. M. Bilash, S. Chavlis, C. D. Johnson, P. Poirazi, J. Basu, Lateral entorhinal cortex inputs modulate hippocampal dendritic excitability by recruiting a local disinhibitory microcircuit. *Cell Rep.* **42**, 111962 (2023). doi: 10.1016/j.celrep.2022.111962; pmid: 36640337
63. H. Pawelzik, D. I. Hughes, A. M. Thomson, Physiological and morphological diversity of immunocytochemically defined parvalbumin- and cholecystokinin-positive interneurones in CA1 of the adult rat hippocampus. *J. Comp. Neurol.* **443**, 346–367 (2002). doi: 10.1002/cne.10118; pmid: 11807843
64. L. Tyan *et al.*, Dendritic inhibition provided by interneuron-specific cells controls the firing rate and timing of the hippocampal feedback inhibitory circuitry. *J. Neurosci.* **34**, 4534–4547 (2014). doi: 10.1523/JNEUROSCI.3813-13.2014; pmid: 24671999
65. N. B. Danielson *et al.*, Sublayer-specific coding dynamics during spatial navigation and learning in hippocampal area CA1. *Neuron* **91**, 652–665 (2016). doi: 10.1016/j.neuron.2016.06.020; pmid: 27397517
66. R. Zemla, J. J. Moore, M. D. Hopkins, J. Basu, Task-selective place cells show behaviorally driven dynamics during learning and stability during memory recall. *Cell Rep.* **41**, 111700 (2022). doi: 10.1016/j.celrep.2022.111700; pmid: 36417882
67. J. J. Moore *et al.*, Sub-cellular population imaging tools reveal stable apical dendrites in hippocampal area CA3. *Nat. Commun.* **16**, 1119 (2025). doi: 10.1038/s41467-025-56289-9; pmid: 39875374
68. T. Butola *et al.*, Hippocampus shapes entorhinal cortical output through a direct feedback circuit. *Nat. Neurosci.* **28**, 811–822 (2025). doi: 10.1038/s41593-025-01883-9; pmid: 39966537
69. B. N. Armbruster, X. Li, M. H. Pausch, S. Herlitze, B. L. Roth, Evolving the lock to fit the key to create a family of G protein-coupled receptors potently activated by an inert ligand. *Proc. Natl. Acad. Sci. U.S.A.* **104**, 5163–5168 (2007). doi: 10.1073/pnas.0700293104; pmid: 17360345
70. C. J. Magnus *et al.*, Ultrapotent chemogenetics for research and potential clinical applications. *Science* **364**, eaav5282 (2019). doi: 10.1126/science.aav5282; pmid: 30872534
71. S. N. Chettih, C. D. Harvey, Single-neuron perturbations reveal feature-specific competition in V1. *Nature* **567**, 334–340 (2019). doi: 10.1038/s41586-019-0997-6; pmid: 30842660
72. L. Carrillo-Reid, S. Han, W. Yang, A. Akrouh, R. Yuste, Controlling visually guided behavior by holographic recalling of cortical ensembles. *Cell* **178**, 447–457.e5 (2019). doi: 10.1016/j.cell.2019.05.045; pmid: 31257030
73. W. Xu, T. C. Südhof, A neural circuit for memory specificity and generalization. *Science* **339**, 1290–1295 (2013). doi: 10.1126/science.1229534; pmid: 23493706
74. A. J. Rashid *et al.*, Competition between engrams influences fear memory formation and recall. *Science* **353**, 383–387 (2016). doi: 10.1126/science.aaf0594; pmid: 27463673
75. S. Kim, S. J. Guzman, H. Hu, P. Jonas, Active dendrites support efficient initiation of dendritic spikes in hippocampal CA3 pyramidal neurons. *Nat. Neurosci.* **15**, 600–606 (2012). doi: 10.1038/nn.3060; pmid: 22388958
76. F. Brandalise, S. Carta, F. Helmchen, J. Lisman, U. Gerber, Dendritic NMDA spikes are necessary for timing-dependent associative LTP in CA3 pyramidal cells. *Nat. Commun.* **7**, 13480 (2016). doi: 10.1038/ncomms13480; pmid: 27848967
77. J. K. Makara, J. C. Magee, Variable dendritic integration in hippocampal CA3 pyramidal neurons. *Neuron* **80**, 1438–1450 (2013). doi: 10.1016/j.neuron.2013.10.033; pmid: 24360546
78. R. K. Mishra, S. Kim, S. J. Guzman, P. Jonas, Symmetric spike timing-dependent plasticity at CA3-CA3 synapses optimizes storage and recall in autoassociative networks. *Nat. Commun.* **7**, 11552 (2016). doi: 10.1038/ncomms11552; pmid: 27174042
79. J. Cichon, W.-B. Gan, Branch-specific dendritic Ca^{2+} spikes cause persistent synaptic plasticity. *Nature* **520**, 180–185 (2015). doi: 10.1038/nature14251; pmid: 25822789
80. J. Voigts, M. T. Harnett, Somatic and dendritic encoding of spatial variables in retrosplenial cortex differs during 2D navigation. *Neuron* **105**, 237–245.e4 (2020). doi: 10.1016/j.neuron.2019.10.016; pmid: 31759808

81. M. E. J. Sheffield, D. A. Dombeck, Calcium transient prevalence across the dendritic arbour predicts place field properties. *Nature* **517**, 200–204 (2015). doi: 10.1038/nature13871; pmid: 25363782
82. J. K. O'Hare, J. Wang, M. D. Shala, F. Polleux, A. Losonczy, Distal tuft dendrites predict properties of new hippocampal place fields. *Neuron* **113**, 1969–1982.e7 (2025). doi: 10.1016/j.neuron.2025.03.029; pmid: 40250428
83. E. O. Mann, O. Paulsen, Role of GABAergic inhibition in hippocampal network oscillations. *Trends Neurosci.* **30**, 343–349 (2007). doi: 10.1016/j.tins.2007.05.003; pmid: 17532059
84. S. Jinno *et al.*, Neuronal diversity in GABAergic long-range projections from the hippocampus. *J. Neurosci.* **27**, 8790–8804 (2007). doi: 10.1523/JNEUROSCI.1847-07.2007; pmid: 17699661
85. A. Joshi, M. Salib, T. J. Viney, D. Dupret, P. Somogyi, Behavior-dependent activity and synaptic organization of septo-hippocampal GABAergic neurons selectively targeting the hippocampal CA3 area. *Neuron* **96**, 1342–1357.e5 (2017). doi: 10.1016/j.neuron.2017.10.033; pmid: 29198757
86. G. G. Szabo *et al.*, Ripple-selective GABAergic projection cells in the hippocampus. *Neuron* **110**, 1959–1977.e9 (2022). doi: 10.1016/j.neuron.2022.04.002; pmid: 35489331
87. Z. Christenson Wick, M. R. Tetzlaff, E. Krook-Magnuson, Novel long-range inhibitory nNOS-expressing hippocampal cells. *eLife* **8**, e46816 (2019). doi: 10.7554/eLife.46816; pmid: 31609204
88. R. Francavilla *et al.*, Connectivity and network state-dependent recruitment of long-range VIP-GABAergic neurons in the mouse hippocampus. *Nat. Commun.* **9**, 5043 (2018). doi: 10.1038/s41467-018-07162-5; pmid: 30487571
89. G. Unal *et al.*, Spatio-temporal specialization of GABAergic septo-hippocampal neurons for rhythmic network activity. *Brain Struct. Funct.* **223**, 2409–2432 (2018). doi: 10.1007/s00429-018-1626-0; pmid: 29500537
90. P. Kaifosh, M. Lovett-Barron, G. F. Turi, T. R. Reardon, A. Losonczy, Septo-hippocampal GABAergic signaling across multiple modalities in awake mice. *Nat. Neurosci.* **16**, 1182–1184 (2013). doi: 10.1038/nn.3482; pmid: 23912949
91. A. D. Madar, A. Jiang, C. Dong, M. E. J. Sheffield, Synaptic plasticity rules driving representational shifting in the hippocampus. *Nat. Neurosci.* **28**, 848–860 (2025). doi: 10.1038/s41593-025-01894-6; pmid: 40113934
92. Y. Li, J. J. Briguglio, S. Romani, J. C. Magee, Mechanisms of memory-supporting neuronal dynamics in hippocampal area CA3. *Cell* **187**, 6804–6819.e21 (2024). doi: 10.1016/j.cell.2024.09.041; pmid: 39454575
93. P. Mehta *et al.*, Functional access to neuron subclasses in rodent and primate forebrain. *Cell Rep.* **26**, 2818–2832.e8 (2019). doi: 10.1016/j.celrep.2019.02.011; pmid: 30840900
94. J. C. Grieger, V. W. Choi, R. J. Samulski, Production and characterization of adeno-associated viral vectors. *Nat. Protoc.* **1**, 1412–1428 (2006). doi: 10.1038/nprot.2006.207; pmid: 17406430
95. D. Ma *et al.*, Role of ER export signals in controlling surface potassium channel numbers. *Science* **291**, 316–319 (2001). doi: 10.1126/science.291.5502.316; pmid: 11209084
96. A. Hofherr, B. Fakler, N. Klöcker, Selective Golgi export of Kir2.1 controls the stoichiometry of functional Kir2.x channel heteromers. *J. Cell Sci.* **118**, 1935–1943 (2005). doi: 10.1242/jcs.02322; pmid: 15827083
97. J. T. Ting, T. L. Daigle, Q. Chen, G. Feng, "Acute brain slice methods for adult and aging animals: Application of targeted patch clamp analysis and optogenetics" in *Patch-Clamp Methods and Protocols*, vol. 1183 of Methods in Molecular Biology, M. Martina, S. Taverna, Eds. (Springer, 2014), pp. 221–242.
98. M. Pachitariu *et al.*, Suite2p: beyond 10,000 neurons with standard two-photon microscopy. bioRxiv 061507 [Preprint] (2016); https://doi.org/10.1101/061507.
99. J. Schindelin *et al.*, Fiji: An open-source platform for biological-image analysis. *Nat. Methods* **9**, 676–682 (2012). doi: 10.1038/nmeth.2019; pmid: 22743772
100. W. E. Skaggs, B. L. McNaughton, K. M. Gothard, E. J. Markus, "An information theoretic approach to deciphering the hippocampal code" in *NIPS'92: Proceedings of the 6th International Conference on Neural Information Processing Systems* (Morgan Kaufmann Publishers Inc., 1993), pp. 1030–1037.
101. V. Robert, J. Basu, basulab-nyu/Robert_Basu_2025. Zenodo (2025); https://doi.org/10.5281/zenodo.16621125.
102. V. Robert, J. Moore, C. Clopath, J. Basu, basulab-nyu/Robert_Basu_2025_code. Zenodo (2025); https://doi.org/10.5281/zenodo.16878595.

ACKNOWLEDGMENTS

New York University (NYU) High Performance Computing resources were used for data analysis. The NYU Genotyping Core Laboratory was used for genotyping mice. We thank M. Dufour and R. Zemla for the early development of the two-photon imaging preparation and head-fixed behavioral setup at the Basu lab. We thank P. Frazel for the mini-prep of the AAV2/5:Dlx-DIO-hM4D(Gi)-mCherry plasmid. We thank M. Long for electrophysiology equipment resources for the project and feedback on the manuscript. We are grateful to O. Bilash, T. Butola, G. Buzsáki, S. Chamberland, M. Druart, M. Hernandez-Frausto, M. Hopkins, D. Lin, R. Piskorowski, R. Tsien, and S. Wang for their input at various stages of the project and helpful comments on the manuscript. **Funding:** This work was funded by National Institutes of Health (NIH) National Institute of Neurological Disorders and Stroke (NINDS) BRAIN Initiative 1R01NS109994 (J.B., C.C.); NIH NINDS 1R01NS109362-01 (J.B.); NINDS 1RM1NS132981-01 (J.B.); a McKnight Scholar Award in Neuroscience (J.B.); a McKnight Endowment Fund for Neuroscience Mathew Pecot URM Award (J.B.); a Klingenstein-Simons Fellowship Award in Neuroscience (J.B.); Alzheimer's Association Research Grant to Promote Diversity – New to the Field AARG-D-NTF (J.B.); an Alfred P. Sloan Research Fellowship (J.B.); a Mathers Charitable Foundation Award (J.B.); a Whitehall Research Grant (J.B.); an American Epilepsy Society Junior Investigator Award (J.B.); a Blas Frangione Young Investigator Research Grant (J.B.); a New York University Whitehead Fellowship for Junior Faculty in Biomedical and Biological Sciences (J.B.); a Leon Levy Foundation Award (J.B.); the Emerald Foundation (J.J.M.); a Young Researchers Bettencourt Prize (V.R.); NIH 5T32MH019524-30 training award (K.O.); NIH T32GM007308 training grant (S.K.R.); NIH NIMH Diversity Supplement training award 3R01MH122391-04S1, parent award R01MH122391PIs Buzsáki/Basu (C.D.J.); NIH NINDS 1U01 NS099720 (B.V.Z.); and NIH NINDS 1U01 NS094330 (B.V.Z.). **Author contributions:** V.R. and J.B. conceived the project and designed experiments; V.R. performed all the experiments and analysis; K.O. assisted with the stereotaxic injections, ex vivo patch-clamp recordings, and immunohistochemistry related to the long-range GABAergic projection to CA3 IN circuit-mapping experiments and also performed the local LEC connectivity experiments; J.J.M. assisted with imaging data analysis; S.K.R. assisted with the CA3 cranial window imaging preparation and in vivo two-photon imaging data acquisition; C.D.J. and R.G.D.L.T. assisted with immunohistochemistry; B.V.Z. provided the AAV2/7:h56D-ChR2-sfGFP construct; C.C. performed the computational modeling; V.R., K.O., and J.B. wrote the paper with input from all authors; and J.B. acquired funding, provided resources, supervised personnel, and managed the project. **Competing interests:** The authors declare that they have no competing interests. **Data and materials availability:** All data are available in the manuscript or the supplementary materials and are deposited at Zenodo (*101*). All original code is available at Zenodo (*102*). Further information and requests for materials and additional details required to reanalyze the data reported here should be directed to and will be fulfilled by the corresponding author. This study used the AAV2/7:h56D-ChR2-sfGFP custom-designed viral reagent, courtesy of B. Zemelman. **License information:** Copyright © 2025 the authors, some rights reserved; exclusive licensee American Association for the Advancement of Science. No claim to original US government works. https://www.science.org/about/science-licenses-journal-article-reuse

SUPPLEMENTARY MATERIALS

science.org/doi/10.1126/science.adn0623
Figs. S1 to S19; Tables S1 to S4; MDAR Reproducibility Checklist

Submitted 22 November 2023; resubmitted 5 May 2025; accepted 29 August 2025; published online 30 October 2025

10.1126/science.adn0623

Science Podcasts

AAAS

Hear the stories behind the latest news and research from *Science*.

LISTEN & SUBSCRIBE

NEW EPISODES EVERY THURSDAY

QUANTUM SIMULATION

Shapiro steps in strongly-interacting Fermi gases

Giulia Del Pace[1,2,3]*, Diego Hernández-Rajkov[2,3], Vijay Pal Singh[4], Nicola Grani[1,2,3], Marcia Frómeta Fernández[2,3], Giulio Nesti[1,2], Jorge Amin Seman[5], Massimo Inguscio[2,3,6], Luigi Amico[4,7,8], Giacomo Roati[2,3]

Driven many-body systems exhibit diverse and complex dynamical behaviors. Here, we report the observation of Shapiro steps in periodically driven Josephson junctions between strongly interacting Fermi superfluids of ultracold atoms. The height and the width of the observed quantized plateaus in the current-potential characteristics mirror the external drive frequency and the junction nonlinear response. Direct measurements of the current-phase relationship showcase how Shapiro steps arise from the synchronization between the relative phase of the two reservoirs and the external drive. Such a mechanism is further supported by the detection of periodic phase-slippage processes, in the form of vortex-antivortex pairs. Our results are corroborated by a circuital model and numerical simulations. Our work may open prospects for studying emergent nonequilibrium dynamics in quantum many-body systems under external drives.

Driven many-body platforms offer a powerful route to probe nonequilibrium quantum dynamics and emergent collective phenomena (*1*). A paradigmatic example is provided by Josephson junctions (JJs) under driving currents. A Josephson junction comprises two superconducting islands separated by a thin insulating barrier. Josephson showed that a dissipationless current I can flow across the junction, maintained solely by the phase difference ϕ between the two superconducting reservoirs (*2*). Above a critical current I_c, the junction transitions into the so-called voltage state: a finite voltage V develops across the junction, which is directly related to the phase difference dynamics as provided by the Josephson-Anderson relation $V = \frac{\hbar}{2e}\dot{\phi}$, with $\hbar$ being the reduced Planck constant and e the electron charge. In this regime, the Josephson current time evolution is characterized by the frequency $\omega_J = 2eV/\hbar$. The junction is thus an element that operates in cycles with a natural frequency controllably set by the externally injected current (*3*, *4*).

When an AC drive with frequency ω is summed to a DC bias, the junction dynamics synchronize with the external drive, resulting in $\omega_J = n\omega$, with n a positive integer. This synchronization yields quantized voltage plateaus, known as Shapiro steps, appearing at $\langle V \rangle_t = n\hbar\omega/2e$ in the time-averaged voltage-current characteristics (*5*). Shapiro steps arise from a phase-locking process where ϕ advances by $2\pi n$ during each cycle of the driving field, undergoing n phase slip processes and establishing coherence between the junction phase and the driven field. Since their observation in superconducting Josephson junctions (SJJs) (*5*), Shapiro steps have been investigated in various nonlinear systems, from charge density waves (*6*), colloidal systems (*7*, *8*), superconducting nanowires (*9*) and nanotubes (*10*), and ^{3}He weak links (*11*). Shapiro steps in SJJs play a crucial role in metrology, in calibration within electronics, and in defining quantum standards (*12*, *13*).

Recent years have witnessed considerable progress in developing and operating circuit architectures employing ultracold atoms (*14*). These atomtronics circuits feature enhanced control and flexibility of their working conditions that may go beyond conventional electronics. One of the most promising atomic platforms for implementing such circuits consists of ultracold Fermi gases (*15*). These systems provide a setting for different regimes of superfluidity, ranging from the Bardeen-Cooper-Schrieffer (BCS) limit of weakly bound fermion pairs to a Bose-Einstein condensate (BEC) of tightly bound molecules, including the intermediate universal, strongly correlated unitary regime (*16*, *17*). In particular, unitary Fermi gases (UFGs) serve as a prototypical example of strongly interacting systems, sharing similarities with other strongly interacting Fermi systems found in nature, from nuclear matter to neutron stars (*18*). Research on quantum transport phenomena within these systems has explored a variety of configurations, including mesoscopic two-terminal setups (*19*), ring geometries (*20*, *21*), optical lattices (*22*–*25*), and scenarios involving disorder (*26*) or periodic modulation of the harmonic trapping potential (*27*–*31*).

Josephson effects have been observed in both three-dimensional (*32*, *33*) and two-dimensional (*34*) unitary superfluids, providing insights into the microscopic properties of these gases. However, despite various theoretical proposals (*35*–*38*), the observation of Shapiro steps in atomic Josephson junctions has remained elusive. Recently, Shapiro steps have been predicted to occur by periodically oscillating the position of a thin tunneling barrier within a weakly interacting BEC (*39*). However, for Fermi superfluids, it remains an open question whether strong interactions could affect the dynamics. Interactions are expected to enhance phase coherence across the junction and potentially reduce decoherence effects associated with the finite compressibility of atomic superfluids (*32*, *33*), but their impact on synchronization processes is yet to be understood. Investigating these effects is crucial for deepening our understanding of strongly interacting systems and for revealing their microscopic behavior under external drives.

In this work, we report the observation of Shapiro steps in a periodically driven atomic Josephson junction connecting two strongly interacting unitary Fermi superfluids. Similar to SJJs, we find that the external driving frequency determines the height of Shapiro steps, whereas the driving amplitude affects their width. Moreover, we access a detailed microscopic understanding of the physical mechanism behind the Shapiro steps by operating the junction in the BEC regime and directly measuring its phase dynamics. By analyzing the current-phase relation under the external drive and observing the phase evolution across different Shapiro steps, we demonstrate the synchronization between the junction phase and the external drive. Both for a BEC and a unitary junction, we observe that the Shapiro dynamics are accompanied by vortex-antivortex pairs emissions, in agreement with the results of (*39*). Our results showcase the response of a many-body strongly interacting system to an external drive, resulting in synchronized dynamics.

Creating and driving the atomic junction

We produce strongly interacting Fermi superfluids of $N \sim 2 \times 10^4$ atom pairs by cooling a balanced mixture of the first and third lowest hyperfine states of ^{6}Li to temperatures $\sim 0.3(1)\ T_c$, where T_c is the superfluid critical temperature (*40*). Interparticle interactions are parameterized by $1/k_F a$, where $k_F = \sqrt{2mE_F}/\hbar$ is the Fermi wave

[1]Department of Physics, University of Florence, Sesto Fiorentino, Italy. [2]European Laboratory for Nonlinear Spectroscopy (LENS), University of Florence, Sesto Fiorentino, Italy. [3]Istituto Nazionale di Ottica del Consiglio Nazionale delle Ricerche (CNR-INO) c/o LENS, Sesto Fiorentino, Italy. [4]Quantum Research Centre, Technology Innovation Institute, Abu Dhabi, UAE. [5]Instituto de Física, Universidad Nacional Autónoma de México, Ciudad de México, Mexico. [6]Department of Engineering, Campus Bio-Medico University of Rome, Rome, Italy. [7]INFN-Sezione di Catania, Catania, Italy. [8]Dipartimento di Fisica e Astronomia, 'Ettore Majorana', Università di Catania, Catania, Italy. *Corresponding author. Email: delpace@lens.unifi.it

vector, E_F the Fermi energy, and a the s-wave scattering length. We tune a in the vicinity of the Feshbach resonance at 690G (*41*), enabling the exploration of various superfluid regimes across the BEC-BCS crossover. In this work, we focus on two different interaction regimes: a UFG with Fermi energy $E_F/h = 11.8(4)$ kHz, and a molecular BEC at $1/k_F a = 3.3(1)$ with $E_F/h = 9.2(3)$ kHz. The gas is confined in the $x-y$ plane using a box-like potential with dimensions $L_x \times L_y$ of 125 μm by 17.5 μm, and along the vertical z direction by a strong harmonic confinement (*40*). The trap configuration establishes a nearly homogeneous in-plane atomic density with the superfluid remaining in the three-dimensional regime. To engineer the atomic JJ, we superimpose a thin repulsive optical barrier onto the atomic sample, which can be displaced along the x axis (Fig. 1A). The barrier intensity profile and position are dynamically controlled by a digital micromirror device (DMD), whose designed pattern is projected onto the atomic plane using a high-resolution microscope objective (*33*, *42*). The barrier features a full width at half maximum of 0.9(1) μm along the x direction (*40*), comparable to the healing length of the investigated superfluids, ranging between 0.6 and 1.7 μm for typical gas parameters. The barrier height, V_0, is set to be larger than the gas chemical potential, μ_0, with $V_0/\mu_0 = 1.3(1)$ for the unitary, and 1.2(1) for the BEC JJs, ensuring that the junction always operates in the tunneling regime (*33*, *42*). Our working conditions are complementary to those reported in (*43*), where Shapiro steps are observed in a weakly interacting BEC junction in the weak link regime.

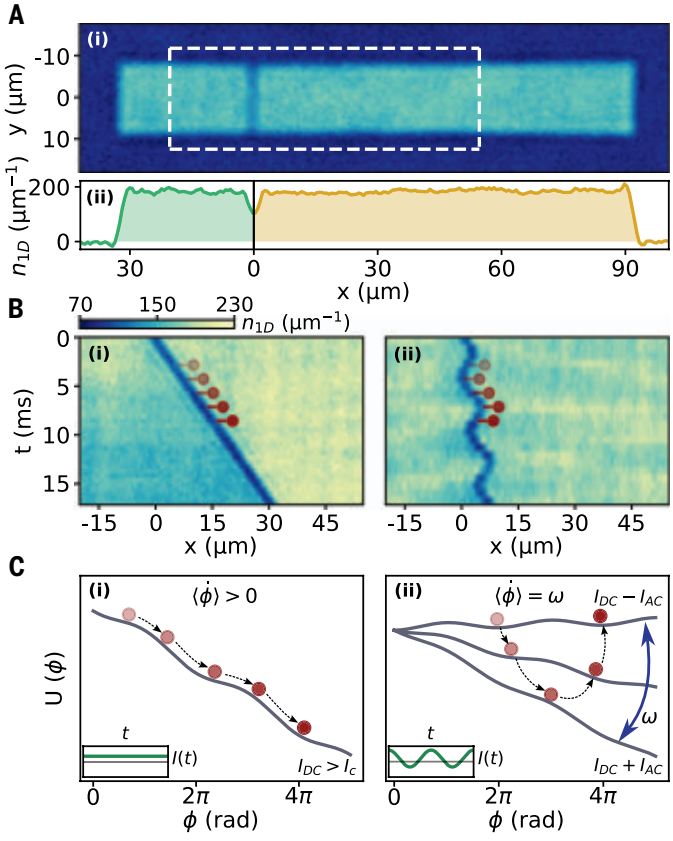


Fig. 1. Current injection in a homogeneous atomic JJ. (**A**) (i) In situ image of the JJ at unitarity, averaged over 15 repetitions. (ii) 1D density profile of the junction integrated along the y direction. (**B**) 1D density profiles as a function of time for (i) $v_{DC} = 1.5$ mm/s and $x_{AC} = 0$, (ii) $v_{DC} = 0.4$ mm/s and $x_{AC} = 2$ μm, modulating with a frequency of 175 Hz. Each row corresponds to the integrated average density profile over five experimental realizations. Red symbols of decreasing transparency mark the timing of the corresponding evolution illustrated in (C). (**C**) Sketch of the phase particle dynamics in the washboard potential for the conditions of (B). (i) The voltage state of the JJ corresponds to the particle rolling down the potential, causing a voltage increase. (ii) Introducing an alternating current modulates the tilt of the potential over time. For an overdamped JJ, the phase particle velocity locks to the external drive, $\langle\dot{\phi}\rangle_t = n\omega$, yielding to a synchronized motion that crosses n potential minima during each modulation cycle. The insets show the current for the two illustrated cases.

We inject currents into our junction by precisely moving the tunneling barrier along specific trajectories controlled with the DMD (*33*, *40*, *42*). The in-plane homogeneous density of the superfluid ensures that the injected current $I(t)$ is independent of its longitudinal position, and it is determined only by the instantaneous barrier velocity $v(t)$. The instantaneous current reads $I(t) = v(t)\tilde{n}L_y = v(t)N/L_x$, with $\tilde{n} = \int n_{3D}(z)dz = N/L_xL_y$ the planar density. To introduce a biased alternating current, we move the barrier according to the trajectory $x(t) = v_{DC}t + x_{AC}\sin(\omega t)$ (*39*), giving rise to the instantaneous injected current $I(t) = I_{DC} + I_{AC}\cos(\omega t)$, with $I_{DC} = v_{DC}N/L_x$, and $I_{AC} = \omega x_{AC}N/L_x$ (Fig. 1B). We explore the junction operation under different driving conditions by tuning the trajectory parameters v_{DC}, x_{AC}, and ω, as illustrated in Fig. 1B for bias (i) and composite current injections (ii). The junction dynamics can be portrayed with the well known washboard potential analogy (*4*), as sketched in Fig. 1C. The phase of the JJ follows the same equation of motion as that of a classical particle subject to a viscous force moving in a tilted washboard potential, where the tilt is given by the external current I. For a DC bias above I_c, the particle enters the running-phase regime, where $\langle\dot{\phi}\rangle_t \neq 0$, and the junction operates resistively [Fig. 1C (i)]. For an AC drive, in the overdamped regime, where friction overtakes inertia, the velocity locks to the driving tilt, resulting in a steady but synchronized descent, crossing n potential wells during each modulation cycle [Fig. 1C (ii)]. This resonant motion locks the mean particle velocity to fixed values $\langle\dot{\phi}\rangle_t = n\omega$, leading to distinct, equally spaced velocity steps, the Shapiro steps. In both cases, the descending movement of the phase particle produces a number of phase-slip events, synchronized with the drive in the AC case.

Shapiro steps in a unitary junction

We probe the response of our junction by measuring the $I - \Delta\mu$ characteristic curves as a function of the bias current, I_{DC}, after three driving periods T (*40*), where $T = 2\pi/\omega$. Here, $\Delta\mu = \mu_L - \mu_R$ represents the chemical potential difference between the the left μ_L and right μ_R reservoirs measured from in situ density images. Curves for $I_{AC} = 0$ and $I_{AC} > 0$ for two example driving parameter sets are shown in Fig. 2, A and B. In the undriven scenario, we recover the hallmark behavior of a current-biased JJ, featuring a zero-imbalance plateau for DC currents below I_c (*33*). For the AC-driven JJ instead, we observe the emergence of distinct plateaus, with number, widths, and heights strongly depending on the driving parameters. To characterize the plateau properties, we perform a phenomenological fit of each step in the $I - \Delta\mu$ curve using multiple, patched sigmoidal functions (*40*), from which we get the height $\Delta\mu_n$, and the width ΔI_n of each step. The step height is in agreement with $\Delta\mu_n = n\hbar\omega$ for various driving frequencies and does not depend on I_{AC} (Fig. 2C): It is determined exclusively by the external driving frequency, whereas the driving strength I_{AC} affects only the position and width of each step (Fig. 2D).

To quantitatively describe the observed $I - \Delta\mu$ characteristics, we exploit the resistively and capacitively shunted junction (RCSJ) circuital model (*3*, *4*). In this model, the junction is set in parallel with resistive and capacitive components, with the total circulating current being

$$I(t) = I_c\sin\phi + \hbar G\dot{\phi} + \hbar C\ddot{\phi} \quad (1)$$

The supercurrent contribution is given by the sinusoidal current-phase relation $I_c\sin\phi$; the resistive and capacitive contributions are $G\dot{\phi}$ and $C\ddot{\phi}$, respectively. Similarly as for SJJ, the Josephson-Anderson relation $\Delta\mu = -\hbar\dot{\phi}$ connects the phase dynamics to the chemical potential build-up (*35*, *44*), with $\Delta\mu$ playing the role of the junction voltage.

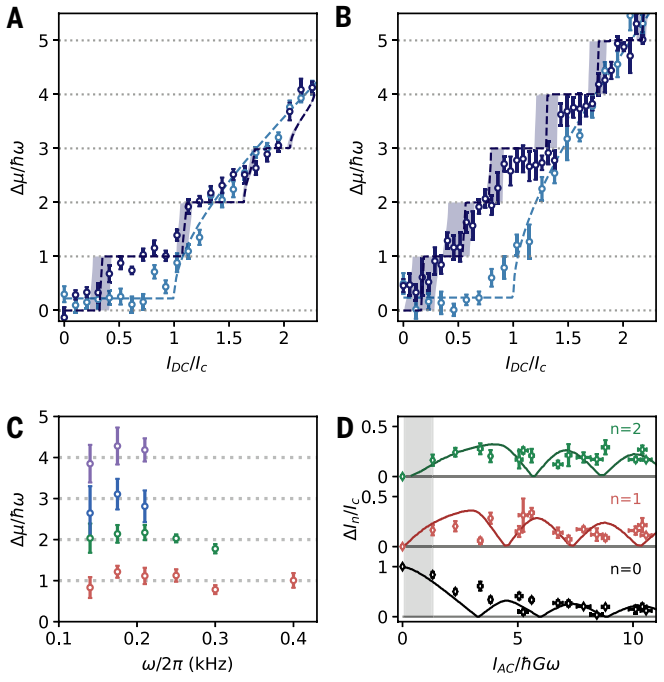


Fig. 2. Shapiro steps in strongly interacting Fermi superfluids at unitarity. (**A** and **B**) Current-voltage characteristic for different AC drive settings (dark blue): $I_{AC}/I_c = 1.6(1)$ and $\omega = 2\pi \times 210$ Hz (A), and for $I_{AC}/I_c = 2.4(1)$ and $\omega = 2\pi \times 175$ Hz (B). In both panels, light blue symbols report the corresponding DC curve at $I_{AC}/I_c = 0$. Dashed light blue lines represent the fit with the stationary solution of the undriven overdamped RCSJ model (*40*); dark blue ones show the results for the driven scenario, where shades account for the fitting error on I_c. (**C**) Shapiro step height characterization. Colors label the 1st (red), 2nd (green), 3rd (blue), and 4th (purple) step. Dotted lines represent $\Delta\mu = n\hbar\omega$. Data points represent an average over at least three measurements at the same ω and different I_{AC}. (**D**) Step half-width characterization: Symbols report the measured step width for $\omega = 2\pi \times 175$ Hz, and variable I_{AC}. Error bars represent the error of the centroid of the multiple sigmoid fit. Solid lines correspond to the numerical solutions of the current-driven overdamped RCSJ model. *G* results from the fit of the DC curve (*40*). The gray shaded area marks the inaccessible parameter region.

The Stewart-McCumber parameter $\beta_c = I_c C/\hbar G^2$ determines the dynamic regime of the junction, discriminating between underdamped ($\beta_c \gg 1$) and overdamped ($\beta_c \ll 1$) (*4*). In the latter, the undriven solution is analytically given by $\Delta\mu = G^{-1}\sqrt{I_{DC}^2 - I_c^2}$, which we use to fit the DC measurements to extract I_c and G. By contrast, in the driven scenario, the $I - \Delta\mu$ characteristic is evaluated by numerically solving Eq. 1. As reported in Fig. 1, A and B, the overdamped solutions of the RCSJ model display the characteristic Shapiro steps matching the measured ones. Even though we estimate $\beta_c \approx 14(2)$ for the unitary superfluid, the overdamped RCSJ numerical solutions well capture the observed step height, owing to the robustness of the Shapiro effect. The precise determination of the nonlinear behavior of the step widths depends on the precise knowledge of the modulation protocol (*40*). However, the step half-widths obtained from the current-driven overdamped RCSJ model are in qualitative agreement with the experimentally measured values (Fig. 2D). Under voltage-driven modulation (*3*, *4*, *11*, *40*), the half-widths of Shapiro steps can be found analytically, $\Delta I_n/I_c = \left|J_n(V_{ac}/\hbar\omega)\right|$, deviating quantitatively at small driving amplitudes with respect to current-driven modulation (*45*). Corrections to the RCSJ caused by compressibility effects can also influence its behavior (*40*).

Phase dynamics and synchronization

To link the Shapiro steps with the phase dynamics, we tune our atomic junction to operate in the BEC regime at $1/k_F a = 3.3(1)$. Here, the reduced interactions allow us to leverage matter-wave interference between the expanding reservoirs to directly measure the relative phase ϕ (*46*), which cannot be accessed at unitarity because of the low contrast of interference fringes (*40*). For a BEC junction, we access both $\Delta\mu - I$ and $\phi - I$ characteristics (*33*), as reported in Fig. 3, A and B, for $\omega = 2\pi \times 175$ Hz, $I_{AC}/I_c = 0$, and $I_{AC}/I_c = 1.4(1)$. In the nonmodulated case for $I_{DC} < I_c$, we recover the expected DC Josephson trend (*33*), i.e., $\phi = \arcsin(I_{DC}/I_c)$. The measured ϕ shows larger error bars only for currents near and above I_c, attributed to the running phase in the voltage state (*40*). The driven scenario displays Shapiro steps with a diminished contrast as compared to the unitary junction, owing to the larger compressibility of the BEC superfluid (*40*). Nevertheless, we observe Shapiro steps in the $I - \Delta\mu$ curve throughout the same frequency range explored for the unitary junction (inset of Fig. 3A). The junction phase ϕ remains well defined within the plateau region even at finite $\Delta\mu$, presenting notable fluctuations only in the transition regions between plateaus (*40*). To support our findings, we compare the experimental results with numerical simulation performed with a dynamical classical-field method under similar experimental conditions (*40*, *47*). The numerical simulations quantitatively agree with our results for $\Delta\mu - I$ and $\phi - I$ characteristics, capturing the smoothness of the Shapiro steps in the experimental data. The agreement with the numerical simulation suggests that the observed lower contrast of the plateaus in the BEC is inherent to our junction. In particular, both the experimental data and the numerical simulation results show a reduction in the Shapiro step height for large ω, when the modulation frequency approaches the vertical trap frequency, which is lower in the BEC regime.

We demonstrate the dynamical synchronization between the junction phase and the external driving by monitoring ϕ as a function of time in the 0th and 1st Shapiro steps (Fig. 3C); the 2nd Shapiro step is shown in fig. S3. The interference fringes show an oscillating behavior in both cases, highlighted by the measured relative phase ϕ (Fig. 3D), which showcases the phase-locking and synchronized dynamics induced by the current drive (Fig. 3E). Note that phase-locking effects have also been observed in a superfluid system in a Floquet-driven tilted double-well potential (*48*). Whereas in the 0th step, the phase oscillates in phase with the injected current without reaching the critical values for phase slips, in the 1st step ϕ reaches this critical limit once every cycle, except for the transient behavior of the first modulation, leading to periodic phase slips, visible as depletions in the integrated interferograms of Fig. 3C (ii) and marked by the red arrows. The phase-slippage process produces a clear spike in ϕ for both the dynamical classical-field simulation and overdamped RCSJ solution, associated with an increase in the error on the measured phase (*40*, *49*).

Depending on the junction dimensionality, phase slips manifest as different topological excitations: solitons in 1D (*4*, *50*), vortex-antivortex pairs in two dimensions (*39*), and vortex rings in three dimensions (*49*). The kind of excitations created is determined by which is energetically favorable (*51*), or arises from a multistep process such as soliton decay into different topological excitations (*51*, *52*). In our BEC junction, we directly observe the presence of vortex-antivortex pairs as localized density depletions in the superfluid after a short time of flight (*40*) (Fig. 3F). The different junction geometry exploited in (*43*) leads instead to the emission of vortex rings during the Shapiro dynamics. For the 1st Shapiro step, we observe vortices generated on the near-left of the barrier (i-ii) that subsequently move toward the bulk of the reservoir (iii-iv). After an additional modulation period, a second vortex-antivortex pair is similarly emitted from the barrier region (v). The dynamical classical-field simulations corroborate this mechanism (figs. S7 and S8): At the end of the first cycle, the phase difference accumulated along the junction releases a solitonic excitation from the barrier, which then quickly decays into vortex-antivortex pairs, via snake instability (*40*, *51*). The periodic emission of vortex-antivortex pairs in Shapiro steps is a proxy of the underlying synchronized phase

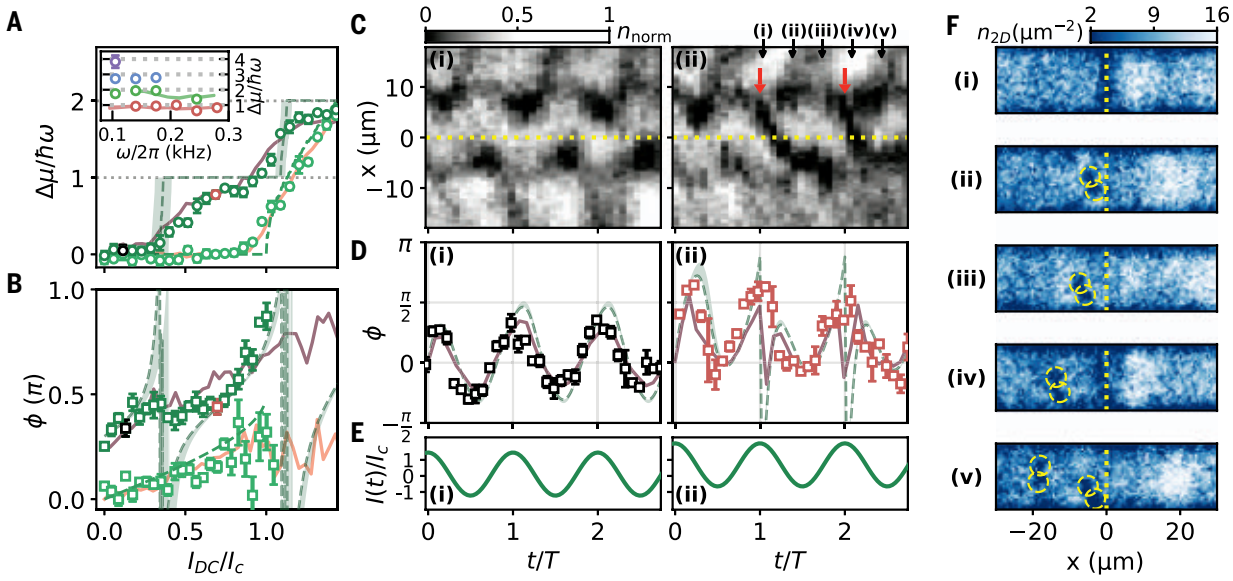


Fig. 3. Phase dynamics and dynamical locking in a driven atomic JJ in the BEC regime. (**A**) Current-voltage characteristic for a BEC junction under DC (light green symbols), and DC+AC drive at $\omega = 2\pi \times 175$ Hz and $I_{AC}/I_c = 1.4(1)$ (dark green symbols). Solid lines represent the numerical simulation results (see main text), with $I_{AC} = 0$ (orange) and $I_{AC}/I_c = 1.4$ (dark purple). Dashed lines represent the fit (light green) with the analytical and numerical solutions (dark green) of the overdamped RCSJ model (*40*). The shaded area accounts for the I_c fitting error. Inset: Shapiro step height characterization for a BEC junction. Symbols report the experimental step height obtained from the average over at least two repetitions plotted following the same color code as for Fig. 1C; dotted lines mark $\Delta\mu = n\hbar\omega$; and the solid lines represent the step height obtained from numerical simulations. (**B**) Current-phase relation under same experimental conditions as in (A), vertically shifted by 0.3π for the DC+AC case. Solid and dashed lines represent the results of the numerical simulation and RCSJ model (*40*), respectively, as in (A). (**C**) Time evolution of the interference pattern between the reservoirs for $I_{AC}/I_c = 1.4(1)$ and $I_{DC}/I_c = 0.14$ (i), $I_{DC}/I_c = 0.83$ (ii), marked by the black and red symbols in (A) and (B). Each row reports the integrated fringe profile, averaged over five repetitions. Red arrows signal the occurrence of phase slips; the yellow dotted line marks the barrier position. (**D**) Measured phase-time evolution from a sinusoidal fit of the fringe patterns. Solid and dashed lines represent the results of the numerical simulation and RCSJ model, respectively. (**E**) Drive current under the same experimental conditions as in (C) and (D). (**F**) Single-shot density profiles in time-of-flight at $t/T = 1.03$ (i), 1.38 (ii), 1.73 (iii), 2.08 (iv), and 2.43 (v), showcasing the vortex emission process. Vortices are marked in yellow dashed circles. The yellow dotted line marks the barrier position.

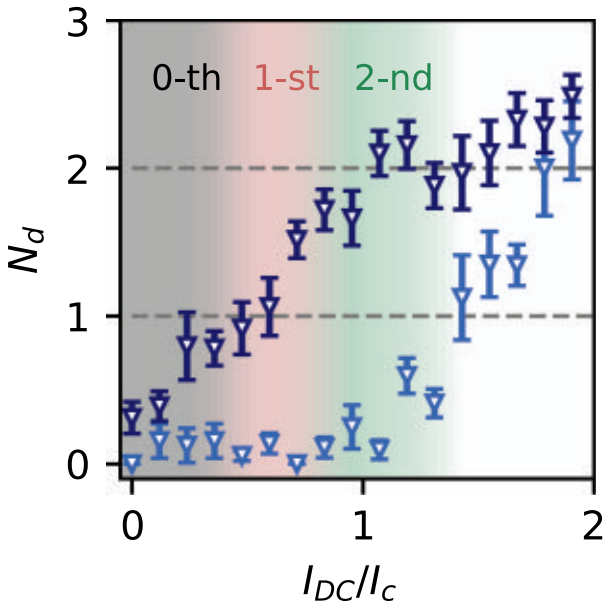


Fig. 4. Vortex-antivortex pairs as phase-slip proxies in a unitary JJ. Number of emitted vortex-antivortex pairs as a function of the bias current I_{DC}/I_c for $I_{AC}/I_c = 0$ (light blue), and $I_{AC}/I_c = 2.8(2)$ (dark blue). We measure the number of vortices after three periods of driving with a frequency $\omega = 2\pi \times 175$ Hz. The background color highlights the regions of the 0th, 1st, and 2nd Shapiro steps, with a color gradient reflecting the measured $\Delta\mu$ under the same driving conditions. Error bars represent the standard deviation of the mean over three to five realizations.

dynamics of the junction, which undergoes n phase-slippage processes in the nth step of each modulation cycle, as illustrated in the washboard potential analogy of Fig. 1C (ii) for $n = 1$.

As a direct measurement of the phase in the unitary regime is challenging (because of strong interactions limiting the fringe contrast), we probe the synchronization dynamics in the strongly interacting regime by detecting the number of emitted vortex pairs N_d as a function of the injected current (Fig. 4), revealing the occurrence of phase-slippage processes. In the nonmodulated case, vortices are observed to proliferate for $I_{DC} > I_c$, signaling a contribution to the junction conductance stemming from collective excitations, in agreement with previous observations in three-dimensional atomic JJs (*42*, *49*). For the AC drive, the number of detected vortex pairs instead shows a steplike trend that closely resembles the Shapiro steps observed in the $I - \Delta\mu$ curve measured under the same driving conditions. In particular, in the 2nd Shapiro step, N_d doubles with respect to the 1st step, highlighting that, as a result of the underlying synchronized phase dynamics, the number of phase slips is proportional to the step number. The dissipative and resistive dynamics giving rise to the Shapiro steps in our atomic JJ are dominated by the collective excitations of the system, playing a role similar to that of quasiparticles produced by Cooper pair breaking in SJJ. Indeed, in all explored configurations, the junction always works in the regime of $\Delta\mu \ll \Delta$, with Δ being the superfluid gap, where broken pairs are energetically suppressed and the only accessible excitations are collective ones—namely, phonons, solitons and vortices (*42*).

Discussion and outlook

We have observed Shapiro steps in a current-driven atomic JJ composed of two weakly coupled strongly interacting Fermi gases. Shapiro steps appear as quantized plateaus in the relative chemical potential—the

analog of the voltage drop in SJJs—occurring at integer multiples of the external driving frequency. As the driving amplitude increases, the widths of these plateaus exhibit a nonlinear dependence, arising from the interplay between the external drive and the nonlinear features of the atomic JJ. We probe the synchronization process at the heart of Shapiro steps by directly accessing the microscopic phase dynamics of the junction, featuring periodic phase-slippage processes that manifest as vortex-antivortex pairs. We note that such a direct microscopic observation is challenging to carry out with the available techniques in solid-state driven JJs, which have several-orders-of-magnitude faster dynamics.

At a fundamental level, our results reflect the interplay between quantum phase coherence and dissipation dynamics in a strongly correlated Fermi system. Our work opens prospects for a deeper understanding of how quasiparticles and quantum phase slips contribute to quantum transport, such as that within driven superconducting networks (*53*–*55*).

Our driven atomtronic circuit can be exploited to investigate driven atomic JJ arrays, whether arranged linearly or in annular configurations (*56*). In turn, this opens the way to simulate important paradigms in quantum synchronization, as provided by Kuramoto-like models (*57*), by driven atomic JJs in the presence of strong interactions and with disordered couplings between the links (*58*, *59*).

In addition, as Shapiro steps provide the voltage standards in quantum electronics (*13*), we could leverage the quantized steps to access a direct measurement of chemical potential differences (*36*). This approach would be specifically valuable in the intermediate regimes of the crossover superfluids, where the equation of state is challenging (*16*).

REFERENCES AND NOTES

1. A. Pikovsky, M. Rosenblum, J. Kurths, *Synchronization: A Universal Concept in Nonlinear Sciences* (Cambridge Univ. Press, 2001).
2. B. Josephson, *Phys. Lett.* **1**, 251–253 (1962).
3. A. Barone, G. Paternò, *Physics and Applications of the Josephson Effect* (Wiley, 1982).
4. M. Tinkham, *Introduction to Superconductivity*, Dover Books on Physics (Dover Publications, ed. 2, 2004).
5. S. Shapiro, *Phys. Rev. Lett.* **11**, 80–82 (1963).
6. G. Grüner, *Rev. Mod. Phys.* **60**, 1129–1181 (1988).
7. M. P. Juniper, A. V. Straube, R. Besseling, D. G. Aarts, R. P. Dullens, *Nat. Commun.* **6**, 7187 (2015).
8. A. P. Stikuts, S. Mishra, A. Ryabov, P. Maass, P. Tierno, *Nat. Commun.* **16**, 2966 (2025).
9. R. C. Dinsmore III, M.-H. Bae, A. Bezryadin, *Appl. Phys. Lett.* **93**, 192505 (2008).
10. I. Bogush, V. M. Fomin, O. V. Dobrovolskiy, *Phys. Rev. B* **111**, 214510 (2025).
11. R. W. Simmonds, A. Marchenkov, J. C. Davis, R. E. Packard, *Phys. Rev. Lett.* **87**, 035301 (2001).
12. B. Jeanneret, S. P. Benz, *Eur. Phys. J. Spec. Top.* **172**, 181–206 (2009).
13. J. Kohlmann, R. Behr, *Development of Josephson Voltage Standards* (InTech, 2011).
14. L. Amico *et al.*, *Rev. Mod. Phys.* **94**, 041001 (2022).
15. J. Polo *et al.*, *Quantum Sci. Technol.* **9**, 030501 (2024).
16. W. Ketterle, M. W. Zwierlein, *Riv. Nuovo Cim.* **31**, 247–422 (2008).
17. W. Zwerger, Ed., *The BCS-BEC Crossover and the Unitary Fermi Gas* (Springer, 2012).
18. M. W. Zwierlein, *Novel Superfluids*, vol. 2 (Oxford University PressOxford, 2014).
19. S. Krinner, T. Esslinger, J.-P. Brantut, *J. Phys. Condens. Matter* **29**, 343003 (2017).
20. Y. Cai, D. G. Allman, P. Sabharwal, K. C. Wright, *Phys. Rev. Lett.* **128**, 150401 (2022).
21. G. Del Pace *et al.*, *Phys. Rev. X* **12**, 041037 (2022).
22. P. T. Brown *et al.*, *Science* **363**, 379–382 (2019).
23. W. Xu, W. R. McGehee, W. N. Morong, B. DeMarco, *Nat. Commun.* **10**, 1588 (2019).
24. M. A. Nichols *et al.*, *Science* **363**, 383–387 (2019).
25. M. Lebrat *et al.*, *Phys. Rev. X* **8**, 011053 (2018).
26. M. Schreiber *et al.*, *Science* **349**, 842–845 (2015).
27. R. Anderson *et al.*, *Phys. Rev. Lett.* **122**, 153602 (2019).
28. P. B. Patel *et al.*, *Science* **370**, 1222–1226 (2020).
29. D. Hernández-Rajkov *et al.*, *New J. Phys.* **23**, 103038 (2021).
30. Z. Yan *et al.*, *Science* **383**, 629–633 (2024).
31. C. Cabrera *et al.*, *Phys. Rev. Res.* **7**, L032018 (2025).
32. G. Valtolina *et al.*, *Science* **350**, 1505–1508 (2015).
33. W. J. Kwon *et al.*, *Science* **369**, 84–88 (2020).
34. N. Luick *et al.*, *Science* **369**, 89–91 (2020).
35. A. Smerzi, S. Fantoni, S. Giovanazzi, S. R. Shenoy, *Phys. Rev. Lett.* **79**, 4950–4953 (1997).
36. S. Kohler, F. Sols, *New J. Phys.* **5**, 94–94 (2003).
37. A. Eckardt, T. Jinasundera, C. Weiss, M. Holthaus, *Phys. Rev. Lett.* **95**, 200401 (2005).
38. J. Grond *et al.*, *New J. Phys.* **13**, 065026 (2011).
39. V. P. Singh, J. Polo, L. Mathey, L. Amico, *Phys. Rev. Lett.* **133**, 093401 (2024).
40. See supplementary materials.
41. G. Zürn *et al.*, *Phys. Rev. Lett.* **110**, 135301 (2013).
42. G. Del Pace, W. J. Kwon, M. Zaccanti, G. Roati, F. Scazza, *Phys. Rev. Lett.* **126**, 055301 (2021).
43. E. Bernhart *et al.*, *Science* **390**, 1130–1133 (2025).
44. F. Meier, W. Zwerger, *Phys. Rev. A* **64**, 033610 (2001).
45. R. Panghotra *et al.*, *Commun. Phys.* **3**, 53 (2020).
46. C. Li, Q. Liang, P. Paranjape, R. Wu, J. Schmiedmayer, *Phys. Rev. Res.* **6**, 023217 (2024).
47. V. P. Singh *et al.*, *Phys. Rev. A* **93**, 023634 (2016).
48. S.-C. Ji *et al.*, *Phys. Rev. Lett.* **129**, 080402 (2022).
49. A. Burchianti *et al.*, *Phys. Rev. Lett.* **120**, 025302 (2018).
50. F. Binanti, K. Furutani, L. Salasnich, *Phys. Rev. A* **103**, 063309 (2021).
51. W. Van Alphen, H. Takeuchi, J. Tempere, *Phys. Rev. A* **100**, 023628 (2019).
52. M. J. Ku, B. Mukherjee, T. Yefsah, M. W. Zwierlein, *Phys. Rev. Lett.* **116**, 045304 (2016).
53. W. Guichard, F. W. Hekking, *Phys. Rev. B Condens. Matter Mater. Phys.* **81**, 064508 (2010).
54. K. Y. Arutyunov, D. S. Golubev, A. D. Zaikin, *Phys. Rep.* **464**, 1–70 (2008).
55. I. M. Pop *et al.*, *Nat. Phys.* **6**, 589–592 (2010).
56. L. Pezzè *et al.*, *Nat. Commun.* **15**, 4831 (2024).
57. Y. Kuramoto, *Chemical Oscillations, Waves, and Turbulence* (Springer Berlin Heidelberg, 1984).
58. D. J. Watts, S. H. Strogatz, *Nature* **393**, 440–442 (1998).
59. B. R. Trees, V. Saranathan, D. Stroud, *Phys. Rev. E Stat. Nonlin. Soft Matter Phys.* **71**, 016215 (2005).
60. G. Del Pace *et al.*, Shapiro steps in strongly-interacting Fermi gases [Data set], Zenodo (2025); https://doi.org/10.5281/zenodo.17303804.

ACKNOWLEDGMENTS

We thank H. Ott and his team for useful discussion during the development of the project. We also thank F. Giazotto, F. Marino, L. Mathey, and K. Xhani for discussions and F. Scazza for careful reading of the manuscript. **Funding:** G.R. and G.D.P. acknowledge financial support from the PNRR MUR project PE0000023-NQSTI. G.R. acknowledges funding from the Italian Ministry of University and Research under the PRIN2017 project CEnTraL and the Project CNR-FOE-LENS-2023. The authors acknowledge support from the European Union - NextGenerationEU for the "Integrated Infrastructure initiative in Photonics and Quantum Sciences" - I-PHOQS (IR0000016, ID D2B8D520, CUP B53C22001750006). This publication has received funding under the Horizon Europe program HORIZON-CL4-2022-QUANTUM-02-SGA via project 101113690 (PASQuanS2.1). J.A.S. acknowledges financial support from CONAHCyT grant CF-2023-I-72; DGAPA-UNAM-PAPIIT grant IN105724; CIC-UNAM grant LANMAC-2024; and European Community's Horizon 2020 research and innovation program under grant agreement no. 871124. **Author contributions:** G.D.P., V.P.S., L.A., and G.R. conceived the experiment. G.D.P., D.H.-R., N.G., M.F.F., and G.N. performed the experimental work, acquired the data, and carried out the data analysis. V.P.S. performed numerical simulations. L.A and G.R. supervised the work. All authors contributed extensively to the discussion and interpretation of the results and took part in writing the manuscript. **Competing interests:** The authors declare that they have no competing interests. **Data and materials availability:** The study involved no new materials preparation. All experimental data and numerical simulation codes shown in this work are available on Zenodo (*60*).

License information: Copyright © 2025 the authors, some rights reserved; exclusive licensee American Association for the Advancement of Science. No claim to original US government works. https://www.science.org/about/science-licenses-journal-article-reuse

SUPPLEMENTARY MATERIALS

science.org/doi/10.1126/science.ads8885
Materials and Methods; Supplementary Text; Figs. S1 to S10; References (*61*–*69*)

Submitted 4 September 2024; accepted 9 October 2025

10.1126/science.ads8885

QUANTUM SIMULATION

Observation of Shapiro steps in an ultracold atomic Josephson junction

Erik Bernhart[1], Marvin Röhrle[1], Vijay Pal Singh[2], Ludwig Mathey[3,4], Luigi Amico[2,5,6], Herwig Ott[1]*

The current-voltage characteristic of a driven superconducting Josephson junction displays discrete steps. This phenomenon, called the Shapiro steps, forms today's voltage standard. In this work, we report the observation of Shapiro steps in a driven Josephson junction in a gas of ultracold atoms. We demonstrate that the steps exhibit universal features and provide insight into the microscopic dissipative dynamics that we directly observe in the experiment. We find that the steps are directly connected to phonon emission and nucleation of solitonic excitations, whose dynamics we follow in space and time. The experimental results are underpinned by extensive numerical simulations based on classical-field dynamics and may enable metrological and fundamental advances.

The Josephson effect is one of the most fundamental phenomena in quantum science and technology, featuring a dissipationless electrical current through a tunnel barrier between two superconductors by virtue of the phase difference of the traversing Cooper pairs' wave function. Above a critical value of the current, a finite voltage occurs across the junction as a result of the formation of superconducting quasiparticles (*1*). The Josephson effect and Josephson junctions have played prominent roles in understanding the notion of macroscopic quantum coherence, which led to important technological applications, such as superconducting quantum interference devices (SQUIDs) (*2*–*6*); they are also the core ingredients of superconducting qubits (*7*–*10*). If an additional microwave field is applied across the Josephson junction, a staircase current-voltage characteristic emerges, referred to as Shapiro steps (*11*). The origin of this effect is photon-assisted tunneling of Cooper pairs through the junction (*5*). Because the height of the steps depends only on the frequency of the microwave radiation, Planck's constant, and the electric charge, Shapiro steps are nowadays used as the voltage standard [see, e.g., (*12*)]. Shapiro steps in superfluid ^{3}He have been investigated (*13*).

The Josephson effect can also be observed in ultracold quantum gases (*14*). This enables the fabrication of atomtronic circuits, which have developed into their own field of research in recent years (*15*–*17*). Additionally, the high degree of control and flexibility over ultracold quantum gases provides unprecedented access to the microscopic physics underlying the system. In particular, Josephson physics has been recently implemented and extensively studied in ultracold atomic systems, both theoretically (*18*–*23*) as well as experimentally in bosonic (*14*, *24*–*26*) and fermionic (*27*, *28*) systems. In implementations with ultracold atoms, the Josephson current-phase relation is realized by moving the barrier through an ultracold gas that is otherwise at rest (*29*, *30*). Shapiro steps in ultracold gases are predicted to appear if the linear translation of the barrier (corresponding to a dc particle current) is combined with a periodic modulation of the position of the barrier (corresponding to an ac particle current), thus emulating the external microwave radiation of the superconducting Josephson junction (*31*).

In this work, we demonstrate the emergence of Shapiro steps at an atomic Josephson junction and quantify their global and local properties. The steps occur in the chemical potential difference, in conjunction with a density imbalance across the junction. We confirm that the step heights in the chemical potential difference $\Delta\mu$ are quantized by the external driving frequency f_m—i.e., $\Delta\mu = nhf_\mathrm{m}$, where n is the step index and h is Planck's constant. By spatially resolving the atomic density, we study the microscopic dynamics and observe the propagation of phonons and density depletions emerging from the barrier, which we identify as solitonic excitations. This paves the way for studying the microscopic dissipative dynamics of Shapiro steps and other related Josephson transport effects. Furthermore, given that the magnitude of the step height relates the chemical potential difference to a tunable frequency and that the density imbalance across the barrier is directly measurable, our results suggest a protocol to measure the equation of state of strongly correlated superfluids.

Experimental system

The experimental setup and the Shapiro protocol are sketched in Fig. 1. We prepare a ^{87}Rb Bose-Einstein condensate in an elongated optical dipole trap. The condensate has a tubelike cylindrical geometry with harmonic transverse confinement (Fig. 1A). The chemical potential is $\mu = h \times 1900\ \mathrm{s}^{-1}$. A movable repulsive barrier with height $V_B = 0.45 \times \mu$ separates the condensate into two parts and thus realizes a weak link (*32*). We probe the system by absorption imaging. To achieve a high accuracy, we perform a matter wave imaging scheme (*33*) to reduce the optical density (*32*).

We implement the dc and ac driving protocol following the proposal of Singh *et al.* (*31*). To this end, we move the barrier with constant velocity v and an additional periodic modulation

$$x(t) = vt + x_\mathrm{m}\sin\left(2\pi f_\mathrm{m} t\right) \tag{1}$$

where x_m is the modulation amplitude and f_m the modulation frequency. We fix the driving time to 33 ms, which means that the final position of the barrier depends on v. At the end, we measure the atom number imbalance $z = (N_\mathrm{R} - N_\mathrm{L})/N$, where N is the total atom number and N_L and N_R are the atom numbers on the left- and right-hand sides, respectively, of the barrier. As a reference z_ref, we also measure the corresponding imbalance without the barrier. Using a simulation of the Gross-Pitaevskii equation, we map $\Delta z = z - z_\mathrm{ref}$ to the chemical potential difference $\Delta\mu$ (*32*). The barrier motion induces an atomic current relative to the barrier of value I, with $I = vI_\mathrm{c}/v_\mathrm{c}$, where I_c is the critical current and v_c is the critical velocity (*32*). The external current then reads $I_\mathrm{ext} = I + I_\mathrm{ac} = I + I_\mathrm{m}\cos(2\pi f_\mathrm{m} t)$, with the bias current I and the modulation current I_m. The parameters that we vary in our protocol are I, I_m, and f_m. In Fig. 1C, we show the measurements of the current-chemical potential characteristics that are obtained without and with ac driving. From the undriven response, we characterize the critical velocity and the critical current of the Josephson junction (*32*). For the periodically driven case, the system features plateaus of constant chemical potential difference occurring at integer multiple of the driving frequency—the steps occur at lower I for stronger I_m. We model our system with extensive classical-field simulations (*32*), which capture the features of our driven Josephson junction well (Fig. 1, D and E).

In a superconducting Josephson junction, where the Shapiro steps arise from photon-assisted tunneling of the Cooper pairs (*34*), the voltage V_n of the n-th Shapiro step is directly given by the energy quantization—i.e., $V_n = n\Phi_0 f_\mathrm{m} = nf_\mathrm{m}h/(2e)$, where Φ_0 is the flux quantum

[1]Department of Physics and Research Center OPTIMAS, RPTU University Kaiserslautern-Landau, Germany. [2]Quantum Research Centre, Technology Innovation Institute, Abu Dhabi, United Arab Emirates. [3]Zentrum für Optische Quantentechnologien and Institut für Quantenphysik, Universität Hamburg, Hamburg, Germany. [4]The Hamburg Centre for Ultrafast Imaging, Hamburg, Germany. [5]Dipartimento di Fisica e Astronomia "Ettore Majorana," Università di Catania, Catania, Italy. [6]INFN-Sezione di Catania, Catania, Italy. ***Corresponding author. Email: ott@physik.uni-kl.de**

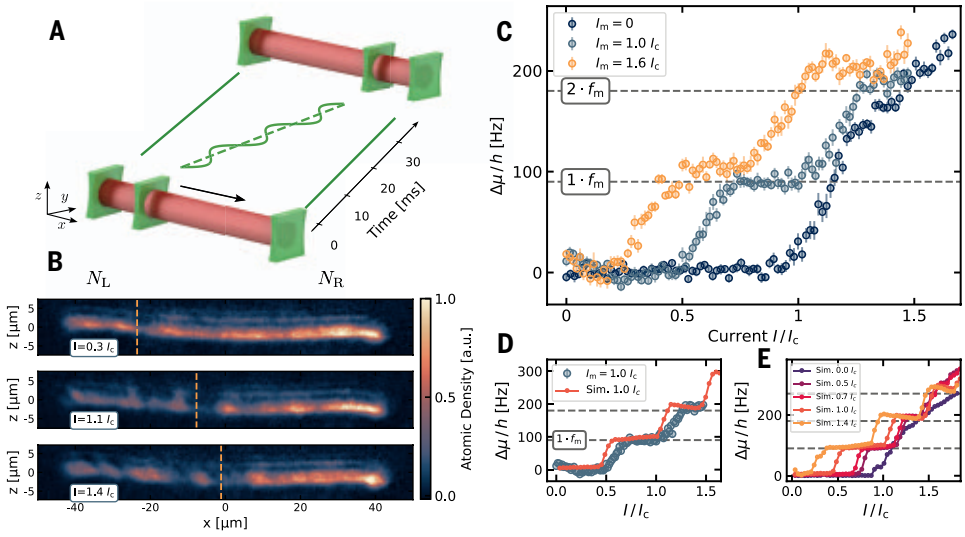


Fig. 1. Shapiro steps in an ultracold atomic Josephson junction. (**A**) The system consists of a cylindrically shaped superfluid, which is split by a movable optical barrier creating a weak link. The barrier as well as the two confining endcaps are realized with tightly focused laser beams. In the measurement protocol, the barrier is moved linearly (dc particle current) through the superfluid with an additional harmonic modulation (ac particle current), which is sketched in the figure. (**B**) At the end of the protocol, a real-space absorption image of the atomic cloud is taken, using matter wave imaging (*32*,*33*). From the atom number imbalance between the two superfluids, their chemical potential difference is derived. The pictures are taken with a modulation current $I_m = 0.8I_c$. The position of the barrier is marked as a dashed orange line. The atomic density is given in arbitrary units (a.u.). (**C**) Measured Shapiro steps for $f_m = 90$ Hz and different modulation amplitudes I_m. The horizontal lines indicate the ideal Shapiro step height, given by Eq. 2. Every data point is the average of about 25 measurement runs, and the vertical bars indicate the errors of the mean. (**D**) Comparison between experiment and classical-field simulation at $T = 35$ nK (*32*). (**E**) Simulations of the system at different I_m (*32*).

and e the elementary charge (*5*, *35*). For our neutral atom implementation, this results in the quantization condition

$$\Delta\mu = nhf_m \tag{2}$$

To confirm this fundamental relation, we vary f_m and determine the height $\Delta\mu$ of the first step (Fig. 2A). In Fig. 2B, we show the results for the simulation and for the experiment by averaging over several realizations with different modulation amplitudes. The simulation reproduces the relation trend accurately, but the experiment measures a 10% larger slope. The reason for this small deviation lies in the uncertainties of the experimental parameters (atom number and trapping potential), which enter the calculation of μ [see also (*32*)]. Taking this into account, we conclude that we indeed confirm the behavior $\Delta\mu = hf_m$ (Fig. 2B). Our results show that the driving protocol is capable of producing a predetermined chemical potential difference, which may enable the transfer of the voltage standard to the realm of ultracold quantum gases (*23*, *36*). In addition, our results are useful in situations where the relation between the atomic density and the chemical potential, $\mu(n)$, is not known. Measuring the density difference at both sides of the junction directly reveals $d\mu(n)/dn$, which is referred to as the inverse thermodynamic density of states. Performing stepwise measurements by decreasing the density allows for the determination of the equation of state $\mu(n)$.

Next, we analyze the width of the Shapiro steps by varying the modulation amplitude I_m/I_c at a fixed modulation frequency of $f_m = 90$ Hz (*32*). In Fig. 2, C and D, the widths of the zeroth and first steps display a Bessel-function behavior as a function of I_m/I_c, which is in agreement with the results of numerical simulations (*32*). To support this observation, we use the analytical prediction of an ac voltage–driven Josephson junction, which yields the step width $I_n = I_c\left|J_n(V_m/V_n)\right|$, where J_n is the Bessel function of the n-th order and V_m the modulation voltage (*5*, *37*). For an ac current–driven junction, this can be mathematically transformed into

$$I_n = I_c\left|J_n\left(\alpha\frac{I_m}{I_c}\right)\right| \tag{3}$$

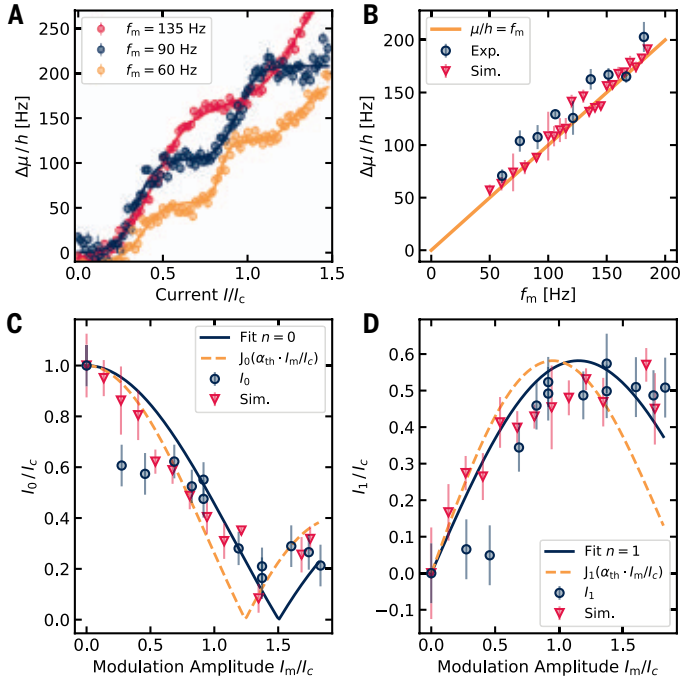


Fig. 2. Characteristics of the Shapiro steps. (**A**) Dependence of the step height on the modulation frequency f_m, where the step height is determined using sigmoid fits (continuous lines). (**B**) Measurements of the step height (dots) are compared with the numerical simulations (triangles) and the prediction $\Delta\mu/h = f_m$ (continuous line). (**C** and **D**) Measurements (dots) and simulation (triangles) of zeroth (C) and first (D) step widths (I_0 and I_1) for varying I_m/I_c. The solid blue lines are a fit to the experimental data, following Eq. 3, where both curves are fitted simultaneously with the same fit parameter α_{fit}, yielding $\alpha_{fit} = 2.15 \pm 0.08$. The dashed orange lines indicate the theoretical prediction, following Eq. 3 (see text).

with $\alpha = RI_c/f_m$. We use the independently determined system parameters R and I_c (*32*) to calculate this parameter, obtaining $\alpha_{th} = 1.93 \pm 0.07$. Using α_{th}, we plot the result of Eq. 3 as the orange dashed line in Fig. 2, C and D. Notably, this fit parameter free model supports the overall trend of our measurements and simulations.

Microscopic dynamics

Compared with solid-state physics, the time and length scales in quantum gas experiments are orders of magnitude larger, which enables the in situ study of collective excitations, quasiparticles, and related microscopic phenomena. To that end, we follow the time evolution of the real-space atomic density. Using only a constant barrier velocity—i.e., no ac particle current—we measure the dc and ac Josephson regime (Fig. 3A). Below the critical current, no imbalance is created, and only a single phononic density wave is emitted from the initial acceleration of the barrier (Fig. 3A, I and II). The group velocity of the emitted phonons coincides with a reference measurement, where a single perturbation creates a phonon wave packet (*32*). In the ac Josephson regime above the critical current, atoms are pushed away by the barrier, and a density depletion remains in its wake (Fig. 3A, III).

In the Shapiro regime, we see that the phase dynamics is instead characterized by two distinct collective excitations: phonons and localized density depletions (Fig. 3, B and C). Phonons are emitted at distinct times in both directions thanks to the oscillatory motion of the barrier. This is particularly visible on the zeroth plateau (Fig. 3, B and C, I). Increasing the constant current I beyond the zeroth plateau yields a chemical potential difference and atom number imbalance; this phenomenon is characterized by the formation of "depletion waves" that move backward compared with the barrier motion (blue lines propagating to the left in Fig. 3, B and C, II and III). These excitations are observed to have a smaller group velocity—i.e., a steeper slope (*32*). By additionally using the phase information of the simulation in Fig. 4A, we observe that such density depletions are accompanied by phase jumps across the density minimum and identify them as solitonic excitations (*38*). Analyzing the transverse phase profile right after the emission (*32*), we find that the solitonic excitations manifest themselves as vortex rings. These solitonic excitations are responsible for most of the reduction in density, ultimately causing the particle imbalance across the junction (Fig. 4, B and C). Specifically, the simulation shows that for the n-th plateau, n solitonic excitations are, on average, emitted backward during one driving cycle (Fig. 3C, II and III) (*32*). This creates the reduced density in the wake of the moving barrier and therefore gives rise to the resistive regime. This statement is supported by the fact that the rate of emitted solitonic excitations displays a steplike behavior in close parallel with the staircase displayed by the chemical potential (fig. S13). Depending on the system geometry, the emerging solitonic excitations can be different. For instance, in the theoretical proposal (*31*), a larger two-dimensional system was used, and vortex-antivortex pairs were generated at the barrier. The appearance of vortex rings has been observed in previous studies (*39*, *40*) as well as the emission of solitons from a barrier (*41*, *42*).

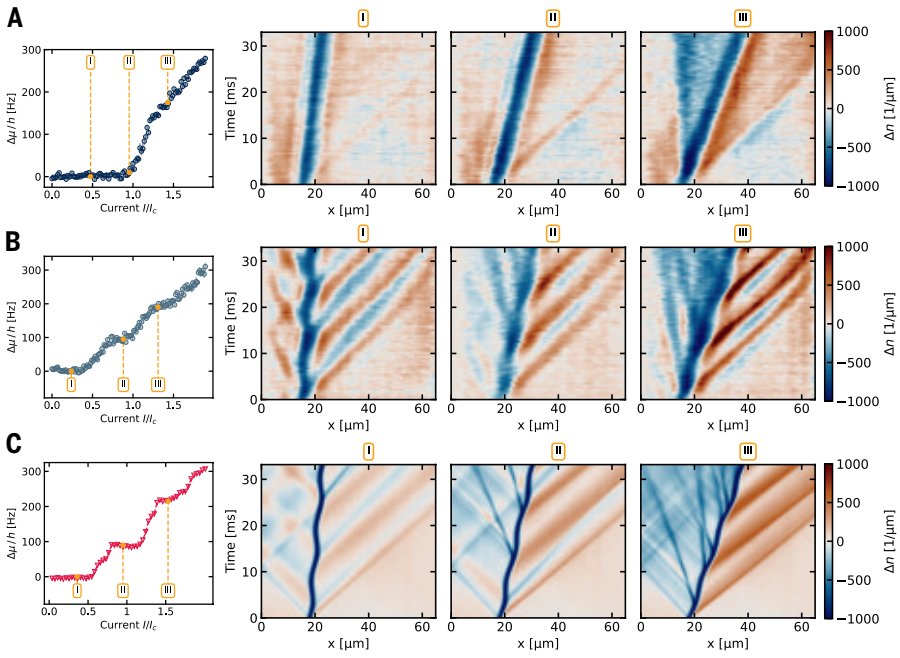


Fig. 3. Microscopic system dynamics. Time evolution of the atomic density in the experiment [(A) and (B)] and in the simulation (C). (**A**) Constant barrier velocity. We show the time evolution for three different currents, indicated in the $I - \Delta\mu$ plot on the left. (**B**) Constant plus periodically modulated barrier velocity (Shapiro protocol), where $I_m = 0.8I_c$ and $f_m = 90$ Hz. (**C**) Classical-field simulations of the driven junction, with $I_m = 0.8I_c$ and $f_m = 90$ Hz. Each horizontal line in the images corresponds to a transversely integrated absorption image, which are stacked together. The color code indicates the relative change of the line density with respect to a reference image without barrier.

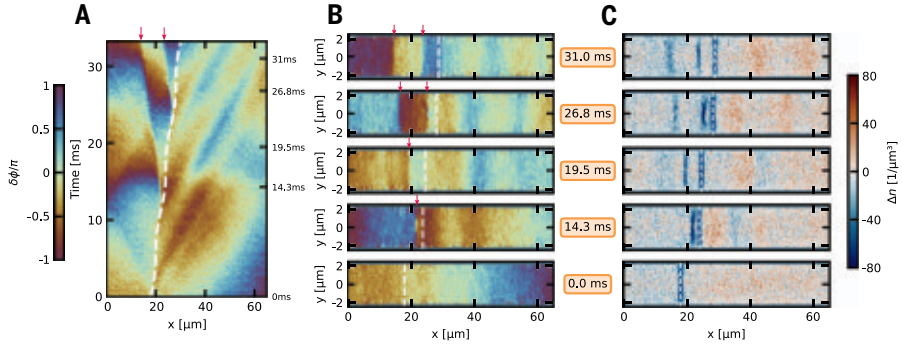


Fig. 4. Dynamics of solitonic excitations. (**A**) Time evolution of the phase $\delta\phi(x, t) = \phi(x, t) - \phi_m(t)$ along the central x line of a single trajectory of the system for $I/I_c = 0.9$, $I_m/I_c = 0.8$, and $f_m = 90$ Hz, where $\phi_m(t)$ is obtained after averaging the wave function over x. The periodic barrier motion (white dashed line) modifies the local phase near the barrier, which results in the creation of solitonic excitations moving to the left. The red arrows in (A) and (B) are a guide to the eye for the position of the solitonic excitations. (**B** and **C**) Snapshots of the phase profile $\delta\phi(x, y)$ of a single trajectory (B) and the averaged density profile $\Delta n(x, y)$ for the central z plane (C) at times $t = 0$, 14.3, 19.5, 26.8, and 31 ms. During each driving cycle, the barrier motion (white vertical dashed line) emits one solitonic excitation, whose subsequent time evolution manifests itself as density dips in (C). The positions of the phase jumps in (A) are marked with red arrows. At time 14.3 ms, the phase profile of a vortex ring is visible (*32*). There are also phononic excitations that propagate in both forward and backward directions. In (C), we show the relative change of the density with respect to a reference cloud without barrier. In (B) and (C), the thermal wings outside the Thomas-Fermi region of the condensate are shaded in gray.

We note that Shapiro steps have also been observed in a complementary experiment with ultracold fermions in the unitary regime and in a molecular Bose-Einstein condensate (*43*). Whereas in our work, vortex rings are the relevant solitonic excitations in the microscopic dynamics, the different geometry observed by Del Pace *et al.* (*43*) leads to the formation of vortex-antivortex pairs.

It is also instructive to compare the microscopic physical mechanism with that of superconductors. Our results effectively demonstrate that both superconducting and atomic junctions are characterized by coherent dynamics leading to a synchronization of the phase difference with the external drive (*2*). Whereas in superconductors, the tunneling of Cooper pairs in the voltage state is mediated by photons from the coherent driving field, the atomic superfluid couples to phonons when crossing the barrier at finite chemical potential difference.

As for the resistive channel, superconductors are characterized by an incoherent tunneling of quasiparticles (namely broken Cooper pairs), which are present in the superconductor at finite temperature (*5*). By contrast, in atomic superfluids, collective excitations, such as solitons and vortices, are the dominant dissipation mechanism, opening the resistive channel. Because they can be observed directly in the experiment, their role for the microscopic physics of Shapiro steps can be studied under clean conditions.

In superconductors, collective excitations have been investigated in complementary studies on Josephson physics, in which phase slips (*44*, *45*), Josephson vortices (*46*), and solitons (*47*) have been observed experimentally. All of these observations have been made with static or pinned excitations; direct observation of the dynamics of such excitations remains challenging. However, we expect that collective phase excitations might also play a role in the Shapiro physics of superconductors, especially in regimes, for example, at very low temperatures, where the quasiparticle density is small.

Discussion and outlook

We have experimentally demonstrated the emergence of Shapiro steps in an ultracold quantum gas by emulating the external microwave field and an alternating particle current across the barrier with a periodic modulation of the barrier position. Using cold atom techniques, we could monitor the coherent dynamics of the system with unprecedented accuracy.

Extensions of the current work include different dimensions, geometries, and particle statistics, as well as superfluid mixtures, dipolar superfluids, and superfluids in optical lattices. These can generate other types of solitons, such as bright solitons or vortices, or defects related to an underlying lattice or competing orders. Equation 2 provides the possibility to measure the equation of state of strongly correlated many-body systems. In the context of superconducting Josephson junctions, our work motivates expanding the understanding of the microscopic dynamics of the Shapiro effect, including the role of collective excitations, such as solitons and vortices in regimes where the quasiparticle density is low. Furthermore, our results demonstrate the potential of atomic superfluids to act as quantum simulators for superconducting circuits.

Toward the development of atomtronic technology, Shapiro steps can be used to fine-tune quantum transport because they combine both superfluid and resistive transport. Stacks of Shapiro steps can be used to create even larger differences in chemical potential over a whole system or as a source for predetermined chemical potential differences.

REFERENCES AND NOTES

1. B. D. Josephson, *Phys. Lett.* **1**, 251–253 (1962).
2. M. Tinkham, *Introduction to Superconductivity* (Courier Corporation, 2004).
3. R. L. Fagaly, *Rev. Sci. Instrum.* **77**, 101101 (2006).
4. D. Koelle, R. Kleiner, F. Ludwig, E. Dantsker, J. Clarke, *Rev. Mod. Phys.* **71**, 631–686 (1999).
5. A. Barone, G. Paterno, *Physics and Applications of the Josephson Effect* (Wiley, 1982).
6. A. J. Leggett, *Jpn. J. Appl. Phys.* **26**, 1986 (1987).
7. J. Clarke, F. K. Wilhelm, *Nature* **453**, 1031–1042 (2008).
8. J. Koch *et al.*, *Phys. Rev. A* **76**, 042319 (2007).
9. M. W. Johnson *et al.*, *Nature* **473**, 194–198 (2011).
10. F. Arute *et al.*, *Nature* **574**, 505–510 (2019).
11. S. Shapiro, *Phys. Rev. Lett.* **11**, 80–82 (1963).
12. R. Pöpel, *Metrologia* **29**, 153–174 (1992).
13. R. W. Simmonds, A. Marchenkov, J. C. Davis, R. E. Packard, *Phys. Rev. Lett.* **87**, 035301 (2001).
14. M. Albiez *et al.*, *Phys. Rev. Lett.* **95**, 010402 (2005).
15. C. Ryu, P. W. Blackburn, A. A. Blinova, M. G. Boshier, *Phys. Rev. Lett.* **111**, 205301 (2013).
16. L. Amico *et al.*, *AVS Quantum Sci.* **3**, 039201 (2021).
17. L. Amico *et al.*, *Rev. Mod. Phys.* **94**, 041001 (2022).
18. S. Giovanazzi, A. Smerzi, S. Fantoni, *Phys. Rev. Lett.* **84**, 4521–4524 (2000).
19. F. Meier, W. Zwerger, *Phys. Rev. A* **64**, 033610 (2001).
20. V. P. Singh, N. Luick, L. Sobirey, L. Mathey, *Phys. Rev. Res.* **2**, 033298 (2020).
21. A. K. Saha, R. Dubessy, *Phys. Rev. A* **104**, 023316 (2021).
22. J. Grond *et al.*, *New J. Phys.* **13**, 065026 (2011).
23. S. Kohler, F. Sols, *New J. Phys.* **5**, 94 (2003).
24. L. J. LeBlanc *et al.*, *Phys. Rev. Lett.* **106**, 025302 (2011).
25. S. Eckel *et al.*, *Phys. Rev. A* **93**, 063619 (2016).
26. S.-C. Ji *et al.*, *Phys. Rev. Lett.* **129**, 080402 (2022).
27. G. Valtolina *et al.*, *Science* **350**, 1505–1508 (2015).
28. N. Luick *et al.*, *Science* **369**, 89–91 (2020).
29. W. J. Kwon *et al.*, *Science* **369**, 84–88 (2020).
30. G. Del Pace, W. J. Kwon, M. Zaccanti, G. Roati, F. Scazza, *Phys. Rev. Lett.* **126**, 055301 (2021).
31. V. P. Singh, J. Polo, L. Mathey, L. Amico, *Phys. Rev. Lett.* **133**, 093401 (2024).
32. See the supplementary materials.
33. L. Asteria, H. P. Zahn, M. N. Kosch, K. Sengstock, C. Weitenberg, *Nature* **599**, 571–575 (2021).
34. A. H. Dayem, R. J. Martin, *Phys. Rev. Lett.* **8**, 246–248 (1962).
35. C. A. Hamilton, *Phys. Rev. B* **5**, 912–923 (1972).
36. C. A. Hamilton, *Rev. Sci. Instrum.* **71**, 3611–3623 (2000).
37. C. A. Hamilton, S. Shapiro, *Phys. Rev. Lett.* **26**, 426–428 (1971).
38. M. J. H. Ku *et al.*, *Phys. Rev. Lett.* **113**, 065301 (2014).
39. A. Burchianti *et al.*, *Phys. Rev. Lett.* **120**, 025302 (2018).
40. K. Xhani *et al.*, *Phys. Rev. Lett.* **124**, 045301 (2020).
41. P. Engels, C. Atherton, *Phys. Rev. Lett.* **99**, 160405 (2007).
42. V. Hakim, *Phys. Rev. E* **55**, 2835–2845 (1997).
43. G. Del Pace *et al.*, *Science* **390**, 1125–1129 (2025).
44. A. G. Sivakov *et al.*, *Phys. Rev. Lett.* **91**, 267001 (2003).
45. R. S. Shaikhaidarov *et al.*, *Nature* **608**, 45–49 (2022).
46. D. Roditchev *et al.*, *Nat. Phys.* **11**, 332–337 (2015).
47. S. Rajasekaran *et al.*, *Nat. Phys.* **12**, 1012–1016 (2016).
48. E. Bernhart *et al.*, Observation of Shapiro steps in an ultracold atomic Josephson junction, Rheinland-Pfälzische Technische Universität Kaiserslautern-Landau (2025); https://doi.org/10.26204/data/14.

ACKNOWLEDGMENTS

We thank G. Roati and G. Del Pace for useful discussions. **Funding:** We gratefully acknowledge financial support by the Deutsche Forschungsgemeinschaft (DFG, German Research Foundation) within the SFB OSCAR (project number 277625399). L.M. acknowledges support by the DFG, namely the Cluster of Excellence "Advanced Imaging of Matter" (EXC 2056), project no. 390715994. The project is cofinanced by the European Regional Development Fund (ERDF) of the European Union and by Fonds of the Hamburg Ministry of Science, Research, Equalities and Districts (BWFGB). **Author contributions:** E.B., M.R., and H.O. conceived the study. E.B. and M.R. performed the experiment and analyzed the data. E.B. performed the Gross-Pitaevskii equation simulations, and V.P.S. modeled classical-field simulations. H.O. supervised the experiment. L.M. and L.A. supervised the theoretical part of the project. E.B. prepared the initial version of the manuscript. All authors contributed to the data interpretation and the writing of the manuscript. **Competing interests:** The authors declare no competing interests. **Data and materials availability:** The study involved no new materials preparation. All data presented in this paper and simulation codes are available online (*48*).

License information: Copyright © 2025 the authors, some rights reserved; exclusive licensee American Association for the Advancement of Science. No claim to original US government works. https://www.science.org/about/science-licenses-journal-article-reuse

SUPPLEMENTARY MATERIALS

science.org/doi/10.1126/science.ads9061
Materials and Methods; Supplementary Text; Figs. S1 to S13; References (*49*–*55*)

Submitted 4 September 2024; accepted 24 October 2025

10.1126/science.ads9061

METABOLISM

NUDT5 regulates purine metabolism and thiopurine sensitivity by interacting with PPAT

Zheng Wu[1]†, Phong T. Nguyen[1]†, Varun Sondhi[1,2], Run-Wen Yao[3,4], Zhifang Lu[5], Tao Dai[1], Jui-Chung Chiang[6], Feng Cai[1], Imani M. Williams[1], Eliot B. Blatt[1], Zengfu Shang[6], Ling Cai[1,7,8], Jing Zhang[3,9], Mya D. Moore[1], Islam Alshamleh[1], Xiangyi Li[1], Tamaratare Ogu[1], Lauren G. Zacharias[1], Rainah Winston[1], Joao S. Patricio[1], Xandria Johnson[1], Wei-Min Chen[6], Qian Cong[3,7,9], Thomas P. Mathews[1], Yuanyuan Zhang[6,7], Limei Zhang[5], Ralph J. DeBerardinis[1,4,7,9]*

Cells generate purine nucleotides through de novo purine biosynthesis (DNPB) and purine salvage. Purine salvage represses DNPB to prevent excessive purine nucleotide synthesis through mechanisms that are incompletely understood. We identified Nudix hydrolase 5 (NUDT5) as a DNPB regulator. During purine salvage, NUDT5 suppresses DNPB independently of its catalytic function but rather through interaction with phosphoribosyl pyrophosphate amidotransferase (PPAT), the rate-limiting enzyme in the DNPB pathway. The NUDT5-PPAT interaction promoted PPAT oligomerization, suppressed PPAT's enzymatic activity, and facilitated disassembly of the purinosome, a metabolon that functions in DNPB. Disrupting the NUDT5-PPAT interaction overcame DNPB suppression during purine salvage, permitting excessive DNPB and inducing thiopurine resistance. Therefore, NUDT5 governs the balance between DNPB and salvage to maintain appropriate cellular purine nucleotide concentrations.

Cells coordinate de novo purine biosynthesis (DNPB) and salvage to maintain purine nucleotide pools (*1*, *2*). Inhibiting DNPB promotes purine salvage (*3*), whereas activating purine salvage represses DNPB to prevent excessive purine synthesis (*4*). Perturbing purine homeostasis impairs the purine-pyrimidine balance, causing replication stress, DNA damage, and cell cycle arrest (*5*). Mutations causing hyperactivity of phosphoribosylpyrophosphate synthetase–1 (PRPS1), the enzyme that produces phosphoribosyl pyrophosphate (PRPP) at the initial step of purine synthesis, drive excessive DNPB through failed feedback inhibition, resulting in hyperuricemia and neurological dysfunction (*6*, *7*).

The ability to engage either DNPB or purine salvage is pivotal for adaptation to stress, including energetic stress. In contrast to salvage, DNPB is energetically demanding and requires metabolic input from the pentose phosphate pathway, nonessential amino acid metabolism, the folate cycle, and oxidative mitochondrial metabolism (*1*). Impairment of mitochondrial respiration drives a shift from DNPB to purine salvage, preventing unnecessary energy expenditure and enabling cell growth (*8*). However, a complete understanding of the interplay between DNPB and purine salvage is lacking.

DNPB enzymes associate into dynamic cytosolic complexes called purinosomes that facilitate purine synthesis by channeling intermediates from one enzyme to the next (*9*–*11*). Purine deprivation induces purinosome formation to enhance DNPB whereas purine repletion leads to purinosome disassembly (*9*). Thus, purinosome disassembly is part of the mechanism by which purine salvage inhibits DNPB. Although several regulators of purinosome assembly have been identified (*1*, *12*–*14*), less is known about purinosome disassembly during purine salvage.

Our search for genes that function in purine homeostasis identified *NUDT5*, which encodes the adenosine diphosphate (ADP)–ribose (ADPR) hydrolase Nudix hydrolase 5 (NUDT5), as a negative regulator of DNPB during purine salvage. NUDT5's catalytic activity was dispensable for this effect. Instead, NUDT5 interacted with phosphoribosyl pyrophosphate amidotransferase (PPAT), the rate-limiting enzyme in DNPB, altering PPAT's oligomeric state, reducing its enzymatic activity and accelerating purinosome disassembly during purine salvage.

Ablation of NUDT5 confers cellular resistance to thiopurines

To identify regulators of purine metabolism, we explored a published CRISPR screen for modifiers of 6-thioguanine (6-TG) sensitivity (*15*). 6-TG is converted to thioguanine nucleotides such as 6-thio-GMP (6-TGMP) by the salvage enzyme hypoxanthine-guanine phosphoribosyltransferase-1 (HPRT1). These nucleotides are incorporated into the genome, causing DNA damage and cell death (Fig. 1A). Guide RNAs targeting *HPRT1* and *NUDT5* were positively selected in 6-TG–treated cells (fig. S1A). Hydrolysis of ADPR by NUDT5 generates ribose-5-phosphate (R5P) (*16*). Because R5P is the precursor of PRPP, a substrate of HPRT1 NUDT5 has a plausible role in 6-TG toxicity by supporting salvage. To validate the screening result, we used CRISPR-Cas9 to delete *HPRT1* or *NUDT5* (ΔHPRT1, ΔNUDT5) in human HeLa cervical carcinoma cells and human A549 lung adenocarcinoma cells (fig. S1B). Loss of NUDT5 or HPRT1 increased the level of their substrates ADPR and hypoxanthine, respectively (fig. S1, C and D), and conferred resistance to 6-TG and another thiopurine, 6-mercaptopurine (Fig. 1B and fig. S1, E to G).

To assess how cells respond to 6-TG in the presence and absence of NUDT5, we performed quantitative proteomics on wild-type (WT) and ΔNUDT5 cells treated with solute or 6-TG (0.5 μg/mL). Pathway analysis revealed changes in protein abundance characteristic of apoptosis and proteasome degradation in WT but not ΔNUDT5 cells (Fig. 1, C and D, and table S1). Annexin V and propidium iodide (PI) staining confirmed a greater increase in apoptosis after thiopurine treatment in WT than that in ΔNUDT5 cells (Fig. 1E and fig. S1H). During thiopurine treatment, WT cells also exhibited more cleaved Poly(ADP-ribose) polymerase (PARP), another apoptosis marker, than ΔNUDT5 and ΔHPRT1 cells. (Fig. 1F and fig. S1I). Conversely, overexpressing NUDT5 increased 6-TG–induced PARP cleavage (fig. S1J).

NUDT5 regulates cellular responses to thiopurines independently of its catalytic function

To test whether NUDT5's role in thiopurine sensitivity is to provide R5P and PRPP, we rescued ΔNUDT5 cells with WT NUDT5 ($NUDT5^{WT}$) or a NUDT5 mutant ($NUDT5^{E112Q}$) lacking catalytic activity (*17*, *18*). $NUDT5^{WT}$, but not an empty vector (EV) or $NUDT5^{E112Q}$, diminished ADPR abundance, confirming $NUDT5^{E112Q}$'s catalytic defect (fig. S1K). However, both $NUDT5^{WT}$ and $NUDT5^{E112Q}$ restored sensitivity to thiopurines (Fig. 1, G and H, and fig. S1, L and M), indicating that NUDT5 regulates thiopurine sensitivity independently of its catalytic function.

Thiopurines suppress mitochondrial metabolism in a NUDT5-dependent manner

Several pathways related to mitochondrial metabolism were suppressed in 6-TG–treated WT cells (fig. S2A and table S1). Mitochondrial electron transport chain (ETC) subunits and tricarboxylic acid (TCA)

[1]Children's Medical Center Research Institute, University of Texas Southwestern Medical Center, Dallas, TX, USA. [2]Division of Pulmonary and Critical Care Medicine, Department of Internal Medicine, UT Southwestern Medical Center, Dallas, TX, USA. [3]Department of Biophysics, University of Texas Southwestern Medical Center, Dallas, TX, USA. [4]Howard Hughes Medical Institute, University of Texas Southwestern Medical Center, Dallas, TX, USA. [5]Department of Biochemistry, University of Nebraska-Lincoln, Lincoln, NE, USA. [6]Department of Radiation Oncology, University of Texas Southwestern Medical Center, Dallas, TX, USA. [7]Harold C. Simmons Comprehensive Cancer Center, University of Texas Southwestern Medical Center, Dallas, TX, USA. [8]Quantitative Biomedical Research Center, Peter O'Donnell Jr. School of Public Health, University of Texas Southwestern Medical Center, Dallas, TX, USA. [9]Eugene McDermott Center for Human Growth and Development, University of Texas Southwestern Medical Center, Dallas, TX, USA. ***Corresponding author. Email: Ralph.DeBerardinis@utsouthwestern.edu** †These authors contributed equally to this work.

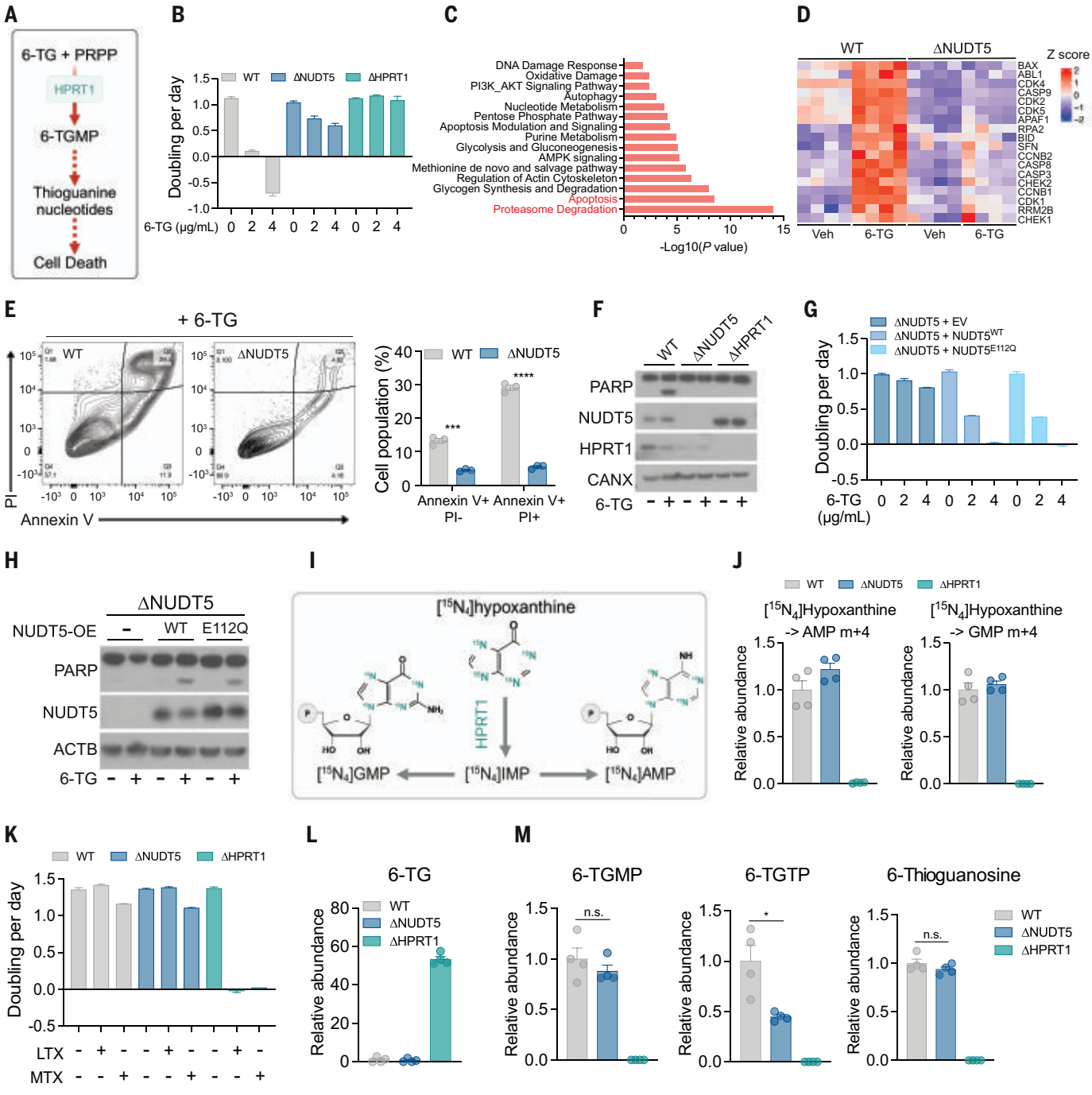


Fig. 1. NUDT5 and HPRT1 regulate thiopurine sensitivity through different mechanisms. (**A**) Simplified schematic illustrating 6-TG metabolism-mediated cell death. (**B**) Growth rates of WT, ΔNUDT5, and ΔHPRT1 HeLa cells treated with the indicated doses of 6-TG. Data are technical replicates from one of three independent experiments. (**C**) Proteomics analysis showing up-regulated pathways in 6-TG–treated WT cells compared with vehicle-treated WT, vehicle-treated ΔNUDT5, and 6-TG–treated ΔNUDT5 cells. (**D**) Heatmap showing abundance of proteins in the apoptosis pathway in WT and ΔNUDT5 HeLa cells treated with or without 0.5 μg/mL 6-TG for 24 hours ($n = 4$). (**E**) Apoptosis analysis in WT and ΔNUDT5 HeLa cells treated with 0.5 μg/mL 6-TG for 48 hours. (Left) Representative contour plots; (right) bar graphs showing the percentage of apoptotic (Annexin V+, PI−) and dead (Annexin V+, PI+) cells; ($n = 3$). (**F**) Western blot assessing cleaved PARP in WT, ΔNUDT5, and ΔHPRT1 HeLa cells treated with 0.5 μg/mL 6-TG for 24 hours. Calnexin (CANX) is the loading control. (**G**) Growth rates of ΔNUDT5 HeLa cells that express EV, NUDT5^{WT}, or NUDT5^{E112Q} treated with the indicated doses of 6-TG. Data are technical replicates from one of three independent experiments. (**H**) Western blot assessing cleaved PARP in ΔNUDT5 HeLa cells that express EV, NUDT5^{WT}, or NUDT5^{E112Q} treated with or without 0.5 μg/mL 6-TG for 24 hours. β-actin (ACTB) is the loading control. (**I**) Schematic illustrating labeling of purine nucleotides from [$^{15}N_4$]hypoxanthine. (**J**) Relative abundance of m+4 AMP and m+4 GMP from [$^{15}N_4$]hypoxanthine in WT, ΔNUDT5, and ΔHPRT1 HeLa cells during 4 hours of tracing; ($n = 4$). (**K**) Growth rates of WT, ΔNUDT5, and ΔHPRT1 HeLa cells treated with DMSO, 1 μM LTX, or 1 μM MTX. Data are technical replicates from one of three independent experiments. (**L** to **M**) Relative abundance of 6-TG (L), 6-T-GMP, 6-T-GTP, and 6-thioguanosine (M) in WT, ΔNUDT5, and ΔHPRT1 HeLa cells treated with 0.5 μg/mL 6-TG for 24 hours; ($n = 4$). Data points in each panel represent an independent sample unless specified. Error bars denote SEM. Multiple *t* test (E) and unpaired, two-sided *t* tests (M) were used for statistical analyses. ***$P < 0.001$; ***$P < 0.001$; *$P < 0.05$; n.s., $P > 0.05$. [Illustrations in panels (A) and (I) created with BioRender.com]

cycle enzymes were depleted in WT but not ΔNUDT5 cells treated with 6-TG (fig. S2B), as reported in acute lymphoblastic leukemia (ALL) cells (*19*). In parental cells, 6-TG decreased oxygen consumption, reduced contributions of oxidative glucose and glutamine metabolism to the TCA cycle, and enhanced the contribution of glutamine-dependent reductive carboxylation, a consequence of ETC suppression (*20*–*22*) (figs. S2C and S3, A to D). All of these alterations were attenuated in ΔNUDT5 cells, indicating that 6-TG's effects on mitochondrial function were NUDT5-dependent.

NUDT5 and HPRT1 regulate cellular thiopurine sensitivity differently

To examine NUDT5's role in purine salvage, we conducted stable isotope tracing with [$^{15}N_4$]hypoxanthine. HPRT1 transfers four ^{15}N nuclei from hypoxanthine into purine nucleotides, which are detected as m+4 isotopologues (Fig. 1I). Depletion of HPRT1 eliminated labeling from [$^{15}N_4$]hypoxanthine (Fig. 1J and fig. S4A). However, WT and ΔNUDT5 cells contained comparable labeling, indicating NUDT5's dispensability for purine salvage (Fig. 1J and fig. S4A). WT and ΔNUDT5 cells were less sensitive than ΔHPRT1 cells to the DNPB inhibitors lometrexol (LTX) and methotrexate (MTX) (Fig. 1K and fig. S4B), also indicating intact purine salvage despite NUDT5 depletion. Lysates from ΔNUDT5 cells expressing EV, NUDT5^{WT}, or NUDT5^{E112Q} had similar HPRT1 enzymatic activity (fig. S4C). Thus, NUDT5 ablation is unlikely to confer 6-TG resistance through blocking 6-TG conversion to 6-TGMP. To confirm this, we measured the relevant metabolites after 6-TG treatment. Intracellular 6-TG was barely detectable in WT and ΔNUDT5 cells after 24 hours of 6-TG treatment (Fig. 1L and fig. S4D). This was not due to defective 6-TG uptake, but rather to its conversion to 6-TGMP, 6-TGTP, and 6-thioguanosine (Fig. 1M and fig. S4E). By contrast, ΔHPRT1 cells accumulated 6-TG but did not produce 6-TGMP, 6-TGTP, or 6-thioguanosine (Fig. 1, L and M, and fig. S4, D and E). These data indicate that NUDT5 supports thiopurine toxicity through a mechanism distinct from HPRT1-mediated purine salvage.

NUDT5 is dispensable for 6-TG–induced DNA damage

Thiopurine incorporation into the genome causes DNA breaks (*23*–*25*). To investigate whether NUDT5 loss mitigated DNA damage during 6-TG treatment, we stained cells for phosphorylated H2A histone family member X (γH2AX), a nuclear DNA damage marker. WT and ΔNUDT5 cells had comparable numbers of γH2AX foci after 48 hours of 6-TG treatment (fig. S4, F and G). Additionally, NUDT5 ablation did not protect cells against ionizing radiation or the DNA-damaging agents cisplatin and etoposide (fig. S5, A to C). Although DNA mismatch repair (MMR) deficiency renders colorectal cancer cells resistant to 6-TG (*23*, *26*), single guide RNA against MMR genes did not protect against 6-TG in the CRISPR screen (fig. S6A). To rule out a role for MMR, we deleted the gene encoding mutator gene L protein homolog 1 (MLH1), a key MMR protein (fig. S6B). MLH1 depletion did not protect against 6-TG (fig. S6C). Therefore, NUDT5 specifically regulates sensitivity to thiopurines.

Thiopurines suppress DNPB in a NUDT5-dependent fashion

Thiopurine-induced cell death may stem from DNPB suppression as thiopurine nucleotides inhibit PPAT (*1*, *27*). 6-TG elicited widespread metabolic changes, including suppression of many purine metabolites, in cells expressing NUDT5 (Fig. 2, A and B, fig. S7A, and table S2). Isotope tracing with [U-^{13}C]glucose revealed that 6-TG suppressed purine nucleotide labeling in a pattern indicating decreased DNPB (Fig. 2C and fig. S7, B and C). However, ΔNUDT5 cells did not display these changes (Fig. 2C and fig. S7C). Suppressed DNPB in WT cells did not result from decreased synthesis of R5P, which was highly labeled under all conditions (fig. S7D). Instead, 6-TG induced an accumulation of labeled R5P and other pentose phosphate pathway metabolites (fig. S7, E to G).

We also cultured cells with [amide-^{15}N]glutamine, which delivers ^{15}N to purine nucleotides largely through DNPB (Fig. 2D). Thiopurines nearly abolished adenosine monophosphate (AMP) and guanosine monophosphate (GMP) labeling in WT but not ΔNUDT5 cells (Fig. 2E and fig. S7H), indicating that thiopurines required NUDT5 to suppress DNPB. In the absence of 6-TG, DNPB was unaffected by knockout or overexpression of NUDT5 (Fig. 2E and fig. S7, H and I). Although thiopurines can impair purine salvage (*28*), the doses we used slightly enhanced the contribution of purine salvage to AMP and GMP in WT cells (fig. S8, A and B), possibly in compensation for DNPB inhibition.

To test whether NUDT5's role in DNPB suppression is restricted to thiopurines, we treated cells with hypoxanthine and inosine to stimulate salvage. Treatment with either hypoxanthine or inosine decreased DNPB as assessed by labeling with [amide-^{15}N]glutamine, and this was alleviated by loss of NUDT5 (Fig. 2, F and G).

To test whether persistent DNPB underlies thiopurine resistance, we treated ΔNUDT5 cells with DNPB inhibitors. ΔNUDT5 cells largely tolerated thiopurines or DNPB inhibitors individually, but concomitant treatment eliminated growth (Fig. 2H and fig. S8C). Supplementing WT cells with hypoxanthine or inosine restored growth during 6-TG treatment, likely by competing with 6-TG for metabolism and providing a source of natural nucleotides to counteract genotoxicity (fig. S8, D and E). Altogether these data indicate that 6-TG induces purine nucleotide insufficiency through NUDT5-mediated DNPB suppression.

NUDT5 binds PPAT to suppress DNPB during purine salvage

Two lines of evidence suggested that NUDT5 binds PPAT: First, the biophysical interactions documented in the ORFeome-based complexes database (BioPlex 3.0) (*29*, *30*) include such an interaction (Fig. 3A). Second, our in silico screen of human protein-protein interactions, which combines coevolution analysis and deep learning, predicted that NUDT5 and PPAT physically associate (*31*). We purified NUDT5 and the glutaminase domain of PPAT and used an in vitro binding assay to demonstrate that these proteins interact directly (fig. S9, A to L). NUDT5 phosphorylation at threonine 45 (T45) increases stability of its dimeric form (*18*). To test whether T45 phosphorylation regulates NUDT5's interaction with PPAT, we generated T45 phosphomimetic (T45D) and T45 phospho-dead (T45A) mutants. Neither mutant affected NUDT5 binding to PPAT or thiopurine sensitivity (fig. S10, A to E).

Supplementing the culture medium with hypoxanthine enhanced the PPAT-NUDT5 interaction in cells that had been cultured in purine-deprived medium (Fig. 3B). AlphaFold3 (*32*) predicted that NUDT5 arginine 70 (R70) resides in the interface between NUDT5 and PPAT and forms salt bridges with PPAT glutamine 26 and glutamate 228 (Fig. 3C). We mutated R70 to alanine and reconstituted ΔNUDT5 cells with NUDT5^{WT}, NUDT5^{R70A}, or NUDT5^{E112Q}. NUDT5^{WT} and NUDT5^{R70A}, but not NUDT5^{E112Q}, reduced cellular ADPR abundance, indicating that NUDT5^{R70A} is catalytically active (Fig. 3D). Epitope-tagged PPAT immunoprecipitated NUDT5^{WT} and NUDT5^{E112Q}, but not NUDT5^{R70A}, confirming that R70 is required for association with PPAT (Fig. 3E). NUDT5^{R70A} also mitigated DNPB suppression by hypoxanthine or inosine (Fig. 3, F and G).

NUDT5 binding suppresses PPAT enzymatic activity

We next tested whether NUDT5 binding modulates PPAT enzymatic activity. We first generated PPAT-null cells (ΔPPAT) that express PPAT under control of doxycycline (fig. S11A). In the absence of doxycycline, these cells required purine bases or nucleosides to grow, consistent with DNPB blockade (fig. S11, B and C). Lysates of cells expressing NUDT5^{WT} or NUDT5^{E112Q} had no detectable PPAT activity (i.e., the same activity as ΔPPAT cells lacking doxycycline), whereas lysates without NUDT5 or with NUDT5^{R70A} exhibited higher activity (fig. S11, D and E). Next, we purified full-length PPAT (fig. S11, F and G), mixed it with purified NUDT5^{WT} or NUDT5^{R70A} in vitro and measured PPAT

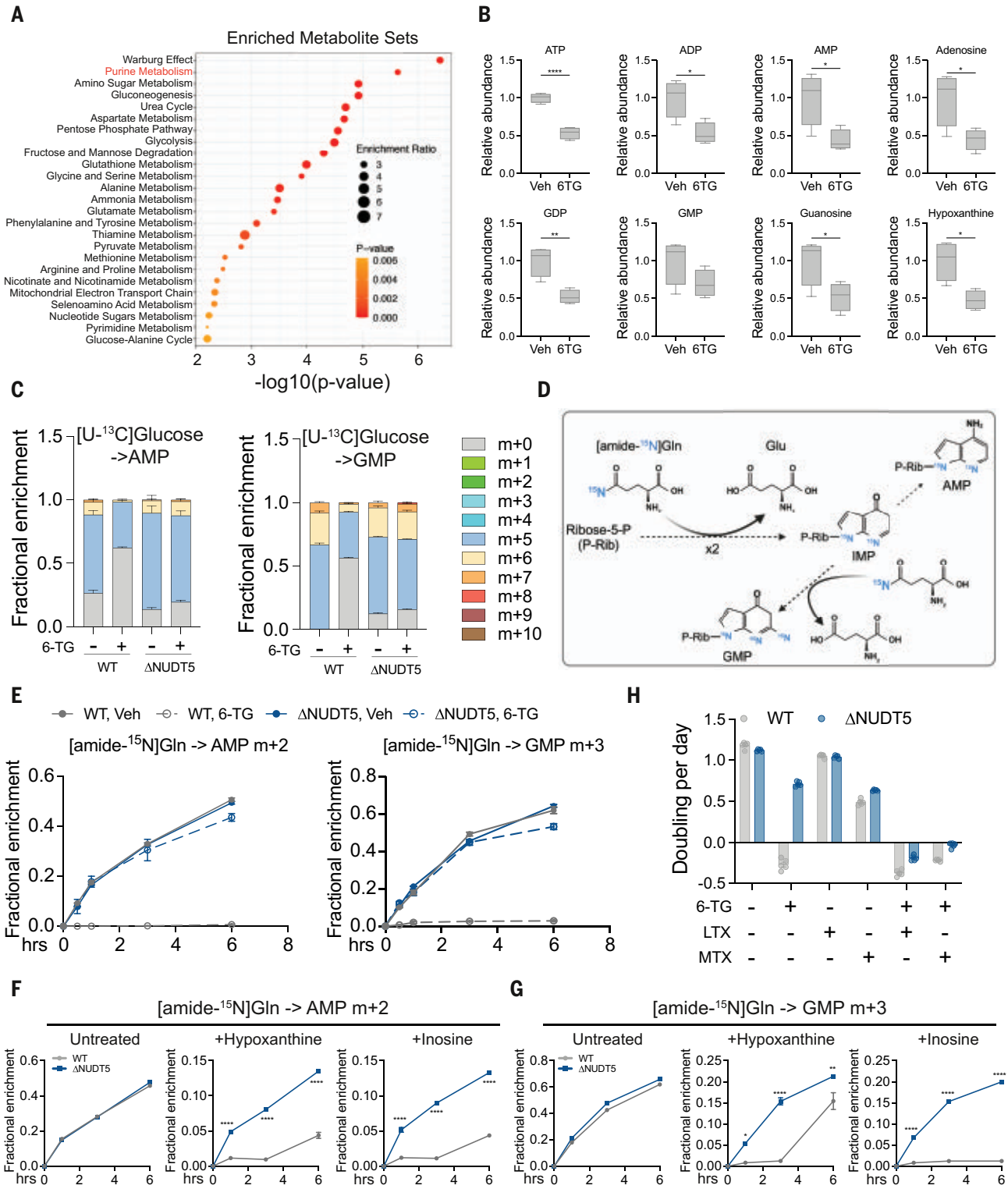


Fig. 2. NUDT5 ablation overcomes thiopurine-induced blockade in de novo purine nucleotide synthesis. (**A**) Metabolite set enrichment analysis comparing vehicle and 24 hours of 0.5 μg/mL 6-TG–treated HeLa cells. (**B**) Relative abundance of the indicated purine metabolites in vehicle or 0.5 μg/mL 6-TG–treated HeLa cells; ($n = 4$). (**C**) ^{13}C labeling in AMP and GMP after 6 hours of culture with [U-^{13}C]glucose in WT and ΔNUDT5 HeLa cells pretreated with vehicle or 0.5 μg/mL 6-TG for 24 hours; ($n = 3$). (**D**) Schematic illustrating labeling of purine nucleotides from [amide-^{15}N]glutamine. (**E**) Time-dependent fractional enrichment of m+2 AMP and m+3 GMP from [amide-^{15}N] glutamine in WT and ΔNUDT5 HeLa cells pretreated with 0.5 μg/mL 6-TG for 24 hours; ($n = 3$). (**F** and **G**) Time-dependent fractional enrichment of m+2 AMP (F) and m+3 GMP (G) from [amide-^{15}N]glutamine in WT and ΔNUDT5 HeLa cells pretreated with or without 20 μM hypoxanthine or inosine for 24 hours; ($n = 3$). (**H**) Growth rates of WT and ΔNUDT5 HeLa cells treated with or without 4 μg/mL 6-TG, 1 μM LTX, 1 μM MTX, or combinations. Data are technical replicates from one of three independent experiments. Data points in each panel represent an independent sample unless specified. Error bars denote SEM. Unpaired, two-sided *t* test (B) and two-way analysis of variance (ANOVA) (F) and (G) were used for the statistical analyses ****$P < 0.0001$; **$P < 0.01$; *$P < 0.05$. [Illustration in (D) created with BioRender.com]

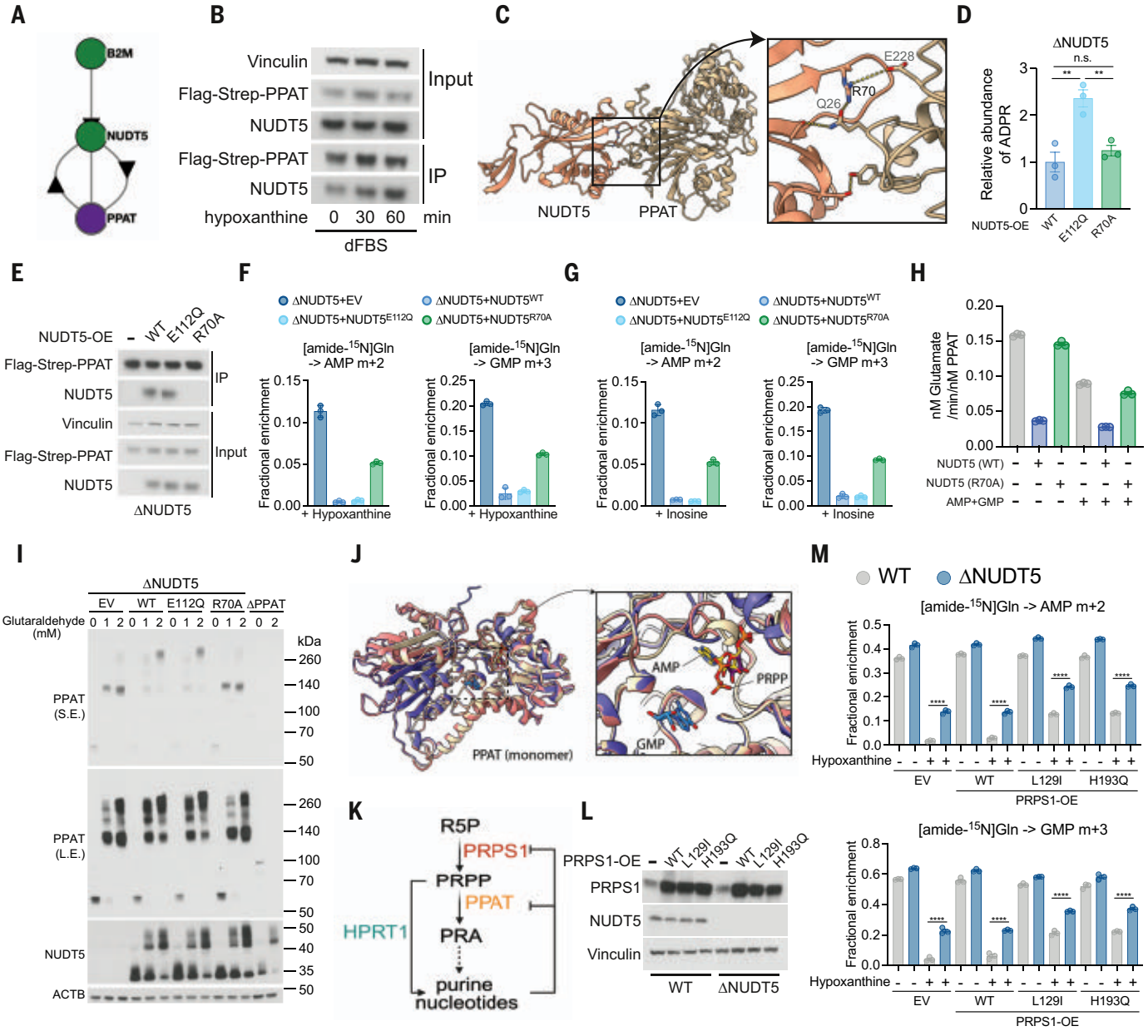


Fig. 3. NUDT5 binds PPAT to suppress de novo purine biosynthesis during purine salvage. (**A**) Bio-plex data showing the interaction between PPAT and NUDT5. (**B**) Western blot showing the interaction between Flag-Strep-PPAT and NUDT5 in cells cultured in dialyzed fetal bovine serum–supplemented medium after 20 μM hypoxanthine treatment at the indicated time points. Vinculin is the loading control for the input samples. (**C**) PPAT-NUDT5 interaction depicted by AlphaFold3. (**D**) Relative abundance of ADPR in ΔNUDT5 HeLa cells that express NUDT5^{WT}, NUDT5^{E112Q}, or NUDT5^{R70A} ($n = 3$). (**E**) Western blot showing interaction between Flag-Strep-PPAT and NUDT5^{WT} or NUDT5^{E112Q} but not NUDT5^{R70A}. Vinculin is the loading control for the input samples. (**F** and **G**) Fractional enrichment of m+2 AMP and m+3 GMP from [amide-^{15}N]glutamine in ΔNUDT5 HeLa cells that express EV, NUDT5^{WT}, NUDT5^{E112Q}, or NUDT5^{R70A} during 4 hours of tracing. The cells were treated with 20 μM hypoxanthine (F) or inosine (G) for 24 hours ($n = 3$). (**H**) Rates of PPAT-catalyzed synthesis of glutamate when incubated with or without NUDT5^{WT} or NUDT5^{R70A}, AMP, and GMP. Data are technical replicates from one of three experiments. (**I**) Western blot showing oligomerization of PPAT and NUDT5 in ΔNUDT5 HeLa cells expressing EV, NUDT5^{WT}, NUDT5^{E112Q}, or NUDT5^{R70A} and ΔPPAT cells. β-actin (ACTB) is the loading control. (**J**) PRPP, AMP, and GMP binding pockets in PPAT overlap as depicted by AlphFold3. (**K**) Schematic illustrating allosteric inhibition of PRPS1 and PPAT in the DNPB pathway. (**L**) Western blot showing overexpression of WT and mutant PRPS1 in WT and ΔNUDT5 cells. Vinculin is the loading control. (**M**) Fractional enrichment of AMP m+2 and GMP m+3 from [amide-^{15}N]glutamine during 4 hours of tracing in WT or ΔNUDT5 cells that express EV, PRPS1^{WT}, PRPS1^{L129I}, or PRPS1^{H193Q} with or without 24 hours of treatment with 20 μM hypoxanthine; ($n = 3$). Data points in each panel represent an independent sample unless specified. Error bars denote SEM. One-way ANOVA (D) and (M) was used for the statistical analyses. ****$P < 0.0001$; **$P < 0.01$; *$P < 0.05$. n.s., $P > 0.05$. [Illustration in (K) created with BioRender.com]

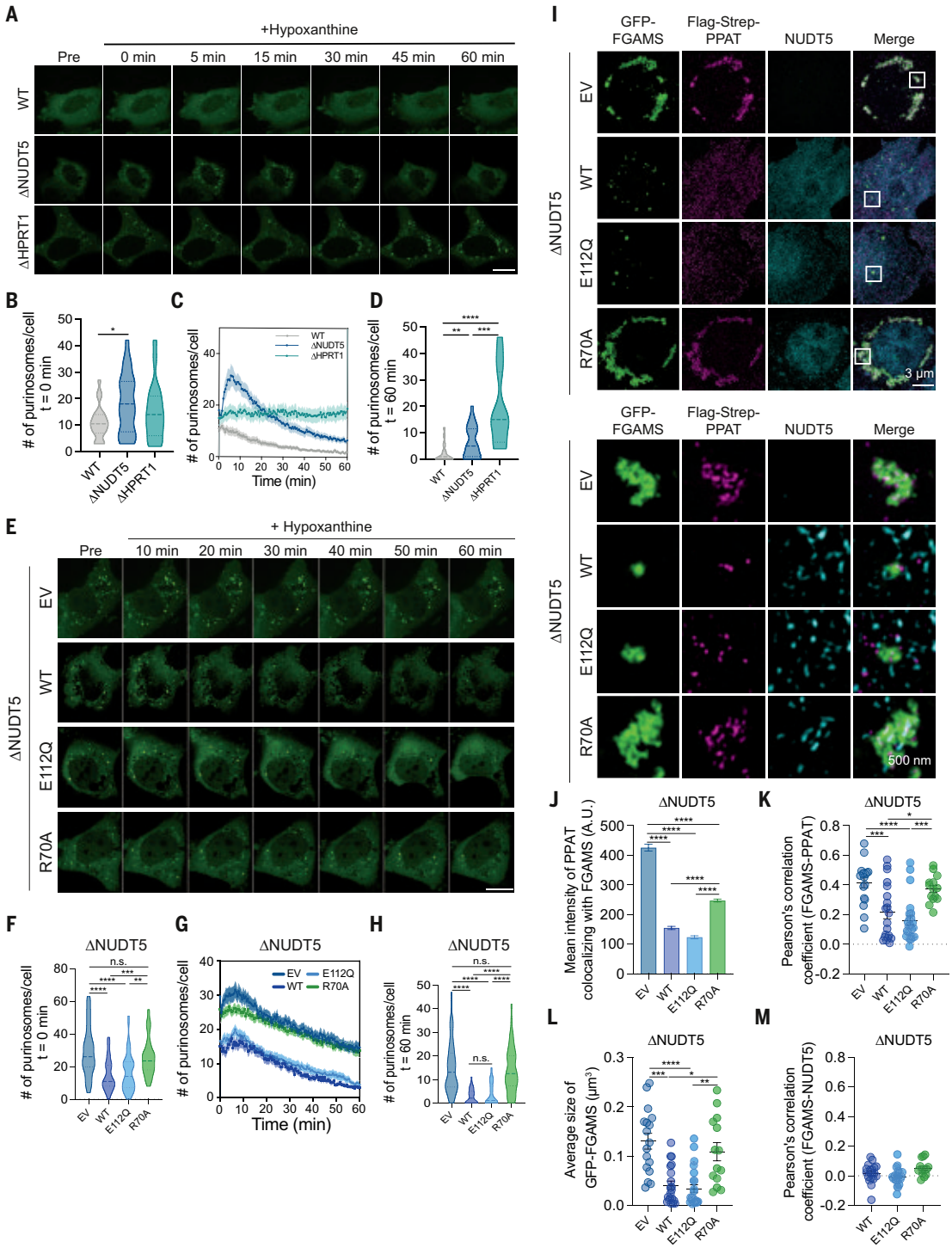


Fig. 4. NUDT5 regulates purinosome dynamics. (**A**) Time-lapse imaging showing purinosome disassembly upon treatment with 20 μM hypoxanthine at t = 0 min in WT, ΔNUDT5, and ΔHPRT1 HeLa cells. The puncta indicate GFP-tagged FGAMS. Scale bar, 10 μm. (**B** to **D**) Quantification of purinosome count at t = 0 min (B), over 1 hour (C), and at t = 60 min (D) after hypoxanthine supplementation in WT ($n = 22$), ΔNUDT5 ($n = 25$), and ΔHPRT1 ($n = 18$) HeLa cells. (**E**) Time-lapse imaging showing dispersal of purinosomes after treatment with 20 μM hypoxanthine at t = 0 min in ΔNUDT5 HeLa cells expressing an EV, NUDT5^{WT}, NUDT5^{E112Q}, or NUDT5^{R70A}. The puncta indicate GFP-tagged FGAMS. Scale bar, 10 μm. (**F** to **H**) Quantification of purinosome count at t = 0 min (F), over 1 hour (G), and at t = 60 min (H) after hypoxanthine supplementation in ΔNUDT5 HeLa cells expressing EV ($n = 42$), NUDT5^{WT} ($n = 39$), NUDT5^{E112Q} ($n = 47$), or NUDT5^{R70A} ($n = 48$). (**I**) Fluorescent images showing GFP-FGAMs (green), Flag-strep-PPAT (magenta), and NUDT5 (cyan) in ΔNUDT5 HeLa cells expressing EV, NUDT5^{WT}, NUDT5^{E112Q}, or NUDT5^{R70A} when cultured in purine-deprived medium. The bottom images are insets from the top images. (**J**) Mean intensity of Flag-Strep-PPAT colocalizing to GFP-FGAMS in (I) ($n > 3000$ for each group). (**K**) Pearson's correlation coefficient of Flag-Strep-PPAT and GFP-FGAMS colocalization in ΔNUDT5 HeLa cells expressing EV ($n = 17$), NUDT5^{WT} ($n = 20$), NUDT5^{E112Q} ($n = 23$), or NUDT5^{R70A} ($n = 14$) in (I). (**L**) Size of GFP-FGAMS puncta in ΔNUDT5 HeLa cells expressing EV ($n = 17$), NUDT5^{WT} ($n = 20$), NUDT5^{E112Q} ($n = 23$), or NUDT5^{R70A} ($n = 14$) in (I). (**M**) Pearson's correlation coefficient of NUDT5 and GFP-FGAMS colocalization in ΔNUDT5 HeLa cells expressing NUDT5^{WT} ($n = 19$), NUDT5^{E112Q} ($n = 23$), or NUDT5^{R70A} ($n = 14$) in (I). Error bars denote SEM. One-way ANOVA (B), (D), (F), (H), (J), (K), and (L) was used for statistical analyses. ****$P < 0.0001$; ***$P < 0.001$; **$P < 0.01$; *$P < 0.05$. n.s., $P > 0.05$.

activity. NUDT5^{WT} but not NUDT5^{R70A} suppressed PPAT activity, with a magnitude of inhibition exceeding the effect of AMP and GMP at physiological concentrations (Fig. 3H).

NUDT5 binding promotes PPAT oligomerization

AMP and GMP promote PPAT tetramerization whereas the PPAT substrate PRPP keeps it in a dimeric state (*33*), indicating that dimeric PPAT is more enzymatically active. We explored whether NUDT5 affects PPAT oligomerization. NUDT5^{WT} and NUDT5^{E112Q}, but not NUDT5^{R70A}, promoted PPAT oligomerization after glutaraldehyde cross-linking in cells (Fig. 3I; fig. S12A shows an AlphaFold3 rendering). Hypoxanthine modestly promoted PPAT oligomerization (fig. S12, B and C), consistent with its positive effect on NUDT5-PPAT interaction. In cell lysates, PRPP is reported to disrupt this interaction, allowing PPAT to adopt its catalytically active dimeric form (*33*). Structural modeling predicts that the PPAT binding pockets for AMP and PRPP overlap with each other (Fig. 3J), allowing AMP to interfere with PRPP binding to PPAT. Therefore, during purine salvage, both the rapid consumption of PRPP by HPRT1 and the appearance of purine nucleotides may enhance NUDT5 binding to PPAT, promoting PPAT oligomerization and suppressing its enzymatic activity.

Purine nucleotides also allosterically inhibit PRPS1, which produces PRPP (*34*) (Fig. 3K). To discriminate between the effects of PRPS1 inhibition and NUDT5 on DNPB, we generated cells overexpressing PRPS1^{L129I} or PRPS1^{H193Q}, mutant alleles from patients with PRPS1 superactivity syndrome (*34*) (Fig. 3L). These mutants partially resist allosteric inhibition by purine nucleotides and display higher levels of DNPB during hypoxanthine treatment (Fig. 3M). Deletion of NUDT5 in cells expressing mutant PRPS1 alleles further enhanced DNPB (Fig. 3M). These data imply that both PRPS1 inactivation and PPAT inhibition by NUDT5 contribute to DNPB suppression during purine salvage.

To explore mechanisms by which NUDT5 might regulate PPAT, we used the standalone version of AlphaFold3 to superimpose structures of PPAT bound to AMP, GMP, or PRPP, and found that NUDT5 is not

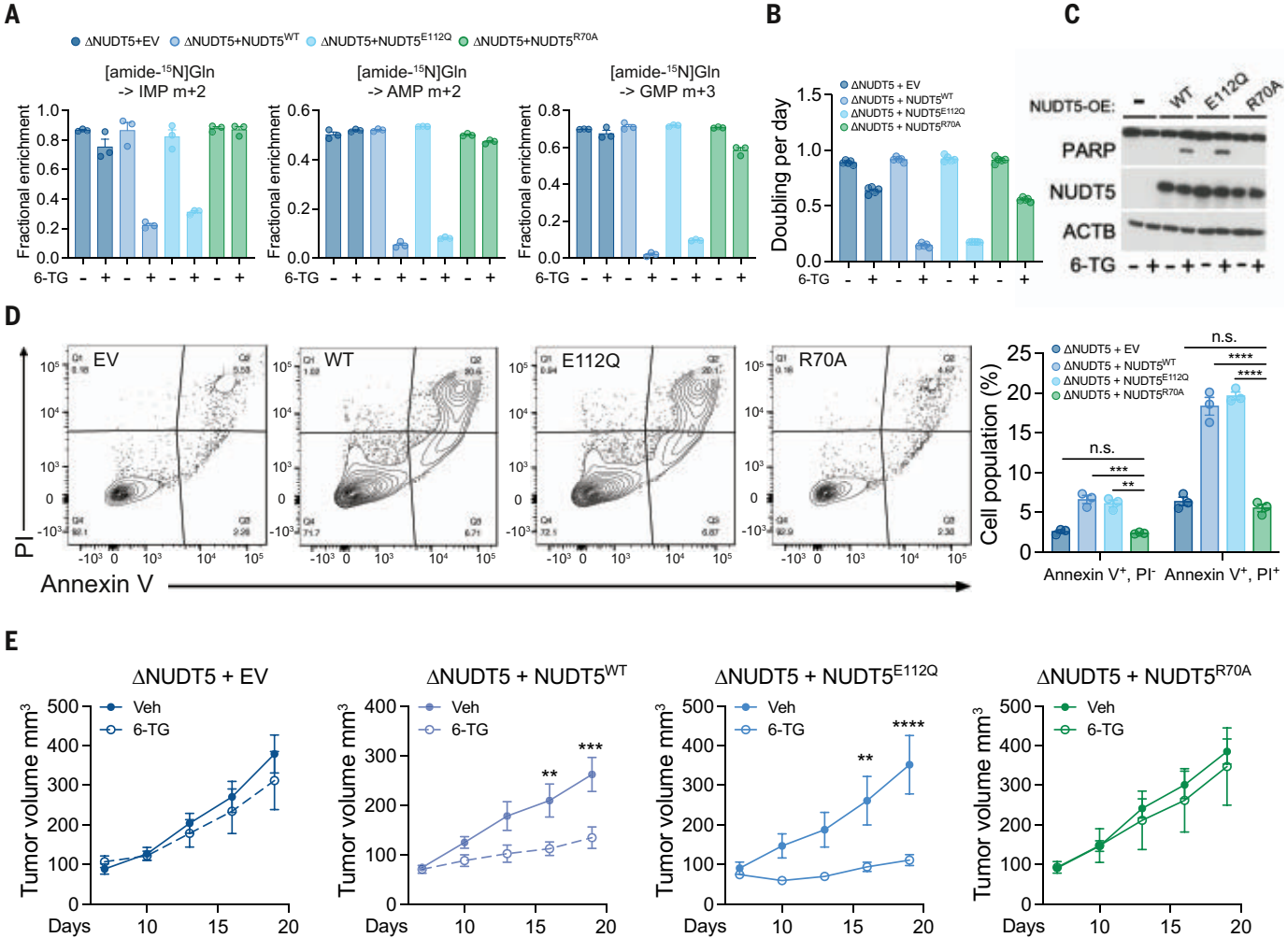


Fig. 5. Disruption of the NUDT5-PPAT interaction induces thiopurine resistance. (**A**) Fractional enrichment of m+2 IMP, m+2 AMP, and m+3 GMP from [amide-^{15}N]glutamine in ΔNUDT5 HeLa cells that express EV, NUDT5^{WT}, NUDT5^{E112Q}, or NUDT5^{R70A} during 6 hours of tracing. The cells were pretreated with 0.5 μg/mL 6-TG for 24 hours; ($n = 3$). (**B**) Growth rates of ΔNUDT5 HeLa cells that express EV, NUDT5^{WT}, NUDT5^{E112Q}, or NUDT5^{R70A}, treated with 2 μg/mL 6-TG. Data are technical replicates from one of three experiments. (**C**) Western blot assessing cleaved PARP in ΔNUDT5 HeLa cells that express EV, NUDT5^{WT}, NUDT5^{E112Q}, or NUDT5^{R70A}, treated with 0.5 μg/mL 6-TG for 24 hours. β-actin (ACTB) is the loading control. (**D**) Apoptosis analysis in ΔNUDT5 HeLa cells that express EV, NUDT5^{WT}, NUDT5^{E112Q}, or NUDT5^{R70A}, treated with 0.5 μg/mL 6-TG for 48 hours. (Left) Representative contour plots. (Right) Bar graphs showing percentage of apoptotic (Annexin V+, PI−) and dead (Annexin V+, PI+) cells; ($n = 3$). (**E**) Subcutaneous growth of ΔNUDT5 HeLa xenografts expressing EV, NUDT5^{WT}, NUDT5^{E112Q}, or NUDT5^{R70A} treated with Vehicle (Veh) or 2 mg/kg 6-TG. EV, Veh ($n = 8$); EV, 6-TG ($n = 6$); NUDT5^{WT}, Veh ($n = 8$); NUDT5^{WT}, 6-TG ($n = 8$); NUDT5^{E112Q}, Veh ($n = 8$); NUDT5^{E112Q}, 6-TG ($n = 8$); NUDT5^{R70A}, Veh ($n = 8$); NUDT5^{R70A}, 6-TG ($n = 8$). Data points in each panel represent an independent sample unless specified. Error bars denote SEM. Two-way ANOVA was used for statistical analysis (D) and (E). ****$P < 0.0001$; ***$P < 0.001$; **$P < 0.01$; n.s., $P > 0.05$.

predicted to induce conformational changes in these binding pockets (fig. S13, A to C) (*32*). PPAT catalyzes two reactions: a glutaminase step to remove ammonia from glutamine and a phosphoribosyltransferase (PRTase) step to conjugate the ammonia to PRPP, producing 5-phosphoribosyl-1-amine (PRA). These reactions are coordinated to ensure efficient delivery of ammonia to PRPP (*35*, *36*). It is possible that in the PRPP-bound state, dimeric PPAT is more effective than tetrameric PPAT at gripping glutamine and facilitating ammonia channeling to the PRPase domain. Therefore, promotion of PPAT oligomerization by NUDT5 binding is potentially linked to the suppressed enzymatic activity.

NUDT5 binds PPAT to stimulate purinosome disassembly

PRA is labile, with a half-life of just a few seconds, and this poses a challenge to maintaining efficient DNPB (*37*). Cells cope with this by assembling PPAT and the other DNPB enzymes into cytosolic complexes called purinosomes, which channel intermediates from PRPP to inosine monophosphate (IMP) (*9*–*11*, *13*, *37*). Purinosomes arise during purine deprivation when the need for DNPB is high, then quickly disassemble during purine supplementation (*9*). To test whether NUDT5 modulates purinosome dynamics, we expressed green fluorescent protein (GFP)-tagged phosphoribosylformyl glycinamidine synthase (FGAMS), a core purinosome protein, in WT, ΔNUDT5, and ΔHPRT1 cells. These cell lines were cultured in purine-depleted medium to induce purinosome formation, indicated by clustering of FGAMS-GFP into punctate structures (*9*, *12*, *13*) (Fig. 4A). NUDT5 deficiency modestly increased basal purinosome abundance (Fig. 4B). After supplementation with hypoxanthine, most punctate FGAMS-GFP structures disappeared in WT cells within 1 hour (Fig. 4, A to D, and movie S1). Hypoxanthine had no effect on punctate FGAMS-GFP in ΔHPRT1 cells (Fig. 4, A to D, and movie S2). In ΔNUDT5 cells, hypoxanthine acutely stimulated punctate FGAMS-GFP, then delayed dispersal, resulting in persistent punctate signals after 1 hour (Fig. 4, A to D, and movie S3). In ΔNUDT5 cells reconstituted with NUDT5, hypoxanthine-induced FGAMS-GFP dispersal was accelerated by $NUDT5^{WT}$ and $NUDT5^{E112Q}$, but not $NUDT5^{R70A}$ (Fig. 4, E to H, and movies S4 to S7). Super-resolution three-dimensional (3D) structured illumination microscopy revealed that $NUDT5^{WT}$ and $NUDT5^{E112Q}$, but not $NUDT5^{R70A}$, impeded PPAT's interaction with FGAMS and reduced the size of FGAMS-GFP without being physically partitioned into purinosomes (Fig. 4, I to M). Most NUDT5 was not colocalized with PPAT, suggesting that these proteins interact transiently in intact cells (Fig. 4I). Together, the data show that NUDT5 negatively regulates purinosome formation and facilitates purinosome disassembly during purine salvage.

Disrupting the PPAT-NUDT5 interaction confers resistance to thiopurines

Cells expressing $NUDT5^{WT}$ or $NUDT5^{E112Q}$ suppressed DNPB upon exposure to thiopurines, whereas cells expressing $NUDT5^{R70A}$ had comparable DNPB under these conditions (Fig. 5A and fig. S14A). Because the PPAT-NUDT5 interaction enabled thiopurine-induced DNPB suppression, we reasoned that loss of the interaction would allow cells to survive thiopurine treatment. Indeed, compared with cells expressing either $NUDT5^{WT}$ or $NUDT5^{E112Q}$, cells expressing $NUDT5^{R70A}$ maintained growth and resisted apoptosis when treated with thiopurines, similar to ΔNUDT5 cells (Fig. 5, B to D, and fig. S14B). Xenografts lacking NUDT5 or expressing $NUDT5^{R70A}$ were also resistant to 6-TG treatment, whereas xenografts expressing $NUDT5^{WT}$ or $NUDT5^{E112Q}$ were sensitive (Fig. 5E).

Discussion

NUDT5 regulates DNPB through two complementary mechanisms: suppression of PPAT enzymatic activity and enabling of purinosome disassembly (fig. S14, C and D). Neither effect requires NUDT5's catalytic activity but both require its association with PPAT. The processes governing purinosome dynamics are incompletely understood, but NUDT5's involvement suggests that disassembly is prompted by PPAT oligomerization. Presumably purinosome disassembly also involves a metabolic signal, but the identity of this signal is unknown. Hypoxanthine prompts purinosome disassembly over time, but this requires both HPRT1 and the transient association of NUDT5 with PPAT. Potential metabolic triggers in this context include increased purine nucleotides, decreased PRPP, or the ability to biochemically inhibit PPAT. When NUDT5 cannot associate with PPAT, hypoxanthine paradoxically induces a transient increase in purinosomes, implying that decisive purinosome disassembly requires rapid suppression of PPAT.

DNPB inhibition activates purine salvage and vice versa, reflecting plasticity in how cells maintain an adequate purine nucleotide supply (*3*, *8*). NUDT5 prevents simultaneous DNPB and salvage. This is likely advantageous because purine overabundance is pathological. Increased purine:pyrimidine ratios induce DNA replication stress and cell cycle arrest (*5*), and excess purine synthesis causes hyperuricemia and associated toxicities. NUDT5 facilitates purine homeostasis by allowing cells to switch off DNPB during salvage.

Thiopurines are used to treat ALL and inflammatory diseases (*38*–*40*). Genetic variants affecting the metabolism of thiopurines to thiopurine nucleotides affect both clinical efficacy and the substantial systemic toxicities associated with these drugs (*40*–*44*). Patients with *HPRT1* variants that impair purine salvage are refractory to thiopurines (*43*), whereas loss-of-function variants in Nudix hydrolase 15 (*NUDT15*), an enzyme involved in thioguanine nucleotide detoxification, increase sensitivity (*42*, *45*). The human relevance of NUDT5's role in thiopurine sensitivity, as shown here and in other recent reports (*46*–*48*), is underscored by the fact that genetic variants promoting *NUDT5* expression are associated with enhanced sensitivity to thiopurine treatment in patients (*49*).

REFERENCES AND NOTES

1. A. M. Pedley, V. Pareek, S. J. Benkovic, *Annu. Rev. Biochem.* **91**, 89–106 (2022).
2. D. H. Tran *et al.*, *Cell* **187**, 3602–3618.e20 (2024).
3. T. Dervieux *et al.*, *Blood* **100**, 1240–1247 (2002).
4. M. S. Hershfield, J. E. Seegmiller, *J. Biol. Chem.* **251**, 7348–7354 (1976).
5. F. F. Diehl *et al.*, *Nat. Cell Biol.* **24**, 1252–1264 (2022).
6. S. Balasubramaniam, J. A. Duley, J. Christodoulou, *J. Inherit. Metab. Dis.* **37**, 669–686 (2014).
7. S. Puusepp *et al.*, *Mol. Genet. Metab. Rep.* **25**, 100677 (2020).
8. Z. Wu *et al.*, *Cell Metab* **36**, 1504–1520.e1509 (2024).
9. S. An, R. Kumar, E. D. Sheets, S. J. Benkovic, *Science* **320**, 103–106 (2008).
10. V. Pareek, H. Tian, N. Winograd, S. J. Benkovic, *Science* **368**, 283–290 (2020).
11. H. Zhao *et al.*, *J. Biol. Chem.* **290**, 6705–6713 (2015).
12. M. C. Chou *et al.*, *Mol. Cell* **83**, 4123–4140.e12 (2023).
13. J. B. French *et al.*, *Science* **351**, 733–737 (2016).
14. C. Doigneaux *et al.*, *J. Biol. Chem.* **295**, 9551–9566 (2020).
15. J. G. Doench *et al.*, *Nat. Biotechnol.* **34**, 184–191 (2016).
16. B. D. G. Page *et al.*, *Nat. Commun.* **9**, 250 (2018).
17. M. Zha *et al.*, *J. Mol. Biol.* **379**, 568–578 (2008).
18. R. H. Wright *et al.*, *Science* **352**, 1221–1225 (2016).
19. F. Zhang, L. Fu, Y. Wang, *Mol. Cell. Proteomics* **12**, 3803–3811 (2013).
20. A. R. Mullen *et al.*, *Nature* **481**, 385–388 (2011).
21. A. R. Mullen *et al.*, *Cell Rep.* **7**, 1679–1690 (2014).
22. P. Pachnis *et al.*, *Sci. Adv.* **8**, eabn9550 (2022).
23. T. Yan, S. E. Berry, A. B. Desai, T. J. Kinsella, *Clin. Cancer Res.* **9**, 2327–2334 (2003).
24. B. F. Pan, J. A. Nelson, *Biochem. Pharmacol.* **40**, 1063–1069 (1990).
25. A. Nowosielska, M. G. Marinus, *DNA Repair* **7**, 48–56 (2008).
26. W. E. Glaab *et al.*, *Carcinogenesis* **19**, 1931–1937 (1998).
27. H. Zalkin, J. E. Dixon, *Prog. Nucleic Acid Res. Mol. Biol.* **42**, 259–287 (1992).
28. G. Weigel, A. Griesmacher, R. A. DeAbreu, E. Wolner, M. M. Mueller, *Thromb. Res.* **94**, 87–94 (1999).
29. E. L. Huttlin *et al.*, *Cell* **184**, 3022–3040.e28 (2021).
30. D. K. Schweppe, E. L. Huttlin, J. W. Harper, S. P. Gygi, *J. Proteome Res.* **17**, 722–726 (2018).
31. J. Zhang *et al.*, *Science* **390**, 6771 (2025).
32. J. Abramson *et al.*, *Nature* **630**, 493–500 (2024).
33. E. W. Holmes, J. B. Wyngaarden, W. N. Kelley, *J. Biol. Chem.* **248**, 6035–6040 (1973).

34. M. A. Becker, P. R. Smith, W. Taylor, R. Mustafi, R. L. Switzer, *J. Clin. Invest.* **96**, 2133–2141 (1995).
35. J. L. Smith, *Curr. Opin. Struct. Biol.* **8**, 686–694 (1998).
36. M. Takaine, R. Morita, Y. Yoshinari, T. Nishimura, *PLOS Biol.* **23**, e3003111 (2025).
37. V. D. Antle *et al.*, *J. Biol. Chem.* **271**, 8192–8195 (1996).
38. K. Schmiegelow, S. N. Nielsen, T. L. Frandsen, J. Nersting, *J. Pediatr. Hematol. Oncol.* **36**, 503–517 (2014).
39. D. R. Wong *et al.*, *J. Crohns Colitis* **11**, 175–184 (2017).
40. P. Sousa *et al.*, *J. Clin. Med.* **9**, 2216 (2020).
41. S. A. Coulthard *et al.*, *Mol. Pharmacol.* **62**, 102–109 (2002).
42. T. Moriyama *et al.*, *Blood* **130**, 1209–1212 (2017).
43. F. Yang *et al.*, *Oncotarget* **9**, 2268–2278 (2017).
44. G. Stocco *et al.*, *Clin. Pharmacol. Ther.* **85**, 164–172 (2009).
45. N. C. Valerie *et al.*, *Cancer Res.* **76**, 5501–5511 (2016).
46. A.-S. M. C. Marques *et al.*, Targeted Protein Degradation of NUDT5 Reveals an Unexpected Non-Enzymatic Role in 6-Thioguanine-Mediated Toxicity. bioRxiv 2025.2003.2016.643557 [Preprint] (2025); doi: 10.1101/2025.03.16.643557.
47. T. -A. Nguyen *et al.*, *Science* **390**, 1143–1150 (2025).
48. A. Strefeler *et al.*, *Nat. Metab.* **7**, 2221–2235 (2025).
49. M. Maillard *et al.*, *J. Clin. Invest.* **135**, e190443 (2025).
50. L. Cai, cailing20 / Wu_et_al_2025_proteomics, Github (2025); https://github.com/cailing20/Wu_et_al_2025_proteomics.

ACKNOWLEDGMENTS

We thank members of the DeBerardinis laboratory for helpful discussions; UT Southwestern Proteomics Core, CRI's Flow Cytometry Core, and Quantitative Light Microscopy Core, a shared resource for the Harold C. Simmons Cancer Center, for assistance with proteomics, cell sorting, and imaging experiments, respectively. We thank J. Garcia-Bermudez for providing the glovebox and G. Hoxhaj for providing reagents. We also acknowledge BIO250039 awarded by NSF ACCESS for providing computer resources. **Funding:** R.J.D. is supported by the NIH (R35CA220449, P50CA196516, and P50CA070907), Howard Hughes Medical Institute Investigator Program, Moody Foundation (Robert L. Moody, Sr. Faculty Scholar Award), and Eugene McDermott Endowment for the Study of Human Growth and Development. Z.W. is supported by the NIH (1K99GM154116). P.T.N. is supported by the NIH (K99GM151439). E.B.B. is supported by the NIH (1T32CA291654-01). L.C. is supported by the NIH (R01CA285336). J.Z. is supported by the NIH (5K99AI180984-02). Q.C. is supported by the NIH (1R35GM160468-01). R.J.D. and T.P.M. are supported by a CPRIT Core Facilities Support Award (RP240494). L.-M.Z. is supported by the NIH (R35GM138157). Y.Z. is supported by the NIH (P30CA142543, KL2TR003981, CTSA-PP-YR1-D-009) and ACS (IRG-21-1542-16). The Quantitative Light Microscopy Core is supported by the NIH (1P30CA142543-01). **Author contributions:** Z.W. and R.J.D. conceived the study. Z.W. and P.T.N. performed most of the experiments and data analyses, assisted by T.D., I.M.W., M.D.M., T.O., I.A., and E.B.B. V.S. generated most of the DNA plasmids. R.Y. conducted all the purinosome analyses. T.P.M. and F.C. developed the LC-MS methods. F.C., L.G.Z., R.W., J.S.P., and X.J. helped with the LC-MS experiments and data analyses. Z.L. and L-M.Z. conducted human PPAT purification. L.C. analyzed the proteomics data. J.Z. and Q.C. helped with the AlphaFold modeling. J.C., X.L., Z.S., W.C., and Y.Z. helped with DNA damage analyses and data interpretation. Z.W. and R.J.D. wrote the paper and all the other authors edited or commented on the paper. **Competing interests:** R.J.D. is an adviser for Vida Ventures, Faeth Therapeutics, Agios Pharmaceuticals, and a founder and adviser at Atavistik Bioscience. The remaining authors declare no competing interests. **Data and materials availability:** Cell lines and plasmids generated for this study are available under a materials transfer agreement. All data are available in the manuscript or supplementary materials. Source data are in table S3. Raw proteomics data have been deposited in MassIVE (accession number: MSV000097432). The codes used for the imaging data analyses in this paper are in data S1 and S2. The codes used for the proteomics analysis in this paper have been deposited in GitHub (*50*). **License information:** Copyright © 2023 the authors, some rights reserved; exclusive licensee American Association for the Advancement of Science. No claim to original US government works. https://www.science.org/about/science-licenses-journal-article-reuse. This article is subject to HHMI's Open Access to Publications policy. HHMI lab heads have previously granted a nonexclusive CC BY 4.0 license to the public and a sublicensable license to HHMI in their research articles. Pursuant to those licenses, the author-accepted manuscript (AAM) of this article can be made freely available under a CC BY 4.0 license immediately upon publication.

SUPPLEMENTARY MATERIALS

science.org/doi/10.1126/scienceadx9717
Materials and Methods; Figs. S1 to S14; Tables S1 to S3; References (*51–61*); MDAR Reproducibility Checklist; Movies S1 to S7; Data S1 and S2

Submitted 3 April 2025; accepted 7 October 2025; published online 6 November 2025

10.1126/science.adx9717

METABOLISM

A non-enzymatic role of Nudix hydrolase 5 in repressing purine de novo synthesis

Tuan-Anh Nguyen[1]†, Jung-Ming G. Lin[1]†, Anne-Sophie M. C. Marques[2,3]†, Maximilian Fottner[4], Ludwig G. Bauer[2,3], Andreas Reicher[1], Diana Daum[1], Lorenzo Scrofani[1], Yusi Liu[2,3], Carol Cheng[2,3], Luna D'Angelo L.d.D.[1], Juan Sanchez[1], Christoph Bueschl[1], Nara Marella[1], Pisanu Buphamalai[1,5], Florian Traversi[6], Maša Bereš[7], Herwig P. Moll[7], Marton Siklos[1], Jakob-Wendelin Genger[1], Gerald Hofstaetter[1], Ludovica Villanti[1], Monika Malik[1], Christoph Klimek[1], Kathrin Runggatscher[1], Bettina Guertl[1], Jesper S. Hansen[2,3], Sarah Dobner[1], Olga Babosova[1], Tina Becirovic[1], Laura P. M. H. de Rooij[1], Emilio Casanova[7,8], Anna Koren[1], D. Sean Froese[6], David S. Rosenblatt[9], Kristaps Klavins[1], Andreas Bergthaler[1,10], Jörg Menche[1,5], J. Thomas Hannich[1], Miriam Abele[1], Sara Sdelci[1,11], Kathrin Lang[4], Kilian V. M. Huber[2,3]*, Stefan Kubicek[1]*

Folate metabolism is intricately linked to purine de novo synthesis through the incorporation of folate-derived one-carbon units into the purine scaffold. By investigating chemical and genetic dependencies caused by mutations in methylenetetrahydrofolate dehydrogenase, cyclohydrolase, and formyltetrahydrofolate synthetase 1 (MTHFD1), we discovered a key role for Nudix hydrolase 5 (NUDT5) in regulating purine de novo synthesis. Genetic depletion and selective chemical degradation showed that a scaffolding role, rather than NUDT5 enzymatic activity, was causing this phenotype. NUDT5 interacted with phosphoribosyl pyrophosphate amidotransferase (PPAT), the rate-limiting enzyme of purine de novo synthesis, to repress the pathway in response to increased purine abundance. Through this mechanism, loss of NUDT5 mediates resistance to purine analogs in cancer treatment and prevents adenosine toxicity in MTHFD1 deficiency.

Folate metabolism is essential for providing one-carbon units for the biosynthesis of several metabolites, which include purines, thymidylate, and methionine (*1*). Consequently, impairment of folate metabolism through genetic mutations or dietary folate deficiency causes varied pathologies, including developmental defects and an increased risk of cancer (*2*–*6*). Therapeutically, the dependence of proliferating cells on this pathway is exploited by the use of antifolates such as methotrexate and pemetrexed in cancer therapy (*7*–*9*).

The folate pathway is compartmentalized between cytoplasm and mitochondria, with additional roles of selected enzymes in the nucleus (*10*, *11*). The usual direction of the folate catalytic cycle of mitochondrial formate production and cytosolic formate utilization can be reversed after mutation of key folate enzymes (*12*). Under these conditions, or after pharmacological inhibition of folate metabolism, destabilization of the folate scaffold might further contribute to the overall phenotype (*13*, *14*). Folate deficiency can also arise from disruption of downstream pathways by "trapping" of all cellular folates as certain species, e.g., as 5-methyltetrahydrofolate (5-MeTHF) in vitamin B12 deficiency (*15*, *16*) and as 10-formyltetrahydrofolate (10-CHO-THF) after pharmacological inhibition of MTHFD1 (*17*).

MTHFD1 is a trifunctional enzyme that catalyzes the cytoplasmic interconversion of 10-CHO-THF, methenyltetrahydrofolate (CH^+-THF), and methylenetetrahydrofolate (CH_2-THF) by its formyltetrahydrofolate synthetase (S) and its combined methylenetetrahydrofolate dehydrogenase and cyclohydrolase (DC) domains (Fig. 1A). Of the MTHFD1 reaction products, CH_2-THF provides one-carbon units for the synthesis of methionine and thymidylate, whereas 10-CHO-THF delivers two of the carbons to the purine scaffold generated in the de novo synthesis pathway. This process might be enhanced by direct interaction of MTHFD1 with the purinosome (*18*). Genetic depletion of MTHFD1 in yeast and human cells results in purine auxotrophy, presumably by preventing purine de novo synthesis (*19*–*24*). By contrast, in cells from patients with MTHFD1 deficiency, purine de novo synthesis is unaffected, but thymidylate and methionine biosynthesis are impaired as a result of point mutations in the DC domain of the enzyme (*25*). To date, no comprehensive studies of the metabolic, pharmacologic, and genetic dependencies caused by loss of distinct MTHFD1 enzymatic activities have been reported. To address this gap in our current understanding, we examined distinct features of MTHFD1 domain activities that control the balance between cellular adenosine dependency and toxicity. We found that the antiproliferative effect of adenosine and other purine analogs in this context was dependent on a scaffolding function of NUDT5, revealing a role of this NUDIX family member in de novo purine synthesis.

Inactivation of distinct MTHFD1 enzymatic activities causes opposing cellular responses to adenosine

We engineered wild-type (WT) human haploid HAP1 cells and derived clonal cell lines that either contained a deletion (knockout, KO) in the *MTHFD1* gene ($MTHFD1^{KO}$) (*11*) or were reconstituted with either the WT allele ($MTHFD1^{recon}$) or catalytically inactive point mutations (*24*, *26*) of the S ($MTHFD1^{K386E}$) (K386→E) or DC ($MTHFD1^{K56R}$) domains (Fig. 1A). We tested proliferation of these cell lines in medium supplemented with either standard serum or with dialyzed serum depleted of metabolites smaller than 10 kDa. $MTHFD1^{KO}$ and $MTHFD1^{K386E}$ cells were sensitive to serum dialysis, whereas the growth of WT, $MTHFD1^{recon}$, and $MTHFD1^{K56R}$ cells was unaffected in these conditions (Fig. 1B and fig. S1). To identify compounds that counteracted the detrimental effects of dialyzed serum on the growth of $MTHFD1^{KO}$ cells, we performed a chemical screen of more than 90,000 structurally diverse small molecules (fig. S1). We realized that mainly adenine-containing compounds, e.g., nicotinamide adenine dinucleotides NADH and NAD^+, flavin adenine dinucleotide (FAD), *S*-adenosylmethionine (SAM), adenosine monophosphate (AMP), or the AMP precursor hypoxanthine (Hyp)—but not other purine or folate analogs—rescued the growth of $MTHFD1^{KO}$ cells (fig. S1). Similarly, adenosine addition reestablished proliferation of S domain inactive $MTHFD1^{K386E}$ cells. However, the addition of adenosine (Ado) to $MTHFD1^{K56R}$ cells harboring the inactivating mutation in the DC domain had the opposite phenotype, because in that context addition of adenosine caused an antiproliferative response (Fig. 1B). These effects occurred in a concentration-dependent manner, and $MTHFD1^{K56R}$ cells became sensitized to adenosine at low micromolar concentrations (IC_{50} ~6 μM; Fig. 1C). Also, other purines, including

[1]CeMM Research Center for Molecular Medicine of the Austrian Academy of Sciences, Vienna, Austria. [2]Centre for Medicines Discovery, Nuffield Department of Medicine, Oxford, UK. [3]Target Discovery Institute, Nuffield Department of Medicine, Oxford, UK. [4]Laboratory for Organic Chemistry (LOC), Department of Chemistry and Applied Biosciences (D-CHAB), ETH Zurich, Zurich, Switzerland. [5]Department of Structural and Computational Biology, Max Perutz Labs, University of Vienna, Vienna, Austria. [6]Division of Metabolism and Children's Research Center, University Children's Hospital, University of Zurich, Zurich, Switzerland. [7]Institute of Pharmacology, Center of Physiology and Pharmacology & Comprehensive Cancer Center (CCC), Medical University of Vienna, Vienna, Austria. [8]Ludwig Boltzmann Institute for Hematology and Oncology, Medical University of Vienna, Vienna, Austria. [9]Department of Human Genetics, McGill University, Montreal, Canada. [10]Institute for Hygiene and Applied Immunology, Center of Pathophysiology, Infectiology and Immunology, Medical University of Vienna, Vienna, Austria. [11]Center for Genomic Regulation, Barcelona, Spain. ***Corresponding author. Email: kilian.huber@cmd.ox.ac.uk (K.V.M.H.); skubicek@cemm.oeaw.ac.at (S.K.)** †These authors contributed equally to this work.

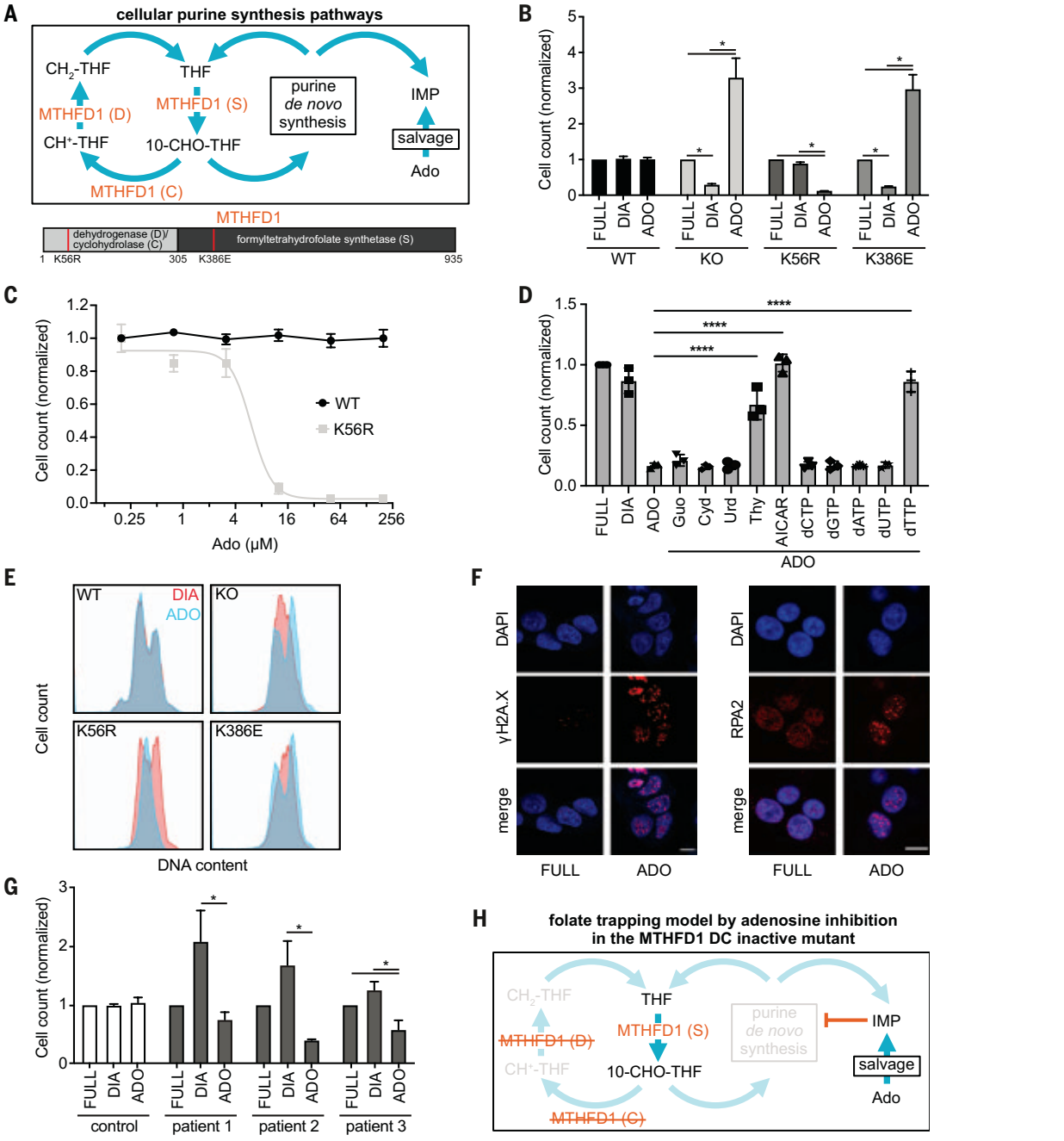


Fig. 1. MTHFD1 enzymatic functions influence adenosine dependency or toxicity. (**A**) Schematic overview of the folate cycle and cellular purine synthesis pathway. Corresponding folate intermediates are generated by the enzymatic functions of the MTHFD1 synthetase (S), cyclohydrolase (C), and dehydrogenase (D) domains. 10-CHO-THF is used for the synthesis of inosine monophosphate (IMP) through the purine de novo synthesis pathway. Alternatively, IMP can be synthesized through the salvage pathway in the presence of exogenous adenosine (Ado). The schematic domain structure of MTHFD1 is shown below with sites of K56R and K386E mutations that ablate the enzymatic reactions of the respective domain. (**B**) Normalized cell counts of WT, MTHFD1^{KO}, MTHFD1^{K386E}, and MTHFD1^{K56R} cells grown for 72 hours in media containing dialyzed serum (DIA) or dialyzed serum supplemented with 50 μM adenosine (ADO). Values are normalized to the respective clone grown in media containing full serum (FULL) ($n = 3$ biological replicates, mean ± SD, $^*P < 0.05$). (**C**) Normalized cell counts of WT and MTHFD1^{K56R} cells at indicated concentrations of adenosine. Cells were cultured in DIA supplemented with respective adenosine concentrations for 72 hours. ($n = 2$ biological replicates, mean ± SD). (**D**) Normalized cell counts of MTHFD1^{K56R} cells cultured at indicated media conditions and with supplemented nucleotides and precursors (50 μM) ($n = 3$ biological replicates, mean ± SD, $^{****}P < 0.0001$). Guo, guanosine; Cyd, cytidine; Urd, uridine; Thy, thymidine; AICAR, 5-aminoimidazole-4-carboxamide ribonucleotide; dCTP, deoxycytidine triphosphate; dGTP, deoxyguanosine triphosphate; dATP, deoxyadenosine triphosphate; dUTP, deoxyuridine triphosphate; dTTP, deoxythymidine triphosphate. (**E**) Representative cell cycle plots for WT and MTHFD1 mutant HAP1 cells in DIA and ADO conditions. (**F**) Representative images of γH2A.X and RPA2 staining of MTHFD1^{K56R} cells with adenosine supplementation (scale bar, 10 μm). (**G**) Growth assays of fibroblasts derived from MTHFD1 deficiency patients in FULL, DIA, and ADO ($n = 3$ biological replicates, mean ± SD, $^*P < 0.05$). (**H**) Schematic overview of the genetic folate trap model. In (B), (D), and (G), comparison of groups carried out by two-way analysis of variance (ANOVA). Single-letter abbreviations for the amino acid residues are as follows: K, lysine; R, arginine; E, glutamic acid.

inosine, hypoxanthine, and AMP, and to a lower extent guanine, guanosine, and guanosine monophosphate (GMP), but not pyrimidines, impaired cell viability (fig. S2A). Moreover, the combinatorial growth deficiencies were not specific to HAP1 cells because we could phenocopy these effects in other cancer cell lines when cells were grown in adenosine-containing medium together with the MTHFD1 DC domain inhibitor LY345899 (*26*) (fig. S2B). Supplementation of thymidine, deoxythymidine triphosphate (dTTP), or 5-aminoimidazole-4-carboxamide ribonucleotide (AICAR) largely reversed these toxic effects in MTHFD1^{K56R} cells (Fig. 1D).

The addition of adenosine caused strong cell cycle changes. In MTHFD1^{KO} and MTHFD1^{K386E} cells, adenosine alleviated the G1-S phase arrest caused by dialyzed serum conditions. By contrast, MTHFD1^{K56R} cells arrested in G1-S phase after adenosine addition (Fig. 1E and fig. S3A). Increases in foci formation for replication protein A2 (RPA2) and phosphorylated histone variant H2AX (γH2A.X) in these conditions (Fig. 1F and fig. S3B) indicated that replication stress and DNA damage caused this phenotype. These effects occurred at adenosine concentrations orders of magnitude lower than the millimolar concentrations normally needed to induce replication stress through nucleotide imbalance (*27*). Again, this phenotype was not specific to HAP1 cells because we observed similar DNA damage effects in fibroblasts from MTHFD1-deficient patients with mutations in the protein's DC domain (Fig. 1G and fig. S4).

Overall, by engineering a specific mutation that inactivates the DC domain of MTHFD1, we have established a genetic "folate trapping" model (*17*). Normally, 10-CHO-THF can be converted to tetrahydrofolic acid (THF) by either the folate cycle or by purine de novo synthesis (Fig. 1 and fig. S5A). However, concomitant inhibition of both pathways—i.e., inhibition of the folate cycle through MTHFD1 DC domain mutation (as also occurring in MTHFD1 deficiency patients), and repression of purine de novo synthesis by adenosine addition—results in the accumulation of cellular folates as 10-CHO-THF (Fig. 1H and fig. S5B). This presumably prevents regeneration of THF (fig. S5C) and thus maintenance of balanced folate and nucleotide abundances, leading to DNA damage and ultimately cell death. We expected that this phenotype might be rescued by genetic and chemical modulators of the folate and purine de novo synthesis pathways.

A genome-wide genetic screen identifies NUDT5 as a modulator of MTHFD1-mediated adenosine response

We performed a genome-wide genetic loss-of-function screen to probe genetic dependencies of the folate-trap conditions. For this, we transduced MTHFD1^{K56R} cells with a CRISPR-Cas9 knockout library targeting 19,114 human genes with an average of four single-guide RNAs (sgRNAs) per gene (*28*). After selection and growth with adenosine (which is toxic in this context) for 2 weeks, we analyzed sgRNA abundance as a proxy for beneficial growth effects after genetic depletion of the respective target gene (Fig. 2A).

Individual depletion of each of three genes rescued adenosine-mediated toxicity: *MTHFD1*, *HPRT1* (*hypoxanthine phosphoribosyl transferase 1*), and *NUDT5* (Fig. 2B). MTHFD1 served as a positive control, as a shift from the MTHFD1^{K56R} mutation to the full knockout was expected to correlate with the transition from adenosine toxicity to adenosine dependency (Figs. 1B and 2C). HPRT1 is a key enzyme in the purine salvage pathway (fig. S5A) (*29*, *30*). We validated the absence of purine-mediated toxicities in MTHFD1^{K56R}HPRT1^{KO} double-mutant cells and showed that adenosine did not cause DNA damage or cell cycle changes in these cells (Fig. 2, D to F, and fig. S6, A and B).

For *NUDT5*, we confirmed that its depletion in the MTHFD1^{K56R} background (MTHFD1^{K56R}NUDT5^{KO}) reestablished cellular proliferation in purine-rich medium and prevented accumulation of aberrant cell cycle and DNA damage signals (Fig. 2, D to F, and fig. S6, A and B). NUDT5 is a hydrolase that functions in the catabolism of adenosine diphosphate (ADP)–ribose and the synthesis of nuclear adenosine triphosphate (ATP) (*31*–*35*). However, to date, a direct association with purine sensing or folate metabolism has not been established (fig. S6C).

NUDT5 is required for the repression of de novo purine biosynthesis in response to adenosine

To assess whether depletion of HPRT1 or NUDT5 affected adenosine uptake or utilization, we performed isotope-tracing metabolomics. We treated WT cells with isotope-labeled adenosine containing five

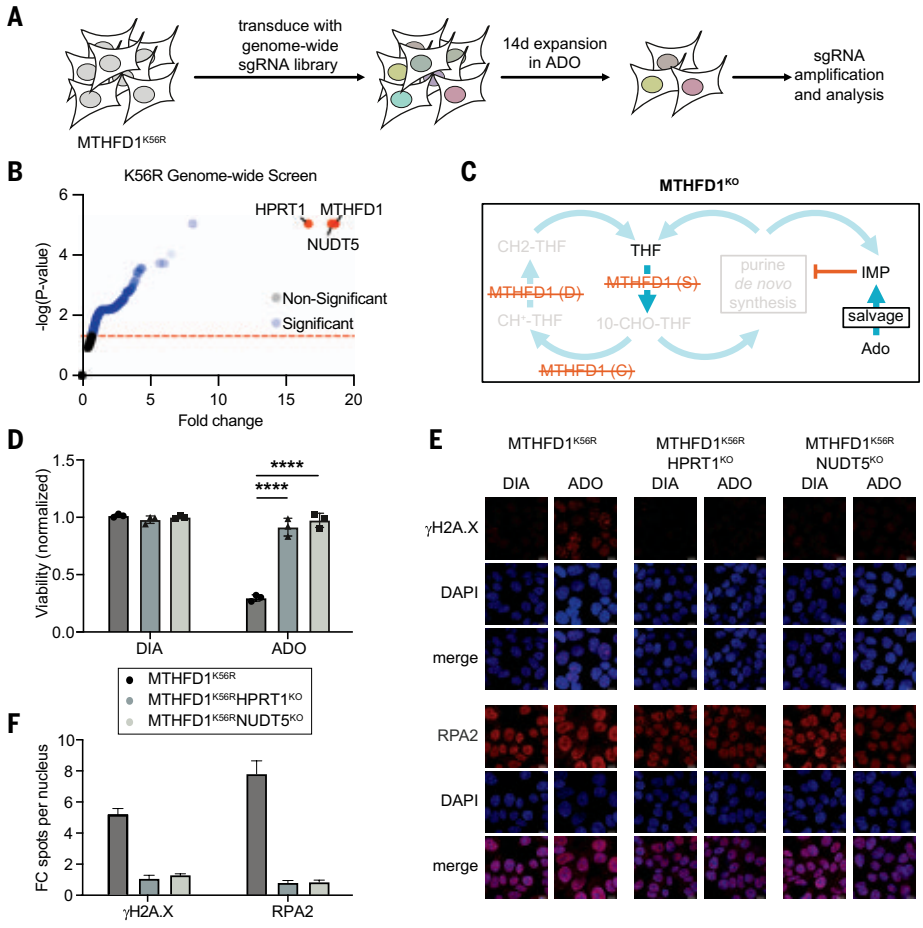


Fig. 2. A genome-wide knockout screen identifies folate trap modulators. (**A**) Schematic overview of the genetic screening strategy. (**B**) Results of the genome-wide KO screen as schematically shown in (A). Genes are ranked by fold change (FC) with the most significantly enriched hits highlighted in red: *HPRT1*, *NUDT5*, and *MTHFD1*. (**C**) Model of folate trap rescue when MTHFD1 is depleted in MTHFD1^{K56R} cells. (**D**) Normalized viability of MTHFD1^{K56R}HPRT1^{KO} and MTHFD1^{K56R}NUDT5^{KO} cells cultured in DIA or ADO for 72 hours. (n = 3, mean ± SD, two-way ANOVA, ****P < 0.0001). (**E**) Representative images of γH2A.X and RPA2 staining of MTHFD1^{K56R}, MTHFD1^{K56R}HPRT1^{KO}, and MTHFD1^{K56R}NUDT5^{KO} cells after being cultured in DIA or ADO for 72 hours. (scale bar, 10 μm). (**F**) Quantification of spots per nucleus from (E) (spots per nucleus values are mean ± SEM from six imaged wells).

heavy ^{15}N atoms. The ^{15}N label was incorporated in a wide set of nucleotides, including inosine monophosphate (IMP), AMP, and GMP (Fig. 3A). By contrast, labeling was almost absent in HPRT1^{KO} cells, corroborating the enzyme's role in nucleotide salvage. The importance of HPRT1 for adenosine salvage in our cell model was further highlighted by AMP containing four heavy nitrogens being the predominant cellular species in WT cells, indicating adenosine processing mainly through inosine and hypoxanthine in HAP1 cells. By contrast, direct conversion of adenosine through adenine phosphoribosyltransferase (APRT) or adenosine kinase (ADK) would have yielded AMP containing five heavy nitrogens. These data indicate that the functional use of exogenous adenosine in intracellular biochemical pathways is required to trigger the folate trap, which is consistent with the model that cellular modulation of the purine salvage pathway may repress purine de novo synthesis activity (figs. S5 and S6).

In contrast to HPRT1^{KO} cells, NUDT5^{KO} cells showed ^{15}N incorporation into IMP, AMP, and GMP in amounts comparable to those in WT cells, indicating that nucleotide salvage was unaffected by NUDT5 (Fig. 3A). To assess whether NUDT5 impacted purine de novo synthesis, we expanded the isotope-tracing setup to concomitantly monitor whether selected metabolites originated from cellular purine salvage or de novo synthesis activity, respectively (Fig. 3B). Specifically, we treated WT, NUDT5^{KO}, MTHFD1^{K56R}, and MTHFD1^{K56R}NUDT5^{KO} cells with isotope-labeled formate (+1 ^{13}C +1 D) that is incorporated into de novo synthesized purines via 10-CHO-THF produced by the MTHFD1 synthetase domain. To assess incorporation of externally added adenosine into various metabolites, we additionally treated cells with isotope-labeled adenosine (+5 ^{15}N). Metabolome analysis by high-resolution mass spectrometry enabled us to clearly discriminate metabolites derived from de novo synthesis (containing heavy carbon atoms) from those derived from adenosine salvage (containing heavy nitrogens).

For all measured metabolites (IMP, AMP, and GMP), adenosine addition resulted in repression of purine de novo synthesis in both WT and MTHFD1^{K56R} cells (Fig. 3C). Depletion of NUDT5 prevented this repression, both in WT and in MTHFD1^{K56R} cells, and resulted in an increased proportion of de novo–derived AMP, GMP, and IMP (Fig. 3C). The same effect was also observable in nucleotides derived from hydrolyzed DNA, in which the lower turnover of DNA resulted in a higher fraction of unlabeled nucleotides (Fig. 3D). The fractional abundances of key de novo synthesis–derived isotopologs (Fig. 3E) indicate that loss of NUDT5—irrespective of MTHFD1 mutational status—enabled cellular purine production through the de novo pathway even when exogenous purines were abundant.

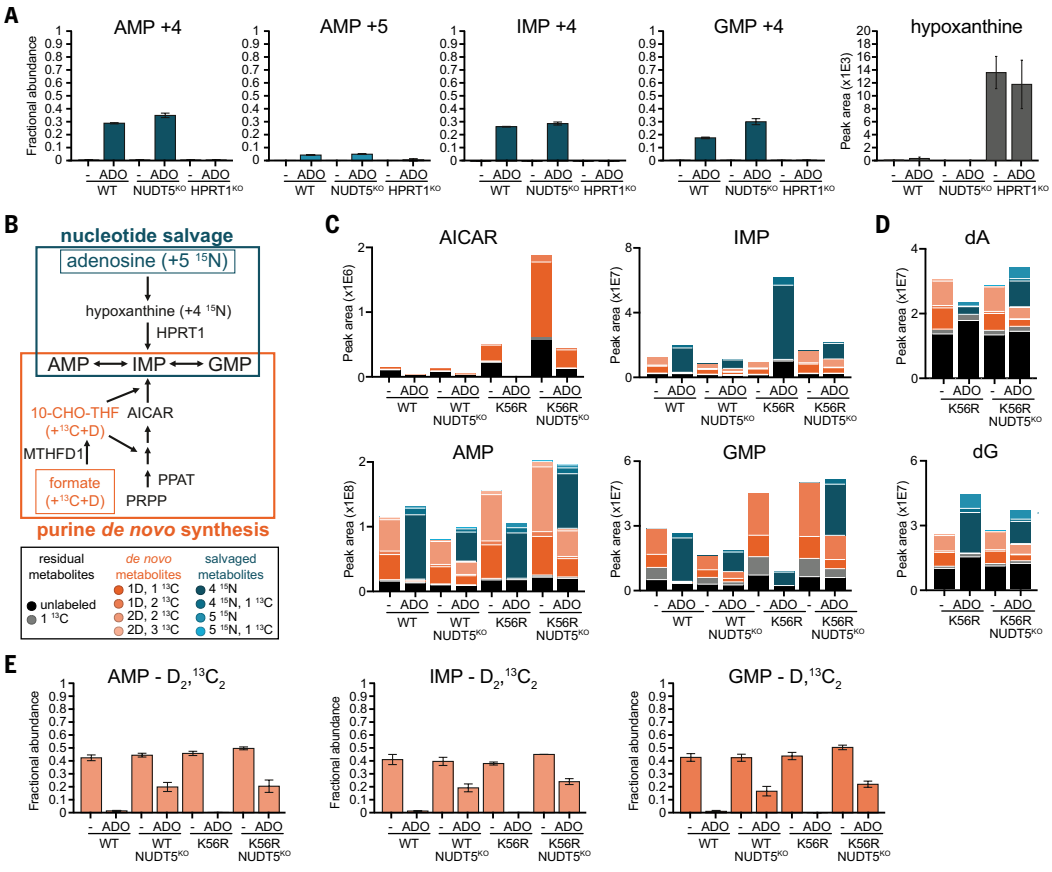


Fig. 3. Loss of NUDT5 causes increased de novo purine synthesis in the presence of salvageable adenosine. (**A**) Quantification of fractional abundance of heavy isotope–labeled metabolites in WT, NUDT5^{KO}, and HPRT1^{KO} cells supplemented with 50 μM $^{15}N_5$-labeled adenosine (ADO) for 24 hours ($n = 2$, mean ± SD). (**B**) Schematic overview of the purine de novo synthesis and salvage pathways indicating labeled precursors used in isotope-tracing experiments. WT, NUDT5^{KO}, MTHFD1^{K56R}, and MTHFD1^{K56R}NUDT5^{KO} cells were grown in DIA with 1 mM labeled formate or with 1 mM labeled formate and 50 μM labeled adenosine (ADO) for 24 hours. (**C**) Peak areas of mass spectrometry signals for metabolites AICAR, IMP, AMP, and GMP, labeled by detected isotope indicating metabolites derived from purine de novo synthesis in shades of red and those derived from salvaged adenosine in shades of blue. (**D**) Peak areas corresponding to deoxyadenosine (dA) and deoxyguanosine (dG) obtained from hydrolyzed DNA, colored as in (C). (**E**) Quantification of fractional abundances of most abundant purine de novo synthesis–derived isotopologs from (C) (mean ± SD).

A NUDT5 scaffolding function rather than enzymatic activity is essential for modulating adenosine responses

Given that NUDT5 can be broadly linked to purine metabolism through its ADP-ribose–converting activity (*31*, *33*), we investigated whether its enzymatic activity contributes to the repression of de novo purine synthesis. We first performed viability assays with the chemical NUDT5 inhibitor TH5427 (*36*) in MTHFD1^{K56R} cells. Even at doses more than 1000 times higher than its biochemical IC_{50} of 29 nM, TH5427 treatment did not rescue the viability of MTHFD1^{K56R} cells when cultured in high-adenosine–containing medium (Fig. 4A). To confirm these results with genetic NUDT5 inactivation, we performed proliferation assays in MTHFD1^{K56R}NUDT5^{KO} cells reconstituted with either NUDT5^{WT} or the catalytically inactive NUDT5^{E112Q} variant (*35*). Both protein variants resensitized MTHFD1^{K56R}NUDT5^{KO} cells to adenosine (Fig. 4A), corroborating our findings with the pharmacological NUDT5 inhibitor. Thus, the enzymatic function of NUDT5 appears to be dispensable for adenosine-mediated toxicity.

Because the genetic depletion of the entire NUDT5 protein rescued the toxic phenotype, the physical presence of its protein scaffold rather

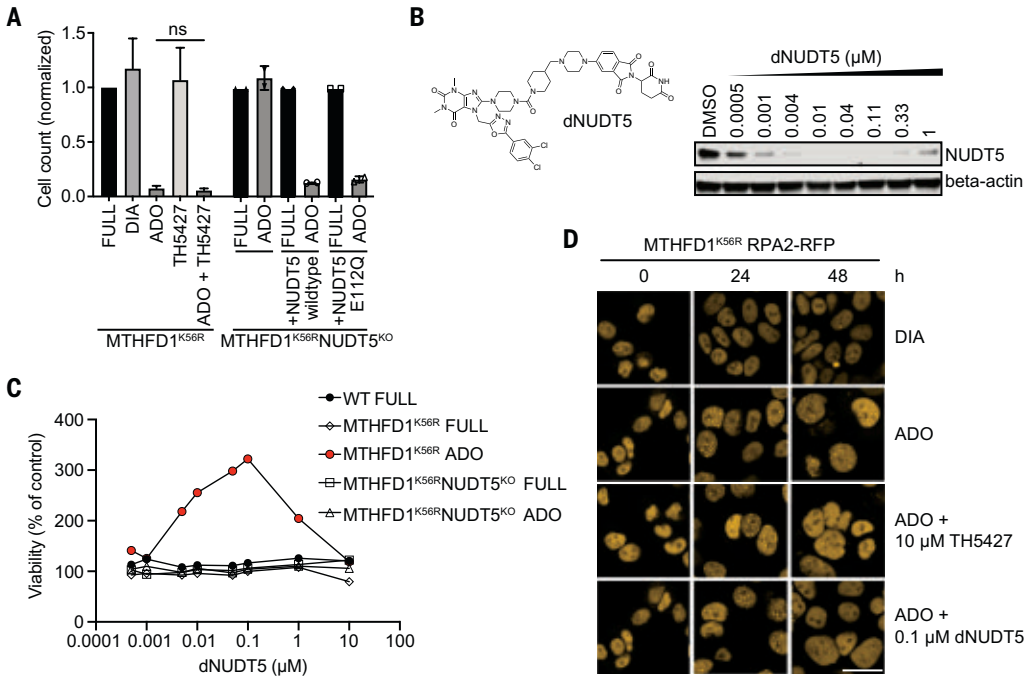


Fig. 4. Knockout or chemical degradation, but not enzymatic inhibition, of NUDT5 prevents adenosine-mediated toxicity. (**A**) Normalized cell counts of MTHFD1^{K56R} cells treated for 72 hours in FULL, ADO, and 10 μM NUDT5 inhibitor TH5427 alone and in combination ($n = 3$ biological replicates, mean ± SD, two-way ANOVA, ns: not significant) and MTHFD1^{K56R}, MTHFD1^{K56R}NUDT5^{KO}, and MTHFD1^{K56R}NUDT5^{KO} cells reconstituted with NUDT5^{wt} or NUDT5^{E112Q} (catalytically inactive) cultured in FULL or ADO ($n = 2$ biological replicates, mean ± SD). Q, single-letter abbreviation for amino acid glutamine. (**B**) Chemical structure of the NUDT5-targeting PROTAC dNUDT5. Representative Western blot of dose-dependent dNUDT5 effects on NUDT5 protein levels after 20 hours treatment in WT cells. (**C**) Dose-dependent effects of dNUDT5 on the growth of WT and MTHFD1^{K56R} cells cultured in FULL or DIA for 72 hours. (**D**) Representative images of RPA2-foci formation of MTHFD1^{K56R} RPA2-RFP (intron-tagged) cells at indicated medium conditions and times (RFP channel; scale bar, 25 μm).

than its enzymatic activity might have dictated the adenosine-mediated toxicity. To dynamically probe a potential scaffolding role, we developed dNUDT5, a proteolysis-targeting chimera (PROTAC) that induces targeted degradation of NUDT5 (*37*). We confirmed that dNUDT5 induced selective NUDT5 degradation in a dose-dependent manner with a maximum degradation at 100 nM (Fig. 4B). We treated both WT and MTHFD1^{K56R} cells with dNUDT5 and performed viability assays in the folate trap conditions. The addition of dNUDT5 did not affect the viability of WT cells, but it prevented adenosine toxicity (Fig. 4C) and accumulation of DNA damage signals (Fig. 4D) in MTHFD1^{K56R} cells. We observed a dNUDT5 dose-response pattern that perfectly matched that of NUDT5 degradation. The maximum rescue of cell viability occurred at 100 nM, the same concentration that also caused maximum degradation (Fig. 4C). Addition of dNUDT5 also mitigated the toxic effects of adenosine addition in the context of patient-derived MTHFD1-deficient fibroblasts (fig. S7A). Thus, we could phenocopy the genetic ablation of NUDT5 with an acute chemical degrader rather than an inhibitor of its enzymatic activity. The combined chemical and genetic evidence indicates that the NUDT5 scaffold rather than the protein's enzymatic activity is required to repress purine de novo synthesis when adenosine is abundant.

The direct interaction of NUDT5 with PPAT represses purine de novo synthesis

To mechanistically explore how the noncatalytic function of NUDT5 represses the purine de novo synthesis pathway, we set out to identify interaction partners of NUDT5. We performed interaction proteomics experiments (*38*) with NUDT5 that was N-terminally tagged with a blue fluorescent protein (BFP) and observed enrichment of three interactors: pyrroline-5-carboxylate reductase 1 and 2 (PYCR1 and 2) and phosphoribosyl pyrophosphate amidotransferase (PPAT) (Fig. 5A). The same factors were also enriched in NUDT5 proximity labeling experiments, in chemical proteomics with a NUDT5 affinity probe (fig. S8, A and B), and in unbiased large-scale protein-protein interaction datasets from other cell lines (*39*). Of these interactors, we focused our attention on PPAT because it catalyzes the rate-limiting step of the purine de novo synthesis pathway. We confirmed that the interaction was reciprocal, because immunoprecipitation of endogenous PPAT resulted in enrichment of NUDT5, irrespective of the cellular background and mutational status of MTHFD1 (Fig. 5B and fig. S8C). Adenosine addition increased the strength of the NUDT5-PPAT interaction (Fig. 5C), and adenosine toxicity in the MTHFD1^{K56R} context was prevented by overexpression of PPAT (Fig. 5D). This finding underscores the relevance of PPAT repression for the phenotype and highlights the importance of PPAT to NUDT5 stoichiometric ratios for active purine de novo synthesis.

To gain insights into the molecular details of the NUDT5-PPAT interaction, we performed structural analyses with AlphaFold3 (*40*). These results predict a "sandwich" binding mode in which two NUDT5 dimers cross-interact with a PPAT tetramer, thereby potentially locking it in an inactive conformation (Fig. 5E). Gel electrophoresis after protein cross-linking (fig. S9A) and native protein gel electrophoresis (fig. S9B) supported a role of NUDT5 in regulating PPAT oligomerization, a process associated with reduced enzymatic activity (*41*, *42*).

From the AlphaFold model, we identified NUDT5$^{70–75}$ as the putative PPAT interaction loop, within which NUDT5^{Y74} points toward the PPAT interface and might function as a key residue critical for the interaction (Fig. 5E). We confirmed that mutation of residue Y74 did not affect NUDT5 catalytic activity (fig. S9C). To test the functional importance of these residues, we systematically reconstituted MTHFD1^{K56R}NUDT5^{KO} cells with mCherry-P2A-NUDT5 constructs that result in the expression of NUDT5 carrying selected point mutations and an mCherry reporter protein with a self-cleaving P2A sequence. We then performed comparative fluorescent competition assays under folate trap and control conditions (Fig. 5F and fig. S9D).

Similarly to the reintroduction of NUDT5^{WT}, inactivating the enzymatic activity of NUDT5 either by abolishing recognition of the adenosine moiety (W28A and W28A/W46A) or catalysis (E112Q) (*35*) did not rescue adenosine toxicity (Fig. 5F). These data corroborate our previous findings that the NUDT5 scaffold, rather than its enzymatic activity, is the key regulator of the phenotype. Also, altering the NUDT5 post-translational modification and dimerization states (*31*) in NUDT5^{T45A} and NUDT5^{T45D} mutants, as well as introducing a NUDT5^{Y74F} mutation, did not rescue adenosine toxicity (Fig. 5F and fig. S9, D and E). However, MTHFD1^{K56R} cells reconstituted with the NUDT5^{Y74E} variant were desensitized to the toxic adenosine conditions and behaved like NUDT5^{KO} cells (Fig. 5F and fig. S9, D and E). Notably, in contrast to NUDT5^{WT}

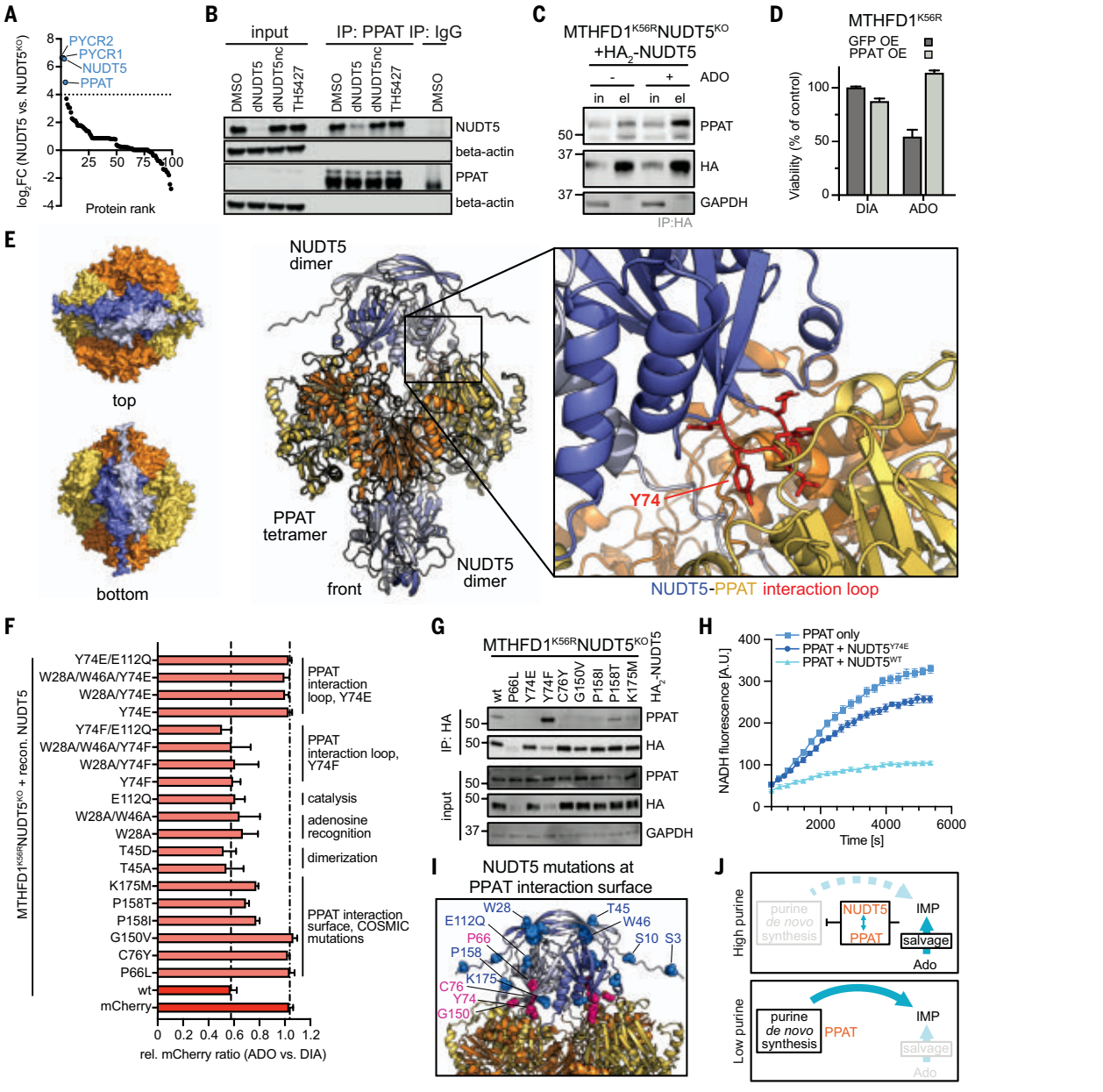


Fig. 5. Adenosine-mediated toxicity is mediated by the interaction of NUDT5 with PPAT. (**A**) Results of BFP pulldown in MTHFD1^{K56R}NUDT5^{KO} cells reconstituted with BFP-NUDT5. Enriched proteins from BFP-NUDT5 pulldown were normalized to NUDT5^{KO} control and ranked according to log_2FC. Hits with log_2FC >4 are highlighted in blue. (**B**) Immunoprecipitation of endogenous PPAT after treatment of WT cells with 100 nM dNUDT5, dNUDT5nc (*37*), or TH5427 for 20 hours. (**C**) Hemagglutinin-tag (HA) pulldown of MTHFD1^{K56R}NUDT5^{KO} cells transfected with HA_2-NUDT5^{wt} (representative blot from two independent experiments). Cells were cultured in DIA or ADO for 3 hours (in, input; el, elution). (**D**) CellTiterGlo viability assay of MTHFD1^{K56R} cells that were transduced at a high multiplicity of infection (MOI) with lenti-EF1alpha-EGFP or lenti-EF1alpha-PPAT and treated for 2 days in ADO ($n = 2$, mean ± SD) (EGFP, enhanced green fluorescent protein). (**E**) AlphaFold3 model of the NUDT5-PPAT complex with the interaction site depicted in detail. (**F**) Results of fluorescence competition assay to test the effects of NUDT5 mutations on adenosine-mediated toxicity in MTHFD1^{K56R} cells. Cells were cultured in DIA (control) or ADO for 72 hours. The population of mCherry-expressing cells in ADO was normalized to cells in DIA. Dashed lines indicate NUDT5^{wt} and mCherry control values (values are mean ± SEM from two independent experiments). (**G**) Pulldown of MTHFD1^{K56R}NUDT5^{KO} cells transfected with indicated HA_2-NUDT5 variants (representative blot from two independent experiments). (**H**) Results of PPAT activity assay together with NUDT5^{wt} or NUDT5^{Y74E} ($n = 3$, mean ± SEM; values are normalized to baseline control). (**I**) Depiction of the AlphaFold3 NUDT5-PPAT interaction surface, highlighting NUDT5 amino acids that maintain PPAT binding when mutated (blue) or that result in lost PPAT binding capacity when mutated (magenta). Single-letter abbreviations for the amino acid residues are as follows: A, alanine; C, cysteine; D, aspartic acid; F, phenylalanine; G, glycine; I, isoleucine; L, leucine; M, methionine; P, proline; T, threonine, V, valine; W, tryptophan; Y, tyrosine. (**J**) Proposed model of the NUDT5-PPAT–dependent purine de novo synthesis pathway regulation at high and low purine conditions.

and NUDT5^{Y74F}, this mutation resulted in loss of the interaction with PPAT, indicating that the rescue of adenosine-mediated toxicity may act through loss of PPAT binding (Fig. 5G and fig. S9, F and G). In biochemical assays with recombinant proteins, addition of NUDT5^{WT} impaired PPAT activity (Fig. 5H), whereas addition of NUDT5^{Y74E} caused only minor effects in PPAT activity. To analyze whether naturally occurring NUDT5 mutations exist that impair PPAT binding, we queried the COSMIC database (*43*). We selected reported NUDT5 patient mutations surrounding the PPAT interaction loop and tested their influence on PPAT binding (Fig. 5I). Conducting assays analogous to the ones

described above, we observed loss of binding for all those mutations that are either directly facing toward the PPAT interface (C76Y and G150V) or had a destabilizing effect on NUDT5 (P66L), whereas the remaining mutations (P158I, P158T, and K175M) still retained some residual PPAT binding (Fig. 5, G and I). The binding strength correlated with the degree of rescue of adenosine-mediated toxicity in MTHFD1^{K56R} cells (Fig. 5F and fig. S9E).

The NUDT5-PPAT interaction controls sensitivity to purine analog cancer drugs

Antimetabolites such as purine analogs inhibit key metabolic pathways and thus are widely used in cancer treatment (*44*). Genetic depletion of HPRT1 and NUDT5 has previously been reported to confer resistance toward the clinically approved anticancer drug 6-thioguanine (6-TG) (*28*). To test whether this resistance also occurred in vivo, we established a mouse xenograft model and observed that NUDT5 depletion prevented the growth inhibitory effects of 6-TG on A549 lung carcinoma cells (fig. S10).

Testing a wide panel of nucleotide analogs, in addition to 6-TG, we found that NUDT5^{KO} cells were also resistant to various other purine analogs, including 6-thioguanosine, 6-thio-2'-deoxyguanosine, 6-mercaptopurine, fludarabine, and cladribine (Fig. 6A). Loss of HPRT1 may prevent the conversion of 6-TG to toxic downstream analogs through the purine salvage pathway, and likewise, rescue of toxicity by NUDT5^{KO} has been attributed to the loss of its enzymatic function and ribose-5-phosphate synthesis, which is an important building block for purine synthesis (*28*). However, we found that, analogous to adenosine toxicity in the folate trap condition, 6-TG toxicity was similarly dependent on the presence of the NUDT5 scaffold rather than its enzymatic activity. Indeed, NUDT5^{Y74E} cells showed comparable resistance patterns to NUDT5^{KO} cells (Fig. 6B) (*37*). Also, HPRT1^{KO} cells exhibited nearly identical resistance patterns, with the notable exception of cladribine and fludarabine, to which HPRT1^{KO} did not confer resistance (fig. S11A).

We validated these differences in drug responses in dose response experiments (Fig. 6, C to E, and fig. S11, B and C). The COSMIC-derived NUDT5 cancer mutations yielded 6-TG resistance patterns (Fig. 6E), which correlated with the extent of PPAT binding (Fig. 5G). Confirming the PPAT dependence of these effects, PPAT overexpression also conferred resistance to 6-TG (Fig. 6F). We extended our studies to other cell line models (Fig. 6, F and G, and fig. S11, B and C). Although some compounds showed context-specific effects, the NUDT5 dependence of thiopurine response was conserved in all models tested (Fig. 6, A to G, and fig. S11, B and C).

Discussion

By initially characterizing the pharmacological and genetic dependencies caused by MTHFD1 mutations, we established that MTHFD1^{K56R} cells constitute a genetic folate trap model in which subphysiological concentrations of adenosine cause toxicity. This model allowed us to systematically identify modulators of the purine de novo synthesis pathways, leading to the discovery of a regulatory role for the NUDIX hydrolase NUDT5 in this context.

We found that a scaffolding rather than an enzymatic role of NUDT5 was essential for repressing purine de novo synthesis. Proteomic profiling revealed that the regulation of this pathway occurred by a direct NUDT5-PPAT interaction, with AlphaFold modeling predicting a tight interaction between two NUDT5 dimers and one PPAT tetramer. Our attempts to experimentally obtain a costructure of these interacting proteins have been unsuccessful. So far, no structure for human PPAT has been reported, and oxidation sensitivity of PPAT as an iron-sulfur cluster protein (*45*) may contribute to the challenges in structurally resolving the complex. To validate the AlphaFold model, we therefore used mutagenesis studies and discovered that single-point mutations in the predicted interaction surface were sufficient to prevent NUDT5 binding to PPAT.

We and others (*46*) observed experimentally that NUDT5 stabilizes PPAT oligomers. That stabilization of such higher-order complexes

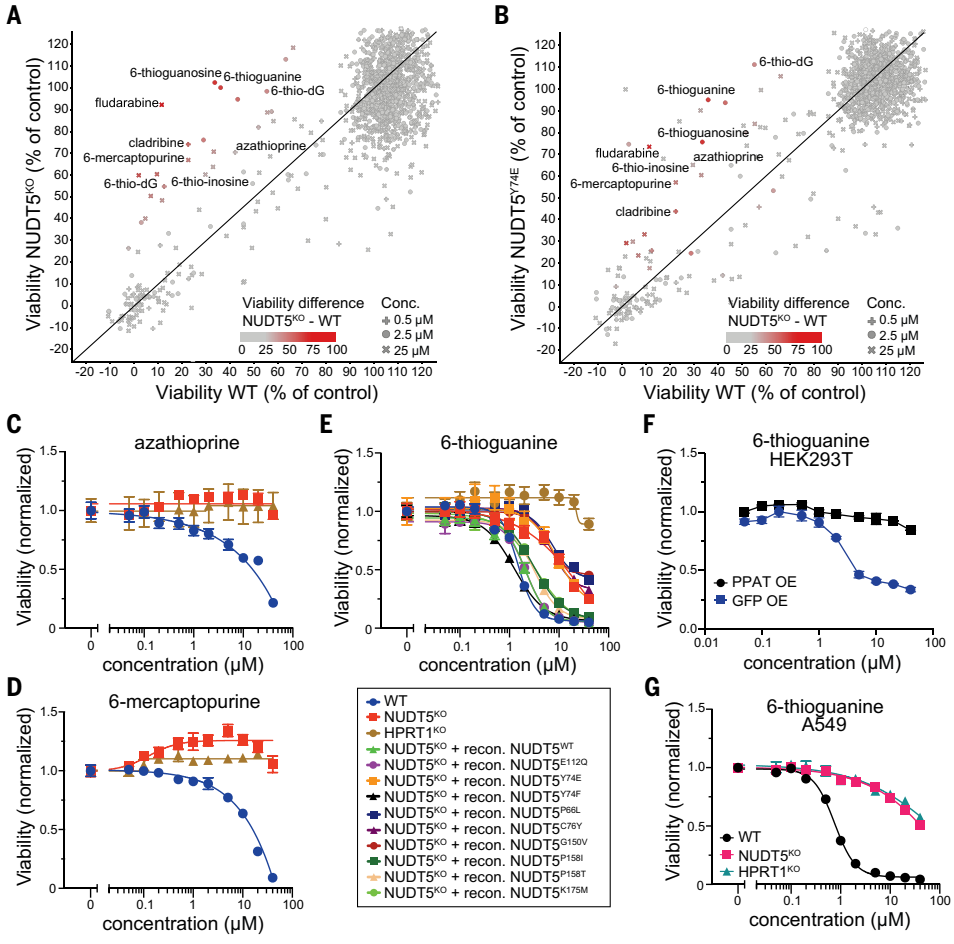


Fig. 6. NUDT5-PPAT interaction controls sensitivity to purine analog cancer drugs. (**A**) Profiling of 422 nucleotide analogs at three concentrations (25, 2.5, and 0.5 µM) for differential viability effects after 72 hours treatment of WT and NUDT5^{KO} cells. (**B**) Same as shown in (A) but comparing WT and NUDT5^{Y74E} cells. (**C** and **D**) Dose-response curves in WT, NUDT5^{KO}, and HPRT1^{KO} cells treated for 72 hours with azathioprine (C) and 6-mercaptopurine (D). (**E**) Dose-response curves of WT, NUDT5^{KO}, HPRT1^{KO}, and NUDT5^{KO} cells reconstituted with different mutant NUDT5 versions to 72 hours 6-thioguanine treatment. (**F**) Dose-response curves of HEK293T cells transiently transfected with overexpression (OE) constructs for green fluorescent protein (GFP) or PPAT treated for 48 hours with 6-thioguanine. (**G**) 6-Thioguanine dose response in parental, NUDT5^{KO}, and HPRT1^{KO} A549 cells. In (C) to (E), and (G), $n = 3$; in (F), $n = 2$, mean ± SEM; values are normalized to control condition.

presumably inhibits PPAT enzymatic function is consistent with reports that found reduced catalytic turnover in PPAT multimers (*41*, *42*). Indeed, we observed that WT NUDT5, but not a PPAT-binding deficient mutant, inhibited PPAT activity in a biochemical assay. In addition to direct PPAT inhibition, NUDT5-containing oligomers may also prevent channeling of product to the next enzyme, phosphoribosylglycinamide synthetase (GART), in purine de novo synthesis or interfere with purinosome formation. Accordingly, NUDT5 may be required for adenosine-mediated purinosome disassembly (*47*). The NUDT5-PPAT interaction appears to be controlled by cellular metabolites, and high-millimolar concentrations of PRPP may disrupt the interaction (*46*). Availability of salvageable adenosine increased the binding of NUDT5 to PPAT. NUDT5^{Y74E}, but not NUDT5^{Y74F}, abolished PPAT binding, indicating that the regulatory switch might occur through allosteric rearrangements or posttranslational modification of this residue (*48*).

Our findings led us to reevaluate the current model of de novo purine synthesis regulation. PPAT is proposed to be regulated through feedback inhibition of AMP and GMP at high-micromolar to -millimolar concentrations (*42*). However, in our reporter assay conditions, MTHFD1^{K56R} cells were already sensitized to adenosine concentrations in the low-micromolar range, indicating that the cellular regulation of purine de novo biosynthesis is several orders of magnitude more sensitive than what biochemical data showed for PPAT alone (Fig. 5J).

Our findings may have translational applications. Consistent with the presence of MTHFD1 CD domain mutations, we found adenosine to exert toxicity in cells from MTHFD1 deficiency patients. Such adenosine-dependent effects may contribute to the observed immunodeficiencies. In cancer, NUDT5 modulates the toxicity of the approved drug 6-TG (*28*, *49*). We found that the rescue mechanism extended to other purine analogs and occurred through loss of PPAT binding rather than loss of the catalytic activity of NUDT5 itself. Thus, modulation of purine de novo synthesis may influence the efficiency of purine analogs in anticancer therapy. This may have clinical implications because drug resistance may evolve through loss of HPRT1 enzymatic function, emerging PPAT binding–deficient NUDT5 mutations, or both.

REFERENCES AND NOTES

1. G. S. Ducker, J. D. Rabinowitz, *Cell Metab.* **25**, 27–42 (2017).
2. P. Burda *et al.*, *J. Inherit. Metab. Dis.* **38**, 863–872 (2015).
3. H. Fu *et al.*, *Dig. Dis. Sci.* **66**, 2368–2379 (2021).
4. A. J. MacFarlane *et al.*, *J. Biol. Chem.* **286**, 44015–44022 (2011).
5. R. Pieroth, S. Paver, S. Day, C. Lammersfeld, *Curr. Nutr. Rep.* **7**, 70–84 (2018).
6. P. J. Stover, *J. Nutr.* **139**, 2402–2405 (2009).
7. N. Gonen, Y. G. Assaraf, *Drug Resist. Updat.* **15**, 183–210 (2012).
8. G. J. Peters, J. H. Hooijberg, G. J. L. Kaspers, G. Jansen, *Trends Food Sci. Technol.* **16**, 289–297 (2005).
9. Y. Lee, K. H. Vousden, M. Hennequart, *Nat. Cancer* **5**, 701–715 (2024).
10. M. S. Field, E. Kamynina, J. Chon, P. J. Stover, *Annu. Rev. Nutr.* **38**, 219–243 (2018).
11. S. Sdelci *et al.*, *Nat. Genet.* **51**, 990–998 (2019).
12. G. S. Ducker *et al.*, *Cell Metab.* **24**, 640–641 (2016).
13. G. Burgos-Barragan *et al.*, *Nature* **548**, 549–554 (2017).
14. Y. Zheng *et al.*, *Cell* **175**, 1546–1560.e17 (2018).
15. B. Shane, E. L. Stokstad, *Annu. Rev. Nutr.* **5**, 115–141 (1985).
16. V. Herbert, R. Zalusky, *J. Clin. Invest.* **41**, 1263–1276 (1962).
17. A. C. Green *et al.*, *Nat. Metab.* **5**, 642–659 (2023).
18. J. He, L. N. Zou, V. Pareek, S. J. Benkovic, *J. Biol. Chem.* **298**, 101853 (2022).
19. C. Staben, J. C. Rabinowitz, *J. Biol. Chem.* **261**, 4629–4637 (1986).
20. J. M. Song, J. C. Rabinowitz, *Proc. Natl. Acad. Sci. U.S.A.* **90**, 2636–2640 (1993).
21. C. K. Barlowe, D. R. Appling, *Mol. Cell. Biol.* **10**, 5679–5687 (1990).
22. C. K. Barlowe, M. E. Williams, J. C. Rabinowitz, D. R. Appling, *Biochemistry* **28**, 2099–2106 (1989).
23. M. G. West, D. W. Horne, D. R. Appling, *Biochemistry* **35**, 3122–3132 (1996).
24. K. E. Christensen, H. Patel, U. Kuzmanov, N. R. Mejia, R. E. MacKenzie, *J. Biol. Chem.* **280**, 7597–7602 (2005).
25. M. S. Field, E. Kamynina, D. Watkins, D. S. Rosenblatt, P. J. Stover, *Proc. Natl. Acad. Sci. U.S.A.* **112**, 400–405 (2015).
26. A. Schmidt *et al.*, *Biochemistry* **39**, 6325–6335 (2000).
27. F. F. Diehl *et al.*, *Nat. Cell Biol.* **24**, 1252–1264 (2022).
28. J. G. Doench *et al.*, *Nat. Biotechnol.* **34**, 184–191 (2016).
29. R. J. Torres, J. G. Puig, *Orphanet J. Rare Dis.* **2**, 48 (2007).
30. M. Vogel *et al.*, *Stem Cells* **37**, 1606–1614 (2019).
31. R. H. Wright *et al.*, *Science* **352**, 1221–1225 (2016).
32. M. Zha, C. Zhong, Y. Peng, H. Hu, J. Ding, *J. Mol. Biol.* **364**, 1021–1033 (2006).
33. H. Qi, R. H. Grace Wright, M. Beato, B. D. Price, *Cell Rep.* **41**, 111866 (2022).
34. J. Carreras-Puigvert *et al.*, *Nat. Commun.* **8**, 1541 (2017).
35. M. Zha *et al.*, *J. Mol. Biol.* **379**, 568–578 (2008).
36. B. D. G. Page *et al.*, *Nat. Commun.* **9**, 250 (2018).
37. A.-S. M. C. Marques *et al.*, bioRxiv 2025.03.2016.643557 [Preprint] (2025). https://doi.org/10.1101/2025.03.16.643557.
38. U. Rix, G. Superti-Furga, *Nat. Chem. Biol.* **5**, 616–624 (2009).
39. E. L. Huttlin *et al.*, *Cell* **184**, 3022–3040.e28 (2021).
40. J. Abramson *et al.*, *Nature* **630**, 493–500 (2024).
41. E. W. Holmes, J. B. Wyngaarden, W. N. Kelley, *J. Biol. Chem.* **248**, 6035–6040 (1973).
42. T. Yamaoka *et al.*, *J. Biol. Chem.* **276**, 21285–21291 (2001).
43. J. G. Tate *et al.*, *Nucleic Acids Res.* **47**, D941–D947 (2019).
44. A. Luengo, D. Y. Gui, M. G. Vander Heiden, *Cell Chem. Biol.* **24**, 1161–1180 (2017).
45. K. Honarmand Ebrahimi *et al.*, *Nat. Chem.* **14**, 253–266 (2022).
46. A. Strefeler *et al.*, *Nat. Metab.* **7**, 2221–2235 (2025).
47. Z. Wu *et al.*, *Science* **390**, eadx9717 (2025).
48. P. V. Hornbeck *et al.*, *Nucleic Acids Res.* **43**, D512–D520 (2015).
49. M. Maillard *et al.*, *J. Clin. Invest.* **135**, e190443 (2025).

ACKNOWLEDGMENTS

We thank the Biomedical Sequencing Facility and the Proteomics and Metabolomics and Chemical Screening Facilities of the Molecular Discovery Platform at CeMM, as well as I. Vendrell, S. Hester, R. Fischer, B. Kessler, and the Proteomics Facility at the Target Discovery Institute in Oxford for their support in generating and analyzing the next-generation sequencing or proteomics data, respectively. We are grateful to J.-L. Venne for technical assistance and all members of the Kubicek and Huber labs for valuable discussions about the project. **Funding:** This work was supported by the European Research Council (ERC) under the European Union's Horizon 2020 research and innovation program (ERC-CoG-772437 to S.K.); Wellcome Trust, Grant Number: 218514/Z/19/Z, Merck Sharp and Dohme Corp. and Janssen Pharmaceutica NV (to L.G.B.); the Innovative Medicines Initiative 2 Joint Undertaking (JU) under grant agreement no. 875510 to K.V.M.H. (the JU receives support from the European Union's Horizon 2020 research and innovation program and EFPIA and Ontario Institute for Cancer Research, Royal Institution for the Advancement of Learning McGill University, Kungliga Tekniska Hoegskolan, Diamond Light Source Limited); the Swiss National Science Foundation (310030_192505 to D.S.F.); the Marie Sklodowska-Curie Postdoctoral Fellowship (grant no. 101106260 to T.-A.N.); and the Austrian Science Fund (FWF) (10.55776/PAT1340623 and 10.55776/TAI2640624 to S.K.; 10.55776/PAT5733623 to H.P.M.; and 10.55776/P36728, 10.55776/P33430, 10.55776/P32900, and 10.55776/DOC59 to E.C.).
Author contributions: Conceptualization: T.-A.N., J.-M.G.L., S.S., K.V.M.H. and S.K.; Formal analysis: T.-A.N., J.G.L., A.-S.M.C.M., M.F., L.G.B., C.B., N.M., P.B., M.S., Y.L., J.S.H., K.K., J.T.H., M.A.; Funding acquisition: K.V.M.H., S.K.; Investigation: J.-M.G.L., T.-A.N., A.-S.M.C.M., M.F., A.R., D.D., L.S., L.G.B., C.C., L.D.L.D.D., J.S., F.T., M.B., H.P.M., M.S., J.G., G.H., L.V., M.M., C.K., Y.L., J.S.H., S.D., O.B., T.B.; Methodology: J.-M.G.L., T.-A.N., A.-S.M.C.M., Y.L., J.S.H., L.G.B., L.C., J.T.H., K.K., K.V.M.H., S.K.; Resources: D.S.F., D.S.R.; Supervision: L.P.M.H.d.R., E.C., A.K., D.S.F., K.K., A.B., J.M., J.T.H., M.A., S.S., K.L., K.V.M.H., S.K.; Visualization: T.-A.N., J.G.L., P.B., L.G.B.; Writing – original draft: T.-A.N., J.-M.G.L., A.-S.M.C.M., L.G.B., K.V.M.H., S.K.; Writing – review & editing: all coauthors. **Competing interests:** J.-M.G.L., A.-S.M.C.M., K.V.M.H., and S.K. have filed a patent application based on inventions described in this manuscript (WO2024127022A1). **Data and materials availability:** All cell lines generated in this study will be made available under a material transfer agreement. RNA-seq data have been deposited in GEO (accession no. GSE201334). Data from the genome-wide knockout screen have been deposited in GEO (accession no. GSE306775). Proteomics measurements have been deposited in PRIDE (PXD067739 – related to Fig. 5A, and PXD067706 – related to fig. S8).
License information: Copyright © 2025 the authors, some rights reserved; exclusive licensee American Association for the Advancement of Science. No claim to original US government works. https://www.science.org/about/science-licenses-journal-article-reuse

SUPPLEMENTARY MATERIALS

science.org/doi/10.1126/science.adv4257
Materials and Methods; Figs. S1 to S11; Tables S1 to S3; References (*50*–*71*); MDAR Reproducibility Checklist

Submitted 18 December 2024; resubmitted 16 May 2025; accepted 20 October 2025; published online 6 November 2025

10.1126/science.adv4257

METHANE EMISSIONS

Global energy sector methane emissions estimated by using facility-level satellite observations

Dylan Jervis[1], Marianne Girard[1], Jean-Philippe W. MacLean[1], David Marshall[1], Jason McKeever[1], Mathias Strupler[1], Antoine Ramier[1], Ewan Tarrant[1], David Young[1], Joannes D. Maasakkers[2], Ilse Aben[2], Tia R. Scarpelli[3]

Methane emissions from energy sector facilities (oil, gas, and coal) represent a substantial contribution to greenhouse gas emissions with substantial mitigation potential. We estimated global 2023 methane emissions from energy sector point sources using the high spatial resolution GHGSat satellite constellation. GHGSat detected 8.30 ± 0.24 million tonnes per year of methane emissions from 3114 emission sites. Detected oil and gas– and coal-emitting sites were found to be emitting 16 and 48% of the time, respectively, above GHGSat's detection limit without obvious continental variation. Compared with the Global Fuel Exploitation Inventory (GFEIv3) estimate, GHGSat's estimate comprises 12% of GFEIv3's total emissions, or 24% over GHGsat-observed locations, with good spatial correlation at the country scale but only weak spatial correlation at 0.2°-×-0.2° grid cell scale.

Methane is the second-most-important contributor to global warming behind carbon dioxide (CO_2). The majority of methane emissions originate from anthropogenic sources (*1*) with a substantial share of these emissions coming from so-called point sources, i.e., sources with localized emitting areas that are commensurate with facility size (order ~100 m). In this work, a point source is defined as a source that can be traced back to an individual facility. The GHGSat satellite constellation combines high spatial resolution (~25 m), good sensitivity (order 100 kg $hour^{-1}$ detection limit), and good coverage (2.4 million km^2 observed in 2023), allowing for attribution of a substantial fraction of emissions to their point of origin as well as the revisit frequency to reveal temporal emissions behavior. In this study, we estimated 2023 annual emissions and temporal intermittency of energy sector point source emission sites across the globe. The 2023 annual emission estimates have been made available at 0.2° × 0.2° gridded spatial resolution.

Methane emissions from the energy sector, oil and gas (O&G) and coal, have been estimated from both bottom-up inventories and top-down measurements (*2*–*20*). Bottom-up emission estimates typically use ground-based measurements from a small sample of emission sources. Top-down emission estimates, on the other hand, estimate emissions from atmospheric measurements of the methane concentration, typically using aircraft- and satellite-mounted instruments. Bottom-up estimates are based on knowledge of the underlying activity or process that produces the emission and are therefore indirect estimates of actual methane emissions and have trouble predicting unexpected emissions and temporal variations. Top-down emission estimates are a more direct estimate of methane emissions but have typically been limited either in spatiotemporal coverage [e.g., aircraft campaigns conducted over the span of weeks in a certain region (*5*, *6*, *8*, *9*, *21*)] or, if they have more extended spatial coverage and correspondingly coarser spatial resolution (e.g., area flux mappers, such as TROPOMI), can only coarsely attribute point source emissions (*20*) or use inversion techniques that require prior information about emission locations (*2*, *3*). Recently, hybrid top-down bottom-up inventories have been developed for some O&G-producing regions (*12*, *22*, *23*). A comparison of top-down and bottom-up estimates at different scales can improve our understanding of the process and methods used to produce both estimates.

Emission estimates from satellite point source and multispectral imagers (e.g., GHGSat, Carbon Mapper, PRISMA, EnMAP, EMIT, Sentinel-2, Landsat) can directly attribute emissions on the ~100-m scale (*8*, *11*, *15*, *24*–*28*). They will, however, miss small or diffuse emissions below the instrument's detection limit [GHGSat has a 50% probability of detection of 100 kg $hour^{-1}$ at 3 m/s wind speed inferred from controlled release measurements (*29*, *30*), whereas a method using a statistical comparison to AVIRIS-NG aircraft detections instead of controlled release measurements estimates a 50% probability of detection of approximately 250 kg $hour^{-1}$ (*31*)]. We note that the detection limit for a given instrument will vary with the observation conditions. The dominant physical factors behind the variation are wind speed and the amount of light collected by the instrument, driven by the surface albedo and solar zenith angle in a given observation (*29*, *30*). Furthermore, workflows involving human review may exhibit context-dependent detection limits: Prior information about the likely emission locations may bias single-blind validation results relative to observations where emission sources are not known a priori (*31*). Because of the fundamental trade-off between spatial resolution and coverage, a large constellation of point source imagers is required to approach the spatiotemporal coverage capabilities of a single area flux mapper. A constellation of point source imagers can achieve near-daily snapshot measurements of a source, building a time series of emissions. Because methane sources in the energy sector can be highly variable, estimating the average emission rate from a given location over a period of months or years requires that multiple snapshot satellite measurements taken over extended time periods be aggregated. We constructed an emission time series of a site through a spatial aggregation procedure: If an O&G or coal plume had an estimated origin location that was within 300 m or 2 km, respectively of another plume detected at a different time, then we deemed the plumes as having originated from the same location or site (figs. S1 and S2). We let the distance criteria be sector specific to account for the fact that, for example, a coal site may emit from distributed locations within its kilometer-scale site footprint, whereas emissions from an O&G site tend to occur from localized infrastructure. The coal mining sector encompasses both localized vent emissions, of which there may be multiple distributed over the surface of the underground mining operations, and more spread-out open-pit mine emissions. Figure 1 shows examples of detected plumes from O&G and coal sites. The materials and methods describe that spatial aggregation procedure in more detail. Observations in which no plumes were detected at a site are also included in the emission time series using knowledge of the observation coverage footprint.

Our annualized point source emission estimate relies on an estimate of the emitting site's emission persistence, the fraction of observations in which a plume is detected at the location. In this way, we present sector and continent resolved site persistence distributions. We compared the GHGSat emission estimates to the most recent global spatially gridded energy sector methane inventory—the recently updated Global Fuel Exploitation Inventory (GFEIv3) (*19*)—at the spatial resolution of GHGSat measurement domains as well as at the national and global levels, providing a specific picture of emissions from the energy sector that is complementary to other top-down and bottom-up estimates. As GFEIv3 country-scale emissions align with the national inventories reported to the United Nations Framework Convention on Climate Change, our comparison at the country-scale has implications for these policy-relevant inventories. We also compared GHGSat estimates to TROPOMI energy sector emission estimates at the global and country scale (*2*).

[1]GHGSat Inc, Montreal, QC, Canada. [2]SRON Netherlands Institute for Space Research, Leiden, Netherlands. [3]Carbon Mapper, Pasadena, CA, USA. ***Corresponding author. Email: dylan.jervis@ghgsat.com**

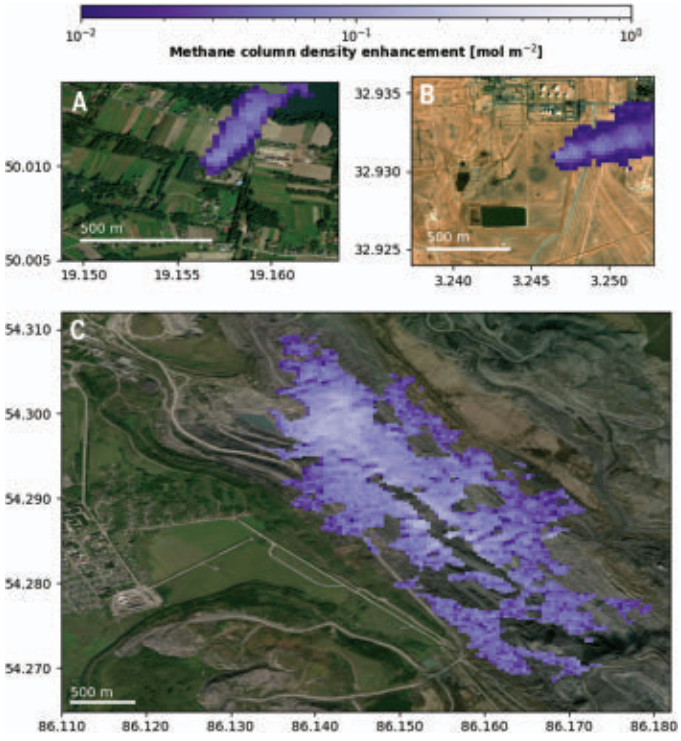


Fig. 1. Example GHGSat methane plume enhancements. Detected plumes from a (**A**) coal vent, (**B**) O&G flare stack, and (**C**) open-pit coal mine.

Temporal emissions behavior

The results presented in this paper were derived from 32,928 clear-sky observations, 14,137 of which were taken over O&G or coal sites that were observed to be emitting by GHGSat in 2023. A total of 11,419 detected plumes have been attributed to 3114 distinct O&G or coal sites alongside "null" observations of these sites in which the site was observed in clear-sky conditions, but no plumes were detected. To be clear, we do not extrapolate our results to locations where we did not detect an emission, whether we observed the locations or not. On average, GHGSat made 26 and 17 observations, respectively (median of 19 and 12 observations), of each emitting O&G and coal site during 2023. The average clear-sky revisit time was 10 and 16 days (median of 5 and 8 days), respectively, for each emitting O&G and coal site. A calculation of the temporal autocorrelation of our 2023 site observations (see supplementary materials) shows a slowly decreasing probability of having observed a site as a function of the time between observations without noticeable periodicity or other temporally correlated features. In many cases, multiple sites were observed within the same observation footprint. See the supplementary materials for a summary of GHGSat measurement details.

The persistence quantifies the fraction of site observations in which a plume was detected at a given location. We use an estimated persistence measure (see materials and methods) to account for the sampling bias that occurs when only a few observations of an emitting site have been taken. An emitting site is a site where at least one emission was detected in N observations. The observed persistence for an emitting site where emissions have been detected in M observations is M/N, which is an unreliable estimate when either M or N is small, especially for the case of intermittent emitters ($M \ll N$). We therefore used an estimated persistence measure $\langle \hat{p} \rangle = \langle p_o(x) p_p(x) \rangle$, which is defined as the mean of the joint probability distribution between the observed $p_o(x)$ and prior $p_p(x)$ persistence probability distributions. The prior persistence distributions are constructed on a per-sector and -continent basis from sites that have been observed at least 20 times. Not only does the estimated persistence provide temporal information about sector emissions, it is also used to estimate the time-averaged emission rate of a site $\hat{Q} = \hat{p} \langle Q_{q \neq 0} \rangle$, with $\langle Q_{q \neq 0} \rangle$ being the average emission rate of the detected plumes. It should be noted that we assume that our measurements are capturing representative and unbiased snapshots of the site's dynamical emission rate behavior from which we may infer an average rate. The materials and methods section discusses considerations when this assumption is broken.

The estimated persistence distributions of sites where GHGSat has detected at least one emission are shown in Fig. 2. Figure 2, A and B, shows the O&G and coal persistence distribution for each continent, respectively, and Fig. 2C shows the average persistence distribution for each sector globally. Figure 2, A and B, suggests that a site's sector is more indicative of its persistence than the continent it is located in: For both O&G and coal, the persistence distributions are largely similar across continents where at least $n = 5$ or more sites have been included in the average. That is, we show evidence of sectoral universality in the emissions persistence. Figure 2C shows that O&G sites are much more intermittent (i.e., less persistent) than coal sites: The average estimated persistence is 0.16 for O&G compared with 0.48 for coal. This means that plumes above GHGSat's detection limit are detected from emitting O&G sites in just 16% of observations compared with that from 48% of observations from emitting coal sites. We also note the flat persistence distribution of coal sites: GHGSat satellites are (approximately) equally as likely to observe a very persistent source as they are to observe a very intermittent or semipersistent source. Our coal persistence estimates are consistent with those of in situ studies of individual coal ventilation shafts, where emission rates were found to vary substantially, including down to negligibly small magnitudes (*32*, *33*).

The measured intermittency of the O&G sector is consistent with the periodic maintenance, leak, and repair events that are specific to the sector (*34*, *35*). A remote sensing measurement campaign conducted over the course of 3 months with the AVIRIS-NG aircraft instrument in the Permian Basin found O&G sources to be intermittent (*5*) (66% of detected sources had a persistence of 0.25 or less). This is consistent with our results (~80% of emitting O&G sites with persistence <20%), accounting for the fact that the persistence distribution estimated from an instrument with higher detection limit will, in general, be lower (*36*).

Because O&G emissions are far more intermittent than those of coal, they demand denser sampling. Given that the probability of detecting an emission from a source with persistence p in N observations is $1-(1-p)^N$, assuming binomial emissions behavior (*37*), ~14 GHGSat overpasses are required for a 90% chance of detecting an O&G release above the instrument's limit versus the ~4 GHGSat overpasses required for coal. The same intermittency likewise inflates the number of passes needed to estimate an O&G site's average emission rate to a given precision. We suggest that these persistence estimates may be relevant to regulatory monitoring frequency requirements, which so far tend to only consider detection limit of the technology (*38*).

We computed the temporal autocorrelation of GHGSat-detected O&G and coal emissions (see supplementary materials). Detection probability after a prior event stayed close to each sector's mean persistence for all lags τ, implying nearly random timing. Only O&G sites may have shown higher probability (within error) at small τ, suggesting day-to-week temporal clustering.

Comparing GHGSat-estimated emissions with those from GFEI

We present the spatial distribution of GHGSat observations and estimated emissions at 0.2°-×-0.2° resolution. This spatial gridding approach was chosen because the 0.2°-×-0.2° resolution is approximately equal to the area of a GHGSat retrieval domain, and it allows for a comparison to the spatially gridded GFEIv3 inventory. The GHGSat-estimated flux in a grid cell with center latitude and longitude coordinates (λ, ϕ) was calculated by summing all estimated site emissions $\hat{Q}$ that are located within ($\lambda \pm 0.1°$, $\phi \pm 0.1°$) and then dividing by the area that a particular

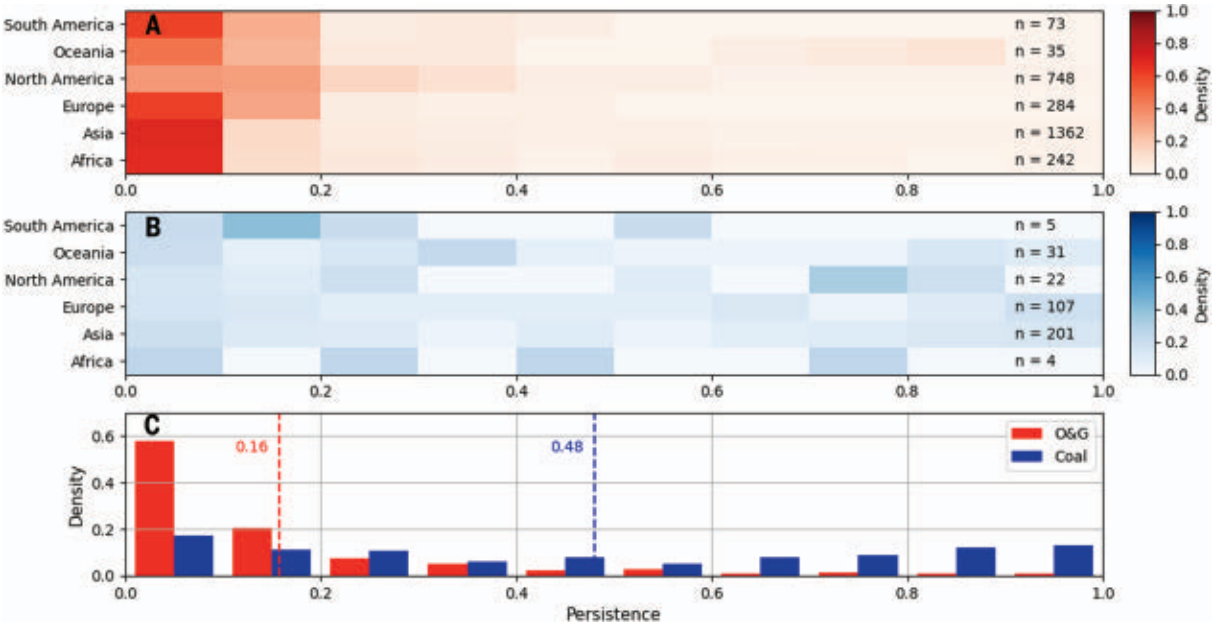


Fig. 2. Average site persistence distributions. (**A**) Persistence distribution for O&G sites by continent with the number of sites *n* included in the average annotated. (**B**) Persistence distribution for coal sites by continent. (**C**) Persistence distributions for all O&G and coal sites. The averages of the persistence distributions are indicated with the vertical dashed line: 0.16 for O&G sites, 0.48 for coal sites.

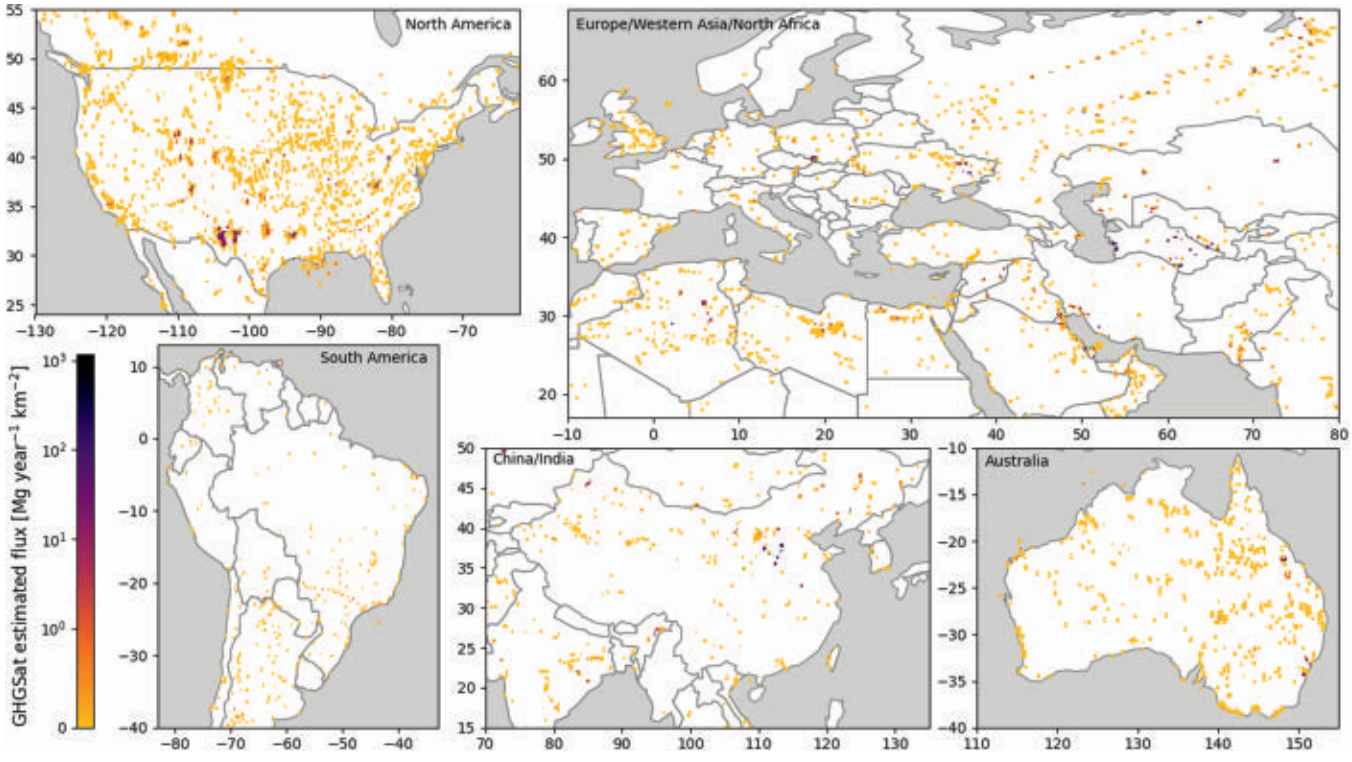


Fig. 3. Map of GHGSat-estimated emissions. GHGSat-estimated emission fluxes are shown at 0.2°-×-0.2° resolution for selected regions around the globe. Each colored area represents a location where GHGSat has made at least one clear-sky retrieval.

grid cell encompasses. A map of gridded GHGSat emission estimates is shown in Fig. 3 for selected regions.

GHGSat-estimated emission fluxes were compared with the GFEI inventory over three different spatial scales: globally, country level, and grid cell level. A map of the difference between GHGSat and GFEIv3 estimated emissions is shown in the supplementary materials.

The total GHGSat emissions estimate is $\widehat{Q}_{tot}$ = 8.30 ± 0.24 million tonnes per year (Mt year^{-1}), with 5.80 ± 0.23 Mt year^{-1} attributed to O&G sites and 2.50 ± 0.06 Mt year^{-1} attributed to coal sites. The GHGSat-estimated total represents 11.7% of the total GFEIv3-estimated emissions (74.3 Mt year^{-1} = 43.7 Mt year^{-1} O&G + 30.7 Mt year^{-1} coal). However, given that the GHGSat constellation only has partial coverage of

locations where GFEIv3 predicts emissions to be originating from, we also compared GHGSat-measured emissions to GFEIv3 predictions only at locations where GHGSat had made at least one successful observation (without necessarily detecting an emission). At these GHGSat-observed locations, the GHGSat-estimated total represents a larger fraction of the GFEIv3-predicted emissions: 35% of the GFEIv3 prediction for O&G (16.4 Mt year^{-1}), 14% of the GFEIv3 prediction for coal (17.8 Mt year^{-1}), and 24% of the GFEIv3 prediction for both combined (34.1 Mt year^{-1}). If we assume that the cumulative GFEIv3 emissions predicted at the GHGSat-observed locations were accurate, then the GHGSat-measured emission fractions could be interpreted as the fraction of emissions observable above GHGSat's detection limit. This would be roughly consistent with a Permian Basin measurement study conducted using an instrument with a 90% probability of detection of 2 kg hour^{-1} (*36*) that estimated that fewer than 35% of total emissions originate from sources above 100 kg hour^{-1}. However, it should be noted that national top-down energy sector emission estimates using TROPOMI measurements between May 2018 and February 2020 were greater than the 2019 GFEIv2 estimates globally (*2*), totaling 95.4 Mt year^{-1} (62.7 Mt year^{-1} O&G + 32.7 Mt year^{-1} coal). Consequently, the global GHGSat estimate represents 8.7% of the global TROPOMI-estimated energy sector emissions total.

In comparing GHGSat-estimated emission totals to GFEIv3-estimated emission totals at GHGSat-observed locations, there is the tacit assumption GFEI is accurate in aggregate. To examine this further, we compared GFEI emission estimates to those from GHGSat at GHGSat-observed locations at both individual–grid cell resolution as well as for multiple grid cells aggregated within a country. We also compared national GHGSat estimates to national TROPOMI estimates. Figure 4, A and B, shows a comparison of GHGSat national emission estimates with those from GFEIv3 and TROPOMI, either for the country total (solid circles for GFEIv3, solid diamonds for TROPOMI) or only at GHGSat-observed aggregated locations in-country (open circles). Because of the mismatch in spatial resolution between the GHGSat and coarser resolution of the TROPOMI gridded estimates (0.5° × 0.6125°), we did not compare them at GHGSat-observed locations. Qualitatively, we observed a correlation between emission rates predicted by GFEIv3 and TROPOMI and those estimated by GHGSat, though the correlation was stronger for the coal sector than for O&G. The correlation can be quantified with both a standard and emission error–weighted Pearson correlation coefficient. When calculating the error-weighted correlation coefficient (see materials and methods), we used the GHGSat-estimated error to weight GHGSat emission estimates and assume zero error for GFEIv3 estimates (as none are provided). Furthermore, because the GHGSat emission error estimate was only defined for locations with nonzero emissions, we only calculated error-weighted correlations over locations with nonzero emissions. The standard correlation coefficients were 0.504 and 0.967 for the O&G and coal sectors, respectively, whereas the error-weighted correlation coefficients were 0.295 and 0.714. For context, a correlation coefficient of –1 would indicate perfect anticorrelation, 0 would indicate zero correlation, and 1 would indicate perfect correlation between variables. Therefore, we observed strong correlation for the coal sector between GHGSat emission estimates and those of GFEIv3 at the country-aggregated scale and moderate correlation for the O&G sector. The correlations were slightly reduced when an error-weighted correlation metric was used, suggesting that the more reliable a GHGSat emission estimate is, the less correlated it is with a GFEIv3 estimate, possibly owing to the repeated targeting of outlier locations where large emissions were detected. Lastly, to quantify how much coverage GHGSat had of GFEIv3-predicted emissions in each country, we defined a coverage fraction measure in the supplementary materials and calculated it for each country.

We also investigated the correlation between GHGSat and GFEIv3 at the resolution of individual 0.2° × 0.2° grid cells (see Fig. 5). The correlation is much weaker compared with the country-aggregated total, with the standard and error-weighted Pearson correlation coefficients equal to, respectively, 0.224 and 0.243 for the O&G sector and 0.183 and 0.233 for the coal sector. That is, the correlation between GHGSat- and GFEIv3-estimated emissions is weak to negligible at the level of individual grid cells and with similar values between the O&G and coal sectors. Maps comparing GHGSat and GFEIv3 gridded emission predictions are shown for selected countries in the supplementary materials.

Discussion

We have produced a global gridded estimate of annual emissions from measured O&G and coal point sources. This annual gridded estimate can help provide a basis for emissions reporting. The GHGSat gridded

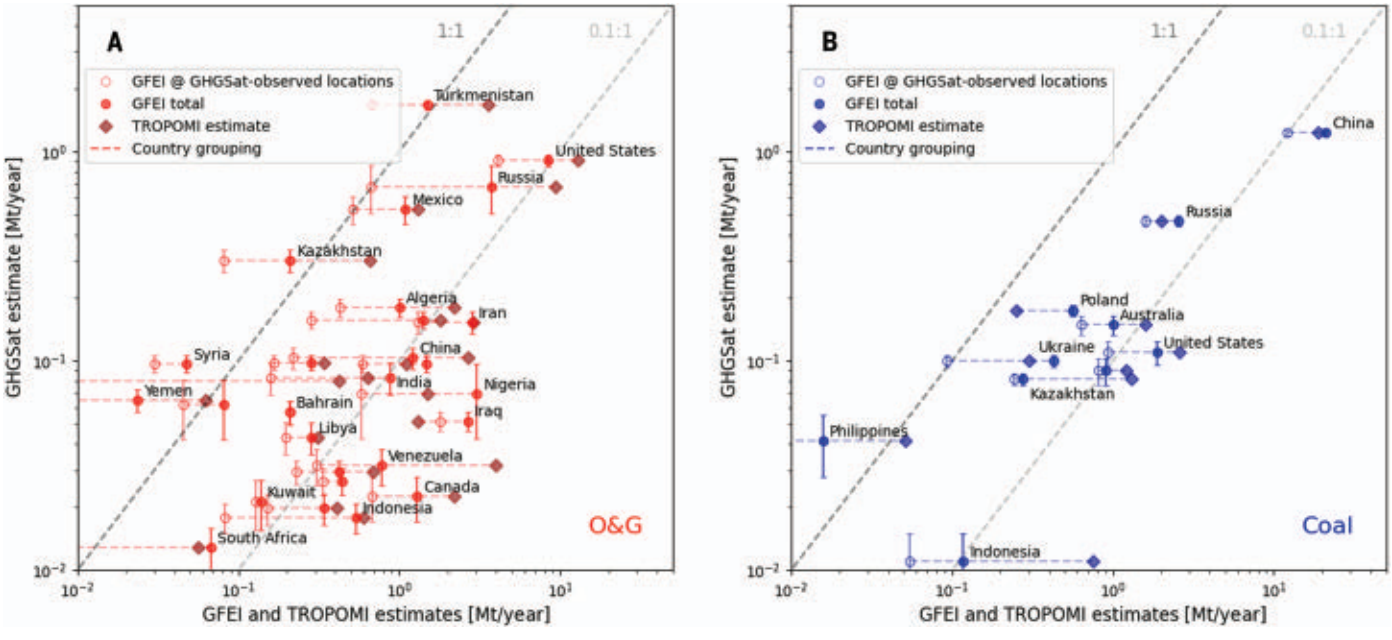


Fig. 4. Spatial correlation of emission estimates between GHGSat and GFEIv3 or TROPOMI. A comparison between GHGSat-estimated and GFEIv3- or TROPOMI-estimated emissions from (**A**) O&G and (**B**) coal for countries.

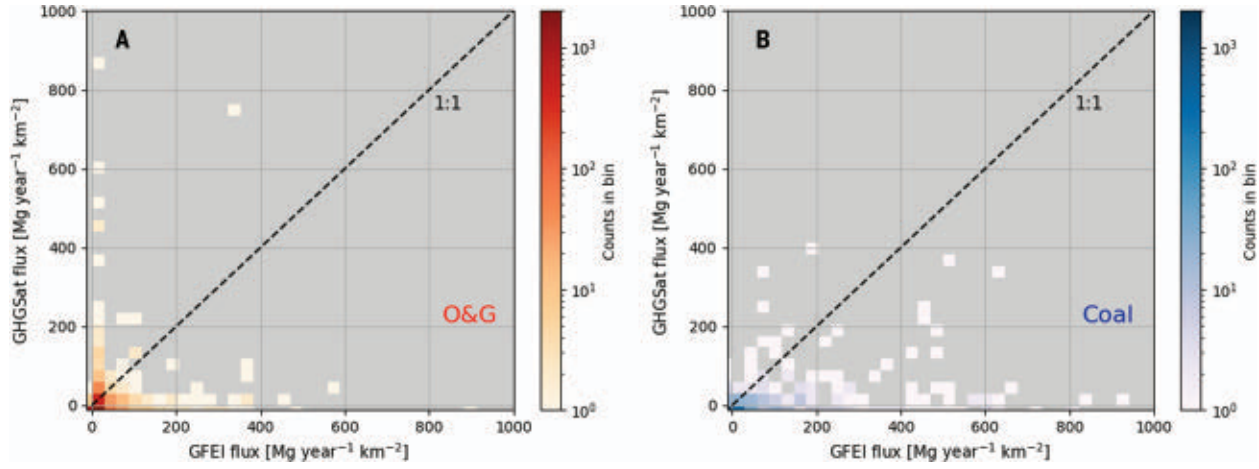


Fig. 5. Correlation between GHGSat and GFEIv3 flux estimates at 0.2°-×-0.2° grid cell resolution for O&G (A) and coal (B). The black dashed line is the 1:1 line. We note that the bins slightly to the negative side of the *x* and *y* axes denote bins where the GFEI and GHGSat flux, respectively, are exactly zero.

emission estimates rely on both detected emissions as well as clear-sky nondetections at emission sites through an estimated emissions persistence measure that is informative in its own right. We have shown good agreement between the GHGSat and GFEIv3 coal emission estimates at the national level and moderate to weak agreement for national O&G emissions but weak to poor agreement at the spatial resolution of individual 0.2° × 0.2° grid cells for both O&G and coal sectors. This suggests that inventory estimates may have trouble accurately estimating emissions at the facility scale. Moreover, the large number of repeated high-resolution observations enables quantification of point source intermittency, providing a globally consistent estimate of temporal emission variability. In presenting our results, it is important to qualify that the site persistence and emission rate estimated by an observing system will depend on the emission rate detection sensitivity of the system (*5*, *39*).

We note that point source measurements can help inform top-down emission estimates from coarser spatial resolution systems by providing more accurate prior mean and prior covariance estimates (*40*). Furthermore, they can provide valuable tip and cue information for more sensitive, higher spatial resolution systems (e.g., airborne and ground-based instruments) for follow-up investigation. The lack of strong per-grid cell agreement between GHGSat-estimated emissions and the bottom-up GFEIv3 prediction suggests that a measurement-informed inventory approach could be beneficial.

REFERENCES AND NOTES

1. M. Saunois *et al.*, *Earth Syst. Sci. Data* **12**, 1561–1623 (2020).
2. L. Shen *et al.*, *Nat. Commun.* **14**, 4948 (2023).
3. Y. Zhang *et al.*, *Sci. Adv.* **6**, eaaz5120 (2020).
4. T. Ehret *et al.*, *Environ. Sci. Technol.* **56**, 10517–10529 (2022).
5. D. H. Cusworth *et al.*, *Environ. Sci. Technol. Lett.* **8**, 567–573 (2021).
6. D. H. Cusworth *et al.*, *Proc. Natl. Acad. Sci. U.S.A.* **119**, e2202338119 (2022).
7. T. R. Scarpelli *et al.*, *Atmos. Chem. Phys.* **22**, 3235–3249 (2022).
8. D. J. Varon *et al.*, *Geophys. Res. Lett.* **46**, 13507–13516 (2019).
9. D. H. Cusworth *et al.*, *Geophys. Res. Lett.* **48**, e2020GL090864 (2021).
10. B. J. Schuit *et al.*, *Atmos. Chem. Phys.* **23**, 9071–9098 (2023).
11. A. K. Thorpe *et al.*, *Sci. Adv.* **9**, eadh2391 (2023).
12. M. R. Johnson, B. M. Conrad, D. R. Tyner, *Commun. Earth Environ.* **4**, 139 (2023).
13. D. Zavala-Araiza *et al.*, *Elementa* **6**, 27 (2018).
14. M. V. Dangeti *et al.*, *Atmos. Chem. Phys.* **24**, 12843–12859 (2024).
15. T.-L. He, R. J. Boyd, D. J. Varon, A. J. Turner, *Proc. Natl. Acad. Sci. U.S.A.* **121**, e2314600121 (2024).
16. J. D. Maasakkers *et al.*, *Environ. Sci. Technol.* **57**, 16276–16288 (2023).
17. M. Crippa *et al.*, *Earth Syst. Sci. Data* **16**, 2811–2830 (2024).
18. D. J. Varon *et al.*, *Atmos. Chem. Phys.* **23**, 7503–7520 (2023).
19. T. R. Scarpelli *et al.*, Using new geospatial data and 2020 fossil fuel methane emissions for the Global Fuel Exploitation Inventory (GFEI) v3. Earth Syst. Sci. Data Discuss [Preprint] (2025); https://doi.org/10.5194/essd-2024-552.
20. T. Lauvaux *et al.*, *Science* **375**, 557–561 (2022).
21. S. Pandey *et al.*, *Environ. Sci. Technol.* **59**, 7931–7947 (2025).
22. B. M. Conrad, D. R. Tyner, H. Z. Li, D. Xie, M. R. Johnson, *Commun. Earth Environ.* **4**, 416 (2023).
23. E. Chan *et al.*, *Commun. Earth Environ.* **5**, 566 (2024).
24. R. Loizzo *et al.*, in *IGARSS 2018-2018 IEEE International Geoscience and Remote Sensing Symposium*, Valencia, Spain, 22 to 27 July 2018. (IEEE, 2018), pp. 175–178.
25. D. J. Varon *et al.*, *Atmos. Meas. Tech.* **14**, 2771–2785 (2021).
26. J. Roger *et al.*, *IEEE Trans. Geosci. Remote Sens.* **62**, 1–12 (2024).
27. D. Jervis *et al.*, *Atmos. Meas. Tech.* **14**, 2127–2140 (2021).
28. J. D. Maasakkers *et al.*, *Sci. Adv.* **8**, eabn9683 (2022).
29. J. Mckeever, D. Jervis, Validation and Metrics for Emissions Detection by Satellite. EarthArXiv [Preprint] (2025); https://doi.org/10.31223/X5DH9Q.
30. A. Ramier *et al.*, High-Resolution Methane Detection with the GHGSat Constellation. EarthArXiv [Preprint] (2025); https://doi.org/10.31223/X5FF0X.
31. J. Worden *et al.*, Commercial Satellite Data Acquisition Program: GHGSat Emission Quality Assessment Report (NASA, 2025); https://earthdata.nasa.gov/s3fs-public/2025-03/CSDA%20GHGSat%20Emission%20Quality%20Assessment%20SMEs%20v1.pdf.
32. J. Swolkień, A. Fix, M. Gałkowski, *Atmos. Chem. Phys.* **22**, 16031–16052 (2022).
33. T. Andersen *et al.*, *Atmos. Environ. X* **12**, 100135 (2021).
34. H. L. Brantley, E. D. Thoma, W. C. Squier, B. B. Guven, D. Lyon, *Environ. Sci. Technol.* **48**, 14508–14515 (2014).
35. A. V. Strizhenok, D. S. Korelskiy, *J. Ecol. Eng.* **20**, 46–51 (2019).
36. W. M. Kunkel *et al.*, *Environ. Sci. Technol.* **57**, 12234–12241 (2023).
37. D. J. Jacob *et al.*, *Atmos. Chem. Phys.* **22**, 9617–9646 (2022).
38. Standards of Performance for New, Reconstructed, and Modified Sources and Emissions Guidelines for Existing Sources: Oil and Natural Gas Sector Climate Review (EPA, 2024); https://www.federalregister.gov/d/2024-13206.
39. K. J. Biener *et al.*, *Environ. Sci. Technol.* **58**, 4948–4956 (2024).
40. S. Naus *et al.*, *Environ. Sci. Technol.* **57**, 19545–19556 (2023).
41. D. Jervis *et al.*, Data for "Global energy sector methane emissions estimated by using facility-level satellite observations," Dryad (2025); https://doi.org/10.5061/dryad.rxwdbrvkp.

ACKNOWLEDGMENTS

We thank D. Jacob and J. East for helpful comments during the writing of this manuscript. **Funding:** The work presented in this paper was carried out as part of the authors' salaried employment; no external funding was received. **Author contributions:** Conceptualization: D.J.; Methodology: D.J.; Investigation: D.J., J.D.M., J.M., M.G., I.A.; Formal analysis: D.J., A.R.; Data curation: D.J., M.G., D.Y., D.M., J.-P.W.M., D.M., J.M., M.S., A.R., E.T.; Visualization: D.J.; Validation: D.J., J.M., M.G., J.D.M.; Software: D.J., E.T., D.Y., A.R.; Resources: T.R.S.; Writing – original draft: D.J.; Writing – review & editing: all authors. **Competing interests:** The authors declare that they have no competing interests. **Data and materials availability:** Gridded emission estimates and site persistence data (with anonymized site locations) are made available at Dryad (*41*).

License information: Copyright © 2025 the authors, some rights reserved; exclusive licensee American Association for the Advancement of Science. No claim to original US government works. https://www.science.org/about/science-licenses-journal-article-reuse

SUPPLEMENTARY MATERIALS

science.org/doi/10.1126/science.adv3183
Materials and Methods; Supplementary Text; Figs. S1 to S15; Tables S1 and S2; References (*42*, *43*)

Submitted 18 December 2024; accepted 10 October 2025

10.1126/science.adv3183

MOLECULAR BIOLOGY

Chromothripsis and ecDNA initiated by N4BP2 nuclease fragmentation of cytoplasm-exposed chromosomes

Ksenia Krupina[1], Alexander Goginashvili[1], Michael W. Baughn[1], Stephen Moore[1], Christopher D. Steele[1,2,3], Amy T. Nguyen[1], Daniel L. Zhang[1], Jonas Koeppel[4,5], Prasad Trivedi[1], Aarti Malhotra[1], David Jenkins[6], Andrew K. Shiau[6], Yohei Miyake[7], Tomoyuki Koga[8]†, Shunichiro Miki[8]‡, Frank B. Furnari[7,8], Peter J. Campbell[4,5], Ludmil B. Alexandrov[1,2,3,7], Don W. Cleveland[1,3]*

Genome instability, including chromothripsis, is a hallmark of cancer. Cancer cells frequently contain micronuclei—small, nucleus-like structures formed by chromosome missegregation—that are susceptible to rupture, exposing chromatin to cytoplasmic nucleases. Through an unbiased, imaging-based small interfering RNA screen that targeted all 204 known and putative human nucleases, we identified a previously uncharacterized cytoplasmic endonuclease, NEDD4-binding protein 2 (N4BP2), that enters ruptured micronuclei and initiates DNA damage, leading to chromosome fragmentation. N4BP2 promoted genome rearrangements (including chromothripsis), formation of extrachromosomal DNA (ecDNA) in drug-induced gene amplification, tumorigenesis, and tumor cell proliferation in an induced model of human high-grade glioma. Analysis of more than 10,000 human cancer genomes revealed elevated N4BP2 expression to be predictive of chromothripsis and copy number amplifications, including ecDNA.

Chromothripsis, the most common type of chromoanagenesis (*1*) and a major driver of genome instability in cancer (*1*–*3*), involves extensive chromosome shattering and random reassembly of fragments, initiated by rupture of aberrantly formed micronuclei (*1*–*4*). Such ruptures expose chromatin to cytoplasmic nucleases, potentially triggering chromosomal fragmentation and rearrangement (*1*, *5*–*10*). We performed an unbiased screen covering all—both reported and putative—human nucleases to identify nucleases whose activity promotes fragmentation of chromosomes within ruptured micronuclei.

Imaging-based screen for human nucleases that fragment micronucleated chromosomes

We first generated a list of all known and putative human nucleases (n = 204, on the basis of the protein function resource https://www.uniprot.org/, combined with relevant literature; table S1) and developed a quantitative imaging-based approach to monitor DNA damage specifically in micronuclei, using phosphorylation of histone H2AX on Ser^{139} (γH2AX) as a marker of DNA double-strand breaks (Fig. 1A and figs. S1A and S2A) (*11*). To systematically induce micronuclei, we used the Dld1-Y human colorectal adenocarcinoma cell model ("Dld1-Y^{MN}") (*9*), in which selective inactivation of the Y chromosome centromere induced controlled missegregation and incorporation of the Y chromosome into micronuclei (fig. S2B), which showed pronounced DNA damage upon micronuclei envelope rupture (Fig. 1C) (*9*, *12*).

Use of Dld1-Y^{MN} allowed nuclease assessment on two levels: (i) DNA double-strand breaks (visualized by γH2AX signals) within Y chromosome–containing micronuclei (Fig. 1A and fig. S1A) and (ii) Y chromosome fragmentation scored on metaphase spreads by DNA fluorescence in situ hybridization (FISH) with Y chromosome–specific probes (Fig. 1B and fig. S2C). Using γH2AX in micronuclei as the primary readout—and benchmarking small interfering (siRNA)–mediated reductions against wortmannin, an inhibitor of γH2AX formation (*11*, *13*)—we screened all 204 nucleases (Fig. 1, A and D), excluding hits that altered γH2AX in the main nucleus (fig. S2D). Neither apurinic/apyrimidinic endonuclease 1 (APE1), previously implicated in promoting DNA breaks in a model of micronuclei-associated inhibition of transcription followed by aberrant DNA repair (*14*), nor three-prime repair exonuclease 1 (TREX1), previously reported to facilitate chromothripsis after induced telomere fusion (*15*, *16*), scored high in the screen (Fig. 1D).

In a secondary screen, we tested whether any of the top 12 candidates from the primary screen influenced the frequency of Y chromosome fragmentation after micronucleation and identified NEDD4-binding protein 2 (N4BP2)—a poorly characterized nuclease reported to nick supercoiled DNA (*17*)—as the top candidate. N4BP2 knockdown markedly reduced γH2AX in micronuclei and the fraction of spreads with fragmented Y chromosomes (Fig. 1B and fig. S2E), whereas similar reduction of TREX1 or APE1 had no effect (fig. S2F). Knockdown of N4BP2 with a different set of siRNAs similarly lowered γH2AX in ruptured micronuclei (GFP-NLS negative, monitored by the efflux of GFP fused to a nuclear localization signal, NLS) and decreased Y fragmentation (Fig. 1, E and F, and fig. S2, G and H). Moreover, CRISPR-Cas9–mediated homozygous disruption of *N4BP2* abolished Y chromosome fragmentation after micronucleation, whereas *TREX1* deletion did not affect either Y chromosome fragmentation or γH2AX level in micronuclei (Fig. 1, G to I, and fig. S2, I and J). These data establish N4BP2 as a key nuclease that drives DNA damage and chromosome fragmentation within ruptured micronuclei. The residual γH2AX in N4BP2 knockout (KO) micronuclei might reflect the action of other nucleases (Fig. 1D and fig. S2E) and/or DNA damage caused by replication, transcription, or repair stress (*18*–*22*).

Fragmentation of chromosomes exposed to N4BP2

We next examined N4BP2 localization and function. Both endogenous N4BP2 (detected by the N4BP2 antibody) and GFP-tagged N4BP2 (N4BP2-GFP) were predominantly cytoplasmic in cancer-derived (Dld1-Y^{MN}, U2OS, HeLa) and near-diploid RPE-1 cells (Fig. 2A and figs. S3A and S8A). Untagged, endogenous N4BP2 formed bright foci inside micronuclei, colocalizing with—or adjacent to—γH2AX foci (Fig. 2A). In rare (<1%) examples, beyond micronuclear puncta, endogenous N4BP2 accumulated within a main nucleus in large, rounded, droplet-like foci, which partially colocalized with bright, abundant γH2AX (fig. S3B), consistent with N4BP2 recruitment after spontaneous rupture of the main nucleus. Furthermore, use of live-cell imaging identified that nuclear entry of N4BP2-GFP into the main nucleus was followed by cell death marked by membrane blebbing, DNA compaction, and cell detachment (fig. S3, C to E).

Both siRNA knockdown and CRISPR-Cas9 KO of *N4BP2* significantly reduced the fraction of γH2AX-positive ruptured micronuclei and the γH2AX signal intensity within them, without affecting intact micronuclei (Fig. 2, B to D, and figs. S4A and S8, C to E). Almost all (95% in Dld-Y^{MN} and 85% in U2OS) of the N4BP2-positive micronuclei

[1]Department of Cellular and Molecular Medicine, University of California at San Diego, La Jolla, USA. [2]Department of Bioengineering, University of California at San Diego, La Jolla, USA. [3]Moores Cancer Center, University of California at San Diego, La Jolla, USA. [4]Department of Haematology, University of Cambridge, Cambridge, UK. [5]Wellcome Trust Sanger Center, Hinxton, UK. [6]Department of Cell and Developmental Biology, University of California at San Diego, La Jolla, USA. [7]Sanford Stem Cell Institute, University of California San Diego, La Jolla, USA. [8]Department of Medicine, University of California at San Diego, La Jolla, USA. ***Corresponding author: Email: dcleveland@health.ucsd.edu** †Present address: Department of Neurosurgery, University of Minnesota, Minneapolis, Minnesota, USA. ‡Present address: Department of Neurosurgery, Institute of Medicine, University of Tsukuba, Tsukuba, Ibaraki, Japan.

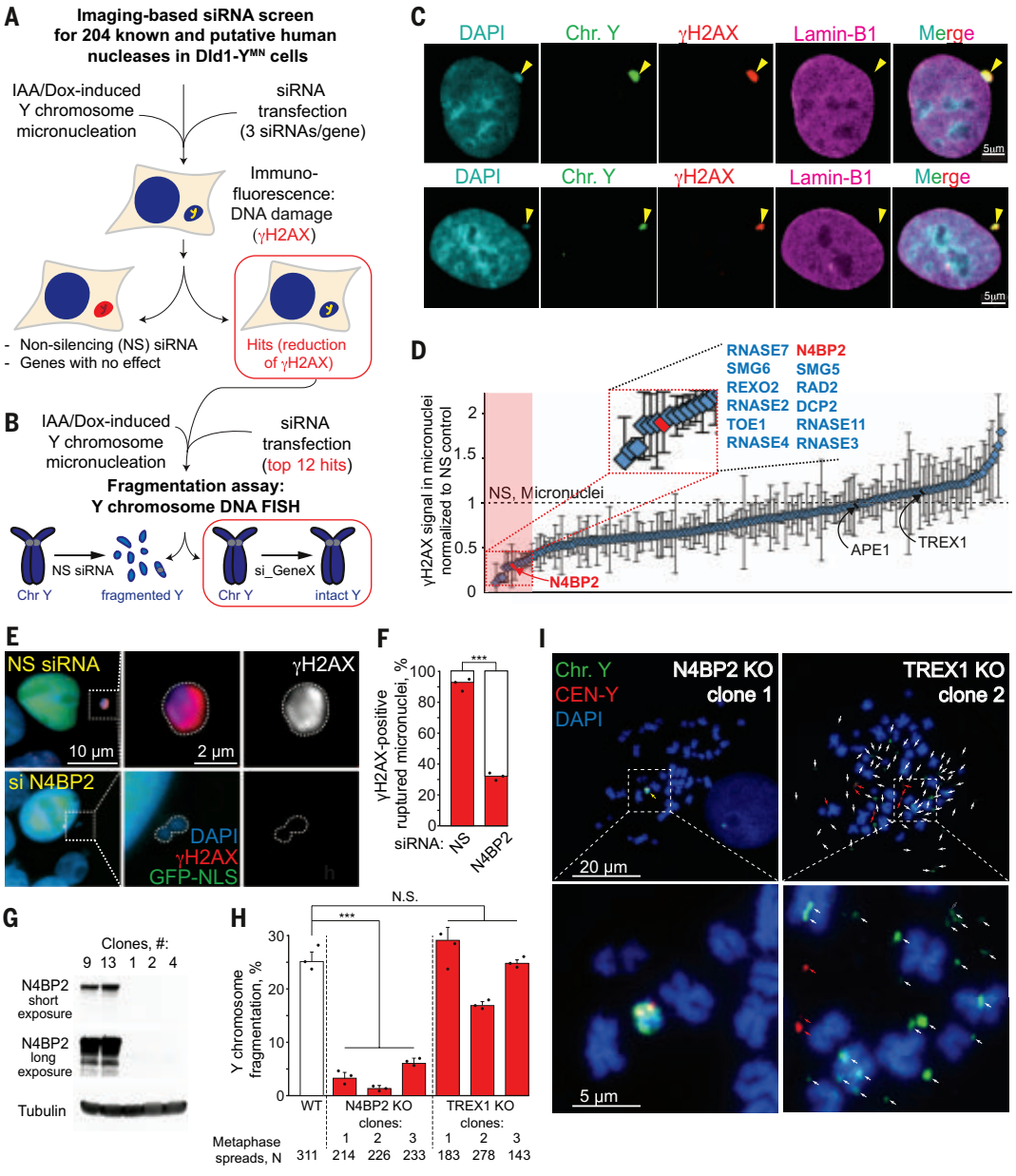


Fig. 1. Imaging-based screen for human nucleases that fragment micronucleated chromosomes. (**A** and **B**) Schematic of siRNA-mediated screen for human nucleases inducing DNA damage and chromosome fragmentation in micronuclei (MN). Dld1-Y^{MN} cells allow for inducible micronucleation of Y chromosome (see also fig. S1A). The MN of MN-induced (for 72 hours) Dld1-Y^{MN} cells transfected with siRNAs targeting 204 nucleases (table S1) were scored for the reduction of DNA damage (with DNA double-strand break marker γH2AX) compared with NS siRNA (negative control, high γH2AX) and γH2AX inhibitor wortmannin (positive control, low γH2AX) [γH2AX immunofluorescence (IF), primary assay shown in (A)]. Next, mitotic spreads from MN-induced Dld1-Y^{MN} cells, transfected with the siRNAs targeting hits identified in a primary assay, were analyzed for the presence of fragmented Y chromosomes through DNA FISH probes against Y chromosome [Y chromosome DNA FISH, secondary assay, shown in (B)]. (**C**) DNA damage in Y chromosome–containing micronuclei with abnormal nuclear envelope in MN-induced Dld1-Y^{MN} cells. Green, Y chromosome paint probe; red, γH2AX; and magenta, lamin B1. Scale bar, 5 μm. (**D**) Distribution of γH2AX signal in micronuclei normalized to NS control (dashed line) for each siRNA of siRNA library (blue rhombuses). Reduction of γH2AX upon wortmannin treatment was used as a baseline. Pink box highlights candidate genes with the strongest γH2AX reduction (zoomed in on top); N4BP2 nuclease is shown as a red rhombus; TREX1 and APE1 are shown as black rhombuses. Mean ± SEM, $n = 3$ independent experiments. (**E** and **F**) Representative images (E) and quantification (F) of DNA damage accumulation (detected with γH2AX, red) in micronuclei with ruptured nuclear envelope (indicated with GFP-NLS efflux from the micronucleus). Scale bar, 2 μm. Mean ± SEM, $n = 3$ independent experiments. (**G**) Immunoblot of N4BP2 with lysates from Dld1-Y^{MN} cells of indicated genotypes. Short and long exposures are shown. Tubulin was used as a loading control. (**H**) Quantification of metaphase spreads from MN-induced Dld1-Y^{MN} cells of indicated genotypes containing fragmented Y chromosome. $n = 3$ independent clones per genotype. (**I**) Representative images of metaphase spreads in Dld1-Y^{MN}, N4BP2 KO clones, and TREX1 KO clones in Dld1-Y^{MN}, after induction of MN for 72 hours. Green, Y chromosome paint probe; red, Y centromere probe. Yellow arrows point at the intact Y chromosome; red arrows, Y centromere fragments; and white arrows, Y chromosome fragments. Scale bars, 20 and 5 μm. DNA was stained with DAPI (blue) in (C), (E), and (I). DOX, doxycycline; IAA, indole-3-acetic acid; N.S., not significant. ***$P < 0.001$.

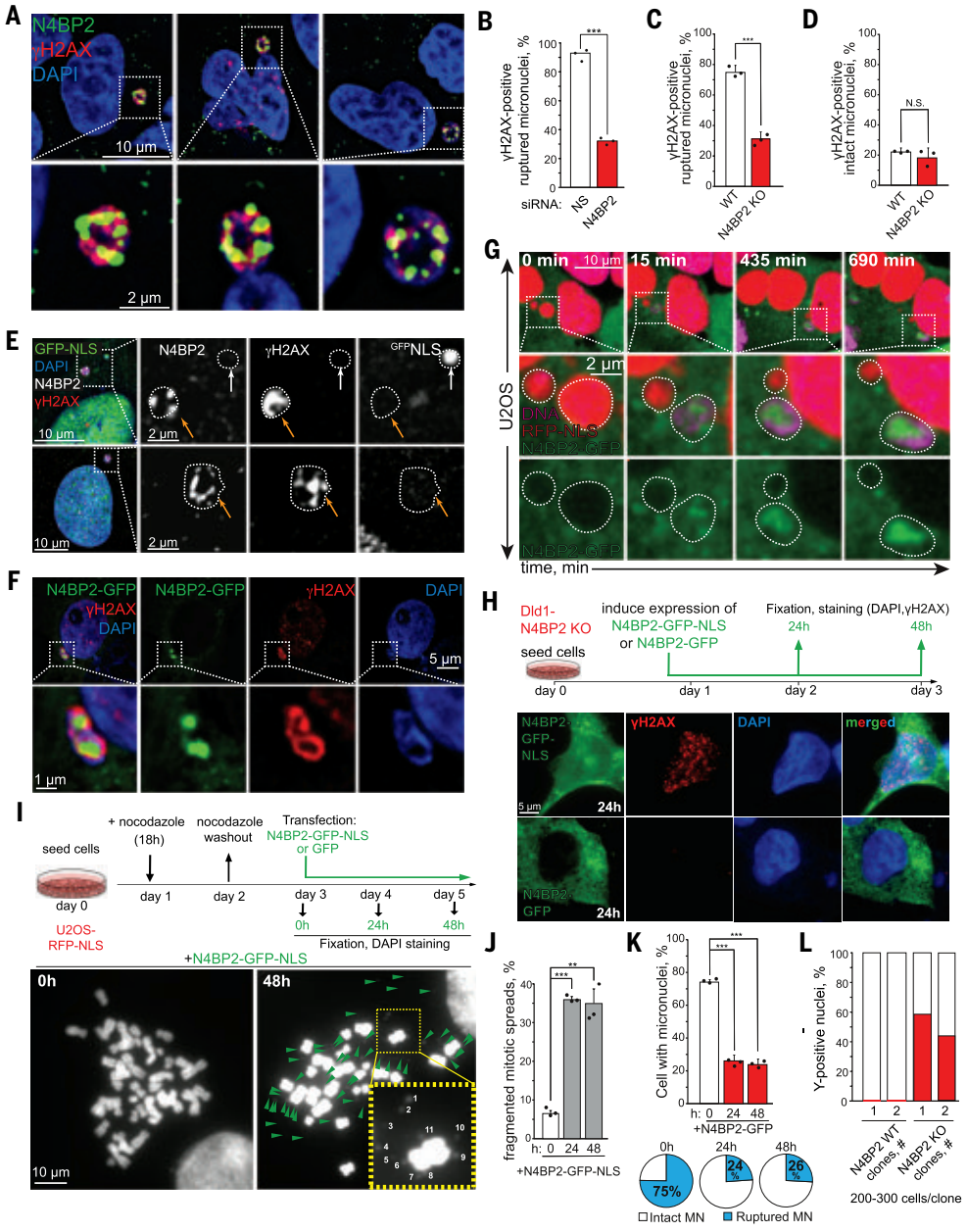


Fig. 2. Fragmentation of chromosomes exposed to N4BP2. (**A**) Representative IF images of MN-induced Dld1-Y^{MN} cells showing localization of endogenous N4BP2 nuclease (green) forming droplet-like foci in MN with extensive DNA damage (γH2AX, red). Scale bars, 10 and 2 μm, as indicated. (**B**) Percentage of γH2AX-positive ruptured MN in GFP-NLS–expressing Dld1-Y^{MN} cells upon indicated siRNA treatments. Mean ± SEM, $n = 3$ independent experiments. (**C**) Percentage of γH2AX-positive ruptured MN in GFP-NLS–expressing Dld1-Y^{MN} cells of the indicated genotypes. See fig. S4A for a scheme of experiment. Mean ± SEM, $n = 3$ independent experiments. (**D**) Percentage of γH2AX-positive intact MN in GFP-NLS–expressing Dld1-Y^{MN} cells of the indicated genotypes. See fig. S4A for a scheme of experiment. Mean ± SEM, $n = 3$ independent experiments. (**E**) Representative IF images of GFP-NLS–expressing U2OS cells, showing localization of endogenous N4BP2 nuclease within ruptured micronuclei (identified by the absence of GFP-NLS, orange arrows) with extensive DNA damage (γH2AX, red). MN were induced by nocodazole. White arrows indicate intact, GFP-NLS–positive micronuclei. Scale bars, 10 and 2 μm, as indicated. (**F**) Representative IF images of Dld1-Y^{MN} cells with induced MN, transfected as indicated, showing localization of N4BP2-GFP–positive (green) inside γH2AX-positive (red) MN. Scale bars, 5 and 1 μm, as indicated. (**G**) Live-cell imaging of U2OS cells expressing N4BP2-GFP and RFP-NLS; MN were induced with nocodazole. N4BP2-GFP enters ruptured MN (identified by the loss of RFP-NLS, occurs at 15-min time point) and gradually accumulates in MN. Scale bar, 10 and 2 μm, as indicated. (**H**) (Top) Schematic of the approach used to target N4BP2-GFP into intact nuclei and micronuclei in N4BP2 KO Dld1-Y^{MN} cells. (Bottom) Representative images of DNA damage accumulation (γH2AX, red) upon targeting N4BP2-GFP-NLS into intact nuclei versus cytoplasmic N4BP2 (N4BP2-GFP). Scale bar, 5 μm. (**I**) (Top) Schematic of the approach used to target N4BP2-GFP into intact nuclei and micronuclei in U2OS cells. (Bottom) Representative images of mitotic spreads upon N4BP2-GFP-NLS expression for 0, 24, and 48 hours. Chromosome fragments are indicated with green arrowheads. Numbers indicate each individual fragment in the zoomed-in area. Scale bar, 5 μm. Quantifications are shown in (J). (**J**) Quantifications of fragmented mitotic spreads (percentage of all spreads) in U2OS cells upon N4BP2-GFP-NLS expression for 0, 24, and 48 hours. $n = 3$ independent experiments per condition, minimum 300 cells per experiment. See schematic of experiment and images of representative mitotic spreads in (I). (**K**) Quantifications of percentage of cells with MN in WT U2OS cells (white column) versus 24 and 48 hours of N4BP2-GFP overexpression (red columns). Pie charts below each corresponding condition show percentage of ruptured (blue, numbers) and intact (white) MN. $N = 3$ independent experiments, 219 cells. See fig. S6G for GFP control. (**L**) Percentage of Y chromosome–positive nuclei in long-term cultured (40 passages) WT and N4BP2 KO Dld1-Y^{MN} cells. Schematic of the experiment is shown in fig. S7, A and B. $n = 3$ independent clones per genotype, ≥200 cells per clone. See also fig. S7. ***$P < 0.001$; **$P < 0.01$.

were ruptured and γH2AX-positive (fig. S4, B and C), indicating that envelope rupture is required for N4BP2-mediated DNA damage. Indeed, live-cell imaging (Fig. 2G and fig. S5, A and B) of cells expressing N4BP2-GFP, as well as fixed-cell imaging of endogenous N4BP2 or N4BP2-GFP, revealed rapid entry of N4BP2 into ruptured micronuclei, which was accompanied by the generation of γH2AX foci (Fig. 2, E and F, and figs. S4, B and C, and S8B). Alteration of N4BP2 levels did not change the proportion of ruptured micronuclei (fig. S4, D to F), indicating that N4BP2 acts on micronuclei after rupture rather than inducing rupture itself. Ruptured micronuclei that accumulated endogenous N4BP2 or N4BP2-GFP displayed a peripheral "rim" of DNA [4′,6-diamidino-2-phenylindole (DAPI) or SiR-DNA] surrounding an apparently DNA-free core (Fig. 2, A, F, and G, and figs. S4, A and B, and S5, A and B), a morphology confirmed by correlative light and electron microscopy (fig. S6, A and B).

To determine whether N4BP2 was sufficient to induce DNA damage, we generated a doxycycline-inducible lentiviral construct encoding N4BP2-GFP fused to an NLS (fig. S6C). Induction in N4BP2 KO Dld1-Y^{MN} cells targeted N4BP2-GFP-NLS to otherwise intact nuclei and micronuclei (Fig. 2H and fig. S6, D and E), which triggered robust γH2AX accumulation within 24 to 48 hours in both asynchronous cultures and cells arrested in G1 with palbociclib (Fig. 2H and fig. S6, D and E). Forced nuclear targeting of N4BP2 also caused a rise in chromosome fragmentation and increased fragment number per mitotic spread (Fig. 2, I to K, and fig. S6F), evidence that N4BP2 is sufficient to drive DNA damage and chromosomal shattering when present in intact nuclei.

Consistent with N4BP2-mediated DNA damage and micronuclear chromosome fragmentation, 24 to 48 hours of overexpression of N4BP2-GFP removed DNA from ruptured micronuclei and accelerated their loss (Fig. 2K and fig. S6G). The entry of cytoplasmic nucleases, including N4BP2, might initiate chromothripsis by shattering a micronucleated chromosome; any residual fragments, if incorporated into a daughter-cell nucleus, can be re-ligated into an aberrant chromosome, but without reacquiring a centromere and telomeres, the outcome would be chromosome loss. The human Y chromosome, which is dispensable for viability and has the weakest human centromere (*23*–*25*), provided an ideal readout: Its loss could have resulted from either (i) missegregation of an intact micronucleated Y chromosome that was transmitted to only one of two daughter cells or (ii) nuclease-driven fragmentation and degradation (fig. S7A). In clonal populations of Dld1-Y^{MN} cells expressing endogenous N4PB2 and passaged for >40 generations, the Y chromosome was completely lost (Fig. 2L and fig. S7, B, D, and E), consistent with previous reports of frequent, spontaneous loss of the Y chromosome (*23*–*25*). By contrast, half of the cells in N4BP2 KO clones retained the Y chromosome (Fig. 2L). Moreover, after 10 days of induced Y centromere inactivation (confirmed in fig. S7G), N4BP2 KO cells kept the Y chromosome at up to threefold higher frequency than wild-type (WT) cells (fig. S7, B to E), reinforcing N4BP2's role in the elimination of micronucleated chromosomes.

N4BP2 promotes ecDNA generation

Chromosome bridges, formed during anaphase and persisting into interphase, have been implicated in initiating chromothripsis in cancer, as well as the formation of extrachromosomal DNA (ecDNA) after bridge fragmentation (*1*, *2*, *4*, *10*, *16*, *26*–*28*). These structures are frequently enclosed by aberrant nuclear envelopes (*10*, *15*, *26*, *29*, *30*), thus permitting entry of cytoplasmic nucleases. To test whether N4BP2 contributes to ecDNA formation, we used a model of ecDNA-mediated resistance to chemotherapy (*26*). High-dose methotrexate (MTX, 640 nM), an inhibitor of dihydrofolate reductase (DHFR) and long-used anticancer drug (*31*), induces DHFR amplification through two distinct mechanisms: (i) formation of DHFR-containing ecDNAs via fragmentation of chromosome bridges with amplified DHFR genes (*26*) or (ii) amplification of DHFR genes within homogenously stained regions (HSRs) via breakage-fusion-bridge (BFB) cycles (Fig. 3A and fig. S9A) (*32*).

We showed that N4BP2 localized to chromosome bridges (Fig. 3, B and C), where it colocalized with γH2AX (Fig. 3C). The siRNA-mediated knockdown of N4BP2 (Fig. 3D) in cells exposed to MTX for 10 days led to more than a twofold reduction in ecDNA-positive cells compared with those treated with nonsilencing (NS) siRNA (Fig. 3, E and F). Given that chromosome bridges remain physically connected to the main nucleus, N4BP2 may act not only on DHFR genes amplified in the bridge but also on nearby nuclear DNA by diffusing through the rupture site, potentially compromising cell viability. In support of this view, cells treated with siN4BP2 showed a twofold increase in cell number compared with NS siRNA- or siTREX1-treated cells (fig. S9B). Despite reduced levels of DHFR-containing ecDNAs, these cells retained a selective advantage by amplifying DHFR within DHFR-containing HSRs on chromosome 5 (fig. S9, C to E).

N4BP2 initiates genome rearrangements and chromothripsis

To directly test the role of N4BP2 in inducing chromosomal rearrangements, we transiently expressed low levels of N4BP2-GFP or GFP alone, concurrently with a 72-hour induction of Y chromosome missegregation in Dld1-Y^{MN} N4BP2 KO cells (Fig. 4A). N4BP2-GFP, but not GFP alone, was expected to induce DNA damage within micronuclei, leading to Y chromosome shattering and, in rare cases, reassembly of chromosome fragments into a chromothriptic chromosome. After transient expression of N4BP2-GFP or GFP, we isolated and expanded clonal cell lines from Dld1-Y^{MN} N4BP2 KO cells and assessed genome integrity in each clone ($n = 88$) (Fig. 4, A to G, and fig. S10, A to E) using FISH (Fig. 4C), spectral karyotyping (SKY) (Fig. 4D), whole-genome sequencing (WGS) (Fig. 4, E to G), and optical genome mapping (OGM) (fig. S10C). In agreement with a role for N4BP2 in promoting genome instability, such rearrangements—including translocations (Fig. 4, C to E, and fig. S10, B and C), tandem duplications (fig. S10, D and E), and chromothripsis (Fig. 4G)—were observed exclusively in clonal isolates of N4BP2 KO cells in which N4BP2-GFP had been transiently expressed ("N4BP2-GFP–derived clones") but not in clones expressing GFP alone ("GFP-derived clones") (Fig. 4B). FISH analysis of metaphase spreads through a Y chromosome–specific probe revealed abnormal signal patterns in N4BP2-GFP–derived clones but not in GFP-derived clones (Fig. 4C and fig. S10A). These findings were further corroborated by SKY (Fig. 4D and fig. S10B, top panel), OGM (fig. S10C), and WGS (Fig. 4, E to G, and fig. S10, D to E).

Furthermore, WGS of the parental Dld1-Y^{MN} clone revealed a pre-existing fusion between a nearly full-length chromosome 3 (196.8 Mb) and an extra copy of the first 41.7 Mb of the p arm of chromosome 1, resulting in a 238.5-Mb fusion chromosome (Fig. 4F, "parental chromosome," and fig. S10B, bottom panel). As larger chromosomes are known to missegregate and be incorporated into micronuclei at high frequency (*33*, *34*), the presence of an immobile, centromereless Y chromosome after the induction of micronuclei formation is expected to further hinder the segregation of such large chromosomes. Consistent with this, we identified an N4BP2-GFP–derived clone that, after induced inactivation of the Y centromere, had not only lost the Y chromosome but also exhibited "focal" chromothripsis of the first 41.7 Mb of the chromosome 1 p arm (Fig. 4G, "derivative clone with chromothripsis").

N4BP2 is associated with chromosome rearrangements in cancer

To further investigate the link between N4BP2 and chromosome rearrangements, we analyzed publicly available cancer genome datasets, including 9691 samples from The Cancer Genome Atlas (TCGA) (*35*) and 667 samples from the Pan-Cancer Analysis of Whole Genomes Consortium (*4*). Across multiple cancer types, N4BP2 copy number gains were more frequent than loss-of-function mutations (fig. S11A). Notably, tumors with high N4BP2 expression in the TCGA dataset exhibited a significantly increased prevalence of chromothripsis (Fig. 4H and fig. S11B), with N4BP2 copy number gains associated with

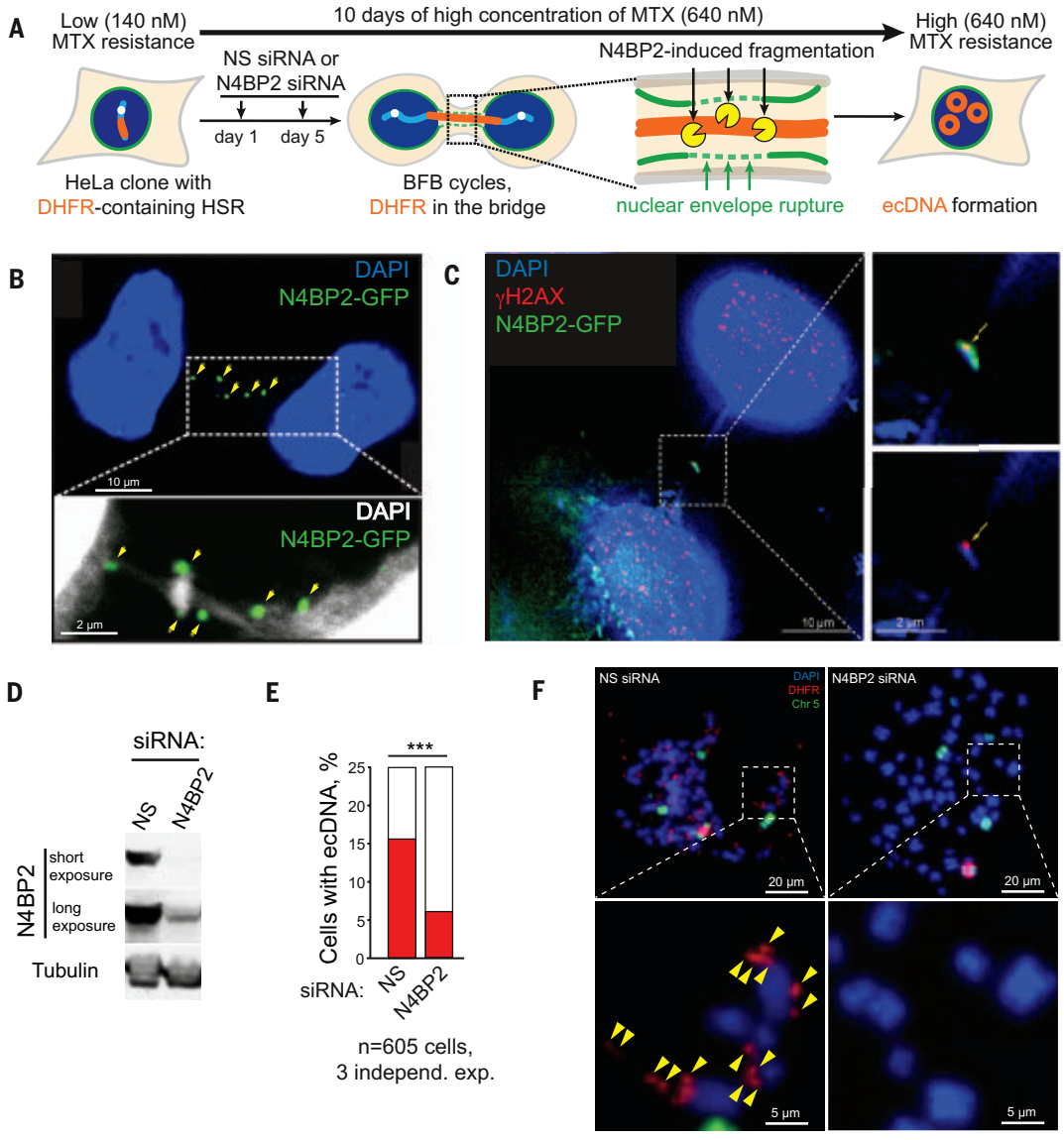


Fig. 3. N4BP2 promotes ecDNA generation. (**A**) Generation of HeLa cells that carry *DHFR*-encoding ecDNA providing resistance to high MTX concentrations. MTX-resistant HeLa clone with amplified *DHFR* gene within the HSR (orange) was treated with high MTX concentration (640 nM) for 10 days, which provided selection pressure and promoted the formation of double minutes (ecDNA) (shown as orange circles). Cells were transfected with indicated siRNAs at day 1 and day 5. N4BP2 is depicted as yellow circles; the ruptured nuclear envelope is represented by a green dashed line. (**B**) Representative image of N4BP2-GFP localizing on a chromatin bridge (yellow arrows) in HeLa clone with amplified *DHFR* gene (zoomed-in view shown below). Scale bars, 10 and 2 µm, as indicated. (**C**) Representative image of HeLa cells from (A) showing colocalization of N4BP2-GFP with γH2AX (red) in the chromatin bridge. Scale bars, 10 and 2 µm, as indicated. (**D**) Immunoblot of N4BP2 with lysates of HeLa cells from (A), transfected with indicated siRNAs. Short and long exposures are shown. Tubulin was used as a loading control. (**E**) Percentage of HeLa cells from (A) with ecDNA, after induction of ecDNA formation with high (640 nM) concentration of MTX for 14 days, treated with indicated siRNAs. $n = 605$ cells from three independent experiments. (**F**) Representative DNA FISH images demonstrating ecDNA-positive mitotic spreads (marked with yellow arrows) upon treatment with NS siRNA versus ecDNA-negative mitotic spreads in N4BP2 siRNA condition. Scale bars, 5 and 20 µm. BFB, breakage-fusion-bridge.

a 3.7-fold increase in chromothripsis ($P = 3.8 \times 10^{-8}$; Fig. 4I). This association was stronger than that observed for *TP53* disruption, the hallmark tumor suppressor gene, which showed a lower odds ratio of 2 (Fig. 4J).

Furthermore, we identified a strong association between elevated N4BP2 expression and an increased number of genomic segments, indicating that tumors with higher N4BP2 levels harbor more complex genomes. This association remained significant after adjusting for both N4BP2 copy number and overall genome aneuploidy (fig. S11C). In addition, tumors with high N4BP2 expression showed a significant increase in the proportion of translocations across the genome (median fold change, 1.26; $P = 0.02$; two-sided Mann-Whitney test; fig. S11D). Elevated *N4BP2* expression was associated with a higher prevalence of genomic amplicons, including ecDNA (odds ratio, 1.38; $P = 0.016$) (fig. S11E). Tumors with high *N4BP2* levels often contained multiple ecDNAs characterized by focal, high-level amplifications (up to 30 copies) across multiple chromosomes. For example, ecDNAs encoding *SOX2* (derived from chromosome 3) were prominent in a lung squamous cell carcinoma with high *N4BP2* levels (Fig. 4K and fig. S11, F and G).

In addition, we performed a comprehensive analysis using the Hartwig Medical Foundation dataset (*36*), a large, well-curated resource containing WGS and matched RNA-sequencing data from 3000 metastatic and

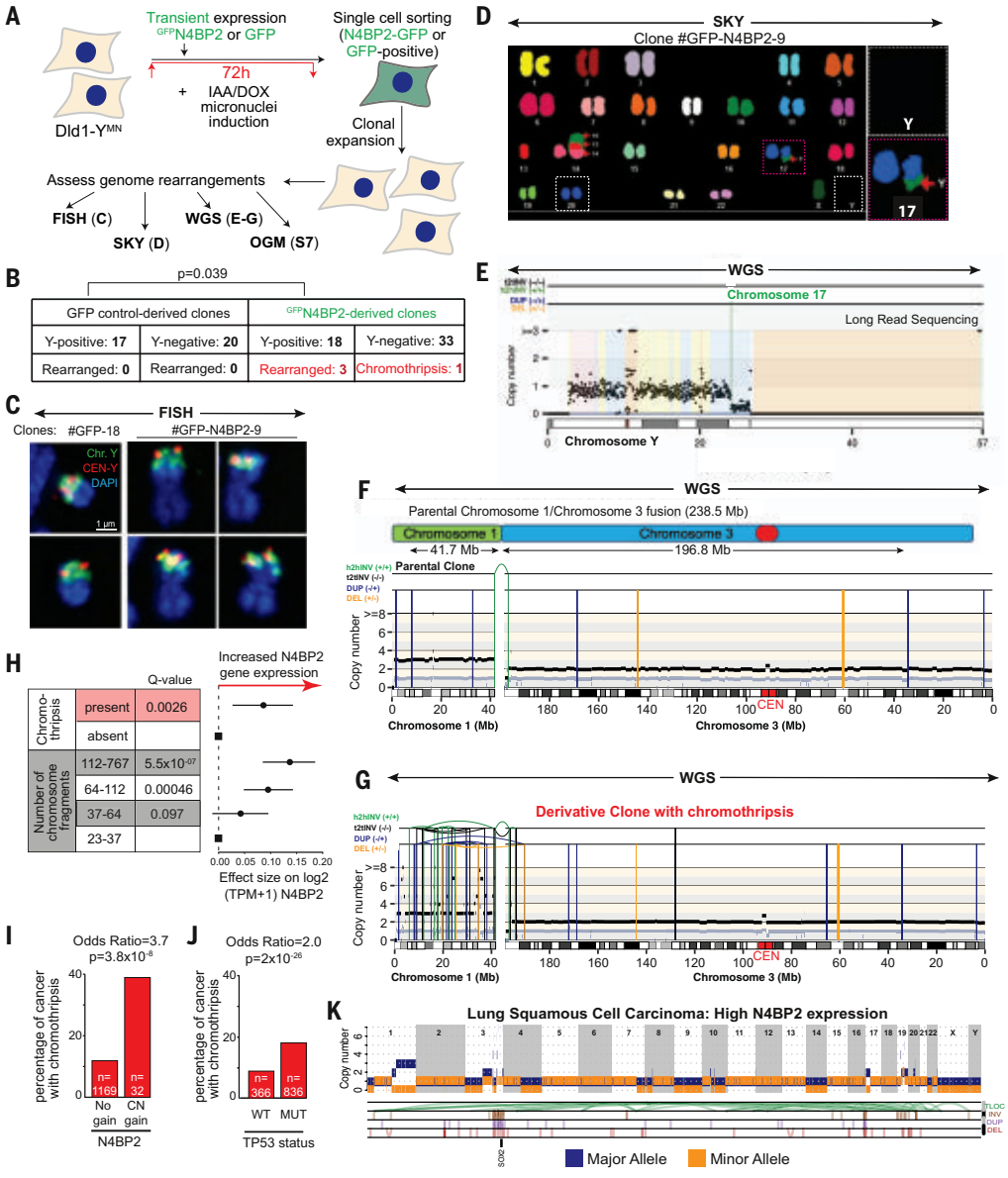


Fig. 4. N4BP2 initiates genome rearrangements and chromothripsis. (**A**) Schematic of a strategy used to assess genome rearrangements induced by N4BP2. Low levels of N4BP2-GFP or GFP were transiently expressed in N4BP2 KO Dld1-Y^{MN} cells; micronuclei were induced by adding DOX/IAA for 72 hours. After single-cell sorting (based on green GFP signal) and clonal expansion, clonal isolates were analyzed by a set of methods (shown below). (**B**) Y chromosome status and chromosomal rearrangements observed in clonal isolates produced in (A). (**C** to **E**) Representative FISH images (C) of a normal Y chromosome without visible defects on metaphase spreads of Dld1-Y^{MN} N4BP2 KO clonal isolate after transient GFP expression (left) and an example of derivative Y chromosomes [also shown with SKY analysis (D) and long-read WGS (E)] from Dld1-Y^{MN}, N4BP2 KO clonal isolate obtained after transient expression of N4BP2-GFP as shown in (A) (right panels). Green, Y chromosome paint probes; red, Y centromere probes; and blue, DAPI. (**F** and **G**) WGS-enabled reconstruction of a preexisting fusion [in a parental clone (F)] between a nearly full-length (196.8 Mb) chromosome 3 and an extra copy of the first 41.7 Mb of the p arm of chromosome 1, producing a large, 238.5-Mb fusion chromosome. (G) N4BP2-GFP–derived clone, in which the first 41.7 Mb of the p arm of chromosome 1 had undergone focal chromothripsis with insertions at three different locations of pieces of chromosome 3 mapped adjacent to the initial chromosome 1–chromosome 3 fusion site. (**H** to **K**) Assessment of the role of N4BP2 in genome rearrangements in cancer using pan-cancer genomics. (H) Independent effect size (*x* axis) of chromothripsis and copy number segmentation (*y* axis) on N4BP2 expression in a multivariate regression model. Chromothripsis is enriched in tumor samples with N4BP2 copy number gains (I), compared with the association of TP53 mutation status [WT indicates no mutation; MUT indicates loss of heterozygosity, homozygous deletion, or driver point mutation or indel (insertion or deletion)] and chromothripsis status across TCGA (two-sided Fisher's exact test) (J). (K) Example of structural variant profile from samples with high expression of N4BP2, exhibiting characteristic signs of ecDNA. Arcs indicate rearrangements between two regions of the genome. CEN, centromere; CN, copy number; DEL, deletion (red); DUP, tandem duplication (purple); INV, inversion (brown); TLOC, translocation (green); TPM, transcripts per million.

primary tumors across diverse cancer types. To test the specificity of N4BP2's association with chromothripsis, we constructed a multivariable model including other genes previously implicated in chromothripsis, such as *TREX1*, *APEX1*, (encoding APE1), and *TP53*. We used both structural equation modeling with the weighted least-squares mean and variance-adjusted estimator, as well as a uniform modeling framework based on generalized linear models (GLMs) (figs. S12 and S13). In addition, we analyzed the TCGA cohort, which is whole-exome sequenced, using GLMs (fig. S14). N4BP2 expression remained significantly associated with chromothripsis in both Hartwig (figs. S12 and S13)

and TCGA datasets (fig. S14), independent of *TP53* status, overall genome complexity, background genomic instability score, and tumor type. These results support the hypothesis that elevated N4BP2 promotes chromosome fragmentation beyond normal expression levels, aligning closely with our experimental data showing that increased N4BP2 activity drives DNA damage, chromosome shattering, and ecDNA formation.

N4BP2-induced DNA damage and ecDNA formation in induced gliomas

Genome rearrangements and ecDNA formation are common features of many human cancers, including glioblastomas, in which they are associated with drug resistance and tumor evolution (*26*, *37*–*39*). To test whether N4BP2 contributes to DNA damage, chromosome fragmentation, and ecDNA formation in vivo, we used an induced high-grade glioma model (*37*) that carries deletion of the *TP53* gene encoding the p53 tumor suppressor and an activating mutation in the gene encoding the platelet-derived growth factor receptor alpha (*PDGFRA*) (deletion of exons 8 and 9a, referred to as $PDGFRA^{\Delta 8\text{-}9}$). This model closely mimics the aggressive, rapidly growing, and invasive behavior characteristic of human glioblastoma (*40*).

We generated *N4BP2* KO, *TREX1* KO, and WT human neural/glial progenitors ("iNPCs") from pluripotent stem cell clones containing *TP53 KO*/$PDGFRA^{\Delta 8\text{-}9}$ driver mutations (Fig. 5A and fig. S15C). These progenitors were engrafted into the brains of *Nod-scid* mice, resulting in the formation of primary glioma tumors ("primary tumor spheres") (*37*). Both iNPCs and primary tumor spheres formed micronuclei spontaneously, with an increased frequency after transient exposure to nocodazole. These micronuclei exhibited ruptured nuclear envelopes, which were indicated with abnormal lamin B1 staining (fig. S15A) (*41*),

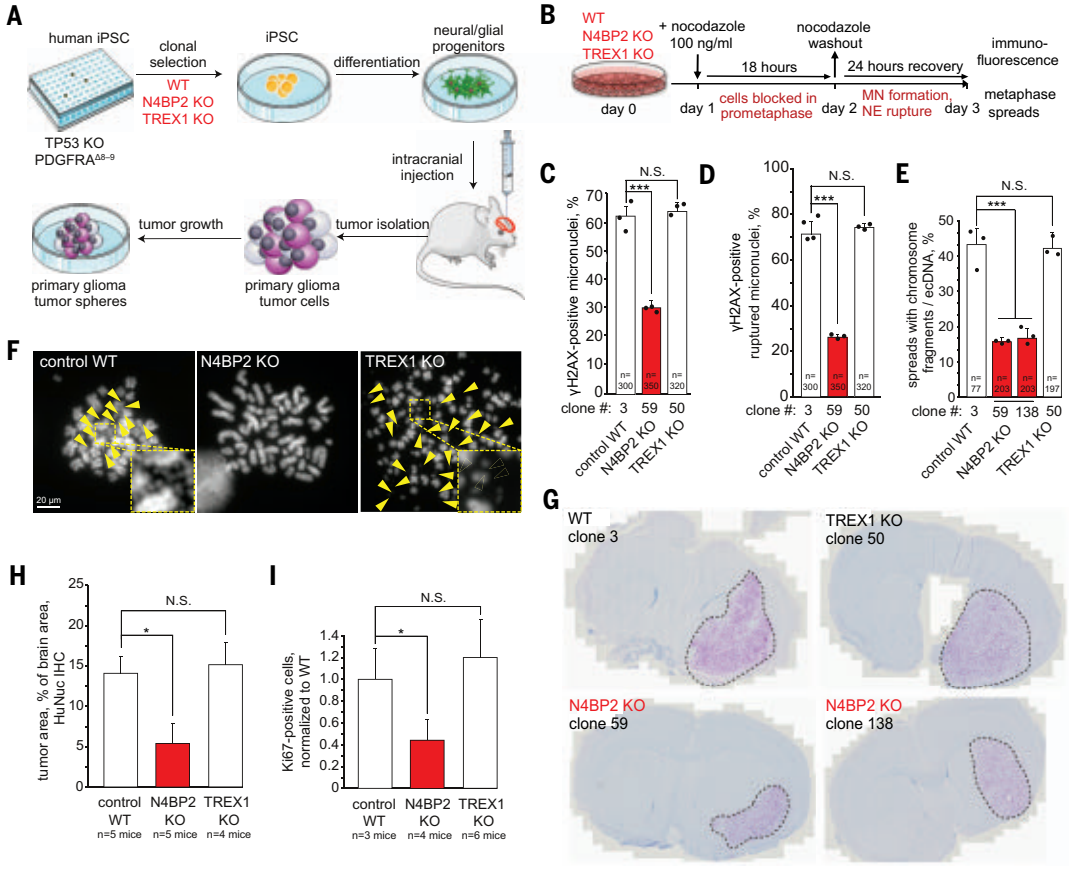


Fig. 5. N4BP2-induced DNA damage and ecDNA formation in induced gliomas. (**A**) Schematic of induced human high-grade glioma generation. Induced pluripotent stem cells (iPSCs) with a combination of driver mutations commonly altered in human glioblastomas were genetically modified (WT, N4BP2 KO, and TREX1 KO) and differentiated into neural/glial progenitor cells, to be intracranially injected into mouse brain to form primary tumors. (**B**) Schematic of the approach used to induce MN in iNPCs and primary tumor spheres [generated as shown in (A)], followed by IF analysis of fixed cells (Fig. 5, C and D, and fig. S12, D and E) and DNA FISH analysis of metaphase spreads (Fig. 5E and fig. S12F). (**C**) Percentage of γH2AX-positive MN in the primary tumor spheres in the absence of N4BP2 or TREX1. $n = 3$ independent experiments per genotype, 970 cells. Three independent experiments per condition. (**D**) Quantification of the fraction of γH2AX-positive ruptured micronuclei (aberrant lamin B1 staining) in primary tumor spheres in the presence and absence of N4BP2 or TREX1. Two independent experiments per genotype, $n = 300$ micronuclei (control), $n = 350$ micronuclei (N4BP2 KO), and $n = 320$ micronuclei (TREX KO). Three independent experiments per condition. (**E**) Quantification of metaphase spreads containing ecDNA in primary tumor spheres in the presence and absence of N4BP2 or TREX1. Three independent experiments per genotype, $n = 77$ spreads (control), $n = 406$ spreads (N4BP2 KO), and $n = 197$ spreads (TREX KO). Three independent experiments per condition. (**F**) Representative images of metaphase spreads in iHGG (induced high-grade glioma) model showing ecDNA (yellow arrowheads); genotypes as indicated. Scale bar, 10 μm. DNA was stained with DAPI (blue). (**G**) Quantification of tumor area on mouse brain sections in the presence and absence of N4BP2 or TREX1 ($n = 5$ mice for control, $n = 5$ mice for N4BP2 KO, and $n = 4$ mice for TREX1 KO). (**H**) Number of dividing tumor cells (Ki67-positive, normalized to WT) in the presence or absence of N4BP2 or TREX1. Sample sizes: $n = 3$ mice (control), $n = 4$ mice (N4BP2 KO), and $n = 6$ mice (TREX1 KO). (**I**) Representative composite images of brain sections showing iHGG tumors, with human nuclei stained in purple and tumor boundaries indicated with dashed lines. Genotypes as indicated. HuNuc, human nuclei; IHC, immunohistochemistry; NE, nuclear envelope.

developed extensive γH2AX-positive DNA damage (fig. S15, A and B), and accumulated N4BP2 (fig. S15B). Loss of N4BP2, but not TREX1, significantly reduced both the production of micronuclei and the occurrence of DNA damage in ruptured micronuclei in iNPCs and primary tumor spheres while decreasing the presence of ecDNA (Fig. 5, B to F, and fig. S15, D to F).

To directly evaluate the impact of N4BP2 on tumor growth and aggressiveness, we analyzed tissue sections from tumors formed by WT, *N4BP2* KO, and *TREX1* KO cells, evaluating both tumor size and the proliferation index of human cancer cells within each tumor. These analyses demonstrated that loss of N4BP2 resulted in less aggressive tumors, characterized by reduced tumor size and fewer proliferating cells compared with tumors formed from WT or *TREX1* KO cells (Fig. 5, G to I).

Discussion

Genome rearrangements are hallmarks of human cancers (*1*, *42*, *43*). Mechanistically, rearrangements can be initiated by DNA double-strand breaks, leading to chromosome translocations, chromothripsis [the major type of chromoanagenesis (*44*)], lost chromosomes, and, in case of circularization of the small remaining fragments, generation of ecDNA. Even as simple an event as a single break, if unrepaired before mitosis, can be sufficient to initiate a chromothriptic cascade in which an acentric chromosome fragment is missegregated into a micronucleus (*45*, *46*). Spontaneous rupture of the micronuclear envelope exposes the previously encapsulated chromatin to cytoplasmic nucleases and chromosome shattering. Using an unbiased cellular screen and multiple cancer cell models, we have identified the largely uncharacterized N4BP2 nuclease to accumulate in foci within ruptured micronuclei (or the main nucleus after envelope breakage in interphase) and induce shattering of cytoplasm-exposed chromosomes, thus initiating multiple rearrangements that can include loss of whole chromosomes, focal chromothripsis, and production of ecDNA. Although N4BP2's structure and in vitro activity have been partially characterized (*47*, *48*), future studies are needed to determine its precise nuclease and/or adenosine triphosphatase activity or activities.

Conceptually, the identification of N4BP2 entry and enhancement of chromatin fragmentation within ruptured micronuclei adds mechanistic support for an "all-at-once" chromosome shattering [as initially proposed (*2*)]. In the broader landscape of human cancer genomes, *N4BP2* amplifications were found in 19 cancer types, with high *N4BP2* expression associated with increased prevalence of chromothripsis, translocations, and ecDNA. Loss of *N4BP2* in a human induced high-grade glioma model led to decreased tumor size and reduced number of micronuclei. Identification of N4BP2 adds a target for potential therapeutic interventions in cancer, with N4BP2 inhibition likely to disrupt initiation of genome rearrangements, including production of ecDNA, and enhancement of its activity expected to selectively target cancer cells with unstable genomes.

REFERENCES AND NOTES

1. K. Krupina, A. Goginashvili, D. W. Cleveland, *Nat. Rev. Genet.* **25**, 196–210 (2024).
2. P. J. Stephens *et al.*, *Cell* **144**, 27–40 (2011).
3. J. O. Korbel, P. J. Campbell, *Cell* **152**, 1226–1236 (2013).
4. I. Cortés-Ciriano *et al.*, *Nat. Genet.* **52**, 331–341 (2020).
5. K. Crasta *et al.*, *Nature* **482**, 53–58 (2012).
6. E. M. Hatch, A. H. Fischer, T. J. Deerinck, M. W. Hetzer, *Cell* **154**, 47–60 (2013).
7. C. Z. Zhang *et al.*, *Nature* **522**, 179–184 (2015).
8. P. Ly, D. W. Cleveland, *Trends Cell Biol.* **27**, 917–930 (2017).
9. P. Ly *et al.*, *Nat. Cell Biol.* **19**, 68–75 (2017).
10. K. Krupina, A. Goginashvili, D. W. Cleveland, *Curr. Opin. Cell Biol.* **70**, 91–99 (2021).
11. T. T. Paull *et al.*, *Curr. Biol.* **10**, 886–895 (2000).
12. P. Trivedi, C. D. Steele, F. K. C. Au, L. B. Alexandrov, D. W. Cleveland, *Nature* **618**, 1049–1056 (2023).
13. I. M. Ward, J. Chen, *J. Biol. Chem.* **276**, 47759–47762 (2001).
14. S. Tang, E. Stokasimov, Y. Cui, D. Pellman, *Nature* **606**, 930–936 (2022).
15. J. Maciejowski, Y. Li, N. Bosco, P. J. Campbell, T. de Lange, *Cell* **163**, 1641–1654 (2015).
16. J. Maciejowski *et al.*, *Nat. Genet.* **52**, 884–890 (2020).
17. T. Diercks *et al.*, *J. Mol. Biol.* **383**, 1156–1170 (2008).
18. E. P. Rogakou, D. R. Pilch, A. H. Orr, V. S. Ivanova, W. M. Bonner, *J. Biol. Chem.* **273**, 5858–5868 (1998).
19. B. M. Sirbu, F. B. Couch, D. Cortez, *Nat. Protoc.* **7**, 594–605 (2012).
20. A. Helmrich, M. Ballarino, L. Tora, *Mol. Cell* **44**, 966–977 (2011).
21. M. T. Hayashi, A. J. Cesare, T. Rivera, J. Karlseder, *Nature* **522**, 492–496 (2015).
22. M. Terradas, M. Martín, L. Tusell, A. Genescà, *DNA Repair* **8**, 1225–1234 (2009).
23. M. Guttenbach, B. Koschorz, U. Bernthaler, T. Grimm, M. Schmid, *Am. J. Hum. Genet.* **57**, 1143–1150 (1995).
24. D. Bachtrog, *Nat. Rev. Genet.* **14**, 113–124 (2013).
25. X. Guo *et al.*, *Hum. Genet.* **139**, 421–446 (2020).
26. O. Shoshani *et al.*, *Nature* **591**, 137–141 (2021).
27. C. Rosswog *et al.*, *Nat. Genet.* **53**, 1673–1685 (2021).
28. R. Gonzalo Parra *et al.*, bioRxiv 2021.06.25.449944 [Preprint] (25 June 2021); https://doi.org/10.1101/2021.06.25.449944.
29. D. R. Hoffelder *et al.*, *Chromosoma* **112**, 389–397 (2004).
30. J. Pampalona, D. Soler, A. Genescà, L. Tusell, *Mutat. Res.* **683**, 16–22 (2010).
31. J. A. Johnston, E. S. Johnson, P. R. Waller, A. Varshavsky, *J. Biol. Chem.* **270**, 8172–8178 (1995).
32. B. McClintock, *Genetics* **26**, 234–282 (1941).
33. S. J. Klaasen *et al.*, *Nature* **607**, 604–609 (2022).
34. T. Bochtler *et al.*, *Genes Chromosomes Cancer* **58**, 392–395 (2019).
35. L. A. Aaltonen *et al.*, *Nature* **578**, 82–93 (2020).
36. F. Martínez-Jiménez *et al.*, *Nature* **618**, 333–341 (2023).
37. T. Koga *et al.*, *Nat. Commun.* **11**, 550 (2020).
38. D. A. Nathanson *et al.*, *Science* **343**, 72–76 (2014).
39. K. M. Turner *et al.*, *Nature* **543**, 122–125 (2017).
40. T. Ozawa *et al.*, *Genes Dev.* **24**, 2205–2218 (2010).
41. N. Y. Chen *et al.*, *Proc. Natl. Acad. Sci. U.S.A.* **116**, 25870–25879 (2019).
42. U. Ben-David, A. Amon, *Nat. Rev. Genet.* **21**, 44–62 (2020).
43. M. R. Stratton, P. J. Campbell, P. A. Futreal, *Nature* **458**, 719–724 (2009).
44. A. J. Holland, D. W. Cleveland, *Nat. Med.* **18**, 1630–1638 (2012).
45. J. S. Z. Li *et al.*, *Nature* **616**, 504–509 (2023).
46. M. L. Leibowitz *et al.*, *Nat. Genet.* **53**, 895–905 (2021).
47. N. Watanabe, S. Wachi, T. Fujita, *J. Biol. Chem.* **278**, 26102–26110 (2003).
48. K. Fukui, S. Kuramitsu, *Mol. Biol. Int.* **2011**, 691735 (2011).

ACKNOWLEDGMENTS

We thank O. Shoshani (Weizmann Institute), P. Ly (Univ. of Texas, Southwestern), and H. Yu (Genentech) for the help with experiments and all current members of Cleveland lab for helpful discussions. We thank D. Pellman (Dana Farber Cancer Center) and S. Tang (Univ. of Virginia) for generating and providing RPE1 cells lacking N4BP2 and for critical scientific inputs and E. Hatch (Hutchinson Cancer Center) for providing plasmids encoding RFP or mCherry tagged with an NLS. The computational analyses reported in this manuscript have used the Triton Shared Computing Cluster at the San Diego Supercomputer Center of UC San Diego. **Funding:** National Institutes of Health (grant R35 GM 122476 to D.W.C.; grants R01ES030993-01A1, R01ES032547-01, U01CA290479-01, and R01CA269919-01 to L.B.A.; and grants R56 NS080939 and R01 CA258248 to F.B.F.). P.T. is supported by a postdoctoral fellowship from the Hope Funds for Cancer Research (no. HFCR 21-04-02). The Ludwig Institute for Cancer Research provided salary support for D.W.C. and F.B.F. and research and salary support for A.K.S.; P.J.C. and J.K. were supported by the core grant from Wellcome Trust to the Wellcome Sanger Institute (220540/Z/20/A). **Author contributions:** Conceptualization: K.K., A.G., and D.W.C. Investigation: K.K., A.G., and D.W.C. Experiments: K.K., A.G., M.W.B., S.M., J.K., C.D.S., P.T., D.L.Z., A.T.N., A.M., D.J., Y.M., T.K., and S.M. Analysis: K.K., A.G., M.W.B., S.M., J.K., C.D.S., P.T., D.L.Z., A.T.N., A.M., D.J., A.K.S., T.K., S.M., F.B.F., P.J.C., L.B.A., and D.W.C. Writing: K.K., D.W.C., A.G., L.B.A., and C.D.S. **Competing interests:** L.B.A. is a co-founder, scientific advisory member, and consultant for io9; has equity; and receives income. The terms of this arrangement have been reviewed and approved by the University of California, San Diego, in accordance with its conflict of interest policies. L.B.A.'s spouse is an employee of Biotheranostics. L.B.A. declares U.S. provisional applications with serial numbers 63/289,601; 63/269,033; 63/483,237; 63/366,392; 63/412,835; and 63/492,348. A.K.S. declares that he has no competing interests but discloses that he is currently an officer, cofounder, and shareholder of FENX Therapeutics. P.J.C. is an academic cofounder of Quotient Therapeutics. D.J. and A.K.S. are employees of FENX Therapeutics, Inc. The other authors declare that they have no competing interests. **Data and materials availability:** All sources of data, codes, and materials are provided in corresponding sections of the materials and methods. All materials are available under materials transfer agreement for noncommercial replication or extension of this work, upon request to corresponding authors. All other information is available in the manuscript or the supplementary materials.

License information: Copyright © 2025 the authors, some rights reserved; exclusive licensee American Association for the Advancement of Science. No claim to original US government works. https://www.science.org/about/science-licenses-journal-article-reuse

SUPPLEMENTARY MATERIALS

science.org/doi/10.1126/science.ado0977
Materials and Methods; Figs. S1 to S15; Table S1; References (*49*–*53*);
MDAR Reproducibility Checklist

Submitted 22 January 2024; resubmitted 28 May 2025; accepted 8 October 2025
10.1126/science.ado0977

EVOLUTION

Infrared radiation is an ancient pollination signal

Wendy A. Valencia-Montoya[1,2]*, Marjorie A. Liénard[3], Neil Rosser[4], Michael Calonje[5], Shayla Salzman[6], Cheng-Chia Tsai[7], Nanfang Yu[7], John R. Carlson[8], Rodrigo Cogni[9], Naomi E. Pierce[1]*† Nicholas W. Bellono[2]*†

Color and scent are well-known pollinator cues. Some plants also produce heat, but its role remains unclear. Here, we report that plant-generated thermal infrared radiation serves as a pollination signal and describe the underlying mechanisms of heat production and infrared detection. Mitochondrial adaptations heat plant reproductive structures in a circadian pattern, radiating infrared that is sufficient to attract beetle pollinators. Beetle antennae contain infrared-activated neurons with thermosensitive ion channels that are structurally tuned to match host plant thermogenesis. Comparative analyses revealed that infrared is among the earliest pollination signals, and indicate a deep-time transition from infrared-based to color-dominated signaling in flowering plants. Our findings uncover an ancient sensory modality shaping the early evolution of pollination, one of the world's most vital processes linking plants and animals.

Plants have evolved an astonishing repertoire of cues to attract pollinators. Although color, scent, and humidity are well-appreciated pollination signals (*1*–*3*), some plants also produce heat (*4*). Similar to endothermic animals, thermogenic plants generate heat as a by-product of cellular respiration (*5*). Thermogenic plants can achieve cellular respiration rates comparable to that of a "hummingbird in flight", leading to an increase in temperature to more than 35°C above ambient temperature (*4*, *6*). Plant thermogenesis has been linked to preventing frost tolerance (*7*), enhancing scent volatilization (*5*, *8*), and providing a warm shelter for pollinators (*9*). However, it may also function as a direct cue (*10*), because thermogenesis occurs exclusively in reproductive organs such as cones (gymnosperms) and flowers (angiosperms), with immense variation in thermal patterns reminiscent of other pollination signals such as color.

Heat produced by flowers and cones can spread through conduction, convection, or infrared radiation (IR). Unlike conduction and convection, IR could represent an effective signal for pollinators because it emanates in all directions and does not require contact. Thermal IR is a sensory cue used by many animals to locate the warm bodies of prey. Snakes, vampire bats, blood-sucking mosquitoes, fire beetles, and flat bugs use IR to localize their endothermic prey, hosts, or forest fires. Considering that most thermogenic plants begin to heat at dusk and are pollinated at night, when IR is especially conspicuous (*5*, *11*), we investigated whether pollinators could use IR as a foraging signal.

Cycads are the oldest living lineage of seed plants pollinated by animals and collectively account for more than half of all known thermogenic plant species (*12*–*16*). These gymnosperms have distinct male and female reproductive organs that are produced on separate plants and engage in daily cycles of volatile emissions that trigger beetle pollinator movement between male (pollen) and female (ovulate) cones (*12*). Extensive fossil evidence suggests that cycad interactions with beetle pollinators are highly specialized and date back at least to the early Jurassic, around 200 million years ago (Ma) (*17*). We therefore focused on cycads and beetles as a model system to investigate the role of thermal IR in plant-pollinator signaling and the early evolution of pollination mutualisms.

Molecular basis of thermogenesis in cycads

We first took thermal images of the cycad *Zamia furfuracea* to confirm that heat production occurs primarily in the sporophylls of pollen-shedding cones (Fig. 1, A to C). Plant thermogenesis is controlled by mitochondrial respiration. During this process, carbohydrates or lipids fuel heat production through alternative oxidase (AOX) or uncoupling proteins, which bypass adenosine 5′-triphosphate (ATP) synthesis to dissipate redox energy as heat (*13*, *18*–*20*). Accordingly, we found that sporophylls from the cycad *Z. furfuracea* contained more mitochondria compared with nonthermogenic tissues and up-regulated *AOX1* just before and during thermogenesis (Fig. 1, D and E, and fig. S1, D to H). We also observed up-regulation of genes related to carbohydrate transport and starch metabolism, as well as numerous starch-filled amyloplasts in sporophyll tissues that were depleted after thermogenesis (Fig. 1, D and E; fig. S2; and tables S1 and S2). These results highlight *AOX1* as a major regulator for respiration across cycads that uses starch as the primary substrate for thermogenesis.

We also found that cones up-regulated circadian clock genes during thermogenesis, including *REVEILLE* (*RVE*) transcription factors, which are involved in afternoon and early evening rhythms (Fig. 1E) (*21*). Indeed, measuring thermogenic activity over time uncovered a strong circadian pattern with a single daily burst of heat production starting in the afternoon and peaking in the early evening (Fig. 1F). We then extended our sampling of thermogenic patterns across the major lineages of the genus *Zamia*, the largest neotropical radiation of cycads, to find that all sampled species were thermogenic and under circadian control (Fig. 1, G and H, and table S3). Thus, thermogenesis in *Zamia* is conserved, energetically expensive, tightly time regulated, and only observed in plant organs involved in pollination (Fig. 1, B and C).

IR is a pollination signal

Cycads are dioecious, with separate male and female plants. We found that in all sampled *Zamia* species, pollen (male) and ovulate (female) plants exhibited distinct circadian dynamics (Fig. 2, A to D, and fig. S3, A to C). Male cones of *Z. furfuracea* heated first and then cooled, whereas female cones entered peak thermogenesis ~3 hours later (Fig. 2D and fig. S3C). This observation led us to investigate the relationship between plant thermogenesis and pollinator behavior. We tracked the movement of *Rhopalotria furfuracea*, the beetle pollinator of *Z. furfuracea*, in an open-field experiment in which female and male plants were placed 50 m apart. By marking beetles with ultraviolet (UV)–fluorescent dyes to track their visits, we discovered that beetles were preferentially drawn to the warmest regions of pollen cones, suggesting that cone thermal patterns might serve as pollination guides (Fig. 2C and figs. S3D and S4). Next, we monitored beetle movement in controlled cages and found that occupancy of male and female cones correlated with the rise and fall of sex-specific cone temperature (Fig. 2D). In fact, we hypothesized that decreases in cone temperature could act as a dynamic signal for the beetles to leave the pollen cones and visit the ovulate cones (Fig. 2D). These experiments demonstrated that beetles actively move between male and female cones during thermogenic events.

In cycads, this "push-pull" pollination mechanism was thought to be primarily driven by the emission of species-specific cone volatiles

[1]Department of Organismic and Evolutionary Biology and Museum of Comparative Zoology, Harvard University, Cambridge, MA, USA. [2]Department of Molecular and Cellular Biology, Harvard University, Cambridge, MA, USA. [3]GIGA Institute, Liège University, Liège, Belgium. [4]Department of Biology, University of Miami, Coral Gables, FL, USA. [5]Montgomery Botanical Center, Coral Gables, FL, USA. [6]Department of Entomology, University of Georgia, Athens, GA, USA. [7]Department of Applied Physics and Applied Mathematics, Columbia University, New York, NY, USA. [8]Department of Molecular, Cellular & Developmental Biology, Yale University, New Haven, CT, USA. [9]Departamento de Ecologia, Universidade de São Paulo, São Paulo, Brazil. ***Corresponding author. Email: wvalenciamontoya@g.harvard.edu (W.V.-M.); npierce@oeb.harvard.edu (N.E.P.); nbellono@harvard.edu (N.W.B.)** †These authors jointly supervised this work.

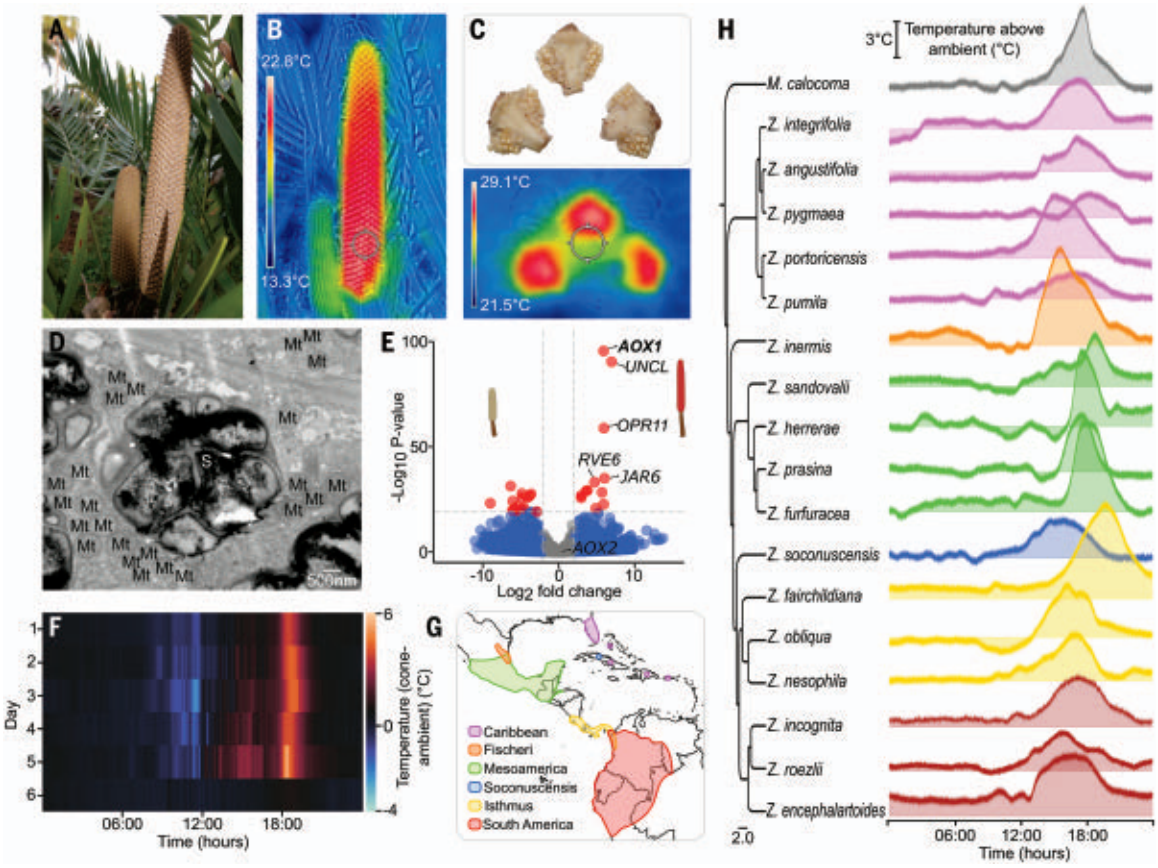


Fig. 1. Thermogenic plants have mitochondrial adaptations to heat their reproductive structures during pollination. (**A**) An open cone of a cycad plant. Cones are the reproductive structures of cycads. (**B**) Thermal infrared image of a cycad male cone heating during pollen release. (**C**) Sporophylls of the cycad *Z. furfuracea* are the primary thermogenic organs. (**D**) Transmission electron micrograph section of a cone sporophyll depicts the densely populated mitochondria (Mt) and starch granules (s) in thermogenic tissues. (**E**) Differential gene expression analysis between nonthermogenic (left) and thermogenic (right) cones. Blue points indicate transcripts with at least a twofold change in expression ($|\log_2 FC| > 2$); red points indicate transcripts meeting this threshold and also showing statistical significance ($-\log_{10} P > 20$). $n = 6$ sporophylls per condition. (**F**) Temperature above or below ambient of a cycad cone releasing pollen over several days. (**G**) Map showing the distribution of all major lineages of *Zamia*, the most diverse genus of neotropical cycads. (**H**) Cone temperature above ambient for 17 different *Zamia* species across all major clades of the *Zamia* radiation "(89 described species) and for the outgroup *Microcycas calocoma*. Colors are the same as for the distributions of *Zamia* clades in (G).

(*12*, *22*). However, the volatiles themselves and other signals, including humidity, can also correlate with plant thermogenesis (*2*, *22*). To tease apart the contribution of heat among these multiple pollination signals, we scanned cycad cones and conducted experiments with artificially heated three-dimensional (3D) models (Fig. 2, E and F). We placed model cones near real cycad plants bearing female or male cones and heated them to match either the average temperature of *Z. furfuracea* cones during thermogenesis or the ambient temperature (Fig. 2, E and F, and fig. S3G). To prevent thermal conduction, models were coated with odorless tangle trap so that beetles would be stuck to cones upon visiting and could not use touch to discern temperature differences between the 3D models; this ensured that temperature was the only variable differing between 3D cones. We found that wild beetle pollinators were more attracted to heated female and male cone models compared with ambient temperature controls (Fig. 2G).

These results suggest that emanating thermal signals such as IR could act as a short- to midrange pollination cue. To further control for convective heat transfer, we devised an enclosure experiment to transmit only thermal IR by covering the heated 3D cones with a polyethylene film (~99% transparent to IR) positioned ~1 cm from the cone surface. In this controlled environment, pollinators preferentially landed on heated female and male cones emitting higher IR, confirming that IR is a pollination signal (Fig. 2H).

Beetle pollinators use specialized antennae to sense IR

We next reasoned that if cycads and their beetle pollinators have evolved a species-specific communication channel, then beetles should also have sensory adaptations for detecting thermal IR. In insects, sensilla are the basic unit of sensory reception, and their morphology and distribution correlate with function (*23*). Most thermosensitive neurons in insects are housed in peg-in-pit coeloconic sensilla, which are small cuticular pits containing sensory pegs (*24*). Therefore, we surveyed coeloconic sensilla in two beetle species, *R. furfuracea* and *Pharaxonotha floridana* (Fig. 3, A to E), both of which are pollinators of thermogenic cycads (*15*, *25*, *26*). In both species, we found that the most distal antennal segment was enriched in sensilla that were morphologically consistent with a thermosensitive function (Fig. 3, A to F, and fig. S5, A to G).

We first used single-sensillum electrophysiology to confirm that sensilla at the antennal tip of the beetle pollinator *P. floridana* were indeed thermosensitive. Heat elicited responses from two morphologically distinct coeloconic sensilla: the first housed a neuron that responded instantly to increased temperature (Fig. 3, G and H), and the second consisted of two classes of neurons that were activated and inhibited by heat (Fig. 3, G and H, and fig. S5, J and K). By contrast, hair-like mechanosensory sensilla responded to touch but not temperature (Fig. 3, G and H). To investigate whether these thermosensitive structures are important for thermal IR sensation, we measured

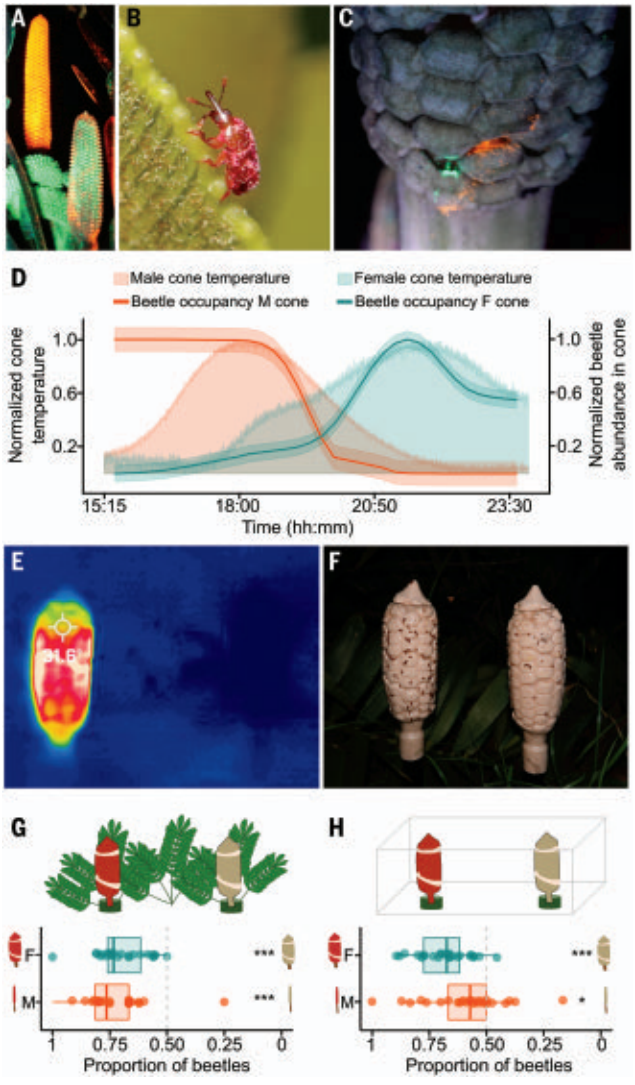


Fig. 2. Thermal IR is a pollination signal for specialized beetle pollinators. (**A**) Male cones of the cycad *Z. furfuracea* releasing pollen marked with UV-fluorescent dyes to track beetle movement. (**B**) A beetle pollinator (*R. furfuracea*) covered in pollen and UV-fluorescent dyes while carrying pollen from male to female plants. (**C**) Female cone of *Z. furfuracea* showing marks of fluorescent dyes left by beetle pollinators during pollen transfer. (**D**) Beetle occupancy of male and female cones during thermogenesis. n = 570 beetles in male cones; n = 278 beetles in female cones. (**E**) Field experiments using heated (left) and nonheated (right) 3D-printed models of female cones. (**F**) Beetle pollinator visits to artificially heated 3D-printed cones (left) versus those at ambient temperature (right). (**G**) Proportion of beetles visiting heated (left) and nonheated (right) 3D-printed models of male and female cones in field experiments. Female cones: n = 25 experiments, n = 1025 beetles, $P < 0.0001$. Male cones: n = 31 experiments, n = 518 beetles, $P < 0.0001$. (**H**) Proportion of beetles visiting heated (left) and nonheated (right) 3D-printed models of male and female cones in cage experiments controlling for conductive and convective heat. Female cones: n = 26 experiments, n = 1187 beetles, $P < 0.0001$. Male cones: n= 25 experiments, n = 1154 beetles, $P < 0.001$. Boxplots represent the interquartile range, and midlines represent the median.

the behavioral responses of immobilized beetles to thermal IR and used a cone odorant (methyl salicylate) as a positive control (Fig. 3I and figs. S5L and S6). Beetles responded to both cues, but only thermal IR responses were abolished by microdissection of the thermosensitive antenna tip (Fig. 3, I and J). These results suggest that beetles detect IR using specialized sensilla at the tips of their antennae.

TRPA1 underlies IR sensing in beetles

To determine the molecular basis of IR sensation, we first performed transcriptome analysis in beetle antennae and other reference organs from *P. floridana*. Transcripts from candidate thermosensitive genes were enriched in the antennae, including *GR28b* (Gustatory Receptor 28b), *IR21a* (Ionotropic Receptor 21a), and several splice variants of *TRPA1* (Transient Receptor Potential Ankyrin 1) (Fig. 4A). In situ hybridization showed that beetle *TRPA1* was restricted to distinct sensory neurons in the most distal antennal segment, which is required for IR sensation (Fig. 4, B and C). *GR28b* and *IR21a*, which detect heating (*27*) and cooling (*28*), respectively, were not coexpressed with *TRPA1* (fig. S7, A to D). Instead, *GR28b* and *IR21a* colocalized within different sensilla, consistent with functional measurements demonstrating two neurons with contrasting responses to temperature (figs. S5K and S7, A to D). Opsins can colocalize with *TRPA1* to facilitate thermal IR sensation in mosquitoes (*29*), but we did not detect opsin expression in the beetle antenna (fig. S9A).

TRPA1 contributes to IR perception in snakes and mosquitoes (*29*, *30*), suggesting that it has a convergent role as a thermal IR sensor across diverse taxa. Because transcripts for a short isoform (B) of *TRPA1* were the most highly expressed in the beetle antenna, we further investigated its putative function as a thermoreceptor using patch-clamp electrophysiology (Fig. 4D). Heterologous expression of *P. floridana TRPA1*(B) exhibited robust responses to temperatures even just slightly above ambient (Fig. 4D and fig. S7). To determine whether *TRPA1*(B) contributes to beetle IR sensation, we exploited the observation that *TRPA1*(B) has ancestral electrophile sensitivity and screened 30 putative antagonists of *TRPA1*(B) using calcium imaging. Whereas common antagonists of vertebrate, fly, and mosquito *TRPA1* failed to block beetle *TRPA1*, we identified AM-0902 as a potent blocker of beetle *TRPA1* (fig. S7, F to I). Ectopic application of AM-0902 to the beetle antennae abolished behavioral responses to thermal IR, but did not affect responses to cone odorants (Fig. 4E and fig. S7E).

We reasoned that if beetle *TRPA1*(B) is specialized for IR sensation, then it should exhibit structural adaptations that enhance thermal sensitivity. To determine the structural basis of heat sensitivity in beetle *TRPA1*(B), we leveraged comparative analysis with *TRPA1*(A), the second most highly expressed isoform in beetle antennae (Fig. 4A). Sequence analysis and AlphaFold (*31*) modeling revealed that the isoforms only differed in a relatively small region, with *TRPA1*(B) having a shorter N terminus (Fig. 4F). Despite exhibiting only this subtle difference, *TRPA1*(B) had significantly greater thermosensitivity compared with *TRPA1*(A) ($P < 0.0001$; Fig. 4G). *R. furfuraceae*, a distantly related beetle species that is also a pollinator of thermogenic cycads, also had *TRPA1*(B) that exhibited enhanced thermosensitivity relative to its *TRPA1*(A) (Fig. 4G). Isoform-specific differences in *TRPA1* thermosensitivity are also present in fruit flies and mosquitoes (*32*), and our findings in beetles suggest that *TRPA1* splicing evolved at least 300 Ma. Additionally, selection analyses of insect *TRPA1*(B) revealed that the N terminus is a hotspot for adaptive evolution (Fig. 4H). Even among beetle pollinators of thermogenic plants, the N terminus exhibited the highest divergence, highlighting its potential role as a modulatory region controlling thermosensitivity properties.

If *TRPA1*(B) is involved in sensing plant species–specific IR signals for pollination, then we hypothesized that species-specific activation ranges would reflect temperature profiles reached by their respective thermogenic host plants. Indeed, *P. floridana TRPA1*(B) exhibited robust heat-evoked activity to temperatures in the thermal range of its thermogenic host plant (*Zamia integrifolia*; Fig. 4, I and J). Similarly, *TRPA1*(B) from the beetle *R. furfuraceae* exhibited a distinct thermal activation range that was differentially tuned to its specific host plant (*Z. furfuracea*) temperature range during thermogenesis (Fig. 4, I and J). These beetle pollinators, from families separated by >140 Ma (*33*), are both attracted to IR signals, suggesting that IR detection may be a widespread

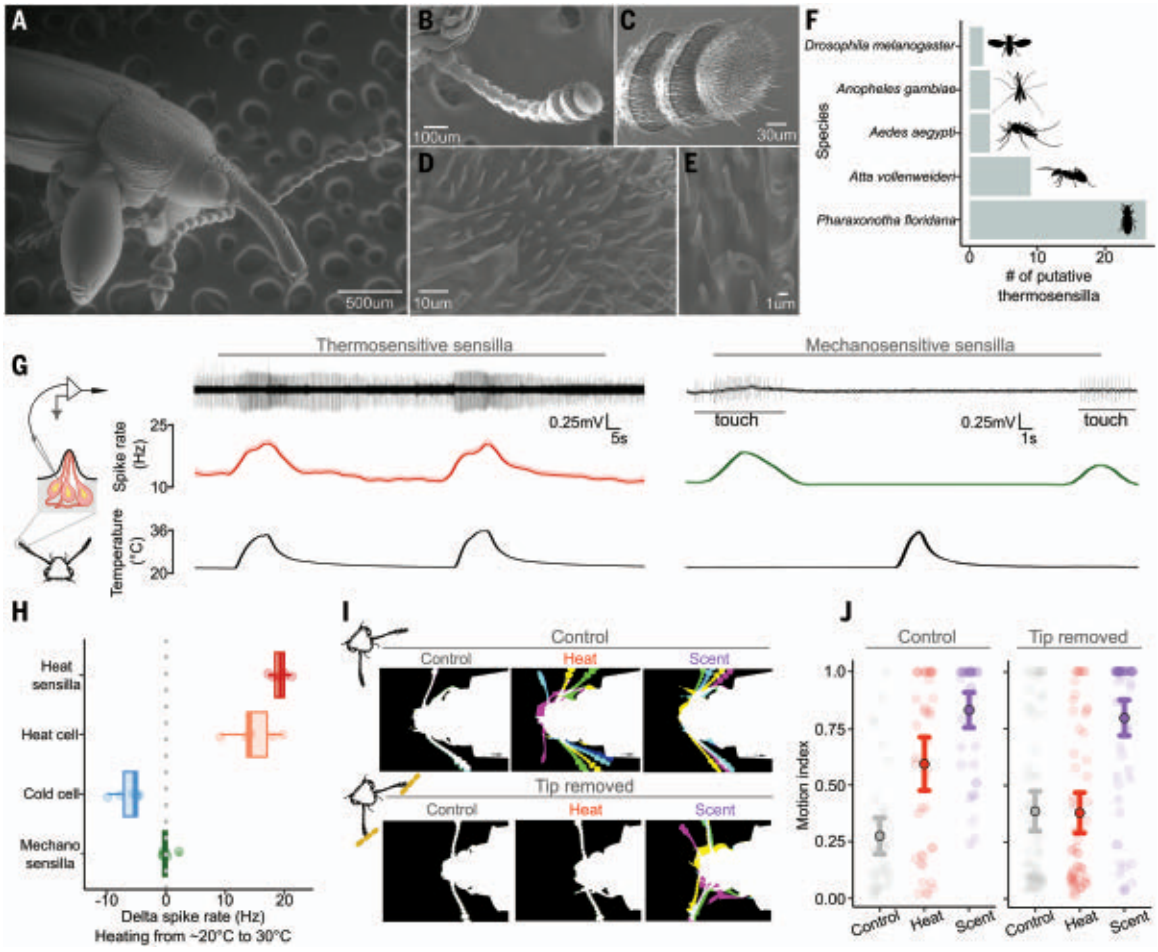


Fig. 3. Pollinators of thermogenic plants have specialized organs at the tip of their antennae to sense thermal radiation. (**A**) Scanning electron micrograph (SEM) images of the beetle pollinator *R. furfuracea*, which pollinates the thermogenic plant *Z. furfuracea*. (**B**) SEM image of an antenna from the beetle pollinator *P. floridana*, which pollinates the thermogenic plant *Z. integrifolia.* (**C**) SEM image of the last three antennal segments of *P. floridana* showing the sensory organs (sensilla). (**D**) Magnified view of sensilla diversity in the terminal antennal segment of *P. floridana*. (**E**) SEM image showing the morphology of a thermosensitive coeloconic peg-in-pit sensillum in the terminal antennal segment of *P. floridana*. (**F**) Number of thermosensitive sensilla ("thermosensilla") in different insect species. (**G**) Left, neuronal responses to heat radiation from a single thermosensitive sensillum located in the terminal antennal segment of the beetle *P. floridana*. Right, neuronal responses to heat radiation and touch from a mechanosensitive sensillum in the terminal antennal segment. (**H**) Changes in firing rate from different antennal sensilla in response to heating from ~20° to ~30°C ($P < 0.0001$ for thermosensitive sensilla responses to heat, $n = 6$ to 7 sensilla; boxplots represent interquartile range, and midlines represent median). (**I** and **J**) Antennal movements of beetle pollinators with (control) and without the last antennal segment (tip removed) in response to heat radiation and cone scent. Colors represent different time frames indicating antennae movement. $n = 40$ to 67 beetles. Error bars represent the 95% confidence interval, and midpoints represent the mean.

strategy among pollinators of thermogenic plants. Thus, our data suggest that *TRPA1*(B) might play an important role in IR sensation and mutualistic plant-pollinator signaling, in contrast to IR detection being previously associated with predation or parasitism (*29*, *30*).

IR signaling predates flower colors

Flowers and cones serve as "billboards" using multiple signals to lure pollinators (*1*). These signals can be effective hierarchically at different spatial and temporal scales (*1*). Floral scent, a long-range signal widely used across seed plants (fig. S8), can attract pollinators over meters (*3*). However, scent becomes uninformative at close range without additional short-range cues such as colors that guide pollinators to nectar (*1*, *3*). We discovered that IR is effective at short- and midrange distances, advertising cones that release and receive pollen. Given the dominance of color as a cue in these ranges, we investigated, in a comparative framework, whether it complements or is redundant to thermal IR by mapping both signals across seed plants.

If ancient plant-pollinator interactions rely on metabolic signals rather than color, then flower and cone colors would probably exhibit lower chromatic contrast under vision models of early pollinators. To investigate beetle color vision, we mined opsins from our transcriptome dataset, identifying a UV and a long-wavelength (LW) opsin (figs. S9 and S10A). Using heterologous expression and spectrophotometry, we found that the UV and LW opsins showed maximum absorbance spectra (λ_{max}) at ~374 nm (UV) and ~490 nm (green) (Fig. 5, A and B). This dichromatic visual system in cycad pollinators is consistent with beetles having lost the short-wavelength opsin from a trichromatic insect ancestor (*34*) (fig. S9).

We next evaluated whether cones and flowers present salient visual signals to key pollinators, including beetles, bees, and butterflies. We recorded reflectance spectra of cones from 23 cycad species (Fig. 5C and fig. S10C) and gathered reflectance spectra data across 1000 species of flowering plants from the FReD database (*35*) (fig. S10B). We mapped both cone and flower reflectance spectra into the respective color space models of the different pollinators (Fig. 5, D to F). Cone spectra did not overlap with beetle opsin sensitivities, suggesting poor discrimination under beetle vision (Fig. 5C). By contrast, flowers exhibited higher chromatic contrast under the visual model of more

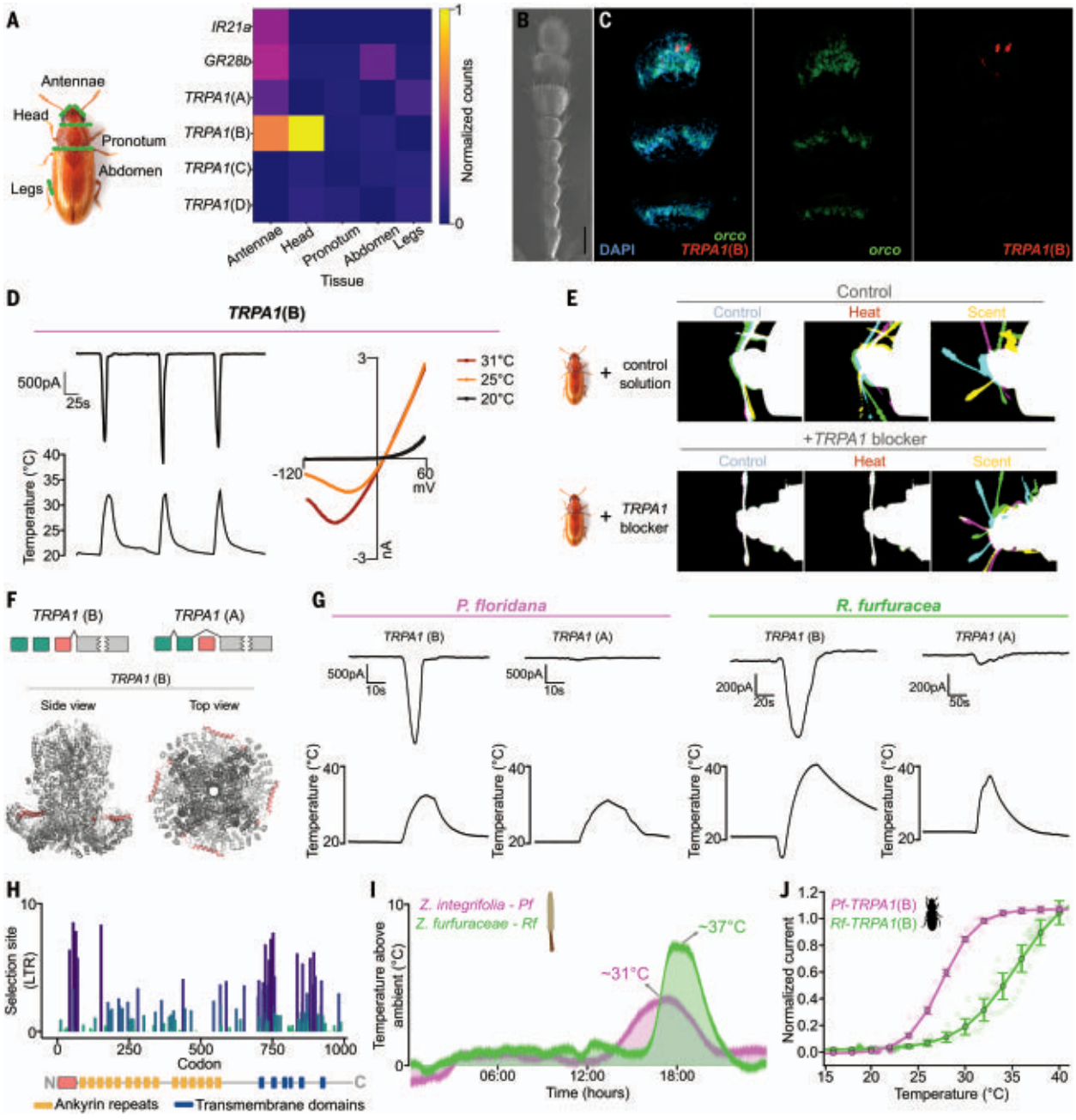


Fig. 4. Molecular basis of IR sensing in pollinators of thermogenic plants. (**A**) Left, beetle tissue samples used for comparative transcriptomics. Right, expression of candidate thermosensitive genes in different organs of the beetle pollinator *P. floridana*. (**B**) SEM image of a beetle antennae. Scale bar, 100 μm. (**C**) In situ hybridization of the last three antennal segments of the beetle pollinator *P. floridana* showing the expression of the candidate thermosensitive gene *TRPA1*(B) and the olfactory sensory neuron marker *orco*. (**D**) Temperature-dependent currents of heterologously expressed *TRPA1*(B). $n = 9$ cells, $P < 0.0001$. (**E**) Antennal movement of beetle pollinators to heat radiation and cone scent for beetles untreated and treated with the *TRPA1* antagonist AM-0902. $n = 32$ beetles, $P < 0.0001$. (**F**) *TRPA1*(B) and *TRPA1*(A) splice isoforms. Colored blocks represent exons that are alternatively spliced (top). AlphaFold structure highlights in color the position of the amino acids encoded by the exon, which is unique to the *TRPA1*(B) variant. (**G**) Temperature-dependent currents of *TRPA1*(B) and *TRPA1*(A) compared across two beetle pollinators (*P. floridana* and *R. furfuracea*). $n = 6$ to 9 cells, $P < 0.0001$. (**H**) Selection analysis of *TRPA1*(B) across >50 species from different insect orders. (**I**) Thermogenic profiles of plants pollinated by *P. floridana* (*Z. integrifolia*, lower temperature, pink) and *R. furfuracea* (*Z. furfuracea*, higher temperature, green). Data are representative of $n = 4$ to 25 plants. (**J**) Heat responses of *TRPA1*(B) channels from *P. floridana* (pollinates lower-temperature cones, pink) and *R. furfuracea* (pollinates higher-temperature cones). $n = 3$ to 9 cells. Error bars represent standard error of the mean.

recent pollinators such as bees and butterflies (Fig. 5, E and F, and fig. S10D). These findings support a shift from ancient metabolic signaling to the diversification and stunning elaboration of color signals characteristic of flowering plants today (Fig. 5H).

To test this pattern, we mapped thermogenesis and color diversity across major families of seed plants. We surveyed the literature (*35*–*38*) and the TRY Plant Trait Database (*39*) and developed an AI pipeline to extract large-scale color data from community-science platforms. We found that thermogenesis has evolved independently in cycads and angiosperms and is disproportionately represented in early-diverging lineages of seed plants (Fig. 5, G and H, and fig. S12), consistent with the fossil evidence (*40*). By contrast, more recently diversified lineages,

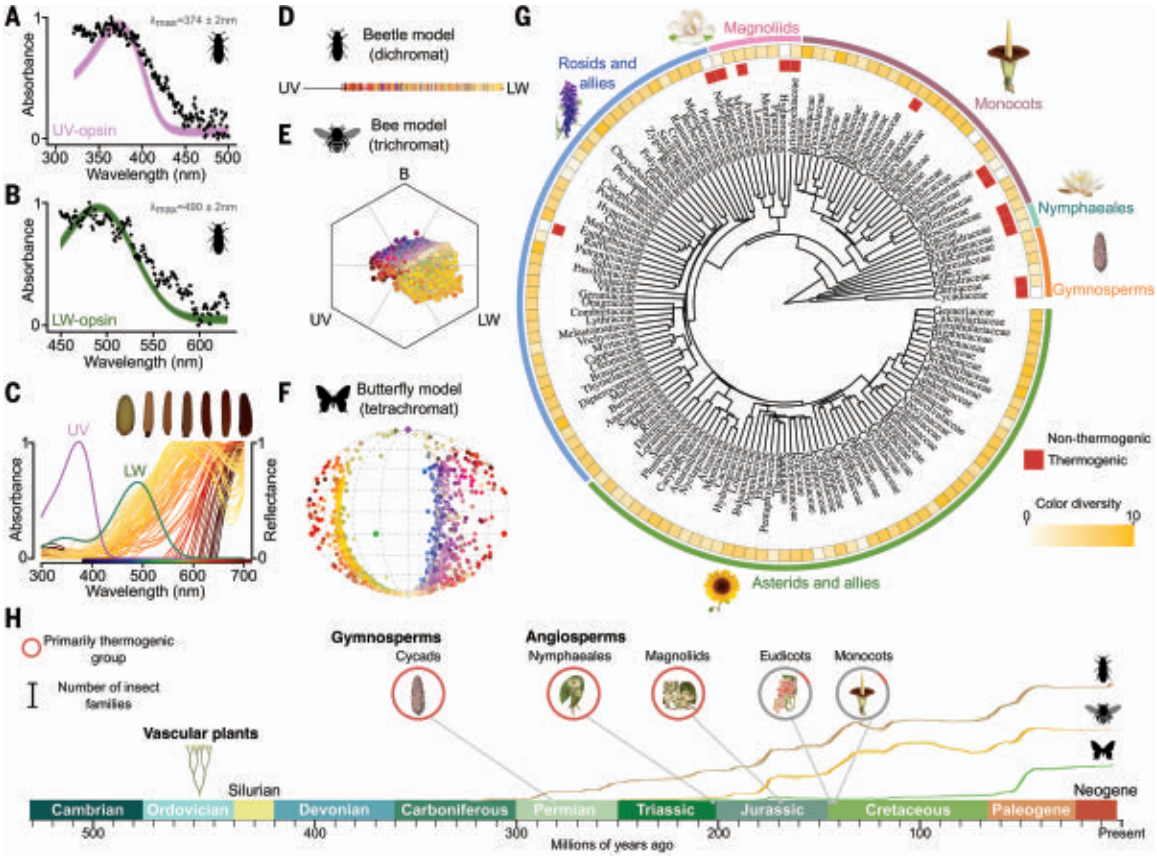


Fig. 5. Thermogenesis is an ancient pollination signal exhibiting a trade-off with color diversity. (**A** and **B**) Absorbance spectra of the two purified beetle opsins, UV and LW. (**C**) Absorbance spectra of the two beetle visual opsins UV and LW with the reflectance spectra of cycad cones pollinated by beetles ($n = 115$ cones, $n = 5$ samples across 23 species). The cones above the plot are representative of the color variation across species. (**D** to **F**) Reflectance spectra of >1000 species of cycads and flowering plants as modeled with the dichromatic visual system of a cycad beetle pollinator (D), the trichromatic visual system of a bee pollinator (E), and the tetrachromatic visual system of a butterfly pollinator (F). Each point represents a cone or flower color projected into the pollinator's perceptual space. Distances between points indicate perceptual contrast; the farther apart, the more distinguishable the colors appear to that visual system. For reference, points are colored using human vision approximations of the color produced by the spectra. (**G**) Thermogenesis and color diversity mapped as traits onto the phylogeny of seed plants (Spermatophyta). (**H**) Timeline of major plant clade evolution and accumulated diversification of insect families through geological time for three large pollinator insect orders: Coleoptera (beetles), Hymenoptera (bees, wasps, and ants), and Lepidoptera (moths and butterflies). Bayesian diversification rates are as estimated in (*41*) using the family-level fossil dataset from (*42*). The scale bar for the number of insect families represents 25 lineages.

such as the rosids and asterids, exhibit diverse colors and are characterized by metabolic investments in a broad range of floral pigments (Fig. 5G). Maximum likelihood models revealed a negative correlation between thermogenesis and color diversity ($P = 1.14 \times 10^{-9}$; figs. S10E and S11 and table S6), indicating an evolutionary trade-off whereby seed plant families that exhibit thermogenesis show low color diversity and vice versa. This negative trade-off is likely mediated by functional redundancy of pollination signals, different metabolic costs associated with heat and color pigment production, and the exploitation of sensory biases of diverse primary pollinator groups.

To further explore the shift from IR- to color-based pollination, we estimated the origin of thermogenesis and gathered fossil data on thermogenic plants and insect pollinators. Because cycads are the oldest living plants pollinated by animals, we first performed ancestral state reconstruction of thermogenesis in this group to pinpoint the evolution of this pollination strategy (fig. S13). We then surveyed family-level fossil records of thermogenic plants (*40*) (table S7) and recent Bayesian estimates of diversification rates for major pollinator insect orders (*41*, *42*) (Fig. 5H and table S8). Collectively, these data support that: (i) thermogenesis evolved at the base of Cycadales in the early Permian (~275 Ma) and represents one of the most ancient pollination syndromes (figs. S12 and S13 and tables S7 and S8); (ii) beetles were ancestrally nocturnal, dichromatic, and among the earliest pollinators of seed plants (*17*, *40*, *43*) (Fig. 5H, figs. S9 and S14, and table S8); and (iii) beetle diversification predated the rise of polychromatic pollinator lineages such as bees and butterflies, which evolved largely concurrently with the adaptive radiation of modern flowering plants, particularly after 50 Ma (*41*, *42*) (Fig. 5H, fig. S9, and table S8). These findings point to an evolutionary shift in pollination signaling strategies that coincided with changes in dominant pollinator groups, each characterized by distinct sensory biases.

Discussion

The evolution of pollination reflects the interplay between plant signals and pollinator sensory abilities. Early pollinator interactions likely recruited ancient molecular machinery already present in plant metabolism and pollinators' senses. Here, we found that the molecular bases of thermogenesis and IR sensing involve the ancient proteins AOX1 and TRPA1, respectively. Although widespread in plants (*44*) and animals (*45*), the up-regulation of these proteins supports specialized adaptations for heat production and detection. The regulatory nature of these adaptations likely contributed to their evolution, with

AOX1-driven thermogenesis emerging independently in nonflowering and flowering plants (*13, 19, 20*) and TRPA1-mediated IR sensation evolving in distantly related beetle pollinators, mosquitoes (*29*), and snakes (*30*). Thus, thermogenesis and IR sensing represent remarkable cases of convergence, where selection repeatedly coopted the same molecular toolkit to enhance thermal signaling and perception across diverse lineages.

Once sensory biases for metabolic cues such as heat evolved in gymnosperm pollinators, early pollinators may have exploited similar cues in nascent groups of flowering plants. Although cycads are currently the most threatened plant order (*46*), they were considerably more diverse and ecologically dominant during the Mesozoic (*47*), coexisting with early-diverging lineages of angiosperms. Fossil evidence from the mid-Cretaceous supports host plant shifts of cycad beetle pollinators to basal angiosperm lineages such as water lilies (Nymphaeaceae) (*43*), which, like cycads, are thermogenic. This early establishment of thermogenesis and IR signaling between gymnosperms and beetles likely set the stage for efficient, insect-mediated pollination at the onset of flowering plants.

Although the earliest flowers were mostly thermogenic and visually inconspicuous (*40*, *48*), color-based syndromes now dominate modern ecosystems. This transition in signaling did not coincide with the origin of flowers (*41*). Instead, this shift occurred alongside the expansion of major groups of diurnal pollinators such as bees and butterflies (*41*), which have retained and elaborated trichromacy. Beetle pollinators of thermogenic plants are dichromatic, yet recent radiations of beetle groups that visit flowers show opsin duplications with putative tri- and tetrachromatic visual systems but only in diurnal species (*49*). These large-scale patterns underscore how pollinator sensory systems are primary drivers shaping the evolution of floral traits. Indeed, as different plant lineages rose to ecological dominance, their signals evolved to tap into the preexisting sensory biases of the widespread pollinator groups. More broadly, our results suggest that metabolic cues such as IR played a pivotal role in the early evolution of biotic pollination, one of the most transformative mutualisms for ecosystems in Earth's history.

REFERENCES AND NOTES

1. R. A. Raguso, *Curr. Opin. Plant Biol.* **7**, 434–440 (2004).
2. S. Salzman *et al.*, *Curr. Biol.* 0 (2023).
3. A. Dahake *et al.*, *Nat. Commun.* **13**, 7773 (2022).
4. R. S. Seymour, P. Schultze-Motel, *Endeavour* **21**, 125–129 (1997).
5. L. B. Thien, H. Azuma, S. Kawano, *Int. J. Plant Sci.* **161** (S6), S225–S235 (2000).
6. C. Lance, *Plant Sci. Lett.* **2**, 165–171 (1974).
7. R. M. Knutson, *Science* **186**, 746–747 (1974).
8. B. J. D. Meeuse, I. Raskin, *Sex. Plant Reprod.* **1**, 3–15 (1988).
9. R. S. Seymour, C. R. White, M. Gibernau, *Nature* **426**, 243–244 (2003).
10. M. J. Harrap, S. A. Rands, N. Hempel de Ibarra, H. M. Whitney, *eLife* **6**, e31262 (2017).
11. R. M. Borges, H. Somanathan, A. Kelber, *Q. Rev. Biol.* **91**, 389–418 (2016).
12. S. Salzman, D. Crook, J. D. Crall, R. Hopkins, N. E. Pierce, *Sci. Adv.* **6**, eaay6169 (2020).
13. Y. Ito-Inaba *et al.*, *Plant Physiol.* **180**, 743–756 (2019).
14. W. A. Valencia-Montoya, D. Tuberquia, P. A. Guzmán, J. Cardona-Duque, *Arthropod-Plant Interact.* **11**, 717–729 (2017).
15. W. Tang, *Bot. Gaz.* **148**, 165–174 (1987).
16. H. Qian, J. Zhang, *J. Syst. Evol.* **52**, 423–430 (2014).
17. C. Cai *et al.*, *Curr. Biol.* **28**, 2806–2812.e1 (2018).
18. C. Claudel, O. Loiseau, D. Silvestro, S. Lev-Yadun, A. Antonelli, *Plant J.* **115**, 874–894 (2023).
19. A. Zulfiqar *et al.*, *PNAS Nexus* **3**, pgae492 (2024).
20. R. Li, J. Li, S. Wang, R. Wang, *Int. J. Mol. Sci.* **23**, 11950 (2022).
21. C. L. Hughes, Y. An, J. N. Maloof, S. L. Harmer, *Plant Direct* **8**, e573 (2024).
22. I. Terry, G. H. Walter, C. Moore, R. Roemer, C. Hull, *Science* **318**, 70–70 (2007).
23. E. Hallberg, B. S. Hansson, *Microsc. Res. Tech.* **47**, 428–439 (1999).
24. M. Nagel, C. J. Kleineidam, *Front. Behav. Neurosci.* **9**, 240 (2015).
25. K. J. Norstog, D. Wm. Stevenson, K. J. Niklas, *Biotropica* **18**, 300–306 (1986).
26. W. Tang, *Am. J. Bot.* **74**, 90–99 (1987).
27. L. Ni *et al.*, *Nature* **500**, 580–584 (2013).
28. C. Greppi *et al.*, *Science* **367**, 681–684 (2020).
29. A. Chandel *et al.*, *Nature* **633**, 615–623 (2024).
30. E. O. Gracheva *et al.*, *Nature* **464**, 1006–1011 (2010).
31. J. Abramson *et al.*, *Nature* **630**, 493–500 (2024).
32. K. Kang *et al.*, *Nature* **481**, 76–80 (2011).
33. D. D. McKenna *et al.*, *Proc. Natl. Acad. Sci. U.S.A.* **116**, 24729–24737 (2019).
34. C. R. Sharkey *et al.*, *Sci. Rep.* **7**, 8 (2017).
35. S. E. J. Arnold, S. Faruq, V. Savolainen, P. W. McOwan, L. Chittka, *PLOS ONE* **5**, e14287 (2010).
36. M. Shrestha *et al.*, *Data Brief* **54**, 110512 (2024).
37. A. Gutiérrez *et al.*, *Sci. Data* **12**, 594 (2025).
38. E. Narbona *et al.*, *Sci. Rep.* **15**, 15927 (2025).
39. J. Kattge *et al.*, *Glob. Chang. Biol.* **26**, 119–188 (2020).
40. D. Peris *et al.*, *Nat. Plants* **10**, 1297–1303 (2024).
41. D. Peris, F. L. Condamine, *Nat. Commun.* **15**, 552 (2024).
42. F. L. Condamine, M. E. Clapham, G. J. Kergoat, *Sci. Rep.* **6**, 19208 (2016).
43. D. Peris *et al.*, *iScience* **23**, 100913 (2020).
44. R. J. Weaver, A. E. McDonald, *Biochim. Biophys. Acta Bioenerg.* **1864**, 149003 (2023).
45. W. A. Valencia-Montoya, N. E. Pierce, N. W. Bellono, *Annu. Rev. Cell Dev. Biol.* **40**, 353–379 (2024).
46. M. P. Griffith *et al.*, *Int. J. Plant Sci.* **176**, 1–10 (2015).
47. M. Coiro, L. J. Seyfullah, *Commun. Biol.* **7**, 328 (2024).
48. H. Sauquet *et al.*, *Nat. Commun.* **8**, 16047 (2017).
49. C. R. Sharkey, G. S. Powell, S. M. Bybee, *Front. Ecol. Evol.* **9**, 676369 (2021).

ACKNOWLEDGMENTS

We thank the Montgomery Botanical Center for providing infrastructure for fieldwork, sample collection, and behavioral experiments, with special thanks to P. Griffith, J. Tucker Lima, M. J. Sanín, X. Gratacos, D. Tucker, and V. Ramirez; the Carlson lab at Yale University, particularly H. Dweck and Y. Luo, and the Garrity lab at Brandeis University for support with single sensillum recordings; E. Soucy and Y. Li at the Harvard Center for Brain Science for help with scanning and printing cycad cones for behavioral experiments, advice on heat delivery systems, and assistance with spectrometer measurements of cycad cones; M. Ericsson and A. Nordstrom at the Harvard Medical School Electron Microscopy Facility for support with imaging; W. Tang and P. Skelley for providing beetle specimens for molecular and behavioral experiments; M. Tevelonis from Botanics Wholesale for generously donating potted cycads for field experiments; the Kampong National Tropical Botanical Garden, the Fairchild Botanical Garden, and the Medellín Botanical Garden (JAUM); B. de Bivort, B. Farrell, and S. Eddy for guidance; C. Allard, P. Villar del Rio, and J. Thibodeau for help with electrophysiology, RNAscope, and behavioral experiments; all members of the Pierce and Bellono labs and members of the Losick, Nett, and Elya labs for their valuable discussions on this work; and G. M. Montoya Giraldo and G. Valencia Ramos for support and encouragement throughout all stages of this project. **Funding:** This work was supported by a Lemann grant to N.E.P and R.C.; a Mind, Brain, and Behavior Interfaculty grant to N.E.P. and N.W.B.; a Harvard Museum of Comparative Zoology Putnam Expedition grant to W.A.V.-M.; a New York Stem Cell Foundation grant to N.W.B.; FRS-FNRS grant MISU F6002.24 to M.A.L.; National Institutes of Health grant R35GM142697 to N.W.B.; a Moore Foundation EPI grant 11561 to N.Y. and C.-C.T. a Harvard OEB and MCZ fellowship to W.A.V.-M.; a Fulbright-Colciencias Fellowship to W.A.V.-M.; and a Harvard Ashford Fellowship in the Natural Sciences to W.A.V.-M. **Author contributions:** Conceptualization: W.A.V.-M., N.E.P., N.W.B.; Formal analysis: W.A.V.-M.; Funding acquisition: N.E.P., R.C., M.A.L., W.A.V.-M., N.W.B.; Investigation: W.A.V.-M., M.A.L., N.R., M.C.; Methodology: W.A.V.-M., N.E.P., N.W.B.; Project administration: N.E.P., N.W.B.; Resources: W.A.V.-M., M.A.L., N.R., M.C., S.S., C.-C.T., N.Y., J.C., R.C., N.E.P., N.W.B.; Supervision: N.E.P., N.W.B.; Visualization: W.A.V.-M.; Writing – original draft: W.A.V.-M., N.W.B.; Writing – review & editing: W.A.V.-M., M.A.L., N.R., M.C., S.S., C.-C.T., N.Y., J.C., R.C., N.E.P, N.W.B. **Competing interests:** The authors declare no competing interests. **Data and materials availability:** All transcriptomic data are available through the Sequence Read Archive (SRA) repository under BioProject accession codes PRJNA1315209 (beetles) and PRJNA1315211 (cycads). *Z. furfuracea* sequences: SRR35626714-SRR35626720; *R. furfuracea* sequences: SRR35658691 to SRR35658697; *P. floridana* sequences: SRR35626828-SRR35626832. Other data are available in the main text, the supplementary materials, and the references therein. **License information:** Copyright © 2025 the authors, some rights reserved; exclusive licensee American Association for the Advancement of Science. No claim to original US government works. https://www.science.org/about/science-licenses-journal-article-reuse

SUPPLEMENTARY MATERIALS

science.org/doi/10.1126/science.adz1728
Materials and Methods; Figs. S1 to S14; Tables S1 to S8; References (*50–114*);
MDAR Reproducibility Checklist

Submitted 20 May 2025; accepted 8 October 2025

10.1126/science.adz1728

THERMAL MANAGEMENT

Mesoporous optically clear heat insulators for sustainable building envelopes

Amit Bhardwaj[1]†, Blaise Fleury[1]†, Bohdan Senyuk[1,2]†, Eldho Abraham[1,2]†, Jan Bart ten Hove[1]†, Taewoo Lee[1,2]†, Vladyslav Cherpak[1]†, Ivan I. Smalyukh[1,2,3,4]*

Mesoporous materials exhibit highly controlled nanoscale structures, often templated by liquid crystalline assemblies of surfactants, with emergent and often designable physical properties. However, scaling their fabrication to be suitable for uses such as envelopes of buildings is challenging. In this work, we describe fabrication of flexible square-meter-sized films and multicentimeter-thick slabs made of three-dimensional spatial graphs of mesopore tubes that have all structural features under 50 nanometers. A solution-based kinetic fabrication process templates growing networks of cylindrical surfactant micelles with thin tubes of polysiloxane-forming gel networks and, upon replacing surfactants and solvents with air, yields lightweight materials with greater than 99% visible-range optical transparency and approximately 10 milliwatts per kelvin per meter thermal conductivity. Such predesigned metamaterials enable transparent thermal barriers for wall-grade insulated glass units, square-meter window retrofits, and unconcentrated solar thermal energy harnessing.

Buildings are responsible for consuming ~40% of all generated energy globally, and much of that energy is wasted in heating and cooling the building interior (*1*–*7*) because building envelopes commonly lack the ability to passively maintain the temperature needed for a comfortable indoor environment. Windows of buildings leak much of the cooling and heating energy (*2*–*5*): Despite constituting on average only ~8% (often ~30% in modern high-end homes) by area of the building envelopes, they are responsible for ~50% of the heat transfer (*2*–*5*). Approaches that aim to address this challenge involve transparent cellulose or silica aerogels and vacuum-insulated glass units, but their deployment is still challenged by issues such as scaling limitations, seal integrity, and high manufacturing costs (*2*–*14*). Recently, cellulose-based aerogel films could be scaled in lateral dimensions while achieving optical characteristics acceptable for window retrofitting applications (*11*), although their thickness could not be scaled beyond several millimeters while retaining transparency, which limits the overall thermal resistance that could be achieved in window units and retrofits. The high nanometers-to-micrometer polydispersity of pores in conventional aerogels is the primary contributor to their hazy appearance, making it difficult for aerogels to meet the stringent optical requirements for applications in windows (*7*–*14*), as well as making them less effective as thermal barriers (*15*, *16*). Despite the recent progress in meticulous nanoscale morphology control (*3*–*14*), the intrinsic limitations of conventional aerogels stem from the lack of well-defined length-scale controlling pores to stay much smaller than both the wavelength of light and mean free path of air molecules at ambient conditions (~60 nm), which is needed to achieve high optical transparency and low thermal conductivity in porous materials (*4*).

Mesoporous materials, including mesoporous silicas, have been developed to exhibit highly controlled monodisperse pores, which are often templated by means of lyotropic liquid crystalline mesophases or kinetic processes that involve mesoscale self-organization of micelles (*17*–*23*). However, such materials have not been reported to be manufactured on building-relevant scales. Similarly, the target physical properties such as thermal insulation and optical transparency have not been systematically studied or optimized.

We report optically transparent, highly thermally insulating preengineered metamaterials made from mesopore networks of polysiloxane tubes as a viable alternative for window insulation (*24*). By tuning mesoscale structure and solid content, we achieved thermal conductivity of 10 to 12 mW K^{-1} m^{-1}, which is much lower than that of still air (~27 mW K^{-1} m^{-1}), as well as average visible-range light transmission >99% (much higher than <92% of glass) with a haze coefficient <1%. We scaled production of these mesoporous optically clear heat insulators (MOCHIs) to square-meter lateral dimensions and slab thicknesses >3 cm, to overall building-relevant scales, while retaining their thermal and optical properties. We fabricated wall-grade insulated glass units with thermal resistance $R \approx 2.64$ m^2 K W^{-1} (15 $foot^2$·hours °F Btu^{-1}) and greater for geometric form factors (thickness) comparable with that of conventional double-pane windows, while also meeting stringent requirements for such glazing applications. Additionally, we demonstrated how such transparent insulation allows for efficient harnessing of unconcentrated solar thermal energy. MOCHI metamaterials could potentially help convert inefficient building envelopes into energy-generating autonomous power plants.

Fabrication of slabs and films of MOCHI metamaterials

By using an optimized procedure that leveraged the out-of-equilibrium self-assembly of surfactant molecules into graph-like networks, which then templated networks of thin nanotubes of polysiloxane to eventually yield our predesigned MOCHI metamaterials (Fig. 1, C to J, and figs. S1 and S2), we fabricated square-meter films and multicentimeter-thick slabs (Fig. 1, A and B; figs. S3 and S4; and movies S1 and S2). Briefly, methyl trimethoxy silane (MTMS) was added to a solution of an aqueous cetylpyridinium chloride (CPCL) surfactant, followed by additions of glacial acetic acid to hydrolyze the silane. Tetramethyl ethylene diamine (TEMED) was used to cross-link the polysiloxane network (tables S1 and S2) (*24*). This mixture was transferred to a prefabricated mold, which was sealed and then kept in a closed chamber to complete gelation at 55°C within 12 to 72 hours, for sample thicknesses of 0.5 to 37.5 mm, respectively (*24*). After removal from the mold, the polysiloxane hydrogels were washed with water and transferred to ethanol at 40°C. Repeated washing with fresh or distilled ethanol completed the solvent exchange and removed the surfactant (*24*). Subsequent carbon dioxide (CO_2)–based supercritical drying replaced ethanol with CO_2 that was then exchanged with air within the mesoporous tubular networks after removal by use of a custom-built supercritical dryer (fig. S3F). The ensuing highly porous MOCHI metamaterials were predesigned to have a polysiloxane solid content of only 5 to 15% by volume (Fig. 1 and fig. S5), fabricated according to recipes shown in tables S1 and S2 (*24*).

Transmission electron microscopy (TEM) imaging and tomographic reconstruction (Fig. 1, C to F; fig. S1; and movies S3 and S4) confirmed that MOCHIs were composed of graph-like networks of thin bicontinuous tubes of polysiloxane. The inner pore diameters were roughly twice the length of CPCL surfactant molecules, and their nanometer-scale thickness and density varied with porosity (Fig. 1, C to I) (*24*). Dimensions of outer internanotube network pores were typically ~30 nm or less. The nanotube orientations exhibited weak orientational correlations with respect to the geometry of the slabs or films that was related

[1]Department of Physics, University of Colorado Boulder, Boulder, CO, USA. [2]International Institute for Sustainability with Knotted Chiral Meta Matter (WPI-SKCM^2), Hiroshima University, Higashi-Hiroshima, Hiroshima, Japan. [3]Materials Science and Engineering Program, University of Colorado Boulder, Boulder, CO, USA. [4]Renewable and Sustainable Energy Institute, National Renewable Energy Laboratory and University of Colorado Boulder, Boulder, CO, USA. ***Corresponding author. Email: ivan.smalyukh@colorado.edu**
†These authors contributed equally to this work.

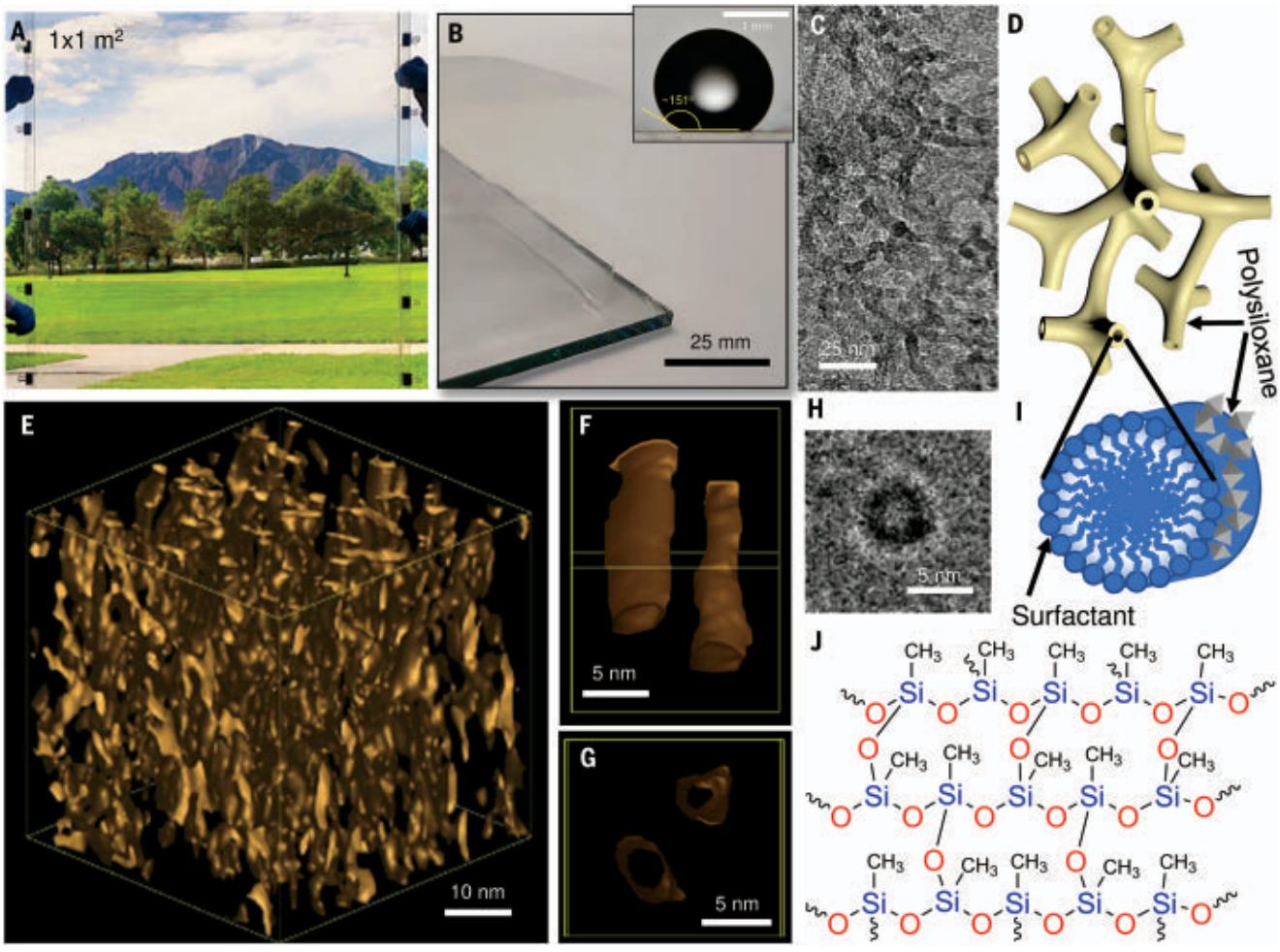


Fig. 1. Large-scale MOCHI metamaterials and their nanoscale morphology. (**A**) Optical photograph illustrating high transparency of a square-meter retrofit with 3-mm-thick MOCHI atop a plastic film. (**B**) A corner perspective view of a 5-cm-thick highly transparent MOCHI slab atop a glass plate. (Inset) A water droplet atop of MOCHI, with a large contact angle highlighting superhydrophobicity (*24*). (**C**) TEM image of a MOCHI, revealing the graph-like networks. (**D**) Corresponding schematic illustration of the nanotube graph network. (**E**) TEM tomographic reconstruction of the nanoscale morphology of MOCHI, demonstrating the orientationally orderly arrangement of hollow polysiloxane tubes within a graph-like network. (**F** and **G**) Zoomed-in tomographic reconstructions of two individual nanotubes viewed from mutually orthogonal perspectives. (**H**) TEM image of an edge-on-oriented polysiloxane tube templated by a cylindrical micelle of surfactant molecules, as shown in (**I**) the schematic. (**J**) Polysiloxane network within the walls of nanotubes.

to the symmetry-breaking at the fabrication-stage solvent exchange and drying (*24*).

The morphology of MOCHIs (Fig. 1D) is much different from that of common aerogels that are typically composed of networks of interconnected particles such as nanospheres and nanofibers with polydisperse pore dimensions that span many orders of magnitude (*4*–*11*), often from nanometers to tens of micrometers. Controlling pore and nanoparticle dimensions in nanocellulose and silica aerogels has been instrumental for achieving desired properties (*4*–*11*) such as optical transparency. However, progress has been limited, and so far, thick slabs of transparent aerogels have not been reported. By exploiting the surfactant self-assembly into cylindrical micellar networks as a guiding mechanism for nanotemplating polysiloxane, we define dimensions of inner pores of nanotubes, distances between them within the graph-like networks, as well as their large-scale partial orientational order and anisotropic properties (Figs. 1 and 2).

Optical, thermal, and other properties

Our MOCHI metamaterials were highly transparent (Figs. 1, A and B, and 2; figs. S6 to S9; and movies S5 to S8), effectively behaving like "frozen air," in contrast to hazy conventional aerogels that are often referred to as "frozen smoke." In Fig. 2B, we illustrate the dramatic differences between transmission of light incident obliquely on edge faces of MOCHIs and conventional window glass, in which glass is nontransparent for large incidence angles owing to the large contrast between refractive indices of glass (1.52) and air (1.0003). Because the refractive index of MOCHIs (1.025 to 1.030) nearly matched that of air, MOCHIs remained highly transparent even at large incidence angles (Fig. 2, A to D). The very small <0.03 difference between the indices of air and MOCHIs as compared with that of glass (>0.5) also caused the net total measured reflection from two MOCHI-air interfaces to be ≈0.02%, which is much lower than the corresponding ~8% reflectivity value for a slab of glass (Fig. 2D, inset).

Furthermore, even the very low reflection from air-MOCHI interfaces disappeared when two slabs of MOCHI were pressed against each other to achieve optical contact (Fig. 2, E and F, and movie S2), which was easier to achieve than with glass because of the comparatively soft nature of MOCHIs. As a result, >99% of normally incident visible light was transmitted, with ≈99.7% visible-range transmission measured with the help of an integrating sphere (*24*). Transmittance remained high (>90%) even for incidence angles >70° and over the entire visible spectrum (Fig. 2, B and F, and fig. S6). Conventional

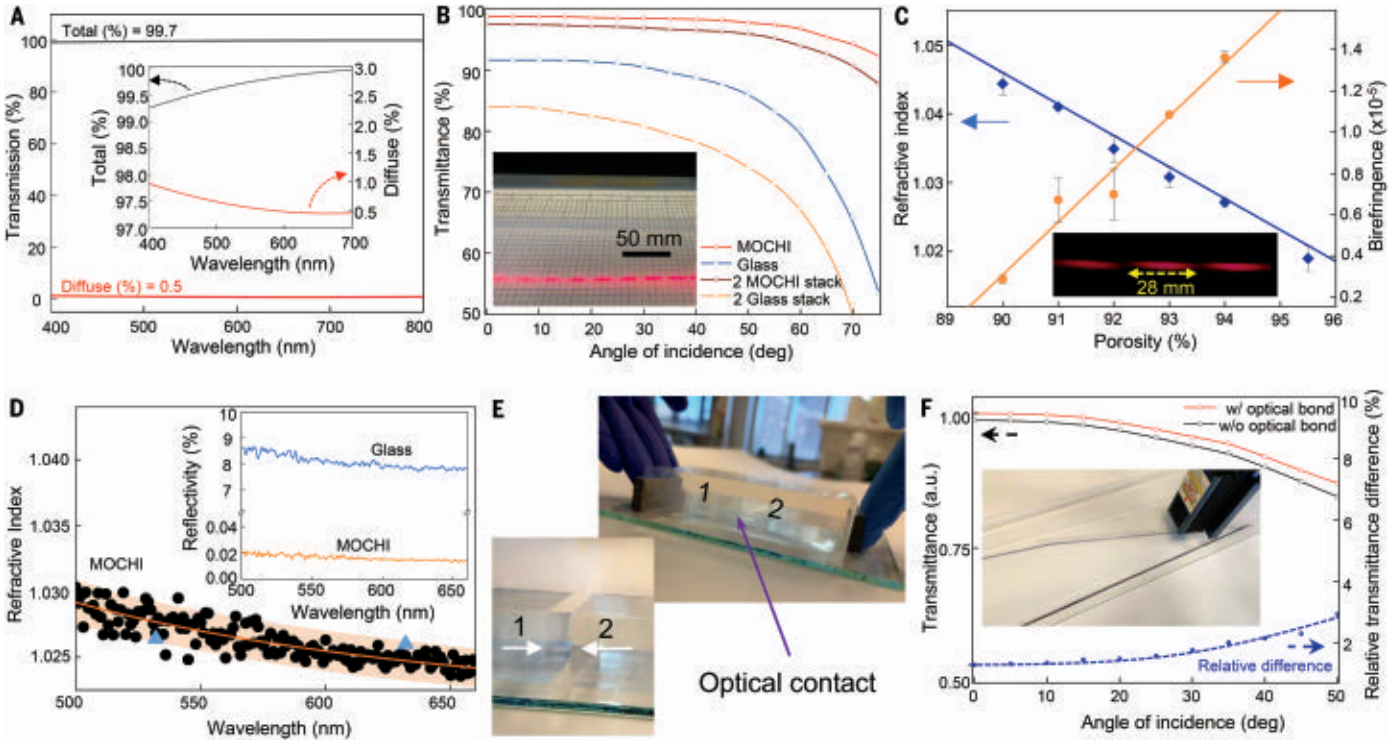


Fig. 2. Optical properties of MOCHI. (**A**) Total and diffuse transmission of 1-mm-thick MOCHI versus wavelength, showing a high average transparency of 99.7% with haze <1%. (Inset) Details of these dependencies. (**B**) Angular dependencies of transmittance for thin MOCHI films for single- and double-stacked MOCHI films as compared with glass counterparts, demonstrating >90% transmittance even at high incidence angles. (Inset) Laser light propagation through monocrystal-like monolithic MOCHI, with the periodic scattered light modulation arising from its birefringence properties. (**C**) Refractive index and birefringence versus porosity of MOCHI. Circular and diamond symbols indicate experimental data; the orange line is based on linear fitting. The refractive index dependence was fit (blue line) with a Arago-Biot relation averaging refractive indices of polysiloxane (1.457) and air (1.0003) at 632 nm, weighted by their volume fractions (*24*). (Inset) A zoomed-in view of modulated scattering laser light traversing through the metamaterial, on a dark background. (**D**) Variation of the average effective refractive index of MOCHI within the visible spectrum, derived from spectral reflectivity measurements. (Inset) Comparison of the spectral dependencies of reflectivity of MOCHI and glass. Blue triangles indicate the data points from independent measurements made by using laser light (*24*). (**E**) Photographs showing two 1-inch-thick MOCHI slabs achieving optical contact upon being pressed toward each other. Photographs were taken under illumination that was optimized to allow visibility of slabs that are generally "invisible" owing to weak surface reflections and transparency. (**F**) Normalized transmittance of MOCHI slabs in (E), before and after optical bonding for different incidence angles, indicating the relative transmittance improvement upon bonding. (Inset) Laser cutting multicentimeter-thick MOCHI slab placed atop glass, defining the shape printed on white underneath.

laser cutting (Fig. 2F, inset, and movie S7) allowed fabrication of multicentimeter-thick slabs of MOCHIs of arbitrary geometric shapes that could be invisibly tiled with other slabs through the creation of optical contacts (*24*).

The morphology of partially orientationally ordered polysiloxane nanotubes (Fig. 1, D to G) led to optical birefringence in the range of 0.2×10^{-5} to 1.4×10^{-5} (Fig. 2C and fig. S8), with the optical monocrystal-like ordering maintained over meter-scale dimensions of slabs defined by the directionality of solvent exchange and drying (*24*). Birefringence increased with porosity and showed a trend different from that of the effective refractive index (Fig. 2C).

Periodically modulated scattering of a laser beam traversing through the slab (Fig. 2, B and C, insets, and fig. S9A) vividly illustrates birefringence properties of these materials on large scales. The $L_s \sim 2.5$ cm modulation period of scattered light corresponds to the beam's polarization state changes from linear to circular (strong scattering) and back to linear (weak scattering) caused by the MOCHI's macroscopic optical-monocrystal-like anisotropic properties. The phase difference between ordinary and extraordinary modes changed by π as the light traversed the distance corresponding to the ~2.5-cm-scale L_s (*24*), within which the beam's polarization state changed from linear to circular (strong scattering) and back to linear (weak scattering). This birefringence is inconsequential for the main envisaged applications of MOCHI as transparent thermal insulators but may find other applications, such as in polarizing optics. The very high visible-range optical transparency also yielded a high color rendering index >99% (*24*), so that viewing through MOCHI preserved natural colors (fig. S9B).

Mesoporous morphology was key to enabling the thermal properties of MOCHIs (Fig. 3A and figs. S10 to S12). Because the pores were much smaller than the mean free path between collisions of air molecules at ambient temperatures and pressures (60 to 70 nm), these molecules collide with the pore walls more often than with each other, so gas conduction of nanoconfined air was strongly inhibited. The tubular polysiloxane network of MOCHIs was also a poor thermal conductor because of its geometric complexity, poor thermal contacts at tubular junctions, and small solid fraction by volume.

The interplay between the conduction contributions caused by the gas and solid network was generally more complex than for conventional aerogels with polydisperse random pores because MOCHIs' inner pores of tubes were monodisperse and small (~5 nm), whereas the 20- to 30-nm intertube pores were controlled by porosity (Fig. 1, C to H). These structural aspects may be a source of apparent two local minima on thermal conductivity versus porosity dependencies (Fig. 3A), although future studies will be needed to confirm this hypothesis. Furthermore, the polysiloxane within MOCHIs strongly absorbed radiation in most of the thermal infrared range that corresponds

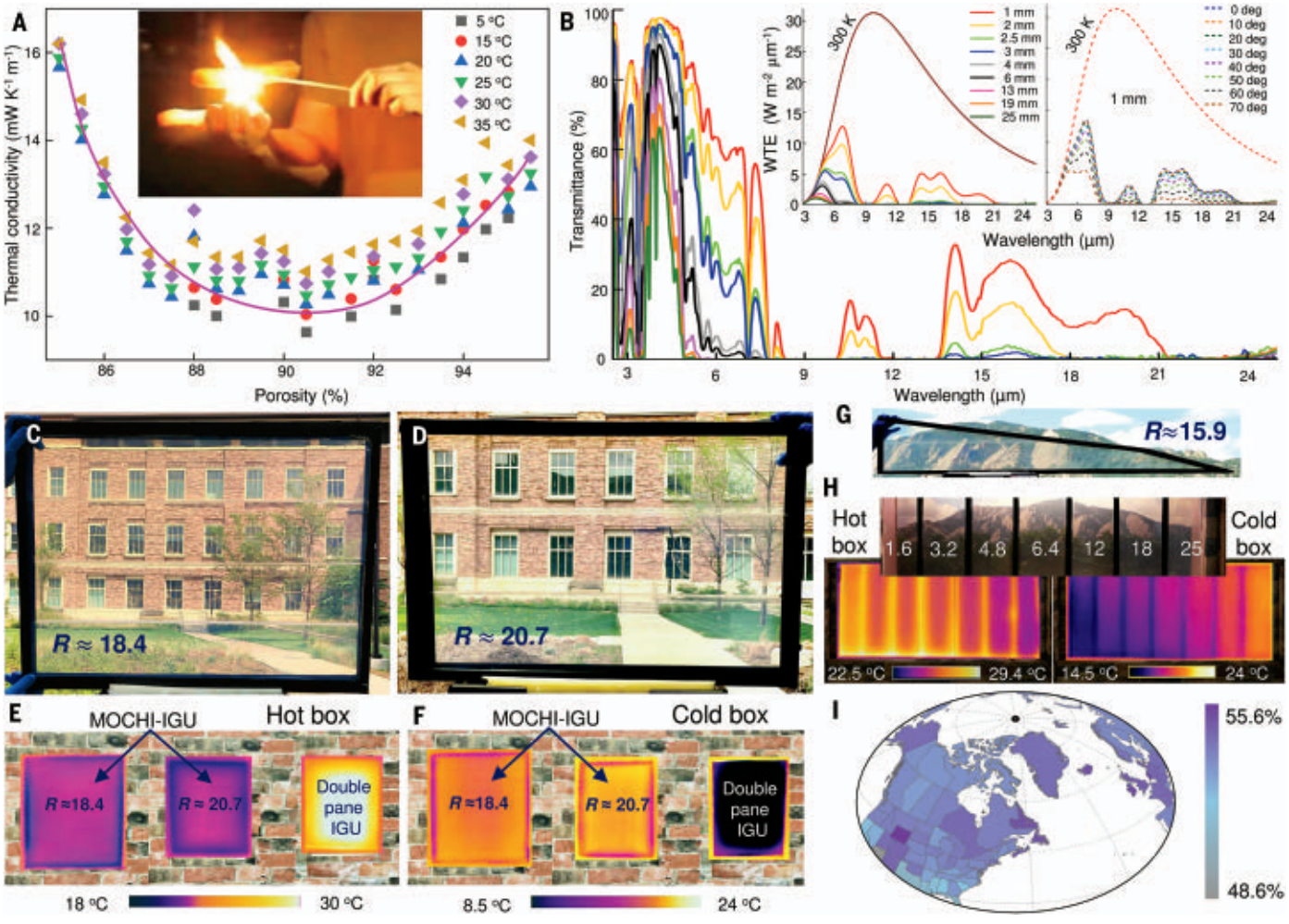


Fig. 3. Thermal barrier properties and impact of using MOCHI in insulating glass units. (**A**) Thermal conductivity of MOCHI versus porosity at different temperatures. The magenta solid line is an eye guide. (Inset) Photograph depicting the fire retardancy and thermal superinsulation of a MOCHI film while protecting from flame (movie S1), allowing for safe on-hand barbecuing. (**B**) Thermal infrared transmittance for MOCHI of varying thickness. (Insets) The weighted infrared transmissive emittance (WTE) per micrometer-unit wavelength (*24*) for blackbody radiation at 300 K, for MOCHI versus (left) thicknesses and (right) light's incidence angle for 1-mm-thick MOCHI. (**C** and **D**) Optical photographs illustrating high transparency and color rendering of MOCHI-IGUs. (C) 52.5 by 65 cm of 35 mm thickness with $R \approx 3.24$ m^2 K W^{-1} and (D) 35 by 50 cm of 37.5 mm thickness with $R \approx 3.65$ m^2 K W^{-1} (*24*), as measured for external and internal temperatures of −4° and 16°C, respectively. (**E** and **F**) Thermal photographs of MOCHI-IGUs shown in (C) and (D) as compared with that of a conventional double-pane IGU with an air gap of 12 mm, in both (E) hot box (at 40°C) and (F) cold box (−10°C) environments. (**G**) Optical photograph of a complex-shaped MOCHI-IGU with lateral dimensions 127.5 by 25 cm and thickness 37.5 mm having $R \approx 2.8$ m^2 K W^{-1} (*24*). *R* values marked in (C) to (G) are in foot^2·hours °F Btu^{-1}. (**H**) Optical and thermal images for MOCHI slabs with varying thickness, ranging from 1.6 to 25 mm, in which the latter were taken above hot and cold boxes at temperatures of 40°C and −10°C, respectively. (**I**) Global map of percentage of a building's heating and cooling energy savings enabled by MOCHI-IGUs replacing single-pane windows, averaged over a year, as estimated for a standard single-family home (*24*).

to blackbody radiation at ambient conditions (Fig. 3B). Thus, the radiative contribution to heat transfer through thick slabs of MOCHI was negligible because sequential processes of absorption and reemission effectively led to thermal-range radiation bouncing back from the slab, which is consistent with our modeling of thermal resistance (fig. S13) and enabling high-*R* insulating glass units (IGUs) with high visible-range transparency (figs. S14 to S18) (*24*).

Optimized-composition MOCHIs were highly insulating, with thermal conductivities of 10 to 12 mW K^{-1} m^{-1} at ambient temperatures (Fig. 3A) and thermal barrier properties useful for many applications (Figs. 3, C to I, and 4). MOCHIs also exhibited mechanical robustness (fig. S19 and movie S9) and could be adhered to plastic films or glass substrates, which allowed for undergoing hundreds of rolling-unrolling (fig. S20) and heating-cooling cycles (fig. S21), as well as accelerated lifetime characterization within an IGU or a retrofit (*24*). Because of composition and large surface area of the mesoporous morphology, MOCHIs were fire retardant (Fig. 3A, inset, and movies S1 and S10), superhydrophobic, and water repellant (Fig. 1B, inset, and movie S6). These MOCHI properties persisted even after ~5 years of being adhered to an interior surface of a window, under dust fouling, chemical exposure, and acid rain (figs. S21, E and F; S22; and S23) (*24*).

Windows, skylights, and solar thermal energy harnessing

The thermal resistance of 2.64 m^2 K W^{-1} (≈15 foot^2·hours °F Btu^{-1}) of optimized MOCHI of 2.5-cm slab thickness allowed for making window units that were insulated better than conventional building walls while having geometric form factors (thickness) comparable with that of the common double-pane windows (Fig. 3, C to I; figs. S14 to S18; and tables S3 to S5). Although relatively thin (3 mm) films of MOCHIs could be rolled and supercritically dried for applications in large-area

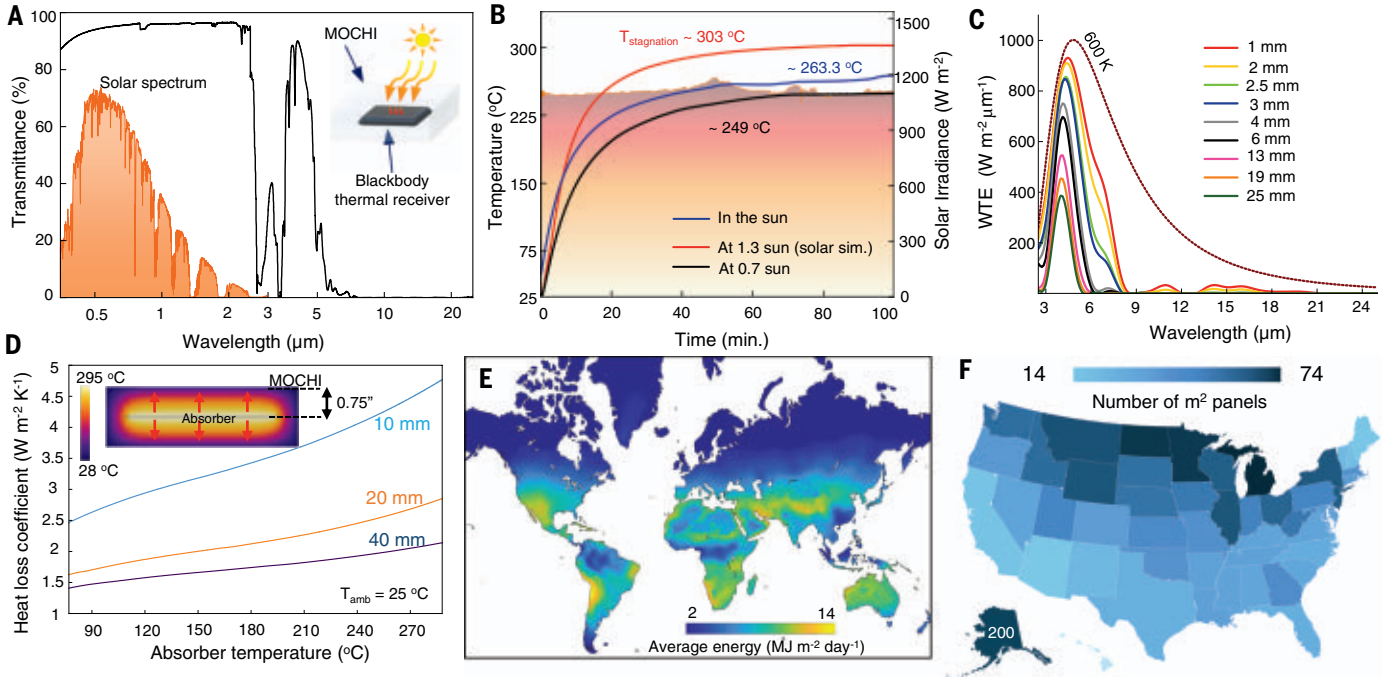


Fig. 4. Solar thermal energy harnessing enabled with MOCHI. (**A**) Spectral transmittance of a MOCHI slab (black curve) showing high transparency in visible and near-infrared ranges, which correspond to solar radiation spectrum (orange) at Earth's surface, along with strong absorption in the part of thermal infrared range >5 μm. (**B**) Stagnation temperatures of a blackbody thermal receiver at various irradiation intensities obtained under ambient conditions (for monitored solar radiation intensity) and by using a solar simulator, as schematically shown in (A), inset (*24*). (**C**) The weighted transmissive emittance per micrometer-unit wavelength (*24*), weighted by 600 K blackbody radiation, for MOCHI slabs of different thicknesses. (**D**) Heat loss coefficient of the solar thermal harnessing system for MOCHI slabs of different thickness. (Inset) The heat escape from absorber through MOCHI. (**E**) Annual average energy generated by a solar thermal panel per square meter per day mapped throughout the world based on the average solar irradiation (*24*). (**F**) A map showing the number of square-meter panels required to meet heating and cooling energy needs for single-family homes in the United States, simulated with EnergyPlus according to the geographical location and average annual energy consumption (*24*).

window retrofits (Fig. 1A), scaling of thick slabs was challenging because the cost of vessels capable of operating at the elevated pressures of CO_2-based supercritical drying is prohibitive for large samples. However, the ability of forming good "optical contact" between edge faces of MOCHI slabs (Fig. 2, E and F, and movie S2) or large-area films allowed for scaling the size of high-*R* MOCHI-IGUs made from overall laterally large and thick MOCHI slabs (Fig. 3, C to I). These slabs could be laser-cut to various geometric shapes (Fig. 2F, inset, and movie S7), providing the ability to make complex-shaped high-*R* IGUs (Fig. 3G) (*24*).

Because MOCHIs effectively blocked thermal-range blackbody radiation under window-relevant conditions (Fig. 3B), high-*R* thermal insulation could be achieved even without using low-emissivity coatings on glass (Fig. 3, C to I) (*24*), with experimentally measured *R* values matching the results of computational modeling (fig. S17 and table S5) (*24*, *25*). However, 3- to 4-mm-thick MOCHI films adhered to the interior of single-pane windows boosted their insulation to be comparable with that of double-pane windows, with $R \approx 0.53$ m^2 K W^{-1} (3 $foot^2$·hours °F Btu^{-1}).

As an additional benefit beyond energy efficiency, the use of MOCHI in IGUs and retrofits also boosts condensation resistance (fig. S21A) and soundproofing (fig. S24) as compared with those of conventional single- and double-pane windows (*24*). IGUs with ≈19- and 25-mm MOCHI slabs between panes reduced the sound transmission level by 25 to 35 dB within the 1- to 5-kHz frequency range and by 15 to 30 dB within the 0.5- to 1-kHz range, performing better than a conventional double-pane IGU by 5 to 10 dB within the entire studied range of sound frequencies.

Accelerated durability testing showed no detectable degradation, indicating an anticipated lifetime of at least 20 years (fig. S21B and tables S6 and S7) (*24*), comparable with that of conventional IGUs. Because MOCHI can be confined between panes of glass, replacing air of conventional double-pane windows, or adhered to protective hard plastic films in retrofits, the window product durability was further enhanced by the glass or plastic confinement. However, even unprotected MOCHIs exhibit good durability under conditions expected for air-purifying disposable windows (fig. S23) (*24*). One of the reasons for selecting polysiloxane (silicone) in our MOCHI designs was that it is already widely used in edge sealing of commercial windows.

The combination of visible-range transparency and thermal insulation is of interest for many applications beyond windows. In one example (Fig. 4), we show how it allows for solar thermal energy harnessing, with the potential utility in compensating for the energy still leaking through building envelopes. By encasing a broadband blackbody solar absorber with our MOCHI, effectively transmitting solar but blocking thermal infrared radiation (Fig. 4A and figs. S25 and S26), we can entrap the absorbed solar thermal energy that can be then used for needs such as heating water or a building interior (Fig. 4, B to D). This energy harnessing yields high stagnation temperatures of ~300°C as the absorber for both solar simulator and ambient conditions (Fig. 4B). At the high temperatures of a blackbody receiver, the blackbody radiation spectrum shifts to shorter wavelengths, at which MOCHIs become semitransparent (Fig. 4C and figs. S25 and S26). Therefore, differently from the ambient temperatures case, the radiative heat transfer becomes important at high stagnation temperatures of the blackbody receiver, causing some heat loss (Fig. 4D). Although one can modify MOCHIs to make them more opaque in the range of 3 to 6 μm (fig. S26A) to further boost the solar thermal energy harnessing, the demonstrated stagnation temperatures (Fig. 4B) are the highest temperatures achieved

for unconcentrated solar radiation, to the best of our knowledge. The harnessed thermal energy can be channeled for heating a building interior or water by use of heat exchangers. Notably, harnessing can be done even on a cloudy day, when ambient solar energy is at ~0.3 sun, which could be particularly advantageous in cold climates. Small parts of the opaque component of the building envelope could become solar heat–based power generators capable of reducing the overall building energy consumption (Fig. 4, E and F).

Discussion

To assess the potential impact of using MOCHIs in building envelopes, we have performed EnergyPlus simulations to estimate the energy saving with the help of MOCHI-IGUs and solar thermal energy generation that could replace other energy sources used for heating and cooling the building interior, such as electricity and gas (*24*). The wall-grade efficient MOCHI-IGUs would allow for increasing the fraction of building envelopes occupied by windows, potentially boosting the window area to 30% from the current 8% while actually reducing the energy wasted for heating (Fig. 3I and figs. S27 and S28). The global variations of solar thermal energy generation per square meter of MOCHI-based solar thermal panel are shown in Fig. 4E and can be converted into interior-heating or solar thermal–powered cooling (*26*) energy or water heating. Typically, solar thermal panels covering a fraction of a single-family home's opaque envelope would be sufficient to meet the heating and cooling needs, as illustrated for US states in Fig. 4F. Having larger areas of solar thermal–harnessing panels would then generate energy beyond building's heating and cooling needs, converting it into an energy-generating plant.

We developed MOCHI metamaterials with high transparency and with thermal conductivity that is lower than that of still air, comparable with that of aerogels used in the Mars Rover (*4*–*12*). Cold-temperature insulation of MOCHI-IGUs stopped 95% of heat transfer, making windows as insulated as high-performing building walls. Self-assembly-based fabrication and optical-contact-enabled scaling of MOCHI slabs and films with diverse geometric form factors is suitable for applications in building envelopes. Our MOCHI can expand the use of insulated glazing in envelopes of future buildings, including in windows, skylights, and porous material–based daylighting (*27*, *28*). Although silicone-based sealants are already widely used in IGUs, our MOCHI could replace the conventional gas fillers with "frozen air" nanosponge-like methyl-silicone-based fillers. Potential applications may extend to greenhouse coverings, protective and heat-insulating apparel (*29*), and space exploration (*15*), whenever simultaneous optical transparency and thermal insulation are needed. MOCHI can be surface-functionalized or modified by adding nanoparticles (*30*) to achieve custom-designed properties that range from solar gain control to air purification (*31*), potentially including disposable insulating air-cleaning windows (*24*).

REFERENCES AND NOTES

1. F. Trubiano, Ed., *Design and Construction of High-performance Homes: Building Envelopes, Renewable Energies and Integrated Practice* (Taylor & Francis, 2013).
2. J. Lovell, *Building Envelopes: An Integrated Approach (Architecture Briefs)* (Princeton Architectural Press, 2010).
3. J. L. Aguilar-Santana, H. Jarimi, M. Velasco-Carrasco, S. Riffat, *Int. J. Low Carbon Technol.* **15**, 112–120 (2020).
4. I. I. Smalyukh, *Adv. Mater.* **33**, e2001228 (2021).
5. M. K. Carroll, A. M. Anderson, S. T. Mangu, Z. Hajjaj, M. Capron, *Sustainability (Basel)* **14**, 2887 (2022).
6. C. Buratti, E. Belloni, F. Merli, M. Zinzi, *Energy Build.* **231**, 110587 (2021).
7. E. Belloni, C. Buratti, F. Merli, E. Moretti, T. Ihara, *Energy Build.* **243**, 110999 (2021).
8. Q. Liu, I. I. Smalyukh, *Sci. Adv.* **3**, e1700981 (2017).
9. R. Hart, S. Selkowitz, C. Curcija, *Build. Simul.* **12**, 79–86 (2019).
10. T. Shimizu, K. Kanamori, A. Maeno, H. Kaji, K. Nakanishi, *Langmuir* **32**, 13427–13434 (2016).
11. E. Abraham *et al.*, *Nat. Energy* **8**, 381–396 (2023).
12. Y. Kobayashi, T. Saito, A. Isogai, *Angew. Chem. Int. Ed.* **53**, 10394–10397 (2014).
13. L. Zhao *et al.*, *Opt. Express* **27**, A39–A50 (2019).
14. Q. Liu *et al.*, *Nano Energy* **48**, 266–274 (2018).
15. R. Wordsworth, L. Kerber, C. Cockell, *Nat. Astron.* **3**, 898–903 (2019).
16. B. Fleury *et al.*, *ACS Appl. Mater. Interfaces* **12**, 34115–34121 (2020).
17. C.-S. Ha, S. S. Park, *Periodic Mesoporous Organosilicas: Preparation, Properties and Applications*, *Springer Series in Materials Science*, vol. 281 (Springer, ed. 1, 2019).
18. C. T. Kresge, M. Leonowicz, W. J. Roth, J. C. Vartuli, J. S. Beck, *Nature* **359**, 710–712 (1992).
19. K. M. McGrath, D. M. Dabbs, N. Yao, I. A. Aksay, S. M. Gruner, *Science* **277**, 552–556 (1997).
20. C. P. Singh *et al.*, *Appl. Phys., A Mater. Sci. Process.* **77**, 585–589 (2003).
21. S. H. Tolbert, A. Firouzi, G. D. Stucky, B. F. Chmelka, *Science* **278**, 264–268 (1997).
22. K. M. McGrath *et al.*, *Langmuir* **16**, 398–406 (2000).
23. M. Kruk, M. Jaroniec, V. Antochshuk, A. Sayari, *J. Phys. Chem. B* **106**, 10096–10101 (2002).
24. Materials and methods are available as supplementary materials.
25. R. Mitchell *et al.*, WINDOW 7 User Manual (Lawrence Berkeley National Laboratory, 2019); https://windows.lbl.gov/window-documentation.
26. C. A. Balaras *et al.*, *Renew. Sustain. Energy Rev.* **11**, 299–314 (2007).
27. M. Ganobjak *et al.*, *J. Build. Eng.* **64**, 105600 (2023).
28. K. McEnaney, L. Weinstein, D. Kraemer, H. Ghasemi, G. Chen, *Nano Energy* **40**, 180–186 (2017).
29. F. Azam *et al.*, *Adv. Mater. Sci. Eng.* **2022**, 1 (2022).
30. Q. Liu, H. Mundoor, G. H. Sheetah, I. I. Smalyukh, *Opt. Express* **28**, 34237–34245 (2020).
31. S. Hu *et al.*, *Environ. Sci. Nano* **11**, 4666–4691 (2024).

ACKNOWLEDGMENTS

We thank B. Borak, K. Burrows, J. Cameron, J. De La Cruz, T. Culp, C. Fitz, J. Gerbi, A. Hess, M. Krarti, M. Lafrance, Q. Liu, P. de Melo, S. Mumme, E. Schiff, M. Sofos, R. Tenent, T. White, and Y. Yuan for discussions. We are grateful to F. Leresche for discussions and the use of a solar simulator, as well as H. Zhao and R. Fei for technical assistance. **Funding:** We acknowledge support of the US Department of Energy (DOE), under the Advanced Research Projects Agency–Energy (ARPA-E) award DE-AR0000743, during which the development of MOCHIs was initiated (J.B.t.H., E.A., V.C., B.S., T.L., B.F., and I.I.S.). We also acknowledge the DOE EERE grant DE-EE0009699 that supported the development of thick slabs of MOCHI and highly insulating glass units based on them (A.B., E.A., B.S., T.L., and I.I.S.). We acknowledge the CU BEST center for the partial support of solar thermal energy harnessing part of this work (A.B. and I.I.S.). **Author contributions:** A.B., B.F., B.S., E.A., J.B.t.H., T.L., and V.C. contributed equally and are listed in the byline in alphabetical order by first name. Conceptualization: I.I.S. Methodology: A.B., B.F., B.S., E.A., J.B.t.H., T.L., V.C., I.I.S. Investigation: A.B., B.F., B.S., E.A., J.B.t.H., T.L., V.C., I.I.S. Funding acquisition: I.I.S. Project administration: I.I.S. Supervision: I.I.S. Writing – original draft: A.B., B.S., E.A., J.B.t.H., T.L., I.I.S. Writing – review & editing: A.B., B.F., B.S., E.A., J.B.t.H., T.L., V.C., I.I.S. **Competing interests:** The authors filed US patent applications related to MOCHI technology (patent no. US 12,241,305 B2); additional patent applications were filed concurrently with the submission of this manuscript (application nos. 63/811,412 and 63/812,787). **Data and materials availability:** All data are available in the main text or in the supplementary materials. Information requests should be directed to the corresponding author. **License information:** Copyright © 2025 the authors, some rights reserved; exclusive licensee American Association for the Advancement of Science. No claim to original US government works. https://www.science.org/about/science-licenses-journal-article-reuse

SUPPLEMENTARY MATERIALS

science.org/doi/10.1126/science.adx5568
Materials and Methods; Supplementary Text; Figs. S1 to S28; Tables S1 to S7; References (*32*–*62*); Movies S1 to S10

Submitted 19 March 2025; resubmitted 6 May 2025; accepted 8 October 2025

10.1126/science.adx5568

MINERAL PHYSICS

Substantial water retained early in Earth's deep mantle

Wenhua Lu[1,2], Ya-Nan Yang[1,2]*†, Tao Long[3], Haiyang Xian[1,2], Yuan Li[1,2]*‡, Zhixue Du[1,2]*

Earth's water was likely acquired early, when our planet was extensively molten because of large to giant impacts. How such early water was retained and distributed within a crystallizing mantle remains unclear. In this study, we investigated partitioning of water between bridgmanite, the first and primary mantle mineral to crystallize, and coexisting melt through systematic high-pressure experiments. Our results demonstrate that partitioning of water into bridgmanite is strongly enhanced by increasing temperature. Thus, appreciable amounts of water may have been retained in the lower mantle after its crystallization. Circulation of such early stored water in Earth's interior could have modulated mantle dynamics and influenced the transition of early Earth to a habitable planet.

Water—hydrogen-bearing species specifically—in the deep mantle is critical for Earth's habitability, thanks to its power to modulate mantle dynamics and possible contributions to surficial environments (*1*). Such deep-sourced water is characterized by primordial hydrogen isotopes (*2*, *3*), suggesting that it may have been acquired early, through accretion of hydrogen-bearing planetesimals or pebbles (*4*, *5*) and/or ingassing of nebular gas (*6*, *7*). During Earth's accretion, deep magma oceans are believed to have been prevalent, likely extending to mid-mantle depth or even the core–mantle boundary owing to large to giant impacts (*8*, *9*). Bridgmanite, the magnesium-endmember perovskite ($MgSiO_3$), is expected to have been the first and dominant mineral crystallized in a deep magma ocean and makes up ~80% of the volume of the lower mantle (*10*). Hence, determining the partition coefficient of water between bridgmanite and silicate melt [$D^{Brg/melt}_{H_2O} = c^{Brg}_{H_2O} / c^{melt}_{H_2O}$, where $c^{Brg}_{H_2O}$ and $c^{melt}_{H_2O}$ are the water contents in bridgmanite (Brg) and silicate melt, respectively] is critical for understanding initial water distribution in a solid mantle.

Most previous high-pressure experiments, however, focus on water solubility in bridgmanite, which gives an upper bound for the water content in bridgmanite, and are limited to the topmost lower mantle conditions (*11*–*20*), that is, <2100 K and <28 GPa. These estimates show a wide range, from <50 parts per million by weight [ppmw (micrograms per gram)] (*11*, *12*, *15*, *20*) to ~200 to 2300 ppmw (*13*, *14*, *16*–*18*). Compounded by experimental inability to quench melt or fluid, $D^{Brg/melt}_{H_2O}$ cannot be directly obtained, and values inferred from earlier experiments remain highly uncertain. Panero *et al*. (*21*) first explored water partitioning at deeper lower mantle conditions (1600 to 2000 K and 25 to 65 GPa) and found a nearly dry bridgmanite (<220 ppmw water), whereas melts at bridgmanite interstices were too small (<200 nm in diameter) for quantification of their water content. First-principles simulations can also readily cover mantle pressure and temperature conditions, yet partitioning of water among solid phases is only available in the absence of melt or fluid phases (*21*–*23*).

In this study, we conducted systematic laser-heated diamond anvil cell experiments to investigate the partitioning of water between bridgmanite and silicate melt under deep magma ocean conditions (Fig. 1 and fig. S1). To quantify $D^{Brg/melt}_{H_2O}$, we used nanoscale secondary ion mass spectrometry (NanoSIMS) to measure the water content of micrometer-size bridgmanite and silicate melt run products (*24*). Coupling this dataset with a magma ocean crystallization model, we found that substantial water in the magma ocean could be retained in the solid lower mantle at high temperatures. Entrainment of such amounts of early water by mantle convection would have had important consequences for the evolution of the deep water cycle through geological time.

Water partitioning between bridgmanite and silicate melt at deep mantle conditions

Synthetic hydrous silicate glass was loaded in diamond anvil cells, compressed to pressures of ~36 to 71 GPa, and melted by double-sided laser heating (see methods in the supplementary materials). Heated regions were typically ~40 to 60 μm in diameter (Fig. 1A and fig. S2). During heating at peak laser power, two-dimensional temperature distributions were obtained every ~50 ms with fluctuations of <62 K (table S1 and fig. S3). Temperatures at crystal–melt interfaces ranged from ~3618 to 4435 K with 1σ uncertainties typically within 200 K, as determined by fitting emissivity transitions from temperature maps (methods, data S1, and code S1).

Quenched samples were subsequently recovered and polished to expose the laser-heated section (methods). A central pocket of quenched melt was surrounded by a liquidus phase, followed by recrystallized silicates with a bulk composition identical to the starting silicate glass (Fig. 1A), indicative of a closed system during melting (*25*). The liquidus phase was depleted in Fe and enriched in Mg compared with coexisting melts, with a stoichiometry of $Mg_{0.71-0.82}Ca_{0.01-0.05}Fe_{0.04-0.08}Al_{0.20-0.35}Si_{0.79-0.89}O_3$ (tables S2 and S3). The liquidus phase was further identified as bridgmanite, showing distinctive Raman peaks at ~350, 580, 730, and 920 cm^{-1} and electron diffraction patterns consistent with an orthorhombic structure of an Al-bearing bridgmanite (*26*) (figs. S4 and S5 and table S4). The bridgmanite phase shows homogeneous chemical compositions at the nanometer scale for major elements (Mg, Si, etc.) and hydrogen-bearing ion OH^+, confirming the absence of possible hydrogen-rich phases, such as brucite or melt inclusions (Fig. 1B, fig. S6, and supplementary text S1). In addition, the Fe–Mg exchange coefficients between bridgmanite and melt range from 0.19 to 0.50, consistent with previous studies (*27*–*32*) (fig. S7). We demonstrate that chemical equilibrium between bridgmanite and silicate melt was likely approached (supplementary text S2), and took temperatures at the bridgmanite–melt interfaces as equilibrium temperatures (methods).

The water content of recovered samples was determined by NanoSIMS (table S2) with a spatial resolution of ~0.7 μm (methods and supplementary text S3). Figure 1C shows that silicate melt was more enriched in water than in neighboring bridgmanite. Water content in bridgmanite and melt was determined to be ~171 to 360 ppmw and ~2808 to 7207 ppmw, respectively, for a starting glass with ~0.3 wt % water. For three experiments with pure water added in the sample chambers (methods), the recovered bridgmanite and melt reached up to 1979 ± 133 ppmw and 63,874 ± 4593 ppmw, respectively. Values for $D^{Brg/melt}_{H_2O}$ were in the range of ~0.024 to 0.087 (Fig. 2 and table S2). At similar temperature and pressure conditions, $D^{Brg/melt}_{H_2O}$ was nearly constant despite widely varying water content in the silicate melt (fig. S8), providing further evidence for equilibrium between bridgmanite and silicate melt.

Water in bridgmanite measured in this study was indigenous and not contaminated by hydrous phases, as our recovered bridgmanite was free of impurity inclusions and showed homogeneous distributions of OH^+ and major elements (Fig. 1B, fig. S6, and movies S1 and S2). The absence of hydrous phases is likely due to such phases being unstable at higher temperatures and bulk water content being

[1]State Key Laboratory of Deep Earth Processes and Resources, Guangzhou Institute of Geochemistry, Chinese Academy of Sciences (CAS), Guangzhou, China. [2]CAS Center for Excellence in Deep Earth Science, Guangzhou, China. [3]Institute of Geology, Chinese Academy of Geological Sciences, Beijing, China. ***Corresponding author. Email: duzhixue@gig.ac.cn (Z.D.); yanan.yang@gu.se (Y.-N.Y.); yuan.li@uni-bayreuth.de (Y.L.)** †Present address: Department of Chemistry and Molecular Biology, University of Gothenburg, Gothenburg, Sweden. ‡Present address: Bayerisches Geoinstitut, University of Bayreuth, Bayreuth, Germany.

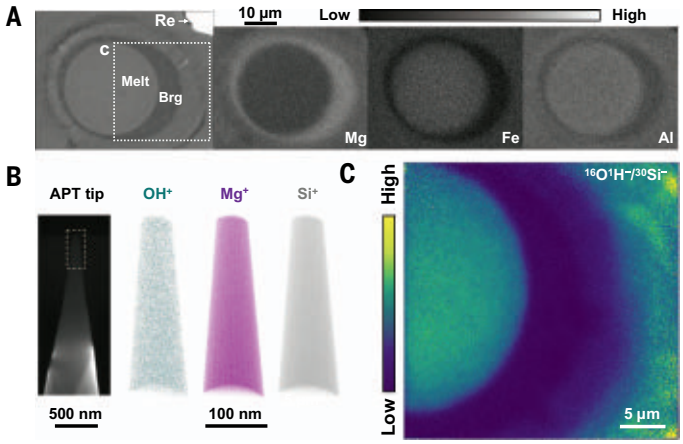


Fig. 1. Recovered high-pressure samples imaged at micro- to nanometer scales. (**A**) Backscattered electron image and elemental (Mg, Fe, Al) distributions of a sample recovered from 56 GPa and 4163 K (sample no. HYM23P1), taken after polishing in parallel to the diamond anvil culet. The central region is Fe-rich silicate melt (labeled "Melt"), surrounded by Fe-depleted bridgmanite (labeled "Brg"). The upper-right bright region is the rhenium (Re) gasket. The scale bar is 10 μm for all four images. (**B**) Three-dimensional distribution of OH^+, Mg^+, and Si^+ ions of recovered bridgmanite (sample no. DACY1P1) obtained by atom probe tomography (APT). (**C**) Water distribution shown by a NanoSIMS secondary ion ratio map of $^{16}O^1H^-/^{30}Si^-$ for the region marked by the dashed square in (A).

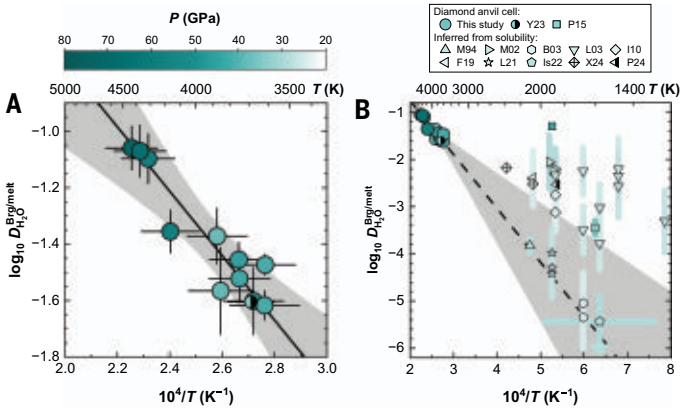


Fig. 2. Partition coefficient of water between bridgmanite and melt ($D_{H_2O}^{Brg/melt}$). (**A**) Logarithmic $D_{H_2O}^{Brg/melt}$ linearly correlates with inverse temperature. Error bars are 1σ. (**B**) Comparison of our results with those inferred from previous solubility experiments. Colored bars across the symbols indicate the ranges of inferred $\log_{10} D_{H_2O}^{Brg/melt}$, as $D_{H_2O}^{Brg/melt}$ was not directly measured in these experiments. The inferred value from (*20*) (Is22) is an upper bound, indicated by the downward-pointing arrow. Original literature data and our methods for inferring $D_{H_2O}^{Brg/melt}$ are summarized in table S5. Gray-shaded areas correspond to a 95% confidence interval in the York linear fitting. The abbreviated references are as follows: Y23 (*24*), P15 (*21*), M94 (*16*), M02 (*17*), B03 (*12*), L03 (*14*), I10 (*19*), F19 (*13*), L21 (*15*), Is22 (*20*), X24 (*36*), and P24 (*18*).

lower in this study (~3618 to 4435 K, ~0.3 to 6 wt % water) than earlier experiments (~1500 to 2200 K, water-saturated). Oxygen defects in bridgmanite induced by trivalent cation substitution with Si could potentially enhance water dissolution in bridgmanite (*13*, *14*). However, in our experiments, Al^{3+} and/or Fe^{3+} was likely substituted by both Si and Mg instead of only Si (fig. S9), diminishing oxygen defects to incorporate hydrogen (see supplementary text S4 for detailed discussions). Alternatively, hydrogen may be coupled with Al by replacing Si without the need of cation vacancies (*18*, *33*). However, the lack of techniques to probe hydrogen speciation at nanoscale prevents us from investigating hydrogen incorporation mechanisms in bridgmanite.

To quantify possible effects of temperature, pressure, and chemical composition on $D_{H_2O}^{Brg/melt}$, we adopted the parameterization as follows

$$\log_{10} D_{H_2O}^{Brg/melt} = a_0 + \sum a_i X_i^j + \frac{b}{T} + \frac{cP}{T} \quad (1)$$

where T and P are temperature in kelvin and pressure in gigapascals, respectively (*34*); X_i^j is the molar fraction of cation i (Si, Al, Fe, Mg, and Ca) in phase j (bridgmanite and silicate melt); and fitting parameters are a_0, a_i, b, and c. An unweighted multilinear stepwise regression was applied to the available dataset ($N = 12$ data points; data S1), and the inverse temperature ($1/T$) term was identified as the sole significant predictor of $\log_{10} D_{H_2O}^{Brg/melt}$, whereas the pressure and compositional effects of Si, Al, Fe, Mg, and Ca were statistically insignificant, with $P > 0.05$. A York linear regression (*35*) was then implemented on the $1/T$ term to account for uncertainties of $D_{H_2O}^{Brg/melt}$ and temperature (code S2), yielding

$$\log_{10} D_{H_2O}^{Brg/melt} = (1.53 \pm 0.59) - \frac{(1.14 \pm 0.23) \times 10^4}{T} \quad (R^2 = 0.86,\ 1\sigma) \quad (2)$$

as shown in Fig. 2A (R^2, coefficient of determination). When extrapolated to lower temperatures of 1500 to 2200 K, our trend is consistent with those inferred from earlier experiments using a multi-anvil press (*12*, *15*, *16*, *20*) but lower than others (*13*, *14*, *17*–*19*, *36*) (Fig. 2B).

Retainment of water in the solid mantle during magma ocean crystallization

We considered a simple model (*37*) to estimate water distribution in the solid mantle after magma ocean crystallization. The magma ocean was assumed to be fully convective and isolated from the core and atmosphere upon crystallization. The chemical isolation was likely due to limited degassing efficiency of water from the magma ocean to the atmosphere, with a solid lip formation on the surface and/or suppression by melt rheology (*38*, *39*). The initial water content was allowed to vary from 0.03 to 0.4 wt %, equivalent to ~1 to 12 ocean masses (1.4×10^{21} to 16.8×10^{21} kg) through nebular ingassing (*40*), likely serving as a lower bound.

A bottom-up crystallization model similar to those in (*41*, *42*) was first considered, in which fractional crystallization was also assumed. For a simple case where the mantle is completely molten, mantle crystals would first form compact cumulates in the lowermost mantle and not re-equilibrate with the residual melt. The same mineral assemblages as in (*41*) were set beforehand to determine bulk D_{H_2O} during crystallization. For transition zone and upper mantle crystallization, bulk D_{H_2O} was estimated from previous experiments (table S6). For the lower mantle, bulk D_{H_2O} was represented by $D_{H_2O}^{Brg/melt}$ from this study, as the contribution from magnesiowüstite is likely minor (*43*) and the role of davemaoite remains largely unknown (*44*). As such, bulk D_{H_2O} was calculated by Eq. 2 as crystallization proceeded (methods). We also considered a scenario of cumulates developing at an intermediate depth of the lower mantle (middle-out crystallization) given a likely crossover of melt–crystal density (*45*). In the latter case, a basal magma ocean above the core–mantle boundary developed in addition to an upper magma ocean (fig. S10). We defined crystallization as complete when the upper magma ocean or basal magma ocean was reduced to a thickness of 50 km.

For the bottom-up crystallization scenario, bulk D_{H_2O} decreased by approximately two orders of magnitude (Fig. 3A) as the crystallization front cooled from ~5300 K to ~2600 K, leading to a large gradient of water content in the solidified lower mantle (Fig. 3B). The higher bulk

D_{H_2O} yielded a water budget for the lower mantle that is ~5 to 100 times higher than that in previous studies (*42*, *46*), which assume constant bulk D_{H_2O} values (~5×10^{-4} to 1×10^{-2}) inferred from solubility experiments (Fig. 3C). Residual melts in the upper magma ocean could have contained up to ~92 wt % of initial water given the incompatibility of water with mantle minerals. This water at shallow depths may have been partially released to the surface after crystallization, forming the primitive hydrosphere (*39*). Model outcomes were consistent given similar variations of bulk D_{H_2O} for middle-out crystallization (fig. S11), except for an additional large reservoir of water in the basal magma ocean. If the hydrous melts were negatively buoyant in the lowermost mantle (*46*), they could have been a potential source of plume-related magmatism (Fig. 4), contributing to the primordial hydrogen isotopes observed in some ocean-island basalts sourced from the deep mantle (*2*, *3*, *47*).

Notably, water incorporated by the compact cumulates should represent a lower bound. In our model, if considering a 1% volume of hydrous melts trapped in the crystal interstices (*48*), the water budget of the bulk solid mantle would have increased by a factor of ~2.5. The water fraction of the lower mantle, however, would have slightly decreased, by ~8%, because early trapped melts were less enriched in water. Nonetheless, the lower mantle was still the largest water reservoir after magma ocean crystallization.

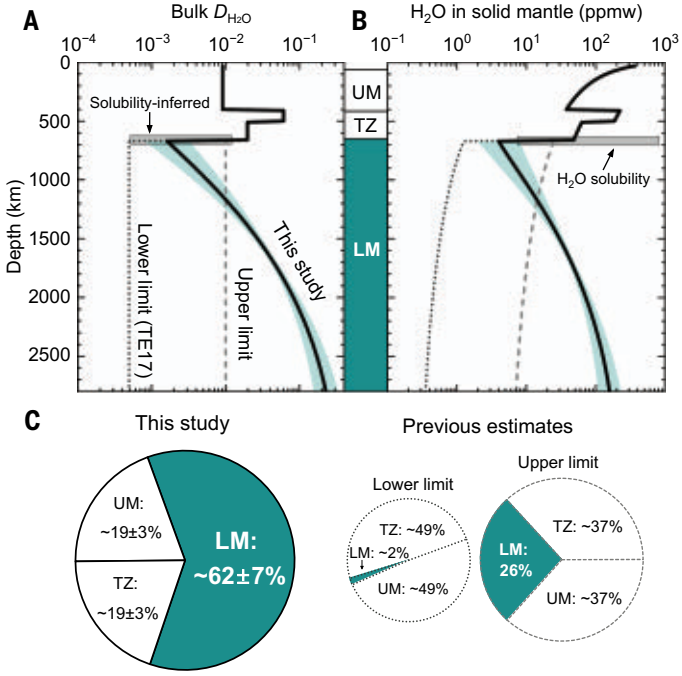


Fig. 3. Partitioning and distribution of water in the solid mantle after bottom-up magma ocean crystallization. (**A**) Comparison of bulk mineral/melt partition coefficient of water (D_{H_2O}) used in our crystallization models and inferred by solubility (gray bar). The lower limit of inferred D_{H_2O} is the same as that used in (*42*) (abbreviated TE17), while the upper limit was set at 1×10^{-2} (Fig. 2B). See main text and methods for the determination of bulk D_{H_2O}. (**B**) Water content in the solid mantle calculated by a fractional crystallization model using D_{H_2O} from (A), assuming two ocean masses of water initially contained in the magma ocean. Water in interstitial melts is not considered. The gray bar represents the range of water solubility of the topmost lower mantle. (**C**) Comparison of the water distribution fraction of the mantle's three layers (expressed as a percentage) derived from this study and previous estimates. The size of the pie charts corresponds to the total mass of water retained in the solid mantle. Uncertainties (1σ) are considered only for bulk D_{H_2O} in the lower mantle from this study, also shown by the light-teal shading in (A) and (B). For simplicity and consistency with previous studies, uncertainties from other model parameters are not included. UM, upper mantle; TZ, transition zone; LM, lower mantle.

Implications for the subsequent evolution of water in Earth's mantle

For the simple scenario above, the solid mantle immediately following magma ocean crystallization could have held at least ~0.08 to 1 ocean masses of water, coinciding with an estimate of ~1 ocean mass in the present-day mantle (*49*). Higher estimates of up to ~10 ocean masses (*50*) may have required endogenous water from Earth's progenitor objects (*4*), hydrous melts trapped in the interstices (*48*), development of a basal magma ocean (*45*), and/or late delivery of water by impacts (*51*). Therefore, the water budget of the present-day mantle could have been established during magma ocean crystallization (Fig. 4). However, the profile of water was most likely modified by a late overturn (*42*) and long-term mantle convection as well as possible hydrogen exchange due to core–mantle (*3*, *52*) and surface–mantle interactions (*53*).

After crystallization, the water budget of the upper mantle may have been comparable to that of the transition zone (Fig. 3). Yet, at the late stage of upper magma ocean crystallization, the dense, water-rich cumulates may have sunk and released their water at the boundary between the transition zone and the lower mantle (*42*). This overturn could have enhanced the water budget of the transition zone, leading to a water distribution profile more similar to that of the present day (Fig. 4C), where the upper mantle is generally dry (*1*) and the transition zone appears to be locally wetter (*54*).

Our model also suggests that the lower mantle could have been the largest water reservoir after crystallization (Fig. 3C). Yet, subsequent

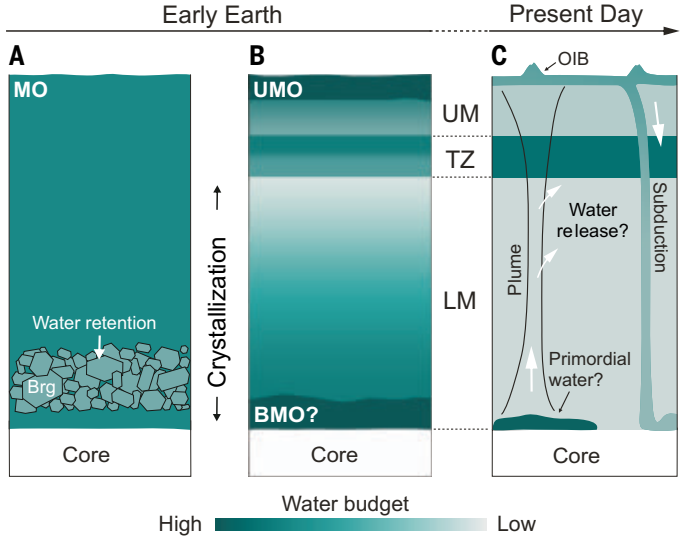


Fig. 4. Evolution of water in Earth's mantle. (**A**) Water was partitioned into bridgmanite during magma ocean (MO) crystallization. (**B**) Initial water distribution in Earth's solid mantle near the end of crystallization, with an upper magma ocean (UMO) and/or basal magma ocean (BMO) present. Substantial water was likely retained in the lower mantle (LM), comparable with that in the transition zone (TZ) or the upper mantle (UM). (**C**) Water cycling through plumes or subduction may have redistributed water from the early mantle, resulting in the present-day profile. Primordial water preserved in the lower mantle could release upon convection and be sampled by some oceanic island basalts (OIB) (*2*,*3*). The colors correspond to relative water budgets. The present-day water budgets of TZ, LM, and subducted slabs are still uncertain (*1*) and are shown here only for illustrative purposes. See main text for detailed discussions.

mantle convection may have continuously modified its initial water distribution (*55*). The extent of mixing and water-induced melting would hinge on water solubility being at present-day mantle conditions, which is poorly constrained. If we assume a lower end of water solubility of ~7 ppmw (*12*, *42*), upwelling from the deep lower mantle would likely have exceeded its solubility limit at the uppermost lower mantle, releasing at least 70% of its original water upon convection (Fig. 4C and fig. S12). On the other hand, if we assume a higher end of water solubility up to ~10^3 ppmw (*13*, *14*, *17*, *18*), the lower mantle may have retained its original water during upwelling.

Secular cooling of Earth's mantle has been suggested to be up to 1000 K since its crystallization to present-day conditions (*56*). If the pronounced temperature dependence from our dataset applies to lower temperatures for the adiabatic mantle, it indicates that water would exhibit strong incompatibility as temperatures decrease. As such, water originally retained in the lower mantle may have been released as the mantle cooled, triggering partial melting. Aggregation and migration of these partial melts could be linked to the viscosity and seismic anomalies observed in the lower mantle (*57*, *58*). Deep water circulation, characterized by upwelling of early water from the deep mantle and downward subduction of surficial water, may have influenced Earth's habitability over geological time.

REFERENCES AND NOTES

1. A. H. Peslier, M. Schönbächler, H. Busemann, S.-I. Karato, *Space Sci. Rev.* **212**, 743–810 (2017).
2. L. J. Hallis *et al.*, *Science* **350**, 795–797 (2015).
3. J. W. Dottin III *et al.*, *Sci. Adv.* **11**, eadr2917 (2025).
4. C. M. O. Alexander *et al.*, *Science* **337**, 721–723 (2012).
5. A. Johansen *et al.*, *Sci. Adv.* **7**, eabc0444 (2021).
6. E. D. Young, A. Shahar, H. E. Schlichting, *Nature* **616**, 306–311 (2023).
7. P. Olson, Z. D. Sharp, *Earth Planet. Sci. Lett.* **498**, 418–426 (2018).
8. M. Nakajima, D. J. Stevenson, *Earth Planet. Sci. Lett.* **427**, 286–295 (2015).
9. W. B. Tonks, H. J. Melosh, *J. Geophys. Res.* **98**, 5319–5333 (1993).
10. T. Irifune, T. Tsuchiya, in *Mineral Physics*, G. D. Price, Ed., vol. 2 of *Treatise on Geophysics*, G. Schubert, Ed. (Elsevier, 2015), pp. 33–60.
11. N. Bolfan-Casanova, H. Keppler, D. C. Rubie, *Earth Planet. Sci. Lett.* **182**, 209–221 (2000).
12. N. Bolfan-Casanova, H. Keppler, D. C. Rubie, *Geophys. Res. Lett.* **30**, 1905 (2003).
13. S. Fu *et al.*, *Geophys. Res. Lett.* **46**, 10346–10357 (2019).
14. K. Litasov *et al.*, *Earth Planet. Sci. Lett.* **211**, 189–203 (2003).
15. Z. Liu *et al.*, *Earth Planet. Sci. Lett.* **570**, 117088 (2021).
16. C. Meade, J. A. Reffner, E. Ito, *Science* **264**, 1558–1560 (1994).
17. M. Murakami, K. Hirose, H. Yurimoto, S. Nakashima, N. Takafuji, *Science* **295**, 1885–1887 (2002).
18. N. Purevjav *et al.*, *Am. Mineral.* **109**, 1036–1044 (2024).
19. T. Inoue, T. Wada, R. Sasaki, H. Yurimoto, *Phys. Earth Planet. Inter.* **183**, 245–251 (2010).
20. T. Ishii, E. Ohtani, A. Shatskiy, *Earth Planet. Sci. Lett.* **583**, 117441 (2022).
21. W. R. Panero, J. S. Pigott, D. M. Reaman, J. E. Kabbes, Z. Liu, *J. Geophys. Res. Solid Earth* **120**, 894–908 (2015).
22. E. R. Hernández, D. Alfè, J. Brodholt, *Earth Planet. Sci. Lett.* **364**, 37–43 (2013).
23. J. P. Townsend, J. Tsuchiya, C. R. Bina, S. D. Jacobsen, *Earth Planet. Sci. Lett.* **454**, 20–27 (2016).
24. Y.-N. Yang *et al.*, *Front Chem.* **11**, 1166593 (2023).
25. F. Nabiei *et al.*, *Geophys. Res. Lett.* **48**, GL092446 (2021).
26. H. Kojitani, T. Katsura, M. Akaogi, *Phys. Chem. Miner.* **34**, 257–267 (2007).
27. E. Ito, A. Kubo, T. Katsura, M. J. Walter, *Phys. Earth Planet. Inter.* **143–144**, 397–406 (2004).
28. C. Liebske, A. Corgne, D. J. Frost, D. C. Rubie, B. J. Wood, *Contrib. Mineral. Petrol.* **149**, 113–128 (2005).
29. R. Nomura *et al.*, *Nature* **473**, 199–202 (2011).
30. D. Andrault *et al.*, *Nature* **487**, 354–357 (2012).
31. S. Tateno, K. Hirose, Y. Ohishi, *J. Geophys. Res. Solid Earth* **119**, 4684–4694 (2014).
32. T. Kim *et al.*, *Geophys. Res. Lett.* **47**, e2020GL089345 (2020).
33. J. M. R. Muir, J. P. Brodholt, *Earth Planet. Sci. Lett.* **484**, 363–369 (2018).
34. J. A. O'Leary, G. A. Gaetani, E. H. Hauri, *Earth Planet. Sci. Lett.* **297**, 111–120 (2010).
35. D. York, N. M. Evensen, M. L. Martínez, J. De Basabe Delgado, *Am. J. Phys.* **72**, 367–375 (2004).
36. L. Xie *et al.*, *Earth Planet. Sci. Lett.* **633**, 118651 (2024).
37. W. Lu, Magma ocean crystallization model for water partitioning in Earth's mantle, Zenodo (2025); https://doi.org/10.5281/zenodo.17221423.
38. D. J. Bower, K. Hakim, P. A. Sossi, P. Sanan, *Planet. Sci. J.* **3**, 93 (2022).
39. Y. Miyazaki, J. Korenaga, *Nature* **603**, 86–90 (2022).
40. P. L. Olson, Z. D. Sharp, *Phys. Earth Planet. Inter.* **294**, 106294 (2019).
41. L. T. Elkins-Tanton, *Earth Planet. Sci. Lett.* **271**, 181–191 (2008).
42. S. M. Tikoo, L. T. Elkins-Tanton, *Philos. Trans. R. Soc. London Ser. A* **375**, 20150394 (2017).
43. N. Bolfan-Casanova, S. Mackwell, H. Keppler, C. McCammon, D. C. Rubie, *Geophys. Res. Lett.* **29**, 89-1–89-4 (2002).
44. H. Chen *et al.*, *Phys. Earth Planet. Inter.* **299**, 106412 (2020).
45. R. Caracas, K. Hirose, R. Nomura, M. D. Ballmer, *Earth Planet. Sci. Lett.* **516**, 202–211 (2019).
46. Z. Du *et al.*, *Geophys. Res. Lett.* **46**, 9466–9473 (2019).
47. E. Hauri *et al.*, *Chem. Geol.* **183**, 99–114 (2002).
48. S. Hier-Majumder, M. M. Hirschmann, *Geochem. Geophys. Geosyst.* **18**, 3078–3092 (2017).
49. M. M. Hirschmann, *Earth Planet. Sci. Lett.* **502**, 262–273 (2018).
50. B. Marty, *Earth Planet. Sci. Lett.* **313–314**, 56–66 (2012).
51. F. Albarède, *Nature* **461**, 1227–1233 (2009).
52. J. Deng, Y. Miyazaki, Q. Yuan, Z. Du, *Nat. Geosci.* **18**, 1056–1062 (2025).
53. M. D. Ballmer *et al.*, *Sci. Adv.* **11**, eadu2072 (2025).
54. X. Huang, Y. Xu, S. Karato, *Nature* **434**, 746–749 (2005).
55. J. W. E. Drewitt, M. J. Walter, J. P. Brodholt, J. M. R. Muir, O. T. Lord, *Earth Planet. Sci. Lett.* **581**, 117408 (2022).
56. G. Fiquet *et al.*, *Science* **329**, 1516–1518 (2010).
57. M. L. Rudolph, V. Lekić, C. Lithgow-Bertelloni, *Science* **350**, 1349–1352 (2015).
58. L. Waszek, N. C. Schmerr, M. D. Ballmer, *Nat. Commun.* **9**, 385 (2018).

ACKNOWLEDGMENTS

We thank X. Yang for help with high-pressure experiments, P. He for electron microprobe analysis, L. Wang and R. Tao for providing reference bridgmanite samples, S. Li for focused ion beam work at Guangzhou Institute of Geochemistry, Chinese Academy of Sciences (GIGCAS), Y. Wang for technical support in atomic force microscopy analysis, Y.-Q. Zhang for preparing NanoSIMS sample mounts, and T. Liu, W. Wang, J. Li, and J. Deng for valuable discussions. We appreciate the comments from the anonymous reviewers, which have improved the quality of this manuscript. This is contribution no. IS-3721 from GIGCAS. **Funding:** Strategic Priority Research Program (B) of the Chinese Academy of Sciences (XDB0840200) to Z.D.; National Natural Science Foundation of China (42150102 and 42394112) to Z.D.; National Natural Science Foundation of China (41903017) to Y.-N.Y.; National Natural Science Foundation of China (42241158) to T.L.; The National Key R&D Program of China (2022YFF0704900) to T.L.; Youth Innovation Promotion Association, CAS (2021353) to H.X.; Key Research Program of Frontier Sciences, CAS (ZDBS-LY-DQC013) to Y.L.; National Science Fund for Distinguished Young Scholars (42225302) to Y.L.; GuangDong Basic and Applied Basic Research Foundation (2025A1515011226) to W.L.; Postdoctoral Fellowship Program of CPSF (GZC20241732) to W.L. **Author contributions:** Conceptualization: Z.D., Y.L.; Methodology: W.L., Y.-N.Y., T.L., H.X., Z.D., Y.L.; Software: W.L.; Validation: W.L., Y.-N.Y., T.L., H.X., Y.L., Z.D.; Formal analysis: W.L., Z.D., Y.-N.Y., T.L., H.X., Y.L.; Investigation: W.L., Z.D., Y.-N.Y., Y.L.; Resources: Y.-N.Y., T.L., H.X., Z.D., Y.L., W.L.; Data curation: W.L., Y.-N.Y., T.L., H.X.; Writing – original draft: W.L.; Writing – review & editing: W.L., Z.D., Y.-N.Y., T.L., H.X., Y.L.; Visualization: W.L., Y.-N.Y., Z.D., Y.L.; Supervision: Z.D., Y.L.; Project administration: Z.D., W.L., Y.L.; Funding acquisition: Z.D., Y.-N.Y., T.L., H.X., Y.L., W.L. **Competing interests:** The authors declare that they have no competing interests. **Data and materials availability:** All data, codes, and details for the synthesis and characterization of all materials are available in the main text or the supplementary materials. The magma ocean crystallization model (*37*) is publicly available on Zenodo. **License information:** Copyright © 2025 the authors, some rights reserved; exclusive licensee American Association for the Advancement of Science. No claim to original US government works. https://www.science.org/about/science-licenses-journal-article-reuse

SUPPLEMENTARY MATERIALS

science.org/doi/10.1126/science.adx5883
Methods; Supplementary Text; Figs. S1 to S19; Tables S1 to S6; References (*59–106*); Movies S1 and S2; Data S1 and S2; Code S1 and S2

Submitted 24 March 2025; accepted 10 October 2025

10.1126/science.adx5883



YOUR NEXT BIG SCIENTIFIC DISCOVERY: A NEW JOB.

Find your next job at ScienceCareers.org

The relevance of science is at an all-time high these days. For anyone who's looking to get ahead in—or just plain get into—science, there's no better, more trusted resource or authority on the subject than *Science* Careers. Here you'll find opportunities and savvy advice across all disciplines and levels. There's no shortage of global problems today that science can't solve. Be part of the solution.

ScienceCareers

FROM THE JOURNAL SCIENCE AAAS

ScienceCareers.org

ScienceCareers



The experiment I didn't plan

Monika Gulia-Nuss

For 20 years, my life has been go, go, go. As a postdoctoral researcher and then a faculty member, I often found myself answering that one last email from a student while helping my children with homework or replying to a text from the lab while attending my son's band concert. I was accustomed to arriving at my office each day before 8 a.m., coffee in hand, ready to tackle a long to-do list. I rarely had a lunch break, and when I did, it was spent at my desk replying to emails. My days were blurred by meetings, lab work, and deadlines, yet I still felt behind. That relentless pace seemed like the only way to be both a scientist and a parent—until a fellowship abroad showed me a new approach to research and life.

After receiving tenure in 2022 I considered taking a sabbatical. But I had 15 people in my lab, a partner who is also in academia with his own lab, and two children in elementary school. I felt I could not step away for a year. Then I connected with researchers in Uruguay seeking a collaborator experienced in my area, tick transgenics, and I got a short-term Fulbright fellowship to explore the opportunity. I envisioned my 3-month stay as an intense period of lab work, data collection, and scientific discoveries. The 5-hour time difference would leave me with enough hours to catch up with my lab and family back home.

When I arrived, I was dismayed to learn that the shuttle to the institute ran on a schedule that limited our work hours to 8 a.m. to 3:30 p.m. Mornings started with shared maté and conversations about our weekends or evenings, followed later by an extended lunch break that was sacred. I felt impatient.

Yet my research progressed steadily. Outside of work, another kind of progress was unfolding. I was still working long hours because of my responsibilities as a lab head, graduate program director, and National Institutes of Health study section member, but the built-in breaks—which often included an evening snack or walk on the *rambla*—made all the difference. I still got my work done, and the slower rhythm also left space for deeper thinking, both in my experiments and in my life. I was learning the value of working with intention rather than urgency, and of leaving room for the parts of life that can't be scheduled. A calmness set in. I found myself laughing more, sleeping better, and enjoying the life I have worked hard to build.

Midway through my fellowship my family arrived for an extended visit, and I took 3 weeks off for a once-in-a-lifetime journey. We wandered through bustling neighborhoods framed by the Andes, stood in silence under a desert sky heavy with stars, and felt the thunder of waterfalls drenching us in mist. I began to notice small things: my daughter's fascination with seashells, my son's growing ease with strangers and his first words of Spanish, the way my spouse and I laughed more instead of just discussing logistics.

When my fellowship ended 8 months ago, I returned with more than a set of data. I came back with a recalibrated sense of how I want to live and work. I no longer treat evenings and weekends as time to catch up on unfinished work; instead, I reserve them for my family and myself. Blocking my calendar so that no one can schedule a meeting during my off hours and letting my lab members know when I will be available has worked wonders. I've built small rituals into my routine—a morning walk, a lunch break away from the screen—and I keep a maté gourd on my desk as a reminder to pause and connect.

These modest changes have reshaped the texture of my days. I find myself more focused in the lab, more patient with my students, and more present with my family. Productivity, I've come to see, is not measured only by research papers and grants. It is also sustained by presence, rest, and the relationships that give meaning to the work. □

Monika Gulia-Nuss is an associate professor at the University of Nevada, Reno. Send your career story to SciCareerEditor@aaas.org.

ILLUSTRATION: ROBERT NEUBECKER

Who's the Top Employer for 2025?



Science 2025 TOP EMPLOYERS

Science Careers' annual survey reveals the top companies in biotech & pharma voted on by *Science* readers.

Explore these highly-rated employers in our interactive experience:
sciencecareers.org/topemployers

TRILLIONS OF MICROBES ONE ESSAY

The NOSTER *Science* Microbiome Prize is an international prize that rewards innovative research by investigators who have completed their terminal degree in the last 10 years and are working on the functional attributes of microbiota. The research can include any organism with the potential to contribute to our understanding of human or veterinary health and disease, or to guide therapeutic interventions. The winner and finalists will be chosen by a committee of independent scientists chaired by a senior editor of *Science*. The top prize includes complimentary membership to AAAS, an online subscription to *Science*, and USD 25,000. Submit your research essay today.



Djenet Bousbaine, Ph.D.
2025 Winner

NOSTER | Science
MICROBIOME
PRIZE

Apply by 14 February 2026 at www.science.org/noster

Sponsored by Noster Inc.